



I. R. IRAN

ISSN: 1728-1431

e-ISSN: 1735-9244



International Journal of Engineering

Journal Homepage: www.ije.ir



TRANSACTIONS A: BASICS

Volume 36, Number 04, April 2023

Materials and Energy Research Center

INTERNATIONAL JOURNAL OF ENGINEERING

Transactions A: Basics

DIRECTOR-IN-CHARGE

H. Omidvar

EDITOR IN CHIEF

G. D. Najafpour

ASSOCIATE EDITOR

A. Haerian

EDITORIAL BOARD

- | | | | |
|------|--|-------|--|
| S.B. | Adeloju, Charles Sturt University, Wagga, Australia | A. | Mahmoudi, Bu-Ali Sina University, Hamedan, Iran |
| K. | Badie, Iran Telecomm. Research Center, Tehran, Iran | O.P. | Malik, University of Calgary, Alberta, Canada |
| M. | Balaban, Massachusetts Ins. of Technology (MIT), USA | G.D. | Najafpour, Babol Noshirvani Univ. of Tech., Babol, Iran |
| M. | Bodaghi, Nottingham Trent University, Nottingham, UK | F. | Nateghi-A, Int. Ins. Earthquake Eng. Seis., Tehran, Iran |
| E. | Clausen, Univ. of Arkansas, North Carolina, USA | S. E. | Oh, Kangwon National University, Korea |
| W.R. | Daud, University Kebangsaan Malaysia, Selangor, Malaysia | M. | Osanloo, Amirkabir Univ. of Tech., Tehran, Iran |
| M. | Ehsan, Sharif University of Technology, Tehran, Iran | M. | Pazouki, MERC, Karaj, Iran |
| J. | Faiz, Univ. of Tehran, Tehran, Iran | J. | Rashed-Mohassel, Univ. of Tehran, Tehran, Iran |
| H. | Farrahi, Sharif University of Technology, Tehran, Iran | S. K. | Sadmezhad, Sharif Univ. of Tech, Tehran, Iran |
| K. | Firoozbakhsh, Sharif Univ. of Technology, Tehran, Iran | R. | Sahraeian, Shahed University, Tehran, Iran |
| A. | Haerian, Sajad Univ., Mashhad, Iran | A. | Shokuhfar, K. N. Toosi Univ. of Tech., Tehran, Iran |
| H. | Hassanpour, Shahrood Univ. of Tech., Shahrood, Iran | R. | Tavakkoli-Moghaddam, Univ. of Tehran, Tehran, Iran |
| W. | Hogland, Linnaeus Univ, Kalmar Sweden | T. | Teng, Univ. Sains Malaysia, Gelugor, Malaysia |
| A.F. | Ismail, Univ. Tech. Malaysia, Skudai, Malaysia | P. | Tiong, Nanyang Technological University, Singapore |
| M. | Jain, University of Nebraska Medical Center, Omaha, USA | X. | Wang, Deakin University, Geelong VIC 3217, Australia |
| M. | Keyanpour rad, Materials and Energy Research Center, Karaj, Iran | H. | Omidvar, Amirkabir Univ. of Tech., Tehran, Iran |

EDITORIAL ADVISORY BOARD

- | | | | |
|-------|--|-------|---|
| S. T. | Akhavan-Niaki, Sharif Univ. of Tech., Tehran, Iran | A. | Kheyroddin, Semnan Univ., Semnan, Iran |
| M. | Amidpour, K. N. Toosi Univ of Tech., Tehran, Iran | N. | Latifi, Mississippi State Univ., Mississippi State, USA |
| M. | Azadi, Semnan university, Semnan, Iran | H. | Oraee, Sharif Univ. of Tech., Tehran, Iran |
| M. | Azadi, Semnan University, Semnan, Iran | S. M. | Seyed-Hosseini, Iran Univ. of Sc. & Tech., Tehran, Iran |
| F. | Behnamfar, Isfahan University of Technology, Isfahan | M. T. | Shervani-Tabar, Tabriz Univ., Tabriz, Iran |
| R. | Dutta, Sharda University, India | E. | Shirani, Isfahan Univ. of Tech., Isfahan, Iran |
| M. | Eslami, Amirkabir Univ. of Technology, Tehran, Iran | A. | Siadat, Arts et Métiers, France |
| H. | Hamidi, K.N.Toosi Univ. of Technology, Tehran, Iran | C. | Triki, Hamad Bin Khalifa Univ., Doha, Qatar |
| S. | Jafarmadar, Urmia Univ., Urmia, Iran | | |

TECHNICAL STAFF

M. Khavarpour; M. Mohammadi; V. H. Bazzaz, R. Esfandiar; T. Ebadi

DISCLAIMER

The publication of papers in International Journal of Engineering does not imply that the editorial board, reviewers or publisher accept, approve or endorse the data and conclusions of authors.

CONTENTS

Transactions A: Basics

S. Norouzi, S. Hossainpour, M. M. Rashidi	Investigating the Effect of Clearance Distance between the Floor of a High-speed Train and Ground on Aerodynamic Forces in Presence of Side Wind	604-614
S. A. Habeeb, A. A. Zinatizadeh, S. A. Mousavi, H. Zangeneh	Visible Light Activated Fe-N-SiO ₂ /TiO ₂ Photocatalyst: Providing an Opportunity for Enhanced Photocatalytic Degradation of Antibiotic Oxytetracycline in Aqueous Solution	615-629
L. Khettache, R. Abdessemed	A New Speed Control Approach of Linear Induction Motor Based on Robust RST Controller and Model Reference Adaptive System Estimator	630-639
V. A. Jha, J. B. Patel, V. A. Sawant, Y. K. Tandel	Flood Hazard Assessment of Water-Front Geosynthetic Reinforced Soil Wall for Dam Regulation Rule Level	640-648
F. Firdaus, I. Fadhilah, N. A. Ahmad, A. A. Mohd Alic	A Light Solution for Device Diversity Problem in a Wireless Local Area Network Fingerprint Indoor Positioning System	649-658
N. Masne, S. Suryawanshi	Effect of Replacement Ratio on Torsional Behaviour of Recycled Aggregate Concrete Beams	659-668
A. Shabanpour, M. Bashiri, R. Tavakkoli-Moghaddam, A. Safi Samghabadi	Integrated Linear Integer Model of a Fleet Allocation and Aircraft Routing Problem with Operational Constraints	669-681
R. Khodadadi, G. Ardeshir, H. Grailu	Compressing Face Images Using Genetic and Gray Wolf Meta-heuristic Algorithms Based on Variable Bit Allocation	682-697
N. Munasir, S. R. Lutfiana, F. Nuhaa, S. Evi, R. Lydia, S. S. Ezaa, T. Ahmad	Graphene Based Membrane Modified Silica Nanoparticles for Seawater Desalination and Wastewater Treatment: Salt Rejection and Dyes	698-708
M. Ahmadigorji, M. Mehrasa	A Robust Renewable Energy Source-oriented Strategy for Smart Charging of Plug-in Electric Vehicles Considering Diverse Uncertainty Resources	709-719
M. Hosseini Nasab, A. Agah	Mapping Hydrothermal Alteration Zones Associated with Copper Mineralization using ASTER Data: A Case Study from the Mirjaveh Area, Southeast Iran	720-732

M. Zamani, R. Shafaghat, B. Alizadeh Kharkeshi	Experimental Investigation on the Effect of Flow Rate and Load on the Hydrodynamic Behavior and Performance of an Archimedes Screw Turbine	733-745
F. Behnamfar, M. Almohammad-albakkar	Development of Steel Yielding Seismic Dampers Used to Improve Seismic Performance of Structures: A Comprehensive Review	746-775
S. A. Haj Seiyed Taghia, H. R. Darvishvand, M. Pourhasan	An Economic Approach to the Confinement of Different Concrete Classes with Carbon and Glass Fibers Reinforced Polymers	776-787
M. Karevan, M. A. Motaleb, A. Jannesari, M. Zeinali	High Energy Release-high Retraction Smart Polymer Fibers used in Artificial Muscle Fabrication	788-796
M. A. R. Pohan, J. Utama	Efficient Sampling-based for Mobile Robot Path Planning in a Dynamic Environment Based on the Rapidly-exploring Random Tree and a Rule-template Sets	797-806
S. D. Thepade, M. R. Dindorkar, P. R. Chaudhari, S. V. Bang	Enhanced Face Presentation Attack Prevention Employing Feature Fusion of Pre-trained Deep Convolutional Neural Network Model and Thepade's Sorted Block Truncation Coding	807-816
I. B. Mulyawati, M. Riza, H. Dermawan, V. Pratiwi	Numerical Simulation of Embankment Settlement in Vacuum Preloading Systems	817-823



Investigating the Effect of Clearance Distance between the Floor of a High-speed Train and Ground on Aerodynamic Forces in Presence of Side Wind

S. Norouzi^a, S. Hossainpour^{*a}, M. M. Rashidi^b

^a Department of Mechanical Engineering, Sahand University of Technology, Tabriz, Iran

^b University of Electronic Science and Technology of China, Chengdu, 610054, Sichuan, PR China

PAPER INFO

Paper history:

Received 02 September 2022

Received in revised form 03 December 2022

Accepted 14 December 2022

Keywords:

Turbulence Model

High Speed

Wall Function

Finite Volume Method

Simulation of Turbulent Flow

ABSTRACT

The main objective of this paper was to propose the real model of the high speed train regarding the side wind disturbance. In the first part of this article, the turbulent air flow around a simplified design of a high-speed vehicle was numerically analyzed using finite volume method and four RANS turbulence models, including $k-\omega$ SST, $k-\epsilon$ RNG, Spalart-Almaras, and Launder and Sharma. The results of numerical simulations regarding the wall function were validated by experimental works and it was shown that in the area near the wall, the SST $k-\omega$ model had the best simulation for the horizontal component of the velocity (21% error). The results of the lift coefficients showed that at short distances from the train floor to the ground due to relatively strong wind with angles less than 0.2 radians, the lift coefficient was negative and as a result, the forces acting on the train were downward. Finally it was shown that by increasing the wind angle, this coefficient gradually becomes positive, which can disrupt the stability of the train. It can be concluded that in trains whose floor to ground distance is more than 0.136 of the train height, the balance is maintained only in the absence of side wind.

doi: 10.5829/ije.2023.36.04a.01

1. INTRODUCTION

The aerodynamic force on the train body, which is created as a result of changing the flow lines, is one of the most important design items. The flow around a train under normal conditions experiences a large-scale separation, which leads to large aerodynamic pressures and less stability. Aerodynamics of trains is a complex issue that needs to be considered for its accurate calculation. Among these things, we can optimize the shape of the train [1], the side wind effect [2-6], pressure changes when the train moves in the tunnel [7-9], the vortices at the end of the train [10], the flow passing under the train [11-13] and the impact of the ground on the air flow [14-17] are only some of the issues that researchers have addressed.

The effect of the ground on the flow around the train can be investigated from two aspects. The first effect is about the relative speed of the ground with the train and

the second effect is about the distance between the floor of the train and the ground. Regarding the relative speed of the train with the ground in the experiments conducted using the wind tunnel, this effect is not considered in the results due to the fact that the ground is fixed in the wind tunnel. Zhang et al. [14] and Xia et al. [15] numerically studied the impact of fixed ground related to moving one. They observed that the boundary layer formed on the ground reduces the drag forces and excess the lift forces. Also, the assumption of a fixed ground increases the speed of flow slippage, which causes the formation of more open vortex structures and, as a result, vortex shedding with a higher frequency [18].

Far less research has been done on the effect of the distance of the floor of the train and the ground. Hajipour Khire Masjidi et al. [19] investigated the effect of the distance from the ground using a moving earth and a simple geometric shape (similar to the geometry that is examined in the first part of this article). Yu et al. [20]

*Corresponding Author Institutional Email: hossainpour@sut.ac.ir
(S. Hossainpour)

and Ismaiel [21] also used an aerodynamic shape to experimentally investigate the effect of distance from the ground on aerodynamic forces. According to their research, when the distance of the bottom of the device and the ground is reduced, the flow rejoins somewhere closer to the front of the model. Also, the lift force is clearly affected by this distance [22].

In today's high-speed trains, the distance between the floor of the train and the rail is very small. For example, one of the reasons for reducing the distance between the floor and the ground is installing panels to absorb noise on the rails [23]. In one of the few studies that was done to determine the effect of floor-to-ground distance on high-speed trains, Kalitzin et al. [24], for the first time, investigated the effect of this distance on the aerodynamic forces and flow field for the ICE3 high-speed train. Since they used the DES turbulence model for their numerical simulation, which is considered as a method with high computational cost, they had to use about 30 million computational cells, which is a very high computational cost in has found For this reason, they assumed the speed of the train to be 49.68 km/h, which is far from the speed of current high-speed trains. For this reason, in this article, firstly, the ability of RANS turbulence models to extract aerodynamic forces has been investigated, and then, using the best turbulence model, the air flow around the high-speed train at real speeds (250 km/h) has been investigated. It is simulated by using computing cells far less and the effect of the distance between the floor of the train and the ground on the aerodynamic forces at real speeds is investigated. Mahzoon and Kharati-Koopae [25] have discussed the effects of the vehicle components and geometry in aerodynamic performance of the high speed trains. They have proposed the optimal length and windshield for the various longitudinal velocities, which can be used in sizing of the train considering its high speed in the design level.

In this article, first, to reach the best turbulence model for simulating the flow around an object, the flow around a rigid object is investigated and the velocity profile at different sections of the end region of the rigid object and the aerodynamic forces acting on it are compared with the experimental values. Despite the different studies done in the aerodynamic performance of the high speed ground vehicles, it seems that the separation area at the end of the bend remains a serious challenge for turbulence models, and there is a need to further examine these models in this area. According to the authors' information, in past studies, cumulative variables such as drag and drag coefficients were mostly calculated, and the amount of error resulting from these models in the reverse flow area has not been specifically studied. In this article, four commonly used models averaged in time with and without using wall functions are examined and the error rate of velocity profile estimation in the areas

near and far from the wall in the separation and return flow area is calculated and reported.

In the second part of this article, the geometry of the ICE3 high-speed train is designed as one of the newest high-speed trains in the world and is simulated using the best turbulence model in the first part of the article, the kwSST model. In this section, firstly, in order to ensure the design of the geometry and computational meshing operations, the simulation of the air flow around this high-speed train at a speed of 50 km/h and without the presence of side winds has been done. Then the profile of aerodynamic forces is compared with the available experimental data of this geometry. According to the authors' knowledge, no article has investigated the effect of side wind and the distance of the train floor from the ground on aerodynamic forces in high-speed trains. In the last stage of this article, the speed of the train has been increased to its actual value, i.e. 250 km/h, and the train has been exposed to side winds with different angles, and the impact of the distance of the train floor from the ground on the speed field and aerodynamic forces acting on the train in the presence of side wind have been investigated.

2. GEOMETRY OF MODEL

In this section, a simplified design of a vehicle is examined in three dimensions. The geometry of this model is designed in ICEM software. The geometry of this simplified model can be seen in 2D-3D in Figure 1.

2. 1. Governing Equations and Boundary Conditions

To simulate the flow passing over the vehicle in Figure 1, the equations of conservation of mass and momentum are used. Equations (1) and (2) represent the time-averaged mass and momentum equations (RANS) for an incompressible fluid in dimensionless form.

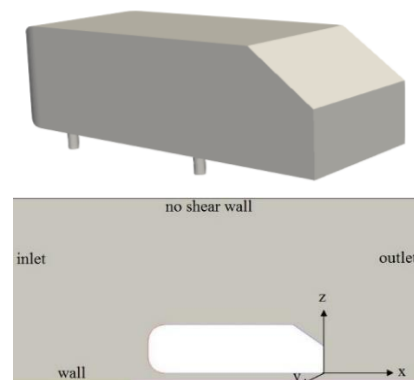


Figure 1. Model geometry: (a) front view; (b) back view (tilt angle 35 degrees); (c) Geometry of the vehicle from the side (inflow direction from left to right)

$$\frac{\partial \bar{u}_i}{\partial x_i} = 0 \quad (1)$$

$$\frac{\partial \bar{u}_i}{\partial t} + \frac{\partial \bar{u}_i \bar{u}_j}{\partial x_j} = -\frac{\partial \bar{P}}{\partial x_i} + \frac{1}{\text{Re}} \frac{\partial}{\partial x_j} \left(\frac{\partial \bar{u}_i}{\partial x_j} - \frac{\partial \tau_{ij}}{\partial x_j} \right) \quad (2)$$

where \bar{u}_i and \bar{P} in these equations are the average values of velocity and pressure respectively, and $\tau_{ij} = \overline{u_i' u_j'}$ is the Reynolds stress tensor. In order to model the Reynolds stress term, many models have been presented so far. To select the best turbulence model, four important and widely used RANS models have been used in this research. These models include k- ω SST, k- ϵ RNG, Spalart-Almaras and Launder and Sharma. The last model is an improved low-Reynolds model based on k- ϵ . The Spalart-Almaras model is a one-equation model that has a lower computational cost than other models. All these models are used together with wall functions. Only the k- ω SST model has been implemented both with and without the wall function and the results were compared.

The boundary conditions of the problem are shown in Figure 1(c). The inlet boundary condition of speed equal to 40 m/s and the outlet boundary condition equal to zero constant pressure are considered. For the ground and the body of the vehicle, the condition of no slip and the upper surface of the wall without shear stress is considered.

2. 2. Numerical Method In this research, the numerical analysis of the flow is done in the OpenFOAM and the simpleFOAM solver and steady solution are used. All terms of Navier-Stokes equations are discretized using second-order methods. The wall functions in the OpenFOAM open source code have been improved to provide acceptable results if the first cell is not exactly in the logarithmic region. The wall functions theory employed in OpenFOAM according to Kalitzin et al. [24]. In the topic of wall functions, the parameter y^+ , which is the dimensionless distance of the first center of the first calculation cell, is calculated from Equation (3):

$$y^+ = \frac{y u_\tau}{\nu} \quad (3)$$

where u_τ is the frictional velocity and y is the distance to the wall. u_τ is calculated from Equation (4). As τ_w is the shear stress of the wall.

$$u_\tau = \sqrt{\frac{\tau_w}{\rho}} \quad (4)$$

Computational meshing has been done using the snappyHexMesh code, and important meshing parameters such as skewness, orthogonality, and aspect ratio have been considered as the general criteria of the computational mesh. In the wall nearby the mesh

accuracy was increased in 5 steps to properly present the velocity and pressure changes regarding the boundary conditions. For reducing the computational time and since we have used the medium size meshes, to increase of velocity and pressure accuracy near the rigid body, smaller meshes have been used in this part. Behind the train, there are flow vortices, positive pressure gradient and flow separation, which can only be correctly predicted with small sized meshes. Figure 2 depicts the side view of the computational grid near the rigid body on central plane.

3. RESULTS

3. 1. Grid Study To check the independency of results from the grid size, the four grid sizes in Table 1 are used. The number of cells in these grids varies from about 2 millions to about 8 and a half millions.

Figure 3 shows the average horizontal and vertical velocity profile in a cross-section in the central plane of the domain ($x=-0.023$ m). As can be seen in this figure, as the number of cells increases, the accuracy of the solution gradually increases and the results converge to a single value. The results of Grid 3 are very close to the results of Grid 4 in most places. For this reason, Grid 3 is used in the rest of this article. Since number of computational cells are equal to 6 millions, near the walls $y^+ > 30$, first computational cell is not located in area under the viscous layer.

3. 2. Investigating the Effect of Wall Function

The results of the velocity field at two different sections are shown in Figure 4 and compared with the empiricals.

As shown in Figure 4, the use of the mentioned wall function reduces the computational cost and also increases the simulation accuracy near the wall. The

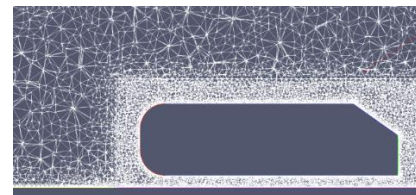


Figure 2. Computational grid side view for the near of rigid body

TABLE 1. Used computing networks

Number of cells	item
2200000	Grid 1
3700000	Grid 2
6600000	Grid 3
8500000	Grid 4

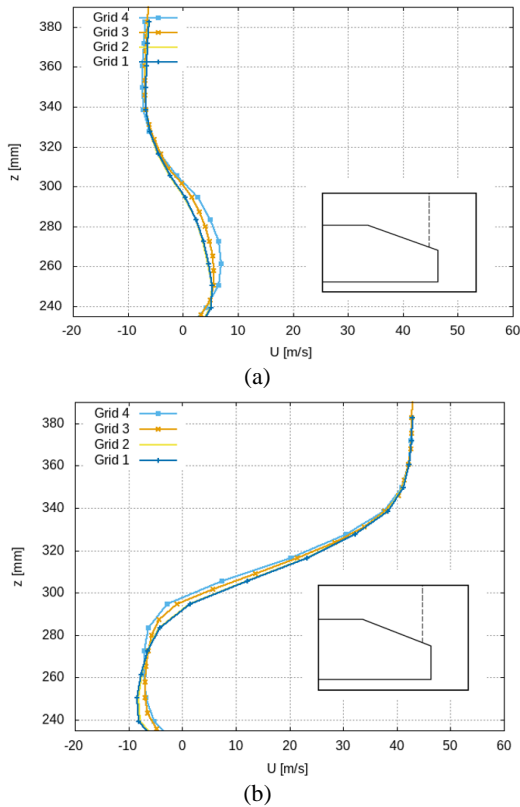


Figure 3. A) horizontal and B) vertical velocity profiles for four different computing grids in cross-section ($x=-0.023$ m)

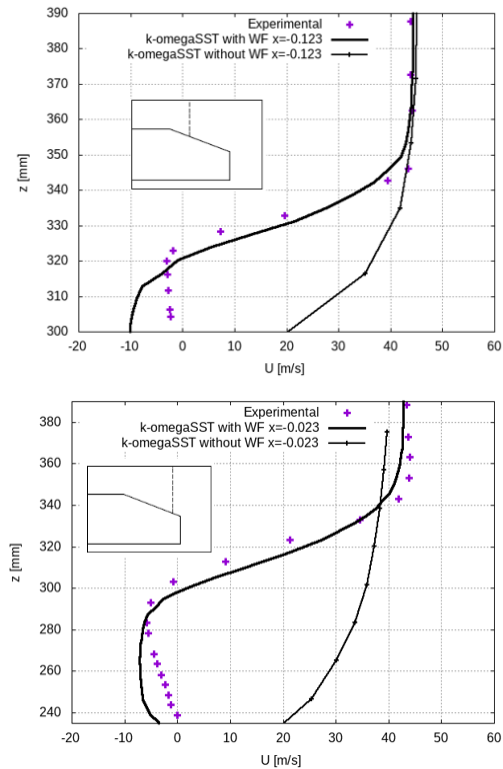
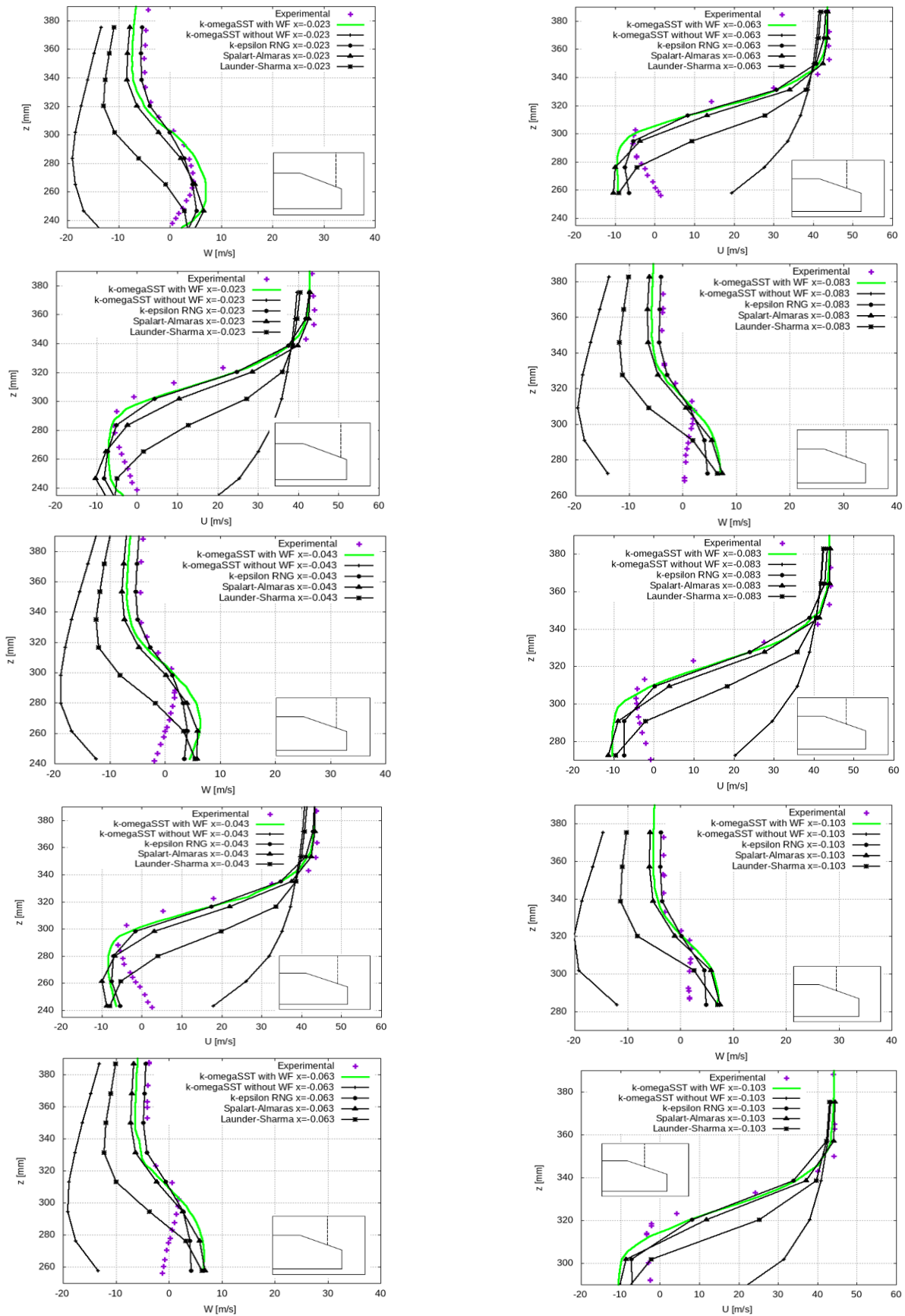


Figure 4. The effect of using the wall function on the horizontal and vertical velocity profile for two vertical sections $x=-0.023$ and $x=-0.123$

results are close to each other at a distance far from the wall for both cases, while near the wall of the solid body where separation and flow reversal occur, the velocity profiles are very different from each other. As can be seen, the SST $k-\omega$ turbulence model using the wall function has provided relatively good results compared to the experimental values.

3. 3. Separation Area behind the Vehicle Figure 5 depicts the profiles of horizontal (u) and vertical velocities (w) at several different vertical sections within (Figure 5) in the tail section using different turbulence models. As can be seen in these sections, near the wall to the height of the vehicle (about $z=310$ mm), the average horizontal velocity component is negative (backward flow) and the vertical velocity component of the air flow is positive (upward flow). This indicates the presence of positive gradient of pressure and return flow in this area.

As can be seen in Figure 5, the error rate of the turbulence models increases when approaching the wall of the vehicle, which is due to the presence of the wall effect and turbulent structures near the wall, as well as the presence of positive pressure and flow reversal, which is always considered as one of the main weaknesses of turbulence models. As can be seen in Figure 5, Lander and Sharma's one-equation model has the lowest and two models, $k-\omega$ SST, $k-\epsilon$ RNG, have the most agreement with the laboratory data.



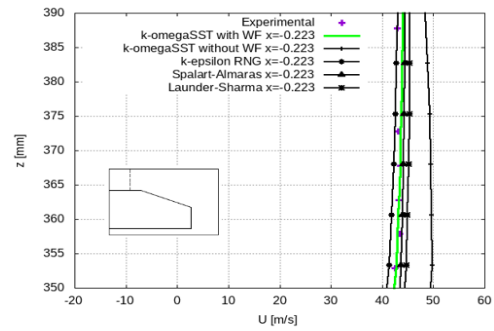
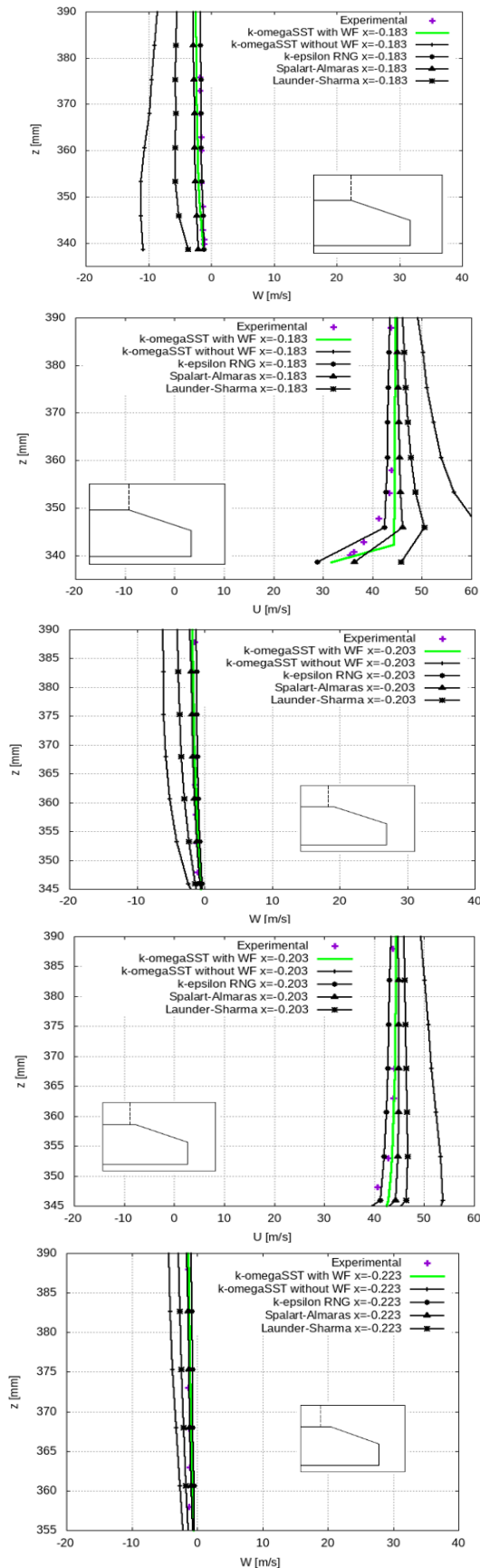


Figure 5. Variation of vertical and horizontal velocities in the tail section using different turbulence models

An important point that should be mentioned is the ability to estimate the average velocity field of these two models near the wall and ($Z < 310$ mm) in the area far from the wall ($Z > 310$ mm). In this research, the difference between the vertical and horizontal velocity profiles predicted by different turbulence models with experimental results was investigated for 10 different sections in the separation area behind the vehicle (the velocity profile of two sections is shown in this article). Table 2 summarized an average of the highest error percentage of different models in 10 different horizontal sections in the separation area.

As shown in Table 2, in the region near the wall ($Z < 310$ mm), the SST $k-\omega$ model has the best simulation in the horizontal component of the average velocity field (21% error), while the RNG $k-\epsilon$ model, although it has shown a little more estimation error (24%), but the vertical component of the velocity has been estimated better in this area. On the other hand, the model has estimated the velocity field in the area slightly away from the wall with an error of 13% for the horizontal velocity field and 12% for the vertical velocity component, which is the best prediction compared to all models. The reason for this is the ability of this model to simulate the return flow and its separation.

3. 4. Investigating the Effect of the Distance between the Floor of the Train and the Ground on Aerodynamic Forces

In the current article, a resized 1:10 size of the ICE3 train was developed, which

TABLE 2. The average maximum relative error of different turbulence models in the separation region (compared to laboratory data) in percentage

Model	Z<310 mm		Z>310 mm	
	W	U	W	U
Launder and Sharma	230	405	110	210
Spalart Almaras	142	150	76	53
$k-\omega$ SST	35	21	20	15
$k-\epsilon$ RNG	29	24	12	13

contains 4 cabins whereas the length (L), width (W) and height (H) are respectively 10.14 meters, 29 0.0 m and 0.36 m (Figure 6). Previous studies by Mahzoon and Kharati-Koopae [25] indicated that in high-speed trains, the impact of wheels on aerodynamic forces can be neglected, so in this study, their effect has been ignored. To investigate the effect of the distance of the floor of the train and the ground on the aerodynamic forces, 4 dimensionless distances from the floor of the train to the ground are considered as $h/H=0.18, 0.136, 0.092,$ and 0.048 .

For numerical simulations, the solution domain with the dimensions of $97W$ as the domain length, $20W$ as the domain height and $40W$ as the solution domain width has been used. The reason for using this large range is the lack of influence of boundary conditions on the flow structures around the train. In this section, flow fields and forces will be examined without considering side winds and considering side winds. Figure 7 shows the boundary conditions and solution domain in this case. The boundary conditions for the upper and side positions are considered symmetrically. To evaluate the relative speed of the train and the ground, the boundary condition of the ground is regarded as a wall with a speed equal to the free flow speed.

The beginning of the train is placed at a distance of $10W$ from the inlet boundary. The boundary condition at the outlet is considered to be fixed pressure and zero pressure. The distance of the train end to the exit boundary is equal to $52W$, which is considered in order to check the vortex profiles behind the train and the lack of influence of the pressure boundary condition at the exit on the flow field at the end of the train. The speed at the inlet is assumed to be uniform on the entire surface of the inlet. In this case, based on the characteristic length ($0.294 \text{ m} = \text{train height}$), flow speed ($v=50 \text{ km/h}$), air density equal to 1.184 kg/m^3 and viscosity $1.855 \times 10^{-5} \text{ kg/m s}$, Reynolds number is equal to $Re=2.58 \times 10^5$ is considered. These specifications are mainly intended to match the previous experimental and numerical data and use them to verify the present work for the flow on the train without the influence of side winds [23]. In this article, to investigate the effect of the distance between the floor of the train and the ground (h in Figure 7) on the

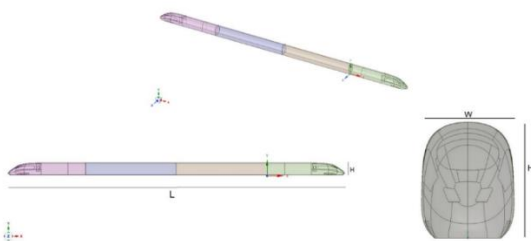


Figure 6. Trimetric, front and side views of the ICE3 high-speed train

aerodynamic forces, 3 dimensionless distances (h/H) have been used, which are represented by symbols h_0, h_1 and h_2 , and the value of this the dimensionless distances are equal to $0.136, 0.092$ and 0.048 , respectively. The side wind speed (in the second part of this section) is equal to 20 km/h and is considered at 5 different angles.

The intended computational grid is done utilizing a grid with cubic organization for train geometry. This computational grid was made using GridPro software and then it was entered into the OpenFoam. Figure 8 shows the method of gridding on the surface of the ground and the surface of the ground near the ground.

Investigating more precisely the velocity and pressure fields, as well as to determine the eddies and turbulence flows created around and behind the train, the unstable URANS models and the $k-\omega$ SST model have been used. In the entire implementation, the time step is determined as the CFL number which is shorter than 0.85 . By this method, the time steps are determined in each time step, based on the simulation results in overall it is about 10^{-4} seconds in overall for time steps. Since the unsteady URANS models have been used, it is necessary to ensure sufficient solution time for the correct estimation of the mean flow parameters such as the mean speed and pressure. Figure 9 illustrates the drag coefficient value on the whole body from in duration time of $0-7$ seconds, which is converged in $\text{time}=5 \text{ s}$.

For checking the independence of the solution from the computational grid, 3 various grids used for the SST $k-\omega$ model (which was chosen in the previous section as the best model in predicting the flow fields around the rigid body). The explained grid strategy is the same for all three grids, but the number of cells in these three grids is 2 million, 4 million, 200 thousand and 8 million cells, respectively. Figures 10-a and 10b show the profile of the

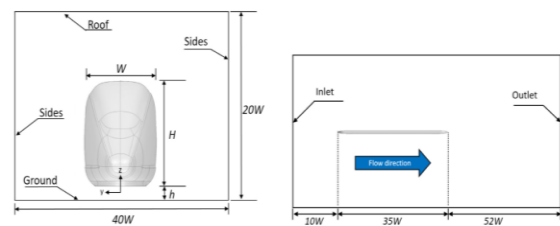


Figure 7. Solution domain and boundaries

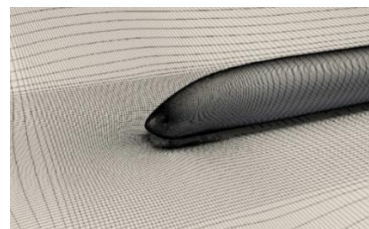


Figure 8. Solution domain and boundary conditions

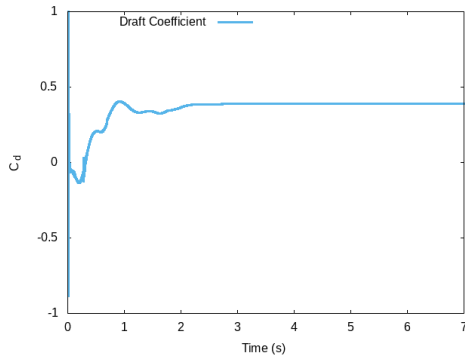


Figure 9. Mean drag coefficient on the train

horizontal and vertical velocity in the cross-section of the distance for the fixed longitudinal speed of 250 km/h. For the rest of the cases, the independence of the solution from the computational grid has been checked. As illustrated in Figure 10, the results for the various meshes are similar which approves the mesh independency of the results. Therefore, in this research, a medium grid size with 4 million two hundred thousand cells has been used.

Figure 11 compares the simulation results with the laboratory findings of xia et al. [18] and Dong et al. [23]. Dong et al. [23] investigated the ICE3 geometry. They simulated by employing LES and RANS hybrid turbulence method, utilizing IDDES method and Reynolds number similar to the present work. Xia et al. [18], studied the geometry of the ICE3 train without the

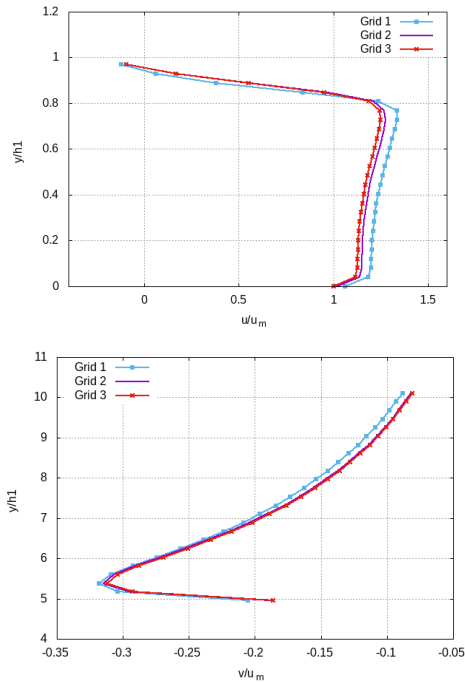


Figure 10. The effect of computational grid on the speed profile a) horizontal and b) vertical at different times

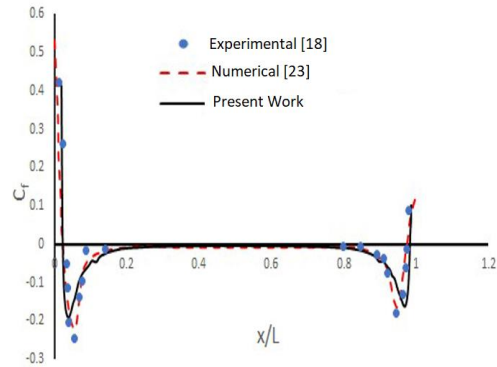


Figure 11. Simulation pressure coefficient comparison with previous experimental and numerical [18, 23]

impact of side wind using a wind tunnel, but in their work, the Reynolds number was considered equal to 1.65×10^6 , which is the same as the Reynolds number employed in the current research is different. Therefore, the laboratory data is slightly different from the simulation of Dong et al. [23] and also the present simulation.

3. 5. High Speed Train in the Presence of Crosswinds

3. 5. 1. Boundary Conditions

The boundary condition is considered exactly like the previous condition (Figure 7) with the difference that the left boundary is considered as the input boundary condition and the right boundary is considered as the output boundary condition.

3. 5. 2. Aerodynamic Forces and Moments

Figure 12 shows the speed diagram including wind speed w , train speed v and wind angle with respect to the direction of train movement β . In this article β is called yaw angle.

The relative speed of the wind to the speed of the train (u) is expressed as follows:

$$u^2 = v^2 + w^2 \tag{5}$$

And the yaw angle is defined as the following relationship.

$$\tan \beta = \frac{w}{v} \tag{6}$$

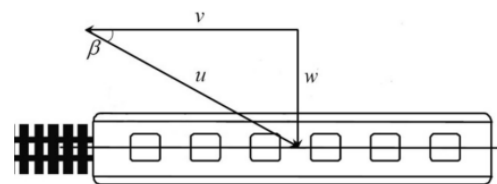


Figure 12. Velocity vector diagram

In the constant wind flow model, constant wind speed is considered. In this case, the aerodynamic forces are obtained from the following relations.

$$F = \frac{1}{2} \rho A C_F(\beta) u^2 \quad (7)$$

where F is the aerodynamic force, C_F is the aerodynamic force coefficient, ρ is the air density, A is the reference area, and h is the reference height. In this section, the $k\omega$ SST turbulence model is used in unsteady form.

3. 5. 3. Investigating the Impact of Train Floor Distance on Aerodynamic Forces at Various Yaw Angles

In this part, the effect of the distance of the train floor and the ground on the aerodynamic forces at various yaw angles will be investigated. For this purpose, 3 different distances from the floor to the ground h_0 , h_1 and h_2 are used and the speed of the wind flow is considered to be constant and equal to 20 m/s. All modes have been investigated for 6 different yaw angles from 0 to 0.5 radians (18 different modes in total).

Figure 13(a) shows the effect of floor to ground distance and yaw angle on the lift coefficient. As it can be seen, in all three distances, with an increase in the wind angle, the lift forces increase, so that for small distances (h_1 and h_2) in yaw angles less than 0.2 radians, the lift coefficient is negative, which means that the result of the vertical forces entering. It is downward on the train and therefore it causes the stability of the train in this direction. By increasing the direction of the wind to more than 0.2, the direction of the lift forces is changed and the lift coefficient is positive, which can cause the instability of the train at these angles.

For greater distances from the floor to the ground (h_0), the lift coefficient is negative only in the absence of side wind, and when the side wind starts, the result of the lift forces is upward and causes the instability of the train. In this case, the maximum value of the lift coefficient is 1.43 at the yaw angle of 0.5.

Figure 13(b) shows the coefficient of side forces acting on the train due to side wind at different distances and angles. As can be seen, the lateral wind forces increase with the decrease of the distance between the train and the ground. The reason for this is the reduction of wind flow under the train. With the further increase of the wind angle and its passing over 0.4 radians, the

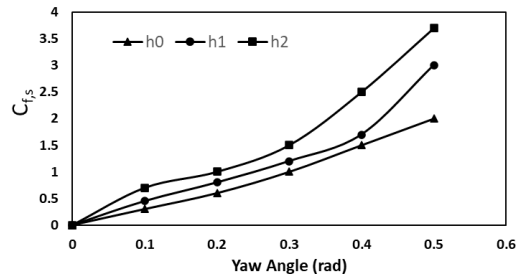


Figure 13. a) lift coefficient and b) drag coefficient related to the high-speed train in the presence of side winds with different angles and 3 different floor-to-ground distances

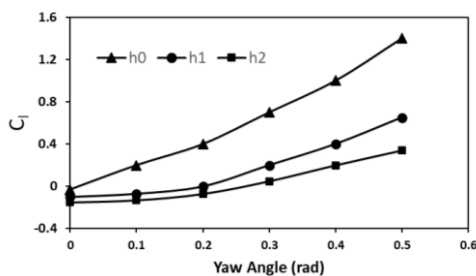
intensity of the increase in the side force increases, which can cause the stability of the train to be disturbed.

4. CONCLUSION

In this article, the influence of the height of the vehicle floor to the ground on the aerodynamic parameters in the presence of side wind flow was investigated. The presence of side wind had a great impact on stability and aerodynamic parameters, so considering its effect in the results, both in boundary conditions and in the analysis of aerodynamic forces, made the model more realistic. In this article, a detailed description of the selection of the turbulence model and its comparison with the previous valid references has been made on the bluff-body aerodynamics. In this article, using the OpenFOAM open source code, the air flow around a vehicle with a speed of 40 m/s (by considering the side wind) using four medium turbulence models taken at different times (in terms of the number of equations and also the working mechanism), including $k\omega$ SST, $k\epsilon$ RNG, Spalart-Almaras and Launder and Sharma with and without using the simulated wall function. The results indicate that Lander-Sharma and Spalart-Almaras models have very high errors (more than 400% for Lander-Sharma model) and these models are not capable of modeling the return flow. While the two models $k\omega$ SST, $k\epsilon$ RNG with the errors less than 25% can be considered as suitable options for checking the return flow. It was observed that the $k\omega$ SST model has a better results in modeling the horizontal component of the velocity near the wall (the error is about 21%), while the $k\epsilon$ RNG model better estimates the vertical part of the flow velocity as well as the flow velocity field in the area far from the wall.

5. REFERENCES

1. Krajnović, S., "Shape optimization of high-speed trains for improved aerodynamic performance", *Proceedings of the Institution of Mechanical Engineers, Part F: Journal of Rail*



- and Rapid Transit*, Vol. 223, No. 5, (2009), 439-452. <https://doi.org/10.1243/09544097JRRT25>
2. Webber, J., Mehdodniya, A., Teng, R., Arafa, A. and Alwakeel, A., "Finger-gesture recognition for visible light communication systems using machine learning", *Applied Sciences*, Vol. 11, No. 24, (2021), 11582. <https://doi.org/10.3390/app112411582>
 3. Baker, C.J., Quinn, A., Sima, M., Hoefener, L. and Licciardello, R., "Full-scale measurement and analysis of train slipstreams and wakes. Part 1: Ensemble averages", *Proceedings of the Institution of Mechanical Engineers, Part F: Journal of Rail and Rapid Transit*, Vol. 228, No. 5, (2014), 451-467. <https://doi.org/10.1177/0954409713485944>
 4. Zhang, L., Yang, M.-z. and Liang, X.-f., "Experimental study on the effect of wind angles on pressure distribution of train streamlined zone and train aerodynamic forces", *Journal of Wind Engineering and Industrial Aerodynamics*, Vol. 174, (2018), 330-343. <https://doi.org/10.1016/j.jweia.2018.01.024>
 5. Adamu, A., Zhang, J., Gidado, F. and Wang, F., "An investigation of influence of windshield configuration and train length on high-speed train aerodynamic performance", *Journal of Applied Fluid Mechanics*, Vol. 16, No. 2, (2022), 337-352. doi: 10.47176/jafm.16.02.1433.
 6. Kargar, F., Mehdipour, R. and Baniamerian, Z., "A numerical investigation on aerodynamic coefficients of solar troughs considering terrain effects and vortex shedding", *International Journal of Engineering, Transactions C: Aspects*, Vol. 28, No. 6, (2015), 940-948. doi: 10.5829/idosi.ije.2015.28.06c.15.
 7. Assadi, A. and Najaf, H., "Nonlinear static bending of single-crystalline circular nanoplates with cubic material anisotropy", *Archive of Applied Mechanics*, Vol. 90, No. 4, (2020), 847-868. <https://doi.org/10.1007/s00419-019-01643-9>
 8. Najafi, M.L. and Nasiri, M., "Identification and prioritizing the effective factors on addition by use of fuzzy analytical hierarchy process (f-AHP)", *Life Science Journal*, Vol. 10, No. 9s, (2013).
 9. Chen, Z., Liu, T., Zhou, X. and Niu, J., "Impact of ambient wind on aerodynamic performance when two trains intersect inside a tunnel", *Journal of Wind Engineering and Industrial Aerodynamics*, Vol. 169, (2017), 139-155.
 10. Rocchi, D., Tomasini, G., Schito, P. and Somaschini, C., "Wind effects induced by high speed train pass-by in open air", *Journal of Wind Engineering and Industrial Aerodynamics*, Vol. 173, (2018), 279-288. <https://doi.org/10.1016/j.jweia.2017.10.020>
 11. Khosravian, E. and Maghsoudi, H., "Design of an intelligent controller for station keeping, attitude control, and path tracking of a quadrotor using recursive neural networks", *International Journal of Engineering, Transactions B: Applications*, Vol. 32, No. 5, (2019), 747-758. doi: 10.5829/ije.2019.32.05b.17.
 12. Assadi, A., Najaf, H. and Nazemizadeh, M., "Size-dependent vibration of single-crystalline rectangular nanoplates with cubic anisotropy considering surface stress and nonlocal elasticity effects", *Thin-Walled Structures*, Vol. 170, (2022), 108518. <https://doi.org/10.1016/j.tws.2021.108518>
 13. Paz, C., Suárez, E. and Gil, C., "Numerical methodology for evaluating the effect of sleepers in the underbody flow of a high-speed train", *Journal of Wind Engineering and Industrial Aerodynamics*, Vol. 167, (2017), 140-147. <https://doi.org/10.1016/j.jweia.2017.04.017>
 14. Zhang, J., Li, J.-j., Tian, H.-q., Gao, G.-j. and Sheridan, J., "Impact of ground and wheel boundary conditions on numerical simulation of the high-speed train aerodynamic performance", *Journal of Fluids and Structures*, Vol. 61, No., (2016), 249-261. doi: <https://doi.org/10.1016/j.jfluidstructs.2015.10.006>
 15. Xia, C., Shan, X. and Yang, Z., "Comparison of different ground simulation systems on the flow around a high-speed train", *Proceedings of the Institution of Mechanical Engineers, Part F: Journal of Rail and Rapid Transit*, Vol. 231, No. 2, (2017), 135-147. <https://doi.org/10.1177/0954409715626191>
 16. Wang, S., Burton, D., Herbst, A., Sheridan, J. and Thompson, M.C., "The effect of bogies on high-speed train slipstream and wake", *Journal of Fluids and Structures*, Vol. 83, (2018), 471-489. <https://doi.org/10.1016/j.jfluidstructs.2018.03.013>
 17. Wang, S., Burton, D., Herbst, A.H., Sheridan, J. and Thompson, M.C., "The effect of the ground condition on high-speed train slipstream", *Journal of Wind Engineering and Industrial Aerodynamics*, Vol. 172, (2018), 230-243. <https://doi.org/10.1016/j.jweia.2017.11.009>
 18. Xia, C., Wang, H., Shan, X., Yang, Z. and Li, Q., "Effects of ground configurations on the slipstream and near wake of a high-speed train", *Journal of Wind Engineering and Industrial Aerodynamics*, Vol. 168, (2017), 177-189. <https://doi.org/10.1016/j.jweia.2017.06.005>
 19. Hajipour Khire Masjidi, B., Bahmani, S., Sharifi, F., Peivandi, M., Khosravani, M. and Hussein Mohammed, A., "Ct-ml: Diagnosis of breast cancer based on ultrasound images and time-dependent feature extraction methods using contourlet transformation and machine learning", *Computational Intelligence and Neuroscience*, Vol. 2022, (2022). doi: 10.1155/2022/1493847.
 20. Yu, E., Jin, Y., Xu, G., Han, Y. and Li, Y., "Aerodynamic stability of typical sea-crossing bridge with streamlined box girder under wave-interfered complex wind fields", *Journal of Wind Engineering and Industrial Aerodynamics*, Vol. 228, (2022), 105101. <https://doi.org/10.1016/j.jweia.2022.105101>
 21. Ismaiel, A., "Wind turbine blade dynamics simulation under the effect of atmospheric turbulence", *Emerging Science Journal*, Vol. 7, No. 1, (2022), 162-176. doi: 10.28991/ESJ-2023-07-01-012.
 22. Zvolenský, P., Grenčík, J., Pultnerová, A. and Kašiar, L., "Research of noise emission sources in railway transport and effective ways of their reduction", in MATEC Web of Conferences, EDP Sciences. Vol. 107, (2017), 00073.
 23. Dong, T., Minelli, G., Wang, J., Liang, X. and Krajnović, S., "The effect of ground clearance on the aerodynamics of a generic high-speed train", *Journal of Fluids and Structures*, Vol. 95, (2020), 102990. <https://doi.org/10.1016/j.jfluidstructs.2020.102990>
 24. Kalitzin, G., Medic, G., Iaccarino, G. and Durbin, P., "Near-wall behavior of rans turbulence models and implications for wall functions", *Journal of Computational Physics*, Vol. 204, No. 1, (2005), 265-291. <https://doi.org/10.1016/j.jcp.2004.10.018>
 25. Mahzoon, M.M. and Kharati-Koopae, M., "The effect of gurney flap and trailing-edge wedge on the aerodynamic behavior of an axial turbine blade", *HighTech and Innovation Journal*, Vol. 2, No. 4, (2021), 293-305. doi: 10.28991/HIJ-2021-02-04-03.

Persian Abstract

چکیده

هدف اصلی این مقاله ارائه مدل واقعی قطار سریع السیر همراه باد جانبی بود. در بخش اول این مقاله جریان هوای آشفته حول یک طرح ساده شده یک خودرو با سرعت بالا به صورت عددی با استفاده از روش حجم محدود و چهار مدل توربولانسی RANS شامل $k-\omega$ SST، $k-\epsilon$ RNG، Spalart-Almaras و Launder and Sharma و همچنین، تأثیر استفاده از تابع دیواره بر نتایج نیز بررسی شده است. نتایج شبیه‌سازی‌های عددی در رابطه با تابع دیواره با کارهای تجربی تأیید شد و نشان داد که در ناحیه نزدیک دیواره، مدل $k-\omega$ SST بهترین شبیه‌سازی را برای مؤلفه افقی سرعت (۲۱ درصد خطا) دارد. نتایج حاصل از لیفت نشان داد که در فواصل کوتاه از کف قطار تا زمین به دلیل وزش باد نسبتاً شدید با زوایای کمتر از ۰.۲ رادیان، ضریب لیفت منفی و در نتیجه نیروهای وارد بر قطار رو به پایین بوده است. در نهایت نشان داده شد که با افزایش زاویه باد، این ضریب به تدریج مثبت می‌شود که می‌تواند پایداری قطار را مختل کند. می‌توان نتیجه گرفت که در قطارهایی که فاصله کف تا زمین آنها بیش از ۰.۱۳۶ برابر ارتفاع قطار است، تعادل فقط در صورت عدم وجود باد جانبی حفظ می‌شود.



Visible Light Activated Fe-N-SiO₂/TiO₂ Photocatalyst: Providing an Opportunity for Enhanced Photocatalytic Degradation of Antibiotic Oxytetracycline in Aqueous Solution

S. A. Habeeb^{a,b}, A. A. Zinatizadeh^{*a,c}, S. A. Mousavi^d, H. Zangeneh^e

^a Department of Applied Chemistry, Faculty of Chemistry, Razi University, Kermanshah, Iran

^b Pharmacy Faculty, University of Babylon, Babylon, Iraq

^c Environmental and Pollution Engineering Group, Environmental Research Center (ERC), Razi University, Kermanshah, Iran

^d Department of Health Engineering, Kermanshah University of Medical Sciences, Kermanshah, Iran

^e Department of Chemical Engineering, Isfahan University of Technology, Isfahan, Iran

PAPER INFO

Paper history:

Received 22 August 2022

Received in revised form 16 December 2022

Accepted 31 December 2022

Keywords:

Photocatalytic Degradation
Nonbiodegradable Antibiotics
Fe-N-SiO₂/TiO₂
Oxytetracycline

ABSTRACT

To probe advantages in Fe-N-SiO₂/TiO₂ nanocomposite system, the visible photocatalytic degradation of the nonbiodegradable antibiotic oxytetracycline (OTC) by unsupported TiO₂ and its modified composites by incorporating each of the Fe, N, and SiO₂ dopants under a series of conditions were investigated. The structural and optical properties as well as the morphology of the prepared nanocomposites were also characterized applying Fourier transform infrared (FT-IR), X-ray diffraction, photoluminescence spectroscopy, UV-visible diffuse reflectance spectra and field emission scanning electron microscopy/Energy-dispersive X-ray spectroscopy (FESEM/EDX). In order to develop two models portraying appropriate functional relationships between two main responses (OTC removal efficiency and its specific removal rate (SRR)) and four numerical variables (OTC concentration, catalysis loading, initial pH and reaction time), two separate multivariate analysis pathways under response surface methodology (RSM) were taken. The results obtained all came down to the maximum SRR (220 OTC mg_{OTC removed}/g_{cat.} h) found at the maximum catalyst dosage of 1.5 g/l, and acidic pH of 3 after 0.5 h. Furthermore, the Fe-N-SiO₂/TiO₂ proved a stable photocatalytic activity during three subsequent reusability experiments, shedding light on its reliable potential for future application.

doi: 10.5829/ije.2023.36.04a.02

1. INTRODUCTION

As a member of one of the most commonly worldwide used classes of antibiotic chemicals aiming significantly for disease prevention and its treatment, oxytetracyclines (OTC) has been frequently detected in the environment, mostly involving water bodies [1, 2]. The environmental contamination caused by OTC is usually originated from pharmaceutical manufacture, livestock farming, and agricultural discharges [3, 4].

Due to be extremely resistant to biodegradation [5], a large number of studies focused on alternative non-biological processes for OTC removal [6]. Providing the opportunity of being carried out at room temperature and

atmospheric pressure while obtaining high levels of mineralization of various pollutants to mainly water, CO₂, and inorganic compounds, throughout the recent decades, photocatalytic technology as an advanced oxidation process (AOP) has been showing great promise in antibiotics degradation [7]. Performing under visible light irradiation is the key to the practical application of photocatalysts. Meanwhile, TiO₂ mediated photocatalysis has been highlighted as one of the most promising approaches to degrade stable organic contaminants in water by producing hydroxyl radicals [8, 9]. Given their sufficiently optical/electric properties, non-toxic nature, high photocatalytic capacity, and long-term chemical stability, metal oxide semi-conductors

*Corresponding Author Email: zinatizadeh@gmail.com
(A. A. Zinatizadeh)

including TiO₂ have been proven in recent publications as potential photocatalysts for successful oxidation as well as antibacterial inactivation of OTC [10, 11].

Possessing a large band gap (3.2 eV) limiting its activation to only ultraviolet (UV) region and low quantum efficiency caused by high e⁻/h⁺ recombination, TiO₂ meets a major drawback in its wide application [12]. Many efforts have been devoted to overcome the limitations improving the visible driven photoactivity and ultimate photocatalytic efficiency of titania photocatalysts [13]. In order to obtain TiO₂-based visible light activated photocatalysts, many strategies including metal ions doping [14], nonmetal ions doping [15], and coupling with other semiconductors containing narrower band gaps [16] have been adopted. Despite some controversial efficiency results obtained under different experimental conditions, introduction of transition metal cations including ferric ion (Fe³⁺) in titania has yet been considered an effective approach towards enhancing the photocatalytic properties within the visible light region [17-19]. Being able to be replaced into TiO₂ network structure due to its electron configuration, different optimum amounts of Fe³⁺ incorporated in TiO₂ as: 0.3 wt.% [20], 0.5 wt.% [21], and 1.0 wt.% [22] have been reported in the literature.

As the leading element which has been investigated extensively in the literature due to its favorable features as a dopant, nitrogen (N) can be easily introduced in the crystal lattice of TiO₂ while suppressing the recombination rate of the photogenerated electron/hole pairs and ultimately facilitating its visible-light photocatalytic activity [23]. Park et al. [24] investigated the enhanced visible driven photocatalytic degradation of methylene orange (MO) N-doped TiO₂ nanocomposite fabricated by using graft polymerization. In another research, Bergamonti and colleagues [25] reported the synthesis of N-TiO₂ photocatalysts employing a variety of precursors as oxysulfate (N-TiA), tetraisopropoxide (N-TiU), and titanium (IV) for MO and rhodamine B (RhB) photodegradation. Based on the results obtained, N-TiA led to the highest photocatalytic activity owing to its capacity absorb higher wavelengths of light in the UV-visible spectrum. Meanwhile, suggesting greater surface area, higher capacities for adsorbing pollutant molecules, and higher photoactivity while being bond-conjugated to TiO₂, SiO₂ has also become a potential candidate in order to obtain enhanced photodegradation efficiencies in the last decades [26]. Chun and coworkers [27-29] thoroughly investigated the adsorption and photodegradation of various dyes using the SiO₂/TiO₂ photocatalyst, shedding light on its high potential.

The present study attempts to compare visible driven photocatalytic degradation of OTC by unsupported TiO₂ nanoparticles and with TiO₂ nanocomposites modified by doping a metal (Fe³⁺), nonmetal (N), and coupling an oxide semi-conductor compound (SiO₂) in order to have

a better understanding of the advantages these modifications can bring along. The experiments successfully resulted in the fabrication of the modified Fe-N-SiO₂/TiO₂ photocatalyst. Following the physicochemical and optical characterization of the as-obtained photocatalysts, As the main objective of the research, effects of four factors including catalyst loading (0.5-1.5 g/l), OTC concentration (50- 200 mg/l), initial pH (3-11), and irradiation time (0.5-6.5 h) were thoroughly investigated.

2. MATERIAL AND METHODS

2.1. Materials Oxytetracycline (OTC) pure powder $\geq 99.9\%$ was ordered from Sigma, USA. Tetra n-butylorthotitanate (TNBOT) $\geq 98\%$, Tetraethyl Ortho Silicate (TEOS) $\geq 98\%$, Ethanol 96%, HCl 37%, NH₃ as the nitrogen source, and Fe(NO₃)₃.9H₂O as Fe⁺³ source were all supplied from Merck, Germany. All the other reagents used were all analytical grade without further requirement for purification. All aqueous solutions were prepared with ultra-pure water.

2.2. Synthesis OF Fe-N-SiO₂/TiO₂ Catalysis Fe-N-SiO₂/TiO₂ photocatalyst was synthesized via the sol-gel technique [21]. 25 ml of TNBOT was dissolved in 100 ml of ethanol under magnetic stirring for 30 min (A solution). Then, 1.6 ml of ethanol was added to TEOS under stirring for 10 min followed by the addition of 4 ml of HCl 37% + 3 ml of ultra-pure water and then further stirred for 30 min (B solution). Next, C solution was prepared by dissolving 0.148 g of Fe(NO₃)₃.9H₂O in 20 ml of ethanol under stirring for 10 min. Ultimately, the mixture of NH₃, and B and C solutions were added to A solution followed by being stirred for about 6 h. The final solution was aged for 48 h. The prepared sample was then dried at 100 °C for approximately 10 h, ultimately being calcinated at 450 °C for 2.5 h.

2.3. Characterization of the Prepared Photocatalysts Using KBr pellets containing the powder samples, an FT-IR spectrometer (MAGNA-560) was applied to record Fourier Transform Infra-Red (FT-IR) spectra. X-ray diffractometer (a Rigaku D-max C III) with Ni-filtered K α radiation and Philips XL30 microscope with accelerating voltage of 10 kV made it possible to obtain X-ray diffraction (XRD) patterns and scanning electron microscopy (SEM) images, respectively leading to a better observation and estimation of the photocatalysts morphology and their structural properties. UV-Vis spectrophotometer (Rayleigh UV 2601 model) and the photoluminescence spectrometer using a photomultiplier tube (Perkin Elmer LS55) were used to study DRS and PL analysis, respectively.

2. 4. Photodegradation Experiments

Photodegradation performance of the synthesized photocatalysts was evaluated by degrading the synthetic OTC wastewater. Reaction suspensions were prepared by adding appropriate amounts of the as-prepared photocatalyst powders into 200 ml of the synthetic OTC wastewater. Solutions were then irradiated by ultraviolet (UV) and visible (Vis) lights for specific time intervals. Experiments were performed for 390 min, and liquid aliquots (5 ml) were withdrawn every 60 min. The samples were then centrifuged to remove the existing particles prior to being analyzed by UV-Vis spectrophotometry. COD concentration of the samples were measured using standard method (5220D) procedures [30]. In each sample, OTC concentration was measured according to its absorbance detected by a UV-Vis spectrophotometer (DR 5000, Jenway) at maximum wavelength of 348 nm. In order to better compare the results, bare Titania was also tested along with the other samples under the same experimental conditions.

2. 5. Experimental Set Up As shown in Figure 1, the photodegradation tests in the laboratory scale were conducted in a suspended batch photoreactor. Being located in a black box, the photoreactor consisted of a 200 ml Pyrex-glass cell. Irradiation sources were a 100-watt tungsten lamp and a UV lamp (HITACHI, emission: 365 nm, constant intensity 60 mW/cm²) which were located at the upper part of the photoreactor. The vertical distance between the solution and the irradiation source was 15 cm. Furthermore, a magnetic stirrer was applied to keep the solution uniformed by providing constant agitation throughout the experiments at the constant temperature of 25±1 °C.

2. 6. Experimental Design As one of the most common experimental methods, response surface methodology (RSM) under Design Expert software (Stat-Ease Inc., version 11.1.2.0) was employed to design the photodegradation tests as well as their mathematical modeling leading to further data analysis [31]. Accordingly, four independent numerical factors including initial OTC concentration, catalyst concentration, reaction time, and initial pH were assessed in terms of their effects on the OTC removal process performance and modeled at 5 levels ($\alpha=\pm 0.5$) by inscribed central composite design (CCID) as shown in Table 1. According to the following equation, a total of 30 operating conditions [32] (Equation (1)) were designed.

$$N = 2^{k-q} + 2 \times k + n_c \quad (1)$$

where k, q, and n_c are considered as the number of factors, a fraction of the number factor (which is zero for full factorial design) and the replicate number of the central point, respectively [32]. The values of the

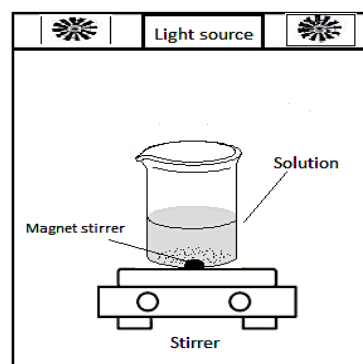


Figure 1. The schematic of the employed photocatalytic batch reactor

TABLE 1. Experimental range and levels of the independent variables

Variables	Range and levels				
	-1	- α	0	+ α	1
A- Initial OTC concentration, mg/l	50	87.5	125	162.5	200
B-Catalyst concentration, g/l	0.5	0.75	1	1.25	1.5
C- Initial pH	3	5	7	9	11
D- Reaction time, h	0.5	2	3.5	5	6.5

responses obtained in the experiments are presented in Table 2.

3. RESULTS AND DISCUSSION

3. 1. Photocatalytic Activity Experiments: Optimization of Fe-N-SiO₂/TiO₂ Each prepared photocatalyst was subjected to a photocatalytic reaction for OTC removal at certain conditions (OTC concentration = 50 ppm and photocatalyst concentration = 0.5g/l) under visible light for 6.5 h (390 min). The prepared samples included pure TiO₂ and its combination with different mass ratios of the dopants (Fe-TiO₂, N-TiO₂, SiO₂-TiO₂, and Fe-N-SiO₂-TiO₂). As observed in Figure 2, pure TiO₂ did not exhibit much visible photoactivity (only 40%). The optimum weight fractions of Fe, N, and SiO₂ as the dopants were obtained at 0.05, 5, and 5 wt. %, respectively, and were further applied in the modified photocatalysts.

Undergoing the same visible light irradiation for 390 min, all of the doped nanocomposites led to higher visible light activities in comparison to the pure TiO₂ as shown in Figure 2. Fe-N-SiO₂/TiO₂, resulting in 91 % OTC removal efficiency, showed the maximum visible-light photocatalytic activity compared to the other doped photocatalysts: Fe-TiO₂ (80%) N-TiO₂ (70%), SiO₂-TiO₂ (64%).

TABLE 2. Experimental conditions for the photocatalytic process

Run	Factor 1	Factor 2	Factor 3	Factor 4	Response 1	Response 2
	A: OTC concentration	B: Catalyst concentration	C: Initial pH	D: Reaction time	OTC removal eff.	SRR
	mg/l	g/l		h	%	mg OTC removed/ g cat. h
1	50	0.5	3	6.5	80.26	12.34
2	50	0.5	3	0.5	56.36	78.35
3	50	0.5	11	0.5	25.26	31.86
4	50	0.5	11	6.5	45.93	7.06
5	50	1.5	3	6.5	86.93	4.45
6	50	1.5	11	0.5	22.09	8.1
7	50	1.5	11	6.5	62.26	3.19
8	50	1.5	3	0.5	60.26	24.2
9	87.5	1	7	3.5	92.1	20.5
10	125	0.75	7	3.5	71.09	29.75
11	125	1	7	3.5	73.35	23.1
12	125	1	7	3.5	75.9	25.28
13	125	1	7	5	83.84	19.01
14	125	1	9	3.5	75	23.561
15	125	1	7	3.5	75.1	25.21
16	125	1	7	3.5	73.4	25.99
17	125	1	7	2	70.9	35.45
18	125	1	7	3.5	73.1	23.2
19	125	1	7	3.5	73.9	25.8
20	125	1	5	3.5	84.5	26.5
21	125	1.25	7	3.5	83.3	20.1
22	162.5	1	7	3.5	78.2	32.04
23	200	0.5	3	0.5	33.5	173
24	200	0.5	11	6.5	31.56	19.42
25	200	0.5	11	0.5	23	119.73
26	200	0.5	3	6.5	53.56	32.96
27	200	1.5	3	6.5	83.98	51.68
28	200	1.5	11	6.5	42.9	8.8
29	200	1.5	3	0.5	70.45	347.2
30	200	1.5	11	0.5	28.3	51.7

The improved visible driven photocatalytic activity of Fe-doped TiO₂ (80%) is attributed to the narrower band gap leading to the enhanced generation of the charge carriers and higher photocatalytic activity [17, 33, 34]. Furthermore, acting as shallow traps in the titania lattice, Fe³⁺ cations lead to a reduction in electron-hole recombination properties, hence increasing not only the electron-hole pair lifetime but also the possibility of reactions between the created electron-hole pair. As for N-doped TiO₂, owing to the formation of a mid-gap (N^{2p}) with an intermediate energy level over top of the

(O^{2p}) valence band [35], introducing nitrogen into the TiO₂ lattice results in its narrower band gap and ultimately enhanced its photocatalytic activity under visible light irradiation. While in SiO₂-TiO₂ composite, the semi-conductor cations entering the lattice of TiO₂ not only provides more available surface for photocatalytic activity, but also enhances its surface acidity. Consequently, coupling SiO₂ with TiO₂ leads to preferentially adsorbing more hydroxyl groups on the surface of the composite and therefore, decreasing its contamination by OTC [36].

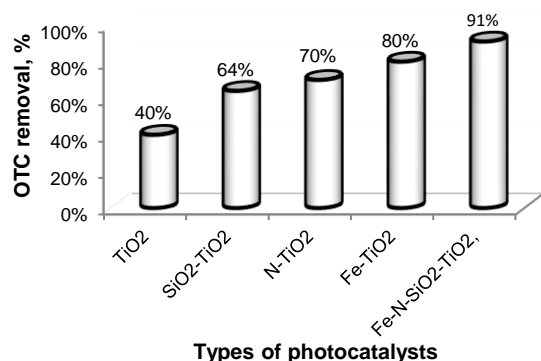


Figure 2. Visible-driven OTC removal efficiency by different photocatalysts at the OTC concentration of 50 ppm and photocatalyst concentration of 0.5g/l for 390 min

Relying on the aforementioned reasons supporting the improved visible driven photocatalytic activity in three modified nanocomposites, Fe-N-SiO₂/TiO₂ obtained the highest OTC removal efficiency, simultaneously benefiting from the addition of Fe³⁺, N, and SiO₂.

3. 2. Characterization of Fe-N-SiO₂/TiO₂ Photocatalyst

3. 2. 1. FT-IR Spectroscopy Figure 3 illustrates the FT-IR spectra of the prepared samples. The bands at 400-800 are related to the vibration of Ti-O and Ti-O-Ti bonds in all of the samples [30]. The presence of dissolved or atmospheric CO₂ in the samples also resulted in a peak at 2400 cm⁻¹. Furthermore, the weak transmittance bands at around 1630 and 3100-3600 cm⁻¹ can be assigned respectively to the bending and stretching vibrations of hydroxyl groups of the adsorbed water molecules in the samples [37]. Owing to the nitrogen atoms being substituted into the TiO₂ network in N-TiO₂ and Fe-N-SiO₂-TiO₂, the peak at 1440 cm⁻¹ was obtained in Figure 3 [38].

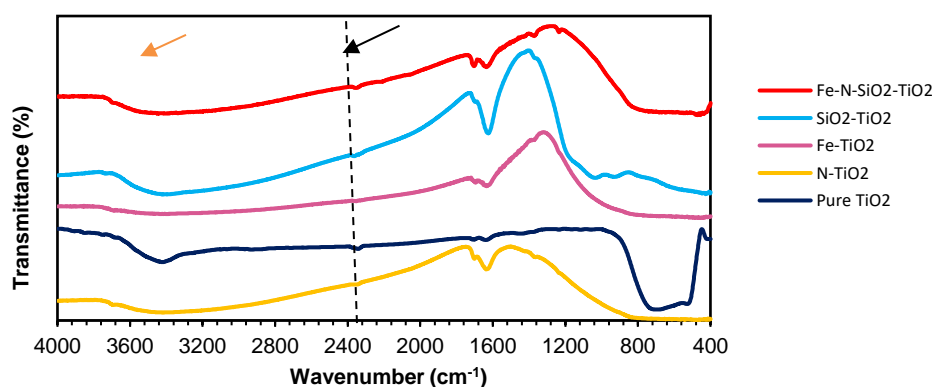


Figure 3. FT-IR spectra of the prepared samples

The asymmetric vibration of Si-O-Si bonds for SiO₂-TiO₂ composites was observed at approximately 1060 cm⁻¹ [50]. The stretching vibrations of Si-OH, SiO groups and Si-O-Ti bonds can be implied by the absorption band at about 900-1000 cm⁻¹ [39].

3. 2. 2. XRD Patterns The XRD pattern was employed to identify crystal structure of the prepared pure TiO₂, SiO₂-TiO₂, N-TiO₂, Fe-TiO₂ and Fe-N-SiO₂-TiO₂ photocatalysts as illustrated in Figure 4. At all samples, the peaks are noted to tetragonal anatase crystalline phase of TiO₂. The diffraction peaks of the 2θ values at 25.1°, 37.25°, 38.63°, 48.12°, 54.48°, 62.54°, 68.9°, 70.57°, and 75.15° were observed which are related to the crystalline phases of anatase. The XRD pattern for the doping amount of Fe (0.05 wt. %) was too low to be detected by XRD [40]. The crystalline size (D) of Fe-N-SiO₂/TiO₂ nanoparticles was calculated by using Debye Scherrer's formula ($D = 0.9\lambda / \beta \cos\theta$), where λ is the wavelength of the X-rays and β is the full width at the half maximum intensity (FWHM) [41]. The results of the calculations for the XRD data showed that the range of particle sizes of Fe-N-SiO₂/TiO₂ NPs are between 19.64 to 46.78 nm, which is close to and supports SEM results.

3. 2. 3. SEM Analysis The SEM images of the Fe-N-SiO₂/TiO₂ nanoparticles are depicted in Figures 5(a)-5(c). As observed in Figure 5(a), the sizes of the nanoparticles were in the range of 22.14-50.87 nm. As an extra provision to calculate the size of the catalyst, Figure 5b presented the particle size distribution of Fe-N-SiO₂/TiO₂ nanoparticles in the range of 10 to 45 nm, in which the most common size range included the values from 26 to 30 nm [42]. The SEM results are the clear evidence that the uniformly distributed nanoparticles are spherical in shape. Providing more active areas for photocatalytic degradation, the porous structure of the as-prepared photocatalysts has also been proven by these images [40]. The EDX result in Figure 5(c) confirms the presence of Fe, N, Si, Ti and O elements in the nanocomposite.

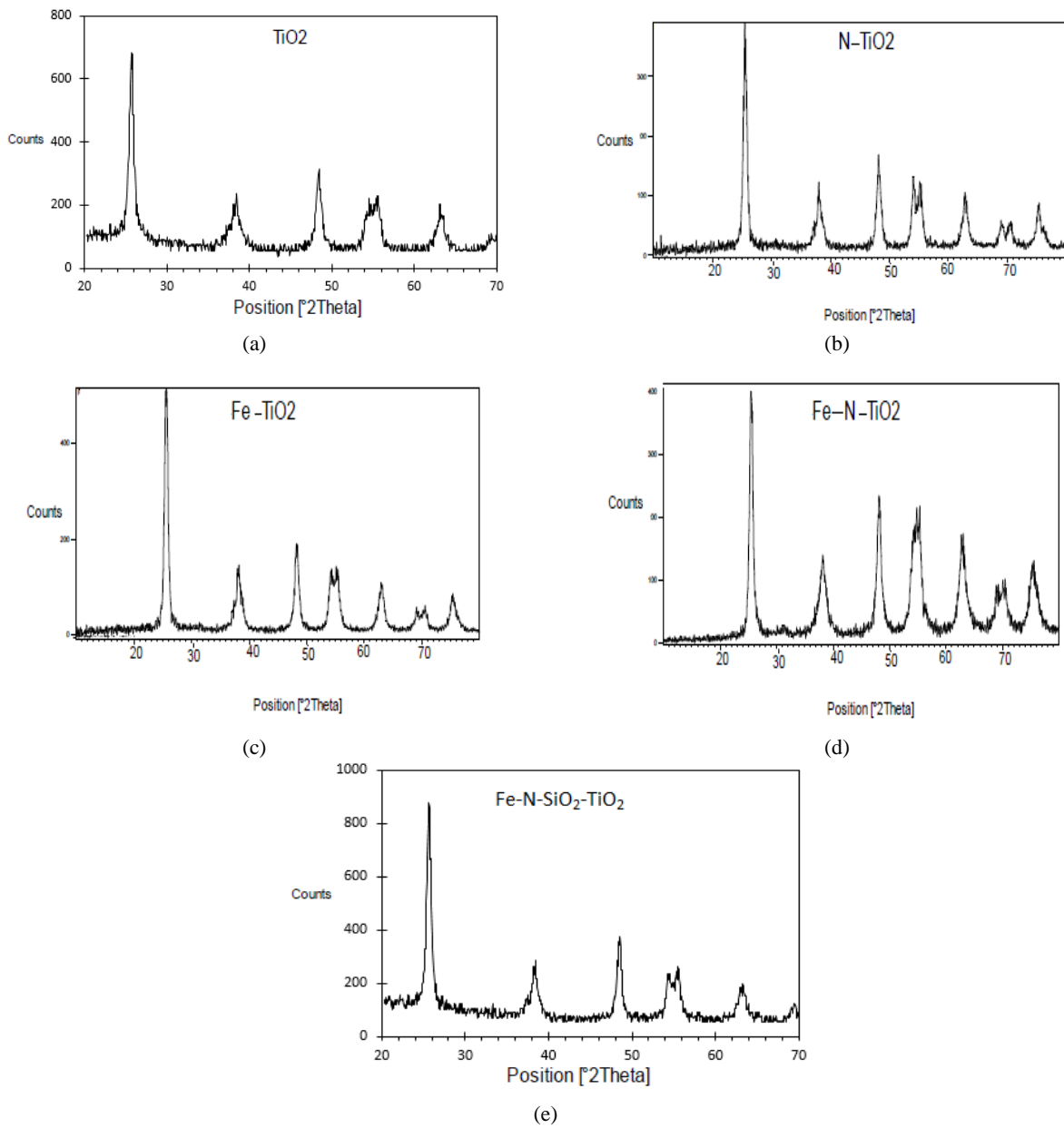
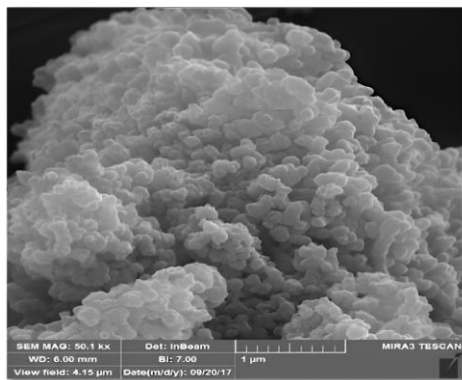
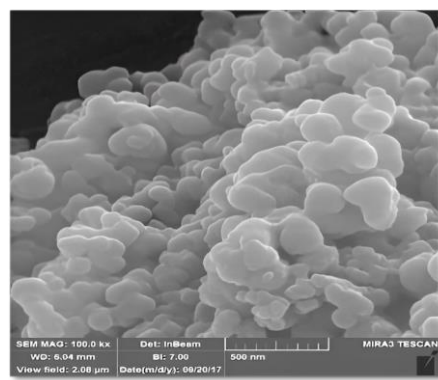


Figure 4. XRD patterns of the prepared samples



(a)



(b)

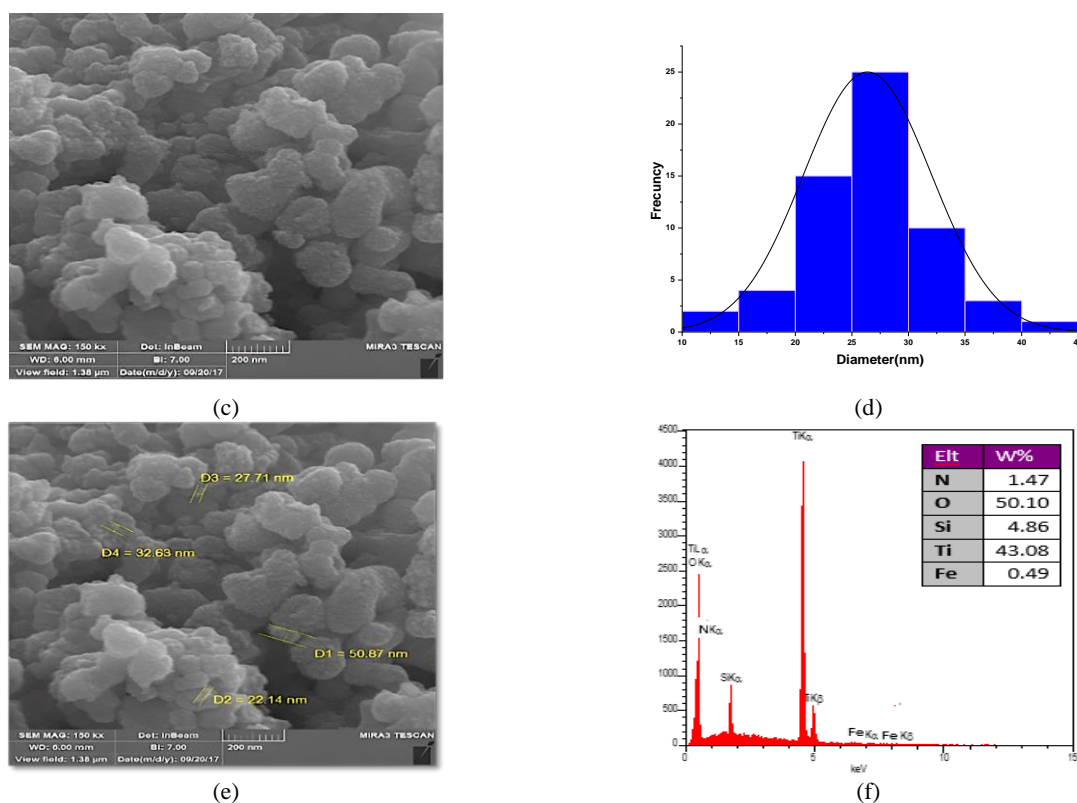


Figure 5. SEM images and EDX spectrum of Fe-N-SiO₂/TiO₂

3. 2. 4. Optical Properties The optical absorption of the synthesized photocatalyst was assessed by UV-Vis DRS analysis and its result was indicated in Figure 6(a). The strong absorption in the visible light region implies the vital role of dopant agents (Fe and N elements) in the reduction of band gap and extension of the absorption edge into a visible light range. Figure 6(b) shows the PL emission spectrum of pure TiO₂ and Fe-N-SiO₂/TiO₂ photocatalysts. The PL intensity of modified nanocomposite is lower than pure TiO₂ due to incorporating Fe, N, and SiO₂ on the TiO₂ surface [43, 44]. Both oxygen vacancies and lattice defects in the structure of the modified TiO₂ sample can act as charge carrier trapping centers and infer the recombination rate of photogenerated h⁺/e⁻ pairs decline.

3. 3. Photodegradation Process Analysis And Modeling

In order to fit the CCID experimental results obtained in OTC photodegradation runs, a response surface model using standard analysis of variance (ANOVA) was developed and the subsequent results are provided in Table 3. Two models, reduced quadratic and reduced 2FI, containing the confidence level of 99 % (probability value <0.0001) were selected for the OTC removal efficiency and specific removal rate (SRR), respectively.

Implying the degree of significance and influence of the coefficients on the responses, the probability values (p-values) and F-values are given in Tables 3 and 4. The insignificant model terms with significantly higher than 0.05 p-values need to be removed from the model equation simplifying the model. As a result, according to p-values for OTC removal, the significant model terms include A (OTC concentration), B (catalyst concentration), C (initial pH), D (reaction time), AB, AD, BC, and B². Meanwhile, for SRR, A, B, C, D, AB, AC, and BC are considered significant model terms. Given the F-values and also multilateral contributions of each variable in the final equation, significant model terms were indicated in terms of their order and subsequent influences on both responses.

Evaluating the accuracy and variability of the model for the OTC removal efficiency and SRR, the high values of the coefficient of determination ($R^2 = 0.9487$ and $R^2 = 0.9570$, respectively) ensures a satisfactory adjustment of the developed models to the experimental data [45]. Furthermore, being very close to the corresponding R^2 value, the adjusted R^2 values of respectively 0.9291 and 0.9458 further confirm the adaptability of the aforementioned models. Predicted R^2 values of both responses are in good agreement with experimental values (Predicted R^2 was about 0.8721 and 0.8900 for OTC removal and SRR, respectively).

According to Table 3, the adequate precision values for OTC removal efficiency and SRR were 23.8605 and 44.2257, respectively, further proving that the models are desirable. Figures 7(a) and 7(b) depict the measured data versus the predicted ones for both models. Furthermore, coefficient of variation (C.V. %) is an important concept allowing us to predict variables within and outside data sets [45]. High reliability and accuracy of experimental work in this study could also be explained by C.V. values of 9.07% and 6.99% for OTC removal and SRR, respectively.

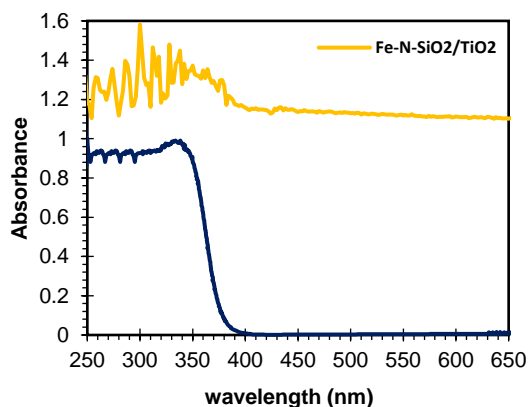
Favoring more effective contacts between the OTC and hydroxyl radicals, the conceivable effect of longer reaction time on the response was observed in both plots.

The three-dimensional (3D) response surface plots represented in Figures. 8 and 9 are applied to assess the interaction effects of the aforementioned variables on both responses. The concentration of OTC was held constant at an average level (125 mg/l) in all of the plots given in Figure 8. In the meantime, increasing the OTC concentration to the maximum level might have an inhibiting role due to the saturation of the photocatalyst active sites with OTC molecules. As a result, the poisoning phenomenon might occur at high OTC loadings, resulting in less production of hydroxyl radicals and superoxide radical anions thereby weakening the degradation efficiency [46].

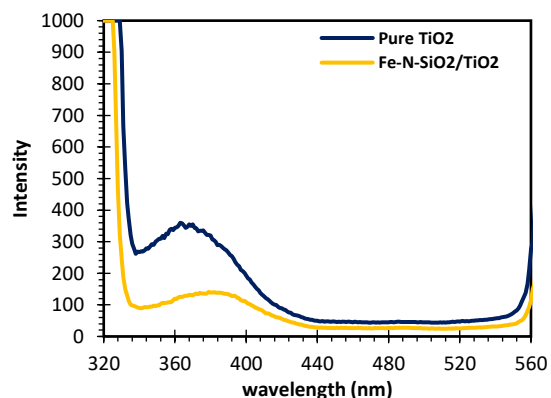
TABLE 3. ANOVA results for the selected models regarding OTC removal efficiency.

Source	Sum of Squares	df	Mean Square	F-value	p-value			
Model	12684.80	8	1585.60	48.53	< 0.0001	Significant	Final Equation in Terms of Coded Factors	
A-OTC conc.	378.72	1	378.72	11.59	0.0027			
B-Cat. conc.	785.50	1	785.50	24.04	< 0.0001			
C-Initial pH	3750.09	1	3750.09	114.78	< 0.0001	OTC removal eff. =		
D-Reaction time	1848.22	1	1848.22	56.57	< 0.0001	+78.18		
AB	227.10	1	227.10	6.95	0.0154	-4.79		A
AD	186.73	1	186.73	5.72	0.0263	+6.90		B
BC	144.84	1	144.84	4.43	0.0475	-15.08		C
B ²	5363.59	1	5363.59	164.17	< 0.0001	+10.58		D
Residual	686.09	21	32.67			+3.77		AB
Lack of Fit	679.76	16	42.48	33.57	0.0005	Significant	-3.42	AD
Pure Error	6.33	5	1.27			-3.01	BC	
Cor Total	13370.89	29				-27.58	B ²	

Fit Statistics						
Std. Dev	Mean	C.V. %	R ²	Adjusted R ²	Predicted R ²	Adeq Precision
5.72	63.01	9.07	0.9487	0.9291	0.8721	23.8605



(a)



(b)

Figure 6. (a) DRS and (b) PL spectra of the prepared photocatalysts

Figures 8(a) and 8(b) demonstrate the influence of B (catalyst concentration) and C (initial pH) on OTC removal efficiency. Being highly influenced by the initial pH of the solution in terms of its photolytic and hydrolytic stability in deionized water while presenting pKa values of 3.22, 7.46, and 8.94, OTC shows repulsive or attractive interactions with the amphoteric nature of the TiO₂-based photocatalyst in different pH levels. Thus, pH is expected to play a key role in OTC photocatalytic degradation experiments. As such, Figures 8(a) and 8(b) show that at an average OTC concentration of 125 mg/l, as initial pH level goes from acidic to basic (3 to 11), OTC removal efficiency decreases, proving the detrimental effect of basic pH levels to OTC mineralization. The observed decreasing trend can be

attributed to the presence of negatively charged OTC molecules at high pH (9 and above), with a high electrical density on the ring system, which tend to attract increasing concentration of reactive species such as an hydroxyl radicals, thus affecting OTC mineralization [47]. The low degree of OTC mineralization implies that consumed OTC mainly transforms to byproducts.

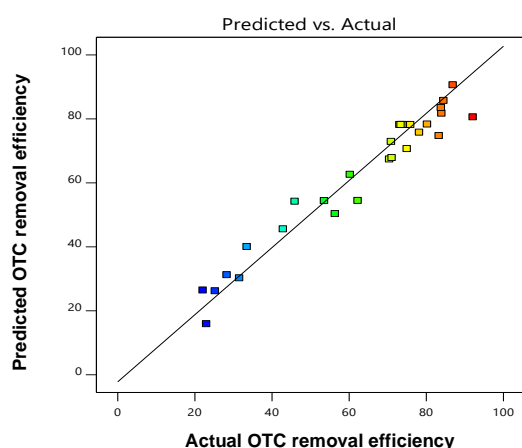
However, it is noted that progressive increase in the catalyst loading from 1 to 1.5 g/l led to a decreasing trend in the response. As observed, at higher than 1g/l catalyst loadings, turbidity increases leading to the unfavorable light scattering phenomenon, and thus, the reduction of light penetration into the suspension [48]. Consequently, the decreased photoactivated volume of the suspension resulted in lower OTC removal efficiencies.

TABLE 4. ANOVA results for the selected models regarding SRR

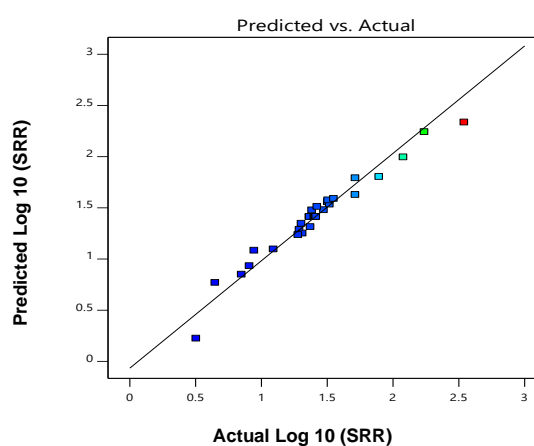
Source	Sum of Squares	df	Mean Square	F-value	p-value	
Model	5.04	7	0.7194	82.82	< 0.0001	Significant
A-OTC conc.	1.73	1	1.73	199.64	< 0.0001	Final Equation in Terms of Coded Factors
B-Cat. conc.	0.2903	1	0.2903	33.42	< 0.0001	
C-Initial pH	0.6458	1	0.6458	74.34	< 0.0001	
D-Reaction time	2.07	1	2.07	237.85	< 0.0001	
AB	0.1769	1	0.1769	20.36	0.0002	
AC	0.0335	1	0.0335	3.86	0.0623	
BC	0.0889	1	0.0889	10.24	0.0041	
Residual	0.1911	22	0.0087			
Lack of Fit	0.1885	17	0.0111	21.23	0.0016	Significant
Pure Error	0.0026	5	0.0005			
Cor Total	5.23	29				

Fit Statistics						
Std. Dev	Mean	C.V. %	R ²	Adjusted R ²	Predicted R ²	Adeq Precision
0.0988	1.41	6.99	0.9570	0.9458	0.8900	44.2257

$$\text{Log}_{10}(\text{SRR}) = +1.41 + 0.3242A - 0.1326B - 0.1978C - 0.3539D + 0.1051AB - 0.0746BC$$



(a)



(b)

Figure 7. Predicted vs. actual values plot for (a) OTC removal efficiency and (b) SRR

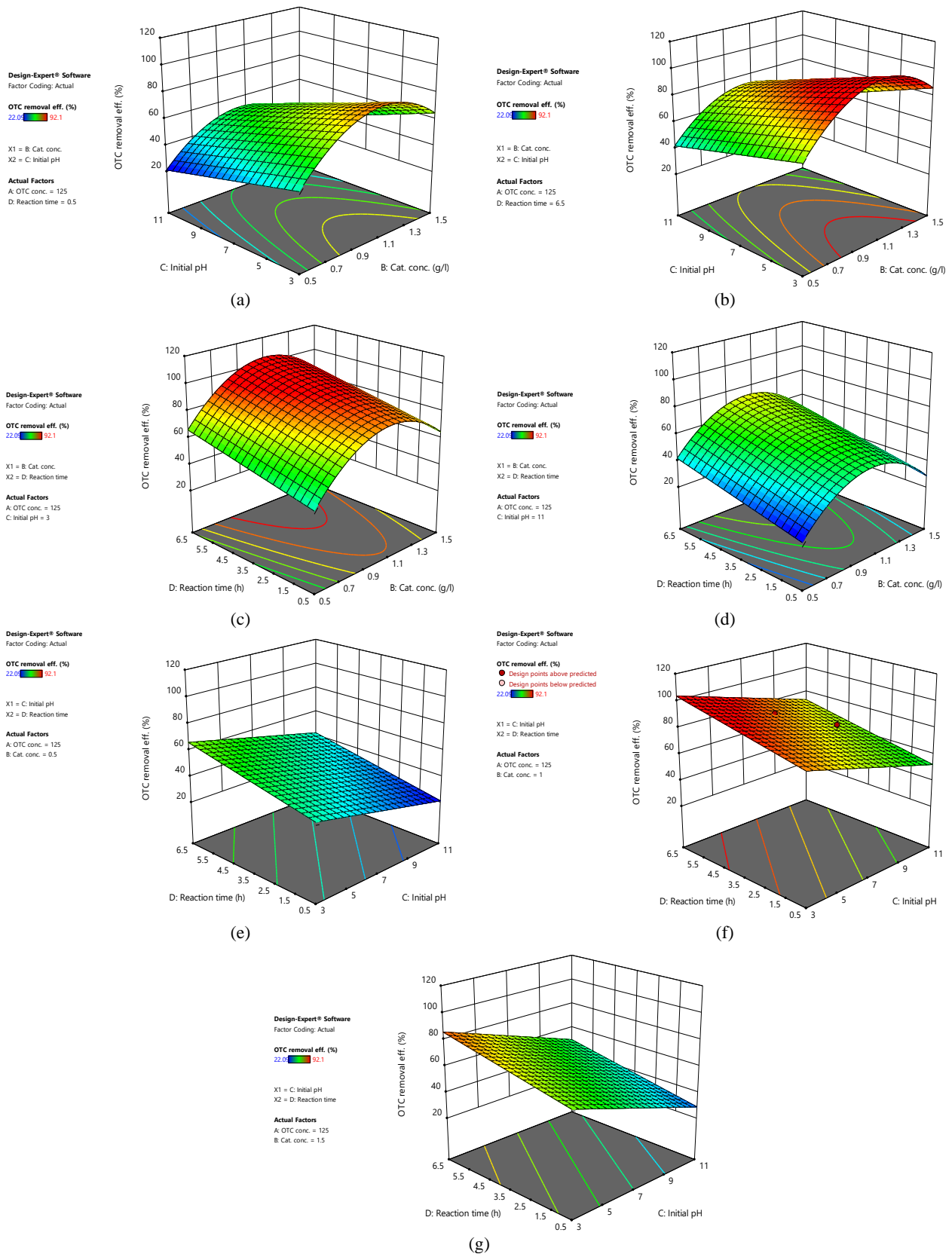


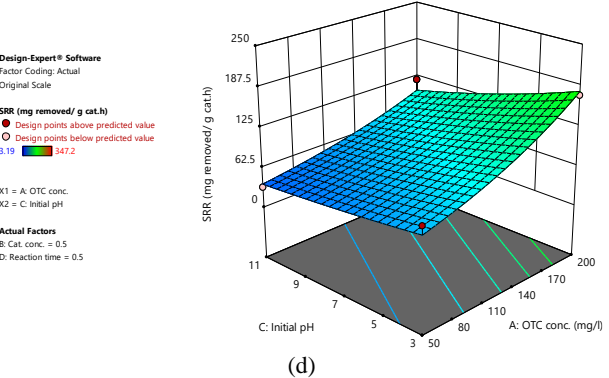
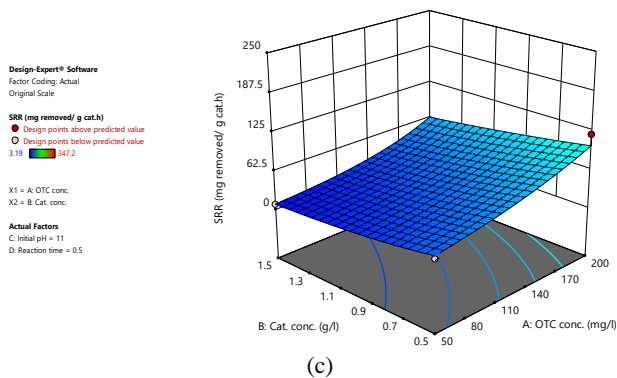
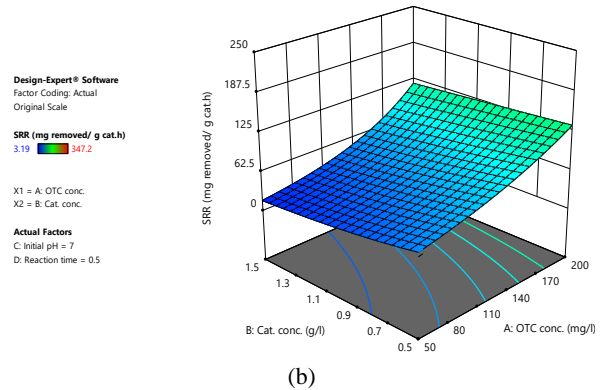
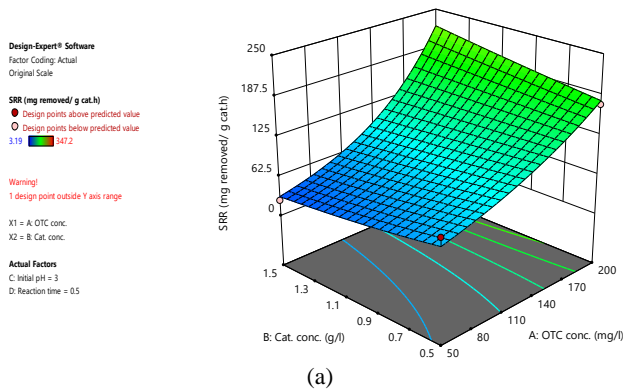
Figure 8. 3D surface plots of OTC removal for the most important pairs of factors: a and b) catalyst concentration and initial pH, c and d) catalyst concentration and reaction time, e, f and g) initial pH and reaction time

As indicated from both plots, the reaction time presented a linear positive effect on the response from 0.5 to 6.5 h. The influence of B (catalyst concentration) and D (reaction time) on the response is plotted in Figures 8(c) and 8(d). The aforementioned impact of catalyst loading on the response is represented again in these two plots, further proving the two consecutive ascending and descending trends observed below and above 1 g/l of catalyst loadings, respectively.

Favoring more effective contacts between the OTC and hydroxyl radicals, the conceivable effect of longer reaction time on the response was observed in both plots. Similarly, initial pH, showed a linear increasing impact on the response at the constant concentration of 125 mg/l of OTC.

Figures 8(e), 8(f), and 8(g) display the 3D surface plots of the response as a function of C (initial pH) and D (reaction time) at three different levels of catalyst concentration (0.5, 1, and 1.5 g/l) and average OTC concentration (125 mg/l). These plots further confirm the linear positive impacts of both initial pH and reaction time on the OTC removal efficiency. Meanwhile, the catalyst loading depicted a parabolic trend opening downward. It means that it has an increasing impact on removal efficiency until reaching catalyst concentration of 1 g/l and then reversing its impact from 1 to 1.5 g/l. In order to assess the overall photocatalytic performance, treatment capacity, and mass efficiency of the prepared

photocatalyst, specific OTC removal rate (SRR) was plotted as a function of different variables in Figures 9(a)-9g. The reaction time remained at the minimum level of 0.5 h. It is clear that reaction time has a decreasing impact on the SRR, referring to the possible surface poisoning of the catalyst. Figure 8 (a, b, and c) represents the response surface plots for the SRR as a function of A (OTC concentration) and B (catalyst concentration) at the minimum reaction time (0.5 h) and different initial pH levels (3, 7, and 11). As observed in these plots, initial pH has a decreasing impact on SRR owing to the repulsive interaction between the catalyst surface and contaminant at higher pH levels. Furthermore, Figures 9d and 9(e) represent the effects of A (OTC concentration) and C (initial pH) at constant minimum reaction time (0.5 h) and minimum and maximum levels of catalyst loading, further highlighting the impacts of catalyst loading and initial pH on this response. The 3D plots given in Figures 9(f) and 9(g) indicate the effects of B (catalyst concentration) and C (initial pH) at the minimum reaction time (0.5 h) and minimum and maximum OTC concentrations (50 and 200 mg/l, respectively). It is noted that at higher OTC concentrations and acidic pH of 3, catalyst loading shows an increasing trend, further confirming the enhanced mass efficiency of the photocatalyst in this condition. According to the plots shown in Figures 9(a), 9(e), and 9(g), maximum SRR of



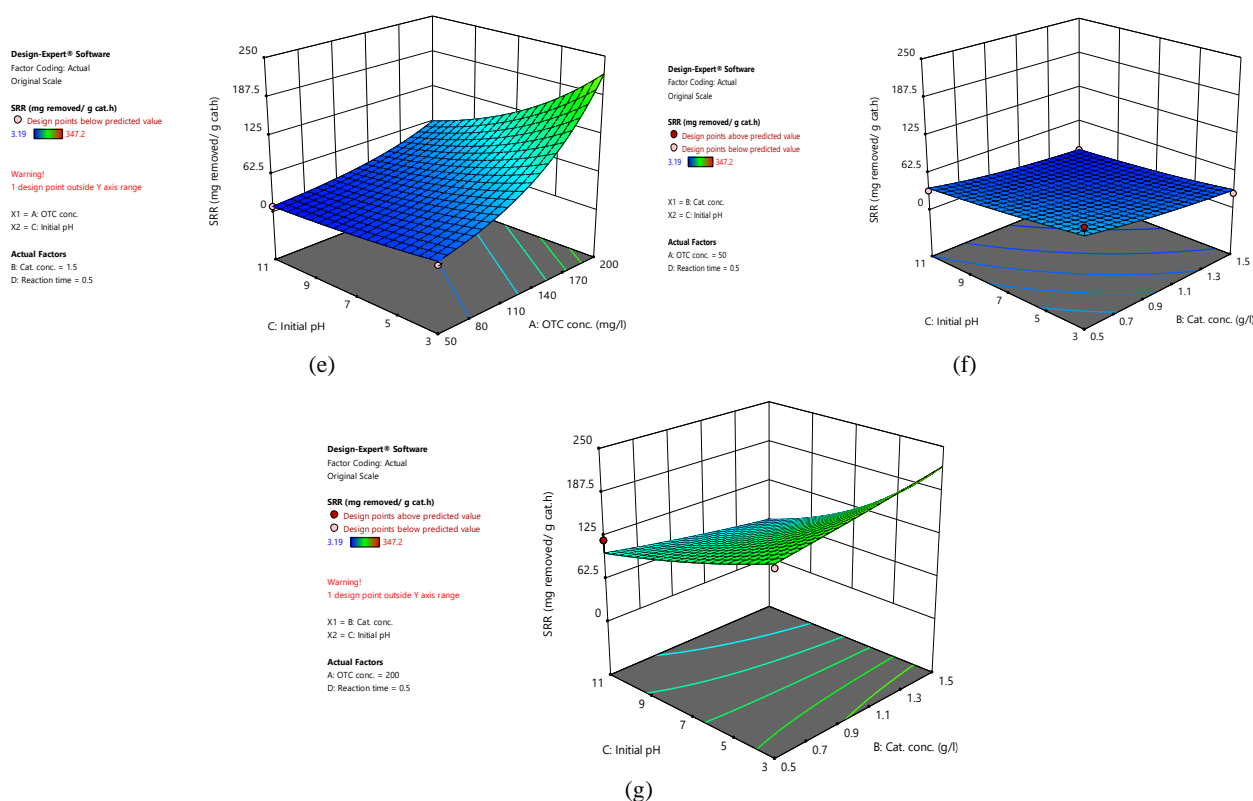


Figure 9. 3D surface plots of OTC removal for the most important pairs of factors: a, b, and c) catalyst concentration and OTC concentration, d and e) OTC concentration and initial pH, f and g) catalyst concentration and initial pH

approximately 220 mg OTC removed/g cat. h was obtained at initial pH of 3, minimum reaction time of 0.5 h, maximum catalyst loading of 1.5 g/l, and maximum OTC concentration of 200 mg/l.

3. 4. Photolytic Degradation of OTC under Controlled pH

A visible photolytic degradation experiment was carried out at the variation of pH values to monitor the OTC removal and mineralization without the addition of the photocatalyst. The results obtained after 6.5 h are given in Figure 9. As can be seen in Figure 10, after 390 min of visible light irradiation, only the range containing a minimum level of 3% to a maximum level of 22% of the initial OTC concentration was degraded at pH levels of 3 to 11 (3, 4.4, 5, 7, 9, and 11), respectively. As aforementioned in the previous part (Figures 8(a) and 8(b) analysis), as pH increases to 9 and above, the negatively charged OTC molecules tend to facilitate the photolytic degradation of OTC and, thus, the formation of more recalcitrant intermediates to mineralization, proving that photocatalysis plays a smaller role at such higher pH levels [47].

Overall, the negligible degree of OTC photolytic mineralization is enough proof of merely sufficient degradation of OTC molecules into more stable

intermediates in comparison to their photocatalytic degradation [47]. Furthermore, in order to assess the contribution of dark adsorption in OTC removal efficiency, the same experiments were carried out in darkness resulting in a minimum 1% to maximum 17% at pH values of 3 to 11 respectively.

3. 5. Reusability of the Fe-N-SiO₂-TiO₂ Photocatalyst

As shown in Figure 11, the reusability of the prepared modified photocatalyst used in the reactions was investigated by the degradation of OTC after 3 cycles under the same conditions. The used photocatalyst after each cycle was regenerated with 60-min aeration under visible light. As can be seen from the results, the photocatalyst could be reused without a significant loss in its activity after 3 successive runs and only an approximate reduction of 2-4% in the process performance was observed. The aforementioned loss might be caused by gradual poisoning and insignificant catalyst loss during supernatant removal after each cycle. Overall, the reusability results indicated the sufficient stability and reliability of the Fe-N-SiO₂/TiO₂ nanocomposite proving its potential for practical application.

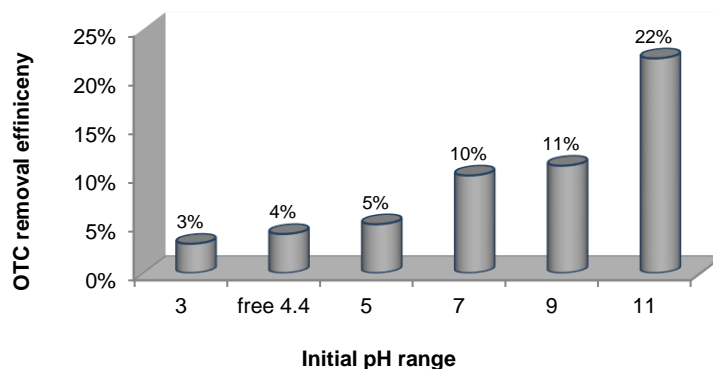


Figure 10. Photolytic degradation of OTC at different pH values (3-11) in the absence of Fe-N-SiO₂/TiO₂ under visible light irradiation for 390 min

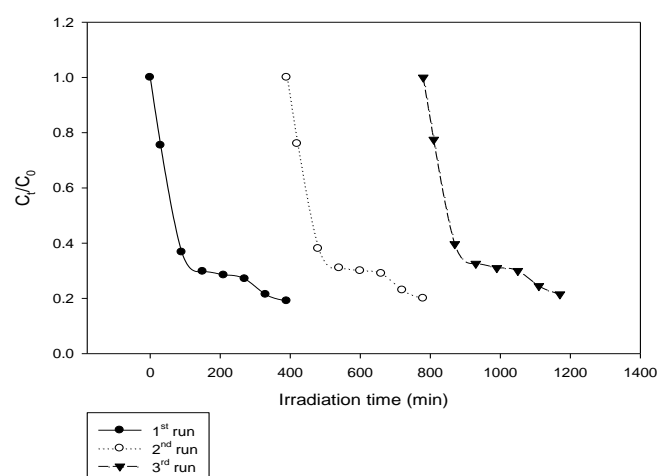


Figure 11. Reusability test of the Fe-N-SiO₂-TiO₂ photocatalyst degrading OTC during three successive runs after regular periodic regeneration using 60-min aeration under visible light

4. CONCLUSION

In the present study, in order to obtain the enhanced photocatalytic decomposition of the nonbiodegradable OTC compounds under visible light, the Fe-N-SiO₂/TiO₂ photocatalyst was successfully synthesized by sol-gel technique and its physical properties were characterized via FT-IR and SEM. The effects of OTC concentration, catalyst concentration, initial pH, and reaction time on the OTC removal efficiency and its SRR were evaluated using CCID under RSM. The reaction time had a positive effect on the OTC removal efficiency while a reverse impact was observed for the initial pH. As for the assessment of the optimum overall performance of the prepared photocatalyst, maximum SRR of 220 mg OTC removed/g cat. h at certain conditions (OTC Conc. = 200 mg/l, catalyst conc. = 1.5 g/l, pH = 3, and reaction time = 0.5 h) was obtained. Furthermore, the Fe-N-SiO₂/TiO₂

nanocomposite could easily be recovered and reused after 3 cycles without considerable loss in its photocatalytic activity.

5. ACKNOWLEDGEMENT

The authors would like to acknowledge Razi University for the financial support of present work to be accomplished and provided necessary facilities.

6. REFERENCES

- Patel, M., Kumar, R., Kishor, K., Mlsna, T., Pittman Jr, C.U. and Mohan, D., "Pharmaceuticals of emerging concern in aquatic systems: Chemistry, occurrence, effects, and removal methods", *Chemical Reviews*, Vol. 119, No. 6, (2019), 3510-3673. doi: 10.1021/acs.chemrev.8b00299.

2. Wang, P. and Yuan, Q., "Photocatalytic degradation of tetracyclines in liquid digestate: Optimization, kinetics and correlation studies", *Chemical Engineering Journal*, Vol. 410, (2021), 128327. doi: 10.1016/j.cej.2020.128327.
3. Wei, Z., Liu, J. and Shangguan, W., "A review on photocatalysis in antibiotic wastewater: Pollutant degradation and hydrogen production", *Chinese Journal of Catalysis*, Vol. 41, No. 10, (2020), 1440-1450. doi: 10.1016/S1872-2067(19)63448-0.
4. Roy, N., Alex, S.A., Chandrasekaran, N., Mukherjee, A. and Kannabiran, K., "A comprehensive update on antibiotics as an emerging water pollutant and their removal using nano-structured photocatalysts", *Journal of Environmental Chemical Engineering*, Vol. 9, No. 2, (2021), 104796. doi: 10.1016/j.jece.2020.104796.
5. Zhu, T.-t., Su, Z.-x., Lai, W.-x., Zhang, Y.-b. and Liu, Y.-w., "Insights into the fate and removal of antibiotics and antibiotic resistance genes using biological wastewater treatment technology", *Science of the Total Environment*, Vol. 776, (2021), 145906. doi: 10.1021/acs.est.9b01131.
6. Phoon, B.L., Ong, C.C., Saheed, M.S.M., Show, P.-L., Chang, J.-S., Ling, T.C., Lam, S.S. and Juan, J.C., "Conventional and emerging technologies for removal of antibiotics from wastewater", *Journal of Hazardous Materials*, Vol. 400, (2020), 122961. doi: 10.1016/j.jhazmat.2020.122961.
7. Baaloudj, O., Assadi, I., Nasrallah, N., El Jery, A., Khezami, L. and Assadi, A.A., "Simultaneous removal of antibiotics and inactivation of antibiotic-resistant bacteria by photocatalysis: A review", *Journal of Water Process Engineering*, Vol. 42, (2021), 102089. doi: 10.1016/j.jwpe.2021.102089.
8. Zangeneh, H., Zinatizadeh, A., Habibi, M., Akia, M. and Isa, M.H., "Photocatalytic oxidation of organic dyes and pollutants in wastewater using different modified titanium dioxides: A comparative review", *Journal of Industrial and Engineering Chemistry*, Vol. 26, (2015), 1-36. doi: 10.1016/j.jec.2014.10.043.
9. Sharma, M., Yadav, A., Mandal, M. and Dubey, K., "TiO₂ based photocatalysis: A valuable approach for the removal of pharmaceuticals from aquatic environment", *International Journal of Environmental Science and Technology*, Vol., No., (2022), 1-16. doi: 10.1016/j.ijhydene.2019.07.241.
10. Pereira, J.H., Reis, A.C., Queirós, D., Nunes, O.C., Borges, M.T., Vilar, V.J. and Boaventura, R.A., "Insights into solar TiO₂-assisted photocatalytic oxidation of two antibiotics employed in aquatic animal production, oxolinic acid and oxytetracycline", *Science of the Total Environment*, Vol. 463, (2013), 274-283. doi: 10.3390/catal11091039.
11. Jia, L., Jin, Y., Li, J., Wei, Z., Chen, M. and Ma, J., "Study on high-efficiency photocatalytic degradation of antibiotics based on a spiral microchannel reactor", *Industrial & Engineering Chemistry Research*, Vol. 61, No. 1, (2021), 554-565. doi: 10.1016/j.jclepro.2020.121725.
12. Chen, D., Cheng, Y., Zhou, N., Chen, P., Wang, Y., Li, K., Huo, S., Cheng, P., Peng, P. and Zhang, R., "Photocatalytic degradation of organic pollutants using TiO₂-based photocatalysts: A review", *Journal of Cleaner Production*, Vol. 268, (2020), 121725. doi: 10.1016/j.jclepro.2020.121725.
13. Basavarajappa, P.S., Patil, S.B., Ganganagappa, N., Reddy, K.R., Raghunath, A.V. and Reddy, C.V., "Recent progress in metal-doped TiO₂, non-metal doped/codoped TiO₂ and TiO₂ nanostructured hybrids for enhanced photocatalysis", *International Journal of Hydrogen Energy*, Vol. 45, No. 13, (2020), 7764-7778. doi: 10.1016/j.ijhydene.2019.07.241.
14. Jiang, D., Otitoju, T.A., Ouyang, Y., Shoparwe, N.F., Wang, S., Zhang, A. and Li, S., "A review on metal ions modified TiO₂ for photocatalytic degradation of organic pollutants", *Catalysts*, Vol. 11, No. 9, (2021), 1039. doi: 10.3390/catal11091039.
15. Akhter, P., Arshad, A., Saleem, A. and Hussain, M., "Recent development in non-metal-doped titanium dioxide photocatalysts for different dyes degradation and the study of their strategic factors: A review", *Catalysts*, Vol. 12, No. 11, (2022), 1331. doi: 10.3390/catal12111331.
16. Del Angel, R., Durán-Álvarez, J.C. and Zanella, R., "TiO₂-low band gap semiconductor heterostructures for water treatment using sunlight-driven photocatalysis", *Titanium Dioxide: Material for a Sustainable Environment*, Vol. 305, (2018). doi: 10.5772/intechopen.76501.
17. Sood, S., Umar, A., Mehta, S.K. and Kansal, S.K., "Highly effective Fe-doped TiO₂ nanoparticles photocatalysts for visible-light driven photocatalytic degradation of toxic organic compounds", *Journal of Colloid and Interface Science*, Vol. 450, (2015), 213-223. doi: 10.1016/j.jcis.2015.03.018.
18. Wang, J., Li, X., Ren, Y., Xia, Z., Wang, H., Jiang, W., Liu, C., Zhang, S., Li, Z. and Wu, S., "The effects of additive on properties of Fe-doped TiO₂ nanoparticles by modified sol-gel method", *Journal of Alloys and Compounds*, Vol. 858, (2021), 157726. doi: 10.1016/j.jallcom.2020.157726.
19. Xia, Z., Xing, S., Wang, H., Zhao, D., Wu, S., Jiang, W., Wang, N., Liu, S., Liu, C. and Ding, W., "Weak-visible-light-driven Fe-doped TiO₂ photocatalyst prepared by coprecipitation method and degradation of methyl orange", *Optical Materials*, Vol. 129, (2022), 112522. doi: 10.1016/j.optmat.2022.112522.
20. Kerkez-Kuyumcu, Ö., Kibar, E., Dayıoğlu, K., Gedik, F., Akın, N. and Özkara-Aydınoğlu, Ş., "A comparative study for removal of different dyes over m-TiO₂ (M= Cu, Ni, Co, Fe, Mn and Cr) photocatalysts under visible light irradiation", *Journal of Photochemistry and Photobiology A: Chemistry*, Vol. 311, (2015), 176-185. doi: 10.1016/j.jphotochem.2015.05.037.
21. Moradi, V., Jun, M.B., Blackburn, A. and Herring, R.A., "Significant improvement in visible light photocatalytic activity of Fe-doped TiO₂ using an acid treatment process", *Applied Surface Science*, Vol. 427, (2018), 791-799. doi: 10.1177/2633366X20906164.
22. Moradi, H., Eshaghi, A., Hosseini, S.R. and Ghani, K., "Fabrication of Fe-doped TiO₂ nanoparticles and investigation of photocatalytic decolorization of reactive red 198 under visible light irradiation", *Ultrasonics Sonochemistry*, Vol. 32, (2016), 314-319. doi: 10.1016/j.ultsonch.2016.03.025.
23. Chung, K.-H., Kim, B.-J., Park, Y.-K., Kim, S.-C. and Jung, S.-C., "Photocatalytic properties of amorphous n-doped TiO₂ photocatalyst under visible light irradiation", *Catalysts*, Vol. 11, No. 8, (2021), 1010. doi: 10.3390/catal11081010.
24. Park, J.T., Kim, D.J. and Kim, J.H., "A facile graft polymerization approach to n-doped TiO₂ heterostructures with enhanced visible-light photocatalytic activity", *Materials Letters*, Vol. 202, (2017), 66-69. doi: 10.1016/j.matlet.2017.05.070.
25. Bergamonti, L., Predieri, G., Paz, Y., Fornasini, L., Lottici, P. and Bondioli, F., "Enhanced self-cleaning properties of n-doped TiO₂ coating for cultural heritage", *Microchemical Journal*, Vol. 133, (2017), 1-12. doi: 10.1016/j.microc.2017.03.003.
26. Joseph, C.G., Taufiq-Yap, Y.H., Musta, B., Sarjadi, M.S. and Elilarasi, L., "Application of plasmonic metal nanoparticles in TiO₂-SiO₂ composite as an efficient solar-activated photocatalyst: A review paper", *Frontiers in Chemistry*, Vol. 8, (2021), 568063. doi: 10.3389/fchem.2020.568063.
27. Chun, H., Yizhong, W. and Hongxiao, T., "Influence of adsorption on the photodegradation of various dyes using surface bond-conjugated TiO₂/SiO₂ photocatalyst", *Applied Catalysis B: Environmental*, Vol. 35, No. 2, (2001), 95-105. doi: 10.1016/S0926-3373(01)00236-3.
28. Chun, H., Yizhong, W. and Hongxiao, T., "Preparation and characterization of surface bond-conjugated TiO₂/SiO₂ and photocatalysis for azo dyes", *Applied Catalysis B: Environmental*, Vol. 35, No. 2, (2001), 95-105. doi: 10.1016/S0926-3373(01)00236-3.

- Environmental*, Vol. 30, No. 3-4, (2001), 277-285. doi: 10.1016/S0926-3373(00)00237-X.
29. Chun, H., Yuchao, T. and Hongxiao, T., "Characterization and photocatalytic activity of transition-metal-supported surface bond-conjugated TiO₂/SiO₂", *Catalysis Today*, Vol. 90, No. 3-4, (2004), 325-330. doi.
 30. Zangeneh, H., Zinatizadeh, A.A., Zinadini, S., Feyzi, M., Rafiee, E. and Bahnemann, D.W., "A novel l-histidine (c, n) codoped-TiO₂-CDS nanocomposite for efficient visible photo-degradation of recalcitrant compounds from wastewater", *Journal of Hazardous Materials*, Vol. 369, (2019), 384-397. doi: 10.1016/j.jhazmat.2019.02.049.
 31. Zulfiqar, M., Samsudin, M.F.R. and Sufian, S., "Modelling and optimization of photocatalytic degradation of phenol via TiO₂ nanoparticles: An insight into response surface methodology and artificial neural network", *Journal of Photochemistry and Photobiology A: Chemistry*, Vol. 384, (2019), 112039. doi: 10.1016/j.jphotochem.2019.112039.
 32. Khuri, A.I. and Cornell, J.A., "Response surfaces: Designs and analyses: Revised and expanded, CRC press, (2018). doi: 10.1201/9780203740774
 33. Larumbe, S., Monge, M. and Gómez-Polo, C., "Comparative study of (n, fe) doped TiO₂ photocatalysts", *Applied Surface Science*, Vol. 327, (2015), 490-497. doi: 10.1016/j.apsusc.2014.11.137.
 34. Moradi, V., Ahmed, F., Jun, M.B., Blackburn, A. and Herring, R.A., "Acid-treated fe-doped TiO₂ as a high performance photocatalyst used for degradation of phenol under visible light irradiation", *Journal of Environmental Sciences*, Vol. 83, No., (2019), 183-194. doi: 10.1016/j.jes.2019.04.002.
 35. Ansari, S.A., Khan, M.M., Ansari, M.O. and Cho, M.H., "Nitrogen-doped titanium dioxide (n-doped TiO₂) for visible light photocatalysis", *New Journal of Chemistry*, Vol. 40, No. 4, (2016), 3000-3009. doi: 10.1039/C5NJ03478G.
 36. Houmard, M., Riassetto, D., Roussel, F., Bourgeois, A., Berthome, G., Joud, J. and Langlet, M., "Morphology and natural wettability properties of sol-gel derived TiO₂- SiO₂ composite thin films", *Applied Surface Science*, Vol. 254, No. 5, (2007), 1405-1414. doi: 10.1016/j.apsusc.2007.06.072.
 37. Zangeneh, H., Zinatizadeh, A.A., Feyzi, M., Zinadini, S. and Bahnemann, D.W., "Photomineralization of recalcitrant wastewaters by a novel magnetically recyclable boron doped-TiO₂- SiO₂ cobalt ferrite nanocomposite as a visible-driven heterogeneous photocatalyst", *Journal of Environmental Chemical Engineering*, Vol. 6, No. 5, (2018), 6370-6381. doi: 10.1016/j.jece.2018.10.001.
 38. Namkhang, P., An, W.-J., Wang, W.-N., Rane, K.S., Kongkachuichay, P. and Biswas, P., "Low temperature synthesis of n-doped TiO₂ nanocatalysts for photodegradation of methyl orange", *Journal of Nanoscience and Nanotechnology*, Vol. 13, No. 3, (2013), 2376-2381. doi: 10.1166/jnn.2013.7087 .
 39. Rosales, A., Ortiz-Frade, L., Medina-Ramirez, I.E., Godínez, L.A. and Esquivel, K., "Self-cleaning of SiO₂- TiO₂ coating: Effect of sonochemical synthetic parameters on the morphological, mechanical, and photocatalytic properties of the films", *Ultrasonics Sonochemistry*, Vol. 73, (2021), 105483. doi: 10.1016/j.ultsonch.2021.105483.
 40. Wan, H., Yao, W., Zhu, W., Tang, Y., Ge, H., Shi, X. and Duan, T., "Fe-n co-doped SiO₂@ TiO₂ yolk-shell hollow nanospheres with enhanced visible light photocatalytic degradation", *Applied Surface Science*, Vol. 444, (2018), 355-363. doi: 10.1016/j.apsusc.2018.03.016.
 41. Bharti, B., Barman, P. and Kumar, R., "Xrd analysis of undoped and fe doped TiO₂ nanoparticles by williamson hall method", in AIP Conference Proceedings, AIP Publishing LLC. Vol. 1675, (2015), 030025, doi: 10.1063/1.4929241.
 42. Habeeb, S.A., Hammadi, A.H., Abed, D. and Al-Jibouri, L.F., "Green synthesis of metronidazole or clindamycin-loaded hexagonal zinc oxide nanoparticles from ziziphus extracts and its antibacterial activity", *Pharmacia*, Vol. 69, No. 3, (2022), 855-864. doi: 10.3897/pharmacia.69.e91057.
 43. Wei, M., Song, N., Li, F., Qi, Z.-n. and Yao, M.-m., "Efficient photodegradation of organic pollutants with co-b codoped TiO₂/SiO₂ composite films under visible light irradiation", *Journal of Materials Science: Materials in Electronics*, Vol. 28, No. 8, (2017), 6320-6327. doi: 10.1007/s10854-016-6315-2.
 44. Rasoulnezhad, H., Hosseinzadeh, G. and Yekrang, J., "Preparation and characterization of nanostructured s and fe codoped TiO₂ thin film by ultrasonic-assisted spray pyrolysis method", *Journal of Nanostructures*, Vol. 8, No. 3, (2018), 251-258. doi: 10.22052/JNS.2018.03.4.
 45. Hosseini, O., Zare-Shahabadi, V., Ghaedi, M. and Azqhandi, M.A., "Experimental design, rsm and ann modeling of tetracycline photocatalytic degradation using LDH@ CN", *Journal of Environmental Chemical Engineering*, Vol. 10, No. 5, (2022), 108345. doi: 10.1016/j.jece.2022.108345.
 46. Reza, K.M., Kumy, A. and Gulshan, F., "Parameters affecting the photocatalytic degradation of dyes using TiO₂: A review", *Applied Water Science*, Vol. 7, No. 4, (2017), 1569-1578. doi: 10.1007/s13201-015-0367-y.
 47. Shaojun, J., Zheng, S., Daqiang, Y., Lianhong, W. and Liangyan, C., "Aqueous oxytetracycline degradation and the toxicity change of degradation compounds in photoirradiation process", *Journal of Environmental Sciences*, Vol. 20, No. 7, (2008), 806-813. doi: 10.1016/S1001-0742(08)62130-0.
 48. Balarak, D., Mengelizadeh, N., Rajiv, P. and Chandrika, K., "Photocatalytic degradation of amoxicillin from aqueous solutions by titanium dioxide nanoparticles loaded on graphene oxide", *Environmental Science and Pollution Research*, Vol. 28, No. 36, (2021), 49743-49754. doi: 10.1007/s11356-021-13525-1.

Persian Abstract

چکیده

برای بررسی مزایای سیستم نانوکامپوزیت Fe-N-SiO₂/TiO₂، تخریب فوتوکاتالیستی آنتی بیوتیک اکسی تتراسایکلین (OTC) توسط TiO₂ و کامپوزیت های اصلاح شده آن با ترکیب هر یک از دوپنت ها شامل N، Fe و SiO₂ تحت شرایط خاصی مورد بررسی قرار گرفتند. خواص ساختاری و نوری و همچنین مورفولوژی نانوکامپوزیت های تهیه شده نیز با استفاده از طیف (FT-IR)، پراش اشعه ایکس، طیف سنجی فوتولومینسانس، طیف های DRS و FESEM/EDX مشخص شد. به منظور توسعه دو مدل که روابط عملکردی مناسب بین دو پاسخ اصلی (بازده حذف OTC و سرعت حذف ویژه آن (SRR)) و چهار متغیر عددی (غلظت OTC، غلظت کاتالیست، pH اولیه و زمان واکنش) را نشان می دهند، دو مسیر تجزیه و تحلیل چند متغیره مجزا تحت روش سطح پاسخ (RSM) بکار گرفته شد. نتایج به دست آمده همگی به حداکثر (220 SRR (mg OTC removed/g cat. h) در حداکثر دوز کاتالیزور ۱.۵ گرم در لیتر و pH اسیدی ۳ پس از ۰.۵ ساعت کاهش یافت. علاوه بر این، Fe-N-SiO₂/TiO₂ یک فعالیت فوتوکاتالیستی پایدار را در طی سه آزمایش پشت سر هم ثابت کرد و پتانسیل قابل اعتماد آن را برای کاربردهای آینده روشن کرد.



A New Speed Control Approach of Linear Induction Motor Based on Robust RST Controller and Model Reference Adaptive System Estimator

L. Khettache^{*a}, R. Abdessemed^b

^a *Departement of Electrical Engineering, Kasdi Marbah Ouargla University, Algeria*

^b *LEB – Research Laboratory, Department of Electrical Engineering, Mostefa Benboulaïd-Batna 2 University, Algeria*

PAPER INFO

Paper history:

Received 05 July 2022

Received in revised form 23 December 2022

Accepted 24 December 2022

Keywords:

End-effect

Field-oriented

Control

Model Reference Adaptive System

RST

Polynomial

ABSTRACT

In this paper, a new model of linear induction motor including the impact of the end-effect on the motor performances is proposed. Moreover, a new strategy of control approach based on the Field-Oriented Control (FOC) technique is suggested and investigated. The proposed approach can provide a robust control strategy and overcome the limitations imposed by FOC technique, which suffers with some drawbacks in linear induction motor (LIM) such as sensitivity to parameter variations and imperfect dynamic tracking performance. In this context, the developed technique combines the benefits provided by the both approaches polynomial (RST) regulator and Model Reference Adaptive System (MRAS) observer, in order to achieve a robust controller by minimizing the external disturbances effects and reducing the influence of parameter variations. Moreover, it is revealed that the proposed control approach enables an improved rotor speed response with a reduced number of overshoot values as function of mass variations, where the recorded maximum overshoot value is 8%. Besides, the developed controller demonstrates a reduced rise and settling time values under wide applied external force conditions. This confirms that the proposed MRAS-RST technique offers a good dynamic response against the parameter variations. The accuracy and control performance of the proposed technique is checked and validated using Matlab/Simulink environment software tool. Simulation results show the effectiveness of the proposed estimator with improved better robustness for RST controller for different reference tracking and disturbance rejection parameters. These significant results make the proposed approach a promising technique dedicated to the design of high-performance controller, which is highly suitable for industrial and electrical applications.

doi: 10.5829/ije.2023.36.04a.03

1. INTRODUCTION

Linear induction motor (LIM), developed Linear induction motor (LIM), developed to achieving linear propulsion, has many advantages such as simple structure, alleviation of gear between motor and the motion devices, reduction of mechanical losses and the size of motion devices, high-speed operation, silence and high-starting thrust force [1-4]. Geometrically, the linear induction motor was inspired from the conventional rotational induction motor structure (RIM). Figure 1 shows a structure of the LIM to be investigated in this work. Besides, when the three phase supply is given to

coil assembly (stator winding) a magnetic field is created, this latter induces currents in the conducting layer on the surface of the secondary linear, which produces a second traveling magnetic field. The interaction of these two magnetic fields produces a thrust force, which tends to move the primary along the surface of the secondary linear at synchronous speed [5]. Basically, the most fundamental difference between LIM and rotary induction motor (RIM) is that LIM has dynamic end-effect phenomenon [6]. On the other hand, many researchers have concentrated on reducing the causes due to end effect and control of LIM's for the performance improvement [7]. To reach this goal, field-oriented

*Corresponding Author Institutional Email: khettache_laid@yahoo.fr
(L. khettache)

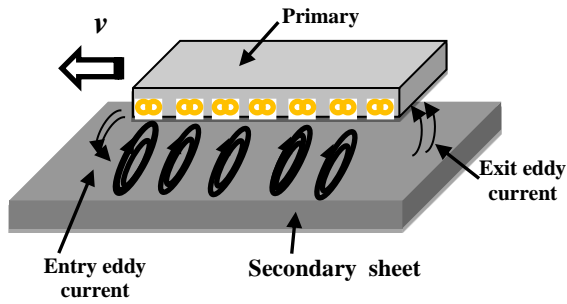


Figure 1. Structure of the LIM

control (FOC) of alternating current (AC) machines is becoming an important research topic of electrical engineering. The associated theory is based on making the AC motor identical to the separately excited DC motor. As well as, this technique (FOC) is performed by two basic methods namely direct and indirect vector control. For the direct FOC, the synchronous speed is computed based on the flux angle, which is available from flux estimator or flux sensors (Hall effects) [8]. In essence, the direct field oriented control can be adopted to decouple the dynamics of the thrust force and the secondary flux amplitude of the LIM. Despite this, a major drawback of this technique based on a proportional-integral (PI) regulator is its dependency on motor parameter variations and as imperfect dynamic tracking performance [9]. In this context, to solve the problem of parametric variations, a RST regulator was proposed.

In the RST design formalism, the most useful method to synthesize this controller is based on the well-known closed-loop poles placement [10]. Hence, the canonical RST structure considered in this contribution consists of three polynomials. In fact, the polynomials R and S allow creation of a feedback control in order to be robust to uncertainties, while the polynomial T is introduced to achieve the desired tracking performance [11]. Moreover, the RST controller is a robust and effective control strategy, that is widely used in industrial applications [12-15]. In addition, the performance studies of sensorless LIM drives concerning the variation effect of these parameters were subject of several previous works such as, the model reference adaptive system (MRAS) [16]. Numerous MRAS estimators based on various quantities have been proposed in the literature so far. These include MRAS based on: reactive power [17-21], rotor flux [22-24], active power [25], PY quantity [26], X quantity [27], q-axis rotor flux [28], d-axis stator voltage [29]. The basic concept of MRAS comprises two mathematical models which are simultaneously evaluated by Holakooie et al. [30]. These models are named respectively “reference model”, which is independent from uncertain model parameters, and “adjustable model” which is instead dependent on such

parameters. Moreover, an adaptation mechanism estimates the desired variable by driving the difference between the reference and adaptive model to zero. Motivated by the above discussed literature review, our main purpose here is to design a robust control based on a combination between a polynomial RST regulator for control speed and MRAS observer for rotor speed estimation in order to achieve high stability and reduced sensitivity to the linear induction machine parameters.

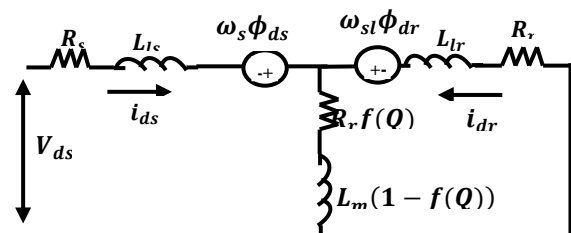
This paper is organized as follows. Section 2 describes the linear induction motor (LIM) dynamic model in the coordinate d-q while a theoretical background of field oriented motor control principle is explained in sections 3. The section 4 presents the structure and stability of the proposed MRAS observer, and its implementation for motor speed estimation. Section 5 deals with RST regulator for speed control. The performance and robustness of the proposed controller scheme are evaluated under MATLAB /SIMULINK environment; and the Simulation results are depicted to confirm the analysis and the efficiency of the proposed technique in section 6. Finally, section 7 summarizes the findings and concludes the paper.

2. MODEL OF LINEAR INDUCTION MOTOR

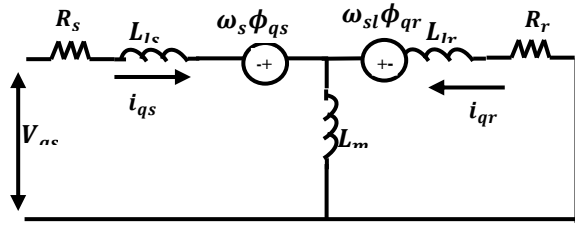
In recent decades, a number of papers on the LIM performance analysis, involving steady and dynamic states, have been published [31]. Gieras et al. [32] and Faiz et al. [33] developed an equivalent circuit by superposing the synchronous wave and the pulsating wave caused by the end-effect. In this section, the dynamic model of the LIM is described based on the d-q model of the equivalent electrical circuit considering end-effects [34].

As illustrated in Figures 2(a) and 2(b), the equivalent circuit of LIM can be separated in two parts, where the first one is independent from the end-effects (identical to the q-axis equivalent circuit of the induction motor) and the second one is dependent on this effect (d-axis in which the parameters vary with the end-effects).

By applying Kirchhoff's-voltage-law (KVL) to above circuits, the below voltage equations of LIM in synchronously rotating frame are expressed as follows:



(a) d-axis equivalent circuit



(b) q- axis equivalent circuit

Figure 2. LIM equivalent electrical circuit taking into account end-effects [5, 31]

$$\begin{cases} V_{ds} = R_s i_{ds} + R_r f(Q)(i_{ds} + i_{dr}) + \frac{d\phi_{ds}}{dt} - \omega_s \phi_{qs} \\ V_{qs} = R_s i_{qs} + \frac{d\phi_{qs}}{dt} + \omega_s \phi_{ds} \\ 0 = R_r i_{dr} + R_r f(Q)(i_{ds} + i_{dr}) + \frac{d\phi_{dr}}{dt} - \omega_{sl} \phi_{qr} \\ 0 = R_r i_{qr} + \frac{d\phi_{qr}}{dt} + \omega_{sl} \phi_{dr} \end{cases} \quad (1)$$

The primary angular frequency can be determined by adding the secondary angular speed with the slip frequency. This will give as follows:

$$\omega_s = \omega_{sl} + \omega_r \quad (2)$$

The transformation of linear speed of the LIM to an angular speed is given below:

$$\omega_r = \frac{\pi}{\tau_p} v \quad (3)$$

with τ_p : is the pole pitch

The linkage fluxes are given by the following equations:

$$\begin{cases} \phi_{ds} = L_{ls} i_{ds} + L_m (1 - f(Q))(i_{ds} + i_{dr}) \\ \phi_{qs} = L_{ls} i_{qs} + L_m (i_{ds} + i_{dr}) \\ \phi_{dr} = L_{lr} i_{dr} + L_m (1 - f(Q))(i_{ds} + i_{dr}) \\ \phi_{qr} = L_{lr} i_{qr} + L_m (i_{ds} + i_{dr}) \end{cases} \quad (4)$$

where Q is an important parameter, it is used to express the end-effects phenomenon:

$$Q = \frac{D R_r}{(L_m + L_{lr}) v} \quad (5)$$

where D denotes the primary length, v the speed of a LIM, and L_{lr} and R_r the secondary inductance and resistance, respectively.

The three-phase magnetizing inductance varying with Q is defined as follows:

$$\hat{L}_m = L_m [1 - f(Q)] \quad (6)$$

where:

$$f(Q) = \frac{1 - e^{-Q}}{Q} \quad (7)$$

Considering the eddy current losses, there is a resistance appearing in the transversal branch, the resistance \hat{R}_r is:

$$\hat{R}_r = R_r f(Q) \quad (8)$$

The dynamic equation of LIM is expressed as follows:

$$F_e = Mv + B\dot{v} + F_L \quad (9)$$

where electromagnetic thrust F_e is defined as follows:

$$F_e = \frac{3\pi}{2\tau_p} \frac{p}{2} (\phi_{ds} i_{qs} - \phi_{qs} i_{ds}) \quad (10)$$

and

$$\begin{aligned} F_e &= \frac{3\pi}{2\tau_p} \frac{p}{2} \frac{L_m (1 - f(Q))}{L_r - L_m f(Q)} (\phi_{dr} i_{qs} - \phi_{qr} i_{ds}) \\ &= Mv + B\dot{v} + F_L \end{aligned} \quad (11)$$

2. FIELD ORIENTED VECTOR CONTROL

The main of the field oriented control is to maintaining constant the d-axis secondary flux and making null the q-axis secondary flux [5, 35]. Figure 3 depicts the dynamic model of FOC applied to LIM considering end-effect in the synchronously rotating reference frame [36].

Under the rotor flux orientation conditions, the rotor flux is aligned on the d-axis of the d-q rotor flux oriented frame and the rotor flux equations can be written as follows:

$$\begin{cases} \phi_{qr} = 0 \\ \phi_{dr} = \phi_r = constant \end{cases} \quad (12)$$

Substituting Equations (12) in the rotor linkage fluxes Equations (4), the rotor currents are derived as in Equations (13) and (14).

$$i_{dr} = \frac{\phi_r - \hat{L}_m i_{ds}}{L_r} \quad (13)$$

with $L_r = L_{lr} + L_m [1 - f(Q)]$

$$i_{qr} = \frac{-L_m i_{qs}}{L_{lr} + L_m} \quad (14)$$

where: L_r is the secondary inductance, L_{lr} the secondary leakage inductance, and L_m the magnetizing inductance.

Using Equations (12) to (14) in stator voltage of Equation (1), the differential equations of decoupling current and voltage compensation can be expressed as follows:

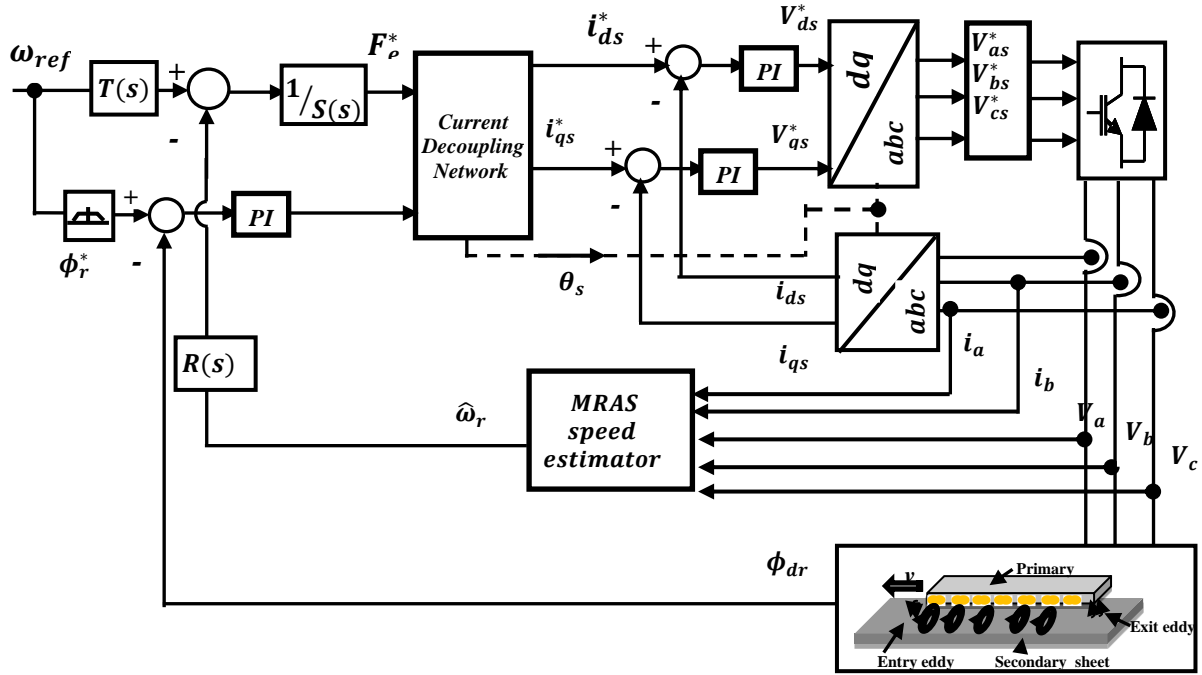


Figure 3. Block diagram of the field oriented control for LIM

$$\begin{cases} V_{ds} = \left(R_s + \hat{R}_r - \frac{\hat{R}_r \cdot \hat{L}_m}{L_r} \right) i_{ds} + \frac{\hat{R}_r}{L_r} \phi_r + \sigma L_s \frac{di_{ds}}{dt} - \omega_s \sigma' i_{ds} \\ V_{qs} = R_s i_{qs} + \sigma' \frac{di_{qs}}{dt} + \omega_s \sigma L_s i_{ds} + \omega_s \frac{\hat{L}_m}{L_r} \phi_r \end{cases} \quad (15)$$

As shown in Equation (15), the stator voltage components are coupled by the d- and q- back electromotive force given by:

$$\begin{cases} E_d = -\frac{\hat{R}_r}{L_r} \phi_r + \omega_s \sigma' i_{ds} \\ E_q = -\omega_s \sigma L_s i_{ds} - \omega_s \frac{\hat{L}_m}{L_r} \phi_r \end{cases} \quad (16)$$

Finally, the feed forward decoupling method [37] is applied in order to have linear terms as provided below:

$$\begin{cases} V'_{ds} = \left(R_s + \hat{R}_r - \frac{\hat{R}_r \cdot \hat{L}_m}{L_r} \right) i_{ds} + \sigma L_s \frac{di_{ds}}{dt} \\ V'_{qs} = R_s i_{qs} + \sigma' \frac{di_{qs}}{dt} \end{cases} \quad (17)$$

$$L_s = L_{ls} + \hat{L}_m \quad (18)$$

$$\begin{cases} \sigma = 1 - \frac{\hat{L}_m^2}{L_s L_m} \\ \sigma' = (L_{ls} + L_m) - \frac{\hat{L}_m^2}{(L_{lr} + L_m)} \end{cases} \quad (19)$$

where: σ, σ' the leakage coefficients associated to cases with and without end-effect, respectively.

Thus, the thrust force is represented in the rotor flux oriented reference frame as follows:

$$F_e^* = K_f \cdot i_{qs}^* \quad (20)$$

$$K_f = \frac{3\pi p}{2\tau_p} \frac{L_m(1-f(Q))}{2L_r - L_m f(Q)} \phi_{dr}^* \quad (21)$$

$$i_{qs}^* = \frac{4\tau_p}{3\pi p} \frac{L_r - L_m f(Q)}{L_m(1-f(Q))} \frac{F_e^*}{\phi_{dr}^*} \quad (22)$$

3. STRUCTURE OF MRAS TECHNIQUE

The model reference adaptive system (MRAS) is one of the most popular adaptive observers used in sensorless drive control applications. In this paper, The MRAS model employs two independent equations for the time derivative of rotor fluxes as shown in Figure 4, where it is obtained from equations of the LIM model in the stationary reference frame α - β . In fact, the system that does not include the estimated rotor speed is called a reference Model (MR), while the other one is called the adaptive Model (MA) [38, 39]. A proportional-integral (PI) control adjusts the error between the reference and adjustable model with the aim of developing a suitable adaptation mechanism, which generates the estimated rotor speed [40].

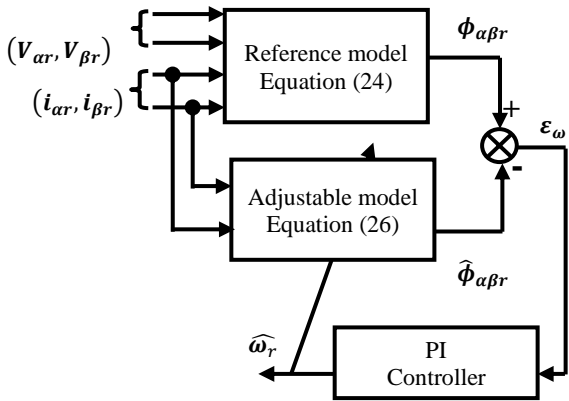


Figure 4. Speed estimation of the linear induction motor using MRAS

3. 1. Reference Model The reference model (MR) is expressed by using stator voltage Equation (1) in stationary reference frame $\omega_s=0$):

$$\begin{cases} V_{\alpha s} = R_s i_{\alpha s} + R_r f(Q)(i_{\alpha s} + i_{\alpha r}) + \frac{d\phi_{\alpha s}}{dt} \\ V_{\beta s} = R_s i_{\beta s} + \frac{d\phi_{\beta s}}{dt} \end{cases} \quad (23)$$

Substituting Equation (13) into (23), and with some mathematical manipulations, the reference model is derived as follows:

$$\begin{cases} \frac{d\phi_{\alpha s}}{dt} = \frac{L_r}{L_m} \left[V_{\alpha s} - \left(\hat{R}_s - \frac{\hat{L}_m}{L_r} \right) i_{\alpha s} - \sigma \frac{di_{\alpha s}}{dt} - \frac{\hat{R}_r}{L_r} \phi_{\alpha r} \right] \\ \frac{d\phi_{\beta s}}{dt} = \frac{L_r + L_m}{L_m} \left[V_{\beta s} - R_s i_{\beta s} - \sigma \frac{di_{\beta s}}{dt} \right] \end{cases} \quad (24)$$

$$\hat{R}_s = R_s + R_r f(Q) \quad (25)$$

3. 2. Adaptive Model Similarly, the adjustable model (MA), is determined by substituting (13) into rotor voltage Equation (1), the expression of (MA) in stationary reference frame ($\omega_{sl}=-\omega_r$) becomes [41]:

$$\begin{cases} \frac{d\hat{\phi}_{\alpha r}}{dt} = - \left(\hat{R}_r - \frac{\hat{L}_m}{L_r} \right) i_{\alpha s} - \frac{\hat{R}_r}{L_r} \hat{\phi}_{\alpha r} - \hat{\omega}_r \hat{\phi}_{\beta r} \\ \frac{d\hat{\phi}_{\beta s}}{dt} = \frac{R_r}{L_r + L_m} \left[L_m i_{\beta s} - \hat{\phi}_{\beta r} \right] + \hat{\omega}_r \hat{\phi}_{\alpha r} \end{cases} \quad (26)$$

where:

$$\hat{R}_r = R_r + R_r f(Q) \quad (27)$$

3. 3. Adaptation Mechanism Model The adaptation algorithm is based on the error between the estimated and the measured rotor fluxes based on the

Lyapunov function. This error is defined by equation (28), and driven to zero by means of a *proportional-integral* PI regulator, where its output generates the estimated rotor speed ($\hat{\omega}_r$) in Equation (29) [42].

$$\varepsilon_{\omega} = \phi_{\beta r} \hat{\phi}_{\alpha r} - \phi_{\alpha r} \hat{\phi}_{\beta r} \quad (28)$$

$$\hat{\omega}_r = \left(K_p + \frac{K_i}{p} \right) \varepsilon_{\omega} \quad (29)$$

The implementation of the MRAS observer is shown in Figure 4.

4. RST CONTROLLER

In this section, the canonical RST regulator elucidated in Figure 5 is proposed in order to achieve the effectiveness and robustness rotor speed control of the LIM.

The polynomials R(s), S(s) and T(s) are obtained by a pole-placement strategy and solutions of the Diophantine equation [13, 40]:

$$A(s)S(s) + B(s)R(s) = P_D(s)P_F(s) = P(s) \quad (30)$$

where: $P(s)$ the desired closed loop poles; it is decomposed into two parts, one representing the desired dominant poles $P_D(s)$ and the other corresponding to the auxiliary poles $P_F(s)$ that are necessary to adjust the sensitivity function as described below. The polynomials R(s), S(s) and T(s) are given by:

$$\begin{cases} R(s) = r_1 s + r_0 \\ S(s) = s_2 s^2 + s_1 s \end{cases} \quad (31)$$

where: $deg(R) = deg(A) = 1$ and $deg(S) = deg(A) + 1$

The closed-loop transfer function is given by:

$$H_{BF}(s) = \frac{T(s)B(s)}{A(s)S(s) + B(s)R(s)} \quad (32)$$

The calculation of the polynomials R and S is carried out starting from the choice of polynomial P:

$$P(s) = p_0 + p_1 s + p_2 s^2 + p_3 s^3 \quad (33)$$

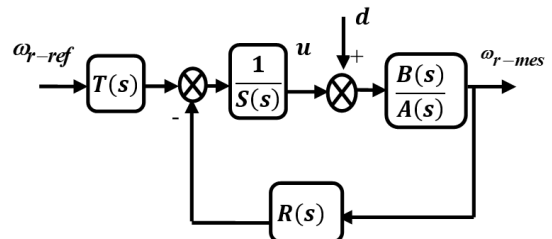


Figure 5. RST closed loop configuration [39]

Within the strategy of robust pole placement, the polynomial $P(s)$ is written as follows:

$$P(s) = P_D(s)P_F(s) = \left(s + \frac{1}{T_c}\right) \left(s + \frac{1}{T_f}\right)^2 \quad (34)$$

such that:

P_D : Command polynomial;

P_F : Filter polynomial;

T_c : Control horizon;

T_f : Filtering horizon;

To determine the coefficients of T , we assume that $T=R(0)$.

In the proposed model, we have:

The denominator A and the numerator B of the transfer function rotor speed is defined by:

$$\begin{cases} A = Js + f \\ B = 1 \end{cases} \quad (35)$$

By identification between Equations (30), (31) and (34), it is possible to obtain a system of four equations with four unknown terms [43]. Thus, we can determine the polynomial coefficients $R(s)$ and $S(s)$ by using Sylvester matrix as follows:

$$\begin{bmatrix} p_0 \\ p_1 \\ p_2 \\ p_3 \end{bmatrix} = \begin{bmatrix} J & 0 & 0 & 0 \\ f & J & 0 & 0 \\ 0 & f & 1 & 0 \\ 0 & 0 & 0 & 1 \end{bmatrix} \begin{bmatrix} s_2 \\ s_1 \\ r_1 \\ r_0 \end{bmatrix} \quad (36)$$

5. SIMULATION RESULTS

The main goal of this paper is the investigation of the speed control of LIM with the consideration of the end-effects. For this purpose, the parameters and data of the LIM used in this research and Gains of RST regulator, PI controllers used to estimate the speed are summarized in Tables 1 and 2, respectively.

TABLE 1. Linear Induction Motor Parameters

Parameters	Values
Primary resistance- R_s	1.25Ω
Secondary resistance- R_r	2.7Ω
Primary leakage inductance- L_{ls}	40.1mH
Secondary leakage inductance- L_{lr}	33.1mH
Magnetizing inductance- L_m	32.6mH
Pole pitch- τ_p	0.0641m
Primary length- D	0.286 m
Mass of the LIM- M	8 kg
Number of pole pairs - p	4

TABLE 2. Regulator values

RST	MRAS
$r_0 = 6056.25$	Kp=0.128
$r_1 = 215.75$	Ki=130
$s_1 = 31.875$	/
$s_2 = 0.125$	/
$T(0) = t=6056.25$	/

In Figure 6, it can be observed the external force of $F_L=50 N$ disturbance at $t= 2.5s$ then the motor reference speed is changed from 150 (rad/s) to 250 (rad/s) at $t=5 s$. Hence, the results display clearly satisfactory performance for the proposed (RST-MRAS) control schema in tracking and a pursuit between measured (blue line) and estimated speed (green line) of the reference speed (red line).

Furthermore, in order to check the robustness of the proposed controllers, the obtained results during modified mass operating condition (M (kg) is doubled from its nominal value) are discussed in figures below.

Figure 7 displays the estimated speed under mass variation ($2 \times M$); very small change has observed in the response shape (the doubled mass does not have any influence on the MRAS observer).

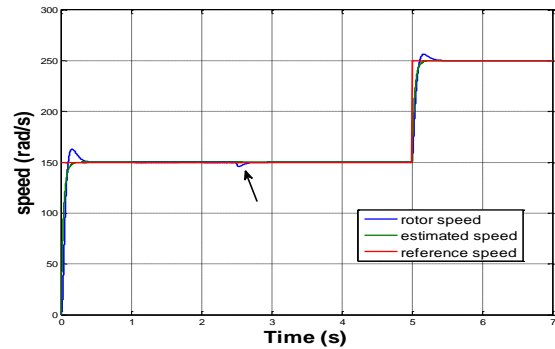


Figure 6. Rotor speed response without mass variation

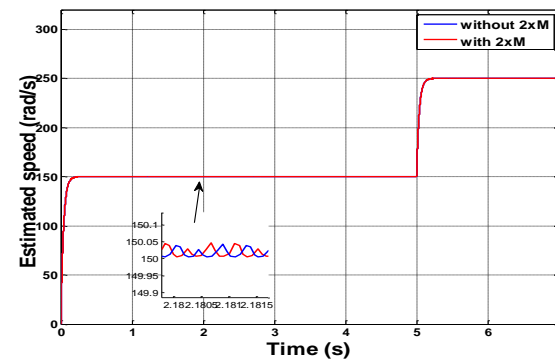


Figure 7. Estimated speed response with mass variation ($2 \times M$)

As one can see, the measured speed follows the reference with negligible error as observed in Figure 8. The speed was reached satisfactory without oscillating when a load force is applied.

From field orientation theory, which based on the decoupling between force and rotor flux linkage, the rotor force can be independently controlled by adjusting stator q component current i_{qs} (see Equation (20)). This can be depicted in Figure 9(b), where the i_{qs} value ($i_{qs}=0.74A$) is determined accordingly to reference force. Figure 9(a) shows that the current component i_{ds} is in direct relation with the rotor flux linkage, which is maintained constant during control simulation ($i_{ds}=18.84A$). Note that the last one change with speed reference variation ($i_{ds} = 26.43 A$) at $t=5 s$.

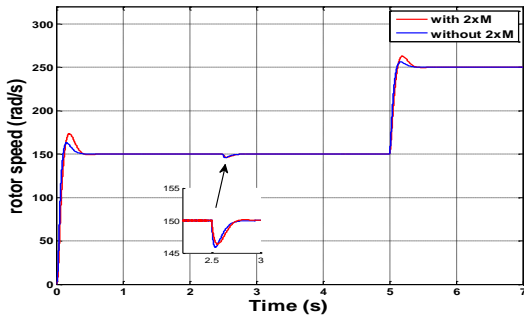
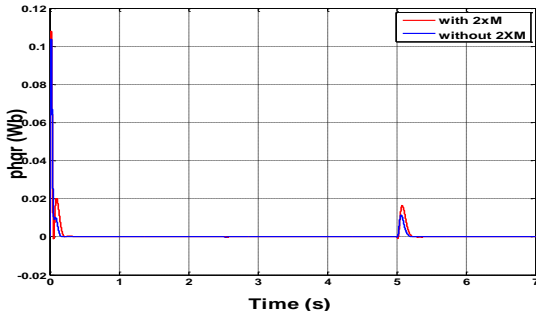
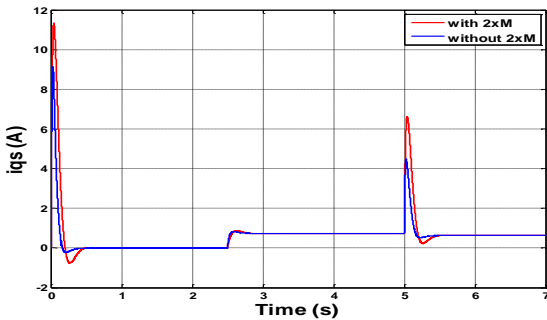


Figure 8. Speed response where blue line is without mass variation and red line is with $2 \times M$



(a) d-axis current



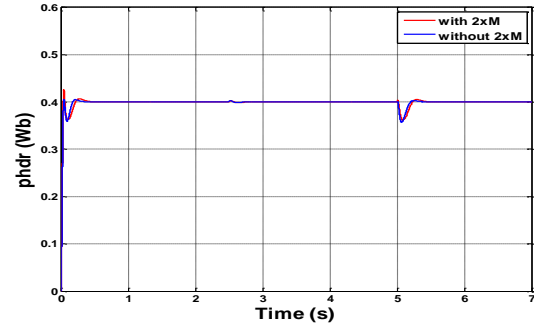
(b) q-axis current

Figure 9. Primary current

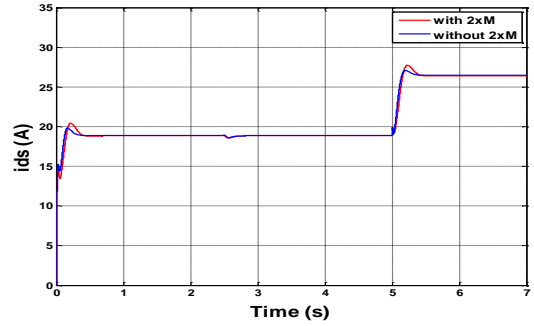
The direct and quadrature rotor flux are shown in Figure 10(a) and Figure 10(b) respectively. It can be seen that ϕ_{dr} converges to reference value $\phi_{dr} = 0.4 Wb$, while ϕ_{qr} is maintained at zero ($\phi_{qr} = 0 Wb$). When the speed reference changes, a remarkable peaks are observed at $t=5 s$. The results indicate good decoupling properties of the vector controller (i.e the Equation (12) is justified).

From Figure 11, the electromagnetic forces increase to reach the peak values 400N and 600N (start-up phenomena) and falls down to be close to zero value because the LIM is operating in no-load. Under load conditions, a high peak force values are observed (300 N and 400 N) at $t = 5 s$.

In order to test the robustness of the proposed controller; a comparative dynamic performance (overshoot, rise time, settling time) is shown in Table 3.



(a) d-axis flux with reference 0.4Wb



(b) q-axis flux with reference 0 Wb

Figure 10. Primary flux

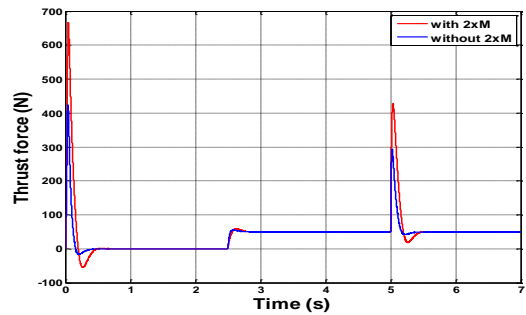


Figure 11. Thrust force

TABLE 3. Rotor speed performance under Mass variation

	M	100% M
	(Ov %)= 7.86%	(Ov %)=15.53%
Rotor speed response (rad/s)	Rise time t_r =0.105	Rise time t_r =0.12
	Peak time t_p =0.161	Peak time t_p =0.1964
	Settling time t_s =0.5	Settling time t_s =0.58

It is important to note that the variation of parameters at the same time deteriorates the performance of the controller (i.e. PI, PID) in terms of response time, oscillation and tracking. Through Table 3, we can say that the response time is significantly reduced with a small overshoot and the oscillation was eliminated. Considering these significant benefits, the proposed controller based on the combination between RST and MRAS estimator is believed to offer new potential directions for high-performance control than recently study [6, 30, 44].

5. CONCLUSION

In this paper, a new model based on field oriented control (FOC) technique is proposed to control a linear induction motor (LIM) by taking into account the end-effects; the FOC is implemented to separately control the produced force and magnetizing flux components. An effective control strategy is proposed using a combined RST regulator and MRAS observer approach to enhance the control procedure by minimizing the effect of parameters variation and reducing the impact of perturbations (external forces) on the control approach. Finally, the effectiveness of the proposed technique is confirmed through MATLAB/SIMULINK simulations, where good tracking to the reference values is recorded under external perturbations and superiority of robustness to internal parameters changes. These significant results make the proposed approach a promising control strategy dedicated to the design of high-performance and reliable controllers, which are highly suitable for industrial and engineering applications. It is worthy to note that this work can be extended by including new advanced techniques based on Artificial Intelligence and deep machine learning to improve the controller performances and stability behavior. However, new complex models and simulations should be developed.

6. REFERENCE

- Loukianov, A., Rivera, J., Alanis, A.Y. and Raygoza, J., "Super-twisting sensorless control of linear induction motors", in 2012 9th International Conference on Electrical Engineering, Computing Science and Automatic Control (CCE), IEEE. (2012), 1-5.
- Kang, G. and Nam, K., "Field-oriented control scheme for linear induction motor with the end effect", *IEEE Proceedings-Electric Power Applications*, Vol. 152, No. 6, (2005), 1565-1572. doi: 10.1049/ip-pa:20045185.
- Lin, F.-J. and Lee, C.-C., "Adaptive backstepping control for linear induction motor drive to track periodic references", *IEEE Proceedings-Electric Power Applications*, Vol. 147, No. 6, (2000), 449-458. doi: 10.1049/ip-pa:20000647.
- Lin, F.-J., Wai, R.-J., Chou, W.-D. and Hsu, S.-P., "Adaptive backstepping control using recurrent neural network for linear induction motor drive", *IEEE Transactions on Industrial Electronics*, Vol. 49, No. 1, (2002), 134-146. doi: 10.1109/41.982257.
- Liu, J., Lin, F., Yang, Z. and Zheng, T.Q., "Field oriented control of linear induction motor considering attraction force & end-effects", in 2006 CES/IEEE 5th International Power Electronics and Motion Control Conference, IEEE. Vol. 1, (2006), 1-5.
- Zhang, L., Dong, Z., Zhao, L. and Laghrouche, S., "Sliding mode observer for speed sensorless linear induction motor drives", *IEEE Access*, Vol. 9, (2021), 51202-51213. doi: 10.1109/ACCESS.2021.3067805.
- Hamzeshbahmani, H., "Modeling and simulating of single side short stator linear induction motor with the end effect", *Journal of Electrical Engineering*, Vol. 62, No. 5, (2011), 302. <https://doi.org/10.2478/v10187-011-0048-5>
- Pucci, M., "Direct field oriented control of linear induction motors", *Electric Power Systems Research*, Vol. 89, (2012), 11-22. <https://doi.org/10.1016/j.epsr.2012.01.012>
- Markov, B. and Tsankova, D., "Mit rule based model reference adaptive control of linear induction motor", *Annals of the Faculty of Engineering Hunedoara*, Vol. 12, No. 3, (2014), 95.
- Poitiers, F., Bouaouiche, T. and Machmoum, M., "Advanced control of a doubly-fed induction generator for wind energy conversion", *Electric Power Systems Research*, Vol. 79, No. 7, (2009), 1085-1096. <https://doi.org/10.1016/j.epsr.2009.01.007>
- Jacknoon, A., Hassan, M. and El Ferik, S., "Design of rst controllers based on intelligent optimization algorithms", in 2016 Conference of Basic Sciences and Engineering Studies (SGCAC), IEEE., (2016), 177-182.
- Abdurraqueeb, A.M., Al-Shamma'a, A.A., Alkuhayli, A., Noman, A.M. and Addoweesh, K.E., "Rst digital robust control for dc/dc buck converter feeding constant power load", *Mathematics*, Vol. 10, No. 10, (2022), 1782. doi: 10.3390/math10101782.
- Boudallaa, A., Chennani, M., Belkhatat, D. and Rhofir, K., "Vector control of asynchronous motor of drive train using speed controller h ∞ ", *Emerging Science Journal*, Vol. 6, No. 4, (2022), 834-850. doi: 10.28991/ESJ-2022-06-04-012.
- Ismail, L.S., Lupu, C. and Alshareefi, H., "Design of adaptive-rst controller for nonlinear magnetic levitation system using multiple zone-model approach in real-time experimentation", *Applied System Innovation*, Vol. 5, No. 5, (2022), 93. <https://doi.org/10.3390/asi5050093>
- Khadraoui, S. and Rakotondrabe, M., "Characterization and rst control of a nonlinear piezoelectric actuator for a robotic hand", *IFAC-PapersOnLine*, Vol. 55, No. 27, (2022), 375-380. <https://doi.org/10.1016/j.ifacol.2022.10.542>
- Lipcak, O., Baum, F. and Bauer, J., "Influence of selected non-ideal aspects on active and reactive power mras for stator and rotor resistance estimation", *Energies*, Vol. 14, No. 20, (2021), 6826. <https://doi.org/10.3390/en14206826>
- Bednarz, S.A. and Dybkowski, M., "Estimation of the induction motor stator and rotor resistance using active and reactive power based model reference adaptive system estimator", *Applied Sciences*, Vol. 9, No. 23, (2019), 5145. <https://doi.org/10.3390/app9235145>

18. Cao, P., Zhang, X. and Yang, S., "A unified-model-based analysis of mras for online rotor time constant estimation in an induction motor drive", *IEEE Transactions on Industrial Electronics*, Vol. 64, No. 6, (2017), 4361-4371. doi: 10.1109/TIE.2017.2668995.
19. Maiti, S., Chakraborty, C., Hori, Y. and Ta, M.C., "Model reference adaptive controller-based rotor resistance and speed estimation techniques for vector controlled induction motor drive utilizing reactive power", *IEEE Transactions on Industrial Electronics*, Vol. 55, No. 2, (2008), 594-601. doi: 10.1109/TIE.2007.911952.
20. Cao, P., Zhang, X., Yang, S., Xie, Z. and Zhang, Y., "Reactive-power-based mras for online rotor time constant estimation in induction motor drives", *IEEE Transactions on Power Electronics*, Vol. 33, No. 12, (2018), 10835-10845. doi: 10.1109/TPEL.2018.2800010.
21. Mapelli, F.L., Tarsitano, D. and Cheli, F., "A rotor resistance mras estimator for ev induction motor traction drive based on torque and reactive stator power: Simulation and experimental results", in 2014 international conference on electrical machines (ICEM), IEEE., (2014), 31-37.
22. Vasic, V., Vukosavic, S.N. and Levi, E., "A stator resistance estimation scheme for speed sensorless rotor flux oriented induction motor drives", *IEEE Transactions on Energy Conversion*, Vol. 18, No. 4, (2003), 476-483. doi: 10.1109/TEC.2003.816595.
23. Agrebi, Y., Yassine, K. and Boussak, M., "Sensorless speed control with mras for induction motor drive", in Proceedings of the 20th International Conference on Electrical Machines (ICEM), Marseille, France., (2012), 2-5.
24. Jo, G.-J. and Choi, J.-W., "A novel method for the identification of the rotor resistance and mutual inductance of induction motors based on mrac and rls estimation", *Journal of Power Electronics*, Vol. 18, No. 2, (2018), 492-501. <https://doi.org/10.6113/JPE.2018.18.2.492>
25. Mapelli, F.L., Bezzolato, A. and Tarsitano, D., "A rotor resistance mras estimator for induction motor traction drive for electrical vehicles", in 2012 XXth International Conference on Electrical Machines, IEEE., (2012), 823-829.
26. Basak, S., Teja, A.R., Chakraborty, C. and Hori, Y., "A new model reference adaptive formulation to estimate stator resistance in field oriented induction motor drive", in IECON 2013-39th Annual Conference of the IEEE Industrial Electronics Society, IEEE., (2013), 8470-8475.
27. Teja, A.R., Chakraborty, C., Maiti, S. and Hori, Y., "A new model reference adaptive controller for four quadrant vector controlled induction motor drives", *IEEE Transactions on Industrial Electronics*, Vol. 59, No. 10, (2011), 3757-3767. doi: 10.1109/TIE.2011.2164769.
28. Yang, S., Cao, P. and Zhang, X., "Stability analysis of q-axis rotor flux based model reference adaptive system updating rotor time constant in induction motor drives", *CES Transactions on Electrical Machines and Systems*, Vol. 1, No. 2, (2017), 109-116. doi: 10.23919/TEMS.2017.7961292.
29. Yu, X., Dunnigan, M.W. and Williams, B.W., "A novel rotor resistance identification method for an indirect rotor flux-orientated controlled induction machine system", *IEEE Transactions on Power Electronics*, Vol. 17, No. 3, (2002), 353-364. doi: 10.1109/TPEL.2002.1004243.
30. Feyzi, M.R. and Holakooie, M.H., "Sensorless indirect field oriented control of single-sided linear induction motor with a novel sliding mode mras speed estimator", *International Journal of Engineering, Transactions A: Basics*, Vol. 28, No. 7, (2015), 1011-1020. doi: 10.5829/idosi.ije.2015.28.07a.07.
31. Boldea, I. and Nasar, S.A., "Linear motion electromagnetic devices, Taylor & Francis, (1997).
32. Gieras, J., Dawson, G. and Eastham, A., "A new longitudinal end effect factor for linear induction motors", *IEEE Transactions on Energy Conversion*, Vol., No. 1, (1987), 152-159. doi: 10.1109/TEC.1987.4765816.
33. Faiz, J. and Jagari, H., "Accurate modeling of single-sided linear induction motor considers end effect and equivalent thickness", *IEEE Transactions on Magnetics*, Vol. 36, No. 5, (2000), 3785-3790. doi: 10.1109/20.908365.
34. Motlagh, S. and Fazel, S.S., "Indirect vector control of linear induction motor considering end effect", in 2012 3rd Power Electronics and Drive Systems Technology (PEDSTC), IEEE., (2012), 193-198.
35. da Silva, E.F., Dos Santos, E.B., Machado, P. and De Oliveira, M., "Dynamic model for linear induction motors", in IEEE International Conference on Industrial Technology, 2003, IEEE. Vol. 1, (2003), 478-482.
36. Cirrincione, M., Accetta, A., Pucci, M. and Vitale, G., "Mras speed observer for high-performance linear induction motor drives based on linear neural networks", *IEEE Transactions on Power Electronics*, Vol. 28, No. 1, (2012), 123-134. doi: 10.1109/TPEL.2012.2200506.
37. Alonge, F., Cirrincione, M., D'Ippolito, F., Pucci, M. and Sferlazza, A., "Active disturbance rejection control of linear induction motor", *IEEE Transactions on Industry Applications*, Vol. 53, No. 5, (2017), 4460-4471. doi: 10.1109/TIA.2017.2697845.
38. Davari, S.A., Wang, F. and Kennel, R.M., "Robust deadbeat control of an induction motor by stable mras speed and stator estimation", *IEEE Transactions on Industrial Informatics*, Vol. 14, No. 1, (2017), 200-209. doi: 10.1109/TII.2017.2756900.
39. Das, S., Kumar, R. and Pal, A., "Mras-based speed estimation of induction motor drive utilizing machines'd-and q-circuit impedances", *IEEE Transactions on Industrial Electronics*, Vol. 66, No. 6, (2018), 4286-4295. doi: 10.1109/TIE.2018.2860530.
40. Wu, S., Liu, Z. and Su, H., "Adaptive sliding mode sensorless vector control of induction motor using sliding mode mras observer", in 2017 36th Chinese Control Conference (CCC), IEEE., (2017), 9124-9129.
41. Reddy, C.U., Prabhakar, K.K., Singh, A.K. and Kumar, P., "Speed estimation technique using modified stator current error-based mras for direct torque controlled induction motor drives", *IEEE Journal of Emerging and Selected Topics in Power Electronics*, Vol. 8, No. 2, (2019), 1223-1235. doi: 10.1109/JESTPE.2019.2901523.
42. Vazifedan, M. and Zarchi, H.A., "A stator resistance estimation algorithm for sensorless dual stator winding induction machine drive using model reference adaptive system", in 2020 11th Power Electronics, Drive Systems, and Technologies Conference (PEDSTC), IEEE., (2020), 1-7.
43. Hachicha, F. and Krichen, L., "Performance analysis of a wind energy conversion system based on a doubly-fed induction generator", in Eighth International Multi-Conference on Systems, Signals & Devices, IEEE., (2011), 1-6.
44. Zhang, L., Xia, Y., Zhang, W., Yang, W. and Xu, D., "Adaptive command-filtered fuzzy nonsingular terminal sliding mode backstepping control for linear induction motor", *Applied Sciences*, Vol. 10, No. 21, (2020), 7405. <https://doi.org/10.3390/app10217405>

Persian Abstract

چکیده

در این مقاله، مدل جدیدی از موتور القایی خطی شامل تاثیر اثر پایانی بر عملکرد موتور پیشنهاد شده است. علاوه بر این، یک استراتژی جدید از رویکرد کنترل مبتنی بر تکنیک کنترل میدان گرا (FOC) پیشنهاد و بررسی شده است. رویکرد پیشنهادی می‌تواند یک استراتژی کنترل قوی ارائه کند و بر محدودیت‌های تحمیل‌شده توسط تکنیک FOC غلبه کند، که با برخی اشکالات در موتور القایی خطی (LIM) مانند حساسیت به تغییرات پارامتر و عملکرد ردیابی دینامیکی ناقص رنج می‌برد. در این زمینه، تکنیک توسعه‌یافته مزایای ارائه شده توسط هر دو رویکرد تنظیم‌کننده چند جمله‌ای (RST) و مشاهده‌گر سیستم مرجع تطبیقی مدل (MRAS) را ترکیب می‌کند تا با به حداقل رساندن اثرات اغتشاشات خارجی و کاهش تأثیر تغییرات پارامتر، به یک کنترل‌کننده قوی دست یابد. علاوه بر این، نشان داده شده است که رویکرد کنترلی پیشنهادی یک پاسخ سرعت موتور بهبود یافته را با کاهش تعداد مقادیر بیش از حد به عنوان تابعی از تغییرات جرم، که در آن حداکثر مقدار بیش از حد ثبت شده ۸٪ است، قادر می‌سازد. علاوه بر این، کنترل‌کننده توسعه‌یافته، مقادیر زمان افزایش و ته‌نشینی کاهش یافته را تحت شرایط نیروی خارجی اعمال شده گسترده نشان می‌دهد. این تایید می‌کند که روش پیشنهادی MRAS-RST پاسخ دینامیکی خوبی در برابر تغییرات پارامتر ارائه می‌دهد. دقت و عملکرد کنترل تکنیک پیشنهادی با استفاده از ابزار نرم افزار محیطی Matlab/Simulink بررسی و تایید می‌شود. نتایج شبیه‌سازی اثربخشی برآوردگر پیشنهادی را با استحکام بهتر برای کنترل‌کننده RST برای پارامترهای مختلف ردیابی مرجع و رد اختلال نشان می‌دهد. این نتایج قابل توجه، رویکرد پیشنهادی را به یک تکنیک امیدوارکننده اختصاص داده شده برای طراحی کنترل‌کننده با کارایی بالا، که برای کاربردهای صنعتی و الکتریکی بسیار مناسب است، تبدیل می‌کند.



Flood Hazard Assessment of Water-front Geosynthetic Reinforced Soil Wall for Dam Regulation Rule Level

V. A. Jha^a, J. B. Patel^{*b}, V. A. Sawant^c, Y. K. Tandel^d

^a Applied Mechanics Department, Dr. S. & S.S. Ghandhy College of Engineering and Technology, Surat, Gujarat, India

^b Civil Engineering Department, Sardar Vallabhbhai National Institute of Technology Surat, Surat, Gujarat, India

^c Civil Engineering Department, Indian Institute of Technology Roorkee, Roorkee, Uttarakhand, India

^d Applied Mechanics Department, Government Engineering College Dahod, Gujarat, India

PAPER INFO

Paper history:

Received 19 July 2022

Received in revised form 01 September 2022

Accepted 03 September 2022

Keywords:

Geosynthetic Reinforced Soil Walls

Prolonged Inundation

Dam Rule Level

Peak Discharge

Hypothesis Test

ABSTRACT

The flood hazard parameter of peak discharge and prolonged inundation due to change in dam regulation is estimated for a water front Geosynthetic Reinforced Soil (GRS) wall on the downstream of large dam. Dam regulation rule level is pre-emptying the reservoir with lower peak discharge to protect the expanding downstream city intruding the flood plain. Present study is to test the hypothesis that rule level has significantly changed peak discharge and inundation duration and also to estimate these two important parameters of flood hazard for different flood return periods. The methodology consists of three parts: first is the categorization of flood data according to major event of flood regulation, second is the distribution test and third is the estimation of design maximum peak discharge and duration of flood. The estimated value of peak discharge and flood duration clearly indicate the implication of dam regulation rule level; the estimated value of peak discharge for 200 years return period is 13.9 lakh Cusecs, which is lower than the flood discharge for year 1968, which was 15 lakh Cusecs, and the estimated flood duration for 10 years return period is 41 days. The most important finding of this study is the substantial increase in duration of flood due to implementation of rule level which will add one more flood hazard parameter for water front geotechnical structure that is prolonged inundation.

doi: 10.5829/ije.2023.36.04a.04

1. INTRODUCTION

The use of geosynthetic materials to increase soil tensile load has been extensively reported in recent decades [1-3]. One of the more common traditional structures, geosynthetic reinforced soil (GRS) walls are reinforced with either geotextile, geogrid, steel strip, or geo-strip in order to increase tensile strength. GRS walls have gained popularity from an environmental standpoint because of their increased flexibility, speed of construction, affordability, and potential for employing locally sourced materials [4]. Because they are affordable, quick and simple to construct, better acceptable to differential settlement, and more tolerant against seismic stresses, GRS walls have occupied a significant amount of area as retaining structures [5, 6]. The rivers are tamed by big

size dams mostly upstream of big cities. The cities expand geometrically and covers the flood plain which increases the flooding area and depth at the same flood discharge. To moderate the flood, dam authority has to take decision of pre-emptying the reservoir for anticipation of flood to come which is called rule level. This reduces peak discharge but duration of flood increase. Flood related hazards are; hydrostatic and hydrodynamic forces, flood-borne debris impact loads, internal and site drainage considerations, and site-specific soil and geotechnical considerations such as soil pressure, bearing capacity, land subsidence, erosion, scour, and shrink-swell potential [7]. For walls potentially subject to inundation, such as those located adjacent to rivers, canals, detention basins or retention basins, a minimum hydrostatic pressure, effective unit

*Corresponding Author Institutional Email: pjb@amd.svnit.ac.in
(J. B. Patel)

weights below the equivalent surface of the pressure head line and rapid drawdown conditions are added in analysis [6]. Normally, reinforced soil structures are not designed for hydrostatic pressures. Where hydrostatic pressures are likely due to submergence; the design should account for such pressure. Proper drainage and prescribed free draining materials are used [8]. Polemio and Lollino [9] observed that upstream water impoundment is generally not considered in the design procedure, probably because this kind of event is believed as exceptional, temporary and without relevant consequences on the embankment stability. Yoo and Jung [10] revealed that the wall failure was mostly caused by poor design and low-quality back fill, despite the fact that rainfall infiltration was the principal triggering mechanism. Flood hazard is one of the major causes of failure if not taken into consideration. The failure database of GRS wall concludes that the maximum number of failures are due to fine grain soil or water ingress either externally or internally [11-13]. The probability analysis for Tapi River has been carried out to estimate peak flood with return periods by different methods [14]. Identification of trend and probability distribution for time series of annual peak, HEC-RAS based hydrodynamic model in prediction of stages and one-dimensional hydrodynamic modelling of flooding and stage hydrographs in the lower Tapi River [15]. A two-dimensional HEC-RAS model was used to analyze the propagation of the flood wave and to assess failure risk on dam downstream areas [16]. A reliable, remote, Early Warning System (EWS) specifically designed for lava flood detection, along with its disaster communication system was successfully implemented in Mount Merapi, Indonesia, coordinated with the local Disaster Deduction Risk (DDR) forum [17]. Fitzgerald et al. [18] gave explanation of how and under which circumstances nonparametric statistics are used. Bargegol et al. [19] used F-distribution in statistical analysis of railway accident in Japan. Samantaray and Sahoo [20] used statistical methods to forecast the stream-flow from four flow data of different stations. Majority of researchers have investigated about peak discharge, it's destroying impact, area of submergence and how to reduce the intensity by diversion, early warning system and flood routing. Dam regulation by rule level is pre-emptying the reservoir in such a way that at no point of time maximum outflow exceeds the pre-decided value. This pre-decided value which is decided by the area of submergence in downstream city or town, further swells and occupy the space through which the flood has to pass. So, this is a vicious circle. When we limit the peak discharge, to pass same volume of flood, the duration of flow will increase. This duration may be prolonged in such a way that it may affect the bearing capacity and metric suction of geotechnical structure in the course of flood line. Perhaps no literature is available which investigated this aspect of dam regulation. The aim

of the study is; firstly, to categorize the flood data on the basis of major event on river Tapi upstream of study area; secondly, to verify the hypothesis that the difference in category is significant or just random for both flood discharge and flood duration; thirdly, to estimate design maximum value of above two parameters for different flood return period; and finally, to consider prolonged inundation as additional flood hazard for geotechnical structure on the bank of non-perennial river.

2. STUDY AREA

For study purpose, a waterfront geosynthetic reinforced earth wall on the bank of river Tapi in the area of south Gujarat in India, which survived several numbers of floods in past has been selected. It lies in the town of Mandavi which is in the proximity of the city Surat in the state of Gujarat of western India. The coordinates of the site are 21.25°N and 73.33°E. The site is on the northern bank of river flowing from east to west. Its chainage from Ukai dam is 3.1 km in lower Tapi Basin. Figure 1 shows lower Tapi basin and Mandavi town in which study area is located.

A gabion facing wall along three sides, 3m to 6m high was constructed to make a large size plain multipurpose raised and paved platform. Figure 2 presents aerial and localized view of study wall. This Riverfront wall's construction was started in July 2017 and completed in February 2018. The completed wall with top platform and side railing is also shown in Figure 2.

The wall is constructed on sloping ground, immediately next to approach road, joining the bank to river. The waterway is touching the wall face in monsoon. A typical sectional view including details of the tallest section of the wall with acting forces is shown in Figure 3. All the de-stabilizing lateral forces and stabilizing vertical forces acting on the wall is shown in Figure 3. These forces are; the active earth pressure force of submerged soil (P_1), the water pressure force (P_2), the active earth pressure force due to surcharge load (P_3), the water pressure force from river side (P_4), the at rest

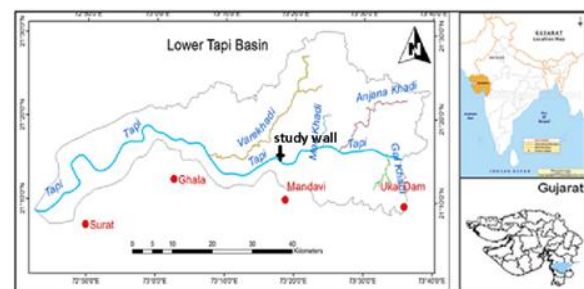


Figure 1. Location of study area in Mandavi town, lower Tapi basin



(a)



(b)

Figure 2. Study wall: (a) aerial view, (b) actual view

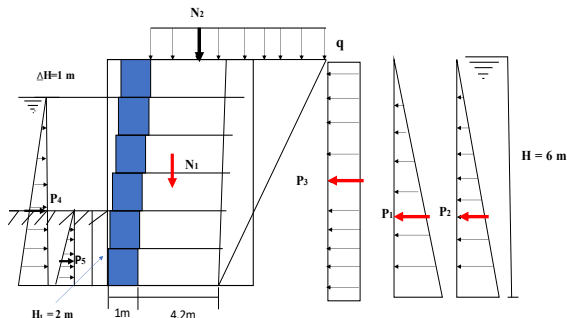


Figure 3. Wall detail with acting forces (tallest section facing waterways)

pressure force of submerged soil from river side (P_5), the gravity force of reinforced earth wall (N_1), and the vertical force due to surcharge load (N_2). The wall is maximum 6m in height from the base, and it is reinforced with Geo-strip of ultimate tensile strength 100 kN/m. The foundation soil below the wall is silty sand (SM) having $C=0$, and $\phi = 30^\circ$. Corrected SPT value of 11 at 1.5m depth and 30 at 4.5m depth shows soil is medium dense to dense below. The satellite image of the study area investigated since year 2002 does not show major scour near the bank.

2. 1. Flood in Lower Tapi Basin

Many of the most serious floods have resulted from heavy rainfall in the Tapi River’s catchment area. The monsoon generally starts in this area during the third week of June and there are occasional heavy rainstorms from the beginning of August to the end of September. The catchment area receives around 90 per cent of its annual rainfall between June and October and most floods occur in August/September. To prevent repeated floods in Surat, a major Dam was constructed in 1972 at village Ukai, which is located about 100 km upstream of Surat. Immediately after the construction of the Ukai dam in 1975, Central Water Commission (CWC) prepared detailed guidelines for the flood control operation of the Ukai reservoir. The guidelines recommended that up to the end of August, the reservoir should be filled maximum up to the level of 103.33m and thereafter be gradually raised up to Full Reservoir Level (FRL) of 105.16m by the end of September. It also prescribed that the reservoir level would not be allowed to go above the full reservoir level FRL of 105.16m. Later, due to increased demand for water and absence of major flood, the State Government relaxed the rule levels and recommended that the reservoir may be filled up to the level of 104.55m by the end of August and then filled up to FRL by 15th September. This consequently reduced the available flood cushion in the reservoir and thus aggravated the problem of flood management. After the major flood of 1994 and 1998, a joint committee with CWC, Central Design Organization, Department of Narmada and Water Resources, Government of Gujarat was formed in 1999 to review the procedure for dam operation for flood control and prepared manual to provide clear guidelines for dam operation. The committees come out with a ‘Manual on Flood Control Operation of Ukai dam in July 2000, which continued to be used in operation of the dam. Table 1 provides compilation of rule level recommended by nodal agency.

The flood of 2006 caused greater damage and affected badly the Surat and Hazira twin-city of Gujarat. It is documented fact that no decision related to rule level was taken till the dam level reached 105.16 m. Then government of Gujarat made strict implementation of rule level after 2006.

After strict implementation of rule level, the flood situation changed for the downstream of the dam. Therefore, a study was needed to assess the flood hazard parameters in this changed scenario. This study is limited to two flood hazard parameters of flood discharge and flood duration.

3. METHODOLOGY

Data for statistical analysis were collected from Ukai dam authority; which were accurately measured and

TABLE 1. Recommended Rule Level of Ukai reservoir [21]

Date	Recommended rule level in m		
	Original Rule Level by CWC, 1975	Later Correction before 1994 flood	New Level by GOG, 2000
1 st July	-	-	97.84 (Min.)
1 st August	-	-	101.50 (Min.)
1 st September	Max. 103.33	104.55	103.63 (Max.)
15 th September	-	FRL 104.55	103.63 (Max.)
1 st October	FRL 105.16	-	105.16 (Max.)

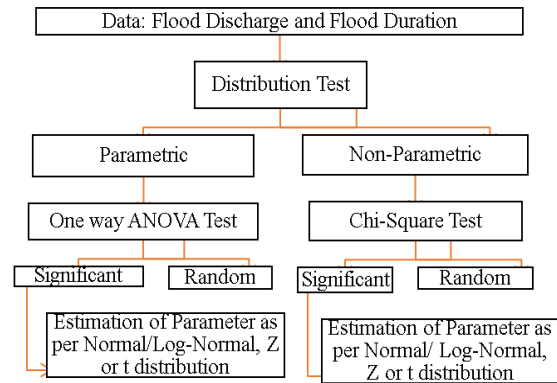


Figure 4. Flow chart showing methodology

provided on request for purely study purpose. Daily outflow data of Ukai (1972-2020) and other peak discharge data (1939-1971) from literature [14] were collected. First, the flood data were categorized on the basis of two major event and tested for its distribution whether it is parametric or non-parametric. Descriptive statistics, histogram, normal and log-normal probability test are carried and graph plotted in excel programming. Hypothesis test of significance, one way ANOVA test for parametric and Chi-square test for non-parametric distribution is conducted. ANOVA test is suitable in analysis of simple random, parametric and independent data, it is using F-test to check the hypothesis, F distribution (Fisher-Snedecor distribution) is also called as variance ratio distribution as it usually defines the ratio of the variance of two normally distributed population. Chi-square is robust for distribution of data and can be used for which parametric assumption cannot be met. It is also flexible in handling data from both two groups and multiple group studies. Therefore, this non-parametric test was used to find significance of flood duration data even with the limitation of sample size. Category with significant difference is selected for estimation of design maximum value. For sample size 30 or less t-value is used, therefore in the estimation of peak discharge and flood duration t-value is taken. These estimated values will be considered for analysis and rectification of flood design parameters of study wall. Main aim of data analysis is whether two basic flood parameters (flood discharge and duration) are significantly changed or the changes are just random after implementation of rule level. Figure 4 shows a flow chart of the methodology adopted in the present study.

4. RESULT AND DISCUSSION

4. 1. Flood Catalog and Categorization of Data

Peak flood discharge data since year 1939 till date is tabulated in Table 2. In the table years, 1972 and 2006, having major event related to flood regulation, are highlighted. In year 1972, multipurpose Ukai dam was

TABLE 2. Peak Discharge Data

Year	Discharge (Lakh cusecs)	Year	Discharge (Lakh cusecs)	Year	Discharge (Lakh cusecs)
1939	5.15	1967	4.55	1995	4.01
1940	2.43	1968	15	1996	2.12
1941	4.81	1969	8.56	1997	4.94
1942	7.58	1970	13.14	1998	10.53
1943	1.79	1971	0.66	1999	3.3
1944	9	1972	2.47	2000	2.38
1945	7.22	1973	5.29	2001	3.09
1946	3	1974	3.06	2002	4.32
1947	2.91	1975	4.56	2003	3.32
1948	2.55	1976	3.81	2004	3.89
1949	6.62	1977	3.09	2005	4.68
1950	3.98	1978	8.88	2006	12.05
1951	1.62	1979	8.58	2007	6.37
1952	1.12	1980	3.17	2008	2.08
1953	0.64	1981	5.73	2009	2.15
1954	6.89	1982	1.33	2010	2.32
1955	2.36	1983	0.78	2011	2.31
1956	3.06	1984	0.5	2012	3.35
1957	1.58	1985	0.5	2013	4.33
1958	6.2	1986	2.86	2014	2.47
1959	13.16	1987	0.5	2015	0.77
1960	2.55	1988	3.3	2016	0.24
1961	7.36	1989	3.1	2017	0.1
1962	7.99	1990	4.9	2018	0.11
1963	2.7	1991	3.68	2019	1.94
1964	2.15	1992	1.84	2020	1.65
1965	1.55	1993	3.35	2021	2.05
1966	3.66	1994	8.87		

constructed with basic purpose of irrigation which changed its focus to more on flood control in coming years. Another major event was strict implementation of flood control after the devastating flood of 2006 which made havoc in downstream city of Surat.

Flood duration data since year 1972 till date with separation of year 2006 is also tabulated in Table 3 for prolonged inundation analysis. In this table “number of days” are taken when the flood just exceeds the base of study wall. The purpose of taking only those days of a year is to know, for how many days the wall will be under inundation.

Both the flood data are categorized as per the major event. Peak discharge data is having three categories: First category is “A” (before construction of Ukai dam when there was no flood control to Ukai dam constructed), second category is “B” (after construction of Ukai dam to strict implementation of rule level), third category is “C” (after strict implementation of rule level till date). Category A is from year 1939 to year 1971, category B is from 1972 to 2006 and category C is from 2007 to 2020. Flood duration data is also divided into two categories; First category is “A” (after construction of Ukai dam to strict implementation of rule level) and second category is “B” (after strict implementation of rule level till date).

TABLE 3. Flood duration data

Criteria- A (1972 to 2006)				Criteria-B (2007 to 2020)	
Year	No of Days*	Year	No of Days*	Year	No of Days*
1972	0	1990	28	2007	30
1973	14	1991	0	2008	3
1974	7	1992	0	2009	0
1975	0	1993	0	2010	19
1976	37	1994	22	2011	11
1977	0	1995	0	2012	23
1978	7	1996	0	2013	59
1979	10	1997	0	2014	12
1980	0	1998	18	2015	6
1981	3	1999	0	2016	4
1982	0	2000	0	2017	0
1983	25	2001	0	2018	0
1984	1	2002	8	2019	63
1985	0	2003	14	2020	22
1986	0	2004	3	2021	14
1987	0	2005	5		
1988	21	2006	33		
1989	1				

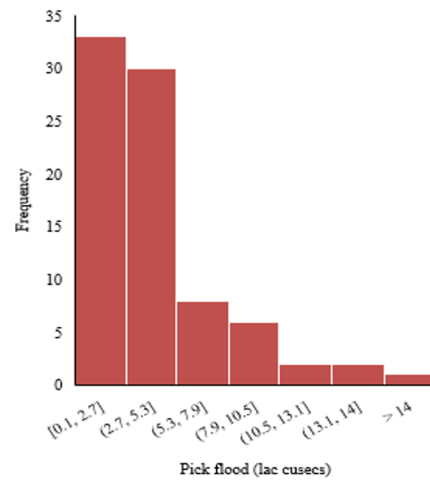
*When the flood just reached above base of study wall in a year

4. 2. Distribution Test

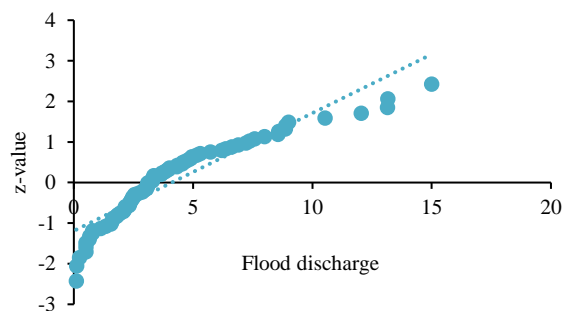
All four data set of peak discharge, (1939-2020), (1939-1972), (1973-2006) and (2007-2020) and two data set of flood duration, (1972-2020) and (2007-2020) are checked for discriptive statistics to know the characteristics of the data (Table 4). The Peak discharge data of Table 2 is plotted in form of histogram showing peak discharge and its frequency, and it is also tested for probability plot test. Both the plot confirms that this data is following log-normal distribution (Figure 5). Similarly flood duration data is plotted as histogram and also tested for probability plot test, but this data does not show any distribution (Figure 6). When this data is taken separately, category C which was flood duration from year 2007 to year 2020 shows log-normal distribution (see Figure 7).

TABLE 4. Estimated flood discharge for different return period

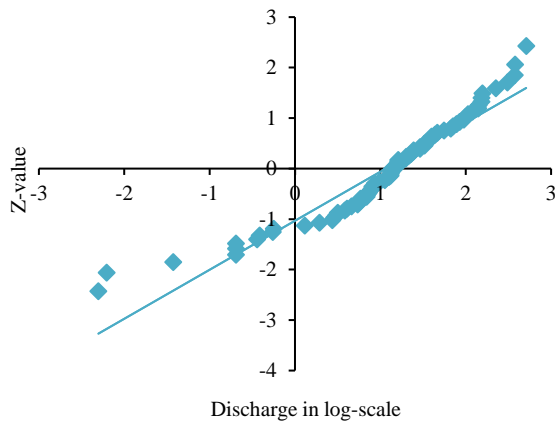
Sr. No.	Return Period	t -value	Discharge (Q) in lakh Cusecs
1	Once in 200 years	3.01	13.9
2	Once in 100 years	2.65	10.8
3	Once in 40 years	2.16	7.70
4	Once in 20 years	1.77	5.80
5	Once in 10 years	1.35	4.32



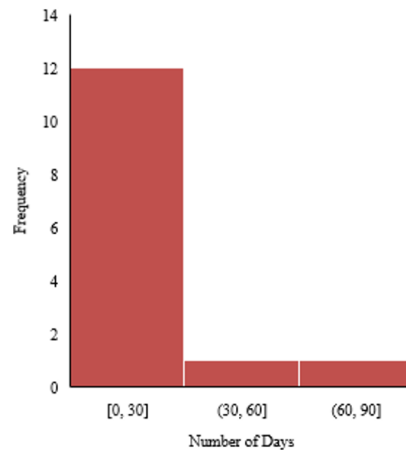
(a) Histogram



(b) Normal probability plot

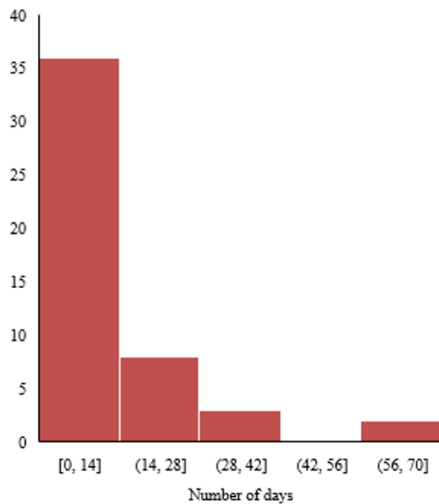


(c) Log-normal probability plot

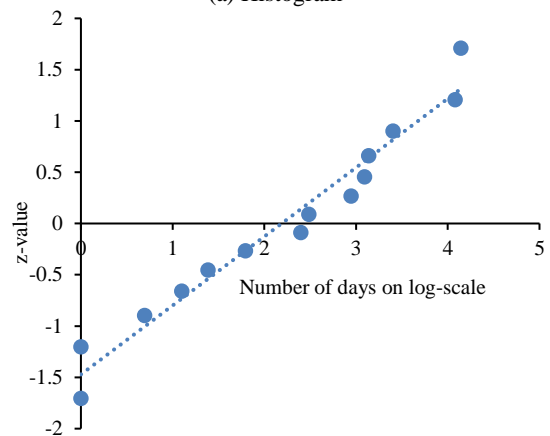


(a) Histogram

Figure 5. Distribution test of Peak Flood Discharge (1939-2020): a) Histogram, b) Normal probability plot) Log-normal probability plot

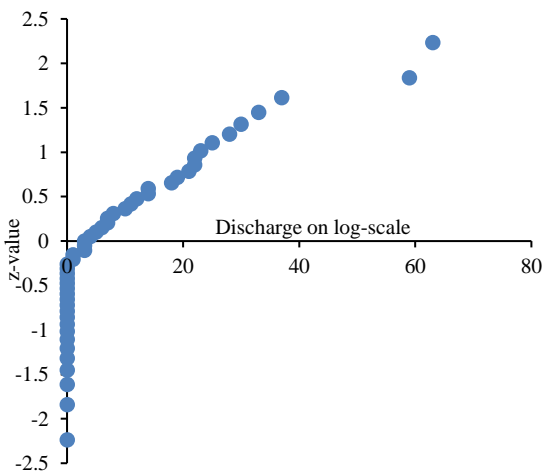


(a) Histogram



(b) Log-normal probability plot

Figure 7. Distribution test of Number of Days of flooding (2007-2020): a) Histogram, b) Log-normal probability plot



(b) Normal probability plot

Figure 6. Distribution test for Number of Days of Flooding (1972-2020): a) Histogram, b) Normal probability plot

4. 3. Hypothesis Verification

For both the flood data, the question was whether difference in data which are divided as per major event i.e., dividing into category A, B, C in case of peak discharge and category A, B in case of flood duration, is significant or random. The meaning of categorization is only there if the difference is significant. Therefore, the hypothesis was whether the difference in category was significant or just by chance. For peak discharge data one-way ANOVA test is carried twice, one taking all three categories and another taking last two categories. In first case the calculated value of “F” equals to 4.78 which is more than value of 3.24 at 5% level of significance, while in another case the calculated value is 5.9, higher than value of 4.21 at 5% level of significance. Therefore, it can be said that the difference is significant so the categorization based on major event for peak discharge is justified.

Since overall flood duration data doesn’t follow any distribution, it is tested on non-parametric Chi-Square test for the hypothesis. The calculated Chi-Square value is 23.21, while the value for 5% level of significance is

9.49 [22]. This shows that the difference is significant and implementation of rule level in year 2006 has changed the scenario of flood in lower Tapi basin i.e., lower discharge with larger duration.

4. 4. Estimation of Flood Parameters Estimation of flood parameters are on the basis of category “C” because after implementation of rule level the pattern of dam outflow changed. Since for category “C” only 14 sample data is available and this category is following log-normal distribution, estimation is based on log-normal t-distribution. Both the values of design maximum flood discharge and design maximum duration of flood are calculated for different flood return period.

4. 5. Design Maximum Peak Discharge The design flood is the most severe of the 100-year event or overtopping flood of lesser recurrence interval [6]. The estimated value of flood discharge in lakh Cubic feet per second (Cusecs) for different return period is listed in Table 4. The flood discharge for 200 years return period is 13.9 lakh Cusecs which is lower than year 1968 flood of 15 lakh Cusecs when Ukai dam was not there. Further this value is just higher than 12.05 lakh Cusecs flood of year 2006 after Ukai dam construction. The reason behind this is flood regulation on the basis of rule level i.e., pre-empting the reservoir in anticipation of possible flood has reduced the peak discharge and increased the duration of flood.

4. 6. Design Maximum Duration of Flood Number of days of wetting is very important parameter in analysis of geotechnical structure for prolonged inundation. If number of days is more than 40 days [10]. There are chances of reduction in bearing capacity, metric suction and shear strength of soil which will ultimately decrease the stability factor of safety of waterfront geotechnical structure. Chances of prolonged inundation has been examined by three ways: First, estimating number of days of wetting using log-normal t-distribution for different return period as shown in Table 5. Second, plotting the graph of flood dispersion throughout monsoon period for major flood as shown in Figure 8, third, comparing average outflow volume of major flood as shown in Table 6.

TABLE 5. Estimated number of days of wetting for different return period in lower Tapi basin

Sr. No.	Return Period	t -value	No of Days of wetting
1	Once in 200 years	3.012	186
2	Once in 100 years	2.65	134
3	Once in 40 years	2.16	85
4	Once in 20 years	1.771	60
5	Once in 10 years	1.35	41

TABLE 6. Average outflow volume of major flood

Year	1994	1998	2006	2013	2019
Total Flood Release in “MCM”	10760	8303	17243	14457	12080
Duration of Flood in Number of Days	22	18	33	59	63
Average Flood Release in “MCM/day”	489	461	522	245	192

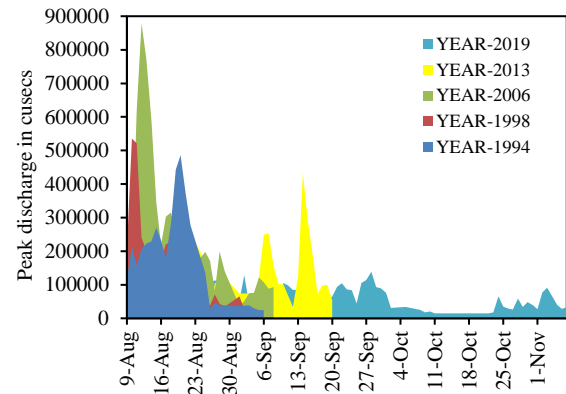


Figure 8. Flood duration graph showing dispersion of flood

For return period of 10 years the wetting days is 41, therefore the downstream waterfront structure must be analyzed for prolonged inundation. The wetting days for return period 200 years is abnormally high, more than 6 months which is higher than monsoon period of 4 months. This shows that once in 200 years, situation will be critical and dam authorities have to go for higher discharge for few days to balance the outflow.

The concentration or dispersion of flood throughout monsoon period for different major flood shown in Figure 8, demonstrated that flood after 2006 are widely dispersed. The highest dispersion is of the flood year 2019 and lowest for the flood year 1994.

Total outflow of water in MCM (Million Cubic Meter) throughout the monsoon season for major floods are taken from Ukai dam data and it is converted into average outflow by dividing it with number of days of flooding. This value can be compared for the parameter of prolonged inundation. Here it can be said that, although in year 2019 total outflow was only 70% of year 2006 outflow, duration of flood was almost double. Therefore, it is finally established that implementation of rule level has increased prolonged inundation.

4. CONCLUSIONS

In this study, flood hazard assessment of water-front GRS wall has been investigated for dam regulation rule

level. Flood data released by Ukai dam authority for lower Tapi basin has been analyzed and tested for hypothesis of strict implementation of rule level in 2006. This was needed to know whether it has changed two main flood hazard parameters; peak discharge and flood duration. It is found that estimated flood discharge for 100 years return period is reduced (10.8 lac cusecs). This value is much lower than year 1968 flood of 15 lakh Cusecs when Ukai dam was not there and also, lower than 12.05 lakh Cusecs flood of year 2006 after Ukai dam construction. Further, it is observed that duration of flood has significantly increased due to implementation of rule level which was not studied before. The estimated value of inundation days is more than 40 for 10 years return period, which is sufficient to create loss of metric suction inside geotechnical structure. Major findings of the study are useful in forecasting the flood discharge and flood duration for Lower Tapi Basin. Other flood parameters, socio-economic impact and change in submergence pattern owing to dam regulation are the future scope of work.

5. REFERENCES

- Sharma, K., Aggarwal, P. and Gupta, K., "Modeling of unreinforced and reinforced pavement composite material using hiss model (research note)", *International Journal of Engineering, Transactions B: Applications*, Vol. 20, No. 1, (2007), 13-22.
- Vafaeian, M. and Abbaszadeh, R., "Laboratory model tests to study the behavior of soil wall reinforced by weak reinforcing layers", *International Journal of Engineering, Transactions B: Applications*, Vol. 21, No. 4, (2008), 361-374.
- Bahrami, M. and Marandi, S., "Large-scale experimental study on collapsible soil improvement using encased stone columns", *International Journal of Engineering, Transactions B: Applications*, Vol. 34, No. 5, (2021), 1145-1155. <https://doi.org/10.5829/ije.2021.34.05b.08>
- Hoseini, M.H., Noorzad, A. and Zamanian, M., "Physical modelling of a strip footing on a geosynthetic reinforced soil wall containing tire shred subjected to monotonic and cyclic loading", *International Journal of Engineering, Transactions B: Applications*, Vol. 34, No. 10, (2021), 2266-2279. <https://doi.org/10.5829/IJE.2021.34.10A.08>
- Berg, R., Christopher, B. and Samtani, N., *Design and construction of mechanically stabilized earth walls and reinforced soil slopes—volume i, us department of transportation, federal highway administration, washington dc, publication no. 2009, FHWA-NHI-10-024 (FHWA GEC 011-Vol I)*.
- Berg, R.R., Samtani, N.C. and Christopher, B.R., *Design of mechanically stabilized earth walls and reinforced soil slopes—volume ii*. 2009, United States. Department of Transportation. Federal Highway Administration.
- Directorate, U.S.F.E.M.A.M., "Engineering principles and practices for retrofitting flood prone residential buildings, Federal Emergency Management Agency, (1995).
- 102, I.S., "Guidelines for design and construction of reinforced soil walls", in Indian Roads Congress., (2014), 1-80.
- Polemio, M. and Lollino, P., "Failure of infrastructure embankments induced by flooding and seepage: A neglected source of hazard", *Natural Hazards and Earth System Sciences*, Vol. 11, No. 12, (2011), 3383-3396.
- Yoo, C. and Jung, H.-Y., "Case history of geosynthetic reinforced segmental retaining wall failure", *Journal of Geotechnical and Geoenvironmental Engineering*, Vol. 132, No. 12, (2006), 1538-1548. [https://doi.org/10.1061/\(asce\)1090](https://doi.org/10.1061/(asce)1090)
- Koerner, R. and Koerner, G., "A data base and analysis of 141 failed geosynthetic reinforced mechanically stabilized earth (mse) walls", in Proc., 26th Central Pennsylvania Geotechnical Conf., (2012).
- Koerner, R.M. and Koerner, G.R., "A data base, statistics and recommendations regarding 171 failed geosynthetic reinforced mechanically stabilized earth (mse) walls", *Geotextiles and Geomembranes*, Vol. 40, (2013), 20-27.
- Koerner, J.R., Soong, T.-Y. and Koerner, R.M., "Earth retaining wall costs in the USA, Geosynthetic Research Institute, (1998).
- Joshi, G., Rana, S. and Shrimali, N., "Peak flood probability analysis for tapi river", *Indian Journal of Applied Research*, Vol. 4, (2014), 187-192. <https://doi.org/10.15373/2249555x/jan2014/57>
- Timbadiya, P., Patel, P. and Porey, P., "One-dimensional hydrodynamic modelling of flooding and stage hydrographs in the lower tapi river in india", *Current Science*, (2014), 708-716.
- Karim, I.R., Hassan, Z.F., Abdullah, H.H. and Alwan, I.A., "2d-hec-ras modeling of flood wave propagation in a semi-arid area due to dam overtopping failure", *Civil Engineering Journal*, Vol. 7, No. 9, (2021), 1501-1514.
- Suwarno, I., Ma'arif, A., Raharja, N.M., Nurjanah, A., Ikhsan, J. and Mutiarin, D., "Iot-based lava flood early warning system with rainfall intensity monitoring and disaster communication technology", *Emerging Science Journal*, Vol. 4, No. 0, (2021), 154-166.
- Fitzgerald, S., Dimitrov, D. and Rumrill, P., "The basics of nonparametric statistics", *Work*, Vol. 16, No. 3, (2001), 287-292.
- Bargegol, I., Najafi Moghaddam Gilani, V. and Abolfazlzadeh, M., "Statistical analysis of the railway accidents causes in iran", *International Journal of Engineering, Transactions C: Aspects*, Vol. 30, No. 12, (2017), 1822-1830. doi: 10.5829/ije.2017.30.12c.02.
- Samantaray, S. and Sahoo, A., "Estimation of flood frequency using statistical method: Mahanadi river basin, india", *H2Open Journal*, Vol. 3, No. 1, (2020), 189-207.
- Thakar, G., "People's committee on gujarat floods 2006: A report", Unique Offset, Ahmedabad, (2007).
- Kothari, C.R., "Research methodology: Methods and techniques, New Age International, (2004).

Persian Abstract

چکیده

پارامتر خطر سیل با دبی اوج و طغیان طولانی مدت به دلیل تغییر در مقررات سد برای دیواره خاک تقویت شده ژئوستنتیکی (GRS) جلوی آب در پایین دست سد بزرگ برآورد شده است. سطح قانون تنظیم سد، مخزن را با دبی اوج کمتر تخلیه می کند تا از شهر در حال گسترش پایین دست که به دشت سیلابی نفوذ می کند، محافظت کند. مطالعه حاضر به منظور آزمون این فرضیه است که سطح قانون به طور قابل توجهی دبی اوج و مدت طغیان را تغییر داده است و همچنین تخمین این دو پارامتر مهم خطر سیل برای دوره های مختلف بازگشت سیل است. روش شناسی شامل سه بخش است: اول طبقه بندی داده های سیل بر اساس رویداد اصلی تنظیم سیل، دوم آزمایش توزیع و سوم برآورد حداکثر دبی پیک طراحی و مدت زمان سیل. ارزش تخمینی دبی اوج و مدت سیل به وضوح نشان دهنده مفهوم سطح قوانین تنظیم سد است. ارزش تخمینی پیک دبی برای ۲۰۰ سال دوره بازگشت ۱۳.۹ لک کیوسک است که کمتر از دبی سیلاب در سال ۱۹۶۸ که ۱۵ لک کوزک بوده است و مدت زمان تخمینی سیل برای ۱۰ سال دوره بازگشت ۴۱ روز است. مهمترین یافته این مطالعه افزایش قابل توجه مدت سیلاب به دلیل اجرای سطح قاعده است که یک پارامتر خطر سیل دیگر را برای سازه ژئوتکنیکی جبهه آب که طغیان طولانی مدت است، اضافه می کند.



A Light Solution for Device Diversity Problem in a Wireless Local Area Network Fingerprint Indoor Positioning System

F. Firdaus*^a, I. Fadhillah^a, N. A. Ahmad*^b, A. A. Mohd Ali^c

^a Department of Electrical Engineering, Universitas Islam Indonesia Kaliurang KM 14.5 Street Yogyakarta, Indonesia

^b Razak Faculty of Technology and Informatics, Universiti Teknologi Malaysia Kuala Lumpur 54100, Malaysia

^c Malaysian Administrative, Modernisation and Management Planning Unit, Putrajaya 62502, Malaysia

PAPER INFO

Paper history:

Received 14 September 2022

Received in revised form 31 December 2020

Accepted 01 January 2022

Keywords:

Device Diversity

Fingerprint

Indoor Positioning System

Received Signal Strength Indicator

Wireless Local Area Network

Wi-Fi

ABSTRACT

The development of location-based services requires an increasingly accurate positioning system technology. Research on outdoor positioning systems has achieved satisfactory accuracy and has been commonly used in various location-based services. The research trend is now shifting toward the Indoor Positioning System (IPS). One technique that is widely used in Wi-Fi-based IPS is fingerprinting. The fingerprinting technique on Wi-Fi uses the Received Signal Strength Indicator (RSSI) value. The problem that occurs is that the results of RSSI measurements on smartphones of different brands will produce different RSSI values, also known as device diversity. Device diversity will cause a decrease in system accuracy. This study aims to offer a solution to the problem of device diversity in Wi-Fi IPS based on RSSI Fingerprinting, i.e., to get a minor distance error. The proposed solution is to modify the original database radio map into two new databases: the difference database and the ratio database. The Difference Database Radiomap was able to reduce the average value of distance errors by 24.3% in Meizu and 28% in OPPO. Then, using the Radiomap database ratio, the average value of distance errors could be reduced by 13% in Meizu and 24% in OPPO. From the calculation, Radiomap database ratio can provide solutions to the problem of device diversity for an Indoor Positioning System better than the difference database radiomap if we looked at reduced distance error.

doi: 10.5829/ije.2023.36.04a.05

NOMENCLATURE

d	Euclidean distance	(x_e, y_e)	The estimated location (IPS measurement results)
S_{m_n}	Value of RSSI (Received Signal Strength Indicator) from the AP (Access Point) to-n at a known location	(RR1, RR2, RR3)	New database and the new test point for the ratio method
S_{i_n}	value of RSSI from the AP to-n at the unknown location	Ea	Initial error, which uses the original database from the results of the RSSI measured value
(x_a, y_a)	The actual location	Eb	New error, using the results of the proposed database modification of the difference or ratio

1. INTRODUCTION

Along with the increasingly widespread development of location-based services, the positioning system technology is developing rapidly such that there is now a need for high standards in the system [1]. Research on the outdoor positioning system is considered to have achieved satisfactory accuracy and has met these

standards, so the system is now commonly used by the general public in various location-based services such as navigation and mapping [2]. The research trend is now shifting toward the indoor positioning system (IPS).

Human activity today tends to be done more in-room; the community generally spends about 80%–90% of all their time in rooms. This situation translates to 80% of data communication being carried out indoors.

*Corresponding Author Institutional Email: firdaus@uii.ac.id
(F. Firdaus), azurati@utm.my (N. A. Ahmad)

Therefore, location-based services in the room have high market potential. Location-based services have led to an increase in IPS research trends in the past decade. However, research on existing IPS has not produced generally optimal, reliable, or ready-to-use methods like the Global Positioning System (GPS) technique for the outdoor positioning system [3]. A good IPS is expected to meet the following aspects: ease of accessibility, simple calculation, and high scalability [4].

One of the devices that can support the ease of accessibility in IPS is the smartphone. In the modern era today, the use of smartphones has drastically increased, supported by various sophisticated smart sensors such as biometric, odometry [5] etc., making smartphones high-potential instruments for IPS. Studies on IPS using smartphones have also been carried out. Subsequently, one by one, research has begun to develop smartphones with built-in sensors for IPS planning. One of these devices involves Wi-Fi data sending technology, which has now become famous in IPS planning.

Positioning system-based Wi-Fi is profitable because it is easily found in various public places and requires relatively cheaper costs. In addition, the Wi-Fi-based positioning system is compatible with outdoor use and various indoor environments to support the high scalability aspects that IPS needs.

Specific techniques must be applied to use Wi-Fi as an instrument in IPS planning. Some commonly-used techniques for positioning systems in indoor-based Wi-Fi are triangulation, trilateration [6], proximity matching, and fingerprinting. Of all the techniques that have been mentioned, fingerprinting techniques are the most widely used because they have high accuracy as they conduct positioning based on references in the original environment [7]. Besides, this method does not require any additional device or tool [8-10]. There are several types of fingerprinting techniques, one of which is the Wi-Fi Received Signal Strength Indicator (RSSI), which matches the Wi-Fi signal strength data received in determining positions. The RSSI-based Wi-Fi fingerprinting technique is the most suitable technique for positioning a system in a room [1].

However, position determination can result in poor precision, when using measurements based on the Wi-Fi RSSI fingerprinting technique involving small cell sizes [7]. The measurement error that appears can worsen if the measurement is made using a smartphone of a different brand due to the manufacturing differences from the Wi-Fi transceiver used by each smartphone [1]. Thus, the main problem with this method is the measurement of RSSI Wi-Fi on smartphones of different brands in the same condition and location, which can produce different RSSI data. The term commonly used for this problem is device diversity. Device diversity can affect the accuracy of the Indoor Positioning System (IPS) that has been built [11]. Therefore, a solution is needed to solve the problem

of device diversity so that the accuracy of IPS can be maintained and the measurement results remain precise; although it is used in a variety of Android smartphones.

2. LITERATURE REVIEW

2. 1. Wi-Fi-based Indoor Positioning System Technology

The indoor positioning system (IPS) has two main objectives: tracking and navigation [8]. Several studies have summarized and examined the performance of various principles and methods that have been proposed in building an IPS [12-14]. The measurement principle uses internal range, signal strength, acceleration, or angles for location determination, along with specific schemes such as triangulation [15], trilateration, hyperbolic location determination, and data matching [12, 16]. The principle of measurement using radio signal technology is divided into several parts; one of which is to use the Wireless Local Area Network (WLAN). To produce an effective and efficient IPS, some measurement principles are combined with one or a combination of two schemes to determine positions.

2. 2. Fingerprinting Technique

Based on the standard provisions in the IEEE 802.11 Standard, Wi-Fi cards and Access Point (AP) wireless networks measure the intensity of radio frequency signals [17]. The fingerprinting technique used for IPS is classified as a data matching scheme, which generally uses signal strength [18] for location mapping where the signal is obtained [1, 19]. One of the most common types of fingerprinting techniques is the Received Signal Strength Indicator (RSSI) [20]. Another type is visual fingerprinting, which uses images from camera sensors, and motion fingerprinting, which utilizes displacement sensors such as accelerometers [1].

2. 3. Wi-Fi IPS Positioning System based on RSSI Fingerprinting

In general, a positioning system using Wi-Fi fingerprinting consists of two phases; the offline phase, where the RSSI measurement from several Access Points (AP) is collected to map a Wi-Fi radio fingerprinting model called the fingerprinting database [13, 21]; and the online phase, which can also be referred to as the location determination phase to determine the position of the device used by matching the Wi-Fi signal received from that location with a database that has been built previously [22, 23]. Figure 1 shows the framework of a Wi-Fi positioning system based on RSSI fingerprinting.

2. 4. Positioning Algorithm: K-Nearest Neighbor (kNN) Algorithm

The kNN algorithm is a method for classifying objects based on learning data closest to the object [24] and to solve user orientation problem [25].

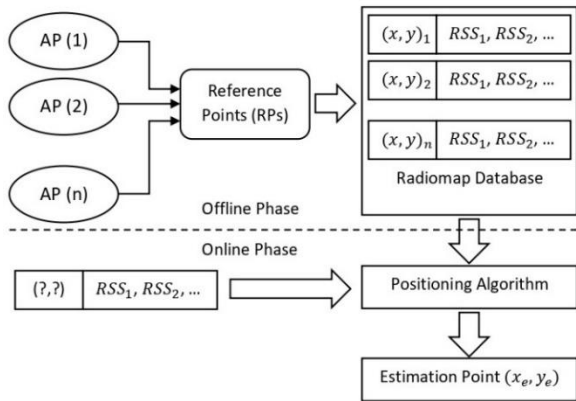


Figure 1. Wi-Fi IPS Positioning System Technology based on RSSI Fingerprinting

The value of K is the smallest amount of Euclidean distance between each AP and the point of location that was not known beforehand. The kNN algorithm is one of the classification methods that are included in the instance-based learning category. That is, this method uses a supervised learning approach, so it requires training known data or labeling. Unknown values will be compared with the known value, and then classified based on the closeness or distance of both values. This algorithm follows the fingerprinting method used in IPS.

The Euclidean distance is calculated using Equation (1) given below [24]:

$$d = \sqrt{(S_{m_1} - S_{i_1})^2 + (S_{m_2} - S_{i_2})^2 + \dots + (S_{m_n} - S_{i_n})^2} \quad (1)$$

where S_{m_n} is the value of RSSI from the AP to-n at a known location, while S_{i_n} is the value of RSSI from the AP to-n at the unknown location.

2. 5. Device Diversity Device diversity (also often referred to as device heterogeneity) is a difference in the results of reading the strong Wi-Fi signals received from different devices [26-27]. This situation generally occurs due to differences in antennas, antenna attenuation, different sensor specifications and [29] chip designs on different devices [27]; note that the difference in the results of this reading can also be found with the same type of device [28].

Park et al. [30] stated that device diversity is an exciting problem to resolve in the design and application of indoor positioning. However, standardization and calibration are not the right solutions for an environment in which the brand of devices varies because these would require sophisticated and expensive equipment. Therefore, one of the calibration efforts is to use detailed signal maps that are robust for use. Several different devices have been proposed, but this effort is less effective in dealing with new types of devices and still requires special equipment and high costs. The other

method is the pre-calibration method; translates the RSS of heterogeneous devices into the benchmark device by a set of conversion formulae. But this method impractical and time-consuming with the increasing number of new mobile devices because formulae must be found and validated in the lab [31].

Therefore, the methods that have been proposed to overcome the problem of device diversity in an indoor positioning system are generally mathematical. Device heterogeneity is eliminated by applying a linear mapping between fingerprints from different devices [29]. Some of these methods are the Unsupervised Learning Algorithm [32], linear regression [33], and hyperbolic location fingerprinting (HLF).

3. MATERIALS AND METHODS

This research was conducted in a computer and simulation laboratory at the Department of Electrical Engineering, Faculty of Industrial Technology, Islamic University of Indonesia. This laboratory has five rooms and one alley. The devices used in the study are smartphones and laptops. Smartphones were chosen from three different brands: Redmi Series 3, Meizu Series Note 5, and Oppo Series F1 Plus, to show device diversity. The laptop was used for data processing and calculating the distance errors used in the study.

This study consists of several stages: determining the number of access points (APs) used, making a database radiomap for each Android. Radiomap is model of network characteristics in a deployment area to estimate a position [34]. Then determining the test point and calculating the approximate location, and then calculating the distance error to examine the differences in the devices. The last step calculates a distance error with a proposed database modification, as shown in Figure 2.

According to the problem limit, the number of access points (APs) used to determine the distance error should be 4; 2 APs were available in the laboratory so 2 additional APs were added. The number of reference points used was 234 based on the length and width of the room, with a distance between one reference point and another reference point being 1 meter. All the rooms and the single hallway/alley in the laboratory were first measured in length and width before the reference point was determined. The layout of the Laboratory is shown in Figure 3.

The next step was to create a database radiomap using three selected Android brands: Redmi Series 3, Meizu Series Note 5, and Oppo Series F1 Plus. The database radiomap is the measurement result at the reference point stored in the database, consisting of the identification of the reference point, the position of each reference point, and the measured data. The most important information

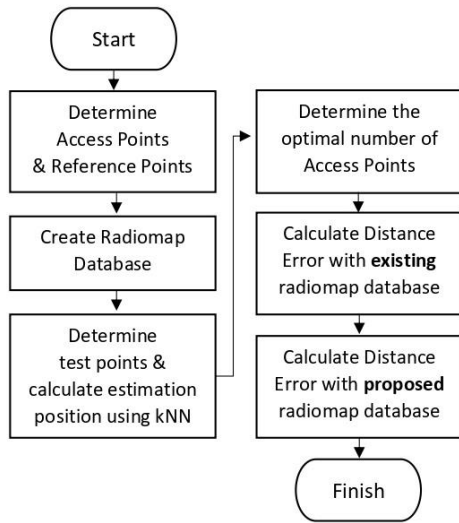


Figure 2. Research Flowchart

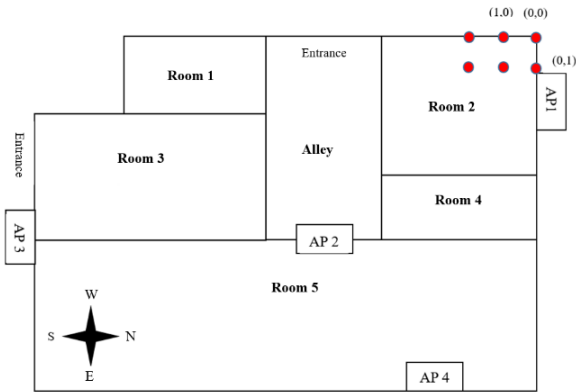


Figure 3. Computer and Simulation Laboratory Layout

in the database radiomap is the result of the Received Signal Strength Indicator (RSSI) value measured from all the available APs.

The radiomap database was created by measuring the RSSI values at each reference point, totaling 234 points, and the number of APs used. Before taking the measurements from each Android, special applications were first installed on the devices to take the RSSI value. The application was also given a Mac Address based on the 4 types of APs used in the study. The application used was Using Wi-Fi developed by Alshami et al. [23].

RSSI indicates the strength of the incoming (received) signal in a receiver. The closer to 0 dBm, the stronger the signal is. The RSSI value is very fluctuating (not constant) depending on multipath fading, environmental conditions, and the distance between the sender and receiver [25]. On IPS fingerprint, each coordinate point (x, y) is represented by a set of RSSI values from several access points (radiomap database). Each access point is represented by an RSSI value, to

obtain this value it is necessary to measure several RSSI values and choose a representative value. In this study, 20 RSSI values will be measured at each point using smartphone, and the mode value will be selected [9]. If at each coordinate point only one RSSI is measured, then the RSSI cannot represent the coordinates so that the accuracy of the IPS system will decrease.

In case of designing of Wi-Fi networks, RSSI values are classified into several groups: -50 dBm is excellent, -70 dBm is good, -80 dBm is low, and -100 dBm is no signal. But in IPS fingerprint there is no such classification, what is important is that each coordinate point has a unique set of RSSI values. That value becomes the difference between one coordinate point and another. The higher the variant value of the RSSI data in radiomap database, the higher the accuracy of the IPS Fingerprint system. High variance in the RSSI data is usually obtained in buildings that have many rooms or have many partitions with various materials.

The RSSI values were measured simultaneously using 3 Android brands at a height of 1 meter from the measured point, as shown in Figure 4. For one reference point, there would be 4 RSSI measured values. For AP1, the measured RSSI value was labelled RSSI1, whereas the RSSI value for AP2 was named RSSI2, and so on. The database radiomap format is summarized in Table 1.

The measurement of the RSSI value starts at the coordinates of x, y (0,0), which means it starts at the corner of one of the rooms in the laboratory, which can be seen in Figure 3 so that later, it would be easier to name each point that has been measured (based on their respective coordinate points). For each coordinate, there are 234 RSSI values, of 4 different types, namely RSSI1, RSSI2, RSSI3, and RSSI4, according to the number of APs used.

The test point was determined after measuring the RSSI and Radiomap database values obtained from the 3 Android brands. The test point taken was 10% of the 234 reference points, and the total test points used were 24 points. These 24 test points were determined randomly and evenly in all rooms in the laboratory by re-measuring the RSSI value at a predetermined point.

Distance error was calculated using the kNN algorithm (k = 3) based on the Redmi Android database with the Redmi test point. At this stage, the distance error could also be calculated using another Android brand, as



Figure 4. RSSI Value Measurement Process

TABLE 1. Format of The Radiomap Database

Coordinates		Redmi				Meizu				Oppo			
x	y	RSSI1	RSSI2	RSSI3	RSSI4	RSSI1	RSSI2	RSSI3	RSSI4	RSSI1	RSSI2	RSSI3	RSSI4

long as the database and test point were sourced from the same Android brand. The purpose of the calculation at this stage was to choose the optimal number of APs to be used in the next stage because the number of APs used will affect the computing load, i.e., the more APs used, the more complex the calculation.

The author used Microsoft Excel software to get a distance error value; the calculation scheme at this stage was to vary the number of APs:

- Scheme 1 used 4 APs
- Scheme 2 used 3 APs
- Scheme 3 used 2 APs

The distance error values in each of the smallest schemes and other considerations were chosen for the optimal use of AP, which would then be used as a reference for the following distance error calculation. The formula for calculating distance errors is given by Equation (2):

$$\text{Distance Error} = \sqrt{\Delta x^2 + \Delta y^2} \quad (2)$$

Remark:

$$\begin{aligned} \Delta x &= x_a - x_e \\ \Delta y &= y_a - y_e \\ (x_a, y_a) &= \text{the actual location} \\ (x_e, y_e) &= \text{the estimated location (IPS measurement results)} \end{aligned}$$

Distance error values were calculated using kNN ($k = 3$). The database was the Android Redmi series, and the test point was Android Redmi, Meizu, and Oppo. The calculation at this stage aimed to examine the effect of the different devices on the distance error value. Calculations were carried out sequentially to produce distance error values for the Android Redmi, Meizu, and Oppo:

- Redmi Series 3 database with the Redmi Series 3 test point
- Redmi Series 3 database with the Meizu Series Note 5 test point
- Redmi Series 3 database with the Oppo F1 Plus Test Point

Once the distance error of each Android brand had been obtained, the next step was to observe and compare the results of the distance error obtained. Differences in the value of the distance errors for each Android brand will point to a solution on how to use the database and test points with different Android brands, so the value of the resulting distance error is not so significant.

At this stage, a solution will be given to overcome the problem of device diversity, that is, by calculating the distance error using the kNN algorithm ($k = 3$) with the

proposed database modification using the difference method and ratio method to improve performance, namely by reducing distance error when using different devices. Before making the calculation, the original database of each Android brand was modified into 2 types of new databases: the difference database and the ratio database.

The number of APs used at this stage was 3 pieces, so the RSSI values were divided into 3 parts: RSSI1, RSSI2, and RSSI3, for each Android brand. The database and test point in the different methods must be modified by way of reducing each other, i.e., reducing the value of one RSSI with another RSSI value, for example, $SR1 = |RSSI1 - RSSI2|$, $SR2 = |RSSI1 - RSSI3|$ dan $SR3 = |RSSI2 - RSSI3|$. A new database radio map (SR1, SR2, SR3) is thus formed. At the test point, the same thing was done for creating a new database, which is to reduce the value of RSSI with one another, and a new test point was formed for the difference method.

In the ratio method (comparison), the database and test point were modified per Equations (3), (4), and (5) given below:

$$RR1 = \frac{RSSI1}{(RSSI1+RSSI2+RSS3)} \quad (3)$$

$$RR2 = \frac{RSSI2}{(RSSI1+RSSI2+RSS3)} \quad (4)$$

$$RR3 = \frac{RSSI3}{(RSSI1+RSSI2+RSS3)} \quad (5)$$

This way, the new database and the new test point for the ratio method are (RR1, RR2, RR3). Once the new database and test point with the different methods and ratios have been obtained, the next step is to calculate the distance error using the kNN algorithm ($k = 3$) for each Android brand and series. The expected outcome in the difference method and this ratio is to reduce the value of distance error when using a different device compared to the original database so that the problem of device diversity can be overcome.

4. RESULTS AND DISCUSSION

Before taking the data to the laboratory, the necessary tools were first prepared, namely 2 additional access points (APs), 2 electric terminals, and a meter measuring device. The next step was to prepare a laboratory and name a location plan at each point. Each point's general location can be seen in Figure 5, where the red points

The calculation at this stage was to find the average value of the distance error via kNN (k = 3) using 3 Aps, with the test point consisting of the Redmi 3 test point, Meizu Note 5, and Oppo F1 Plus. The average value of the distance error produced by the Redmi test point was expected to be smaller than when using the Meizu and Oppo test points because the database is the Redmi database itself.

The average value of the distance error would be taken as it is calculated using the kNN algorithm (k = 3) with 24 test points from the three types of Android brands. The results of the average distance error that was obtained is shown in Figure 7.

From the results of the graph as shown in Figure 7, the average value of the distance error for k = 3 obtained with the Redmi Android test point was 2.7, whereas the android Test Point Meizu produced an average distance error of 3.2, and the test point using Android OPPO produced an average distance error of 3.68. From the obtained results, the assumption from the start, before the calculation, is proven—namely, that the average value of the distance error produced by the Android Redmi test point will be smaller compared to the average value of the distance error using the Android Meizu and Oppo test points. This concept proves the notion of device diversity, where, by using a different device, the average value of the distance error produced will also be different. The use of the Meizu and OPPO devices resulted in an increase in the average distance error by 18.5% and 36.3%, respectively.

Given the problem of device diversity seen in the calculation as a result of using a different test point, a proposal was made to overcome it, namely via database modification using the difference and ratio methods; then, 2 types of new databases were created and used in the calculation for each method.

Both of these methods use the same previous calculation: to find distance error using the kNN algorithm (k = 3) to improve performance so that the distance error generated by the different devices would be smaller than before.

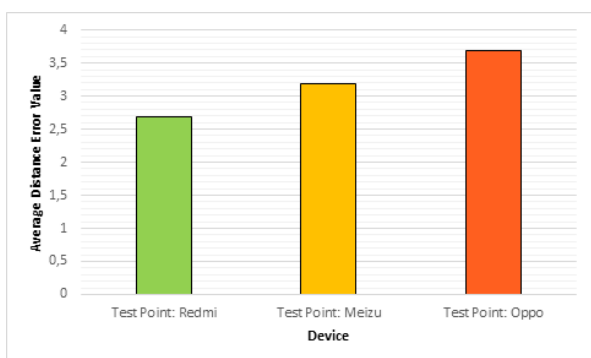


Figure 7. Graph of Average Distance Error for 3 Different Devices (radiomap database : Redmi)

The distance error results obtained after calculating the difference method and the ratio method showed a reduced distance error produced by each Android brand, as shown in Figure 8 below. The decrease in the average distance error (%) by using this proposed database modification is calculated using Equation (6).

$$Decreased\ Error = \frac{(Ea - Eb)}{Ea} \times 100\% \quad (6)$$

Ea is Initial error, which uses the original database from the results of the RSSI measured value. Eb is new error, using the results of the proposed database modification of the difference or ratio.

From the graph shown in Figure 8, the Android Redmi Series 3 results in a distance error value, using the original database, of 2.7, while for the difference database, the resulting error value is 2.17. Moreover, the ratio database also produced a smaller error compared to the original database, which is 2.56. Using equation (6), the average value of the distance error for the difference database decreased by 19.6%. As for the original database, the average distance error decreased in value by 5.2%.

On the Android Meizu Note 5 Series using the difference database, the ratio database produced an error that was smaller than the original database. The difference database produced a distance error of 2.42, while the ratio database produced a distance error of 2.78. This result is significantly different from the distance error generated using the original database, which was 3.2. The decrease in the average distance error in the difference database is 24.3%, whereas the ratio database was 13%.

The Android Oppo F1 Plus series produced a smaller distance error value when using the ratio database with a difference of 2.8 and 2.65. The original database of the distance error produced an error of 3.68. The decrease in average distance error using the difference database was 28%. Meanwhile, in the original database, the average decrease in the distance error was 24%.

Previous research preformed also used the kNN algorithm on IPS Fingerprint resulted in an accuracy of

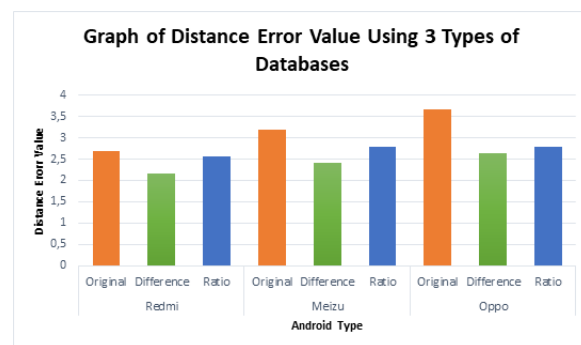


Figure 8. Graph of Comparison of Distance Error (radiomap database: Redmi)

2.94 m. Research conducted by Xia et al. [1] which uses a more complex algorithm (a multi-layer perceptron for indoor positioning), with a positioning accuracy of 2.3 m. The two studies have not paid attention to the aspect of device diversity. In the data reported by Nguyen et al. [4] stated that the IPS Fingerprint technique that uses Wi-Fi proposed by Zhou et al. [27], He et al. [6] and Korayem et al. [5] each can achieve an accuracy of 3.2m and 5.3m. While in research conducted by Choi and Jang [7], the accuracy that can be achieved is 86% in a cell with a size of 2.7 x 2.8 meters. The best accuracy in this study was 2.17m, still better than the previous studies mentioned above. This research has also overcome the problem of device diversity which has not been discussed in previous studies.

RSSI data collection on a building to create a radiomap database is low cost because it only requires a smartphone and an operator. It is just that manually collecting RSSI data requires quite a long time. Then several solutions have been proposed using the indoor propagation model to create a radiomap database in short time [9]. This research does not touch on RSSI data collection techniques, but on processing RSSI data to create a new database radiomap. Data processing is also only carried out by calculating the difference in RSSI (reduction operation), so that the additional computational needs will not be high either.

5. CONCLUSION

The results of calculating the average value of the distance error using the proposed modification, the Difference Database Radiomap and the ratio database, can provide solutions to the problem of device diversity for an Indoor Positioning System (IPS) using fingerprinting techniques, which only require a light computing system. The decrease in the distance error that occurred with the Redmi 3 Series Android smartphones using the modified difference database was 19.6%, while for the ratio database, the decreased distance error was 5.2%. On Android smartphones, Meizu Note 5 Series showed a decreased average distance error, with a difference database, of 24.3%, and using a ratio database, the average distance error decreased by 13%. As for the Android smartphone, Oppo F1 Plus, using the difference database and ratio database, the decrease in the average distance error was 28% and 24%, respectively.

Based on the research above, several suggestions to improve future research are to use devices that have not been used in this study so that more devices can be compared. Besides, the test location could include more than one location, and the number of original databases can be increased to more than one to compare the distance error value.

6. ACKNOWLEDGEMENTS

This work was supported by the Fundamental Research Grant Scheme R.K130000.7814.5F228, and a research grant from the Department of Electrical Engineering, Universitas Islam Indonesia (EE UII). Hence, the authors would like to thank Universiti Teknologi Malaysia (UTM) and EE UII for their support.

7. REFERENCES

1. Xia, S., Liu, Y., Yuan, G., Zhu, M., and Wang, Z. "Indoor fingerprint positioning based on Wi-Fi: An overview." *ISPRS International Journal of Geo-Information*, Vol. 6, No. 5, (2017). <https://doi.org/10.3390/ijgi6050135>
2. Hadian Jazi, S., Farahani, S., and Karimpour, H. "Map-merging in multi-robot simultaneous localization and mapping process using two heterogeneous ground robots." *International Journal of Engineering, Transactions A: Basics*, Vol. 32, No. 4, (2019), 608-616. <https://doi.org/10.5829/ije.2019.32.04a.20>
3. Hamidi, H., and Valizadeh, A. "Improvement of navigation accuracy using tightly coupled Kalman filter." *International Journal of Engineering, Transactions B: Applications*, Vol. 30, No. 2, (2017), 1293-1301. <https://doi.org/10.5829/idosi.ije.2017.30.02b.08>
4. Nguyen, K. A., Luo, Z., Li, G., and Watkins, C. "A review of smartphones-based indoor positioning: Challenges and applications." *IET Cyber-systems and Robotics*, Vol. 3, No. 1, (2021), 1-30. <https://doi.org/10.1049/csy2.12004>
5. Korayem, M. H., Peydaie, P., and Azimirad, V. "Investigation on the effect of different parameters in wheeled mobile robot error." *International Journal of Engineering, Transactions A: Basics*, Vol. 20, No. 2, (2007), 195-210.
6. He, S., and Chan, S.-H. G. "INTRI: Contour-Based Trilateration for Indoor Fingerprint-Based Localization." *IEEE Transactions on Mobile Computing*, Vol. 16, No. 6, (2017), 1676-1690. <https://doi.org/10.1109/TMC.2016.2604810>
7. Choi, M. S., and Jang, B. "An accurate fingerprinting based indoor positioning algorithm." *International Journal of Applied Engineering Research*, Vol. 12, No. 1, (2017), 86-90. Retrieved from <https://yonsei.pure.elsevier.com/en/publications/an-accurate-fingerprinting-based-indoor-positioning-algorithm>
8. Mrindoko, N. R., and Minga, D. L. M. "A Comparison Review of Indoor Positioning Techniques." *International Journal of Computer*, Vol. 21, No. 1, (2016), 42-49. <https://doi.org/10.1093/hmg/1.8.655-a>
9. Firdaus, F., Ahmad, N. A., and Sahibuddin, S. "Accurate indoor-positioning model based on people effect and ray-tracing propagation." *Sensors*, Vol. 19, No. 24, (2019). <https://doi.org/10.3390/s19245546>
10. Firdaus, F., Ahmad, N. A., and Sahibuddin, S. "A review of hybrid indoor positioning systems employing WLAN fingerprinting and image processing." *International Journal of Electrical and Computer Engineering Systems*, Vol. 10, No. 2, (2019), 59-72. <https://doi.org/10.32985/ijeces.10.2.2>
11. Kim, Y., Shin, H., Chon, Y., and Cha, H. "Smartphone-based Wi-Fi tracking system exploiting the RSS peak to overcome the RSS variance problem." *Pervasive and Mobile Computing*, Vol. 9, No. 3, (2013), 406-420. <https://doi.org/https://doi.org/10.1016/j.pmcj.2012.12.003>
12. Mautz, R. "Overview of current indoor positioning systems." *Geodesy and Cartography*, Vol. 35, No. 1, (2009), 18-22.

- <https://doi.org/10.3846/1392-1541.2009.35.18-22>
13. Subedi, S., and Pyun, J. Y. "A survey of smartphone-based indoor positioning system using RF-based wireless technologies." *Sensors*, Vol. 20, No. 24, (2020), 1-32. <https://doi.org/10.3390/s20247230>
 14. Batistić, L., and Tomic, M. "Overview of indoor positioning system technologies." In 2018 41st International Convention on Information and Communication Technology, Electronics and Microelectronics (MIPRO), 473-478. <https://doi.org/10.23919/MIPRO.2018.8400090>
 15. Firdaus, Ahmad, N. A., and Sahibuddin, S. "Fingerprint indoor positioning based on user orientations and minimum computation time." *Telkomnika (Telecommunication Computing Electronics and Control)*, Vol. 17, No. 4, (2019), 1740-1749. <https://doi.org/10.12928/TELKOMNIKA.V17I4.12774>
 16. Mendoza-Silva, G. M., Torres-Sospedra, J., and Huerta, J. "A meta-review of indoor positioning systems." *Sensors*, Vol. 19, No. 20, (2019). <https://doi.org/10.3390/s19204507>
 17. Wang, H., Ma, L., Xu, Y., and Deng, Z. "Dynamic Radio Map Construction for WLAN Indoor Location" in Third International Conference on Intelligent Human-Machine Systems and Cybernetics, IEEE, (2011). <https://doi.org/10.1109/IHMSC.2011.110>
 18. Zulkiflie, S. A., Kamaruddin, N., and Wahab, A. "Dynamic navigation indoor map using wi-fi fingerprinting mobile technology." *Bulletin of Electrical Engineering and Informatics*, Vol. 9, No. 2, (2020), 739-746. <https://doi.org/10.11591/eei.v9i2.2066>
 19. Pérez-Navarro, A., Torres-Sospedra, J., Montoliu, R., Conesa, J., Berkvens, R., Caso, G., Costa, C., Dorigatti, N., Hernández, N., Knauth, S., ... Wilk, P. "Challenges of fingerprinting in indoor positioning and navigation." *Geographical and Fingerprinting Data for Positioning and Navigation Systems: Challenges, Experiences and Technology Roadmap*, No. July 2018, (2018), 1-20. <https://doi.org/10.1016/B978-0-12-813189-3.00001-0>
 20. Pascacio, P., Casteleyn, S., Torres-Sospedra, J., Lohan, E. S., and Nurmi, J. "Collaborative indoor positioning systems: A systematic review." *Sensors*, Vol. 21, No. 3, (2021), 1-39. <https://doi.org/10.3390/s21031002>
 21. Mashuk, M. S., Pinchin, J., Siebers, P. O., and Moore, T. "A smart phone based multi-floor indoor positioning system for occupancy detection." in *IEEE/ION Position, Location and Navigation Symposium, PLANS 2018 - Proceedings*, No. December, (2018), 216-227. <https://doi.org/10.1109/PLANS.2018.8373384>
 22. Wang, J., and Park, J. G. "An enhanced indoor positioning algorithm based on fingerprint using fine-grained csi and rssi measurements of ieee 802.11n wlan." *Sensors*, Vol. 21, No. 8, (2021). <https://doi.org/10.3390/s21082769>
 23. Alshami, I. H., Ahmad, N. A., Sahibuddin, S., and Firdaus, F. "Adaptive Indoor Positioning Model Based on WLAN-Fingerprinting for Dynamic and Multi-Floor Environments." *Sensors*, Vol. 17, No. 8, (2017). <https://doi.org/10.3390/s17081789>
 24. Yudha, D. P., Hasbi, B. I., and Sukarna, R. H. "Indoor Positioning System Berdasarkan Fingerprinting Received Signal Strength (Rss) Wifi Dengan Algoritma K-Nearest Neighbor (K-Nn)." *ILKOM Jurnal Ilmiah*, Vol. 10, No. 3, (2018), 274-283. <https://doi.org/10.33096/ilkom.v10i3.364.274-283>
 25. Firdaus, Ahmad, N. A., Sahibuddin, S., and Dzyiauddin, R. A. "Modelling the Effect of Human Body around User on Signal Strength and Accuracy of Indoor Positioning." *International Journal of Integrated Engineering*, Vol. 12, No. 7, (2020), 72-80. <https://doi.org/10.30880/ijie.2020.12.07.008>
 26. Wang, L., Liu, J., and Zhou, W. A Survey on Motion Detection Using WiFi Signals. <https://doi.org/10.1109/MSN.2016.040>
 27. Zhou, B., Li, Q., Mao, Q., and Tu, W. "A robust crowdsourcing-based indoor localization system." *Sensors*, Vol. 17, No. 4, (2017), 1-16. <https://doi.org/10.3390/s17040864>
 28. Xue, J., Liu, J., Sheng, M., Shi, Y., and Li, J. "A WiFi fingerprint based high-adaptability indoor localization via machine learning." *China Communications*, Vol. 17, , (2020), 247-259. <https://doi.org/10.23919/J.CC.2020.07.018>
 29. Li, Y., Williams, S., Moran, B., and Kealy, A. "A Probabilistic Indoor Localization System for Heterogeneous Devices." *IEEE Sensors Journal*, Vol. 19, No. 16, (2019), 6822-6832. <https://doi.org/10.1109/JSEN.2019.2911707>
 30. Park, J. G., Curtis, D., Teller, S., and Ledlie, J. "Implications of device diversity for organic localization." *Proceedings - IEEE INFOCOM*, No. July 2011, (2011), 3182-3190. <https://doi.org/10.1109/INFCOM.2011.5935166>
 31. Yang, F., Xiong, J., Liu, J., Wang, C., Li, Z., Tong, P., and Chen, R. "A pairwise SSD fingerprinting method of smartphone indoor localization for enhanced usability." *Remote Sensing*, Vol. 11, No. 5, (2019). <https://doi.org/10.3390/rs11050566>
 32. Li, L., Yang, W., Bhuiyan, M. Z. A., and Wang, G. "Unsupervised learning of indoor localization based on received signal strength: Unsupervised learning of indoor localization." *Wireless Communications and Mobile Computing*, Vol. 16, , (2016). <https://doi.org/10.1002/wcm.2678>
 33. Zhang, L., Meng, X., and Fang, C. "Linear Regression Algorithm against Device Diversity for the WLAN Indoor Localization System." *Wireless Communications and Mobile Computing*, Vol. 2021, , (2021). <https://doi.org/10.1155/2021/5530396>
 34. Meneses, F., Moreira, A., Costa, A., and Nicolau, M. J. Radio maps for fingerprinting in indoor positioning. *Geographical and Fingerprinting Data for Positioning and Navigation Systems: Challenges, Experiences and Technology Roadmap*. Elsevier Inc. <https://doi.org/10.1016/B978-0-12-813189-3.00004-6>

Persian Abstract

چکیده

توسعه خدمات مبتنی بر مکان مستلزم یک فناوری سیستم موقعیت یابی دقیق و فزاینده است. تحقیقات در مورد سیستم های موقعیت یابی در فضای باز به دقت رضایت بخشی دست یافته است و معمولاً در خدمات مختلف مبتنی بر مکان استفاده می شود. روند تحقیقات اکنون به سمت سیستم موقعیت یابی داخلی (IPS) در حال تغییر است. یکی از تکنیک هایی که به طور گسترده در IPS مبتنی بر Wi-Fi استفاده می شود، اثر انگشت است. تکنیک انگشت نگاری در Wi-Fi از مقدار نشانگر قدرت سیگنال دریافتی (RSSI) استفاده می کند. مشکلی که رخ می دهد این است که نتایج اندازه گیری های RSSI در گوشی های هوشمند برندهای مختلف، مقادیر RSSI متفاوتی را تولید می کند که به عنوان تنوع دستگاه نیز شناخته می شود. تنوع دستگاه باعث کاهش دقت سیستم می شود. این مطالعه با هدف ارائه راه حلی برای مشکل تنوع دستگاه در Wi-Fi IPS بر اساس اثر انگشت RSSI، یعنی دریافت یک خطای فاصله جزئی است. راه حل پیشنهادی اصلاح نقشه رادیویی پایگاه داده اصلی به دو پایگاه داده جدید است: پایگاه داده تفاوت و پایگاه داده نسبت. نقشه رادیویی پایگاه داده تفاوت توانست میانگین خطاهای فاصله را ۲۴.۳ درصد در Meizu و ۲۸ درصد در OPPO کاهش دهد. سپس، با استفاده از نسبت پایگاه داده Radiomap، مقدار متوسط خطاهای فاصله را می توان ۱۳٪ در Meizu و ۲۴٪ در OPPO کاهش داد. از محاسبات، نسبت پایگاه داده Radiomap می تواند راه حلی را برای مشکل تنوع دستگاه برای یک سیستم موقعیت یابی داخلی بهتر از نقشه رادیویی پایگاه داده تفاوت ارائه دهد، اگر به کاهش خطای فاصله نگاه کنیم.



Effect of Replacement Ratio on Torsional Behaviour of Recycled Aggregate Concrete Beams

N. Masne*, S. Suryawanshi

Department of Civil Engineering, S. V. National Institute of Technology, Surat, India

PAPER INFO

Paper history:

Received 21 November 2022

Received in revised form 26 December 2022

Accepted 28 December 2022

Keywords:

Construction Waste

Demolition Waste

Solid Waste Management

Torsion

Diagonal Cracks

ABSTRACT

In the past two decade, researchers have studied the flexural, shear and bond behaviour of recycled aggregate concrete (RAC) beams. This work intends to analyze the behaviour of RAC beams under pure torsion, despite the lack of information on its behaviour under pure torsion. The coarse recycled concrete aggregates (RCA) extracted from construction and demolition (C & D) waste was used to replace natural coarse aggregates (NCA) in 0 %, 50 %, and 100 % ratio. Their recycling could help preserve the environment and promote sustainability through solid waste management. Six beams, each of size 150 x 250 x 1800 mm were prepared and tested. To detects minor deformation and to achieve the same strength through the out-of-plane direction, 250 mm inbuilt cantilever projections were provided on opposite faces of the beams at a span of 1000 mm along the longitudinal axis. The ultimate torsional capacity of tested beams was lower by 7.41 %, 8.60 % and 13.58 % than ATENA-3D (FEM) for 0 %, 50 % and 100 % RCA. The change in the replacement ratio of aggregate has a low impact on the ultimate torque and angle of twist. Based on the experimental and analytical results, it was established that the torque resistance capacity of the RAC beam was reduced as the % of RCA increased. Similar crack patterns and failure behaviour were observed in RAC and NAC beams in both studies. Therefore, it is practically possible to apply RAC in structural applications under pure torsional loading.

doi: 10.5829/ije.2023.36.04a.06

1. INTRODUCTION

Torsion progresses in structural elements as an effect of asymmetrical loading, member shape, or structural framing. Stairway lateral beams, bridge decks, and spiral stairs are examples of RC components exposed to strongly eccentric stresses and torsional loading. Several structural components in bridges and buildings are exposed to considerable torsional moments that influence the design. Torsion design has become important in reinforced concrete beams in construction. Recognizing the significance of the issue, a research has been done on the torsional performance of steel fibre concrete [1]. The behaviour of RC members in pure torsion has been subject of extensive investigation. The pure torsional performance of RAC beams has not yet been thoroughly addressed, and limited research on the torsional performances of RAC beams is available in the literature.

In seismic torsion, RAC beams fail similar to regular concrete beams [2, 3]. According to Sarsam et al. [4], the application of RCA in RAC is nearly conceivable in torsionally loaded structural elements. The analytical (ATENA-3D) and experimental study showed that altering RCA does not degrade pure torsional behaviour of RAC solid beams and the utilization of RAC in structural applications has become an essential aspect [5, 6]. These studies demonstrated the significance of RAC beams in pure torsional design; as a result, this investigation explored the structural behaviour of RAC beams subjected to pure torsion. On the other hand, NCA are an essential component of RAC, but their availability is decreasing day by day. To overcome this, RCA can be a substitute for NCA in concrete. According to the Central Pollution Control Board of India [7], India had 1.8 million tonnes of RCA each year. The Indian Standard IS: 383 [8] for coarse and fine aggregates allows

*Corresponding Author Institutional Email: nsmasne@gmail.com
(N. Masne)

the use of RCA up to 20% in reinforced concrete elements. The C&D waste will be the one source of RCA. The reusing of C&D waste on a large scale has the potential to significantly reduce natural aggregate consumption and contribute to environmental preservation [9] and solid waste management. Different types of waste materials are used to manufacture of concrete for pavement and structural application [10-14]. RAC is becoming an appealing structural material in the building sector. The idea of utilizing RCA in structural concrete is gradually obtaining scalability at present, and investigation in this scope is improving. The tensile strength [15], compressive strength [16], toughness and ductility index [17], and constitutive relationship [18] of RAC have been found in the literature, which showed worthy agreement with the NAC. Many structural engineers and researchers also studied the flexural [19], shear [20], and bond [21] performance of RAC elements, but slight work has been found on the torsion. The research work related to reducing carbon emissions mention that, the globe moves toward sustainable sources and the research toward innovation with new technologies should be transparent and acceptable at large scale [22, 23]. Except the investigation by Sarsam et al. [4], and Masne et al. [6] no test data on the torsional behaviour of RAC beams is available in literature. The current study was conducted to bridge this gap. This study will help to facilitate the safe structural application of RAC beam in pure torsion.

2. MATERIALS AND METHODS

2.1. Materials This experiment employed grade 53 OPC with a fineness of 3080 cm²/g and a specific gravity of 3.14 accordance with IS-12269 [24]. As fine aggregate (FA), zone II river sand that conforms to IS-383 [8] was utilized (fineness modulus = 2.80). The NCA with a size of 20 mm was utilized, according to IS-383 [8]. Deformed TMT steel bars were used as reinforcement of Grade Fe500. The steel bars were tested in a 1200 kN capacity UTM to obtain their mechanical properties as per the procedure recommended in IS-1608 part-I. To achieve the requisite quality of new concrete in the experiment, a polycarboxylic ether-based high-range water-reducing additive (HRWRA) according to IS-9103 was utilized. The admixture dosage was kept at 0.77 % by the weight of cement. Concretes were mixed and cured with tap water, ensuring with IS-456. The coarse RCA were obtained from tested concrete specimens at the concrete laboratory by using mechanical breaker and jaw crusher to prepare concrete. The waste concrete specimens were composed of a variety of beam-column junctions with varying compressive strengths of 20-30 MPa. It was unable to assess the original concrete's quality from such specimens. Because of this, there was

no accurate information about the quality of the concrete specimens that were used to make the RCA in this study. The size fractions of RCA after sieving 35 % on 4.75 - 10 mm, 22.5 % on 10 - 12.5 mm, 22.5 % on 12.5 - 16 mm, and 20 % on 16 mm-20 mm respectively, are shown in Figure 1. The obtained RCA was sieved and stored in separate bags so that these fractions could be blended manually.

The mechanical and physical characteristics of both aggregates are shown in Table 1. The aggregate characteristics like water absorption, specific gravity, and residual adhering mortar of RCA are very important when preparing the correct concrete mix. The RCA was porous, less dense, and absorbs extra water than NCA. These RCA particles were spherical and extra fines were broken off during crushing and impact testing was observed from Table 1. The impact and crushing tests are used to determine the aggregate durability. Residual mortar in the interfacial transition zone (ITZ) of RAC can readily be broken off, which is common in concrete. Under the load, the remaining mortar on RCA would break off, but NCA has no such coat to fail.

2.2. Concrete Mixtures In accordance with IS-10262, the absolute volume method was utilized to create concrete mix grade of the M30 using NCA and RCA. The IS-456 was used to cast concrete. Table 2 presents the NAC and RAC mix proportions of concrete.



Figure 1. Comparison of different size fraction of NCA and RCA

TABLE 1. Characteristics of the coarse aggregates

Aggregate Type	NCA	RCA
Size (mm)	4.75-20	4.75-20
Water Absorption (%)	1.05	3.85
Specific gravity	2.64	2.45
Aggregate Crushing Value (%)	21.10	25.40
Aggregate Impact Value (%)	15.30	20.80

TABLE 2. Concrete mix proportions

Mix	M-R00	M-R50	M-R100
% of RCA	0.00	50.00	100.00
Cement	1.00	1.00	1.00
W/C ratio	0.40	0.40	0.40
FA	1.67	1.67	1.67
NCA	2.82	1.41	0.00
RCA	0.00	1.30	2.60
HRWRA	0.77	0.77	0.77

In the absolute volume technique, the volume of compacted concrete equals the total volume of all ingredients. The approach described in earlier study [19] was followed while using the RCA particles in the saturated surface dry (SSD) state. In laboratory, the concrete was mixed using a tilting-drum mixer. Before mixing began, measured quantities in terms of weights of concrete materials such as cement, fine aggregate, NCA, and RCA were kept ready in bags. To wet the coarse aggregates, one-third of total water was introduced to the mixer along with coarse aggregates before mixing. Following that, one-third quantity of the cement was added and the constituents were mixed for approximately one minute. Then the fine aggregates were added, followed by the remaining cement and water. The entire mixing time was limited to 30 minutes. A coat of oil was applied to the interior surface of the moulds used to cast the test specimens. Following completion of mixing, concrete was poured into the moulds for a period of 24 hours and then de-moulded. In this study, changed ratios of RCA were considered for the same grade of concrete, so that water content was constant for all the mixt to achieve workability and strength.

2. 3. Test Specimens

Concrete's compressive strength IS-516 [25] and its tensile strength IS-5816 [26] were measured using 150 x 300 mm cylinders. Prisms measuring 100 x 100 x 500 mm were made to test the concrete's flexural strength IS-516 [25]. All the samples were cured in water for 28 days before testing. Meantime, six beams were casted into three groups based on % of RCA. The first group was considered a reference group, which consisted of two beams cast from NCA-concrete denoted by B-R00. The second and third groups consisted of two beams each, cast from 50 % and 100 % RCA-concrete, denoted by B-R50 and B-R100, respectively, and the average or best of two from each group is reported. All the beams were reinforced with the same transverse and longitudinal steel shown in Figure 2. All the stirrups were anchored with 135° hooks to resist the torsion specified in CSA-14 [27]. To avoid local failure, the spacing of stirrups in the end zone and lever arms was curtailed to 50 mm c/c.

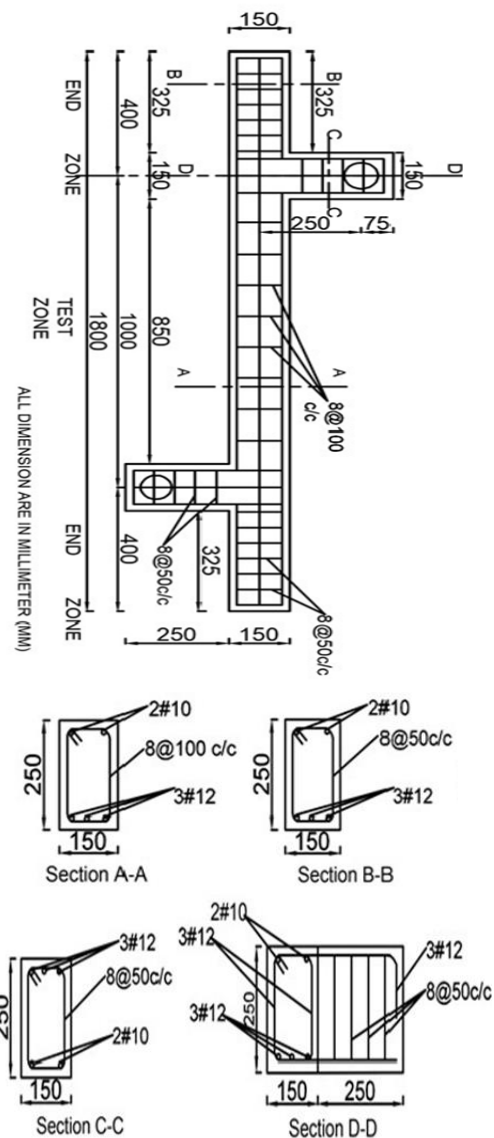


Figure 2. Details of steel reinforcement specimen

The torsion specimens were formed by pouring concrete into the mould and compacting with a needle vibrator on a level and clean surface of lab. The beams were covered with a plastic sheet shortly after casting to prevent evaporation, and demoulded 24 hours. All beams wrapped in gunny bags and cured in the laboratory for 28 days.

2. 4. Test Set-up

The test set-up for torsion was planned and manufactured in the structural laboratory. Figure 3 shows the schematic diagram of a typical setup. The specimen was put on roller support at a distance of 1350 mm aligned with the specimen so that the ends of the specimen could freely rotate, extend, and contract shown in Figures 3 and 4. At both ends of the specimen, roller supports were positioned to ensure free rotation and

elongation. The load was applied through a steel spreader beam supported by rollers above the lever arms.

Previously, metal mechanisms were used to hold the beam while applying a torsional load. This type of apparatus causes errors in the detection of slight deformation because it permits slippage and gaps between the metal clamping and the beam. To overcome this problem and to achieve the same strength through the out-of-plane direction where the matrix carries the primary load, 250 mm inbuilt cantilever projections were provided on opposite sides of the beams at a span of 1000 mm along the longitudinal axis. The free span of the beam subjected to pure torsion was 850 mm, and the effective range was 1000 mm. To measure the vertical deformations in the RAC beam two linear variable displacement transducers (LVDT) were attached to the bottom of lever arm. The LVDTs and load sensor were connected to the data collecting system. The tested beams were gradually loaded with a hydraulic jack with a 1000 kN capacity till failure at the middle of the spreader beam. The recorded data were load at first crack, the crack pattern, crack angle, crack width, angle of twist, and the overall performance of the specimen when subjected to pure torsion. The spreader beam and hydraulic jack were knotted by a string in the actual test set up, as shown in Figure 4, in such a manner that it should not affect the test setup and readings at any level throughout the test.

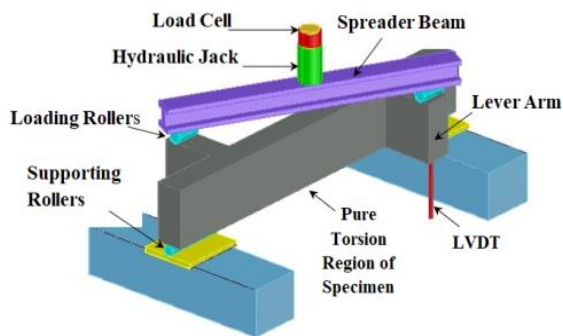


Figure 3. Schematic diagram of test set up



Figure 4. Front and side view of actual test set-up

3. RESULTS AND DISCUSSIONS

This investigation aims to verify the compatibility of RCA in concrete for structural use. The presentation of the outcomes is organized in the same sequence as that in which the experiment was conducted and compared with finite element model by ATENA-3D software.

3.1. Concrete Density Table 3 shows the densities of all hardened concrete combinations. When the densities of the NAC and RAC mixes were compared, it was found that 50 % and 100 % RCA in concrete reduces the density by 1.92 % and 3.75 %, as compared to 0 % RCA. These results showed that RCA does not affect the density of concrete largely. The density of RAC was mostly affected by the residual adhering mortar of RCA.

3.2. Mechanical Properties of Concrete Table 3 specifies the mechanical properties of concrete for all mixes. The concrete's elastic modulus was determined by using the IS-456. The ratio of the compressive strength to the flexural strength of concrete is known as brittleness. When the brittleness property of concrete increases, its tensile strength decreases. This means that once the concrete has achieved its tensile strength, it loses its ability to resist loads and cracks developed in the concrete. With increased brittleness, the bond between cement paste and RCA breaks, and aggregates burst. Table 3 showed that the 0 % and 50 % RCA produced similar compressive, tensile, flexural and modulus of elasticity of concrete i.e. 0.80 %, 3.16 %, 1.00 %, and 0.39 %. Meanwhile for a similar grade of concrete, RAC with 100 % RCA produced inferior compressive, tensile and flexural strength, i.e. 13.12 %, 23.35 %, and 25.27 %, respectively, which considerably caused in a higher brittleness ratio i.e. 13.93 %, as shown in Table 3. In the majority of circumstances, it was expected that the mechanical qualities of RAC would be inferior to those of conventional concrete as found in the literature [4, 5]. RAC with 100 % RCA had low mechanical properties because the aggregate-cement paste bond broke down. This caused the RAC to be less durable. The NAC specimens, on the other hand, failed due to aggregate and cement matrix fracture. The modulus of elasticity of

TABLE 3. Test beam material and experimental parameters

Mix Id	M-R00	M-R50	M-R100
Density (Kg/m ³)	2400	2354	2310
Compressive strength (MPa)	37.10	36.80	32.23
Tensile Strength (MPa)	4.11	3.98	3.15
Flexural Strength (MPa)	4.55	4.50	3.40
Brittleness	8.15	8.17	9.47
Modulus of Elastic (GPa)	30.45	30.33	28.38

RAC experiences strain when compressed and resulting in an inferior modulus of elasticity i.e. 6.79 % for B-R100 than B-R00, same observations were found in literature [4, 16].

3. 3. Test Analysis under the Influence of Different Load Levels and Angle

Table 4 shows the test analysis under different load level and angles of test beams, which were very helpful to understand the detailed test load information. The average of two beams is reported in Table 4. As the load level changes, the cracks angle and crack pattern were also changes on the concrete surface of test beams.

3. 4. Effect of RCA on Torsional Strength

From Table 5, it was observed that the cracking torque for B-R50 and B-R100 was lower by 10.56 % and 27.60 % than B-R00 beam and the ultimate torque for B-R50 and B-R100 was reduced by 6.79 % and 23.2 % than B-R00 beam. The torque resistance capacity of B-R100 was less than that of B-R00 beams at every state of loading i.e. 27.60 % at cracking, 20.30 % at yielding, 23.24 % at ultimate and 28.64 % at failure state respectively. It will help to decide the required changes in a modification to the current standards. Because RAC has an inferior elastic modulus than NAC and the twist angle of beams

at every loading state increases as the ratio of RCA was increased. Similar torsional behaviour was mentioned in the experimental work [4, 5]. Table 5 summarized data when RCA grows, the cracking torque to ultimate torque capacity decreases. Because of the poorer ITZ of older RCA, the cracking torque to ultimate torque ratio for B-R50 and B-R100 beams was reduced by 3.22 % and 4.68 %, than the B-R00 beams. The average of two beams is reported in Table 5. This result indicates slightly inferior than NAC, but considerable behaviour of RAC beam in torsion as found in the literature [2-5].

3. 5. Effect of RCA Content on Cracking Behaviour

Crack origination and the crack pattern were the important constraints of this experiment. At the commencement of the experiment, no cracks were seen as the load increased linearly. Concrete generally resisted torsion until the beam cracked. In testing, the first crack was detected in the test zone on the longer face of the beams, then it spread diagonally to the other faces, which formed a spiral crack. This is because the main paths of compressive and tensile and spiral around the beams in directions that are 45 degrees apart from the beam's axis [26]. As the torque reached its ultimate torsional strength, a 45°- 62° diagonal crack was observed as displayed in Figure 5. The angle of the primary diagonal crack depends on the principal stress orientation and the diagonal compressive stress angle. RAC beam diagonal crack angles increased with RCA.

As an example crack behaviour of beam B-R50-01 and B-R50-02 was examined, shown in Figure 6. To understand the cracking behaviour under different load level two beams with same concrete mix are reported from all the beams with average torque in Figure 6. The first crack was observed diagonally at average torque of 5.25 kN.m. As the load increases, more diagonal cracks were emerged on the longer side beams at yield state 6.88 kN.m. As the torque near is peak, a major diagonal crack occurred. After the average peak torque of 8.50 kN.m

TABLE 4. Test analysis under different load levels and angle

Beam Type	Load Level	Stage of loading	Observations
B-R00	0.65Tu	Crack stage	45° diagonal cracks, can close after unloading
B-R50	0.61Tu		
B-R100	0.60Tu		
B-R00	0.80Tu	Yield stage	Larger and more number of 45° cracks, that did not recover after unloading
B-R50	0.81Tu		
B-R100	0.83Tu		
B-R00	Tu	Ultimate stage	Complete 45° diagonal cracks
B-R50	Tu		
B-R100	Tu		
B-R00	0.85Tu	Failure stage	Concrete lump caving, brittle failure
B-R50	0.85Tu		
B-R100	0.85Tu		
			Complete diagonal cracks, same as B-R00 beams, crack angle change
			Complete diagonal cracks, faster and larger than B-R00 and B-R50 beams crack angle increases from 52°
			Concrete lump caving is a brittle failure mode same as B-R00.
			Concrete lump caving is a brittle failure mode that is more severe than B-R00 and B-R50 beams and crack angle increases to 62°.

TABLE 5. Measured torque and corresponding angle of twist at cracking, yield, ultimate, and failure state

State of Loading		B-R00	B-R50	B-R100
Cracking State	T_{cr} (kN.m)	5.87	5.25	4.25
	θ_{cr} (rad/m)	0.012	0.012	0.014
Yield State	T_y (kN.m)	7.29	6.88	5.81
	θ_y (rad/m)	0.022	0.022	0.025
Ultimate state	T_u (kN.m)	9.12	8.50	7.00
	θ_u (rad/m)	0.043	0.044	0.047
Failure State	T_f (kN.m)	8.25	7.37	5.87
	θ_f (rad/m)	0.053	0.054	0.058

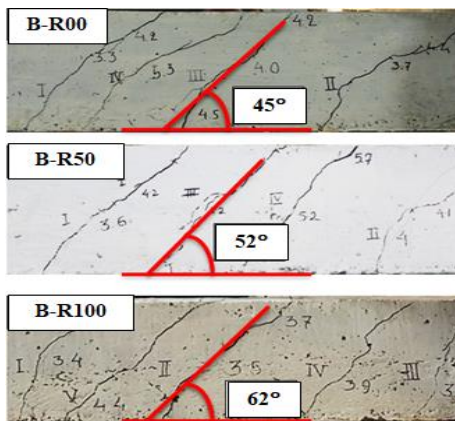


Figure 5. Angle of major diagonal cracks

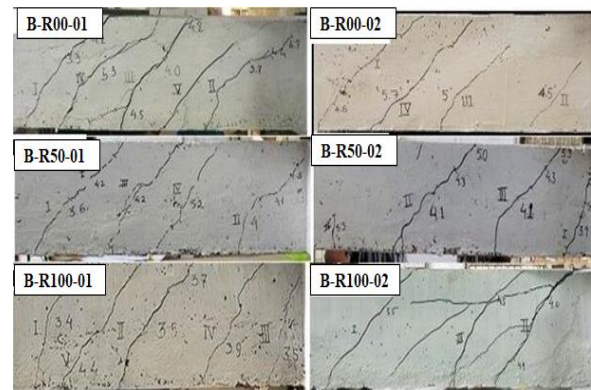


Figure 7. Comparison of crack pattern in test region for all specimens

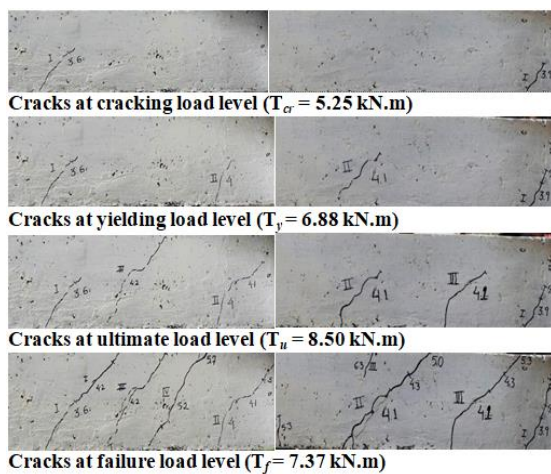


Figure 6. Comparison of cracking under different load levels (B-R50-01 and B-R50-02)

was reached, the torque decreases gradually to 7.37 kN.m. All the emerging cracks were parallel to first diagonal crack with increasing load from cracking to failure level. The failure mode indicated a diagonal tensile failure in all the beam.

Figure 7 shows the crack pattern in test region for all the six tested beams at their final state. The crushing of the concrete cover was detected only when the beams were twisted much beyond their ultimate limit for all the beams. Concrete crushing perpendicular to diagonal cracks was found at 0.047 rad/m and increased to 0.058 rad/m. This resulted in crushing of concrete cover because of excessive twisting deformation, as the torque increases. It was an indication toward the end of the experimentation. The width of the crack was measured with a hand microscope that could count to at least 0.02 mm. The width of the cracks measurements were made at the middle of the widest face as the crack width was the maximum at this point and the best of the two is reported. The detected performance of crack width was the same in all beams. When torque approaches its

ultimate torque, it's possible that the beam will break because of the excessive expansion of one large crack relative to the other cracks in the beam. When the types of concrete beams were tested for torsion, similar cracks with excessive expansion were found in the literature [1]. The structures may become unusable as a result of these excessive wide cracks in beams. The recommended limiting value of crack width in IS-456 and in ACI-318 [28] is 0.30 mm and 0.41 mm, respectively, for NAC. The ITZ from the old mortar and new mortar meet the RCA, this ITZ might grow and crack. When it comes to crack width in torsion, the use of RCA was not a concern for structural concrete beams since it has less influence, as found in the test region, as shown in Figure 8 (a, b, c). The crack width was measured for both beams of each mix and best of two results are reported in Figure 8.

3. 6. Finite Element Model Comparison with Test

The diagonal cracking patterns observed in ATENA-3D FEM software and experiment for the test beams were similar, shown in Figure 9. Due to the huge amount of data collected from each test specimen, the average torque-twist curve for each factor was found by averaging the data from the two beam specimens that were tested together. Figure 10 displays the average torque-twist curves for all the beams that were tested in this study. It was also found that, the ATENA-3D FEM software torque-twist curves of test beams was nearly same when compared with the experimental curves.

Figure 10 shows the normalised measured average torque-twist curve in the test and compared with ATENA-3D (FEM) for all the beams. The overall behaviour from cracking to failure state of all curve was similar in both results. Pre-cracking and post-cracking behaviour of each pair (one test and one ATENA-3D) of beam was identical in both methods. The following noteworthy remarks were made in light of this study. (a) Beams B-R00 had similar torque-twist behaviour before and after the maximum torque achieved in both methods.

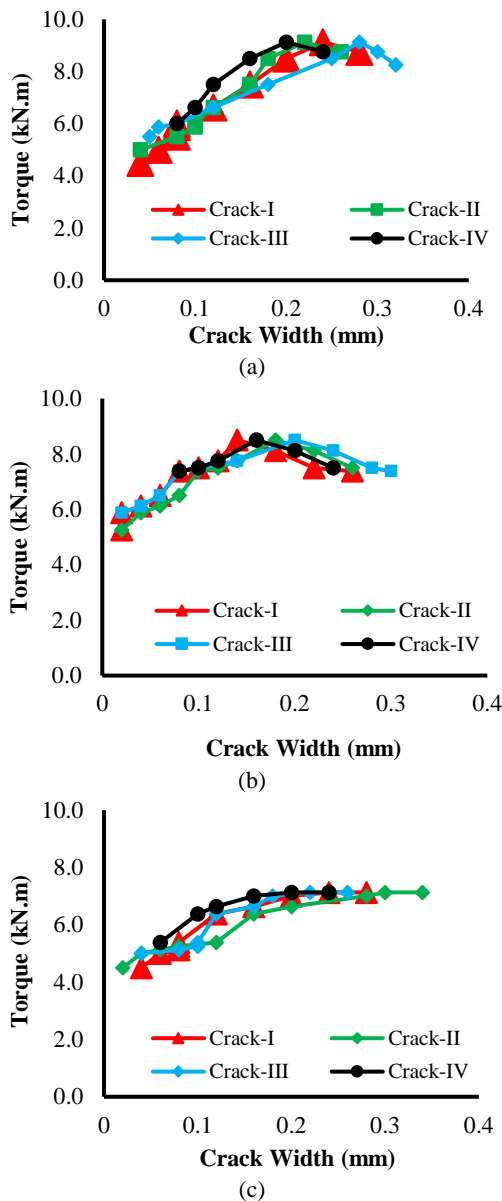


Figure 8. (a) Crack width for B-R00, (b) Crack width for B-R50 and (c) Crack width for B-R100

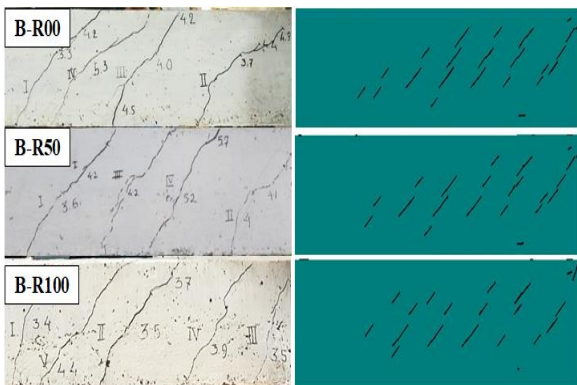


Figure 9. Comparison of Test and ATENA-3D (FEM) cracks

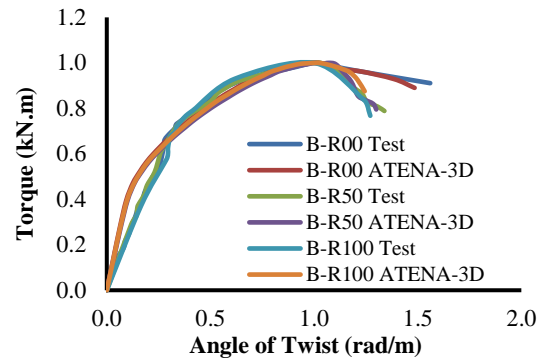


Figure 10. Normalised average test and ATENA-3D (FEM) torque-twist curve

(b) Beams B-R50 had equal torque-twist behaviour upto peak torque, then B-R50 curve turned as the B-R100 curve in both methods. (c) As the level of RCA replacement increases, the area beneath the torque-twist curve decreases in the both methods. (d) Adding RCA to concrete reduces torque-twist curve slopes after the peak, demonstrating RAC brittleness rather than NAC in both methods. The preceding observation suggests that B-R00 and B-R50 beams perform similarly up-to peak torque. The B-R50 and B-R100 behave similar after peak. The change in the replacement ratio of aggregate has a low impact on the ultimate torque and angle of twist; the effect was not enough to discourage the use of RCA in RAC beams in pure torsion in both methods. For the achieved results in the literature [4, 5], also agree that well after the outcome of torsional behaviour, crack pattern and failure mode of RAC beams. So, the use of RAC in structural applications under pure torsional loading is practically possible.

From Table 6, the cracking torque of tested beam was lower by 3.77 %, 4.19 % and 9.18 % than ATENA-3D (FEM) for 0 %, 50 % and 100 % replacement ratio, respectively. The ultimate torque of tested beams was lower by 7.41 %, 8.60 % and 13.58 % than ATENA-3D (FEM) for 0 %, 50% and 100% replacement ratio of NCA by RCA. The cracking and ultimate torque for 0% and 50% RCA was not influed much as compare to 100%

TABLE 6. Measured (Test) and ATENA-3D (FEM) torque at cracking, and ultimate state

Beam ID		B-R00	B-R50	B-R100
Cracking Torque (kN.m)	Test (Ex)	5.87	5.25	4.25
	ATENA-3D (An)	6.10	5.48	4.68
	Ex/An	0.96	0.95	0.91
Ultimate Torque (kN.m)	Test (Ex)	9.12	8.50	7.00
	ATENA-3D (An)	9.85	9.30	8.10
	Ex/An	0.92	0.91	0.87

RCA. Similar finding was reported in the literature [6]. It can be concluded that full replacement of NCA by RCA will be possible in the structural concrete with due care.

3. 7. Comparisons of Measured (Test) and ATENA-3D (FEM) with Skew Bending Theory and Space Truss Analogy

To determine whether the existing approach for designing torsional beam of NAC can be applied to RCA beam in their current state. The usually accepted methods of skew bending theory [29, 30] and space truss analogy [28, 30, 31] have been considered for comparison against the experimentally and analytically ATENA-3D (FEM) obtained values of average ultimate torsional moments. The ACI codes [28] issued between 1971 and 1995 were based on Kamiński and Pawlak's [32] and Hsu's [33] skew bending hypothesis. Indian code's provisions for torsion are also based on the skew bending theory. The space truss analogy has replaced the skew bending theory, which was based on the plane truss analogy for shear recognized by Ritter [34] and Morsch [35]. The space truss theories were initially sensible and have been adopted in several building codes, among them: CSA [27], ACI 318-14/318R [28], GB-50010 [36], AS-3600, and BS EN 1992-1-1 [37]. Figure 11 shows that both methods give same value as compared to measured (test) and ATENA-3D (FEM) with small accuracy differences.

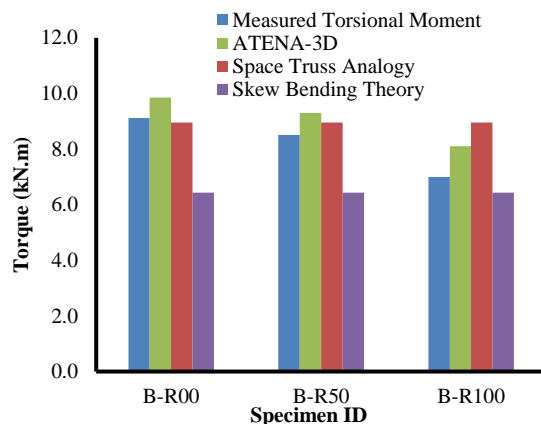


Figure 11. Comparisons of measured (Test) and ATENA-3D (EFM) torsional strength with Skew Bending Theory and Space Truss Analogy

4. CONCLUSIONS

The successful experimental pure torsion study of RCA beams determined that 50 % RCA was closely matched with 0 % RCA and that of 100 % RCA decreases the mechanical properties marginally lower than the 0 % RCA. It is due to weakened ITZ from the residual mortar. However, the torsional capability of the beam was

reduced as the RCA content increased in the RAC. The analytical and experimental torque resistance capacity of 50 % RAC beams was reduced by 5.58 % and 6.79 % as compared to NAC beams and for 100 % RAC it was lowered by 17.76 % and 23.24 %. The ultimate torque value of tested beams was lower by 7.41 %, 8.60 % and 13.58 % than ATENA-3D (FEM) value for 0 %, 50 % and 100 % RCA. Also, the torque-twist behaviour and orientation of cracks were also identical in all the beams in both methods. The crack width of 100 % RCA beams was greater, but this variation was not much different from 50 % and 0 % RCA concrete beams. Based on the experiments and analytical results, it was established that the torque resistance capacity of the RAC beam was reduced as the % of RCA increased. The replacement of RCA in concrete has no major effect on the overall torsional behaviour RAC beam compared with NAC beams in pure torsion after comparing the experimental and analytical results. It can be concluded that full replacement NCA by RCA will be possible in the structural concrete with due care. The results of this investigation will be useful to add value to the state of the art with respect to the application of RCA in structural beams and current code design procedures in pure torsion. The recycling of waste concrete could help to preserve the environment and promote sustainability through solid waste management. The findings specify that additional large-scale studies are required to establish a consensus about its pure torsional performance of RAC beams and to enhance the database for structural concrete.

5. REFERENCES

- Okay, F. and Engin, S., "Torsional behavior of steel fiber reinforced concrete beams", *Construction and Building Materials*, Vol. 28, No. 1, (2012), 269-275. <https://doi.org/10.1016/j.conbuildmat.2011.08.062>
- Fu, J.L., Liu, B.K., Ma, J.W. and Zhou, H., "Experimental study on seismic behavior of recycled aggregate concrete torsion beams with abaqus", in *Advanced Materials Research*, Trans Tech Publ. Vol. 1079, (2015), 220-225.
- Wang, X., Liu, B. and Zhang, C., "Seismic behavior of recycled aggregate concrete beams under cyclic torsion", *Construction and Building Materials*, Vol. 129, (2016), 193-203. <http://dx.doi.org/10.1016/j.conbuildmat.2016.10.101>
- Sarsam, F., Salih, N. and Hussein, M., "Assessment of reinforced recycling aggregate concrete beams under torsional moment", *International Journal of Engineering and Technology*, Vol. 7, (2018), 623-628. <http://dx.doi.org/10.14419/ijet.v7i4.20.2740>
- Pawar, A.J. and Suryawanshi, S., "Comprehensive analysis of stress-strain relationships for recycled aggregate concrete", *International Journal of Engineering, Transactions B: Applications*, Vol. 35, No. 11, (2022), 2102-2110. <http://dx.doi.org/10.5829/ije.2022.35.11b.05>
- Masne, N. and Suryawanshi, S., "Analytical and experimental investigation of recycled aggregate concrete beams subjected to pure torsion", *International Journal of Engineering*,

- Transactions A: Basics*, Vol. 35, No. 10, (2022), 1959-1966. <http://dx.doi.org/10.5829/ije.2022.35.10a.14>
7. Kartam, N., Al-Mutairi, N., Al-Ghusain, I. and Al-Humoud, J., "Environmental management of construction and demolition waste in kuwait", *Waste Management*, Vol. 24, No. 10, (2004), 1049-1059. <https://doi.org/10.1016/j.wasman.2004.06.003>
 8. Standard, I., "Is: 383 (2016) coarse and fine aggregate for concrete-specification", Bureau of Indian Standards, New Delhi, (2016).
 9. Sormunen, P. and Kärki, T., "Recycled construction and demolition waste as a possible source of materials for composite manufacturing", *Journal of Building Engineering*, Vol. 24, (2019), 100742. <https://doi.org/10.1016/j.jobe.2019.100742>
 10. Beiram, A. and Al-Mutairee, H., "Effect of using waste rubber as partial replacement of coarse aggregate on torsional strength of square reinforced concrete beam", *International Journal of Engineering, Transactions B: Applications*, Vol. 35, No. 2, (2022), 397-405. <https://doi.org/10.5829/ije.2022.35.02b.16>
 11. Nurhanim, A., "State of art reviews on physico-chemical properties of waste concrete aggregate from construction and demolition waste", *Iranian (Iranica) Journal of Energy & Environment*, Vol. 13, No. 4, (2022), 340-348. doi: 10.5829/ije.2022.13.04.03.
 12. Odeyemi, S., Abdulwahab, R., Akinpelu, M., Afolabi, R. and Atoyebi, O., "Strength properties of steel and bamboo reinforced concrete containing quarry dust, rice husk ash and guinea corn husk ash", *Iranian (Iranica) Journal of Energy & Environment*, Vol. 13, No. 4, (2022), 354-362. doi: 10.5829/ije.2022.13.04.05.
 13. Kanthe, V., "Effect of superplasticizer on strength and durability of rice husk ash concrete", *Iranian (Iranica) Journal of Energy & Environment*, Vol. 12, No. 3, (2021), 204-208. doi: 10.5829/ije.2021.12.03.04.
 14. Hadad, O., Soltani, O., Azizian, H. and Mam Ghaderi, V., "Investigating the simultaneous effect of macro fly ash and oak bark ash on mechanical properties of concrete", *Iranian (Iranica) Journal of Energy & Environment*, Vol. 12, No. 3, (2021), 234-240. doi: 10.5829/ije.2021.12.03.08.
 15. Xiao, J., Li, W., Fan, Y. and Huang, X., "An overview of study on recycled aggregate concrete in china (1996–2011)", *Construction and Building Materials*, Vol. 31, (2012), 364-383. <https://doi.org/10.1016/j.conbuildmat.2011.12.074>
 16. Malešev, M., Radonjanin, V. and Marinković, S., "Recycled concrete as aggregate for structural concrete production", *Sustainability*, Vol. 2, No. 5, (2010), 1204-1225. doi: 10.1007/978-81-322-2187-6_139.
 17. Suryawanshi, S., Singh, B. and Bhargava, P., "Characterization of recycled aggregate concrete", in *Advances in Structural Engineering: Materials*, Volume Three, Springer. Vol., No. Issue, (2015), 1813-1822.
 18. Suryawanshi, S., Singh, B. and Bhargava, P., "Equation for stress-strain relationship of recycled aggregate concrete in axial compression", *Magazine of Concrete Research*, Vol. 70, No. 4, (2018), 163-171. <https://doi.org/10.1680/jmacr.16.00108>
 19. Fathifazl, G., Razaqpur, A.G., Isgor, O.B., Abbas, A., Fournier, B. and Foo, S., "Flexural performance of steel-reinforced recycled concrete beams", *ACI Structural Journal*, Vol. 106, No. 6, (2009). <https://doi.org/10.14359/51663187>
 20. Rahal, K. and Alrefaei, Y., "Shear strength of recycled aggregate concrete beams containing stirrups", *Construction and Building Materials*, Vol. 191, (2018), 866-876. <https://doi.org/10.1016/j.conbuildmat.2018.10.023>
 21. Fathifazl, G., Razaqpur, A.G., Isgor, O.B., Abbas, A., Fournier, B. and Foo, S., "Bond performance of deformed steel bars in concrete produced with coarse recycled concrete aggregate", *Canadian Journal of Civil Engineering*, Vol. 39, No. 2, (2012), 128-139. <https://doi.org/10.1139/L11-120>
 22. Shiravi, A. and Firoozzadeh, M., "A novel proposed improvement on performance of a photovoltaic/water pumping system: Energy and environmental analysis", *Iranian (Iranica) Journal of Energy & Environment*, Vol. 13, No. 2, (2022), 202-208. doi: 10.5829/ije.2022.13.02.11.
 23. Esmaeili Shayan, M., Hayati, M., Najafi, G. and Esmaeili Shayan, S., "The strategy of energy democracy and sustainable development: Policymakers and instruments", *Iranian (Iranica) Journal of Energy & Environment*, Vol. 13, No. 2, (2022), 185-201. doi: 10.5829/ije.2022.13.02.10.
 24. 12269, I., "Ordinary portland cement-53 grade specification", Bureau of Indian Standards: New Delhi, India, (2013).
 25. 516:, I., "Method of tests for strength of concrete", IS: 516-1959 (Reaffirmed 2004), (2004).
 26. Standard, I., "Method of tests for strength of concrete", Bureau of Indian Standards, Manak Bhavan, Vol. 9, (1959).
 27. 3-14, C.A., "Design of concrete structures", Canada, (2014).
 28. Wight, J., Barth, F., Becker, R., Bondy, K., Breen, J., Cagley, J., Collins, M., Corley, W., Dolan, C. and Fiorato, A., "Aci committee 318," building code requirements for structural concrete (aci 318-05) and commentary (aci 318r-05)", Am. Concr. Institute, Farmingt. Hills, MI, Vol. 430, (2003).
 29. Pillai, S., U. and Menon, D., "Reinforced concrete structures.3rd ed, Tata McGraw-Hill, (2009).
 30. Subramanian, N., "Design of reinforced concrete structures.1st ed, Oxford University Press, (2013).
 31. Wight, J.K. and MacGregor, J.G., "Reinforced concrete, Pearson Education UK, (2016).
 32. Kamiński, M. and Pawlak, W., "Load capacity and stiffness of angular cross section reinforced concrete beams under torsion", *Archives of Civil and Mechanical Engineering*, Vol. 11, No. 4, (2011), 885-903. [https://doi.org/10.1016/S1644-9665\(12\)60085-5](https://doi.org/10.1016/S1644-9665(12)60085-5)
 33. Hsu, T.T., "Torsion of structural concrete-behavior of reinforced concrete rectangular members", *Special Publication*, Vol. 18, (1968), 261-306.
 34. Lee, J., Lim, H. and Yoon, S., "Diagonal crack width of re members with high strength materials", *International Journal of Civil and Environmental Engineering*, Vol. 10, No. 7, (2016), 833-838. doi: 10.5281/zenodo.1339325.
 35. Kurrer, K.E., "Kurt beyers beitrag zur baustatik", *Beton-und Stahlbetonbau*, Vol. 115, No. 1, (2020), 62-80. <https://doi.org/10.1002/best.201900078>
 36. Administration of Quality Supervision, I. and China, Q.o.t.P.s.R.o., *National standard of the people's republic of china: Bauxite*. 2009, Standard Press of China Beijing, China.
 37. Code, P., "Eurocode 2: Design of concrete structures-part 1–1: General rules and rules for buildings", *British Standard Institution, London*, (2005).

Persian Abstract

چکیده

در دو دهه گذشته، محققان رفتار خمشی، برشی و پیوند تیرهای بتن بازیافتی (RAC) را مورد مطالعه قرار داده‌اند. این کار در نظر دارد رفتار پرتوهای RAC را تحت پیچش خالص، علیرغم کمبود اطلاعات در مورد رفتار آن تحت پیچش خالص، تجزیه و تحلیل کند. سنگدانه‌های درشت بتن بازیافتی (RCA) استخراج شده از ضایعات ساخت و ساز و تخریب (D & C) برای جایگزینی سنگدانه‌های درشت طبیعی (NCA) در نسبت ۰٪، ۵۰٪ و ۱۰۰٪ استفاده شد. بازیافت آنها می‌تواند به حفظ محیط زیست و ارتقای پایداری از طریق مدیریت زباله جامد کمک کند. شش تیر با ابعاد ۱۵۰*۲۵۰*۱۸۰۰ میلی‌متر تهیه و مورد آزمایش قرار گرفت. برای تشخیص تغییر شکل جزئی و دستیابی به استحکام یکسان در جهت خارج از صفحه، برجستگی‌های ۲۵۰ میلی‌متری کنسول داخلی در وجوه مخالف تیرها در دهانه ۱۰۰۰ میلی‌متر در امتداد محور طولی ارائه شد. ظرفیت پیچشی نهایی تیرهای آزمایش شده ۷.۴۱ درصد، ۸.۶۰ درصد و ۱۳.۵۸ درصد کمتر از ATENA-3D (FEM) برای ۰٪، ۵۰٪ و ۱۰۰٪ RCA بود. تغییر در نسبت جایگزینی سنگدانه تأثیر کمی بر گشتاور نهایی و زاویه پیچش دارد. بر اساس نتایج تجربی و تحلیلی، مشخص شد که ظرفیت مقاومت گشتاور پرتو RAC با افزایش درصد RCA کاهش می‌یابد. الگوهای ترک مشابه و رفتار شکست در تیرهای RAC و NAC در هر دو مطالعه مشاهده شد. بنابراین، عملاً امکان اعمال RAC در کاربردهای سازه‌ای تحت بارگذاری پیچشی خالص وجود دارد.



Integrated Linear Integer Model of a Fleet Allocation and Aircraft Routing Problem with Operational Constraints

A. Shabanpour^a, M. Bashiri^b, R. Tavakkoli-Moghaddam^{*c}, A. Safi Samghabadi^a

^aDepartment of Industrial Engineering, Payame Noor University, Tehran, Iran

^bDepartment of Industrial Engineering, Faculty of Engineering, Shahed University, Tehran, Iran

^cSchool of Industrial Engineering, College of Engineering, Tehran University, Tehran, Iran

PAPER INFO

Paper history:

Received 21 September 2022

Received in revised form 27 December 2022

Accepted 28 December 2022

Keywords:

Airline Scheduling

Fleet Assignment

Aircraft Maintenance Routing

Long Term Planning

ABSTRACT

One of the topics that have been studied a lot in the field of airline industry optimization is related to flight planning, and air fleets, and how they relate to each other, which is called airline scheduling. Despite the high importance of this issue in the profitability of airline companies and the proper use of their resources, the high computational complexity of these models has led to considering each of them in a mathematical model separately, and as a result, the accuracy of the final decision will be decreased. So far, many articles have studied various relevant issues, in some cases, efforts to create integration in the process can be observed. However, there is a few operational views of the issue, and some key requirements were neglected due to the simplification of provided models. In this study, an integrated model of the two main stages of airline planning, including fleet allocation and aircraft maintenance routing, is considered simultaneously, and the performance of the developed model is investigated using real data from one of the airlines. Also, a sensitivity analysis of the model to some relevant parameters confirms the validity of the developed mathematical model and the solution algorithm. Then, a comparative study was investigated to compare the performance of the developed model with the operational method, including solving sub-problems stepwise. Also, the results are compared with the developed and similar method from the previous studies. The results confirm the superiority of the developed mathematical model.

doi: 10.5829/ije.2023.36.04a.07

NOMENCLATURE

Sets

$I(J)$	Set of scheduled flight legs
K	Set of all aircraft
M	Set of the maintenance stations
A	Set of airports

Parameters

trt_k	Time needed for an aircraft k to prepare for the next flight.
t_{max}	Maximum cumulative flight time of aircraft k .
c_{max}	Maximum number of aircraft departures.
mt_k	Time needed for maintenance for aircraft k .
v_{min}^k	Least number of maintenance has to be done for aircraft k in the planning horizon.
N	A big number.
dt_i	Departure time of flight leg i .
ft_i	Duration of flight leg i .
et_m	Time of closing the maintenance station m .

fd_k	Cumulative flight time of each aircraft at the start of planning.
tp_i	Ticket price of flight leg i .
pn_i	Number of flight leg i passengers.
cap_k	Capacity of aircraft k .
op_{ka}	1 if the aircraft k seating airports a at the start of scheduling; 0, otherwise.
s_{ia}	1 if the flight leg i departure from airport a ; 0, otherwise.
d_{ia}	1 if the flight leg i ends in airport a ; 0, otherwise.
ml_{ma}	1 if maintenance station m is located in airport a ; 0, otherwise.
O	Dummy start point
D	Dummy destination point

Variables

x_{ijk}	1 if flight legs i and j assign sequence to aircraft k ; 0, otherwise.
y_{imk}	1 if aircraft k going to maintenance station m after covering flight legs i ; 0, otherwise.
z_{mik}	1 if flight legs i covers by aircraft k in station m ; 0, otherwise.

*Corresponding Author Email: tavakkoli@ut.ac.ir (R. Tavakkoli-Moghaddam)

1. INTRODUCTION AND LITERATURE REVIEW

Aviation is one of the largest global industries, and in the modern era, the aviation industry has contributed greatly to the growth and development of the global economy, so the aviation industry has accounted for 3.5% of the world's gross domestic product [1]. Regardless of this issue, this industry indirectly affects economic growth by creating potential in creating employment. Nowadays, airports are not limited to only one place for air travel, and many recreational facilities such as dining, shops, rest, etc., are offered in them. Since the first commercial flights took off in the early 20th century, the industry has been growing at a tremendous pace. About 4.5 billion passengers traveled by the airlines in 2019, and more than 65 million people worldwide currently work in the airlines or related industries. Of this amount, about 10.2 million people are directly employed in full-time jobs in this industry [2].

Optimizing processes to increase revenues and reduce costs is one of the things that have been the focus of airline companies since their establishment. Considering that the main source of revenue for airlines is related to the movement of passengers, it is very important to have an optimal schedule of flights to meet the demand. On the other hand, the most important costs of airlines are related to flight operations and air fleets, which include about 10-20% of the total costs [3]. The next factor that has a significant impact on the profitability of organizations is related to lost sales, delays, and flight cancellations. In 2007, the airlines of the United States suffered a loss equivalent to 31.2 billion dollars due to delays [4]. This makes airline organizations seriously avoid situations that lead to delays or cancellations. To reduce this possibility, preventive measures are needed during flight planning.

Airline planning is usually divided into four steps including flight scheduling, fleet assignment, aircraft maintenance routing, and crew allocation. Air fleet planning, as an important and expensive resource of each airline, is carried out in fleet assignment and aircraft maintenance routing stages. In these steps, it is determined by which aircraft and in what sequence each flight will be made. There are many strict restrictions during this planning such as the maximum number and flight hours of each plane or the existence of a minimum time between two consecutive flights, which airlines are required to comply with in planning. Due to the sharp increase in the complexity of the model, these limitations are not considered in many studies, which makes it impossible to use them operationally.

So far, various articles and models have been published in the field of flight planning. Most of the primary proposed models have dealt with the tactical discussions of the issue and have refrained from examining the issue operationally. The maintenance

requirements are the first things that must be observed for having an operational mathematical model in the field of airline planning. As mentioned earlier, three types of maintenance requirements, including the number of landings and take-offs, total flight time, and the number of days since the last maintenance, are defined in the airline safety rules, and any model that does not consider these items is not operational. In this section, the research done in the past on the topic of airline planning has been described and divided according to its characteristics.

The first group of articles takes a tactical look at airline scheduling. One of the first articles in this field was presented by Feo and Bard [5] who considered some maintenance constraints in a multi-commodity flow network model and tried to minimize the maintenance costs for a type of fleet. Daskin and Panayotopoulos [6] developed an integer model and used a combined method of Lagrangian simplification and a heuristic method to solve it. Kabbani and Patty [7] developed a new concept called "flight line" and scheduled a three-day schedule. They chose the night to do the scheduling and used an innovative two-step approach to the solution. Clarke et al. [8] used the salesman problem for modeling and planning an aircraft flight based on some maintenance constraints. Next, in 1998, the concept of the flight line was used by Gopalan and Talluri [9].

Barnhart et al. [10] defined a chain of flights and defined the objective function based on reducing the overall costs of this chain. Mak and Boland [11] have also used the salesman problem to model aircraft routing. They calculated the upper and lower bounds for this problem and then determined the optimal solution [11]. Sriram and Haghani [12] assumed that all maintenance activities are performed during the night. Therefore, they determined some pairs of origin and destination in such a way that the maintenance visits of each plane happen every four days. They used an innovative method to solve the model and developed another model at the end of the article, which was not solved [12]. Liang et al. [13] have developed a one-day aircraft routing planning model based on the time-space network. They focused on maximizing the revenue from flights and tried to prevent short connections in flights. They extended their paper by extending the planning period to one week on 2013 [14]. Jamili [15] has developed a mixed-integer programming (MIP) model by considering extra time for landing and take-offs to create robustness and has used a meta-heuristic method to solve it. Khanmirza, et al. [16] developed a model for fleet allocation and added restrictions to count the number and balance the planes and passengers. They used a developed method based on the genetic algorithm to solve the model. Next, Ozkir and Ozgur [17] developed a simple model of fleet allocation and

aircraft routing and focused on developing an innovative solution method for it. The proposed method is two-stage, and the answers generated in the first stage are improved later.

Several developed models have incompletely included operational constraints in their models. Sarac, et al. [18] used the set partitioning problem to model the aircraft routing problem. Their goal was to minimize the remaining time of legal but unused repairs before repairs, and they tried to send the planes to repairs as late as possible [18]. Eltokhy et al. [19] developed a linear integer model for the problem from a derivative method. In the next study by Eltokhy et al. [20], they also developed a solution method. Wen et al. [21] focused a lot on the limited resources in maintenance stations. Due to the assumption of carrying out maintenance during the night, other constraints are implicitly included in the model. Saltzman [22] studied a daily recurring schedule for planning a fleet type and tried to satisfy the maintenance constraints by considering the maximum time interval of three days between two consecutive repairs.

The approach of creating integration in route planning is also very important in other fields, among which we can mention shipping. By converting the operating limits of cumulative flight hours and the number of cumulative flights into speed limits and the amount of ship fuel consumption and maintaining the minimum number of repairs in a period of time, we can mention the articles published in this field, including Pasha et al. [23]. The common operational and time requirements between these two issues are quite clear and the movement of this category of articles towards integration in decision-making can be seen. So that all kinds of operational, time, fuel consumption, speed, environmental and financial constraints have been investigated in an integrated problem.

As can be seen in Table 1, a few articles that have been published in the integration of airline planning stages have addressed the issues of mandatory restrictions on maintenance visits. Another point that is evident in this case is related to the shortness of the planning period in most of the articles. According to the existing conditions in the airlines, the results of the model that does not consider the mentioned topics, including mandatory maintenance visits and proper planning period, cannot be implemented in the operational environment. Therefore, one of the important weaknesses in this field is related to the non-operational nature of existing models, which exists due to the high complexity of airline planning stages.

This paper is attempted to provide an integrated model of the two main stages of the airline planning process, including fleet allocation and aircraft routing, which includes the constraints related to the requirements of periodic maintenance visits and has a

long planning period. Also, the mentioned model deals with other relevant requirements, such as the initial location of the aircraft and the working hours of the repair stations.

2. PROBLEM DEFINITION

The main processes of airline planning include four steps flight scheduling, fleet assignment, aircraft maintenance routing, and crew scheduling. The high complexity of integrating and solving these problems at

TABLE 1. Summary of the literature review

Authors	Planning period (day)	Maintenance constraints		
		Take-offs number	Cumulative flight hour	Last day from the repair
Feo & Bard [5]	–	×	×	×
Daskin & Panayotopoulos [6]	–	×	×	×
Kabbani & Patty [7]	3	×	×	×
Clarke et al. [8]	–	×	×	×
Barnhart et al. [10]	7	×	×	×
Gopalan & Talluri [9]	3	×	×	×
Mak & Boland [11]	–	×	×	×
Sriram & Haghani [12]	7	×	×	✓
Sarac et al. [18]	1	✓	×	×
Liang et al. [13]	1	×	×	×
Huari et al. [24]	1	✓	✓	✓
Liang & Chaovalitwongse [14]	7	×	×	×
Al Thani, et al. [25]	7	✓	✓	✓
Jamili [15]	1	×	×	×
Eltoukhy et al. [19]	4	✓	×	×
Safaei & Jardine [26]	7	✓	✓	×
Kenan et al. [27]	1	×	×	×
Eltoukhy et al. [20]	4	✓	×	×
Deng et al. [28]	10	✓	×	×
Ruan, et al. [29]	4	✓	✓	✓
Xu et al. [30]	–	×	×	×
Wen, et al. [21]	1	×	×	×
Saltzman [22]	1	×	×	✓
This paper	10	✓	✓	✓

the same time, due to the volume of calculations and available calculation methods, causes that in most cases, as in Figure 1, these problems were examined and solved separately and sequentially. So that the output of each stage was used as the input of the next stage. This issue caused non-optimal solutions for problems to be delayed or even impossible [31].

The flight schedule is the first issue that should be questioned during the planning of an airline. The output of this step includes the origin, destination, take-offs, and landing time of all airline flights in a certain period. The purpose of this stage is to create a timetable to maximize the airline's revenue in relation to the expected demand from passengers. Usually, all other operations of the airline are based on the output of this stage. In most cases, these timetables are repeated daily or weekly [31].

The first issue that is addressed after the flight schedule is determined is the allocation of the fleet. The purpose of this stage is to allocate the types of the existing fleet of the airline to the flights planned in the previous stage [32]. According to the article of Al Thani and Haouari [25], the type of aircraft refers to a specific model of aircraft. Aircraft belonging to the same type have the same cabin style and equal seat numbers, and this is different from an aircraft family. An aircraft family includes different aircraft types with only the same cabin style. It should also be noted that at this stage, only the issue of allocating types of aircraft to scheduled flights is discussed, and the one-to-one allocation of existing aircraft is not an issue [32].

Another activity that must be put on the agenda for airline planning is the allocation of each aircraft to each scheduled flight. In other words, a sequence of flights that are required to be covered must be defined for each aircraft. During this stage, there are a large number of constraints that must be considered while solving the problem, the most important of which is related to meeting the requirements related to maintenance visits of each aircraft. Preventive maintenance visits are performed before the number of flights of each aircraft reaches a predetermined value [33]. A feasible route for an aircraft consists of several consecutive flights, each flight must be covered by one aircraft, and there is no time overlap between them. These paths must have the following conditions:



Figure 1. Airline's steps for flights scheduling

- The landing airport of the first flight must be the same as the departure airport of the second flight.
- The second flight request time must be greater than the first flight's seating time plus the time needed to prepare for the next flight.
- The cumulative flight time and take-off number of airplanes should not exceed a certain amount.
- It should not be more than a certain number of days since the last repair of the aircraft.

Because maintenance visits are required only after some flights and only possible in some airports (usually hub airports) when connecting two flights after a maintenance visit, the time and place of repairs are also It should be included in the above conditions. The problem of aircraft routing in all its forms is considered a very complex problem [34].

After the mentioned steps, it is necessary to plan how to serve the crew on the flights. This step involves assigning crew to each flight while complex work rules and reducing crew costs should be on the agenda [33]. Crew scheduling includes a sequence of duty periods with night rest between them, which starts at a specific location and ends at the same location, which is called the crew base. Carrying out this process step by step causes inefficiency and failure to achieve the optimal answer. This step-by-step process is used to help reduce complexity, which is somewhat successful in this matter, but this reduction in complexity comes at the cost of reducing the quality of the final solution. It seems that integrating the planning process can be very effective in improving the obtained response.

3. PROPOSED MATHEMATICAL MODEL

Assuming that the flight schedule is available, the purpose of the proposed model is to achieve an integrated model of two main processes with the high computational complexity of fleet allocation and aircraft routing. For this purpose, three types of arcs according to the connection network were used in this research. Flight vectors connect two consecutive flights to the flight flow of an aircraft, repair vectors direct the aircraft to the repair station after a flight, and auxiliary vectors are responsible for returning the repaired aircraft to the flight cycle.

This model is presented based on the connection network, in which flights are displayed as points and possible connections between them as vectors. Considering that it has been tried to make the model have the most features of an operational model, the flight cost of each plane has been considered different in each of the flights. Other things such as the capacity of each plane and the number of passengers on the route are also considered in this model. The objective function of the model is based on choosing the options

that create the most profitability for the airline. The presented model has features that completely separate it from the previous models. The first feature is adding a decision variable as an auxiliary vector to the model, which is responsible for returning the aircraft to the planning cycle after completing the repairs. Another point that is considered in this model, unlike most of the previous models, is related to considering the initial location of the aircraft at the beginning of the planning period. This makes the planning operational. One of the most important strengths of this model is related to having control over the current state of the aircraft at every moment of planning. It should be noted that other things such as making a distinction between the time required for a maintenance visit and the time required to prepare the aircraft between two consecutive flights, separating the repair station from the airport, reducing the parameters related to the definition of scheduled flights, etc. Other features are added to the model. Using the nomenclature mentioned before the introduction, the mathematical model is presented as follows:

$$\text{Max } u = \sum_{k=1}^K \sum_{i=1}^I \sum_{j=1}^I \sum_{m=1}^M (pn_i * tp_i) * (x_{ijk}) \quad (1)$$

s.t.

$$\sum_{k=1}^K \sum_{j=1}^I x_{ijk} + \sum_{k=1}^K \sum_{m=1}^M y_{imk} = 1 \quad \forall i \in I - \{O, D\} \quad (2)$$

$$\sum_{i=1}^I \sum_{a=1}^A x_{oik} * s_{oa} * op_{ka} + \sum_{m=1}^M \sum_{a=1}^A y_{omk} * s_{oa} * op_{ka} \geq 1 \quad \forall k \in K \quad (3)$$

$$\sum_{j=1}^I x_{jik} + \sum_{m=1}^M z_{mik} = \sum_{j=1}^I x_{ijk} + \sum_{m=1}^M y_{imk} \quad \forall k \in K, i \in I - \{O, D\} \quad (4)$$

$$\sum_{i=1}^{I-D} y_{imk} = \sum_{i=1}^I z_{mik} \quad \forall k \in K, m \in M \quad (5)$$

$$\sum_{m=1}^M z_{mik} \leq \sum_{j=1}^{I-D} \sum_{m=1}^M y_{imk} \quad \forall k \in K, i \in I \quad (6)$$

$$\sum_{i=1}^I x_{oik} + \sum_{m=1}^M y_{omk} = 1 \quad \forall k \in K \quad (7)$$

$$dt_i + ft_i + trt_k - dt_j \leq N * (1 - x_{ijk}) \quad \forall k \in K, i \in I, j \in I \quad (8)$$

$$\sum_{k=1}^K x_{ijk} \leq \sum_{a=1}^A d_{ia} * o_{ja} \quad \forall i \in I, j \in I \quad (9)$$

$$dt_i + ft_i + mt_k - et_m \leq N * (1 - y_{imk}) \quad \forall m \in M, i \in I, k \in K \quad (10)$$

$$\sum_{k=1}^K y_{imk} \leq \sum_{a=1}^A d_{ia} * ml_{ma} \quad \forall m \in M, i \in I \quad (11)$$

$$\sum_{k=1}^K z_{mik} \leq \sum_{a=1}^A o_{ia} * ml_{ma} \quad \forall m \in M, i \in I - \{D\} \quad (12)$$

$$\sum_{i=1}^I \sum_{j=1}^I x_{ijk} \leq c_{max} \quad \forall k \in K \quad (13)$$

$$\sum_{i=1}^I \sum_{j=1}^I ft_j * x_{ijk} + fd_k \leq t_{max} \quad \forall k \in K \quad (14)$$

$$\sum_{i=1}^I \sum_{m=1}^M y_{imk} = 1 \quad \forall k \in K \quad (15)$$

$$x_{ijk} \in \{0,1\} \quad \forall k \in K, i \in I, j \in I \quad (16)$$

$$y_{imk} \in \{0,1\} \quad \forall k \in K, i \in I, m \in M \quad (17)$$

$$z_{mik} \in \{0,1\} \quad \forall k \in K, i \in I, m \in M \quad (18)$$

In this model, the objective function maximizes the total revenue of the airline by selling tickets to passengers. Constraint (2) tries to ensure that all flights are covered by exactly one aircraft. Constraint (3) ensures that the flight path of each aircraft starts from the airport where it was based at the beginning of the planning period.

Constraints (4) to (7) are used to create balance in planning. The purpose of constraint (4) is to logically switch between decision vectors so that if an aircraft is sent to the repair station, the next vector should return the aircraft to the planning cycle. While the previous vector was a flight vector, the next vector is only allowed to take two states, a flight vector or a repair vector. Constraint (5) causes correct change between the repair vector and auxiliary vector in repair stations. In Constraint (6), it is only possible to use the auxiliary vector to return the aircraft to the flight cycle if the related repair vector has already been set. Despite Constraint (7), the use of the entire fleet is guaranteed during the planning of at least one flight or one repair.

Constraints (8) and (9) are used to ensure the consistency of consecutive flights during the planning process. In this way, in Constraint (8), the coincidence of two consecutive flights in terms of time is checked in such a way that the landing time of the first flight plus the minimum time required for the preparation of the plane is before the time of the next flight. While in Constraint (9), their compatibility is examined in terms of origin and destination airports.

Constraints (10) to (12) are responsible for the correct planning of the repairs of an aircraft in terms of time and place of repairs. In such a way, Constraint (10) of the working time of the repair station and the completion of the repair visits before the end of the working time has been examined. While Constraint (11) examines the sameness of the scheduled repair location with the destination airport of the previous flight. Constraint (12) examines the coincidence of the origin airport of the next flight with the repair station.

Constraints (13) to (17) are related to the review of aircraft maintenance and repair requirements. In this regard, Constraint (13) examines the number of flights made by each aircraft since the last repair. At the same time, Constraints (14) examine the cumulative time of

flights performed by each aircraft. It is necessary to explain that the amount of previous flights made by each aircraft is counted. Constraint (15) determines the minimum number of maintenance visits of each aircraft on the planning horizon. Constraints (16) to (18) are related to determining the binaryness of the decision variables of the model.

4. COMPUTATIONAL RESULTS

To check the validity of the presented model, it tried to analyze the real data of an airline company, and for this purpose, the available flight and fleet data of Ata Airlines Company (as Appendices 1 and 2) were used¹, which information is stated in Table 2. The used information includes the origin, destination, time, and duration of the planned flights during a week. Other required information, including the type and number of air fleets, operating costs, etc., was also collected from the company's website¹. In addition to the proposed model, the collected data were solved with the conventional step-by-step method and the work conducted by Ruan et al. [29] as an updated and similar article, and the results were used to confirm the performance. The reason for choosing the mathematical model [29] is the high similarity of its features and constraints to our model proposed in this paper So that both models are modeled using the connection network and the objective function of both is based on increasing the profitability of the airline. Also, the constraints used to maintain the balance and sequence of flights (constraints 2 to 10) and operational constraints (constraints 11 to 15) provide a similar function. The main difference between these two models is the absence of one of the decision variables (decision variable z to return the plane to the flight schedule) in [29], as well as how the restrictions are set differently, and these differences do not hinder the possibility of comparing the two models. For similarity in comparison results, the objective function of the mentioned paper was also replaced, despite the high similarity. The comparison with the stepwise method was also done by solving the fleet allocation problem and transferring its results as input data to the aircraft routing problem, as explained in section 2. The presented model was solved according to the information provided in the previous section and three modes. In the first case, the scheduled flights of this airline in 2 days, including 110 flights and 15 separate destinations, were examined under the title of small statistical population. The second studied mode was related to 4 days of the flight schedule of this airline, including 220 flights and 18 separate destinations, and at the end, the statistical population

with a large size was related to 1 week of the flight schedule with 347 flights to 18 flight destinations.

All these three statistical populations were solved with a precise method using GAMS software, and the results are shown in Table 6. Also, all three assumed cases are solved by the stepwise method, and a comparison of the amount of the objective function and its solution time with the exact solution method has been made. To increase the validity of the proposed integrated model, a comparison with one of the new articles by Ruan et al. [29] was also made, and the results were reported. This article was chosen due to the similarity in key features to the proposed model, including considering all the repair limitations and also the solution time of four days. By using the mentioned comparisons, the performance of the proposed model can be compared with the most important related cases. The first comparison with the step-by-step method shows how the proposed model performs in our comparison of the common practice method in airline scheduling, while the comparison made with the selected paper compares the performance of the model with the latest research achievements. It should be mentioned that the selected article related to Ruan et al. [29] should have presented several features similar to the proposed model, the most important of which are similar repair restrictions (considering all repair requirements), relatively similar parameters, and The solution time indicated the appropriate ratio. To compare the two models from the point of view of the amount of the objective function and the non-identity of the models in this matter, the objective function of the model proposed in this article was replaced, and the models were solved with the same input information. The things that are comparable in the mentioned comparison are related to the two key issues of the value of the objective function (here, the profitability rate) and the solution time.

As shown in Table 2, despite the 28% increase in solving time in the large sample compared to the stepwise method, an improvement of more than 18% is seen in the final answer. In medium and small samples, despite the improvement of 20% and 12%, respectively, in the value of the objective function compared to the stepwise method, the solution time is also in a suitable range. Meanwhile, the comparison of the proposed method with the paper of Ruan et al. [29] indicates an improvement of between 1.5 and 4.5 percent in the obtained answers, and the solution time has also improved significantly compared to this paper. It should be noted that meta-heuristic methods have been used in the article by Ruan et al. [29] due to the long time needed to solve the model accurately. One of the most important reasons for this improvement is the return of repaired planes to the planning cycle. This has caused flights to be reassigned to the aircraft at the correct time

¹ <https://www.ataair.ir>

TABLE 2. Performance comparison of the proposed model

Problem Size	Small	Medium	Large	
Aircraft number	21	21	21	
Maintenance Station	15	18	18	
Flights number	110	207	347	
Objective Function Value	*	2,987,985	27.187.168	33.793.258
	**	2,629,426	21.749.707	22.722.487
	***	2,943,164	25.963.745	33,318,585
Solution Time	*	4.664	33.637	87.938
	**	10.635	31.126	68.438
	***	3255.032	5869.866	9014.326

* Proposed model ** Stepwise model *** Selected model from [27]

and place after the repairs. Also, the improvement created in modeling, including reducing the number of parameters used to define flights and replacing complex constraints with simpler constraints, has caused a significant reduction in model-solving time.

In addition to the above analysis, several related sensitivity analyzes were conducted to determine the accuracy of the model's performance. In the first case, the state of change of the objective function relative to the changes in the allowed flight time of the aircraft was investigated. For this issue, two different parameters, including t_{max} to show the maximum allowed flight hours of each plane and c_{max} for the maximum number of landings and take-offs allowed in the model are used. To determine the correctness of the model's performance, it is expected that by reducing the allowed time or the number of landings and take-offs of the aircraft, the operating costs will increase, and as a result, the amount of the objective function will decrease. Therefore, to measure this issue by keeping one of these two parameters constant, the value of the other parameter is changed. The result of these changes can be observed in Figure 2.

As shown in Figure 2, the amount of the objective function has an increasing trend with an increase in the parameters of the allowed flight time. It can also be seen that for the trend line, fixed parameters with lower values have a lower objective function value than higher values in both parameters. As a result, in this analysis, the correct performance of the model is observed for changes in the allowed flight time.

The next analysis that can be examined in this regard is related to the number of scheduled repairs per change in the amount of allowed flight time. It is expected that the number of repairs will decrease as the flight time increases. For this purpose, the sensitivity analysis of the model was done, and the results are shown in Figure 3. In this figure, it is evident that the

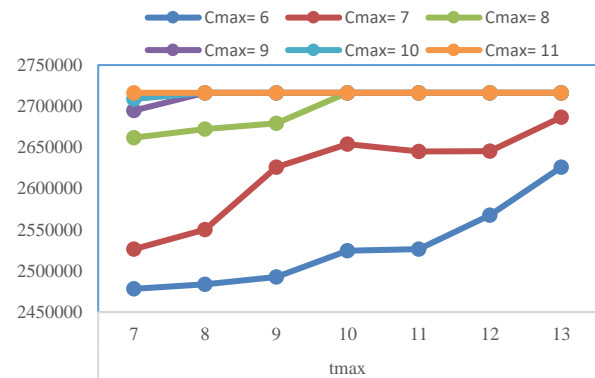


Figure 2. Changes of the objective function for parameter t_{max} for different values of parameter c_{max}

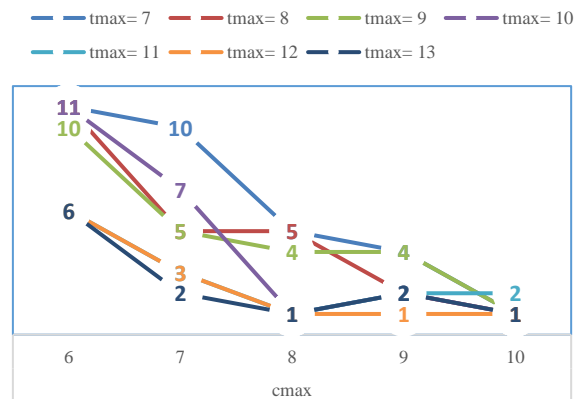


Figure 3. Changes of the planned maintenance number for c_{max} for different values of t_{max}

number of planned repairs of the model decreases due to an increase in time and the number of allowed flights of each plane.

- Improvement in the answers obtained compared to the conventional step-by-step method and reviewed articles, and as a result, increasing the profitability of the airline company.
 - Consideration of all maintenance requirements and usability in all real issues.
 - Long planning period and the possibility of using the model in operational mode.
- Bringing repaired aircraft back into the planning cycle.

5. CONCLUSION

This article, while introducing the airline planning process, it was tried to focus on integrating the two main stages of this process. The presented integrated linear integer model is proposed for the ten-day scheduling of two major airline scheduling processes. These two stages, which include fleet allocation and

aircraft routing, are presented in one model, unlike common mathematical models that analyze each stage separately. The presented model takes into account all operational limitations and maintenance visits, and as a result, it can be used operationally.

The presented model is solved using three different sizes of real data, and the result is compared with the stepwise solution method as one of the fastest available solution methods and one of the recent studies with a similar structure that produces one of the best possible solutions. According to the obtained results, it seems that the results of the proposed model have produced much better results and can be used in an operational mode so that the proposed model could improve the results by 12 - 20 percent improvement compared to the stepwise method and also could improve the results by 1.5 - 4.5 percent improvement compared to the model presented in the selected article. The numerical analysis confirms that solving the proposed model by GAMS software can compete with the stepwise model and has produced far better results than the selected model in terms of time efficiency.

One of the topics suggested for future research is the development of the level of integration in the model presented to other parts of planning. Another interesting topic is related to the development of the solving method for the presented model. Due to the widespread of heuristic and meta-heuristic algorithms, this potential method can be used to improve the time and quality of the achievable solution. Also, smartening the flight selection process and integrating it with the current model is another attractive direction for future study. Another interesting topic for future research is the use of studies conducted in the field of shipping in airline planning research or vice versa.

6. REFERENCES

- Shaw, S., "Airline marketing and management, Routledge, (2016).
- Group, A.T.A., "Facts & figures", (2014).
- Shaukat, S., Katscher, M., Wu, C.-L., Delgado, F. and Larrain, H., "Aircraft line maintenance scheduling and optimisation", *Journal of Air Transport Management*, Vol. 89, (2020), 101914. doi: 10.1016/j.jairtraman.2020.101914.
- Ball, M., Barnhart, C., Dresner, M., Hansen, M., Neels, K., Odoni, A., Peterson, E., Sherry, L., Trani, A. and Zou, B., "Total delay impact study: A comprehensive assessment of the costs and impacts of flight delay in the united states", (2010). <https://rosap.ntl.bts.gov/view/dot/6234>
- Feo, T.A. and Bard, J.F., "Flight scheduling and maintenance base planning", *Management Science*, Vol. 35, No. 12, (1989), 1415-1432. doi: 10.1287/mnsc.35.12.1415.
- Daskin, M.S. and Panayotopoulos, N.D., "A lagrangian relaxation approach to assigning aircraft to routes in hub and spoke networks", *Transportation Science*, Vol. 23, No. 2, (1989), 91-99. doi: 10.1287/trsc.23.2.91.
- Kabbani, N.M. and Patty, B.W., "Aircraft routing at american airlines", in proceedings of the agifors symposium, (1992).
- Clarke, L., Johnson, E., Nemhauser, G. and Zhu, Z., "The aircraft rotation problem", *Annals of Operations Research*, Vol. 69, (1997), 33-46. doi: 10.1023/A:1018945415148.
- Gopalan, R. and Talluri, K.T., "The aircraft maintenance routing problem", *Operations research*, Vol. 46, No. 2, (1998), 260-271. doi: 10.1287/opre.46.2.260.
- Barnhart, C., Boland, N.L., Clarke, L.W., Johnson, E.L., Nemhauser, G.L. and Shenoi, R.G., "Flight string models for aircraft fleetling and routing", *Transportation Science*, Vol. 32, No. 3, (1998), 208-220. doi: 10.1287/trsc.32.3.208.
- Mak, V. and Boland, N., "Heuristic approaches to the asymmetric travelling salesman problem with replenishment arcs", *International Transactions in Operational Research*, Vol. 7, No. 4-5, (2000), 431-447. doi: 10.1111/j.1475-3995.2000.tb00209.x.
- Sriram, C. and Haghani, A., "An optimization model for aircraft maintenance scheduling and re-assignment", *Transportation Research Part A: Policy and Practice*, Vol. 37, No. 1, (2003), 29-48. doi: 10.1016/S0965-8564(02)00004-6.
- Liang, Z., Chaovalitwongse, W.A., Huang, H.C. and Johnson, E.L., "On a new rotation tour network model for aircraft maintenance routing problem", *Transportation Science*, Vol. 45, No. 1, (2011), 109-120. doi: 10.1287/trsc.1100.0338.
- Liang, Z. and Chaovalitwongse, W., "A network-based model for weekly aircraft maintenance routing with integrated fleet assignment problem", *Manuscript, Department of Industrial Engineering and Management, Peking University, Beijing, China*, (2011). doi: 10.1287/trsc.1120.0434.
- Jamili, A., "A robust mathematical model and heuristic algorithms for integrated aircraft routing and scheduling, with consideration of fleet assignment problem", *Journal of Air Transport Management*, Vol. 58, (2017), 21-30. doi: 10.1016/j.jairtraman.2016.08.008.
- Khanmirza, E., Nazarahari, M. and Haghbeigi, M., "A heuristic approach for optimal integrated airline schedule design and fleet assignment with demand recapture", *Applied Soft Computing*, Vol. 96, (2020), 106681. doi: 10.1016/j.asoc.2020.106681.
- Özkar, V. and Özgür, M.S., "Two-phase heuristic algorithm for integrated airline fleet assignment and routing problem", *Energies*, Vol. 14, No. 11, (2021), 3327. doi: 10.3390/en14113327.
- Sarac, A., Batta, R. and Rump, C.M., "A branch-and-price approach for operational aircraft maintenance routing", *European Journal of Operational Research*, Vol. 175, No. 3, (2006), 1850-1869. doi: 10.1016/j.ejor.2004.10.033.
- Eltoukhy, A.E., Chan, F.T., Chung, S. and Qu, T., "Optimization model and solution method for operational aircraft maintenance routing problem", in Proceedings of the world congress on engineering. Vol. 2, (2017).
- Eltoukhy, A.E., Chan, F.T., Chung, S.H. and Niu, B., "A model with a solution algorithm for the operational aircraft maintenance routing problem", *Computers & Industrial Engineering*, Vol. 120, (2018), 346-359. doi: 10.1016/j.cie.2018.05.002.
- Wen, X., Sun, X., Ma, H.-L. and Sun, Y., "A column generation approach for operational flight scheduling and aircraft maintenance routing", *Journal of Air Transport Management*, Vol. 105, (2022), 102270. doi: 10.1016/j.jairtraman.2022.102270.
- Saltzman, R.M. and Stern, H.I., "The multi-day aircraft maintenance routing problem", *Journal of Air Transport Management*, Vol. 102, (2022), 102224. doi: 10.1016/j.jairtraman.2022.102224.

23.	Pasha, J., Dulebenets, M.A., Fathollahi-Fard, A.M., Tian, G., Lau, Y.-y., Singh, P. and Liang, B., "An integrated optimization method for tactical-level planning in liner shipping with heterogeneous ship fleet and environmental considerations", <i>Advanced Engineering Informatics</i> , Vol. 48, (2021), 101299. doi: 10.1016/j.aei.2021.101299.	7	Tehran	Mashhad	8:34	01:20
		8	Mashhad	Tehran	9:00	01:20
		9	Mashhad	Sari	9:04	01:10
		10	Tehran	Ahvaz	9:05	00:50
24.	Haouari, M., Shao, S. and Sherali, H.D., "A lifted compact formulation for the daily aircraft maintenance routing problem", <i>Transportation Science</i> , Vol. 47, No. 4, (2013), 508-525. doi: 10.1287/trsc.1120.0433.	11	Tehran	Bandarabbas	9:20	01:45
		12	Tabriz	Mashhad	9:57	02:00
25.	Al-Thani, N.A., Ahmed, M.B. and Haouari, M., "A model and optimization-based heuristic for the operational aircraft maintenance routing problem", <i>Transportation Research Part C: Emerging Technologies</i> , Vol. 72, (2016), 29-44. doi: 10.1016/j.trc.2016.09.004.	13	Mashhad	Esfahan	10:49	01:30
		14	Ahvaz	Tehran	10:55	00:50
		15	Sari	Mashhad	10:55	01:10
26.	Safaei, N. and Jardine, A.K., "Aircraft routing with generalized maintenance constraints", <i>Omega</i> , Vol. 80, (2018), 111-122. doi: 10.1016/j.omega.2017.08.013.	16	Tehran	Mashhad	11:25	01:20
		17	Tehran	Kish	11:25	01:45
		18	Bandarabbas	Tehran	11:50	01:45
27.	Kenan, N., Diabat, A. and Jebali, A., "Codeshare agreements in the integrated aircraft routing problem", <i>Transportation Research Part B: Methodological</i> , Vol. 117, (2018), 272-295. doi: 10.1016/j.trb.2018.08.008.	19	Mashhad	Tabriz	13:00	02:00
		20	Mashhad	Tehran	13:00	01:20
28.	Deng, Q., Santos, B.F. and Curran, R., "A practical dynamic programming based methodology for aircraft maintenance check scheduling optimization", <i>European Journal of Operational Research</i> , Vol. 281, No. 2, (2020), 256-273. doi: 10.1016/j.ejor.2019.08.025.	21	Tehran	Sabzevar	13:05	01:00
		22	Esfahan	Mashhad	13:10	01:30
		23	Mashhad	Tehran	13:40	01:20
		24	Kish	Tehran	14:00	01:45
29.	Ruan, J., Wang, Z., Chan, F.T., Patnaik, S. and Tiwari, M.K., "A reinforcement learning-based algorithm for the aircraft maintenance routing problem", <i>Expert Systems with Applications</i> , Vol. 169, (2021), 114399. doi: 10.1016/j.eswa.2020.114399.	25	Tehran	Kermanshah	14:50	01:00
		26	Sabzevar	Tehran	15:00	01:00
		27	Tehran	Shiraz	15:05	01:20
30.	Xu, Y., Wandelt, S. and Sun, X., "Airline integrated robust scheduling with a variable neighborhood search based heuristic", <i>Transportation Research Part B: Methodological</i> , Vol. 149, (2021), 181-203. doi: 10.1016/j.trb.2021.05.005.	28	Mashhad	Tehran	15:40	01:20
		29	Tabriz	Tehran	16:00	01:00
31.	Papadakos, N., "Integrated airline scheduling: Decomposition and acceleration techniques", IC-PARC (centre for Planning and Resource Control), (2006), 1-38. doi: 10.1016/j.cor.2007.08.002.	30	Tehran	Kish	16:35	01:45
		31	Kermanshah	Tehran	16:50	01:00
		32	Tehran	Shiraz	17:00	01:20
32.	Bazargan, M., "Airline operations and scheduling, Routledge, (2016).	33	Shiraz	Tehran	17:20	01:20
33.	Ahmed, M.B., Mansour, F.Z. and Haouari, M., "Robust integrated maintenance aircraft routing and crew pairing", <i>Journal of Air Transport Management</i> , Vol. 73, (2018), 15-31. doi: 10.1016/j.jairtraman.2018.07.007	34	Tehran	Qheshm	17:45	01:50
		35	Tehran	Tabriz	18:05	01:00
		36	Kish	Tehran	18:40	01:45
34.	Parmentier, A., "Aircraft routing: Complexity and algorithms", Rapport de stage de master, École des Ponts ParisTech, (2013).	37	Shiraz	Kish	19:10	01:00
		38	Tehran	Kish	19:50	01:45
		39	Tehran	Mashhad	19:50	01:20
		40	Tabriz	Tehran	20:00	01:00
		41	Tehran	Ahvaz	20:10	00:50
		42	Qheshm	Tehran	20:30	01:50
		43	Kish	Shiraz	20:50	01:00
		44	Tehran	Mashhad	21:30	01:20
		45	Tehran	Tabriz	22:00	01:00
		46	Ahvaz	Tehran	22:00	00:50
		47	Mashhad	Tehran	22:00	01:20
		48	Kish	Tehran	22:10	01:45

APPENDIX 1. Ata airline flight schedule between 2022/04/12 to 2022/04/18

Row	Date	Origin	Destination	Flight time	Flight duration
1	2022/04/12	Tehran	Tabriz	5:00	01:00
2		Tabriz	Tehran	6:02	01:00
3		Orumie	Tehran	6:25	01:00
4		Tehran	Mashhad	6:48	01:20
5		Tabriz	Tehran	7:00	01:00
6		Tehran	Tabriz	7:54	01:00

49	Shiraz	Tehran	22:40	01:20	91	Mashhad	Tehran	19:20	01:20
50	Tehran	Orumie	23:40	01:00	92	Tehran	Qheshm	19:20	01:50
51	Tabriz	Tehran	5:55	01:00	93	istanbul	Tabriz	19:30	01:15
52	Tehran	Tabriz	6:10	01:00	94	Tehran	Shiraz	19:40	01:20
53	Orumie	Tehran	6:23	01:00	95	Tabriz	Tehran	20:00	01:00
54	Tehran	Kermanshah	7:17	01:00	96	Mashhad	Tehran	20:00	01:20
55	Tehran	Tabriz	7:50	01:00	97	Kish	Tehran	20:30	01:45
56	Tabriz	Tehran	8:06	01:00	98	Ahvaz	Tehran	21:00	00:50
57	Kermanshah	Tehran	8:50	01:00	99	Tehran	Mashhad	21:40	01:20
58	Mashhad	Kish	9:03	02:00	100	Qheshm	Tehran	21:50	01:50
59	Tehran	Mashhad	9:15	01:20	101	Tehran	Tabriz	22:00	01:00
60	Tehran	Qheshm	9:30	01:50	102	Shiraz	Tehran	22:00	01:20
61	Tehran	Bandarabbas	9:53	01:45	103	Tehran	Orumie	22:50	01:00
62	Tabriz	Tehran	9:55	01:00	104	Tehran	Tabriz	5:02	01:00
63	Tehran	Esfehan	10:35	01:00	105	Tabriz	Tehran	5:57	01:00
64	Mashhad	Esfehan	11:00	01:30	106	Tehran	Ahvaz	6:09	00:50
65	Kish	Tehran	11:00	01:45	107	Orumie	Tehran	6:28	01:00
66	Esfehan	Kish	11:50	01:15	108	Tabriz	Tehran	7:00	01:00
67	Tehran	Mashhad	11:50	01:20	109	Tehran	Tabriz	7:58	01:00
68	Tehran	Kish	11:50	01:45	110	Ahvaz	Tehran	8:06	00:50
69	Kish	Esfehan	12:00	01:15	111	Tehran	Mashhad	8:40	01:20
70	Qheshm	Tehran	12:20	01:50	112	Tehran	Bandarabbas	9:05	01:45
71	Bandarabbas	Tehran	12:40	01:45	113	Tehran	Mashhad	9:35	01:20
72	Esfehan	Mashhad	13:20	01:30	114	Tabriz	Tehran	10:00	01:00
73	Kish	Esfehan	13:35	01:15	115	Tehran	Kish	10:20	01:45
74	Tehran	Kish	13:45	01:45	116	Mashhad	Esfehan	10:50	01:30
75	Mashhad	Tehran	14:10	01:20	117	Kish	Tehran	11:00	01:45
76	Tehran	Tabriz	14:20	01:00	118	Bandarabbas	Tehran	11:39	01:45
77	Esfehan	Kish	14:20	01:15	119	Mashhad	Tehran	11:45	01:20
78	Kish	Tehran	14:40	01:45	120	Tehran	Shiraz	11:50	01:20
79	Tehran	Ahvaz	14:50	00:50	121	Kish	Esfehan	12:00	01:15
80	Tehran	Mashhad	15:20	01:20	122	Kish	Shiraz	13:00	01:00
81	Esfehan	Tehran	15:30	01:00	123	Tehran	Mashhad	13:10	01:20
82	Mashhad	Tehran	15:40	01:20	124	Esfehan	Mashhad	13:30	01:30
83	Tabriz	istanbul	16:00	01:15	125	Mashhad	Kish	13:30	02:00
84	Kish	Mashhad	16:30	02:00	126	Tehran	Kish	13:40	01:45
85	Ahvaz	Tehran	16:50	00:50	127	Shiraz	Tehran	14:10	01:20
86	Mashhad	Tehran	17:40	01:20	128	Esfehan	Kish	14:20	01:15
87	Tehran	Mashhad	17:40	01:20	129	Tehran	Esfehan	14:30	01:00
88	Tehran	Kish	17:45	01:45	130	Shiraz	Kish	14:50	01:00
89	Tehran	Tabriz	18:00	01:00	131	Mashhad	Tehran	15:20	01:20
90	Tehran	Ahvaz	19:05	00:50	132	Mashhad	Tehran	16:00	01:20

133	Esfehan	Kish	16:20	01:15	175	Shiraz	Tehran	12:50	01:20
134	Kish	Mashhad	16:30	02:00	176	Mashhad	Tabriz	13:00	02:00
135	Kish	Tehran	16:30	01:45	177	Ahvaz	Tehran	13:00	00:50
136	Tehran	Orumie	16:35	01:00	178	Esfehan	Mashhad	13:10:	01:30
137	Kish	Tehran	16:50	01:45	179	Bandarabbas	Esfehan	13:20	01:30
138	Tehran	Kish	17:45	01:45	180	Mashhad	Tehran	13:40	01:20
139	Tehran	Mashhad	17:45	01:20	181	Kish	Tehran	13:40	01:45
140	Tehran	Tabriz	18:00	01:00	182	Tehran	Sabzevar	15:00	01:00
141	Orumie	Tehran	18:20	01:00	183	Tehran	Kish	15:00	01:45
142	Kish	Esfehan	18:30	01:15	184	Tehran	Mashhad	15:00	01:20
143	Tehran	Qheshm	19:05	01:50	185	Esfehan	Tehran	15:40	01:00
144	Tehran	Kish	19:15	01:45	186	Mashhad	Tehran	15:40	01:20
145	Mashhad	Tehran	19:20	01:20	187	Tabriz	Tehran	16:00	01:00
146	Tabriz	Tehran	20:00	01:00	188	Tehran	Kish	16:15	01:45
147	Mashhad	Tehran	20:00	01:20	189	Sabzevar	Tehran	16:50	01:00
148	Kish	Tehran	20:10	01:45	190	Mashhad	Tehran	17:20	01:20
149	Tehran	Shiraz	20:15	01:20	191	Tehran	Orumie	17:30	01:00
150	Esfehan	Tehran	20:40	01:00	192	Kish	Tehran	17:30	01:45
151	Tehran	Mashhad	21:30	01:20	193	Tehran	Qheshm	17:40	01:50
152	Qheshm	Tehran	21:40	01:50	194	Tehran	Tabriz	18:00	01:00
153	Tehran	Tabriz	22:00	01:00	195	Tehran	Shiraz	18:10	01:20
154	Shiraz	Tehran	22:20	01:20	196	Tehran	Bandarabbas	18:40	01:45
155	Tehran	Orumie	22:50	01:00	197	Kish	Tehran	18:40	01:45
156	Tehran	Ahvaz	5:35	00:50	198	Orumie	Tehran	19:30	01:00
157	Tabriz	Tehran	6:00	01:00	199	Tabriz	Tehran	20:00	01:00
158	Tehran	Mashhad	6:05	01:20	200	Shiraz	Tehran	20:20	01:20
159	Orumie	Tehran	6:25	01:00	201	Tehran	Kish	20:20	01:45
160	Tehran	Tabriz	6:55	01:00	202	Qheshm	Tehran	20:30	01:50
161	Ahvaz	Tehran	7:17	00:50	203	Bandarabbas	Tehran	21:10	01:45
162	Tehran	Tabriz	7:57	01:00	204	Tehran	Mashhad	21:30	01:20
163	Mashhad	Tehran	8:20	01:20	205	Tehran	Tabriz	22:00	01:00
164	Tehran	Mashhad	8:55	01:20	206	Kish	Tehran	22:50	01:45
165	Mashhad	Tehran	9:00	01:20	207	Tehran	Orumie	22:50	01:00
166	Tabriz	Tehran	9:00	01:00	208	Tehran	Ahvaz	5:00	00:50
167	Tehran	Esfehan	9:05	01:00	209	Tehran	Tabriz	5:00	01:00
168	Tabriz	Mashhad	10:00	02:00	210	Mashhad	Tehran	5:50	01:20
169	Tehran	Shiraz	10:40	01:20	211	Tabriz	Tehran	6:10	01:00
170	Mashhad	Esfehan	10:50	01:30	212	Orumie	Tehran	6:28	01:00
171	Tehran	Ahvaz	11:00	00:50	213	Ahvaz	Tehran	7:00	00:50
172	Esfehan	Bandarabbas	11:00	01:30	214	Tabriz	Tehran	7:00	01:00
173	Tehran	Mashhad	11:20	01:20	215	Tehran	Tabriz	8:00	01:00
174	Tehran	Kish	11:20	01:45	216	Tehran	Mashhad	8:20	01:20

217	Tehran	Ahvaz	8:50	00:50	259	Orumie	Tehran	6:52	01:00
218	Tehran	Kermanshah	9:00	01:00	260	Tabriz	Mashhad	7:50	02:00
219	Tehran	Orumie	9:05	01:00	261	Tehran	Tabriz	7:57	01:00
220	Tehran	Bandarabbas	9:20	01:45	262	Tehran	Ahvaz	8:30	00:50
221	Tabriz	Tehran	10:00	01:00	263	Tehran	Kermanshah	8:50	01:00
222	Mashhad	Sari	10:30	01:10	264	Qheshm	Mashhad	9:00	02:00
223	Ahvaz	Tehran	10:50	00:50	265	Tabriz	Tehran	9:50	01:00
224	Orumie	Mashhad	11:00	02:00	266	Tehran	Qheshm	9:53	01:50
225	Orumie	Tehran	11:00	01:00	267	Ahvaz	Tehran	10:08	00:50
226	Kermanshah	Tehran	11:00	01:00	268	Mashhad	Tabriz	10:50	02:00
227	Bandarabbas	Mashhad	12:00	02:00	269	Kermanshah	Tehran	10:58	01:00
228	Sari	Mashhad	12:20	01:10	270	Tehran	Tabriz	11:48	01:00
229	Tehran	Tabriz	13:00	01:00	271	Mashhad	Tehran	11:50	01:20
230	Tehran	Mashhad	14:00	01:20	272	Tehran	Mashhad	12:05	01:20
231	Mashhad	Orumie	14:00	02:00	273	Qheshm	Tehran	12:38	01:50
232	Tehran	Esfahan	14:05	01:00	274	Tehran	Esfahan	13:50	01:00
233	Mashhad	Esfahan	14:10	01:30	275	Tabriz	Tehran	14:00	01:00
234	Mashhad	Bandarabbas	14:40	02:00	276	Tehran	Ahvaz	14:10	00:50
235	Tabriz	Tehran	16:00	01:00	277	Mashhad	Tehran	14:20	01:20
236	Esfahan	Tehran	16:00	01:00	278	Esfahan	Ahvaz	15:40	00:50
237	Esfahan	Kish	16:00	01:15	279	Tehran	Kish	15:50	01:45
238	Tabriz	Istanbul	16:00	01:15	280	Tabriz	Tehran	16:00	01:00
239	Esfahan	Mashhad	16:20	01:30	281	Ahvaz	Tehran	16:00	00:50
240	Mashhad	Kish	16:20	02:00	282	Tehran	Orumie	16:00	01:00
241	Bandarabbas	Tehran	17:30	01:45	283	Tehran	Shiraz	16:40	01:20
242	Tehran	Tabriz	17:55	01:00	284	Ahvaz	Esfahan	17:30	00:50
243	Kish	Esfahan	18:00	01:15	285	Tehran	Mashhad	17:55	01:20
244	Mashhad	Ahvaz	18:40	00:50	286	Orumie	Tehran	18:00	01:00
245	Tehran	Kish	19:05	01:45	287	Tehran	Tabriz	18:05	01:00
246	Kish	Mashhad	19:20	02:00	288	Kish	Esfahan	18:20	01:15
247	Istanbul	Tabriz	19:30	01:15	289	Shiraz	Tehran	19:00	01:20
248	Tabriz	Tehran	20:00	01:00	290	Shiraz	Kish	19:00	01:00
249	Tehran	Shiraz	20:10	01:20	291	Esfahan	Tehran	19:20	01:00
250	Ahvaz	Mashhad	21:20	01:30	292	Tehran	Abadan	19:55	01:00
251	Kish	Tehran	21:30	01:45	293	Tabriz	Tehran	20:00	01:00
252	Tehran	Orumie	21:50	01:00	294	Mashhad	Ahvaz	20:10	01:30
253	Tehran	Tabriz	22:00	01:00	295	Esfahan	Kish	20:20	01:15
254	Mashhad	Tehran	22:20	01:20	296	Kish	Shiraz	20:40	01:00
255	Shiraz	Tehran	22:20	01:20	297	Tehran	Tabriz	22:00	01:00
256	Tabriz	Tehran	5:50	01:00	298	Kish	Tehran	22:10	01:45
257	Tehran	Tabriz	6:00	01:00	299	Abadan	Tehran	22:10	01:00
258	Mashhad	Qheshm	6:20	02:00	300	Ahvaz	Mashhad	22:50	01:30

2022/04/17

301	Tehran	Orumie	22:50	01:00	329	Bandarabbas	Tehran	15:40	01:45	
302	Tehran	Yazd	4:41	01:00	330	Tabriz	Tehran	16:00	01:00	
303	Tehran	Tabriz	4:43	01:00	331	Mashhad	Tehran	16:20	01:20	
304	Tabriz	Tehran	5:54	01:00	332	Kish	Esfahan	16:40	01:15	
305	Orumie	Tehran	6:20	01:00	333	Tehran	Orumie	17:30	01:00	
306	Yazd	Tehran	6:40	01:00	334	Tehran	Tabriz	18:00	01:00	
307	Tabriz	Tehran	6:45	01:00	335	Ahvaz	Tehran	18:00	00:50	
308	Tehran	Zahedan	7:20	01:50	336	Tehran	Qheshm	18:40	01:50	
309	Tehran	Tabriz	7:54	01:00	337	Esfahan	Kish	18:50	01:15	
310	Tehran	Ahvaz	8:25	00:50	338	Tehran	Shiraz	19:30	01:20	
311	Tehran	Ardebil	8:53	01:00	339	Orumie	Tehran	19:30	01:00	
312	Tehran	Kermanshah	9:10	01:00	340	Tabriz	Tehran	20:00	01:00	
313	Tabriz	Tehran	10:00	01:00	341	Tehran	Ahvaz	20:00	00:50	
314	2022/04/18	Zahedan	Tehran	10:00	01:50	342	Kish	Tehran	21:00	01:45
315		Ahvaz	Tehran	10:30	00:50	343	Qheshm	Tehran	21:30	01:50
316		Ardebil	Tehran	11:00	01:00	344	Shiraz	Tehran	21:50	01:20
317		Mashhad	Tehran	11:00	01:20	345	Tehran	Tabriz	22:00	01:00
318		Esfahan	Bandarabbas	11:00	01:15	346	Ahvaz	Mashhad	22:00	01:30
319		Kermanshah	Tehran	11:00	01:00	347	Tehran	Orumie	22:50	01:00
320		Tehran	Tabriz	12:00	01:00					
321		Tehran	Mashhad	12:30	01:20					
322	Tehran	Bandarabbas	13:00	01:45						
323	Bandarabbas	Esfahan	13:20	01:15						
324	Tehran	Esfahan	13:40	01:00						
325	Tehran	Kish	14:05	01:45						
326	Tehran	Mashhad	14:10	01:20						
327	Mashhad	Ahvaz	15:00	01:30						
328	Esfahan	Tehran	15:40	01:00						

APPENDIX 2: Ata airline air fleets

Row	Type of air fleet	Number of fleets	Passenger capacity
1	Boeing MD-83	8	170
2	Airbus A320	3	168
3	Boeing 737	2	136
4	EMB-145	3	50

Persian Abstract

چکیده

یکی از موضوعاتی که تحقیقات زیادی را در زمینه بهینه‌سازی صنعت هوایی به خود اختصاص داده است به برنامه‌ریزی پروازها، ناوگان هوایی و نحوه ارتباط این دو با یکدیگر مرتبط می‌شود که به اختصار برنامه‌ریزی خطوط هوایی نامیده می‌شود. با وجود اهمیت بسیار بالای این موضوع در سودآوری شرکت‌های هوایی و استفاده مناسب از منابع آنها، پیچیدگی محاسباتی بالای این مدل‌ها سبب تفکیک این مساله به زیرمسائل مجزا و در نتیجه کاهش دقت پاسخ نهایی شده است. تاکنون مقالات زیادی در زمینه‌های مختلف این موضوع منتشر شده است که در بعضی از موارد تلاش برای ایجاد یکپارچگی در فرآیند دیده می‌شود ولی در اکثر آنها نگاه عملیاتی به موضوع وجود نداشته و بعضی از الزامات کلیدی به دلیل ساده‌سازی مدل‌ها مغفول مانده است. در این مقاله مدلی یکپارچه از دو مرحله اصلی برنامه‌ریزی خطوط هوایی شامل تخصیص ناوگان و مسیریابی تعمیرات محور هواپیما ارائه شده و عملکرد این مدل با استفاده از داده‌های واقعی یکی از خطوط هوایی ایران مورد بررسی قرار گرفته است. در ادامه مقایسه عملکرد این مدل با روش عملیاتی شامل حل مرحله به مرحله زیرمسائل و یکی از مقالات جدید و مشابه در این حوزه مورد بررسی قرار گرفته و بهبود نتایج نشان داده شده است. همچنین تحلیل حساسیت مدل نسبت به بعضی از پارامترها انجام شده و صحت عملکرد آن را تایید نموده‌اند.



Compressing Face Images Using Genetic and Gray Wolf Meta-heuristic Algorithms Based on Variable Bit Allocation

R. Khodadadi^a, G. Ardeshir^{*a}, H. Grailu^b

^a Faculty of Electrical & Computer Engineering, Babol Noshirvani University of Technology, Babol, Iran

^b Faculty of Electrical Engineering, Shahrood University of Technology, Shahrood, Iran

PAPER INFO

Paper history:

Received 24 November 2022

Received in revised form 11 January 2023

Accepted 14 January 2023

Keywords:

Genetic Algorithm

Gray Wolf Algorithm

Face Recognition

Face Compression

Block Division

Variable Bit Allocation

ABSTRACT

In image processing, compression plays an important role in monitoring, controlling, and securing the process. The spatial resolution is one of the most effective factors in improving the quality of an image; but, it increases the amount of storage memory required. Based on meta-heuristic algorithms, this article presents a compression model for face images with block division and variable bit allocation. Wavelet transform is used to reduce the dimensions of high spatial resolution face images. In order to identify important and similar areas of identical macroblocks, genetic algorithms and gray wolves are used. A bit rate allocation is calculated for each block to achieve the best recognition accuracy, average PSNR, and SSIM. The CIE and FEI databases have been used as case studies. The proposed method has been tested and compared with the accuracy of image recognition under uncompressed conditions and using the common SPIHT and JPEG coding methods. Recognition accuracy increased from 0.18% for 16×16 blocks to 1.97% for 32×32 blocks. Additionally, the gray wolf algorithm is much faster than the genetic algorithm in reaching the optimal answer. Depending on the application type of the problem, the genetic algorithm or the gray wolf may be preferred to achieve the maximum average PSNR or SSIM. At the bit rate of 0.9, the maximum average PSNR for the gray wolf algorithm is 34.92 and the maximum average SSIM for the genetic algorithm is 0.936. Simulation results indicate that the mentioned algorithms increase PSNR and SSIM by stabilizing or increasing recognition accuracy.

doi: 10.5829/ije.2023.36.04a.08

1. INTRODUCTION

In general, the process of compression and recognition reduces the quality of the image by increasing the compression ratio. The study of block transform coding systems has been conducted in a variety of domains of discrete two-dimensional transformations. As a result, most coding systems in this regard rely on sinusoidal transformations (such as DFT or DCT) that provide more accurate and closer estimates of information packaging and computational complexity. Choosing a particular transform for a particular application depends on the amount of reconstruction error that can be tolerated and the computational resources available. The JPEG format uses a DCT conversion method that offers a good compromise between information packing capability and computational complexity. One of the challenges of

facial recognition systems is maintaining the rate of image recognition. Today, due to the advancement of technology, most cameras are equipped with high resolution, which is usually expressed in megapixels. High spatial resolution, on the other hand, is one of the most important factors for increasing image quality, resulting in a larger storage volume. Reducing the resolution to a lower limit will decrease recognition accuracy, and the higher the resolution, the desired quality.

Many face recognition applications capture images with low resolution. Because face recognition methods are trained on high resolution face images, they perform poorly on low resolution images. Compression rates for lossy methods are much higher than those for lossless methods. The smaller the image size, the faster it can be compressed and transferred, and it requires less storage

*Corresponding Author Institutional Email: g.ardeshir@nit.ac.ir
(G. Ardeshir)

space. A point that is preferable to other aspects. Due to this, the proposed method, which allows simultaneous access to high compression rates while maintaining or improving the accuracy of image recognition, is suitable for the intended applications. However, these methods always result in distortions by destroying some of the primary data. At lower bit rates, the amount of distortion increases. The most important application of face images is in the recognition of people, and as such, the amount of distortion may be so high that it reduces the accuracy of recognition, it is important to provide a method that does not reduce the recognition rate.

Mobile phones and social networks have led to an increase in the production of digital content today. Recent advances in compression methods such as H.265 or HEVC have enabled CCTV images to be compressed and encoded in high quality [1]. As a general rule, the smaller the images, the faster they will be compressed and transmitted, and the less storage space they will require [2]. As the volume of information in circulation is so large, managing and optimizing these processes is of utmost importance. Therefore, it is very important to compress images. Images are usually compressed in such a way that some details are lost. When the removed details are noisy and do not contain important and real details of the face, the recognition percentage may even be increased. The primary objective of image compression is to reduce the number of bits necessary to display an image, since the transfer of images is a costly process [3]. Image compression begins with identifying data redundancy, and among the types of data redundancy, we can mention cryptographic redundancy [4], inter-pixel redundancy [5], and psychovisual redundancy [6]. The main objective of image compression algorithms is to reduce all types of image redundancy. As a result, the type of algorithm to use depends on how the image is to be used. Video surveillance systems place a high value on the compression of face images, and the images are always designed to consume the least amount of bandwidth possible. Therefore, infrastructure equipment should be considered much smaller, with lower energy consumption and lower costs.

By compressing facial images, in addition to removing redundancies, the distortion resulting from compression should not affect or even increase the recognition percentage of the system. Face images with a low degree of spatial resolution are compressed under conditions in which the distance between two eyes is approximately 90 pixels and the image dimensions are approximately 180-200 pixels. However, in this article, facial images with a high degree of spatial resolution have been evaluated, and, therefore, the conditions considered are for images larger than the approximate dimensions, usually $200 \times \times$.

Finding compression methods that have minimal impact on image processing systems is an interesting area of research. Meta-heuristic algorithms have recently emerged with significant power in solving optimization problems [7]. The optimization of objective criteria in compression by examples of these algorithms has been investigated. However, the impact these improvements have on the compression of face recognition systems has received less attention.

In this article, a compression method is used to allocate the bit budget from meta-heuristic algorithms (genetics and gray wolf) for identifying valuable areas without reducing the recognition rate of facial images. An optimization problem can be solved in a variety of ways. A number of these methods [8, 9] are derived from natural processes. The genetic algorithms are under the search algorithms and instead of directly dealing with the values of the parameters of the problem, they operate on a coded representation of the set of parameters. To find solutions to the problem and optimize the objective function of the problem, they search a population of points in a search space without knowing the gradient information related to the objective function. A genetic algorithm is a type of evolutionary algorithm that uses biological methods such as inheritance and mutation. One of these algorithms, inspired by the genetics of living organisms, seeks to find an optimal state within a reasonable period of time [10]. The gradient of the objective function is used as a guide in most computational optimization methods. However, these methods often encounter difficulties if, for example, the objective function is discontinuous and its derivative cannot be calculated. Genetic algorithms are often beneficial to regression-based prediction methods [11]. It is, however, the aim of the discussion to identify a suitable answer among a variety of samples that will provide an optimal learning system that delivers high accuracy and significant speed. In this case, the topic is to identify the best learning system with a high level of accuracy and significant speed from a variety of samples. In this learning system, in fact, the loop process of accessing the optimal estimation of the bit rate of each of the blocks separately, is performed, provided that the recognition accuracy of images is equal to the condition without compression (the highest value of recognition accuracy) or even greater if it is possible.

Genetic algorithms are usually based on repetition, most of their parts are chosen at random, and they are considered to be meta-heuristic methods for discrete optimization. The popularity of meta-heuristic methods can be attributed to their flexibility, derivative-free mechanism, and ability to avoid getting stuck in local optima. These methods [12] are relatively simple and are founded on very simple concepts. This article also discusses the gray wolf algorithm, which is based on

collective intelligence and the life of gray wolves [13]. In these animals, the leader, or alpha, makes decisions regarding areas such as attack and timing. According to this algorithm, the hunting method of this kind of animal involves tracking, chasing and approaching the prey. It involves following and encircling the prey until it stops moving, and then attacking it. In order to model wolf social behavior, a random population of solutions is generated, and the most appropriate is referred to as (α). As well as the second best solution, other solutions are known as wolves of packs (ω). As such, the gray wolf algorithm uses the following three answers to guide hunting (optimization).

Meta-heuristic algorithms are designed to find the optimal solution within a reasonable amount of time. A process can be optimized by improving it, as we know. Essentially, optimization involves adjusting inputs, the characteristics of a device, a mathematical process, or an experiment in order to achieve the minimum or maximum output [14]. To achieve a reasonable and good answer at the right time, instead of searching all the states, we use various meta-heuristic methods [15]. While working in a lossy environment, an image data compression algorithm [16] should preserve most of the data's features and be less complex in algorithmic terms. The general nature of these methods [17-19] usually begins with a set of variables and continues until the objective function reaches a minimum or maximum value. The image of a face is one of the most popular and widely used images. There is a growing importance of the issue of identity verification in surveillance systems [20], control systems [21] and security systems [22]. Most of these systems require a large database of face images of different people, especially when they are used in large, international and significant organizations. Meanwhile, the effectiveness of these systems is highly dependent on the correct identification of facial features and the correct detection of facial areas [23]. Some features of the face play an instrumental role in face recognition, and it is critical not to lose this information when compressing images. When compressing face images, it is a priority to maintain the quality of valuable features of the face at an appropriate level, particularly at low bit rates [24]. As part of the proposed method, it is automatically determined for each image to decompose the input image $I(i,j)$ into several levels (L), and to use the approximate sub-image of each level as the basis for further processing. This means that after the implementation of the last decomposition step in the proposed method, the approximation sub-image is delivered to the segmentation block as the input image with low level resolution. In this research, A meta-heuristic algorithm (genetics and gray wolf) is responsible for allocating the bit budget in this research. In part 2, previous research on image compression methods, especially those for face images, is reviewed. In

section 3, the proposed method will be described in detail, and its evaluation results will be compared to those obtained from several reference methods. In section 4, we discuss the conclusion.

2. RELATED WORKS

Most of the methods that have been proposed for image compression are general-purpose, which is an advantage since they can be applied to a wide variety of images. On the other hand, it is a negative point and does not take into account the content of the images. As a consequence, all-purpose methods are not able to optimally utilize the abundance of images within a limited set of categories (face, medical, text, etc.). The use of smart optimization methods can offer much better solutions to these problems. Meta-heuristic optimization methods and evolutionary algorithms are effective and constructive methods for solving feature selection problems. With approximate algorithms, it is possible to find effective (near-optimal) solutions to difficult optimization problems. A heuristic, a meta-heuristic, and a super-heuristic are examples of approximate algorithms. We present meta-heuristic algorithms to solve the problem of heuristic algorithms getting stuck in local optimal points and converge prematurely to them. Meta-heuristic algorithms can be classified according to a variety of factors:

- I. Based on a single answer and the population as a whole
- II. Natural and non-natural designs
- III. Memory and non-memory
- IV. Definite and probable
- V. Algorithms based on collective intelligence.

The use of smart optimization methods can provide much better solutions to these problems. As a consequence, meta-heuristic optimization methods and evolutionary algorithms are effective and constructive methods for solving feature selection problems. Nowadays, it is possible to compress images using various classical or meta-heuristic algorithms, and in this regard, many experts have presented various ideas [25]. To learn algorithms and repeat the process, many calculations must be made in order to use these methods and different functions to approach learning, optimization, decision-making, etc. A learning system, however, must be able to find the optimal answer with high accuracy among various samples. Based on the proposed method, the loop process of accessing the optimal bit rate estimation for each of the blocks is based on the assumption that the accuracy of image recognition is equivalent to the discussed methods, or even higher if possible.

The number of compression methods for natural images and even text images is relatively small in

comparison. As a result, no specific classification has been provided for these methods. One of the reasons for the low number of methods may be the lack of serious attention paid to the uniqueness of these images [26]. Face images are usually compressed using images with a low spatial resolution (usually images with a dimension of 200×200), and in most cases, the use of high resolution images has not been investigated. In relevant applications, there is a very limited amount of space allocated for storing face images [27]. Recent years have seen the introduction of intelligent and meta-heuristic methods for solving image compression problems. Unlike precise optimization methods, these algorithms look for points close to the global optimum, based on rules that govern natural phenomena. As a result of meta-heuristic methods, optimal solutions can be found at acceptable computational costs, but there is no guarantee that they will lead to the optimal solution, and the results are entirely random. Consequently, these methods are also known as imprecise methods [28], as random mechanisms have a significant impact on their structure. The most influential and widely used approaches include genetic algorithms [29], differential evolution algorithms [30], particle swarm algorithms [31], ant colony algorithms [32], honey bee algorithms [33], used in various industries today. Asiedu et al. [34] presented a face recognition algorithm based on wavelet transforms and compression coefficient values. Based on sparse representation (SRC), the classification method compares residual errors between test samples and reconstruction samples. The algorithm not only improves recognition and reliability, but it also reduces detection time to some extent [35]. A matrix of facial features is extracted and classified. Compared with reconstructed samples. The results using the ORL¹ and FERET [36] databases have shown that this method provides better recognition capability, accuracy, and recognition speed than traditional methods.

He and Chen [37] proposed a novel variable block size for a face image compression method (E2EFIC), whose parameters can be automatically optimized based on gradient feedback. Image compression uses a network (GAN). The metrics should be applied directly to the image compression scheme. This scheme has been demonstrated to be effective by showing a performance improvement of 71.71%, 48.28%, and 52.67% when compared with JPEG2000, WebP, and neural network encodings. This is under the same face accuracy measurement. To enhance face recognition in low-resolution images, a Generative Adversarial Network is employed by Shahbakhsh and Hassanpour [38]. The network considers image edges and reconstructs high-frequency details in order to preserve the structure of the face. Any face recognition method can benefit from the

proposed technique for generating super-resolved features. In order to preserve the structure of the face, the proposed network considers image edges and recovers high-frequency details. Using the generated high resolution features, any face recognition method can be improved in terms of recognition accuracy.

Selimović et al. [39] performed content-aware compression by prioritizing the areas of the image that are more relevant to the interpretation of the image and compressing them at a higher bit, i.e. without loss or with less loss. Encodes information about the rest of the image. By examining multiple regions of interest (MS-ROI), a convolutional neural network (CNN) is able to locate different regions of interest within an image. It is expressed as a sensitivity map that characterizes the relevance of different regions of the image and provides a merit value for every pixel. As a result of this information, compression is guided. This method [40] examines the recognition of remote face recognition (FR) schemes within the framework of compact image recognition (CS). Using predictors such as autoencoder that provide compact measurements, error images can be obtained as the difference between original and predicted images. Subsampled measurements of the thin error image and part of the original image are then transmitted. At the destination end, the test image is reconstructed from the CS error image and the partial information. Following the reconstruction of the image, principal component analysis is used to extract significant features. The performance of the proposed method has been evaluated on both AR and ORL databases, with 93.99% accuracy for the former and 91.5% accuracy for the latter.

Asghari Beirami and Mokhtarzade [41] proposed a new method for FR called multiscale Gabor covariance-based ensemble Log-euclidean SVM (MGcov-ELSVM), which utilizes descriptors of Gabor magnitude and phase derived from multiscale face representations. MGcov-ELSVM begins by producing multiscale representations of faces. In the second stage, Gabor magnitude and phase features are derived from multiscale face images. The Gabor magnitude and phase features are then used to generate covariance descriptors. As a final step, log-Euclidean SVM classifiers are used to classify covariance descriptors, and a majority voting method is used to determine the recognition results. According to experimental results from two face databases, ORL and Yale, the MGcov-ELSVM outperforms some recent FR methods. Elad et al. [24] described compressing face images by changing the geometric shape to a standard form, dividing the resulting image into blocks, and then coding each block according to the vector quantization (VQ) method. The method has been used to exploit the excess of the same facial features in different individuals. This was done by converting images to standard form and

¹ <https://paperswithcode.com/dataset/orl>

using VQ in order to increase compression efficiency, particularly at low bit rates. One disadvantage of this method is the long training time for the VQ data culture. In addition, there is the relatively large external memory required to store this data culture in both the encoder and decoder. Another disadvantage of this method is the visual disruptions created by the block method and the separate coding of each block in the image. Al-Khafaji et al. [42] introduced a new mathematical iterative polynomial model to represent both coding bases. The model proposes an efficient hybrid way where coefficients are represented as lossless while residuals are presented as a lossy but with minimum loss, which ensures effective performance in terms of compression ratios and quality. Results show that while the technique has some limitations, the proposed system achieves equivalent compression ratios as the standard JPEG technique, but with superior quality for the same compression ratio.

Discrete Wavelet Transform (DWT) is used by Qiuyu and Suozhong [43] to encode the wavelet coefficients of the three areas of the face image. These coefficients are then coded according to the importance specified in the image quality. The embedded block coding algorithm with optimal shortening (EBCOT) is applied in this method. Facial recognition technology has advanced significantly over the past ten to fifteen years. Algorithms for recognizing and identifying faces can be applied. For face recognition, some researchers have used genetic algorithms [44]. In this algorithm, an optimal subset of the extracted features is sought. Sun and Yin [45] applied a genetic algorithm to select a 3D diagnosis. Liu and Wechsler [46] used an evolutionary tracking method based on a genetic algorithm to recognize faces.

In this plan, the axes defined in PCA space are rotated to determine the basis of the face. The existing methods do not provide satisfactory general classification, so a better feature selection and integration method is needed to improve the accuracy and precision of general classification. Even though evolutionary algorithms have powerful structures for classifying data and learning patterns, the difficulty of training and using a comprehensive network that includes all the desired features is another issue with these algorithms. This paper does not place a high priority on computational processing time. Based on genetic and gray wolf algorithms, this paper proposes assigning variable bits to each block of face images. It is important to pay attention to the recognition rate in addition to the process of compressing images and dividing the appropriate bit budget for each block. Although due to the nature of compression, the information and redundant details of the image are removed, the recognition percentage for the images should be calculated in a way that does not decrease from the recognition accuracy in uncompressed conditions or even increases if possible. In this way, if we

can identify areas of the face image that are of low value and importance with the aid of genetic algorithms and gray wolves, fewer bits will be assigned to each block and redundant information will be removed. In contrast, we can assign a higher bit rate to high-value portions of face images (such as the eyes, nose, and mouth) that contain facial details. As a result, the face image is encoded using SPIHT, and after decoding and applying the wavelet transform, it is saved. All test images are subjected to the loop described above. To conclude, the recognition accuracy criterion was used to determine the appropriate choice of bit block rate using principal component analysis (PCA). According to the explanations provided, each method has its advantages and disadvantages and is used for different purposes and functions in different fields. We will next examine how to allocate a variable bit budget between image blocks using the algorithms used in the proposed method.

3. PROPOSED METHOD

A suitable bit budget is proposed in this paper article for the image blocks and a map of the importance of face images is provided. For this reason, an importance map is created for the valuable regions of the face images, which can be analyzed to determine the region of interest (ROI) and valuable regions. The areas of the face details can be assigned a higher priority and bit rate than other areas. The meta-heuristic algorithms of the proposed method take into account the objective function of recognition rate. This objective function seeks to find the bit string length (BSL) assigned to each block that does not reduce the recognition rate during compression. The highest recognition rate is recorded in the output as soon as the meta-heuristic algorithm has reached the termination condition (maximum repetition).

Because the input image is divided into equal-sized blocks, it is possible to remove redundancy and allocate fewer bits in some blocks with less critical information. Conversely, if a block contains facial image details that have more value and information (such as eyes, nose, and mouth), more bits should be allocated to that block. In the training database set, 70% of the images are included, while in the test database set, 30% of the images are randomly selected. In the section on dimension reduction, discrete wavelet transforms are used. Three modes with dimensions 16, 32, and 64 have been divided into blocks. As test steps, we have applied two meta-heuristic algorithms, one based on evolutionary structure (genetics) and the other based on collective intelligence (gray wolf). Algorithms described above are responsible for identifying valuable areas in the face and allocating the required amount of bits. These algorithms begin with a population of 10 and a number of generations.

We evaluated the results of the algorithms with the images in the test gallery set without compression, as well as compressed (JPEG) and SPIHT coding. In order to verify the termination condition, the classification department has been assigned the task of classifying and identifying the correctness of the images using principal component analysis. The process view of the proposed method is shown in Figure 1.

Final steps in the process are to evaluate and compare the results of the recognition test and the accuracy of image recognition for the set of compressed images. The following sections provide more information about the facade process.

3. 1. Facial Database The spatial resolution of face images is 1536×2048 (high), 480×640 (relatively high), and 150×200 (low). In the existing face image compression methods, images with a low spatial resolution (such that the distance between two eyes is

about 90 pixels, and the image dimensions are 180-200 pixels) have been employed, high-resolution face images have not been examined. In most existing methods for compressing face images, images with a low spatial resolution (normal images with dimensions of approximately 200×200 pixels) are used. As the selected images in this paper require high spatial resolution analysis, CIE¹ and FEI² images are used. These databases present simulation results. In the CIE database, there are 300 color images (for 30 individuals) with dimensions of 2048×1536. Figure 2 illustrates examples of images from the CIE database.

In the FEI database, there are 2000 images (for 200 people) with dimensions of 640×480, and there are 100 images of males and females in color. Most of the faces in this photo are taken from FEI students and staff ranging in age from 19 to 40, and they all have distinctive hairstyles and cosmetics. Figure 3 shows FEI database images.

3. 2. Discrete Wavelet Transform This article proposes a method in which input images (high resolution) are received and reduced in dimensions using wavelet transforms. There are two purposes for which wavelet transforms are used. First, the high resolution images are reduced to the lowest possible level, and the horizontal, vertical, and diagonal details are left out, leaving only the approximate image of low resolution as a measurement criterion. For this reason, with one goal, image detail has been removed (compressed), and with another goal, the dimensions have been reduced so that the processing can be carried out at a faster rate.

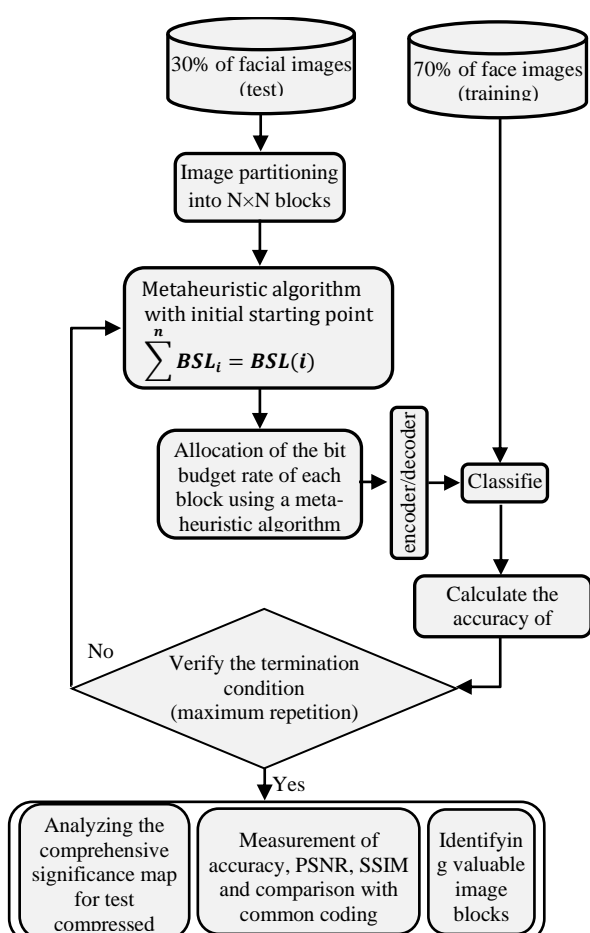


Figure 1. Compression process and recognition accuracy calculation



Figure 2. Images of the CIE database [50]



Figure 3. Images of the FEI database [51]

¹ https://www.researchgate.net/figure/Example-images-of-CIE-database_fig3_343240268

² <https://fei.edu.br/~cet/facedatabase.html>

Based on the level reduction number selected for wavelet transformation, the output of this section consists of a series of images with a lower resolution and smaller dimensions than the original images. In other words, every time wavelet analysis is applied to an image, its dimensions are cut by a quarter. As an example, if a two-level wavelet decomposition is applied to an image, the approximate dimensions at the second level will be approximately one-sixteenth of the original dimensions. Thus, wavelet transforms are used to reduce dimensionality. The number of levels of decomposition in the proposed method is automatically determined for each image, and after the last decomposition step (L), the approximate sub-image is provided to the segmentation block as an input image with low-level resolution. In each level of wavelet decomposition, there are three subbands of details, called horizontal (D^d), vertical (D^v), and diagonal (D^b). EN is calculated by dividing the energy of each subband by the total number of pixels in that subband. The analysis of the input image continues automatically in the proposed method until a level where at least one of the subbands of that level of analysis meets the following condition, at which point parameter L equals the number of the analysis level (or, equivalently, the energy of at least one subband exceeds the threshold value T). The significant value will be determined by Equation (1). The parameter T is a threshold whose value is determined by a coefficient (α) of the energy normalized by the area of the input image.

$$E_N \geq T \quad (1)$$

The α parameter for each subband in each level and for the whole image is fixed at 0.1, which was selected empirically. Because the larger the value of α is chosen, the more compression we will achieve, but the amount of distortion will also increase. Additionally, larger values result in a reduction in the accuracy of detail subband estimation.

$$T = \frac{\alpha \times \sum_{i=1}^M \sum_{j=1}^N I(i,j)^2}{M \times N} \quad (2)$$

According to relation (2), M and N represent the dimensions of the input image. As a result of the proposed method, the larger the value of L, the greater the reduction in the dimensions of the input image. Therefore, the amount of compression will also increase. Figure 4 shows the output of horizontal, vertical, and diagonal levels, as well as the sub-image of the approximation of the fourth level (L=4).

3. 3. Image Block Division It is possible to divide an image into blocks both in a fixed and in a variable manner [47]. Monochrome images are segmented based on their brightness [48] and color images are segmented based on their color components [49]. On the other hand, image and texture edges are also useful features for segmentation [50]. As a result of the proposed method, it is possible to change the dimensions of the blocks

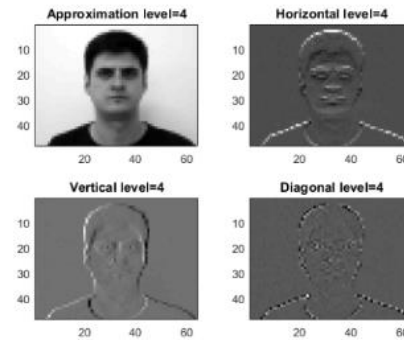


Figure 4. Approximate details of sub-images, horizontal, vertical, and diagonal decompositions up to the fourth level

uniformly. In the second step of the proposed method, these conditions have been specified. This is to facilitate the evaluation of results for image segmentation with 8×8 , 16×16 , 32×32 , 64×64 , and 128×128 blocks. At this stage, the output of the dimensionality reduction diagram block (low-resolution images) is segmented accordingly. In the proposed method, default values are provided for the three states of equal blocks due to a limited number of pages to present the results. We have therefore divided each image into equal blocks of 16×16 , 32×32 and 64×64 dimensions and analyzed their results. Table 1 provides instructions for dividing the number of images into blocks.

In the next step of the proposed method, the values of the number of blocks will be the initial population members of our search space algorithm for bit budget allocation. As explained above, in the first step (reduction of dimensions by the wavelet transform method), the number of reduction levels determines the size of the output images (low-resolution images). If we choose the original input images from the CIE database, and we use the first step of the proposed method, we will obtain images with a scale of 64×48 . Based on the default block size of 16 by 16, if the second step (block division section) is completed, 12 blocks will be created for the image.

3. 4. Bit Rate Per Block

A meta-heuristic algorithm is designed so that a suitable bit budget is allocated to each block for each bit rate with a fixed bit string value. Meta-heuristic algorithms (genetics and gray wolf) have been applied to the investigated data to determine the appropriate bit budget for each block.

TABLE 1. Block division of images

Size of the image	64×48	128×96	256×192	512×384	1024×768	2048×1536
Blocks totaled	12	48	192	768	3072	12288

Using the meta-heuristic algorithms mentioned above, the proposed method extracts the most valuable and most effective features related to valuable face image blocks. If we can allocate a suitable bit budget rate to critical areas of the face, such as the eyes, nose, mouth, etc., then this is the most appropriate answer. There is no doubt that other areas, such as the background, will have less value, and therefore a shorter bit string length will be considered for them. Simply stated, genetic and gray wolf algorithms identify and allocate the desired bit rate for each image block. These meta-heuristic algorithms are used to determine the value between the blocks of an image.

The genetic algorithm does not require any special prerequisites in order to solve the problem. As a result of this feature, genetic algorithms have become powerful optimization tools. The genetic algorithm, like many stochastic methods, does not guarantee finding the optimal solution to a problem and only assists in finding a relatively good solution to the problem. In the proposed method, the search space is comprised of the number of image segmentation blocks. The proposed method considers a maximum of 10 primary populations for the statistical population. There are 70% of chromosomes in the population that are considered for crossover, and 30% for mutation. Genetic algorithm of the proposed method selects crossover and mutation coefficients of 3 and 2, respectively. The selection process is based on a roulette wheel. Upon reducing the dimensions and dividing the approximate image (the last level of decomposition), the number of blocks will equal the number of genes of the genetic algorithm. Since the total length of the bit string is fixed, it is important to note that after determining the values assigned to each gene, their sum equals the total length of the bit string.

For each block in the iteration loop, the algorithm determines the appropriate gene value and provides stopping conditions. Whenever the objective function requires a large number of computations, convergence is considered to be faster. In the proposed method, a stop condition is used to achieve the highest detection accuracy possible. Gray wolf algorithm were presented in 2014 based on the gray wolf's life [14]. A group's leader (α) determines how attacks and timing should be handled by these animals, which live in groups.

- Tracking, chasing, and approaching
- Following and surrounding the hunt
- Assaulting the prey

According to the proposed method based on the gray wolf algorithm, it is assumed that we have three viable solutions. However, we have no idea of the location of the prey in the initial search space. For 3D modeling, it is therefore necessary to first determine the points around the prey. It then moves toward the prey and attacks it. These relationships are used to determine the bait's location.

$$\vec{D} = |\vec{C} \cdot \vec{X}_p(t) - \vec{X}(t)| \quad (3)$$

$$\vec{X}(t+1) = \vec{X}_p(t) - \vec{A} \cdot \vec{D} \quad (4)$$

Here, t is the current iteration of the algorithm, \vec{A} and \vec{C} are the coefficient vectors, (\vec{X}_p) is the prey position vector, and \vec{X} is the gray wolf position vector. As a result of the following relationship, we can also obtain the vectors \vec{A} and \vec{C} .

$$\vec{A} = 2 \vec{\alpha} \vec{r}_1 - \vec{\alpha} \quad (5)$$

$$\vec{C} = 2 \vec{r}_2$$

In the above relationship, (\vec{r}_1) and (\vec{r}_2) are random vectors in the interval [0 and 1]. An intelligent optimization algorithm makes a compromise between exploration and mining by adjusting its control parameters. An optimization algorithm with a large number of control parameters does not necessarily result in better performance. The fewer the parameters, the greater the possibility of adjusting these parameters to increase the speed of convergence and avoid becoming stuck in the local optimum. But the gray wolf optimization algorithm lacks any parameter control. During the optimization process, the parameter (α) is the only parameter that changes.

The parameter $\vec{\alpha}$ also decreases from 2 to zero during the algorithm execution process. To mathematically model the prey approaches, the value of a is reduced. It should be noted that the range of changes of A will also decrease with a . In other words, A is a random value in the interval $[-2a, 2a]$, where a decreases from 2 to 1 during the steps of solving the iteration of the algorithm. For the random values of A in the interval $[1,1]$, the next position of The search agent can be anywhere between the current position of the agent and the position of the prey. In the gray wolf algorithm, the position of the wolves is updated according to the position of α , β , and δ . Other solutions (called ω wolves) should change their positions to converge to the optimal solution, according to the following relations.

$$\vec{D}_\alpha = |\vec{C}_1 \cdot \vec{X}_\alpha - \vec{X}| \quad (7)$$

$$\vec{D}_\beta = |\vec{C}_2 \cdot \vec{X}_\beta - \vec{X}| \quad (8)$$

$$\vec{D}_\delta = |\vec{C}_3 \cdot \vec{X}_\delta - \vec{X}| \quad (9)$$

$$\vec{X}_1 = \vec{X}_\alpha - \vec{A}_1(\vec{D}_\alpha) \quad (10)$$

$$\vec{X}_2 = \vec{X}_\beta - \vec{A}_2(\vec{D}_\beta) \quad (11)$$

$$\vec{X}_3 = \vec{X}_\delta - \vec{A}_3(\vec{D}_\delta) \quad (12)$$

$$\bar{X}(t+1) = \frac{\bar{X}_1 + \bar{X}_2 + \bar{X}_3}{3} \quad (13)$$

The wolves may sometimes need to move apart in order to find prey, and they may not always congregate. A random value greater than 1 or less than -1 is used to model such phenomena. As a result, if $|A| > 1$, the wolves will move away from the prey, whereas if $|A| < 1$, the wolves will be forced to attack the prey. For example, if we have an image (low resolution) with dimensions of 64×48 and a total number of blocks of 12, and we want to compress it at a bit rate of $BPP = 0.5$, in this situation, the output data bit string length (BSL) will be equal to 1536 and the number of genes on each chromosome or the number of attacking wolves will be equal to 12. Consequently, the pattern of dividing these 1536 bits into 12 (genes/wolves) and selecting the optimal place to allocate the most appropriate bit budget to each block (in terms of the highest recognition accuracy across all images, and how to swap the values of genes/wolves) is the responsibility of the meta-heuristic algorithm (Genetics/Gray Wolf). It is very significant to pay attention to the fact that the number of genes of each chromosome or the number of invading wolves after combining does not increase more than the amount considered in the bit budget allocation ($BSL=1536$). A mutation process is used to increase or decrease each of the (genes/wolves) in the proposed method so that the budget amount does not change. Essentially, our method of comparing the accuracy of the recognition is based on the fact that the size of the total bit string of each block should equal the length of the output bit string if the same conditions apply as usual. Therefore, the fitting function used in meta-heuristic algorithms (genetics/gray wolf) of the proposed method is chosen in a way that converges at the same time to the highest recognition accuracy of all images, the highest average PSNR and the highest average SSIM. As a result, the condition of stopping the function and exiting the process loop is met.

3. 5. Coding/Decoding In compression processes, the most vital part, which happens to have the most computational complexity, is related to image encoding and decoding. In the proposed method of this article, SPIHT coding is used due to the production of integrated sequences, high encoding efficiency, and low computational complexity [51]. It is also possible to express one of the benefits of this type of coding in terms of the transmission process. The transmission is designed as a progressive transmission. It can be stopped at any time during the encoding process to achieve the highest image quality at the available bit rate. It was found by Xiang et al. [52], the way of coding in the proposed method is that the bit rate of each of the image blocks is determined by meta-heuristic algorithms (genetics and

gray wolf) and then unique coding is done for each block through the implementation of the SPIHT coder and finally the output bit string for each block is generated. As we know, in compression methods, there is always some overhead, which is insignificant, because the number of pixels in the image is large. The compressor unit performs the functions of the reconstruction unit, as it is aware of the quality of the final image in advance. After reducing the dimensions of the input images using wavelet transformation, the approximate sub-image obtained at the end of the compression path is used as an independent face image in the next step. As a result, it is never necessary to encode in the SPIHT method the details of the suggested dimensionality reduction method. A block of the low-resolution image is received as input at a time. This input image, as we know, is the result of reducing the dimensions of the original image using the proposed method based on the wavelet transform. In fact, it is the last subband of the wavelet decomposition approximation. After the dimension reduction process and the search for budgeting for key blocks in the face image have been completed, the low-frequency coefficients of the image are sorted and coded using the SPIHT method. The approximate sub-image can be obtained from the photo wavelet transform method after obtaining the output bit string and the data values of the reduction levels and image dimensions in the image reconstruction section.

3. 6. Accuracy Measurement DCT conversion is one of the most popular compression methods (including JPEG), but it is not suitable due to problems such as hardware complexity and computational costs. In contrast, an algorithm such as JPEG-LS¹ does not suffer from the problem of hardware complexity to a certain extent, since it uses the correlation method between pixels, but it is not efficient at improving the compression speed of images. The use of appropriate color space conversion algorithms increases the speed and quality of compressed images in this regard [53]. Researchers have studied methods such as fractal coding to increase speed, which utilizes similarity in different areas of the image [54]. Principal component analysis is a method that has proven successful in the recognition of faces [55]. PCA is used in the proposed method to extract features for recognition. The advantages of this method include its simplicity of application and use, its positive effects on large databases, and its acceptable efficiency level. Many researchers have worked to improve it [56]. A number of studies have also focused on the problem of choosing the most appropriate eigenvectors. This is with the objective of increasing and improving PCA's efficiency by removing noise eigenvectors and reducing processing time. The PCA method is therefore used to remove

¹ <https://jpeg.org/jpegls/>

correlations in the data by imaging the data in a new space [57]. Based on the explanations provided, the secondary objective of this research is to develop an identification system based on principal component analysis (PCA). For each sample, we consider one vector or array of information or features. In order to obtain an average vector, we first average the vectors of all samples. According to Equation (14), an image containing n samples and b dimensions can be displayed as a vector variable.

$$X_i = [x_{i1}, x_{i2}, \dots, x_{in}]^T \quad i = 1, 2, \dots, b \quad (14)$$

With relation (14) where the n th sample is included in the i -th band, the data is presented in the modified coordinate system with the vector variable resulting from relation (15).

$$Y_i = X_i - \left(\frac{1}{n} \sum_{k=1}^n x_{ik}\right) [1]_{n1}, \quad i = 1, 2, \dots, b \quad (15)$$

The distance between each sample and the mean vector is then calculated, resulting in a matrix. Multiplying the obtained matrix by its transpose yields the covariance matrix.

$$C(i, j) = \frac{1}{n} (Y_i Y_j^T) \quad i = 1, 2, \dots, b, \quad j = 1, 2, \dots, b \quad (16)$$

In the next step, we calculate the eigenvalues and eigenvectors of this matrix, and after calculating the eigenvalues, we sort them in descending order. Each eigenvalue has its own eigenvector, and the larger the value of an eigenvalue, the greater the differentiation in the data in that dimension. The proposed method uses 70% of the low-resolution facial images of each individual in the database as training images. Test images were evaluated on the remaining 30% of images (with low resolution). For the first experiment, the system is trained using seven random images of each person in the FEI database, which contains 280 images. For the purpose of this test, the remaining three images of each person in the database, which contains 120 images, are considered. In the first step of the proposed method, the size of the feature vector is determined by the number of reduction levels. In the second test, 300 images from the CIE database were examined. For this step, 210 images are used for training and 90 images for testing. In order to measure the accuracy of the recognition of the set of images, PCA transformation has been used to extract the features of the images. In a situation where we are trying to increase or maintain the accuracy of image recognition in comparison to conventional methods, the performance of the recognition system is acceptable. The process of creating the database for the proposed method is shown in Figure 5.

Therefore, meta-heuristic algorithms (genetics/gray wolf) will be used to achieve the research's sub-goal, which is to detect and identify the image recognition algorithm with the highest accuracy value based on PCA

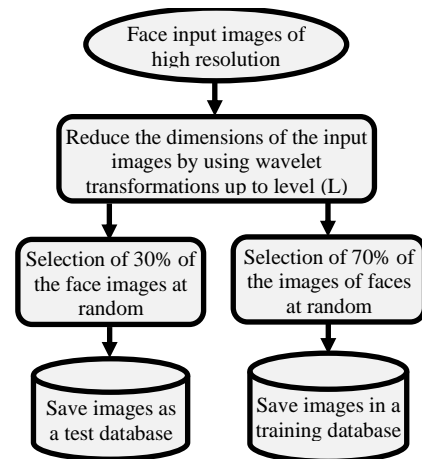


Figure 5. Training and test phases for creating the proposed method's database

transformation. The optimal vector proposed by the algorithm (genetics/gray wolf) for allocating the bit budget of each image block is determined when the efficiency and accuracy of the recognition of the test images are at their peak. Face recognition is based on the following recognition accuracy criteria (17):

$$Accuracy = \frac{\sum true\ positive + \sum true\ negative}{\sum total\ population} \quad (17)$$

The term (correct positive) refers to the number of images that belong to the positive category and have been properly classified. This refers to the number of images that are classified as negative by the classifier and have been correctly identified as such. It is significant to note that the denominator of the above fraction is the total number of images that have been verified.

4. TEST RESULTS

For a better comparison, the test results were reviewed and evaluated in two databases, CIE and FEI. Researchers compared uncompressed random test images and compressed images using SPIHT and JPEG coding methods as well as meta-heuristic genetics and gray wolf methods. The simulations have been performed in MATLAB R2016. The conditions have been selected in such a way that the performance of the algorithms in each of the different situations has been evaluated and compared, including the change in the bit rate, the change in the division of blocks, and the change in the reduction levels in the two databases. In the simulations, an Intel Core (TM) i5 processor with 2.4 GHz processing speed and 6 GHz RAM memory is used.

All three tests are conducted using FEI database images, the number of reduction levels is 4, 3, and 2, and the dimensions of the images after reduction are 48x64, 96x128, and 192x256, respectively. A second step

involves examining the images from the CIE database, and determining that the reduction levels are 5, 4, and 3, and this subsequently leads to the same size images as those in the first step. The total number of blocks in each step is 12. For all three tests, the dimensions of dividing the blocks into the two stages are 16, 32, and 64, respectively. The bit value assigned to each block must be an integer, and the maximum value of the bit string (BSL) will be rounded to the lower integer value in each test. As a result of the changes in the dimensions of the block division, the compression ratios for each test will differ slightly, and the assumptions and parameters of both tests (two databases) summarized in Table 2. Tables 3, 4 and 5 present simulation results for the set of FEI database images based on the assumptions in Table 2. We report the average values for PSNR, SSIM, and CR ratio in uncompressed and compressed conditions using SPIHT, JPEG coding methods, and genetic algorithms and gray wolf algorithms. In the context of image compression and recognition, it is critical to note that recognition efficiency does not necessarily decrease or remain constant at all bit rates; in other words, it may be slightly increased in some cases. As an example, in the third experiment, where the block division is 64, for a bit rate of 0.5, there is a relative increase in recognition efficiency. are illustrated below images. Figure 6 illustrates; the accuracy of image recognition in the division of 16, 32, and 64 blocks for bit rates ranging from 0.2 to 1 in the FEI database.

TABLE 2. assumes the parameters of the FEI and CIE databases

Database	The number of images in the database		The reduction levels (L)	Image dimensions after reduction	Size of the block	The block number
	Training	Test				
	FEI	280				
			3	128×96	32×32	
			2	256×192	64×64	
			5	64×48	16×16	
			4	128×96	32×32	
CIE	210	90	3	256×192	64×64	

TABLE 3. Recognition percentages for different bit rates in the FEI database

Bit Per Pixel	Conpration Ratio	Size of the block	Performance averages in recognition				
			Original	SPIHT	JPEG	GA	GWO
0.2	40.0261	16×16	99.16	97.5	97.83	97.5	97.5
	40.0098	32×32	97.5	98.33	98.96	99.16	98.33
	40.0016	64×64	99.16	99.16	98.33	99.16	99.16
0.3	26.684	16×16	97.5	97.5	97.5	97.5	97.5

0.4	26.6696	32×32	100	99.16	97.5	99.16	100
	26.6678	64×64	98.33	98.33	98.33	99.16	99.16
	20.013	16×16	100	98.33	97.5	99.16	99.16
0.5	20.0008	32×32	98.33	97.5	97.5	100	98.16
	20.0008	64×64	99.16	98.33	97.3	99.16	99.16
	16	16×16	98.33	97.5	97.5	98.33	98.33
0.6	16	32×32	99.16	99.16	97.5	99.16	99.16
	16	64×64	99.16	99.16	98.33	100	100
	13.3348	16×16	99.16	98.33	97.5	99.16	99.16
0.7	13.3348	32×32	100	100	97.5	100	100
	13.3334	64×64	97.5	97.5	98.33	98.33	98.33
	11.4307	16×16	98.33	98.33	96.66	99.16	99.16
0.8	11.4294	32×32	99.16	99.16	97.5	100	100
	11.4287	64×64	96.66	96.66	98.33	98.33	99.16
	10.0024	16×16	98.33	98.33	97.5	99.16	99.16
0.9	10.0004	32×32	99.16	98.33	97.5	99.16	99.16
	10.0002	64×64	98.33	98.33	97.5	98.33	99.16
	8.8915	16×16	97.5	97.5	97.5	99.16	100
1	8.889	32×32	99.16	99.16	96.66	100	99.16
	8.889	64×64	98.33	98.33	97.5	98.33	98.33
	8	16×16	97.5	98.33	97.5	98.33	99.16
1	8	32×32	99.16	98.33	97.5	99.16	99.16
	8	64×64	97.5	98.33	97.5	98.33	100

TABLE 4. Average PSNR values for different bit rates in the FEI database

Bit Per Pixel	Conpration Ratio	Size of the block	Performance of average PSNR (dB)				
			Original	SPIHT	JPEG	GA	GWO
0.2	40.0261	16×16	22.92	17.92	17.09	15.17	16.09
	40.0098	32×32	22.13	21.03	17.33	18.70	20.20
	40.0016	64×64	21.62	21.49	17.44	22.03	28.75
0.3	26.684	16×16	22.69	19.37	17.24	15.50	16.64
	26.6696	32×32	21.99	21.38	16.95	22.68	25.29
	26.6678	64×64	21.58	21.53	17.52	24.68	28.94
0.4	20.013	16×16	23.04	20.53	17.18	19.71	21.69
	20.0008	32×32	21.93	21.56	17.16	23.61	21.77
	20.0008	64×64	21.84	21.81	17.41	28.30	27.60
0.5	16	16×16	22.35	20.85	17.03	18.45	20.83
	16	32×32	22.44	22.22	17.33	24.15	23.26
	16	64×64	21.76	21.73	17.21	28.42	27.57
0.6	13.3348	16×16	22.85	21.32	17.09	22.97	23.05
	13.3948	32×32	22.10	21.92	17.56	27.75	30.02
	13.3334	64×64	21.67	21.67	17.43	24.84	28.18
0.7	11.4307	16×16	22.65	21.64	17.23	22.93	21.78

	11.4294	32×32	21.79	21.70	17.17	25.97	23.22
	11.4287	64×64	21.53	21.53	17.53	27.59	20.12
	10.0024	16×16	23.00	22.15	17.05	20.95	25.88
0.8	10.0004	32×32	22.04	21.97	17.03	26.52	25.67
	10.0002	64×64	21.73	21.71	17.37	27.58	25.19
	8.8915	16×16	22.51	21.92	17.23	21.88	23.14
0.9	8.889	32×32	22.74	22.65	17.29	23.88	29.66
	8.889	64×64	21.86	21.86	17.63	32.51	34.92
	8	16×16	22.60	22.16	16.97	20.71	20.79
1	8	32×32	22.10	22.03	17.10	24.34	26.43
	8	64×64	21.32	21.33	17.30	32.49	25.27

TABLE 5. Average SSIM values for different bit rates in the FEI database

Bit Per Pixel	Conpration Ratio	Size of the block	Performance of the SSIM on average				
			Original	SPIHT	JPEG	GA	GWO
	40.0261	16×16	0.787	0.428	0.581	0.529	0.447
0.2	40.0098	32×32	0.766	0.602	0.625	0.648	0.684
	40.0016	64×64	0.781	0.720	0.690	0.782	0.828
	26.684	16×16	0.774	0.489	0.582	0.498	0.529
0.3	26.6696	32×32	0.758	0.635	0.624	0.721	0.741
	26.6678	64×64	0.781	0.742	0.692	0.817	0.839
	20.013	16×16	0.784	0.542	0.587	0.633	0.649
0.4	20.0008	32×32	0.762	0.666	0.625	0.779	0.712
	20.0008	64×64	0.786	0.762	0.690	0.840	0.824
	16	16×16	0.770	0.580	0.576	0.594	0.669
0.5	16	32×32	0.774	0.701	0.631	0.787	0.748
	16	64×64	0.786	0.770	0.694	0.842	0.871
	13.3348	16×16	0.780	0.607	0.583	0.719	0.719
0.6	13.3348	32×32	0.769	0.709	0.632	0.819	0.852
	13.3334	64×64	0.786	0.777	0.691	0.861	0.865
	11.4307	16×16	0.769	0.629	0.585	0.736	0.721
0.7	11.4294	32×32	0.760	0.715	0.627	0.795	0.750
	11.4287	64×64	0.782	0.777	0.693	0.867	0.831
	10.0024	16×16	0.781	0.663	0.583	0.693	0.805
0.8	10.0004	32×32	0.764	0.729	0.625	0.798	0.812
	10.0002	64×64	0.784	0.780	0.693	0.862	0.827
	8.8915	16×16	0.776	0.676	0.580	0.750	0.751
0.9	8.889	32×32	0.780	0.751	0.630	0.816	0.861
	8.889	64×64	0.788	0.786	0.695	0.936	0.924
	8	16×16	0.774	0.689	0.577	0.724	0.682
1	8	32×32	0.768	0.745	0.629	0.786	0.881
	8	64×64	0.777	0.776	0.689	0.911	0.880

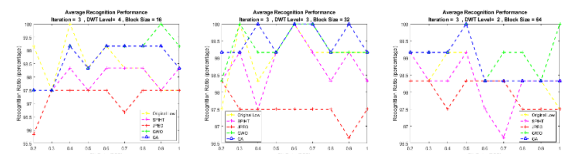


Figure 6. Accuracy of image recognition in the division of 16, 32, and 64 blocks for bit rates ranging from 0.2 to 1 in the FEI database

Figure 7 shows the average PSNR for images in 16, 32, and 64 block divisions for bit rate values between 0.2 and 1.

Figure 8 shows the average SSIM images with bit rates ranging from 0.2 to 1 in the FEI database divided into 16, 32, and 64 blocks.

Using the test image set of the FEI database as an example, the results of the image importance map calculated by dividing the 64×64 blocks (the third test from the first stage) at each of the bit rates from 0.2 to 1 are illustrated in Figure 9.

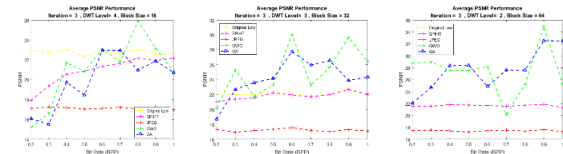


Figure 7. Average PSNR for images in 16, 32, and 64 block divisions for bit rate values between 0.2 and 1

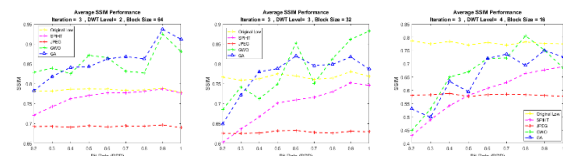


Figure 8. Average SSIM of images with bit rates ranging from 0.2 to 1 in the FEI database

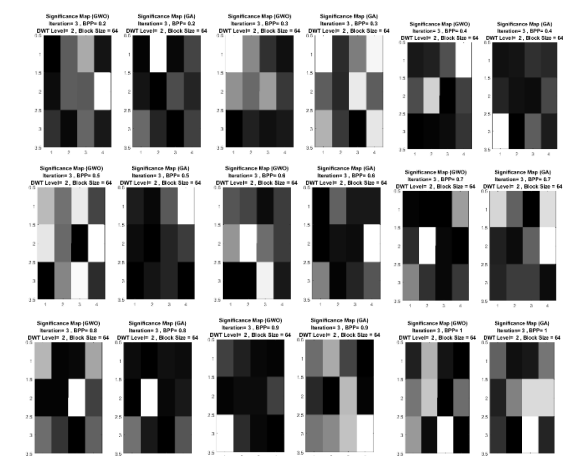


Figure 9. illustrates the importance of image compression in genetic and gray wolf methods for bit rate values ranging from 0.2 to 1 in the FEI database

Figure 10, for example, shows the amount of total processing time for genetic and gray wolf meta-heuristic algorithms with 16, 32, and 64 block allocations for bit rates ranging from 0.2 to 1.

Based on the CIE database, simulation results related to accuracy, average PSNR, and SSIM parameters are presented in Figures 11, 12, and 13.

As shown in Figure 14, the total amount of processing computing time for genetic and gray wolf meta-heuristic algorithms is calculated by dividing bit rate values from 0.5 to 1 into 16, 32, and 64 blocks.

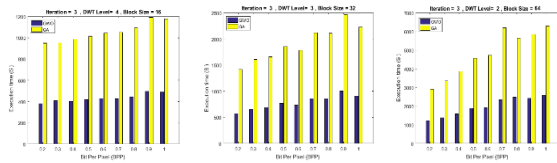


Figure 10. Comparison of execution times for genetic and gray wolf methods with block allocations of 16, 32, and 64 in the FEI database for bit rates 0.2 to 1

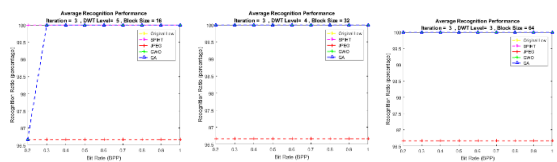


Figure 11. shows the accuracy of image recognition in the CIE database based on the division of 16, 32, and 64 blocks

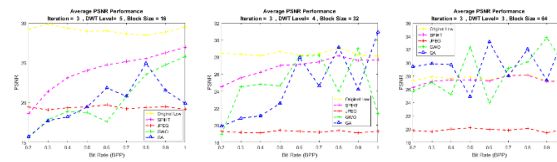


Figure 12. Average PSNR of images for bit rates ranging from 0.2 to 1 for images divided by 16, 32, and 64 blocks

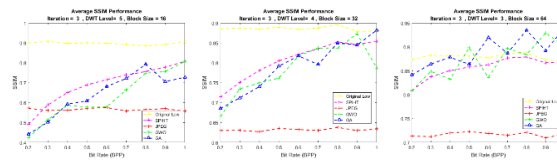


Figure 13. Average SSIM of images for bit rates between 0.2 and 1 for 16 blocks, 32 blocks, and 64 blocks

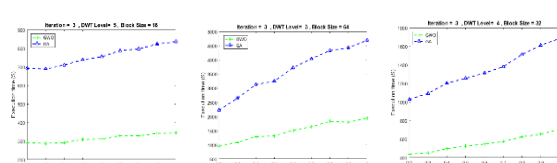


Figure 14. Comparison of execution times for genetic and gray wolf methods with 16, 32, and 64 blocks allocated for bit rates of 0.2 to 1 in CIE database

The meta-heuristic algorithm of genetics and gray wolf is used in this article to identify significant blocks and assign appropriate bits to each block. As a result, the coefficients of the image blocks have been encoded with the SPIHT method. The accuracy criterion has been evaluated to determine the accuracy of image recognition and the effectiveness of the proposed method. It is used in conjunction with learning and testing images obtained from a principal component analysis (PCA) process. Based on a comparison of the accuracy of the test images at different bit rates with JPEG methods, SPIHT will be the final method for testing the proposed method. When comparing the proposed method with the SPIHT coding curve and evaluating its recognition efficiency in accordance with the bit rate criterion, it is apparent that it can maintain significant and effective features in recognition. In Table (6), we present the percentage of recognition rate and the performance efficiency of the proposed method compared with the without compression method (Original) and the compression methods (SPIHT and JPEG).

The results shown in the graphs related to accuracy recognition (Table 6) indicate that at some bit rates, the accuracy value of face image recognition will be higher than without image compression. As stated in the abstract, we are looking for a method in which compression does not decrease the recognition rate compared to the original conditions (without compression) and even increases it.

As evidence of this claim, a bit rate of 0.7 is obtained for all three block modes of 16, 32, and 64 bits. By using meta-heuristic algorithms (genetics and gray wolf), the proposed method has significantly improved SSIM and PSNR over SPIHT and JPEG. According to the structure of the meta-heuristic algorithms that follow the search in the problem space, part of the time will be allocated for the calculations of the iterative loops until the objective function is reached. Therefore, in a new approach to reach the final goal, meta-heuristic algorithms can be used as a way to reduce the amount of time spent on computing. In the following research, the authors will focus on reducing computing time by using meta-heuristic algorithms and comparing them. On the other hand, based on this idea, future research could be done

TABLE 6. values of image recognition accuracy in meta-heuristic algorithms for blocks 16, 32 and 64 in terms of percentage

Method name	Original			SPIHT			JPEG		
Dimensions of blocks	64×64	32×32	16×16	64×64	32×32	16×16	64×64	32×32	16×16
GA	0.56	0.46	0.18	0.56	0.74	0.64	0.84	1.97	1.16
GW	0.93	0.16	0.37	0.93	0.44	0.83	1.21	1.67	1.35

on variable image segmentation based on a quad tree similar to the H.265 method. Additionally, a new approach to development and future activities can be proposed and evaluated using deep learning methods.

5. CONCLUSION

When presenting the latest image compression algorithms, it has always been a priority to eliminate coding redundancy (shortest length for fewer code words), spatial or temporal redundancy, and irrelevant information caused by the data being removed by the human eye. On the other hand, the pace of upgrading equipment and updating capabilities within existing systems is continuously increasing. Therefore, there is a need for algorithms capable of providing high quality and efficient performance in the field of image compression. Since high resolution is an essential component of increasing quality, this article proposes the use of meta-heuristic algorithms to compress images with high resolution based on dimension reduction and bit budget allocation for dividing image blocks in wavelet transformation by using a method derived from dimension reduction.

6. REFERENCES

- Lin, C.-H., Chung, K.-L. and Fang, J.-P., "Adjusted 4: 2: 2 chroma subsampling strategy for compressing mosaic videos with arbitrary rgb color filter arrays in hevc", in Signal and Information Processing Association Annual Summit and Conference (APSIPA), 2014 Asia-Pacific, IEEE., (2014), 1-7.
- Mohammed, R.B. and van Silfhout, R., "High bandwidth data and image transmission using a scalable link model with integrated real-time data compression", *e-Prime-Advances in Electrical Engineering, Electronics and Energy*, Vol. 1, (2021), 100017. <https://doi.org/10.1016/j.prime.2021.100017>
- Joshi, K., Gill, S. and Yadav, R., "A new method of image steganography using 7th bit of a pixel as indicator by introducing the successive temporary pixel in the gray scale image", *Journal of Computer Networks and Communications*, Vol. 2018, (2018). <https://doi.org/10.1155/2018/9475142>
- Chaudhary, P., Gupta, R., Singh, A., Majumder, P. and Pandey, A., "Joint image compression and encryption using a novel column-wise scanning and optimization algorithm", *Procedia Computer Science*, Vol. 167, (2020), 244-253. <https://doi.org/10.1016/j.procs.2020.03.218>
- Nadu, T., "Removing coding and inter pixel redundancy in high intensity part of image", (2019).
- Bajit, A., Nahid, M., Tamtaoui, A. and Benbrahim, M., "A psychovisual optimization of wavelet foveation-based image coding and quality assessment based on human quality criterions", *Advances in Science, Technology and Engineering Systems Journal*, Vol. 5, No. 2, (2020), 225-234. doi: 10.25046/aj050229.
- Rajabi Moshtaghi, H., Toloie Eshlaghy, A. and Motadel, M.R., "A comprehensive review on meta-heuristic algorithms and their classification with novel approach", *Journal of Applied Research on Industrial Engineering*, Vol. 8, No. 1, (2021), 63-89.
- Emara, M.E., Abdel-Kader, R.F. and Yasein, M.S., "Image compression using advanced optimization algorithms", *Port-Said Engineering Research Journal*, Vol. 21, No. 1, (2017), 95-108. doi: 10.12720/jcm.12.5.271-278.
- Jino Ramson, S., Lova Raju, K., Vishnu, S. and Anagnostopoulos, T., "Nature inspired optimization techniques for image processing—a short review", *Nature Inspired Optimization Techniques for Image Processing Applications*, Vol., No., (2019), 113-145. doi: 10.1007/978-3-319-96002-9_5.
- Omari, M. and Yaichi, S., "Image compression based on genetic algorithm optimization", in 2015 2nd World Symposium on Web Applications and Networking (WSWAN), IEEE., (2015), 1-5.
- Xu, S., Chang, C.-C. and Liu, Y., "A novel image compression technology based on vector quantisation and linear regression prediction", *Connection Science*, Vol. 33, No. 2, (2021), 219-236. <https://doi.org/10.1080/09540091.2020.1806206>
- AL-Bundi, S.S. and Abd, M.S., "A review on fractal image compression using optimization techniques", *Journal of Al-Qadisiyah for Computer Science and Mathematics*, Vol. 12, No. 1, (2020), Page 38-48. <https://doi.org/10.29304/jqcm.2020.12.1.674>
- Mirjalili, S., Mirjalili, S.M. and Lewis, A., "Grey wolf optimizer", *Advances in Engineering Software*, Vol. 69, (2014), 46-61. <https://doi.org/10.1016/j.advengsoft.2013.12.007>
- Kumar, A., Singh, S. and Kumar, A., "Grey wolf optimizer and other metaheuristic optimization techniques with image processing as their applications: A review", in IOP Conference Series: Materials Science and Engineering, IOP Publishing. Vol. 1136, (2021), 012053.
- Oloyede, M., Hancke, G., Myburgh, H. and Onumanyi, A., "A new evaluation function for face image enhancement in unconstrained environments using metaheuristic algorithms", *EURASIP Journal on Image and Video Processing*, Vol. 2019, No., (2019), 1-18. <https://doi.org/10.1186/s13640-019-0418-7>
- Cuevas, E., Trujillo, A., Navarro, M.A. and Diaz, P., "Comparison of recent metaheuristic algorithms for shape detection in images", *International Journal of Computational Intelligence Systems*, Vol. 13, No. 1, (2020), 1059-1071.
- Sheraj, M. and Chopra, A., "Data compression algorithm for audio and image using feature extraction", in 2020 4th International Conference on Computer, Communication and Signal Processing (ICCCSP), IEEE., (2020), 1-6.
- Cuevas, E., Zaldívar, D. and Perez-Cisneros, M., "Applications of evolutionary computation in image processing and pattern recognition, Springer, (2016).
- Geetha, K., Anitha, V., Elhoseny, M., Kathiresan, S., Shamsolmoali, P. and Selim, M.M., "An evolutionary lion optimization algorithm-based image compression technique for biomedical applications", *Expert Systems*, Vol. 38, No. 1, (2021), e12508. doi: 10.1111/exsy.12508.
- Bian, N., Liang, F., Fu, H. and Lei, B., "A deep image compression framework for face recognition finding the optimum structure of cnn for face recognition", (2019). <https://doi.org/10.48550/arXiv.1907.01714>
- El-Kenawy, E.-S.M., Mirjalili, S., Abdelhamid, A.A., Ibrahim, A., Khodadadi, N. and Eid, M.M., "Meta-heuristic optimization and keystroke dynamics for authentication of smartphone users", *Mathematics*, Vol. 10, No. 16, (2022), 2912. <https://doi.org/10.3390/math10162912>
- Reddy, C.V. and Siddaiah, P., "Hybrid lwt-svd watermarking optimized using metaheuristic algorithms along with encryption for medical image security", *Signal & Image Processing*, Vol. 6, No. 1, (2015), 75. doi: 10.5121/sipij.2015.6106.
- Hasan, M.K., Ahsan, M.S., Newaz, S.S. and Lee, G.M., "Human face detection techniques: A comprehensive review and future

- research directions", *Electronics*, Vol. 10, No. 19, (2021), 2354. <https://doi.org/10.3390/electronics10192354>
24. Elad, M., Goldenberg, R. and Kimmel, R., "Low bit-rate compression of facial images", *IEEE Transactions on Image Processing*, Vol. 16, No. 9, (2007), 2379-2383. doi: 10.1109/TIP.2007.903259.
 25. Soni, N., Sharma, E.K. and Kapoor, A., "Hybrid meta-heuristic algorithm based deep neural network for face recognition", *Journal of Computational Science*, Vol. 51, (2021), 101352. <https://doi.org/10.1016/j.jocs.2021.101352>
 26. Mascher-Kampfer, A., Stögner, H. and Uhl, A., "Comparison of compression algorithms' impact on fingerprint and face recognition accuracy", in *Visual Communications and Image Processing 2007*, SPIE. Vol. 6508, (2007), 350-361.
 27. Vila-Forcén, J.E., Voloshynovskiy, S., Koval, O. and Pun, T., "Facial image compression based on structured codebooks in overcomplete domain", *EURASIP Journal on Advances in Signal Processing*, Vol. 2006, (2006), 1-11. doi: 10.1155/ASP/2006/69042.
 28. Liang, Y., Lai, J.-H., Yuen, P.C., Zou, W.W. and Cai, Z., "Face hallucination with imprecise-alignment using iterative sparse representation", *Pattern Recognition*, Vol. 47, No. 10, (2014), 3327-3342. doi: 10.1016/j.patcog.2014.03.027.
 29. Subban, R., Mankame, D., Nayeem, S., Pasupathi, P. and Muthukumar, S., "Genetic algorithm based human face recognition", in *Proc. of Int. Conf. on Advances in Communication, Network, and Computing, CNC*. (2014), 417-426.
 30. Yang, Y., Liu, J., Tan, S. and Wang, H., "A multi-objective differential evolutionary algorithm for constrained multi-objective optimization problems with low feasible ratio", *Applied Soft Computing*, Vol. 80, (2019), 42-56. <https://doi.org/10.1016/j.asoc.2019.02.041>
 31. Ramadan, R.M. and Abdel-Kader, R.F., "Face recognition using particle swarm optimization-based selected features", *International Journal of Signal Processing, Image Processing and Pattern Recognition*, Vol. 2, No. 2, (2009), 51-65.
 32. Kaur, S., Agarwal, P. and Rana, R.S., "Ant colony optimization: A technique used for image processing", *International Journal of Computer Science and Technology*, Vol. 2, No. 2, (2011), 173-175.
 33. Bencherqui, A., Daoui, A., Karmouni, H., Qjidaa, H., Alfidid, M. and Sayyouri, M., "Optimal reconstruction and compression of signals and images by hahn moments and artificial bee colony (ABC) algorithm", *Multimedia Tools and Applications*, Vol. 81, No. 21, (2022), 29753-29783. <https://doi.org/10.1007/s11042-022-12978-x>
 34. Asiedu, L., Essah, B.O., Iddi, S., Doku-Amponsah, K. and Mettle, F.O., "Evaluation of the dwt-pca/svd recognition algorithm on reconstructed frontal face images", *Journal of Applied Mathematics*, Vol. 2021, (2021), 1-8. <https://doi.org/10.1155/2021/5541522>
 35. Lu, L., Hu, X., Chen, S., Sun, L. and Li, C., "Face recognition based on weighted wavelet transform and compressed sensing", in *2016 8th International Conference on Wireless Communications & Signal Processing (WCSP)*, IEEE. (2016), 1-5.
 36. Phillips, P.J., Moon, H., Rizvi, S.A. and Rauss, P.J., "The feret evaluation methodology for face-recognition algorithms", *IEEE Transactions on Pattern Analysis and Machine Intelligence*, Vol. 22, No. 10, (2000), 1090-1104.
 37. He, T. and Chen, Z., "End-to-end facial image compression with integrated semantic distortion metric", in *2018 IEEE Visual Communications and Image Processing (VCIP)*, IEEE. (2018), 1-4.
 38. Shahbakhsh, M.B. and Hassanpour, H., "Empowering face recognition methods using a gan-based single image super-resolution network", *International Journal of Engineering, Transactions A: Basics*, Vol. 35, No. 10, (2022), 1858-1866. doi: 10.5829/ije.2022.35.10a.05.
 39. Selimović, A., Meden, B., Peer, P. and Hladnik, A., "Analysis of content-aware image compression with vgg16", in *2018 IEEE International Work Conference on Bioinspired Intelligence (IWOB)*, IEEE., (2018), 1-7.
 40. Biswas, S., Sil, J. and Maity, S.P., "On prediction error compressive sensing image reconstruction for face recognition", *Computers & Electrical Engineering*, Vol. 70, (2018), 722-735. doi: 10.1007/s11042-017-5007-0.
 41. Asghari Beirami, B. and Mokhtarzade, M., "Ensemble of log-euclidean kernel svm based on covariance descriptors of multiscale gabor features for face recognition", *International Journal of Engineering, Transactions B: Applications*, Vol. 35, No. 11, (2022), 2065-2071. doi: 10.5829/ije.2022.35.11b.01.
 42. AL-Khafaji, G.K., Rasheed, M., Siddeq, M. and Rodrigues, M., "Adaptive polynomial coding of multi-base hybrid compression", *International Journal of Engineering, Transactions B: Applications*, Vol. 36, No. 2, (2023), 236-252. doi: 10.5829/ije.2023.36.02b.05.
 43. Qiuyu, Z. and Suozhong, W., "Color personal id photo compression based on object segmentation", in *PACRIM. 2005 IEEE Pacific Rim Conference on Communications, Computers and Signal Processing*, 2005., IEEE., (2005), 566-569.
 44. Bala, J., Huang, J., Vafaie, H., DeJong, K. and Wechsler, H., "Hybrid learning using genetic algorithms and decision trees for pattern classification", in *IJCAI (1)*, (1995), 719-724.
 45. Sun, Y. and Yin, L., "A genetic algorithm based feature selection approach for 3d face recognition", in *The Biometric Consortium Conference, (Hyatt Regency Crystal City, Arlington, Virginia USA)*, Citeseer., (2005).
 46. Liu, C. and Wechsler, H., "Evolutionary pursuit and its application to face recognition", *IEEE Transactions on Pattern Analysis and Machine Intelligence*, Vol. 22, No. 6, (2000), 570-582.
 47. Kahu, S.Y. and Bhurchandi, K.M., "Jpeg-based variable block-size image compression using cie la* b* color space", *KSII Transactions on Internet and Information Systems (TIIS)*, Vol. 12, No. 10, (2018), 5056-5078. doi: 10.3837/tiis.2018.10.023.
 48. Pantanowitz, L., Liu, C., Huang, Y., Guo, H. and Ronde, G.K., "Impact of altering various image parameters on human epidermal growth factor receptor 2 image analysis data quality", *Journal of Pathology Informatics*, Vol. 8, No. 1, (2017), 39. doi: 10.4103/jpi.jpi_46_17.
 49. Giuliani, D., "Metaheuristic algorithms applied to color image segmentation on hsv space", *Journal of Imaging*, Vol. 8, No. 1, (2022), 6. doi: 10.3390/jimaging8010006.
 50. Mobahi, H., Rao, S.R., Yang, A.Y., Sastry, S.S. and Ma, Y., "Segmentation of natural images by texture and boundary compression", *International Journal of Computer Vision*, Vol. 95, No. 1, (2011), 86-98. doi: <https://doi.org/10.48550/arXiv.1006.3679>
 51. Jin, Y. and Lee, H.-J., "A block-based pass-parallel spihit algorithm", *IEEE Transactions on Circuits and Systems for Video Technology*, Vol. 22, No. 7, (2012), 1064-1075. <https://doi.org/10.1109/TCSVT.2012.2189793>
 52. Xiang, T., Qu, J. and Xiao, D., "Joint spihit compression and selective encryption", *Applied Soft Computing*, Vol. 21, (2014), 159-170. doi: 10.1016/j.asoc.2014.03.009.
 53. Kumar, M., Powduri, P. and Reddy, A., "An rgb image encryption using diffusion process associated with chaotic map", *Journal of*

- Information Security and Applications*, Vol. 21, (2015), 20-30. doi: 10.1016/j.jisa.2014.11.003.
54. Tang, Z., Wu, X., Fu, B., Chen, W. and Feng, H., "Fast face recognition based on fractal theory", *Applied Mathematics and Computation*, Vol. 321, (2018), 721-730. <https://doi.org/10.1016/j.amc.2017.11.01>
55. Satone, M. and Kharate, G., "Feature selection using genetic algorithm for face recognition based on pca, wavelet and svm", *International Journal on Electrical Engineering and Informatics*, Vol. 6, No. 1, (2014), 39.
56. Poon, B., Ashraful Amin, M. and Yan, H., "Performance evaluation and comparison of pca based human face recognition methods for distorted images", *International Journal of Machine Learning and Cybernetics*, Vol. 2, (2011), 245-259. doi: 10.1007/s13042-011-0023-2.
57. Timotius, I.K., Setyawan, I. and Febrianto, A.A., "Face recognition between two person using kernel principal component analysis and support vector machines", *International Journal on Electrical Engineering and Informatics*, Vol. 2, No. 1, (2010), 55-63. doi: 10.15676/IJEEL.2010.2.1.5.

Persian Abstract

چکیده

فشرده‌سازی نقش مهمی در نظارت، کنترل و امنیت پردازش تصویر دارد. وضوح مکانی یکی از موثرترین عوامل در بهبود کیفیت تصویر است، اما میزان حافظه ذخیره سازی مورد نیاز را افزایش می دهد. این مقاله بر اساس الگوریتم‌های فراابتکاری، یک مدل فشرده‌سازی برای تصاویر چهره با تقسیم بلوک و تخصیص بیت متغیر ارائه می کند. تبدیل موجک برای کاهش ابعاد تصاویر چهره با وضوح فضایی بالا استفاده می شود. به منظور شناسایی مناطق مهم و مشابه ماکروبلوک های یکسان، از الگوریتم های ژنتیک و گرگ های خاکستری استفاده می شود. یک تخصیص نرخ بیت برای هر بلوک برای دستیابی به بهترین دقت تشخیص، میانگین PSNR و SSIM محاسبه می شود. پایگاه های اطلاعاتی CIE و FEI به عنوان مطالعات موردی استفاده شده اند. روش پیشنهادی با دقت تشخیص تصویر در شرایط فشرده نشده و با استفاده از روش های رایج کدگذاری JPEG و SPIHT آزمایش و مقایسه شده است. دقت تشخیص از ۰/۱۸ درصد برای بلوک های ۱۶×۱۶ به ۱/۹۷ درصد برای بلوک های ۳۲×۳۲ افزایش یافته است. علاوه بر این، الگوریتم گرگ خاکستری در رسیدن به پاسخ بهینه بسیار سریعتر از الگوریتم ژنتیک است. بسته به نوع کاربرد مشکل، الگوریتم ژنتیک یا گرگ خاکستری ممکن است برای دستیابی به حداکثر میانگین PSNR یا SSIM ترجیح داده شود. ماکزیمم متوسط PSNR برای الگوریتم گرگ خاکستری برابر ۳۴/۹۲ و ماکزیمم متوسط SSIM برای الگوریتم ژنتیک برابر ۰/۹۳۶ در نرخ بیت ۰/۹ بدست آمده است. نتایج شبیه سازی نشان می دهد که الگوریتم های مذکور با تثبیت یا افزایش دقت تشخیص، PSNR و SSIM را افزایش می دهند.



Graphene Based Membrane Modified Silica Nanoparticles for Seawater Desalination and Wastewater Treatment: Salt Rejection and Dyes

N. Munasir^{*a}, S. R. Lutfiana^a, F. Nuhaa^b; S. Evi^a, R. Lydia^a, S. S. Ezaa^c, T. Ahmad^d

^a Department of Physics, Faculty of Mathematics and Sciences, Universitas Negeri Surabaya (UNESA), Indonesia

^b Department of Chemistry, FSAD, Institut Teknologi Sepuluh Nopember Surabaya (ITS), Indonesia

^c Department of Physics, Universitas Teknologi Malaysia (UTM), Malaysia

^d Department of Physics, Universitas Negeri Malang (UM), Indonesia

PAPER INFO

Paper history:

Received 05 December 2022

Received in revised form 27 December 2022

Accepted 14 January 2023

Keywords:

Graphen Oxide

Polysulfones Membrane

Nanoparticle Silica

Desalination

Filtration

ABSTRACT

The clean water crisis in Indonesia is increasing every year, and waste from the textile industry sector can also add to this problem. There are various water treatment processes to deal with the clean water crisis, one of which is the desalination process using graphene oxide. With the addition of hydrophilic nanoparticles, graphene oxide (GO) membranes can increase roughness and have good mechanical strength. SiO₂ nanoparticles also have a high specific surface to absorb water or are hydrophilic. This study aims to determine the ability of the GO-SiO₂/Psf membrane to reject salt (NaCl solution) and filtering of methylene blue solutions. Membrane prepared by variations of Tetraethyl orthosilicate (TEOS) 0.6; 0.8; 1.0; and 1.2 ml for GO/SiO₂ composite synthesis. The results showed that the GO-SiO₂/Psf membrane could absorb methylene blue solution. The most optimum absorption value occurred at a TEOS concentration of 0.8 ml and had the most effective salt rejection value for NaCl solution equal to 67.22%.

doi: 10.5829/ije.2023.36.04a.09

NOMENCLATURE

C_f	The salt concentrations in feed	A	Area (m ²)
C_p	The salt concentrations in permeate	SR	Salt-rejection (%)
J_w	The permeate water flux (L m ⁻² h ⁻¹)	F	Flux flow
V	Volume (m ³)	A	The water permeability coefficient (L m ⁻² h ⁻¹ bar ⁻¹)
$TEOS$	Tetraethyl orthosilicate, Si(OH) ₄	Psf	Polysulfones , performance thermoplastics

1. INTRODUCTION

Indonesia is the largest archipelagic country in the world with a sea area of 5.8 million km² and only 2.01 million km² of land area. By having an existing sea area, Indonesia has great potential to be able to utilize and treat sea water as an alternative to meet the needs of clean water. The average total demand for clean water (for the household, industrial and agricultural sectors) in Java from 1991-2020 is 79.41 billion m³ and is predicted to increase to 86.65 billion m³ from 2021-2050. There is an increase of 9.12% for the clean water demand. Based on the results of calculating water availability using the

CSIRO (*Commonwealth Scientific and Industrial Research Organization*) model based on rainfall and air temperature, from 1991-2020, the Java Island region had an average water availability of 620.19 billion m³. Furthermore, it is estimated that in 2021-2050 the average availability of water will decrease to 544.51 billion m³, or decreased by 12.20% (or 75.68 billion m³), so the estimated economic value due to water loss in this range will increase by IDR 3.85 trillion.

The scarcity of clean water is caused by several factors, including the amount of water demand that continues to increase and exceeds its supply capacity, as well as the result of irresponsible human activities [1, 2].

*Corresponding Author Institutional Email:
munasir_physics@unesa.ac.id (N. Munasir)

The scarcity of clean water also has an impact on the lower middle-class community because they have to provide funds to meet the needs of clean water. Global water scarcity is driven by water quantity and water quality issues, and measures expansion in clean water technologies (i.e. desalination and reuse of treated wastewater) “to reduce the number of people suffering from water scarcity” as urgently needed by the United Nations Sustainable Development Goal (SDGs 6.0) [3].

Meanwhile, the textile industry sector has increased every year. The textile industry can produce approximately 700 tons of dyes per year globally [4]. Methylene blue is one of the dyes used in the textile industry as a basic ingredient in production. Methylene blue is a heterocyclic aromatic compound that is often used in the textile, silk, and wool industries [5]. This can lead to the release of dye waste that endangers the surrounding environment and can damage aquatic organisms [6]. Based on data from the World Resources Institute (WRI), Indonesia is ranked 51st with a high-risk level of clean water crisis (high 40–80% possibility). To deal with the scarcity of clean water, there are various kinds of water treatment processes, one of which is the desalination process.

Desalination is a water purification technique by separating the levels of substances from water [7, 8] by reducing ions to the required level according to human needs [9]. The desalination process can be carried out using graphene oxide. Graphene oxide offers an unusually high surface area, mechanical durability, atomic thickness, nano-sized pores and reactivity to polar and non-polar water pollutants. These characteristics provide high selectivity and water permeability, and thus provide excellent water purification efficiency. It also has the ability to adsorb and photocatalyzed water pollutants, so it has great potential for filtration materials, even for seawater desalination [7].

The addition of graphene oxide (GO) to the composite can affect the magnetization value so that it has super paramagnetic properties and can be used to absorb methylene blue [10, 11]. The GO membranes contain groups such as epoxide, carboxyl, and hydroxyl which can bind to water. Graphene oxide membranes also have good mechanical strength, so they are easy to fabricate and have the potential to be produced on an industrial scale [12-14]. However, pure GO membranes have a finely stacked structure and have limited improvement in membrane performance. Based on the Cassie-Wenzel theory, there is an effective method to overcome the weakness of GO membranes, namely the addition of hydrophilic nanoparticles to increase surface roughness [15].

SiO₂ nanoparticles have properties that can carry a large number of hydroxyl groups, and the concentration of hydroxyl groups is directly proportional to the specific surface area of the amorphous silica. Also, have a high

specific surface so that they can absorb water or are hydrophilic, and on the surface of SiO₂ there are abundant siloxane groups (Si-O-Si) that can bridge oxygen atoms [16, 17]. From such characteristic, there are many advantages, such as the broad application of biomedical and biotechnological applications, agricultural applications, industrial applications, environmental applications, and water purification. In water purification, SN can reduce biological oxygen demand, perform antimicrobial strength as a filter for water-oil mixture, and filter methylene blue, commonly used in the textile and paper industry, as waste disposal from a textile factory.

There are three graphene derivatives: graphite, GO, and reduced graphene oxide (rGO). Graphite is the primary material of carbon which is amorphous and stacked and rich in carbon and oxygen. GO is the result of graphite oxidation which increases the amount of oxygen, and some Van der Waals bonds have been released. So, the thickness of the sample has been reduced. Reduced Graphene Oxide (rGO) is a graphene oxide in which the carbon atoms of graphene undergo oxidation and reduction. In the oxidation process, there are several oxygen and hydrogen atoms bonded to carbon atoms, the result of this oxidation process is called GO. While in the reduction process, some hydrogen and oxygen bonds are released from graphene oxide so that a structure almost similar to graphene is obtained.

From various previous studies, silica nanoparticles have shown great application potential in some fields, such as chemistry, biomedicine, biotechnology, agriculture, environmental improvement, and wastewater purification. With superior properties such as mesoporous structure, high surface area, adjustable pore size/diameter, morphology, biocompatibility, modifiability, anti-bacterial, as an excellent encapsulating agent for various bioactive molecules: proven safe for targeted drug delivery, and polymer hybridization ability [18].

In a study conducted by Sun et al. [16] using a GO-SiO₂ membrane as an oil-in-water separator, it was found that the incorporation of SiO₂ nanoparticles with GO can expand and increase water permeability with oil rejection (>99%) for various types of oil-in-water emulsions [15, 19, 20]. The GO/SiO₂ hybrid composite membrane has good hydrophilicity and thermal properties, able to reject high rhodamine B dye molecules (99%), high permeation and water resistance, so it is very good to be developed as a high-performance material for water treatment [21]. SiO₂-GO/Psf hybrid membrane presents the best overall properties, including water permeation rate, protein rejection and antifouling ability [22, 23]. The SiO₂-GO nanohybrid has high hydrophilicity and good dispersibility properties derived from silica nanoparticles which are densely and uniformly coated on the GO surface and serve as a space layer of GO [21, 22]. The

GO-SiO₂/Psf composite under UV irradiation during filtration greatly reduces the formation of fouling and produces a high flux recovery ratio, and is effective for filtration and remove organic pollutants [24].

Previous studies on graphene membranes have shown good performance as seawater desalination membranes [7]. Furthermore, silica nanoparticles can be applied as adsorption of dyes in water (such as methylene blue); In addition, SiO₂ nanoparticles also have good antibacterial and hydrophilic properties. In this study, substituted graphene silica nanoparticles and polysulfone polymers were fabricated into membranes using the phase inversion method. This study is expected to improve the performance of membranes in desalination and adsorption of dyes to obtain decent water quality, healthy for consumption. GO/SiO₂-Psf membrane performance in salt rejection (for desalination) and dye filtration in water (MB) will be discussed in this paper.

2. MATERIALS AND METHOD

2. 1. Materials Some of the materials used include graphite powder produced from coconut shell extract, NaNO₃ (Merck, for analysis), KMnO₄ (Merck, for analysis), H₂O, H₂O₂ (Merck, 30%), NH₄OH (Merck, 25%), distilled water, and TEOS which were all obtained from Edu Lab, H₂SO₄ (Merck, 95-97%) was obtained from Indofa-Industry, HCl (Merck, 37%) was obtained from Mallinckrodt, NMP solvent was obtained from Sigma-Aldrich, PSF (Polysulfone) was obtained from Sigma-Aldrich (average Mw ~35,000), and Methylene blue (M9140, Sigma-Aldrich).

2. 2. Synthesis Method

2. 2. 1. Synthesis of Graphene (GO) The hummer method was used, in which 5 grams of graphite powder, 2.5 grams of NaNO₃, and 120 ml of H₂SO₄ were placed in a 500 ml beaker with an ice bath and stirred for 30 minutes to form a black solution. Then, 15 grams of KMnO₄ were added slowly and stirred for 30 minutes at a controlled temperature of 20°C to form a purple solution, and then stirred again for 3 hours at room temperature to form a brown solution. Then 150 ml of H₂O was added and the temperature was held at 95°C. The mixture was stirred for 3 hours at a controlled temperature of 95°C-100°C to form a dark yellow solution [25]. Then 50 ml of H₂O₂ (30%) was added slowly, then washed with HCl (1M) and H₂O until the yellow color of the solution disappeared and the pH of the solution became neutral, then sonicated for 1 hour and filtered to produce a black gel. Furthermore, the black gel was dried at a temperature of 60°C for 6 hours and produced GO.

2. 2. 2. Synthesis of GO/SiO₂ Composite It was carried out by the TEOS hydrolysis method, where 12,5

mg of GO was mixed with 150 ml of ethanol distilled water using a ratio of 1:5 and then sonicated for 30 minutes. Then, ammonia was added until the PH of the mixture was close to 9. Then, 0.6 ml to 1.2 ml of TEOS concentration were added to the solution and stirred for 30 minutes. Then it was stirred at room temperature for 24 hours, centrifuged and washed with ethanol, then dried for 12 hours at 60°C producing a GO/SiO₂ composite [24].

2. 2. 3. Fabrication of GO/SiO₂-Psf Membrane

Using the phase inversion method, 1 gram of polysulfone was added to 5.469 ml of NMP and stirred for 3 hours. Then 0.0333 gram of GO/SiO₂ composite was added to obtain a 0.5 wt% solution and sonicated for 30 minutes to shorten the dissolution process. No air bubbles were formed in it. Then the solution was formed on a glass plate and soaked in distilled water for 24 hours. Then it was dried for 24 hours at room temperature, which finally produced a GO/SiO₂-Psf membrane [26].

2. 3. Characterizations

2. 3. 1. Characterization of GO/SiO₂ and GO/SiO₂-Psf Membrane

Phase and crystal structure analysis of nanoparticles (GO, SiO₂) and GO/SiO₂ nanocomposites used X-Ray Diffraction (PANalytical X'Pert Pro) plus Expert High Score Plus software; using monochromatic radiation CuK α (40kV/40 mA) taken at an angle of $5^{\circ} \leq 2\theta \leq 90^{\circ}$ at a rate of 0.02°/min at room temperature. Functional group analysis using infrared wave absorption test using FTIR (Shimadzu Brand, Type: IR-Prestige 21). Lattice vibration analysis in Graphene phase using Raman spectroscopy (wavelength range 4000-200 cm⁻¹), and to observe the morphology of GO/SiO₂ nanocomposite and GO/SiO₂-Psf membrane using the Scanning electron microscope/SEM test (FEI Brand, Type: Inspect-S50). UV-Visible test to analyze the adsorption of methylene blue dye in water. And the analysis of the hydrophilicity of the membrane surface with the CAA 2320 Contact Angle instrument.

2. 3. 4. Filtration of NaCl Solution

GO/SiO₂-Psf was placed in a funnel Buchner flask and a hose was connected to a vacuum pump (Rocker 300) (Figure 1). The vacuum pump was turned on, then the membrane was dripped with 10 ml of NaCl solution (as sea-water synthetic) at a pressure of 650 mmHg for all variations of the GO/SiO₂-Psf membrane. The membrane that has been passed through the NaCl solution is then weighed.

2. 3. 5. Filtration of Methylene Blue in Aqueous

The 20- ppm methylene blue solution was passed through a 12.25 cm² GO-SiO₂/PSF membrane placed in a Buchner flask funnel and connected to a vacuum pump (Rocker 300) using a tube (Figure1). The vacuum pump

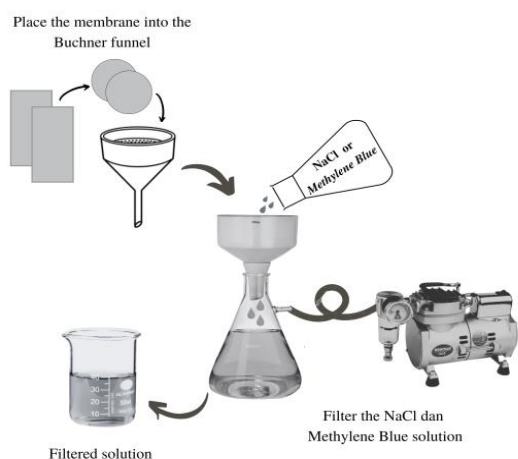


Figure 1. Filtration test with GO/SiO₂-Psf

was turned on, then the membrane was dripped with 10 ml of methylene blue solution at a pressure of 650 mmHg for all variations of the GO-SiO₂/PSF membrane. The results of the filtered methylene blue solution will be subjected to a UV-Visible test to determine the absorbance [27]. The results of the filtered methylene blue solution will be tested by UV-Vis (Shimadzu 1800) with a wavelength of 200-600 nm, to determine the absorption.

Methylene blue (C₁₆H₁₈N₃SCl) is one of the most commonly used dyes for dyeing wool, cotton and silk. Since sewage or water containing dyes can cause serious environmental problems and the availability of healthy water for consumption, it is necessary to treat these wastes before being discharged into the environment [28].

2. 3. 6. Salt-Rejection Test A salt-rejection test was carried out to determine the efficiency of the membrane in filtering NaCl solution. Salt-rejection (SR) can be obtained by the following formula [9]:

$$\text{Salt-rejection} = \frac{C_f - C_p}{C_f} \times 100 \quad (1)$$

where, C_f is the mean salt concentration in feed stream, and C_p is the salt concentration in the permeate.

2. 3. 5. Flow-Flux Test The membrane flux test was carried out to measure the optimization parameters of the membrane. The *filtrate flow flux* (J) can be obtained by the formula [9]:

$$J = \frac{V}{At} \quad (2)$$

where A is membrane area (m²), V is the volume of filtrate generated (liter), and t is process time (hours).

3. RESULT AND DISCUSSION

3. 1. X-Ray Diffraction of Composite Diffraction analysis of Graphene (GO) material and GO/SiO₂ composite is presented in Figure 2. The peak at $2\theta = 10.21^\circ$ is associated with the (002) GO plane in the GO/SiO₂ composite, but this peak does not appear. It is associated with weak diffraction, and the presence of graphite oxide heaps, in which SiO₂ is coated with a GO sheet, causes GO diffraction to appear [20]. The similarity of the diffraction peaks for GO and the GO/SiO₂ composite is indicated at positions $2\theta = 21.8^\circ$ and 26.2° . And the presence of a widened peak at $2\theta = 23.31^\circ$ indicates that silica is amorphous [27].

3. 2. Functional Group of Composite The functional group analysis of the characteristics for GO materials and GO/SiO₂ composites is presented in Figure 3. The results of the analysis showed the presence of silanol groups and Si-O silicates and C-H carbon groups.

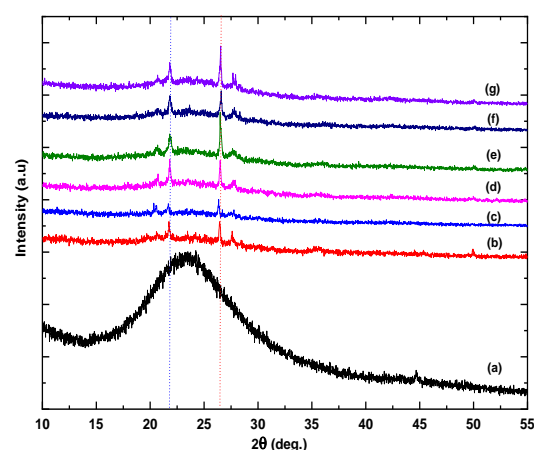


Figure 2. Pattern Diffraction of SiO₂ (a), Graphite (b), GO (c) and GO/SiO₂-Psf Composite (d-g)

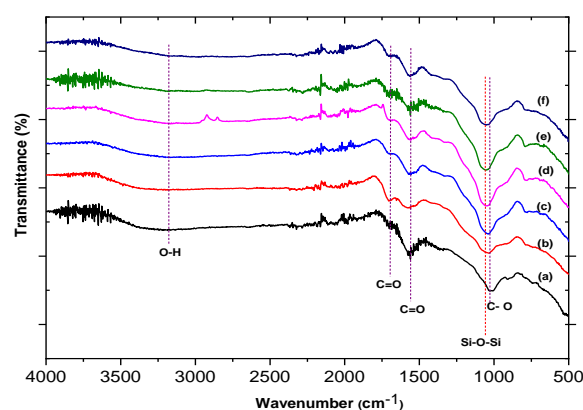


Figure 3. Functional group of GO and GO/SiO₂-Psf: (a) Graphite, (b) GO, and (c-f) composite

These functional groups are a representation of the composite material [11, 29]. The GO/SiO₂ composite exhibits a new peak at 1100 cm⁻¹, characteristic of the Si-O-Si asymmetric vibration. The presence of this absorption proves that silica is on the GO surface [20]. In addition, the peak at 1600-1735 cm⁻¹ is associated with the C=O vibration of the carboxylate group. The decreasing C=O absorption peak in the composite was due to the interaction of C=O with GO to become Si-O-C indicating a bonding interaction between GO and Silica.

3. 3. Morphology of GO, GO/SiO₂ Composite and GO/SiO₂-Psf Membrane

The morphology of GO/SiO₂ composite material and GO/SiO₂-Psf membrane with NPM solvent during the membrane preparation process is presented in Figure 4. The shape of the particles varies, it appears that the particles have several (small) pores, and between the stacks of particle arrangement there are quite large voids. Particle sizes also vary, small and large, this affects the formation of voids which will later play a role in forming the density of the membrane material.

The morphology of the GO/SiO₂-Psf membrane material prepared by the phase inversion method is presented in Figure 5. It can be seen on the surface of the membrane and its cross section. On the surface of the membrane, pores of varying sizes were seen, and these were identified as water inlet channels through the membrane through the cavities formed on the inside of the membrane. The size and shape of the cavity is influenced by the type of membrane polymer (polysulfone) and the composite material embedded in the membrane. Figure 5(b) shows a cross-sectional view of the modified composite membrane with the topical asymmetrical morphology of the membrane fibers. The middle layer represents the predominant morphology with finger-like structures. This finger-like structure is

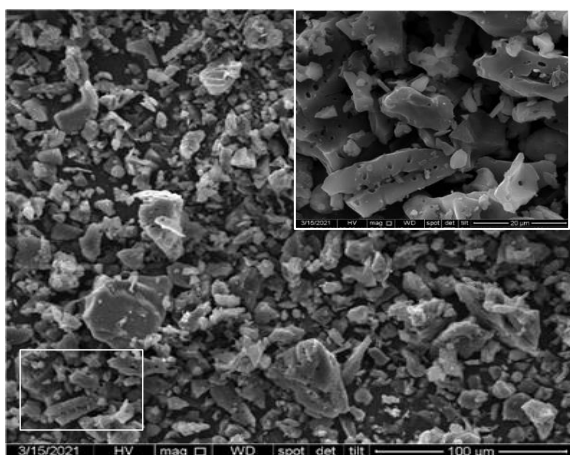


Figure 4. Morphology of GO/SiO₂ composite

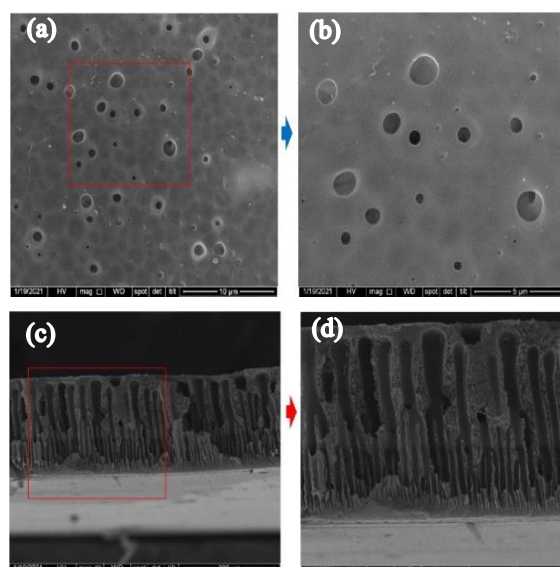


Figure 5. Morphology of GO/SiO₂-Psf membrane: (a-b) surface pores, (c-d) cross-sectional view

characteristic of an asymmetrical membrane where the cross-section of the membrane consists of a finger structure with a porous underlayer [29]. The formation of a porous surface on GO-SiO₂-Psf is caused by an increase in the hydrophilic nature of the solution, which will accelerate the rate of solvent exchange [29, 30]. The addition of GO into the membrane causes a larger cavity. In theory, the more macro-voids appear, the greater the membrane's permeability [29].

3. 4. Hydrophobicity of GO/SiO₂-Psf Membrane

The hydrophilic nature of the membrane has an essential role in filtration performance. In principle, the hydrophilicity of the membrane can be determined by the water contact angle.

The contact angle of GO/SiO₂-Psf polysulfone membrane with NMP solvent is presented as follows, for the weight percent of GO/SiO₂ composite (for SiO₂, Wt% ≈ 0.5%) with the percentage of composite material varied: 0.6; 0.8; 1.0; and 1.2%. Figure 5 and Table 1 show that the angle is smaller than 90° (hydrophobic): each membrane sample shows an average contact angle of: 75.41°; 70.16°; 76.78°; and 74.25°. The lower the contact angle, the higher the membrane hydrophilicity [30, 31]. The greater contact angle value is caused by the surface tension between the membrane and the water. On the other hand, for the SiO₂-Psf membrane contact angle (without GO) the contact angle is 71.13°, approximately the same as the GO/SiO₂-Psf membrane. This indicates that the membrane is hydrophilic or slightly water-loving (contact angle (θ) (0° ≤ θ ≤ 90°) [32, 33]. Furthermore, a small contact angle generally results in better hydrophilicity, increased water flux, and resistance to

TABLE 1. Contact Angle of GO/SiO₂-Psf (0.5%) Membrane with DMAC and NMP Solvents

PSF-0,5% GO/SiO ₂	Contact Angle (degrees) with DMAC solvent			Contact Angle (degrees) with NMP solvent		
	Right	Left	Average	Right	Left	Average
0.60 ml TEOS	76.13	81.02	78.58	74.39	76.44	75.41
0.80 ml TEOS	61.78	60.36	61.07	69.71	70.61	70.16
1.00 ml TEOS	82.71	82.53	82.62	72.65	80.90	76.78
1.0 ml TEOS	70.24	70.86	70.55	74.79	73.72	74.25
0.5% SiO ₂ -PSF	69.91	72.44	71.18	70.43	71.84	71.13

Impurities [34]. Thus, the experimental results obtained in this study are in accordance with the literature [35].

3. 5. Anti-Bacterial of GO/SiO₂ Composite The disc diffusion test was carried out to determine the inhibitory power of the compound on bacterial growth. Bacterial suspension (\varnothing 600 nm 0.1) was rubbed on the surface of Muller Hinton Agar (MHA) media on a Petri dish using a sterile cotton swab. A paper disk containing 20 l of the test compound was placed on the surface of the MHA. Incubation was carried out for 48 hours at 30°C. The clear zone formed around the disc was expressed as the inhibitory power of the compound against bacterial growth. Anti-bacterial test in this study, using 2 types of bacteria, namely *Escherichia coli* and *Staphylococcus aureus*.

The results of the antimicrobial test of GO/SiO₂ against *Escherichia coli* and *Staphylococcus aureus* with the disc diffusion method (Table 2 and Figure 6) showed that the inhibitory power of *E. coli* was stronger than *S. aureus*; The increase in GO-SiO₂ (ppm) concentration further strengthens the antibacterial activity of the *E. coli* stable. Thus, the membrane material will be confirmed to have resistance to bacterial growth (*E. coli* and *S. aureus*) [36]. Bacterial-mediated infections can cause various acute or chronic diseases and antibiotic resistance in pathogenic bacteria has become a serious health problem.

Graphene-based materials have been very well studied due to their outstanding bactericidal activity on various bacteria. The use of GO material in membrane preparation will provide biosafety advantages [22]. Likewise, the presence of SiO₂ nanoparticles, also has excellent properties as an anti-bacterial material [36, 37].

3. 6. Salt-rejection of NaCl Solution Based on Table 3, the results of the salt-rejection calculation, the Cp value is obtained from the total solid NaCl dissolved in freshwater with a salt density of 2.16 g/ml, and the Cf value is obtained from the initial concentration in the NaCl solution, which is 27.79 g/ml. The GO/SiO₂-Psf membrane with a TEOS (0.8 ml) showed the most effective results for seawater desalination because the GO/SiO₂-Psf membrane was able to filter out NaCl compounds in solution by 67.22%. The high salt-rejection value is caused by the distribution of silica grains on the membrane being very tight so that the pores are getting smaller and able to filter NaCl compounds efficiently [13]. The research of Zeng et al. [38] showed that an increase in membrane thickness due to the pore density of SiO₂, can help reduce conductive losses in bulk water and increase salt rejection ability, but energy efficiency is limited by maximum liquid flux.

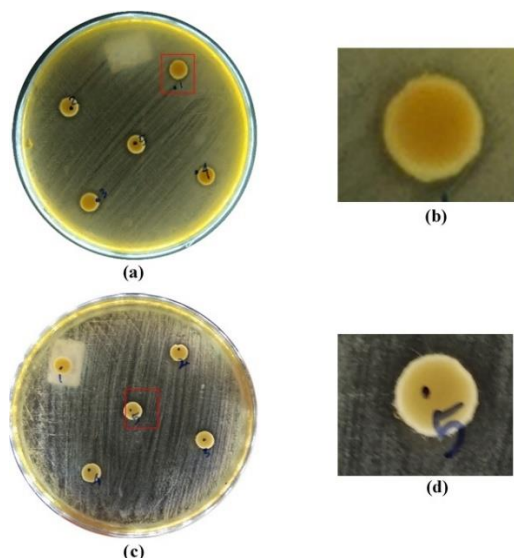
The GO/SiO₂-Psf membrane with TEOS concentrations of 1.0 ml and 1.2 ml decreased because the ratio of matrix and filler was not balance.

TABLE 2. Antimicrobial of GO-SiO₂ compounds against *E. coli* and *S. Aureus*

Bacterial	Test repeats	Inhibition zone diameter (cm) at various concentrations of GO-SiO ₂ compounds				
		100 ppm	200 ppm	300 ppm	400 ppm	500 ppm
<i>Escherichia coli</i>	1	0.83	0.94	1.01	1.08	0.97
	2	0.79	0.83	0.91	0.95	1.04
	3	0.93	0.94	0.94	0.98	1.01
<i>Staphylococcus aureus</i>	1	0.55	0.55	0.55	0.55	0.55
	2	0.55	0.55	0.55	0.55	0.55
	3	0.55	0.55	0.55	0.55	0.55

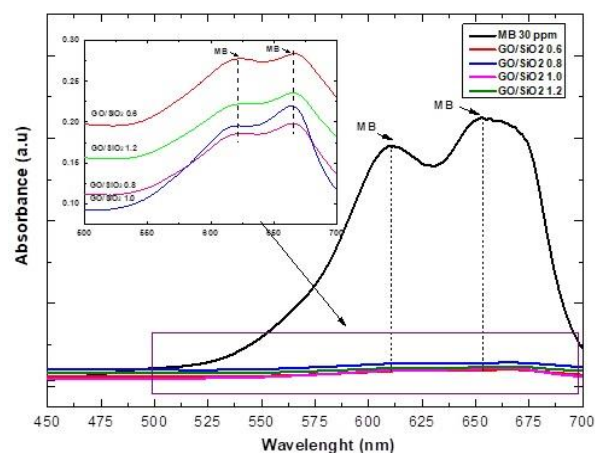
TABLE 3. The results of the calculation of flow flux

Wt% Membrane	Time (Hour)		Flux (L.m ⁻² .h ⁻¹)	
	NaCl (sea-water synthetic)	Methylene Blue	NaCl (sea-water synthetic)	Methylene Blue
GO/SiO ₂ (0.6)	0.13	0.12	79.37	81.30
GO/SiO ₂ (0.8)	0.17	0.16	47.46	51.55
GO/SiO ₂ (1.0)	0.15	0.14	53.71	59.88
GO/SiO ₂ (1.2)	0.16	0.15	48.88	54.05

**Figure 6.** Photograph of antimicrobial of GO/SiO₂: (a-b) *E. coli* and (c-d) *S. aureus*

3. 6. Filtration of Methylene Blue in Aqueous By using 20 ppm methylene blue was then carried out a filtration test. The methylene blue solution was filtered using a GO/SiO₂-Psf membrane with various concentrations of TEOS 0.6; 0.8; 1.0; and 1.2 ml. The results of the methylene blue solution filtration test (Figure 2) show that the methylene blue solution, which has been filtered using a GO/SiO₂-Psf membrane, appears to change in color before and after filtering.

The UV-Vis test was carried out using a wavelength of 200 to 600 nm, and the absorbance value of each sample was obtained (Figure 3). The methylene blue solution without passing through the GO-SiO₂/Psf membrane obtained an absorbance value of 1.206 at a wavelength of 291 nm. Figure 7 shows the results of the UV-Vis test showing the relationship between wavelength and absorbance. The UV-Vis absorption spectrum of GO/SiO₂ nanocomposite has a strong absorption in the range of 200-650 nm. In the composite for TEOS (0.6 ml), GO showed a characteristic peak at 325 nm, for TEOS (0.8 ml) it decreased starting at the

**Figure 7.** Dye absorption in water (Methylene Blue) by GO/SiO₂ nanocomposite

peak of 280 nm. For TEOS (1.0 and 1.2 ml) indicates a stable position and continues to increase. The maximum absorption peak corresponds to the π - π^* transition bond in the C=C aromatic structure and the π - π^* transition in the carbonyl group (C=O). The characteristic peak shifts to 270 nm for GO due to the presence of reduced graphene [19, 39, 40].

The Methylene blue, which was passed through the GO/SiO₂-Psf membrane in one time filtering (Figure 8(a)) decreased the absorbance value, where the most optimum absorbance occurred in the membrane with a TEOS concentration of 0.8 ml, which was 0.396 at a wavelength of 291 nm. This is to the literature conducted by Junaidi et al. [15] where the absorbance of methylene blue can be carried out using silica. This also supports the statement of Akhter et al. [18] that the higher the silica content used, the larger the surface area, so the more effective it is to absorb methylene blue. However, on membranes with TEOS concentrations of 1.0 ml and 1.2 ml, there was an increase in the absorbance value due to the unbalanced and uneven matrix and filler content during the manufacture of the membrane, which caused the membrane to be less than optimal in the filtering process.

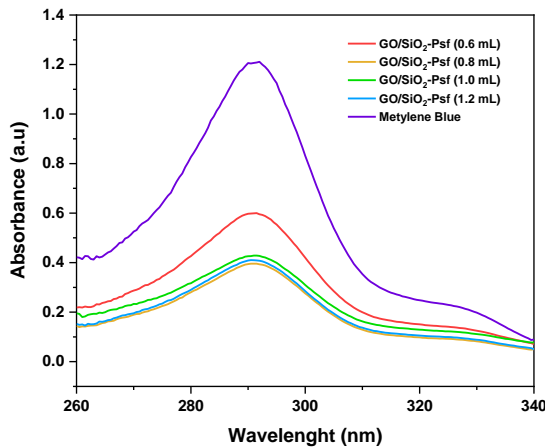


Figure 8. UV-Vis. test of Methylene Blue solution 1 times filtering

Based on Figure 8(b), the methylene blue solution that has been passed through the GO/SiO₂-Psf membrane 5 times has been filtered (Figure 9). There is a significant decrease in the absorbance value compared to the 1 filter (Table 4). The more the filtering process uses the GO/SiO₂-Psf membrane, the lower the methylene blue content in the solution. According to previous research, the content of methylene blue in the solution that has passed through the membrane decreases when the filtration test is completed [26].

Visually (Figure 10) there is a significant color change, and it is relatively clearer when the color change is by the results of the UV-Vis test that has been carried out. The GO/SiO₂-Psf membrane with TEOS 0.8 ml at 5 times of filtration obtained a negative absorbance value (Table 3), which indicates that the sample does not contain methylene blue analyte or that the methylene blue content contained in the solution is below the detection limit of the UV spectrometer method. So, it can be said that the addition of SiO₂ to the membrane can maximize

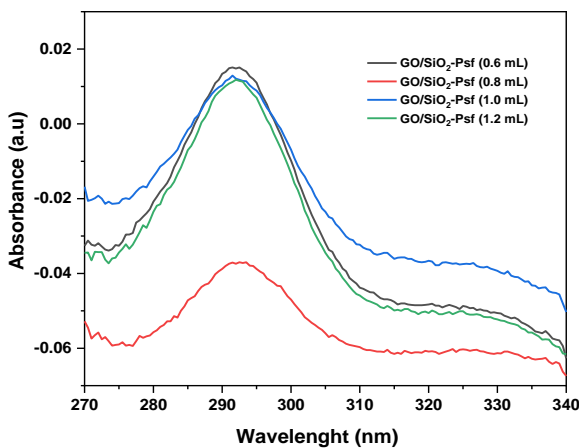


Figure 9. UV-vis test of Methylene Blue solution 5 times filtering

TABLE 4. Comparison of absorbance values of Methylene Blue solution one-times filtering and fives-times filtering

Wt% Membrane	Absorbance (a.u)	
	1 times filtering	5 times filtering
GO/SiO ₂ (0.6)	0.599	0.015
GO/SiO ₂ (0.8)	0.396	-0.037
GO/SiO ₂ (1.0)	0.428	0.012
GO/SiO ₂ (1.2)	0.409	0.011

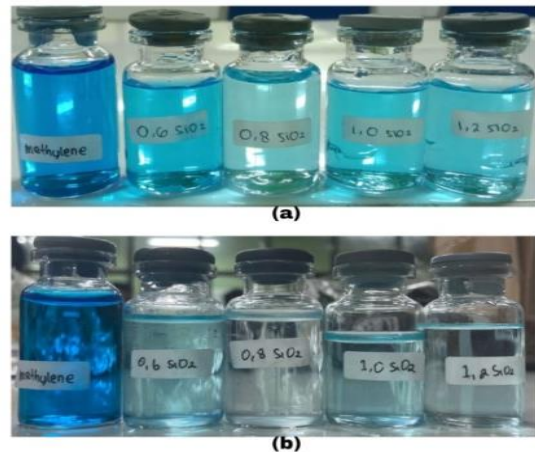


Figure 10. Methylene Blue solution filtration test results (a) 1 filter, (b) 5 filters

the membrane as an absorbent [19], and the GO-SiO₂/PSF membrane with 0.8 ml TEOS is more effective in filtering methylene blue solutions.

3. 7. Flow Flux of NaCl Solution

Based on the experimental results, the data obtained are as in Table 3. The magnitude of the flow flux value is affected for different GO-SiO₂/Psf membrane samples, the greater the composition of SiO₂ in the flow-flux membrane the greater. The value of the flow flux for NaCl solution and methylene blue water can be seen in Table 3. A low flux value indicates a low membrane permeability, so it can be said that the membrane is more optimal in filtering the solution, the resulting water quality is cleaner (from impurities), especially salt molecules. and methylene-blue molecules (natural dyes).

The filtering time of the solution greatly affects the value of the resulting water flux, where the longer the filtering time, the GO/SiO₂-Psf membrane has a tight pore size. The GO/SiO₂-Psf membrane with a TEOS concentration of 0.8 ml had the lowest flux value, namely 47.46 L.m⁻².h⁻¹ in NaCl solution and 51.55 L.m⁻².h⁻¹ in methylene blue ocean. The decrease in flux in the membrane can be caused by the closure of several pores in the membrane. The membrane flux will decrease as the filtering time increases [15-17, 41]. The GO/SiO₂-Psf

membrane with a TEOS concentration of 0.8 ml has a tight pore size so that it is more efficient for filtering NaCl and methylene blue solution

3. 8. Flow Flux of NaCl Solution and Methylene-Blue in Water Figure 11(a) is the result of one filter where the methylene blue solution is still concentrated. Figure 11(b) is the result of 5 times filtering, where the methylene blue solution is relatively clearer. Visually, it can be seen that the GO/SiO₂-Psf membrane can reduce or absorb methylene blue gradually. Based on the results of the filtration test on the methylene blue solution 5 times filtering, the GO/SiO₂-Psf membrane with a TEOS concentration of 0.8 ml looked the brightest, it was by the flux test that had been carried out.

The filtering time of the solution greatly affects the value of the resulting water flux, where the longer the filtering time, the GO/SiO₂-Psf membrane has a tight pore size. The GO/SiO₂-Psf (0.8 ml) membrane had the lowest flux value, namely 47.46 L.m⁻².h⁻¹ in NaCl solution and 51.55 L.m⁻².h⁻¹ in methylene blue ocean. The decrease in flux in the membrane can be caused by the closure of several pores in the membrane. The membrane flux will decrease as the filtering time increases [42]. The GO/SiO₂-Psf (0.8 ml) membrane has a tight pore size so that it is more efficient for filtering NaCl and methylene blue solutions.

In addition, the graphene structure that forms thin sheets of net (the order of nanometers) is very effective

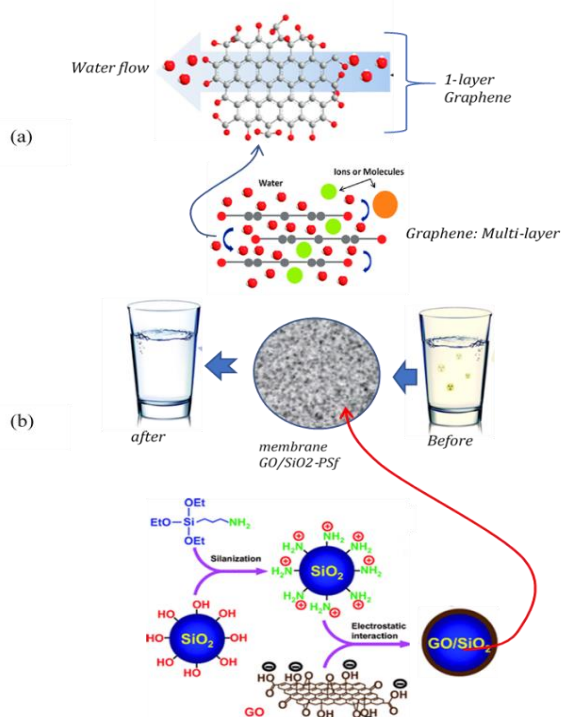


Figure 11. Filtration model of GO/SiO₂-Psf membrane: (a) water-flow in layer graphene, (b) fresh-water after filtrations

for filtering water molecules. GO modified with SiO₂ in the membrane system is believed to be more effective in the filtration and absorption of pollutants in water (Figure 11). Graphene oxide (GO) has unique characteristics that make it an excellent material for water purification applications. Chemically stable in water, provides high water permeability through its 2D nanochannels, and has excellent antifouling and antibacterial properties [43]. Graphene has unique physicochemical properties, extraordinarily high surface area, mechanical resistance, atomic thickness, nano-sized pores, and polar reactivity of polar and non-polar water, thus providing high selectivity and water permeability and thus providing excellent water purification efficiency. Graphene material has great potential as a membrane for water desalination, GO for good adsorption, and photocatalysis of water pollutants. On the other hand, SiO₂ nanoparticles have good adsorption properties due to their high surface area and porosity, so they can be promoted as membrane fillers [39, 40, 43-46].

4. CONCLUSIONS

In conclusion, we have successfully developed GO membranes by substituting SiO₂ nanoparticles in GO/SiO₂ nanocomposite formations. This membrane has flexible properties and hydrophilicity for separating dyes and rejecting salt in water. The incorporation of SiO nanoparticles between the GO layers expands the vertical interlayer nano-channels, increasing the water permeability. The suitable anti-bacterial property further strengthens this membrane's application for healthy water filtration consumption. In this study, excellent results were obtained, where the Flow Flux of NaCl Solution and Methylene-Blue in Water was 79.37% and 81.30%, respectively, with a salt-rejection rate of 67.22%. However, the results of this study can still be developed further to be applied as a membrane in ultrafiltration systems.

5. ACKNOWLEDGMENTS

The authors would like to thank the State University of Surabaya, especially the Department of Physics for allowing the use of laboratory facilities and LPPM-UNESA which provided grants through competitive research, with the contract number: B/36699/UN38.3/LK.04.00/ 2022.

6. REFERENCES

1. Taufik, M., Khairina, E., Hidayat, R., Kalalinggi, R. and Fadhurrohman, M.I., "Study of government's strategy on clean water availability in indonesia", *Jurnal Kesehatan Lingkungan*

- Indonesia*, Vol. 21, No. 1, (2022), 111-121. doi: 10.14710/jkli.21.1.111-121.
2. Shehu, B. and Nazim, F., "Clean water and sanitation for all: Study on sdgs 6.1 and 6.2 targets with state policies and interventions in nigeria", *Environmental Sciences Proceedings*, Vol. 15, No. 1, (2022), 71. doi: 10.3390/envirosci.2022015071.
 3. Van Vliet, M.T., Jones, E.R., Flörke, M., Franssen, W.H., Hanasaki, N., Wada, Y. and Yearsley, J.R., "Global water scarcity including surface water quality and expansions of clean water technologies", *Environmental Research Letters*, Vol. 16, No. 2, (2021), 024020. doi: 10.1088/1748-9326/abbfc3.
 4. Slama, H.B., Chenari Bouket, A., Pourhassan, Z., Alenezi, F.N., Silini, A., Cherif-Silini, H., Oszak, T., Luptakova, L., Golińska, P. and Belbahri, L., "Diversity of synthetic dyes from textile industries, discharge impacts and treatment methods", *Applied Sciences*, Vol. 11, No. 14, (2021), 6255. doi: 10.3390/app11146255.
 5. Tehubijuluw, H., Subagyo, R., Yulita, M.F., Nugraha, R.E., Kusumawati, Y., Bahruji, H., Jalil, A.A., Hartati, H. and Prasetyoko, D., "Utilization of red mud waste into mesoporous zsm-5 for methylene blue adsorption-desorption studies", *Environmental Science and Pollution Research*, Vol. 28, (2021), 37354-37370. doi: 10.1007/s11356-021-13285-y.
 6. Gupta, V., Gupta, B., Rastogi, A., Agarwal, S. and Nayak, A., "A comparative investigation on adsorption performances of mesoporous activated carbon prepared from waste rubber tire and activated carbon for a hazardous azo dye—acid blue 113", *Journal of Hazardous Materials*, Vol. 186, No. 1, (2011), 891-901. doi: 10.1021/am300889u.
 7. Homaeigohar, S. and Elbahri, M., "Graphene membranes for water desalination", *NPG Asia Materials*, Vol. 9, No. 8, (2017), e427-e427. doi: 10.1038/asm.2017.135.
 8. Fa, Z., "Porous graphene for sea water desalination considering the effects of fluorine/nitrogen modification: A molecular dynamic study", in IOP Conference Series: Materials Science and Engineering, IOP Publishing. Vol. 926, (2020), 012011.
 9. Aende, A., Gardy, J. and Hassanpour, A., "Seawater desalination: A review of forward osmosis technique, its challenges, and future prospects", *Processes*, Vol. 8, No. 8, (2020), 901. doi: 10.3390/pr8080901.
 10. Ahmad, H.H. and Alahmad, W., "Modeling the removal of methylene blue dye using a graphene oxide/tio2/sio2 nanocomposite under sunlight irradiation by intelligent system", *Open Chemistry*, Vol. 19, No. 1, (2021), 157-173. doi: 10.1515/chem-2021-0025.
 11. Kusumawati, R., "Synthesis and characterization of fe3o4@ rgo composite with wet-mixing (ex-situ) process", in Journal of Physics: Conference Series, IOP Publishing. Vol. 1171, No. Issue, (2019), 012048.
 12. Salverda, M., Thirupathi, A.R., Pakravan, F., Wood, P.C. and Chen, A., "Electrochemical exfoliation of graphite to graphene-based nanomaterials", *Molecules*, Vol. 27, No. 24, (2022), 8643. doi: 10.3390/molecules27248643.
 13. Mbayachi, V.B., Ndayiragije, E., Sammani, T., Taj, S. and Mbuta, E.R., "Graphene synthesis, characterization and its applications: A review", *Results in Chemistry*, Vol. 3, (2021), 100163. doi: 10.1016/j.rechem.2021.100163.
 14. Kigozi, M., Koech, R.K., Kingsley, O., Ojeaga, I., Tebandeke, E., Kasozi, G.N. and Onwualu, A.P., "Synthesis and characterization of graphene oxide from locally mined graphite flakes and its supercapacitor applications", *Results in Materials*, Vol. 7, (2020), 100113. doi: 10.1016/j.rinma.2020.100113.
 15. Junaidi, N.F.D., Othman, N.H., Fuzil, N.S., Shayuti, M.S.M., Alias, N.H., Shahrudin, M.Z., Marpani, F., Lau, W.J., Ismail, A.F. and Aba, N.D., "Recent development of graphene oxide-based membranes for oil–water separation: A review", *Separation and Purification Technology*, Vol. 258, (2021), 118000. doi: 10.1016/j.seppur.2020.118000.
 16. Sun, J., Bi, H., Su, S., Jia, H., Xie, X. and Sun, L., "One-step preparation of go/sio2 membrane for highly efficient separation of oil-in-water emulsion", *Journal of Membrane Science*, Vol. 553, (2018), 131-138. doi: 10.1016/j.memsci.2018.02.029.
 17. Taufiq, A., Teraningtyas, A., Kusumawati, D.H. and Supardi, Z.A.I., "Nanosized fe3o4/sio2 core-shells fabricated from natural sands, magnetic properties, and their application for dye adsorption", *Engineering and Applied Science Research*, Vol. 49, No. 3, (2022), 340-352. doi: 10.14456/EASR.2022.35.
 18. Akhter, F., Rao, A.A., Abbasi, M.N., Wahocho, S.A., Mallah, M.A., Anees-ur-Rehman, H. and Chandio, Z.A., "A comprehensive review of synthesis, applications and future prospects for silica nanoparticles (SNPS)", *Silicon*, (2022), 1-16. doi: 10.1007/s12633-021-01611-5
 19. Ou, X., Yang, X., Zheng, J. and Liu, M., "Free-standing graphene oxide–chitin nanocrystal composite membrane for dye adsorption and oil/water separation", *ACS Sustainable Chemistry & Engineering*, Vol. 7, No. 15, (2019), 13379-13390. doi: 10.1021/acssuschemeng.9b02619.
 20. Naseeb, N., Mohammed, A.A., Laoui, T. and Khan, Z., "A novel pan-go-SiO₂ hybrid membrane for separating oil and water from emulsified mixture", *Materials*, Vol. 12, No. 2, (2019), 212. doi: 10.3390/ma12020212.
 21. Du, Y.-c., Huang, L.-j., Wang, Y.-x., Yang, K., Zhang, Z.-j., Wang, Y., Kipper, M.J., Belfiore, L.A. and Tang, J.-g., "Preparation of graphene oxide/silica hybrid composite membranes and performance studies in water treatment", *Journal of Materials Science*, Vol. 55, (2020), 11188-11202. doi: 10.1007/s10853-020-04774-5.
 22. Wu, H., Tang, B. and Wu, P., "Development of novel sio2-go nanohybrid/polysulfone membrane with enhanced performance", *Journal of Membrane Science*, Vol. 451, (2014), 94-102. doi: 10.1016/j.memsci.2013.09.018.
 23. Zhu, Z., Jiang, J., Wang, X., Huo, X., Xu, Y., Li, Q. and Wang, L., "Improving the hydrophilic and antifouling properties of polyvinylidene fluoride membrane by incorporation of novel nanohybrid go@SiO₂ particles", *Chemical Engineering Journal*, Vol. 314, No., (2017), 266-276. doi: 10.1016/j.cej.2016.12.038.
 24. Kusworo, T.D., Aryanti, N., Utomo, D.P., Hasbullah, H., Lingga, F.F., Yulfarida, M., Dalanta, F. and Kurniawan, T.A., "Simultaneous photocatalytic and membrane filtration using graphene oxide (go)/ SiO₂ composite for enhanced removal of organic pollutant and ammonia from natural rubber-laden wastewater", *SSRN Electronic Journal*, (2022). doi: 10.2139/ssrn.4017566
 25. Aher, A., Cai, Y., Majumder, M. and Bhattacharyya, D., "Synthesis of graphene oxide membranes and their behavior in water and isopropanol", *Carbon*, Vol. 116, (2017), 145-153. doi: 10.1016/j.carbon.2017.01.086.
 26. Gholami, F., Zinadini, S., Zinatizadeh, A., Noori, E. and Rafiee, E., "Preparation and characterization of an antifouling polyethersulfone nanofiltration membrane blended with graphene oxide/ag nanoparticles", *International Journal of Engineering, Transaction A: Basic*, Vol. 30, No. 10, (2017), 1425-1433. doi: 10.5829/ije.2017.30.10a.02.
 27. Munasir, N., Kusumawati, R., Kusumawati, D., Supardi, Z., Taufiq, A. and Darminto, D., "Characterization of fe3o4/rgo composites from natural sources: Application for dyes color degradation in aqueous solution", *International Journal of Engineering, Transaction A: Basic*, Vol. 33, No. 1, (2020), 18-27. doi: 10.5829/IJE.2020.33.01A.03.
 28. Yavari, M. and Salman Tabrizi, N., "Adsorption of methylene blue from aqueous solutions by silk cocoon", *International*

- Journal of Engineering, Transaction C: Aspect*, Vol. 29, No. 9, (2016), 1191-1197. doi: 10.5829/idosi.ije.2016.29.09c.02.
29. Kusworo, T.D., Susanto, H., Aryanti, N., Rokhathi, N., Widiasta, I.N., Al-Aziz, H., Utomo, D.P., Masithoh, D. and Kumoro, A.C., "Preparation and characterization of photocatalytic psf-tio2/go nanohybrid membrane for the degradation of organic contaminants in natural rubber wastewater", *Journal of Environmental Chemical Engineering*, Vol. 9, No. 2, (2021), 105066. doi: 10.1016/j.jece.2021.105066.
 30. Agbaje, T.A., Al-Gharabli, S., Mavukkandy, M.O., Kujawa, J. and Arafat, H.A., "Pvdf/magnetite blend membranes for enhanced flux and salt rejection in membrane distillation", *Desalination*, Vol. 436, (2018), 69-80. doi: 10.1016/j.desal.2018.02.012.
 31. Jaleh, B., Etivand, E.S., Mohazzab, B.F., Nasrollahzadeh, M. and Varma, R.S., "Improving wettability: Deposition of tio2 nanoparticles on the O₂ plasma activated polypropylene membrane", *International Journal of Molecular Sciences*, Vol. 20, No. 13, (2019), 3309. doi: 10.3390/ijms20133309.
 32. Shakir, F., Hussein, H.Q. and Abdulwahhab, Z.T., "Synthesis and characterization of nano silica from iraqi sand by chemical precipitation with different acid types", in AIP Conference Proceedings, AIP Publishing LLC. Vol. 2660, (2022), 020140.
 33. Xu, B. and Zhang, Q., "Preparation and properties of hydrophobically modified nano-sio₂ with hexadecyltrimethoxysilane", *ACS Omega*, Vol. 6, No. 14, (2021), 9764-9770. doi: 10.1021/acsomega.1c00381.
 34. Guo, J., Farid, M.U., Lee, E.-J., Yan, D.Y.-S., Jeong, S. and An, A.K., "Fouling behavior of negatively charged pvdf membrane in membrane distillation for removal of antibiotics from wastewater", *Journal of Membrane Science*, Vol. 551, (2018), 12-19. doi: 10.1016/j.memsci.2018.01.016.
 35. Mosayebi, M., Salehi, Z., Doosthosseini, H., Tishbi, P. and Kawase, Y., "Amine, thiol, and octyl functionalization of go-fe₃o₄ nanocomposites to enhance immobilization of lipase for transesterification", *Renewable Energy*, Vol. 154, (2020), 569-580. doi: 10.1016/j.renene.2020.03.040.
 36. Khaleel, I.H., Alkhafaji, A.A., Miran, H.A. and Jaf, Z.N., "Synthesis, characterization, photoluminescence, and antibacterial activities of silica-graphene oxide composites", *Canadian Journal of Physics*, Vol. 99, No. 12, (2021), 1105-1113. doi: 10.1139/cjp-2020-0538.
 37. Kumar, P., Huo, P., Zhang, R. and Liu, B., "Antibacterial properties of graphene-based nanomaterials", *Nanomaterials*, Vol. 9, No. 5, (2019), 737. doi: 10.3390/nano9050737.
 38. Zeng, J., Wang, Q., Shi, Y., Liu, P. and Chen, R., "Osmotic pumping and salt rejection by polyelectrolyte hydrogel for continuous solar desalination", *Advanced Energy Materials*, Vol. 9, No. 38, (2019), 1900552. doi: 10.1002/aenm.201900552.
 39. Fonseca, S., Cayer, M.-P., Ahmmed, K.T., Khadem-Mohtaram, N., Charette, S.J. and Brouard, D., "Characterization of the antibacterial activity of an SiO₂ nanoparticulate coating to prevent bacterial contamination in blood products", *Antibiotics*, Vol. 11, No. 1, (2022), 107. doi: 10.3390/antibiotics11010107.
 40. Zhang, T., Xue, Q., Zhang, S. and Dong, M., "Theoretical approaches to graphene and graphene-based materials", *Nano Today*, Vol. 7, No. 3, (2012), 180-200. doi: 10.1016/j.nantod.2012.04.006.
 41. Li, X., Zhu, B. and Zhu, J., "Graphene oxide based materials for desalination", *Carbon*, Vol. 146, (2019), 320-328.
 42. Kadhim, R.J., Al-Ani, F.H., Al-Shaeli, M., Alsahy, Q.F. and Figoli, A., "Removal of dyes using graphene oxide (GO) mixed matrix membranes", *Membranes*, Vol. 10, No. 12, (2020), 366. doi: 10.3390/membranes10120366.
 43. Alnoor, O., Laoui, T., Ibrahim, A., Kafiah, F., Nadhreen, G., Akhtar, S. and Khan, Z., "Graphene oxide-based membranes for water purification applications: Effect of plasma treatment on the adhesion and stability of the synthesized membranes", *Membranes*, Vol. 10, No. 10, (2020), 292. doi: 10.3390/membranes10100292.
 44. Karimi Pasandideh, E., Kakavandi, B., Nasser, S., Mahvi, A.H., Nabizadeh, R., Esrafil, A. and Rezaei Kalantary, R., "Silica-coated magnetite nanoparticles core-shell spheres (Fe₃O₄@ SiO₂) for natural organic matter removal", *Journal of Environmental Health Science and Engineering*, Vol. 14, No., (2016), 1-13. doi: 10.1186/s40201-016-0262-y.
 45. Al-Maliki, R.M., Alsahy, Q.F., Al-Jubouri, S., Salih, I.K., AbdulRazak, A.A., Shehab, M.A., Németh, Z. and Hernadi, K., "Classification of nanomaterials and the effect of graphene oxide (GO) and recently developed nanoparticles on the ultrafiltration membrane and their applications: A review", *Membranes*, Vol. 12, No. 11, (2022), 1043. doi: 10.3390/membranes12111043
 46. Yang, Y., Zhang, M., Song, H. and Yu, C., "Silica-based nanoparticles for biomedical applications: From nanocarriers to biomodulators", *Accounts of Chemical Research*, Vol. 53, No. 8, (2020), 1545-1556. doi: 10.1021/acs.accounts.0c00280

Persian Abstract

چکیده

بحران آب پاک در اندونزی هر سال در حال افزایش است و ضایعات صنعت نساجی نیز می تواند به این مشکل بیفزاید. فرآیندهای مختلف تصفیه آب برای مقابله با بحران آب پاک وجود دارد که یکی از آنها فرآیند نمک زدایی با استفاده از اکسید گرافن است. با افزودن نانوذرات آبدوست، غشاهای اکسید گرافن (GO) می توانند زبری را افزایش داده و از استحکام مکانیکی خوبی برخوردار باشند. نانوذرات SiO₂ همچنین سطح ویژه بالایی برای جذب آب دارند یا آبدوست هستند. این مطالعه با هدف تعیین توانایی غشاء GO-SiO₂/Psf در دفع نمک (محلول NaCl) و فیلتر کردن محلول های متیلن بلو انجام شد. غشاء تهیه شده توسط تغییرات تترائیل ارتوسیلیکات (TEOS) 0.6; 0.8; و 1.0 میلی لیتر برای ستر کامپوزیت GO/SiO₂ نتایج نشان داد که غشاء GO-SiO₂/Psf می تواند محلول متیلن بلو را جذب کند. بهینه ترین مقدار جذب در غلظت TEOS 0.8 میلی لیتر و موثرترین مقدار دفع نمک برای محلول NaCl برابر با ۶۷.۲۲ درصد بود.



A Robust Renewable Energy Source-oriented Strategy for Smart Charging of Plug-in Electric Vehicles Considering Diverse Uncertainty Resources

M. Ahmadigorji*^a, M. Mehrasa^b

^a Department of Electrical Engineering, Nour Branch, Islamic Azad University, Nour, Iran

^b Univ. Grenoble Alpes, CNRS, Grenoble INP, G2ELAB, 38000 Grenoble, France

P A P E R I N F O

Paper history:

Received 08 January 2022

Received in revised form 29 January 2023

Accepted 09 February 2023

Keywords:

Multi-objective Optimization

Plug-In Electric Vehicle

Renewable Energy Sources

Robustness

Smart Charging

Uncertainty Resources

A B S T R A C T

Nowadays, the notion of plug-in electric vehicle (PEV) as a valuable tool of energy management has been extensively employed in smart distribution grids. The main advantage of clean energy as well as elastic behaviour of operation in both electrical load/generation modes can sufficiently justify the utilization of such emerging technology. Moreover, the specific capability of renewable energy sources (RESs) in terms of contribution in PEV smart charging/discharging scheme would cause to remarkable techno-economic benefits in smart grids. However, the load demand, RES generation and also the electrical energy price encounter with uncertainty in practice required to be properly handled. Hence, a non-deterministic optimization model based on information gap decision theory (IGDT) is proposed in this paper to specify a robust PEV smart charging pattern. To solve the multi-objective proposed IGDT-based PEV smart charging (IGDT-PSC) model, the multi-objective version of particle swarm optimization (MOPSO) is utilized to define a set of Pareto optimal solutions. Furthermore, the final solution among the Pareto solutions is selected by means of a linear fuzzy satisfaction rule. The simulation results for a test smart microgrid comprising a PEV, a set of RES units and a load demand verify the effectiveness of the proposed IGDT-PSC model.

doi: 10.5829/ije.2023.36.04a.10

NOMENCLATURE

TC	Cost of purchased electrical energy (\$).	CS_{int} / CS_{fin}	Initial/final charging state of the plug-in electric vehicle battery (%).
ϕ^t	Set of hours in a day (i.e. {0,1,...,24}).	$\gamma_{ch} / \gamma_{dch}$	Charging/discharging efficiency of the plug-in electric vehicle battery (%).
UP_t	Upstream power supplied by the main grid at hour t (kW).	$P_{ch,t}^{PEV} / P_{dch,t}^{PEV}$	Charging/discharging power of the plug-in electric vehicle battery at hour t (kW).
EP_t	Electrical energy price at hour t (Cent/kWh).	CS_t	Charging state associated with the plug-in electric vehicle battery at hour t (%).
LD_t	Load demand at hour t (kW).	CS^{min} / CS^{max}	Lowest/highest charging state value (%).
P_t^{PV}	Output power of the photovoltaic system at hour t (kW).	α_t / β_t	Binary variables showing the charging/discharging status of the plug-in electric vehicle battery at hour t .
P_t^{WT}	Output power of the wind turbine at hour t (kW).	$P_{ch}^{max} / P_{dch}^{max}$	Maximum permissible charging/discharging power of the plug-in electric vehicle battery (kW).
P_t^{PEV}	output power of the plug-in electric vehicle at hour t (kW).	$SE_{min}^{PEV} / SE_{max}^{PEV}$	Minimum/maximum value of the stored energy in the plug-in electric vehicle battery. (kWh).
E_{max}^{PEV}	Rated capacity of the plug-in electric vehicle (kWh).	RP	Robustness controlling parameter used in information gap decision theory.
E_t^{PEV}	Remained energy of the plug-in electric vehicle battery at hour t (kWh).	$\mu_{(o)}$	Boudry value related to r_z of the uncertain variable (o).
$\mathcal{I}_{z(o)}$	Robust zone associated with the uncertain variable (o).	δ	A user-defined value between 0 and 1 controlling the selection pressure of the leader associated with each cell.

*Corresponding Author Institutional Email: ahmadigorji@yahoo.com
(M. Ahmadigorji)

Please cite this article as: M. Ahmadigorji, M. Mehrasa, A Robust Renewable Energy Source-oriented Strategy for Smart Charging of Plug-in Electric Vehicles Considering Diverse Uncertainty Resources, *International Journal of Engineering, Transactions A: Basics*, Vol. 36, No. 04, (2023), 709-719

LD_t^{exp}	Expected value of the load demand at hour t (kW).	τ	A user-defined value between 0 and 1 controlling the selection pressure of the cell elimination.
EP_t^{exp}	Expected value of the electrical energy price at hour t (Cent/kWh).	Δt	Time step (h).
$P_t^{PV,exp} / P_t^{WT,exp}$	Expected value of the photovoltaic/wind turbine output power at hour t (kW).	Subscripts	
VE_k / PS_k	Velocity/position of the particle k .	t	Hour.
GBT^{iter}	The best position ever discovered among the population until iteration $iter$.	k	Number of candidate solution in particle swarm optimization.
PBT_k^{iter}	Best position arisen for the particle k until iteration $iter$.	ch / dch	Related to the charging/decharging.
C_1, C_2	Two predefined weighting factors regulating the moving step toward the particle's best position ever discovered and the best position ever discovered among the population, respectively.	i	Related to the number of each objective function.
r_1, r_2	Two random values with uniform distribution lying in the range of (0,1).	n	Related to the number of each Pareto optimal solution.
Greek Symbols		ld / pv	Related to the load demand/photovoltaic unit.
λ	Inertial coefficient representing the particle's tendency to move along the previous position.	wt / pr	Related to the wind turbine/electrical energy price.

1. INTRODUCTION

Green-house gases emission and so human health concerns, shortage and low accessibility of fossil fuel as well as its increasing price in world markets, low operation costs and also using the potential of energy storage are of the main techno/economic/enviromental incentives of the PEV application. The essential flexibility of the PEVs in both performance modes of electrical source/load has recently absorbed the attention of academic and industrial individuals to more investigate and exploit the operational advantages of such technology in modern power systems [1, 2]. At the same context, the extensive potential of RESs such as photovoltaic (PV) units, wind turbine (WT) units, fuel cells, geothermal energy, battery energy storage system (BESS), etc., as supportive low-emission cost power sources has been growingly taken into consideration in smart distribution grids [3-5]. In this way, the helpful role of PV/WT units in charging a PEV battery specifically in off-peak electrical energy prices can potentially lead to reduction in operation costs. At the same context, the valuable feature of battery discharging throughout the peak load interval of the main grid, aiming to more reduction of the operation costs, can further highlight the beneficial aspects of the PEVs [6]. Hence, based on contributory partnership of the PV/WT units, this paper concentrates on presenting a reasonable cost-effective PEV charging/discharging framework (called hereafter PEV smart charging (PSC)) in order to achieve the techno/economical purposes of all participants. In general, the main participants of PEV-equipped smart grids are PEV user (driver), grid operator and charging station owner. Thus, the PEV charging/discharging optimization can be variously implemented based on each of participants' interest. Load balancing, peak load shaving, cost minimization are among the main expectation of the grid operator from the smart PEV

charging approach [7, 8]. On the other hand, the owner of charging station essentially seeks to earn more revenue from injecting (selling) the PEVs' stored energy especially within the peak price period. Without loss of the generality, the grid operator and the charging station owner is assumed to be identical in this paper. At this condition, the main target of the formulated PSC model is to sufficiently supply the load demand by focusing on reduction in total cost as much as possible. Additionally, the PEV user's interest is an important issue less emphasized in the recent research works. Based on this issue, in this paper, a comprehensive PSC model is proposed wherein the whole participants' desire are simultaneously taken into account. To incorporate the key role of the PEV user, the presented PSC model permits the PEV user to previously announce his/her desired arrival and departure time to/from the charging station as well as the interested initial and final charging state (CS) pertaining to the PEV battery. The data transmission infrastructure is practically provided by wireless communication technology employing the specialized applications installed at smart phones, etc. In this regard, immediately after receiving the required data of PEV user, the grid operator/charging station owner seeks to optimize the PEV terminal power (i.e. charging/discharging pattern) along a day considering all other relevant inputs including the load, PV/WT generation profiles as well as the economic data and constraints associated with both grid and PEV. Subsequently, the PEV user is informed from the optimization result (i.e. variation trend of the PEV terminal power) based on the technical specifications he/she announced before arrival to the charging station.

On the other hand, the load demand, PV/WT generation and also the electrical energy price are intrinsically exposed to the uncertainty in real-world smart grids, which has not been considered in the literature. In this way, to ensure a reliable and robust

decision outputs hedged against the uncertain characteristics of the mentioned parameters, an efficient uncertainty modeling approach should be utilized. Generally speaking, the well-known probabilistic [9-11] and possibilistic methods [12-14] are usually observed in recent research works to model the various uncertainty resources. In the former, the probability distribution function (PDF) of the uncertain variables is mandatory while the latter characterize the uncertain resources via their membership function. However, each of these two methods encounter with functional challenges somehow. Within the probabilistic methods, the PDF of some uncertain variables are not available or the uncertain variables do not follow any definite PDF. Moreover, in some cases, sufficient previously recorded data is not available to constitute an accurate PDF. On the other hand, the membership function is structurally formed according to the prior experience of the expert system, which is generally a non-trivial task in practice. Therefore, in this paper, the notion of IGDT is utilized to handle the uncertainty resources of the load, PV/WT generation and electrical energy price within the proposed PSC model. Two distinguished advantages of the IGDT versus the probabilistic/possibilistic methods can be enumerated. The first is the proficient performance of the IGDT under the least or no historical data about the past of uncertainty resources. Also, the second advantage is presenting a robust optimization outputs all protected against the worst fluctuation of the uncertain variables varying within their own robust zones [15-17]. Within the formulated IGDT-PSC model, the four uncertain variables including the load, PV/WT generation and electrical energy price competitively try to extend their relevant robust zones. Since these uncertain parameters are fundamentally heterogeneous, thus, the suggested non-deterministic IGDT-PSC model is in the form of a multi-objective optimization problem. To solve this problem, the multi-objective variant of PSO (i.e. MOPSO) is utilized to create a set of non-dominated Pareto solutions. Finally, to reach the best compromise solution among the Pareto solutions generated by the MOPSO, a well-known fuzzy-based satisfaction rule is employed.

The main contributions of this paper are as follows: 1) an IGDT-PSC model is proposed considering four uncertainty resources of load, PV/WT output and also electricity price; 2) the proposed model is comprehensive such that the techno-economic interests of all participants, i.e. the PEV user, grid operator and charging station owner, are concurrently met. To assess the effectiveness of the formulated IGDT-PSC model, it is implemented on a small-scale microgrid including an electrical load, a set of PV/WT generation units and also a PEV. The simulation results including the daily profiles of the PEV terminal power (and so its CS) is optimally calculated by simultaneous application of the proposed

IGDT-PSC model, MOPSO and fuzzy-based satisfaction rule.

The rest of the paper is categorized as follows. In section 2, the suggested mathematical representation of the proposed deterministic PSC (DPSC) model is presented. The IGDT definition, the mathematical formulation of the proposed IGDT-PSC model, the MOPSO performance in creation of the non-dominated solutions and ultimately the fuzzy decision-making strategy is presented in section 3. Section 4 includes the simulation results obtained by simultaneous application of the proposed IGDT-PSC model, MOPSO and fuzzy-based rule aiming to specify the robust PEV charging/discharging scheme. Section 5 highlights the conclusion remarks.

2. THE PROPOSED DPSC MODEL

In this section, the mathematical formulation of the proposed DPSC model together with the associated technical constraints is presented.

2.1. The Objective Function of the Proposed DPSC Model

The DPSC framework presented in this research work aims to minimize the daily cost of the electrical power procured from the main grid. In this regard, the mathematical representation of the suggested DPSC model specifying the optimal daily trend of the PEV terminal power (and so the pertinent CS) can be depicted as follow:

$$DOF = \min TC \quad (1)$$

$$TC = \sum_{\forall t \in \phi^f} (UP_t \times EP_t) \quad (2)$$

where TC denotes the electrical energy purchase cost. As illustrated in Equation (1), the main goal of the proposed DPSC model is to adequately meet the load power based on the minim TC imposed to the grid operator.

2.2. Constraints The following equality/inequality constraints, related to both PEV battery and the main grid, are incorporated into the proposed DPSC model:

- Power balance should be satisfied all the day:

$$UP_t = LD_t - P_t^{PV} - P_t^{WT} - P_t^{PEV} \quad \forall t \in \phi^f \quad (3)$$

$$P_t^{PEV} = (CS_t - CS_{t-\Delta t}) \times \left(\frac{E^{PEV}}{\Delta t} \right) \quad \forall t \in \phi^f \quad (4)$$

By Comparing CS_t and $CS_{t-\Delta t}$ as well as assuming $\Delta t=1h$, three performance statuses for a PEV is defined as below:

$$\begin{cases} CS_t > CS_{t-1}; & \text{charged} \\ CS_t < CS_{t-1}; & \text{discharged} \\ CS_t = CS_{t-1}; & \text{no operation (idle)} \end{cases} \quad \forall t \in \phi^f \quad (5)$$

• The variation trend of CS for the PEV battery during the time period between entering/leaving the charging station is determined by Equations (6)-(8). Furthermore, the time-based remaining energy of the PEV battery is calculated via Equation (9):

$$CS_{t \leq AT} = CS_{int} \quad (6)$$

$$CS_{t \geq DT} = CS_{fin} \quad (7)$$

$$CS_{(AT < t < DT)} = CS_{(t-1)} + \left(\frac{E_t^{PEV}}{E_{max}^{PEV}} \right) \quad \forall t \in \phi^f \quad (8)$$

$$\begin{aligned} E_t^{PEV} &= P_t^{PEV} \times (\Delta t = 1hr) \\ &= \gamma_{ch} \times P_{ch,t}^{PEV} - \left(\frac{P_{dch,t}^{PEV}}{\gamma_{dch}} \right) \quad \forall t \in \phi^f \end{aligned} \quad (9)$$

• The functional restriction imposed to the charging/discharging rate, CS and stored energy of the PEV battery (affirmed by the manufacturer to prevent the loss of battery lifetime) is represented as follows:

$$P_{ch,t}^{PEV} \leq \alpha_t \times P_{ch}^{max} \quad \forall t \in \phi^f \quad (10)$$

$$P_{dch,t}^{PEV} \leq \beta_t \times P_{dch}^{max} \quad \forall t \in \phi^f \quad (11)$$

$$\alpha_t + \beta_t \leq 1 \quad \forall t \in \phi^f; \alpha_t, \beta_t \in \{0,1\} \quad (12)$$

$$CS^{min} \leq CS_t \leq CS^{max} \quad \forall t \in \phi^f \quad (13)$$

$$SE_{min}^{PEV} \leq E_t^{PEV} \leq SE_{max}^{PEV} \quad \forall t \in \phi^f \quad (14)$$

$$SE_{min}^{PEV} = CS^{min} \times E_{max}^{PEV} \quad \forall t \in \phi^f \quad (15)$$

$$SE_{max}^{PEV} = CS^{max} \times E_{max}^{PEV} \quad \forall t \in \phi^f \quad (16)$$

3. THE PROPOSED IGDT-PSC MODEL

In this section, the notion of IGDT as the uncertainty handling approach employed in this paper is firstly described in subsection 3.1. Afterwards, the mathematical formulation of the proposed IGDT-PSC model is presented in subsection 3.2. Since the IGDT-PSC model is a multi-objective optimization problem, the evolution procedure of the multi-objective PSO (MOPSO), utilized for solving the suggested model, is presented in subsection 3.3. Eventually, the fuzzy satisfaction-based decision rule used to select the best solution between the Pareto optimal solutions, created by the MOPSO, is elucidated in subsection 3.4.

3.1. The Information Gap Decision Theory (IGDT)

In real-world power systems, the planning/operation

process encounter with several economic/technical uncertainties. To model such uncertainty resources, the familiar probability distribution function (PDF) [9-11] for probabilistic approaches and fuzzy membership function [12-14] for possibilistic techniques have been recurrently employed in recent studies. Nevertheless, the PDF of the uncertain variables is not reachable or not appropriate for precise uncertainty modeling in most practical cases. Furthermore, the altering behaviour pertaining to some other uncertain variables does not follow a definite PDF. On the other hand, a fuzzy membership function requires the preceding skills of the expert individuals that are not available in some circumstances. Accordingly, a worthwhile uncertainty characterizing approach like IGDT can be an advantageous tool to cope with such uncertainty resources.

The main goal of the IGDT is to maximize the robustness of the decision outputs in a non-deterministic optimization problem. Within the IGDT, the permissible variation of the uncertain variables from their expected values is circumscribed to a boundary parameter namely robust zone. Based on this issue, IGDT attempts to maximize the toleration of the decision-making strategy versus any probable value realized for the uncertain variables throughout their own robust zones [15-17]. In other word, the robust solution achieved by the IGDT is secure against the worst-case deviation of the uncertainty resources all over their own robust zones.

Mathematically speaking, not surpassing the objective function of the non-deterministic problem from a predefined value is defined as the robustness of the decision-making procedure. The predefined value is the numerical value of the objective function associated with the related deterministic problem where no uncertainty resource is incorporated.

There are numerous methods to represent the variation behaviour of the uncertainty resources within the IGDT technique. The envelope bound is used in this paper for this purpose [18-20]. Let assume an optimization problem wherein X and Y denote the set of decision and uncertain variables, respectively. Considering the boundary value of μ , the envelope bound method characterizing the robust zones of the Y (i.e. rz) can be illustrated as follows:

$$Y \in rz(\mu, Y^{exp}) \quad (17)$$

$$rz(\mu, Y^{exp}) = \left| \frac{Y - Y^{exp}}{Y^{exp}} \right| \leq \mu \quad (18)$$

where Y^{exp} is the expected (forecasted) value of the Y . According to Equation (18), the Y members can freely change within their own rz interval, confined by μ , as below:

$$(1-\mu)Y^{exp} \leq Y \leq (1+\mu)Y^{exp} \quad (19)$$

The chief role of the IGDT is to maximize the robust zone μ aiming to achieve a set of decision variables X immunized against any possible fluctuation of the Y members within their own robust zones represented in Equation (19). To better insight, consider $f^*(X,Y)$ as the numerical value of the non-deterministic objective function. Since more deviation of the Y members from their own expected values results in escalating the $f^*(X,Y)$, the highest value of $f^*(X,Y)$ to confirm the maximum robustness befalls when all Y members reach to their own upper bounds (i.e. $Y=(1+\mu).Y^{exp}$). Hence, the IGDT trying to attain the most extended rz for the set of Y can be mathematically formulated via Equations (20)-(22):

$$\max_X \mu(X, f(X)) \quad (20)$$

$$Y \in rz(\mu, Y^{exp}) \quad (21)$$

$$f^*(X, (Y=(1+\mu)Y^{exp})) \leq (1+UB).f(X) \quad (22)$$

where UB is a selective limiting value predefined by the decision-maker. The UB value is directly relies on the decision-maker prospect such that how much robustness, as shown in Equation (22), is desired to realize.

3. 2. Mathematical Representation of the Suggested IGDT-PSC Model The DPSC model developed in section 2 is exposed to the multifold uncertainties in practical environment. As explicated beforehand, the uncertainty resources of this paper comprise the load demand, PV/WT output power, and also the electrical energy price which should be incorporated into the DPSC model given in Equations (1)-(16).

To mathematically formulate the IGDT-PSC model, the set of decision variables (X), uncertain variables (Y), robust zones (rz), and boundary enveloping values (μ) are considered as follow:

$$X = \{\alpha_t, \beta_t, P_t^{PEV}\} \quad (23)$$

$$Y = \{LD_t, P_t^{PV}, P_t^{WT}, EP_t\} \quad (24)$$

$$rz = \{rz_{ld}, rz_{pv}, rz_{wt}, rz_{pr}\} \quad (25)$$

$$\mu = \{\mu_{ld}, \mu_{pv}, \mu_{wt}, \mu_{pr}\} \quad (26)$$

Based on Equation (18), the set of rz associated with the four uncertainty resources of the proposed IGDT-PSC model can be illustrated as follows:

$$rz_{ld} = \left| \frac{LD_t - LD_t^{exp}}{LD_t^{exp}} \right| \leq \mu_{ld} \quad (27)$$

$$rz_{pv} = \left| \frac{P_t^{PV} - P_t^{PV,exp}}{P_t^{PV,exp}} \right| \leq \mu_{pv} \quad (28)$$

$$rz_{wt} = \left| \frac{P_t^{WT} - P_t^{WT,exp}}{P_t^{WT,exp}} \right| \leq \mu_{wt} \quad (29)$$

$$rz_{pr} = \left| \frac{EP_t - EP_t^{exp}}{EP_t^{exp}} \right| \leq \mu_{pr} \quad (30)$$

Considering Equations (27)-(30), the worst-case value of the uncertain variables are: $(1+\mu_{ld}).LD_t^{exp}$ for the load demand, $(1-\mu_{pv}).P_t^{PV,exp} / (1-\mu_{wt}).P_t^{WT,exp}$ for the PV/WT output power and $(1+\mu_{pr}).EP_t^{exp}$ for the electrical energy price. Therefore, the extended form of the IGDT-PSC model can be mathematically demonstrated by Equations (31)-(35):

$$\max (\mu_{ld}, \mu_{pv}, \mu_{wt}, \mu_{pr}) \quad (31)$$

s.t.

$$ROF \equiv TC(UP, CS, LD, P^{PV}, P^{WT}, EP, P^{PEV}) \leq (1+RP).DOF \quad (32)$$

$$TC = \sum_{\forall t \in \phi^t} (UP_t \cdot (1+\mu_{pr}).EP_t) \quad (33)$$

$$UP_t = (1+\mu_{ld}).LD_t - (1-\mu_{pv}).P_t^{PV} - (1-\mu_{wt}).P_t^{WT} - P_t^{PEV} \quad \forall t \in \phi^t \quad (34)$$

$$\text{Equations (3) to (16)} \quad (35)$$

It is evident that the proposed IGDT-PSC model presented in Equations (31)-(35) is characteristically a multi-objective optimization problem. The MOPSO algorithm is employed to solve this model and so generate a set of Pareto optimal solutions. In the following, the step-by-step performance of MOPSO is described.

3. 3. Multi-objective Particle Swarm Optimization (MOPSO) In the following, the original PSO is briefly reviewed in subsection 3.3.1. Then, the dominance theory raised in multi-objective optimization problems is mathematically elucidated in section 3.3.2. Finally, the step-by-step evolutionary performance of the MOPSO is described in section 3.3.3.

3. 3. 1. Brief Description of the Original PSO The original PSO inspires from group movement of the fishes/birds herd (population). This metaheuristic optimization algorithm and also its enhanced variants have been numerously utilized in recent power system problems [21-24]. In original PSO, each member of the population (i.e. each candidate solution) is generally known as a particle which can be iteratively evolved by means of adaptive movement toward two other positions in the feasible search space. The first is the best position arisen for each particle (PBT) and the second is the best

position ever discovered among the population (*GBT*). To mathematically represent the chronological movement of each PSO particle, consider an optimization problem with m decision variables. The velocity and position of the particle k can be respectively indicated by Equations (36) and (37):

$$VE_k = [ve_k^1, ve_k^2, \dots, ve_k^m] \quad (36)$$

$$PS_k = [ps_k^1, ps_k^2, \dots, ps_k^m] \quad (37)$$

Thus, the iterative update for both VE_k and PS_k is as follows:

$$VE_k^{iter+1} = \lambda \cdot VE_k^{iter} + c_1 \cdot r_1 \cdot (PBT_k^{iter} - PS_k^{iter}) + c_2 \cdot r_2 \cdot (GBT^{iter} - PS_k^{iter}) \quad k \in \{1, 2, \dots, N_{sol}\} \quad (38)$$

$$PS_k^{iter+1} = PS_k^{iter} + VE_k^{iter+1} \quad (39)$$

where N_{sol} and $iter$ are respectively symbolized for the number of particles and counter of PSO iterations. Furthermore, c_1 and c_2 are two predefined weighting factor regulating the moving step toward the particle's *PBT* and population's *GPT*, respectively (classically $c_1 + c_2 = 4$ [21-24]). The inertial coefficient λ depicts the particle's tendency to move along the previous position. In general, this factor is initialized with a high value and gradually drops to the lower values along with the PSO iterations. Ultimately, r_1 and r_2 are two random values with uniform distribution lying in the range of (0,1).

The update approach of Equations (38)-(39) is iteratively replicated up to the termination condition (i.e. reach to the maximum iteration number). The *GBT* in the last iteration ($iter_{max}$) is designated as the PSO best solution.

3. 3. 2. Dominance Theory A multi-objective optimization problem with u decision variable and nb objective functions can be mathematically demonstrated as follows (without loss of the generality, a maximization problem is taken into account):

$$F(X) = [f_1(X), f_2(X), \dots, f_{nb}(X)] \quad (40)$$

$$X = [x_1, x_2, \dots, x_u] \quad (41)$$

$$EC(X) = \bar{0}, \quad IC(X) \leq \bar{0} \quad (42)$$

where $EC(X)$ and $IC(X)$ are clique of the equality and inequality constraints, respectively. If X_1 and X_2 are two feasible candidate solutions, X_2 is dominated by X_1 when the following conditions are concurrently fulfilled:

$$\forall i \in \{1, 2, \dots, nb\} \Rightarrow f_i(X_1) \geq f_i(X_2) \quad (43)$$

$$\exists i' \in \{1, 2, \dots, nb\} \Rightarrow f_{i'}(X_1) > f_{i'}(X_2) \quad (44)$$

3. 3. 3. The MOPSO Step-By-Step Algorithm

Compared with original PSO, the *GBT* is replaced by the notion of "leader" selected among a set of non-dominated solutions (namely Pareto optimal solutions) in every iteration of the MOPSO. Moreover, the mentioned Pareto solutions are stockpiled in a specific archive known as "repository". Accordingly, the step-by-step algorithm of MOPSO aiming to generation of non-dominated solutions (repository members) can be elucidated as follows [25, 26]:

1. A predefined number of initial candidate solutions (population) are created with respect to allowable range of the decision variables as well as problem constraints.
2. Compute the values of all the objective functions for every particle. The *PBT* for each particle is the same as generated in the previous step.
3. Based on the dominance theory introduced in section 3.3.2, a certain number of particles are specified as the non-dominated (Pareto) solutions and then keep them in the repository.
4. A leader among the repository members is selected for every particle. For this purpose, the Pareto frontier made by MOPSO is divided to a number of adjoining cells using the grid constitution presented by Sepehrzad et al. [25]. In this case, assuming np_b as the number of repository members located in cell b (i.e. size of cell b), the leader selection probability associated with the cell b can be calculated based on Boltzmann function, as follows:

$$P_b^{sl} = \frac{\exp(-\delta \cdot np_b)}{\sum_{np_j} \exp(-\delta \cdot np_j)} \quad (45)$$

where δ is a user-defined value between 0 and 1 controlling the selection pressure of the leader associated with each cell. The less the cell size is, the more the probability of leader selection for that cell. Calculating the leader selection probability for all cells, one cell is accidentally selected for each particle based on Roulette Wheel method [27]. Subsequently, one member of the specified cell is randomly selected as the leader. The mentioned mechanism is repeated for all particles out of the repository.

5. For each particle, the velocity and position are evolved analogous to the method presented in Equations (38)-(39), respectively. The *GBT* in Equation (38) is substituted by the associated leader of the particle. The new *PBT* for each particle is dependent on the dominance condition between the previous *PBT* and the updated position of that particle. In this context, if the updated position dominates the previous *PBT*, the new *PBT* is switched to the updated position; otherwise, the *PBT* remains unchanged. If none of the updated position and previous *PBT* can dominate each other, the new *PBT* is randomly determined among them.

6. Investigate the dominance status for the updated particles and then add the non-dominated particles to the

repository of the preceding iteration. The updated repository is checked and so the dominated members are eliminated.

7. If the number of repository members surpasses a definite value, the excessive members should be discarded. Thus, the Boltzmann operator of Equation (45) is transformed to Equation (46) in this condition with the aim of calculating the elimination probability for cell b (P_b^{ce}):

$$P_b^{ce} = \frac{\exp(-\tau \cdot np_b)}{\sum_{np_j} \exp(-\tau \cdot np_j)} \quad (46)$$

where τ (another real value in the interval (0,1)) controls the selection pressure of the cell elimination. Likewise the approach in step 4, one cell is stochastically selected and then, one of its members is randomly removed. However, opposed to the step 4, the more the size of a cell is, the more the probability of selection for removing the associated members. The removing procedure is continued till the repository size comes back to the pre-allocated value.

8. Check the stopping condition as realization of the $iter_{max}$. If true, the last residual members of the repository are reported as the best found Pareto optimal solutions. Otherwise, return to the step 4.

3.4. Fuzzy-Based Satisfaction Rule To select the final solution amongst the set of Pareto solutions created by the MOPSO, a linear fuzzy rule is utilized. This approach is commonly employed while no preference/priority between the objectives is considered [28]. Based on Equations (43)-(44) and also the lettering of section 3.3.2, the fuzzy value ($\mathcal{G}_{X_n}^i$) is computed for Pareto solution X_n as below:

$$\mathcal{G}_{X_n}^i = \begin{cases} 1 & f_i(X_n) > f_{i,max} \\ \frac{f_i(X_n) - f_{i,min}}{f_{i,max} - f_{i,min}} & f_{i,min} \leq f_i(X_n) \leq f_{i,max} \\ 0 & f_i(X_n) < f_{i,min} \end{cases} \quad (47)$$

where $f_{i,min}$ and $f_{i,max}$ are the lowest and highest value of the f_i . Considering N_{pb} as the number of Pareto solutions, the X_n having the maximum $\mathcal{G}_{X_n}^i$ is identified as the final solution using the following selective max-min function:

$$\max_{n=1:N_{pb}} \min_{i=1:nb} \mathcal{G}_{X_n}^i \quad (48)$$

4. SIMULATION RESULTS

In this section, the input data used for the simulation process are first presented in subsection 4.1. In the following, subsection 4.2 includes the numerical results

obtained by application of the proposed IGDT-PSC, MOPSO and the fuzzy satisfaction method on a test micro smart grid. Finally, subsection 4.3 presents a kind of comparative results aiming to appraise the robustness of the suggested IGDT-PSC model based on different values of RP .

4. 1. Data Used for the Simulation Study To analyze the efficiency of the suggested IGDT-PSC model in terms of specifying a robust techno-economic scheme for the PEV smart charging, a test microgrid schematically depicted in Figure 1 is considered. As demonstrated in Figure 1, the test microgrid comprises a load demand, a set of PV/WT units and a PEV. The variation trend of the load demand, PV/WT generation and electrical energy price are depicted in Figures 2 and 3, respectively. The descriptive data related to the PEV (with maximum power of 3.5 kW) and PV/WT units are presented in Table 1. It is assumed that the PEV arrives the charging station at 4:00 by $CS_{in}=0.4$ and leave there at 23:00 by $CS_{fin}=0.8$. Moreover, CS^{min} and CS^{max} are supposed to be 0.2 and 0.9, respectively. The tunable parameters of the MOPSO are depicted in Table 2. Moreover, the computational coding associated with the proposed IGDT-PSC model, the MOPSO and the fuzzy satisfaction approach are all implemented in MATLAB 7.5 software. Additionally, the hardware package utilized for the execution of the simulations consists of a PC equipped by a core™ i5 2.3 GHz CPU and also a 4 GB RAM.

4. 2. Numerical Results for the Test Microgrid In the proposed IGDT-PSC model solved through MOPSO, the profiles of Figures 2 and 3 including the load power, PV power, wind power and the electrical

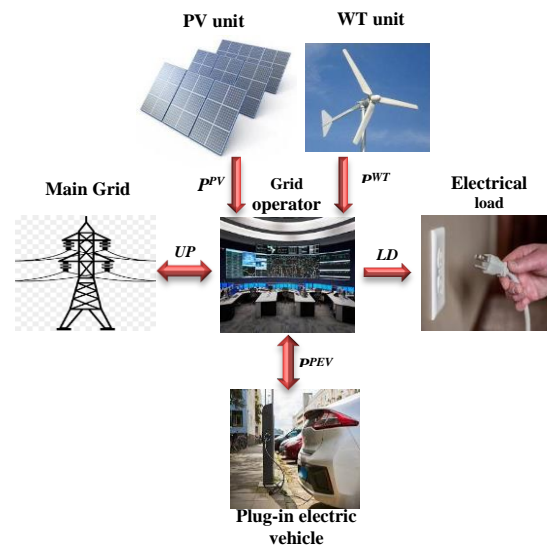


Figure 1. The schematic illustration of the test microgrid used for the simulation studies

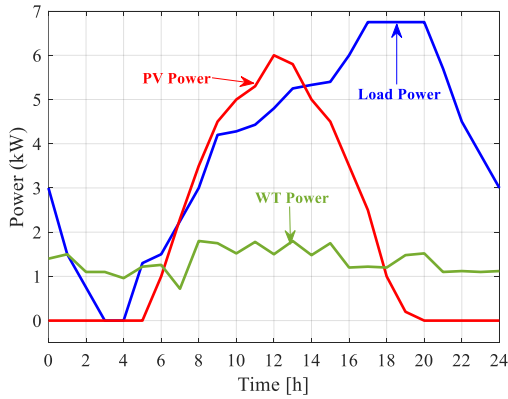


Figure 2. The daily profile of load power, PV power, and WT power

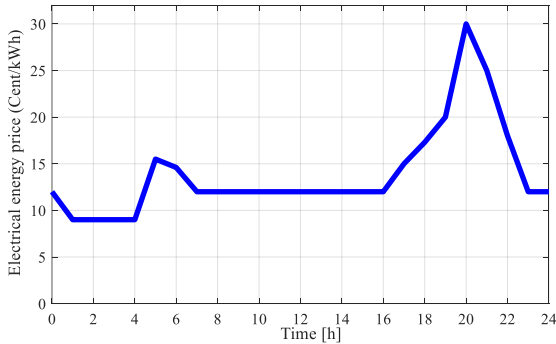


Figure 3. The daily profile of electrical energy price

TABLE 1. The descriptive data of PEV and PV/WT units

List of data	Value
P_{max}^{PV} (rated power of PV unit)	7 kW
P_{max}^{WT} (rated power of WT unit)	2 kW
$P_{ch}^{max} / P_{dch}^{max}$	-3.5/+3.5 kW
E_{max}^{PEV}	24 kWh

TABLE 2. Tunable parameters of the MOPSO

List of tunable parameters	Assigned values
Number of population	80
Maximum number of repository members	20
$Iter_{max}$	100
δ, τ	0.4
C_1, C_2	2

energy price should be taken into account for analyzing the numericals results pertaining to the test microgrid. This analysis encompasses the results associated with the optimal daily profiles of the grid power, PEV power, and

the CS of PEV all demonstrated in Figures 4 and 5 for $UB=0.25$ and $UB=0.75$, respectively. It is seen from Figures 2 and 3 that within the interval of maximum PV/WT generation wherein the electrical energy price remains constant, the proposed IGDT-PSC enables the PEV to be persistently charged for both $UB=0.25$ and $UB=0.75$.

However, comparing the obtained results of the PEV power for the cases of $UB=0.25$ and $UB=0.75$, it can be realized that the proposed robust optimization strategy can force the PEV to be more in charging mode in the case of $UB=0.25$. Nevertheless, during this operating status, the CS of PEV would possess its maximum values according to Figures 4(a) and 5(a). Within the interval of RESs' maximum generation, the moderate level of load consumption is also devoted in which the grid power is appointed to provide the load demand despite the RESs' generation for both $UB=0.25$ and 0.75 .

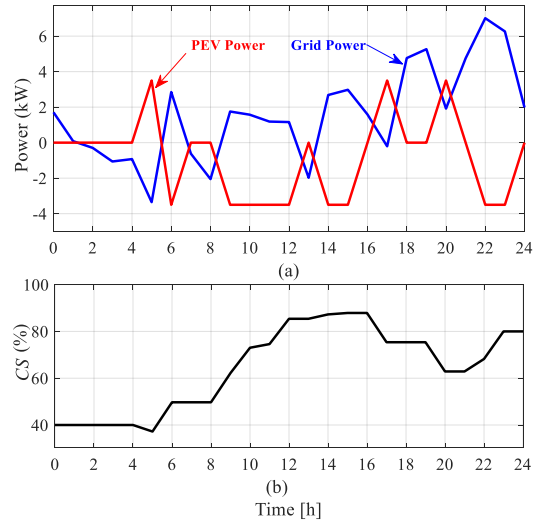


Figure 4. (a) PEV and grid power, (b) CS, all for $UB=0.25$

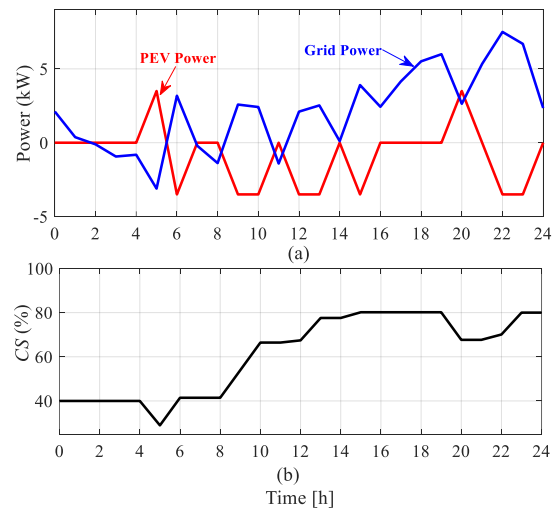


Figure 5. PEV and grid power, (b) CS, all for $UB=0.75$

Since the electrical energy price is increased throughout the interval [19h, 22h] with its top value at $t=20h$, the proposed strategy causes optimal PEV discharging especially at $t=20h$ for both $UB=0.25$ and 0.75 , as exhibited in Figures 4(a) and 5(a), respectively. It is worth mentioning that the PEV is kept in discharging mode for $UB=0.25$ more than $UB=0.75$. Within the interval [19h, 22h], the CS of PEV experiences a significant drop that must be compensated to attain its desired value at the departure time leading to the charging mode activation of the PEV, as seen from both Figures 4(b) and 5(b). In this condition, the grid power (with relatively high value) along with the WT unit are responsible for supplying the load demand and PEV charging power.

4. 3. Comparative Results This section firstly evaluates the variation trend of envelope bounds $\{\mu_{lp}, \mu_{pv}, \mu_{wt}, \mu_{pr}\}$ while the UB value is increased accordingly. As it is expected, Figure 6 verifies that the higher value of UB causes a larger envelope bounds demonstrating a further robustness feature. In this way, the most

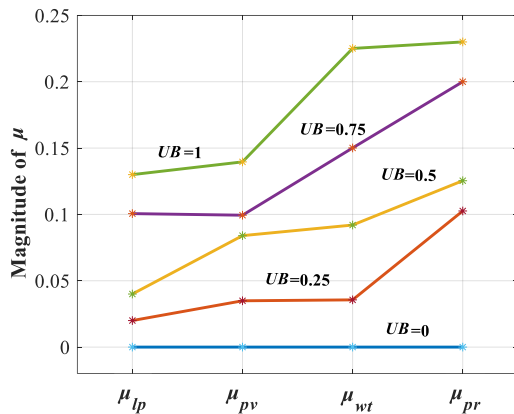


Figure 6. The alteration trend of envelope bounds considering various UB

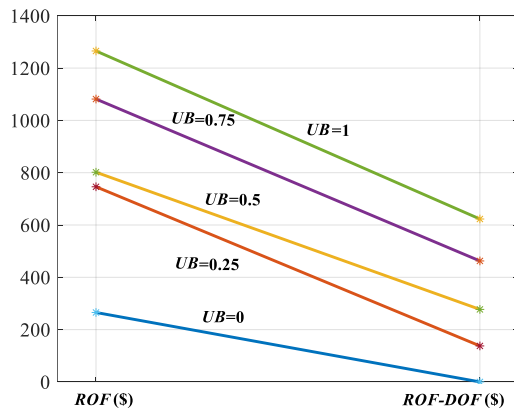


Figure 7. The alteration trend of ROF and $ROF-DOF$ considering various UB

robustness feature for each envelope bound is belong to $UB=1$. Among the envelope bounds, the minimum and maximum increments are respectively achieved for μ_{lp} and μ_{pr} wherein the μ_{pr} has the most increment from zero to 0.25. Moreover, when the UB value is increased from 0.5 to 0.75, three envelope bounds $\{\mu_{lp}, \mu_{wt}, \mu_{pr}\}$ encounter relatively high augmentation as depicted in Figure 6 validating a significant enhancement on the robustness of the proposed IGDT-PSC. However, it is worth noting that the least increment occurs for μ_{pv} while the UB is changed from 0.5 to 0.75. Figure 7 illustrates the results of the ROF and also $ROF-DOF$ (as a robustness indice) obtained from the proposed IGDT-PSC model for disparate UB values of $\{0, 0.25, 0.5, 0.75, 1\}$. When the UB is changed from 0 to 0.25, the ROF approaches approximately three times more than its initial value. Despite this noticeable ascent, there is only \$50 difference between the ROF values associated to $UB=0.25$ and $UB=0.5$ as observed in Figure 7.

5. CONCLUSION

In this paper, a robust decision-making framework for the PEV smart charging in a RES-oriented microgrid is suggested. The RESs including PV and WT units are utilized to collaboratively participate in the PEV charging strategy along a day. On the other hand, the proposed model is exposed to intrinsic uncertainty in practice. The daily profiles of load demand, output power of the PV/WT units as well as the electrical energy price are of the essential uncertainty resources which should be inevitably integrated with the proposed model. Since the mentioned uncertainty resources have low-frequency nature, the well-known IGDT technique is utilized to characterize their fluctuating/unpredictable behaviour. Regarding the heterogeneous features of the uncertainty resources as well as the restricted ROF value (controlled by predefined UB), the formulated IGDT-PSC model is a multi-objective optimization problem. Hence, the MOPSO algorithm is utilized to solve this model. Subsequently, the final solution (i.e. optimal envelope bound of the robust zone associated to every uncertain variable) amongst the set of Pareto solutions is determined using a linear max-min fuzzy-based rule.

6. REFERENCES

- Jin, Y., Yang, L., Du, M., Qiang, J., Li, J., Chen, Y. and Tu, J., "Two-scale based energy management for connected plug-in hybrid electric vehicles with global optimal energy consumption and state-of-charge trajectory prediction", *Energy*, Vol. 267, (2023), 126498. doi: 10.1016/j.energy.2022.126498.
- Abdallahman, A. and Zhuang, W., "Dynamic pricing for differentiated pev charging services using deep reinforcement learning", *IEEE Transactions on Intelligent Transportation Systems*, Vol. 23, No. 2, (2020), 1415-1427.

3. Wang, L., Jiang, S., Shi, Y., Du, X., Xiao, Y., Ma, Y., Yi, X., Zhang, Y. and Li, M., "Blockchain-based dynamic energy management mode for distributed energy system with high penetration of renewable energy", *International Journal of Electrical Power & Energy Systems*, Vol. 148, (2023), 108933. doi: 10.1016/j.ijepes.2022.108933.
4. Ullah, K., Hafeez, G., Khan, I., Jan, S. and Javaid, N., "A multi-objective energy optimization in smart grid with high penetration of renewable energy sources", *Applied Energy*, Vol. 299, (2021), 117104. doi: 10.1016/j.apenergy.2021.117104.
5. Ali, A.O., Elmarghany, M.R., Abdelsalam, M.M., Sabry, M.N. and Hamed, A.M., "Closed-loop home energy management system with renewable energy sources in a smart grid: A comprehensive review", *Journal of Energy Storage*, Vol. 50, (2022), 104609. doi: 10.1016/j.est.2022.104609.
6. Wan, Y., Qin, J., Li, F., Yu, X. and Kang, Y., "Game theoretic-based distributed charging strategy for pevs in a smart charging station", *IEEE Transactions on Smart Grid*, Vol. 12, No. 1, (2020), 538-547.
7. Zahedmanesh, A., Muttaqi, K.M. and Sutanto, D., "Active and reactive power control of pev fast charging stations using a consecutive horizon-based energy management process", *IEEE Transactions on Industrial Informatics*, Vol. 17, No. 10, (2020), 6742-6753. doi: 10.1016/j.tii.2020.10.010.
8. Martinez-Piazuelo, J., Quijano, N. and Ocampo-Martinez, C., "Decentralized charging coordination of electric vehicles under feeder capacity constraints", *IEEE Transactions on Control of Network Systems*, Vol. 9, No. 4, (2021), 1600-1610.
9. Caetano, H.O., Desuó, L., Fogliatto, M.S. and Maciel, C.D., "Distribution systems cost reduction based on switches upgrades: A stochastic approach", *Electric Power Systems Research*, Vol. 216, (2023), 108523. doi: 10.1016/j.epsr.2022.108523.
10. Peng, S., Lin, X., Tang, J., Xie, K., Ponci, F., Monti, A. and Li, W., "Probabilistic power flow of ac/dc hybrid grids with addressing boundary issue of correlated uncertainty sources", *IEEE Transactions on Sustainable Energy*, Vol. 13, No. 3, (2022), 1607-1619.
11. Hashemi, S. and Naderi, R., "Application of random radial point interpolation method to foundations bearing capacity considering progressive failure", *International Journal of Engineering, Transactions B: Applications*, Vol. 36, No. 2, (2023), 264-275. doi: 10.5829/IJE.2023.36.02B.07.
12. K., S.H., L., A., R., A., A., M. and Mohamed K., "Fuzzy logic control of maximum power point tracking controller in an autonomous hybrid power generation system by extended kalman filter for battery state of the charge estimation", *International Journal of Engineering, Transactions B: Applications*, Vol. 36, No. 2, (2023), 199-214. doi: 10.5829/IJE.2023.36.02B.02.
13. Maghzi, P., Mohammadi, M., Pasandideh, S. and Naderi, B., "Operating room scheduling optimization based on a fuzzy uncertainty approach and metaheuristic algorithms", *International Journal of Engineering, Transactions B: Applications*, Vol. 35, No. 2, (2022), 258-275. doi: 10.5829/ije.2022.35.02b.01.
14. Günay, E.E., Kremer, G.E.O. and Zarindast, A., "A multi-objective robust possibilistic programming approach to sustainable public transportation network design", *Fuzzy Sets and Systems*, Vol. 422, (2021), 106-129. doi: 10.1016/j.fss.2020.09.007.
15. Tabandeh, A. and Hossain, M.J., "Hybrid scenario-igdt-based congestion management considering uncertain demand response firms and wind farms", *IEEE Systems Journal*, Vol. 16, No. 2, (2021), 3108-3119.
16. Khaloie, H., Vallée, F., Lai, C.S., Toubeau, J.-F. and Hatzigiorgiou, N.D., "Day-ahead and intraday dispatch of an integrated biomass-concentrated solar system: A multi-objective risk-controlling approach", *IEEE Transactions on Power Systems*, Vol. 37, No. 1, (2021), 701-714.
17. Hashemi, S., Arasteh, H., Shafiekhani, M., Kia, M. and Guerrero, J., "Multi-objective operation of microgrids based on electrical and thermal flexibility metrics using the nnc and igdt methods", *International Journal of Electrical Power & Energy Systems*, Vol. 144, (2023), 108617. doi: 10.1016/j.ijepes.2022.108617.
18. Yan, X., Gao, C., Song, M., Chen, T., Ding, J., Guo, M., Wang, X. and Abbas, D., "An igdt-based day-ahead co-optimization of energy and reserve in a vpp considering multiple uncertainties", *IEEE Transactions on Industry Applications*, Vol. 58, No. 3, (2022), 4037-4049.
19. Najafi, A., Pourakbari-Kasmaei, M., Jasinski, M., Lehtonen, M. and Leonowicz, Z., "A medium-term hybrid igdt-robust optimization model for optimal self scheduling of multi-carrier energy systems", *Energy*, Vol. 238, (2022), 121661. doi: 10.1016/j.energy.2021.121661.
20. Izadi, M., Hosseini, S.H., Dehghan, S., Fakharian, A. and Amjadi, N., "Resiliency-oriented operation of distribution networks under unexpected wildfires using multi-horizon information-gap decision theory", *Applied Energy*, (2023), 120536. doi: 10.1016/j.apenergy.2022.120536.
21. Wang, W., Huang, Y., Yang, M., Chen, C., Zhang, Y. and Xu, X., "Renewable energy sources planning considering approximate dynamic network reconfiguration and nonlinear correlations of uncertainties in distribution network", *International Journal of Electrical Power & Energy Systems*, Vol. 139, (2022), 107791. doi: 10.1016/j.ijepes.2021.107791.
22. Fernandes, P.B., Oliveira, R. and Neto, J.F., "Trajectory planning of autonomous mobile robots applying a particle swarm optimization algorithm with peaks of diversity", *Applied Soft Computing*, Vol. 116, (2022), 108108. doi: 10.1016/j.asoc.2021.108108.
23. Jiang, Y., Li, X., Qin, C., Xing, X. and Chen, Z., "Improved particle swarm optimization based selective harmonic elimination and neutral point balance control for three-level inverter in low-voltage ride-through operation", *IEEE Transactions on Industrial Informatics*, Vol. 18, No. 1, (2021), 642-652.
24. Seyyedi, A.Z.G., Armand, M.J., Shahmoradi, S., Rashid, S.M., Akbari, E. and Al-Hassanawy, A.J.K., "Iterative optimization of a bi-level formulation to identify severe contingencies in power transmission systems", *International Journal of Electrical Power & Energy Systems*, Vol. 145, (2023), 108670. doi: 10.1016/j.ijepes.2022.108670.
25. Sepehrzad, R., Rahimi, M.K., Al-Durra, A., Allahbakhshi, M. and Moridi, A., "Optimal energy management of distributed generation in micro-grid to control the voltage and frequency based on pso-adaptive virtual impedance method", *Electric Power Systems Research*, Vol. 208, (2022), 107881. doi: 10.1016/j.asoc.2014.11.052.
26. Yu, D., Lv, Q., Srivastava, G., Chen, C.-H. and Lin, J.C.-W., "Multiobjective evolutionary model of the construction industry based on network planning", *IEEE Transactions on Industrial Informatics*, Vol. 19, No. 2, (2022), 2173-2182.
27. Elsheikh, A.H., Abd Elaziz, M., Ramesh, B., Egiza, M. and Al-qaness, M.A., "Modeling of drilling process of gfrp composite using a hybrid random vector functional link network/parasitism-predation algorithm", *Journal of Materials Research and Technology*, Vol. 14, (2021), 298-311.
28. Karimi, N., Feylizadeh, M.R., Govindan, K. and Bagherpour, M., "Fuzzy multi-objective programming: A systematic literature review", *Expert Systems with Applications*, (2022), 116663. doi: 10.1016/j.eswa.2022.116663.

Persian Abstract

چکیده

امروزه مفهوم خودروهای برقی به عنوان یک ابزار ارزشمند مدیریت انرژی به طور وسیعی در شبکه‌های توزیع هوشمند به کار گرفته شده است. مزیت عمده انرژی پاک و همچنین عملکرد انعطاف‌پذیر خودروهای برقی در هر دو حالت تولیدی/ مصرفی می‌تواند به اندازه کافی استفاده از این فناوری‌های نوظهور را توجیه نماید. علاوه بر این، ویژگی خاص منابع انرژی تجدیدپذیر در قالب مشارکت در برنامه شارژ/دشارژ هوشمند خودروهای برقی منجر به مزایای فنی- اقتصادی قابل توجهی در شبکه‌های هوشمند گردد. اما، تقاضای بار الکتریکی، تولید منابع تجدیدپذیر و همچنین قیمت انرژی الکتریکی با مقوله عدم قطعیت مواجه بوده که می‌بایست به طور مناسبی به آن رسیدگی گردد. به همین جهت، در این مقاله یک مدل بهینه‌سازی غیرقطعی بر پایه نظریه تصمیم‌گیری بر اساس شکاف اطلاعات به منظور تعیین یک برنامه مقاوم برای شارژ هوشمند خودروی برقی ارائه گردیده است. جهت حل مدل چندهدفه و مقاوم پیشنهادی، از نسخه چندهدفه الگوریتم بهینه‌سازی ذرات با هدف تولید یک گروه از پاسخ‌های بهینه نامغلوب (پارتو) استفاده گردیده است. همچنین، پاسخی نهایی از میان پاسخ‌های بهینه پارتو به کمک یک روش فازی خطی تعیین می‌گردد. نتایج شبیه‌سازی برای یک ریزشبکه هوشمند متشکل از یک خودروی برقی، یک گروه از منابع تجدیدپذیر و یک بار الکتریکی، اثربخشی مدل مقاوم پیشنهادی جهت شارژ هوشمند خودروی برقی را تایید می‌کند.



Mapping Hydrothermal Alteration Zones Associated with Copper Mineralization using ASTER Data: A Case Study from the Mirjaveh Area, Southeast Iran

M. Hosseini Nasab*, A. Agah

Mining Department, University of Sistan and Baluchestan, Zahedan, Iran

PAPER INFO

Paper history:

Received 29 May 2022

Received in revised form 22 January 2023

Accepted 03 February 2023

Keywords:

Mirjaveh

Hydrothermal Alteration

Copper Exploration

Principal Components Analysis

Logical Operator

Spectral Angle Mapper

ABSTRACT

In this research, ASTER satellite images and the combined algorithm of band ratios with the method of logical operators with the determination of the threshold limit based on ground, laboratory and experimental studies have been used in order to highlight hydrothermal alterations. Image transformation techniques such as specialized band ratio and principal component analysis are used to map lithologic units and alteration minerals. Supervised classification technique, i.e. Spectral Angle Mapper (SAM) is applied to detect subtle differences between index alteration minerals associated with actual copper localities in the region. The results show that the integration of image transformation techniques and supervised classification of ASTER data with field studies and geochemical exploration is highly effective in targeting new copper mineralization prospects. Copper mineralization is found in siliceous veins that strike from north-south to northeast-southwest across the region. Remote sensing evidence supports the presence of propylitic and argillic alteration, which can be useful for searching for copper-gold type deposits. Kaolinite and pyrophyllite play a role in identifying argillic alteration zones, and muscovite, epidote and chlorite minerals are very important in identifying pyropilitic and phyllic areas and in mineral exploration. Based on remote sensing processing, according to the detection of various alterations (phyllic, pyrophyllite and argillic) in this area, possible copper mineralization was detected in the central part of the studied area. The approach used in this research provides a quick and cost-effective means of initiating comprehensive geological and geochemical exploration programs in the study area and elsewhere in similar areas.

doi: 10.5829/ije.2023.36.04a.11

1. INTRODUCTION

Today, remote sensing is critical in geological projects because it can offer important information on structural examinations such as alteration zone identification, line extraction, geomorphological phenomena, and so on. The use of remote sensing to detect alteration zones for the purpose of mineral exploration goes back to the 1970s [1]. The study of wallrock alteration may give significant information on the mineralization type, characteristics of mineralizing solutions, physicochemical conditions of minerals, and mineralization depth since the same rock-type ores cause the wallrock alteration. Another benefit of researching alteration mineral zones is that they are frequently utilized as a useful guide for mineral exploration owing to their greater extension compared to

mineral horizons and simpler recognition of such zones in the desert because of color and other physical characteristics.

The most common uses of satellite remote sensing data for regional-scale mineral survey projects in the past decade have been mineral discovery via hydrothermal alteration and mapping of structural geology [1-16]. The phyllic alteration region is typically defined by pyrite-quartz-sericite rocks with a high OH-Al absorbance peak at 2.20 μm , which corresponds to Advanced Spaceborne Thermal Emission and Reflection Radiometer band 6 [3]. Supergene processes often influence the argillic alteration region. Plagioclase is chemically changed to different clay minerals (such as montmorillonite, kaolinite, and illite), which collectively exhibit an OH-Al absorbance peak at 2.17 μm , which corresponds to

*Corresponding Author Email: hosseininasab@eng.usb.ac.ir
(M. Hosseini Nasab)

Advanced Spaceborne Thermal Emission and Reflection Radiometer band 5. The mineralogy of magnetite, pyrite, sericite, chlorite, carbonates and epidote in the propylitic alteration region is varied, with Fe-OH, Mg absorbance peaks in the 2.35 μm , which corresponds to Advanced Spaceborne Thermal Emission and Reflection Radiometer band 8 [17].

Multispectral remote sensing sensors including the Advanced Spaceborne Thermal Emission and Reflection Radiometer (ASTER), Landsat Multispectral Scanner (MSS), Landsat Thematic Mapper/Enhanced Thematic Mapper+ (TM/ETM+), HyMap, the Airborne Visible/Infrared Image Spectrometer (AVIRIS), and Hyperion hyperspectral have been successfully and extensively used for mapping alteration mineral assemblages and fractures/faults related to exploring copper deposits, which is a critical component in the discovery of copper resources [1, 18-23].

Since the 1970s, remote sensing data has been an indispensable tool for determining changes. The Landsat series of satellite sensors, including TM, ASTER, and ETM, provide vast and ongoing data for the investigation of a range of ores. The governing concept is that different minerals have different VNIR and SWIR spectrum properties. Crosta and Moore were the first to utilize TM data to derive modification information in the 1980s. Researchers utilized TM pictures to extract mineral alteration information using the band ratio technique and Principal Components Analysis (PCA) toward the end of the twentieth century [24]. Many researchers expanded innovative methods to extract alteration and mineralization information in the early twenty-first century, which resulted in effective prospecting findings [9, 25-35]. Crosta et al. [36] were the first to utilize PCA and ASTER data to extract alteration data in Patagonia, Argentina. Other researchers later used ASTER data to achieve important achievements in a variety of fields [37-45].

A comprehensive remote sensing research for copper exploration in the Mirjaveh area, which is situated in the Nehbandan-Khash zone (in Iran's southeast), has not yet been reported. Based on this, the goals of this research are: (1) to indicate the hydrothermal alteration map of minerals and geological structural features such as faults and fractures related to copper mineralization in Mirjaveh region using ASTER satellite data. (2) to prospect of areas with high potential of copper mineralization using the integration of robust image processing techniques into ASTER spectral and thermal bands. and (3) to develop a cost-effective exploration approach to explore for copper mineralization in the region and other remote areas around the world.

2. GEOLOGIC SETTINGS

The investigated region is found on the geological maps

of Zahedan (1: 250,000) and Mirjaveh (1: 100000), as well as in Iran's Nehbandan-Khash zone (Figure 1).

The western boundary of the Nehbandan-Khash zone is the Nehbandan fault, while the southern edge with the Makran is the Bashagard fault region. The eastern edge of the Nehbandan-Khash zone is west of Afghanistan and Pakistan, and the western border is the Nehbandan fault. This zone is also known as the colored melange zone because of the presence of melange ophiolites in eastern Iran [46]. The Nehbandan-Khash flysch basin, according to recent research [47, 48], is the weld zone between the Afghanistan and Lut block, or the Sistan weld region. The zone is divided by a sedimentary environment (Sefidabeh basin) into two assemblages of ophiolitic melange (Retuk assemblages in the west, but not in the east). The region includes basal volcanic, metamorphic (schistose structure) strata, and intrusive masses, the newest of which is Quaternary alluvial deposits, according to stratigraphic investigations on the map of Mirjaveh (scale 1:500,000) (Figure 2). Due to the temporal range of rock sequences, this region is geologically young, and its Quaternary deposits are made up of a variety of rock sequences. In the research region, the most well-known rock sequences are:

- A) The fault system limits, severely breaks, and deforms tectonic mixes (colored melanges) composed of basaltic to ultrabasic rocks with blocks of serpentine ultrabasic, which frequently protrude in the form of a narrow strip in the region.
- B) Intrusive mass
- C) Metamorphic rocks
- D) Alluvial sediments
- F) Terrigenous sedimentary rocks

2. 1. Geology of Deposit Area The zone is located in the Nehbandan-Khash region, and it contains a tiny portion of the Mirjaveh (scale 1: 100000). Sandstone, siltstone, mudstone, and volcanic sandstone, as well as lime, tuff, and alluvial deposits, make up the majority of the exploration area.

Copper mineralization may be seen in the region in the shape of siliceous veins. The main trend of copper mineralized siliceous veins is north-south to northeast-southwest. Most shale strata and tectonized sandstone, as well as volcanic rocks (p^{sv}), have been cut by these siliceous veins. Mineralization effects are visible in the shape of space-filling in the rock fractures and joints, and the rock orientation is shear. In addition, iron oxides and hydroxides act as cement in the formation of rock.

Mineralizing streaks are often controlled by northeast-southwest faults. With modest halos of argillic and sericite changes, the argillic and siliceous alterations are the most common. Iron hydroxides and potentially copper ores, have formed in the oxidant fraction as a result of secondary reactions.

Faults of various lengths and orientations may be found in this region. Faults having a northeast-southwest

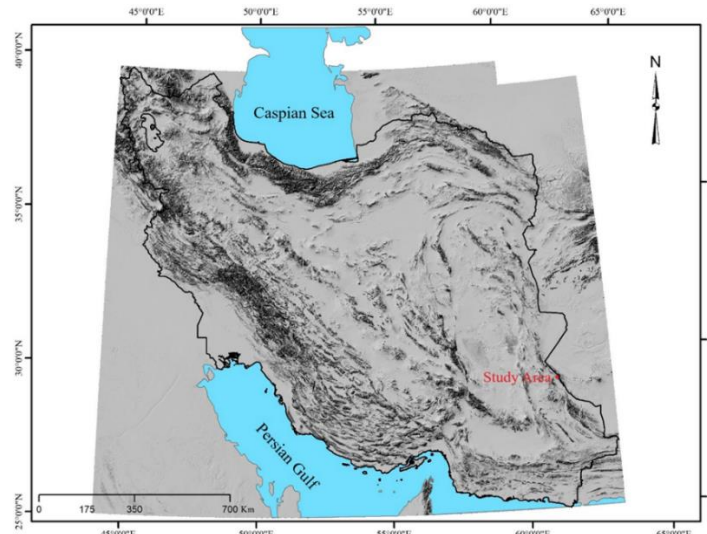


Figure 1. Image of Iran from a digital elevation model (DEM), showing the research area's location

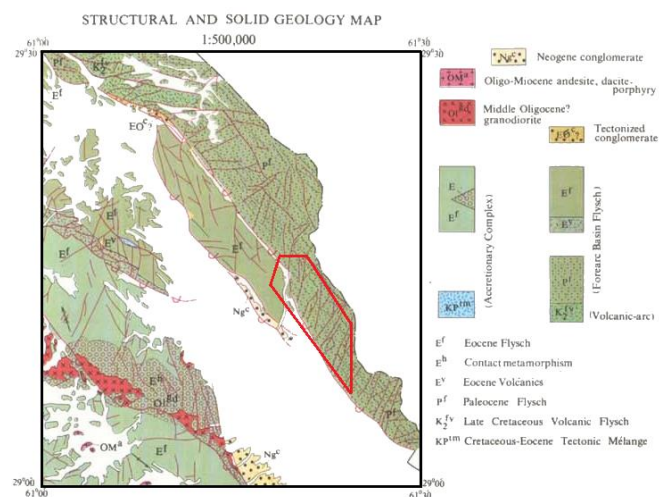


Figure 2. The studied area on a geological 1: 500000 map of Mirjaveh

extension, on the other hand, are more common and primarily regulate mineralization processes.

According to the Mirjaveh map (scale 1: 500000), the research area's outcrop units, from old to new, are as follows:

- Paleocene units:

(P^{sv2}): Tuff, lapilli tuff, mudstone, and sandstone are all found in this unit. The unit's main trend is northwest-southeast, and it has a wide dispersion throughout the area.

(P^{sv4}): This Paleocene unit contains a wide range of rock types, including mudstone, siltstone, green shale, and lime. This unit's main trend is northwest-southeast.

- Eocene units:

(E^{s2}): This Eocene unit contains siltstone, mudstone, and grain-size sandstones with a little olive to grey, purple, or

blue thin-layer lime. The dynamo-thermal technique was used to change this unit. As a result, all of the stones have been somewhat changed. In fine-grained sediments, phyllic and slate tissues associated with sericite growth are common. Sandstones are typically granular, and they may crystallize into schist or coarse quartzite. This unit's main trend is northwest-southeast.

- The Oligocene unit:

(EO^c): This Oligocene unit, which comprises conglomerate and sandstone, has a limited distribution throughout the region. This unit's main trend is northwest-southeast.

- Quaternary units:

(Q^{f1}): This category includes older alluvial fans with vegetation and numerous terraces (t¹).

Alluvial sediments of the present era (Q^{al}):

The Qal mark on the map distinguishes the alluvial sediment samples of the current period that develop around seasonal rivers from other alluvial deposits. These newly formed and deposited sediments are still being produced and deposited.

3. METHODOLOGY

ASTER satellite images are processed for remote sensing interpretation. The following methods demonstrated the ability of ASTER images to provide data for the detection of hydrothermal alteration useful for mineral exploration. In addition, the techniques used in the study area are useful for identifying mineralization zones with high potential. Using logic operator mapping algorithms, PCA and SAM methods, Landsat ASTER image data of the study area were processed to map hydrothermal alteration zones.

3. 1. Remote Sensing Data Characteristics and Per-processing

In 1999, the ASTER sensor was launched as part of the TERRA satellite. This sensor offers 14 distinct bands of spectral data for ground resources. There are three bands in the near-infrared and visible spectra (52%-86%), with a spatial resolution of 15 m and three-dimensional vision provided by the BACKWARD and NADIR components. In addition, there are six bands in the shortwave infrared spectra (1.6-2.43) with a spatial resolution of 30 m. Moreover, there are five bands in the thermal infrared spectra (5.125-11.650), with a spatial resolution of 90 m (Table 1).

The data from ASTER level 1T has been geometrically and radiometrically adjusted. The pixel amounts of the ASTER L1T are the sensor's radiance value. The atmospheric correction module was used to extract surface leaving radiance data and remove the effects of air scattering and absorption. In the present study, the SWIR and VNIR bands of the ASTER were additionally corrected using the Fast Line-of-Sight Atmospheric Analysis of Spectral Hypercubes (FLAASH) algorithm. The ASTER 30-m resolution SWIR bands were resampled to match the 15-m resolution VNIR bands in order to apply the image processing techniques. To retain the original pixel amounts in the resampled pictures, the nearest neighbor resampling technique was used.

3. 2. Image Processing Methods In the present study, various image processing techniques, such as band ratio, false-color combination, and principal component analysis, were utilized to detect changed areas. The features of each method, as well as the outcomes, are given in the following sections.

3. 2. 1. False Color Combination Method The false-color combination was utilized to visually understand the changed regions using satellite data. Due to adsorption, the minerals kaolinite, halloysite, muscovite, dickite, and pyrophyllite (index of phyllic and argillic alteration zones) exhibit a high reflection in SWIR band 4 and a low reflection in band 6 according to standard curves (Figure 3). Furthermore, the minerals chlorite, calcite, and epidote (propylitic zone index) are

TABLE 1. ASTER sensor specifications

Spectrometer	Band	Wavelength (µm)	Radiometric resolution (bits)	Spatial resolution (m)
VNIR	1	0.520-0.600	8	15
	2	0.630-0.690	8	15
	N3	0.780-0.860	8	15
	B3	0.780-0.860	8	15
	4	1.600-1.700	8	30
SWIR	5	2.145-2.185	8	30
	6	2.185-2.225	8	30
	7	2.235-2.285	8	30
	8	2.295-2.365	8	30
	9	2.360-2.430	8	30
TIR	10	8.125-8.475	12	90
	11	8.475-8.825	12	90
	12	8.925-9.275	12	90
	13	10.25-10.95	12	90
	14	10.95-11.65	12	90

reflected the least in band 8 and the most in bands 5 and 4 (Figure 4).

Bands 8, 6, and 4 of ASTER are shown in Figure 5 as a red-green-blue composite. The separation of the various spectral changes and lithological units in the research region is visualized and enhanced using this false-color composite. The chosen bands are the most effective for creating a color composite because they correspond to the absorption characteristics of the argillic, propylitic, and phyllic zones. Figure 5 depicts the majority of lithological units with spectral characteristics linked to Mg-Fe-OH and Al-OH minerals. Because of the high reflection in band 4 and strong absorbance characteristics in band 6, argillic and phyllic alteration zones with significant Al-OH absorbance features (halloysite, muscovite, kaolinite, dickite, and pyrophyllite minerals) show as a pinkish shade. In band 8, propylitic alteration zones (chlorite, epidote, and calcite minerals) are shown in green tone owing to Fe-OH-Mg absorbance characteristics (chlorite, epidote, calcite minerals). Bold pink pixels may be seen in certain regions of this type, which are associated with places with extensive argillic alteration (alunite).

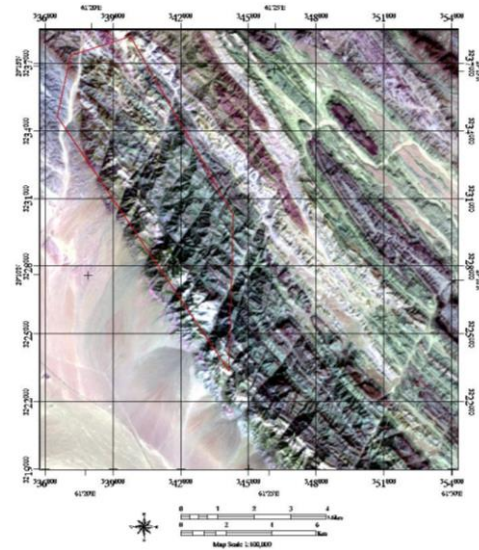


Figure 5. The false-color combination of 468 ASTAR sensors (argillic alteration in pink and propylitic alteration in green) is visible

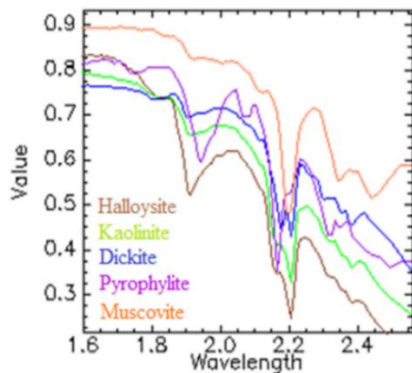


Figure 3. Reflection of argillic and phyllic index minerals in the USGS standard curve

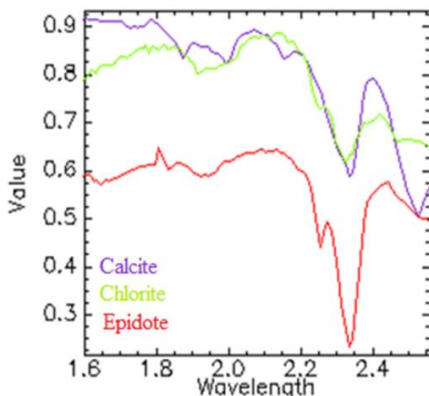


Figure 4. Reflection of propylitic index minerals in the USGS standard curve

3. 2. 2. Logical Operator Mapping Algorithms

For each pixel, the logic operator’s algorithm is specified based on a combination of different band ratios. In this study, for the study range of a series of band ratios to define the algorithm associated with silica-rich hydrothermal zones (hydro silica, chalcedony and opal), Propylitic alteration in relation to carbonate and chlorite-epidote minerals separately, argillic alteration in the presence of alunite-kaolinite minerals and phyllite alteration with sericite-muscovite index minerals have been used algorithms according to Table 2. Finally, the logic operators used for these purposes each provide a definite value of true (value one for the desired pixel) or false (value of zero for the desired pixel) for each pixel of the image. For each algorithm for the target, an image is generated with pixel value values of one and zero, which specifies pixels with a value equal to a target area. Each of these band ratios in the defined algorithm has a specific threshold value. This value is calculated based on statistical methods from relative images using Equation (1) and is used as a suitable coefficient in combining different band ratios in Table 2. It is worth noting that in certain cases this value has been changed due to experience and knowledge of the study area.

$$\text{Threshold} = \mu + 2\sigma \tag{1}$$

In this regard, μ is the mean and σ are the standard deviations.

For all operators defined in the algorithms, a band ratio of 3 to 2 is used to mask the vegetation. In order to map areas with high silica, the band ratio of 4 to 7 in the SWIR range shows areas with high alteration. For silica minerals, regions with the presence of alteration have less

TABLE 2. Logical operator algorithms used to map altered rocks in area study

Alteration type	Algorithm
Phyllic	$(\text{float}(b3)/(b2) \leq 1.22) \text{ and } (\text{float}(b4)/(b6) \geq 1.22) \text{ and } (\text{float}(b5)/(b6) \geq 1.15) \text{ and } (\text{float}(b7)/(b6) \geq 1.02)$
Argillic	$(\text{float}(b3)/(b2) \leq 1.22) \text{ and } (\text{float}(b4)/(b6) \geq 1.22) \text{ and } (\text{float}(b5)/(b6) \leq 1.15) \text{ and } (\text{float}(b7)/(b6) \geq 1.02)$
Propylitic (Calcite-Dolomite)	$(\text{float}(b3)/(b2) \leq 1.22) \text{ and } (\text{float}(b6)/(b8) \geq 0.83) \text{ and } (\text{float}(b13)/(b14) \geq 0.94) \text{ and } (b5 \geq b6) \text{ and } (b7 \geq b8) \text{ and } (b9 \geq b8)$
Propylitic (Epidote-chlorite)	$(\text{float}(b3)/(b2) \leq 1.22) \text{ and } (\text{float}(b6)/(b8) \geq 0.83) \text{ and } (\text{float}(b13)/(b14) \leq 0.94) \text{ and } (\text{float}(b5)/\text{float}(b4+b6)) \text{ and } (b5 \geq b6) \text{ and } (b6 \geq b7) \text{ and } (b7 \geq b8) \text{ and } (b9 \geq b8)$
Silica-rich hydrothermal alteration	$(\text{float}(b3)/(b2) \leq 1.22) \text{ and } (\text{float}(b4)/(b7) \geq 1.24) \text{ and } \text{float}(b13)/(b12) \geq 1.34) \text{ and } (\text{float}(b12)/(b11) \geq 1.13)$

reflection at wavelengths between 2 and 2.4 μm than regions without alteration. The reason for this is the property of adsorption of water molecules in the range of 2.26 to 2.4 micrometers. The bandwidth ratio of the TIR range of ester images to highlight high silica areas using a 13 to 12 bandwidth ratio with absorption at a wavelength of 9.619 μm , so high silica areas are characterized by non-alteration areas by reflecting each pixel in the SWIR area. To identify rocks containing silica-rich hydrothermal alterations, an image with a value of one pixel for target points and zero for other points in the algorithm was prepared. Figure 6 shows the silica-rich hydrothermal zones.

Mapping of propylitic hydrothermal alteration has been characterized using band ratios defined in the SWIR and TIR spectral ranges. The spectral adsorption index of calcite at 11.2 μm and chlorite-epidote with adsorption at 10.2 μm were used to isolate propylitic alteration associated with carbonate and epidote-chlorite minerals (Figure 7). Emission of calcite in the upper 13 band and

is less in band 14, while it is the opposite for epidote and chlorite (Figure 8). In the logical operator defined for the separation of propylitic alteration with two classes of calcite and epidote-chlorite minerals from the band ratio of 6 to 8 in the SWIR range to highlight the adsorption of both groups at a wavelength of 2.31 to 2.33 μm and to separate the two forms. The band ratio of 13 to 14 in the TIR range of the ester image has been revealed by selecting the threshold of 0.94, two groups of indicators of this alteration.

Detection of argillic and phyllite alterations in the SWIR range of ester images has been used to map the OH-Al adsorption spectrum with a band ratio of 4 to 5 at 2.165 μm and a band ratio of 4 to 6 at 2.2 μm , respectively. A band ratio of 5 to 6 has been used to distinguish between the two alterations. The 7 to 6 band ratio is used to display pixels with a wavelength of 2.2 μm for argillic and phyllite alteration. Figures 9 and 10 show the manifestations of these alterations in the study area.

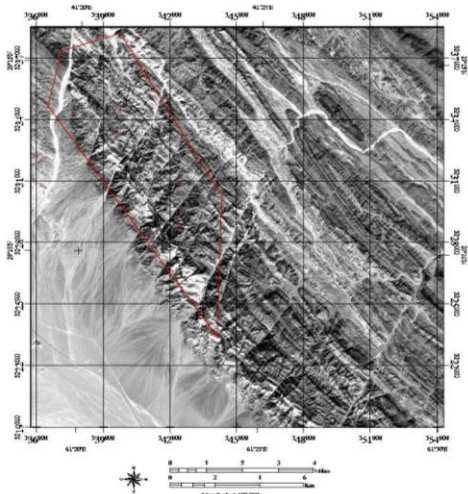


Figure 6. Maps of Silica-rich hydrothermal alteration using logical operator algorithms include

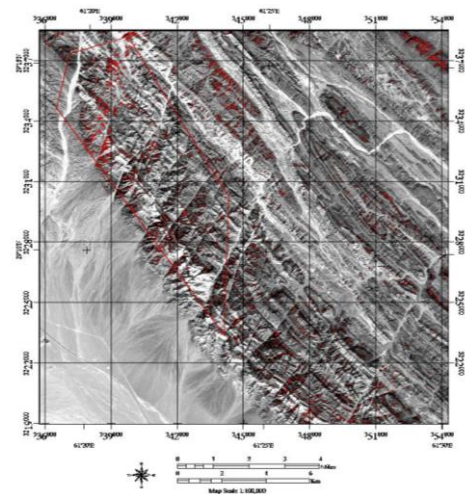


Figure 7. Maps of propylitic rocks (epidote-chlorite) using logical operator algorithms include

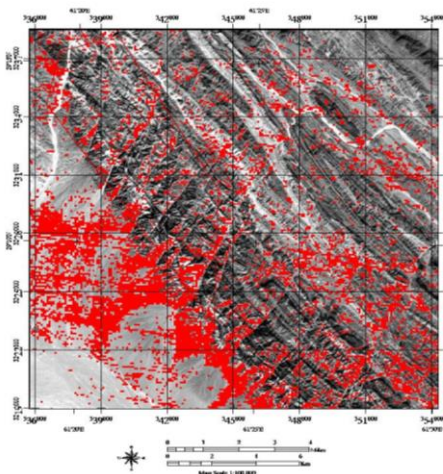


Figure 8. Maps of propylitic rocks (calcite-dolomite) using logical operator algorithms include

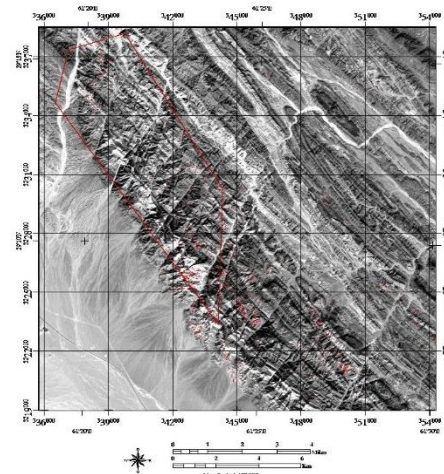


Figure 9. Maps phyllic rocks using logical operator algorithms include

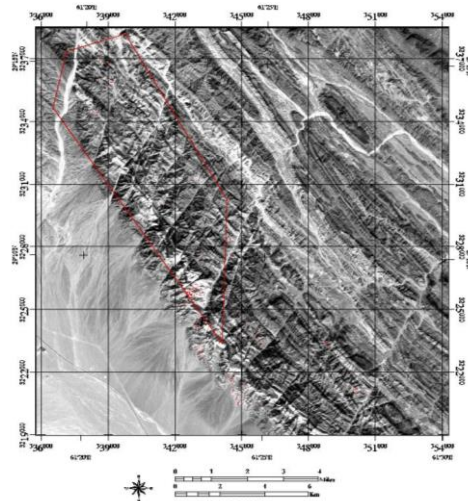


Figure 10. Maps of argillic rocks using logical operator algorithms include

3. 2. 3. Principal Component Analysis Method

By selecting multiple sets of principle components and decreasing dimensions, principal component analysis in ENVI5.3 is a commonly used technique for isolating noise and extracting mineral information. Different minerals that have experienced the same modification have undergone comparable geologic occurrences and have chemical compositions that are similar. In this research, PCA was used to map the particular changes of interest utilizing the ASTER VNIR+SWIR bands. For identifying zones of hydrothermal alteration associated with Cu mineralization, the absorbance characteristics of indicator minerals were examined. A PC picture may improve a mineral or mineral group by including eigenvector loadings that contain unique contributions (sign and magnitude) for absorbance and reflective bands of alteration minerals or mineral groups. The picture tone for the improved target mineral will be bright if the

loading in the reflective band of the mineral is positive and dark if it is negative [49].

In this research, principal component analysis was initially conducted on ASTER bands 1-9. Based on the phyllic modification index minerals' reflection in band 7 and their absorbance in band 6 in principal component analysis, PC5 reveals the most important difference in the eigenvector of these two bands. Thus, this PC was identified to be the most suited PC for the recognition of phyllic alteration and epithermal Cu mineralization. Figure 11 depicts the final picture. In principal component analysis, PC4 was selected as the most appropriate PC to show this alteration based on the reflection of index minerals of argillic alteration (kaolinite) in band 5 and their absorbance in band 6. Figure 12 depicts the picture produced from this study. PC9 was selected as the most appropriate to exhibit this alteration picture produced from this study based on the

reflection of index minerals of propylitic alteration (epidote, chlorite) in band 9 and their absorbance in band 8. The white pixels in this picture indicate propylitic modification (Figure 13). Figure 14 depicts a color picture of PCs obtained for various modifications.

Based on the eigenvector matrix of the ASTER bands obtained from the PCA, the PC4, PC9, and PC5 pictures may include spectral information linked to argillic, propylitic, and phyllic alteration zones (Table 3). From the SWIR and VNIR spectral regions of ASTER, the

eigenvector loadings provide suggestive information about the spectral properties of alteration minerals. As a result, a PC with strong eigenvector loadings for suggestive bands of an alteration mineral or mineral group with opposing signs accentuates that mineral or mineral group as bright or dark pixels in the PC picture. Positive loading in a reflecting band accentuates the alteration mineral by depicting it as bright pixels, while negative loading in a reflective band shows it as dark pixels [49].

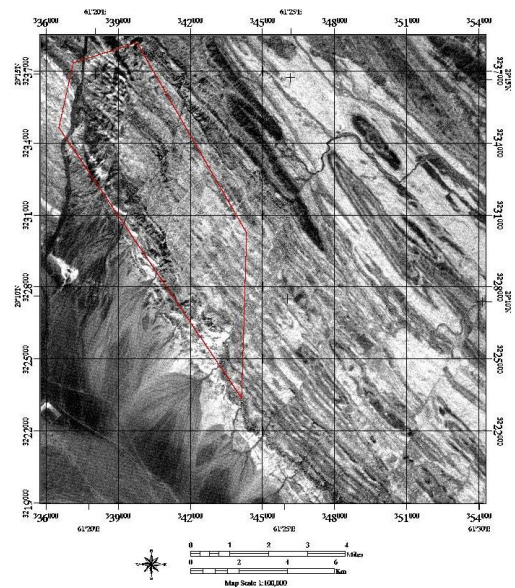


Figure 11. PC5 image of the main components (bright pixels shows phyllic alteration)

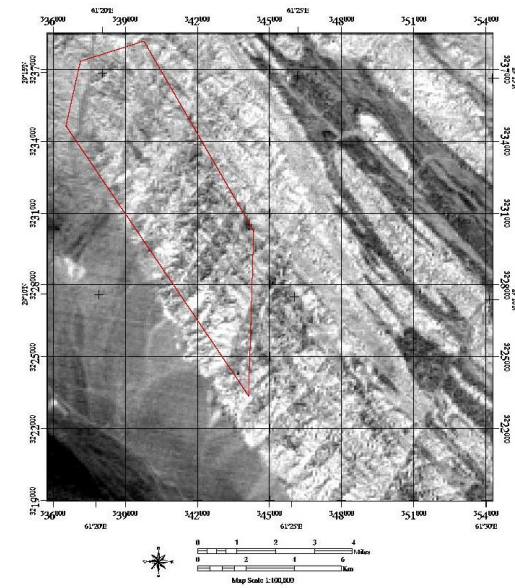


Figure 12. PC4 image of the main components (bright pixels shows argillic alteration)

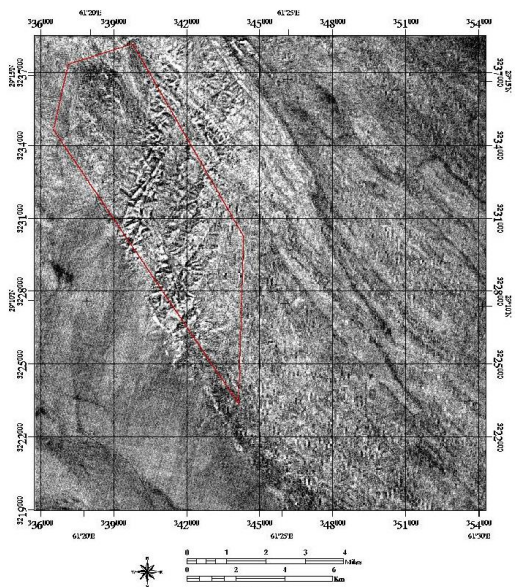


Figure 13. PC9 image of the main components (bright pixels shows propylitic alteration)

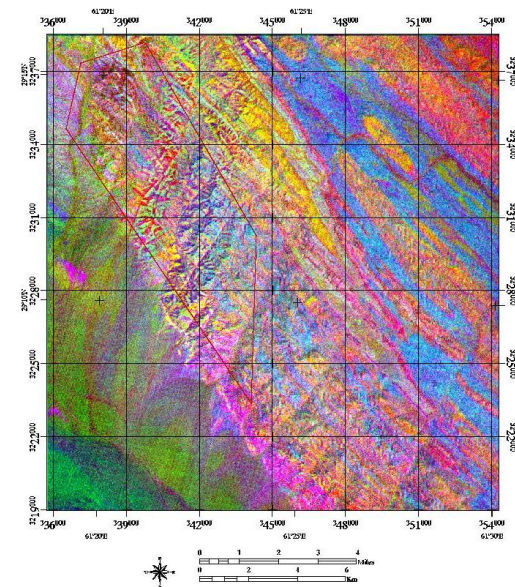


Figure 14. Image of RGB (PC4, PC9, PC5). The red and pink pixels show argillic alteration; the blue part specifies the phyllic alteration. The green pixels show propylitic alteration

TABLE 3. Eigenvector matrix of Principal Components Analysis (PCA) on VNIR and SWIR bands of ASTER data

Eigenvector	Band 1	Band 2	Band 3	Band 4	Band 5	Band 6	Band 7	Band 8	Band 9
PCA1	-0.256	-0.286	-0.291	-0.325	-0.273	-0.275	-0.273	-0.260	-0.320
PCA2	0.159	0.172	0.178	0.186	0.162	0.153	0.151	0.149	0.217
PCA3	0.472	0.510	0.434	-0.195	-0.293	-0.261	-0.217	-0.170	-0.238
PCA4	-0.050	-0.008	0.050	0.134	0.101	-0.013	-0.137	-0.094	0.092
PCA5	-0.509	0.029	0.360	0.218	-0.431	-0.438	0.118	0.366	0.172
PCA6	-0.085	0.052	0.004	0.745	0.138	-0.072	-0.038	-0.187	-0.593
PCA7	0.410	0.019	-0.533	0.222	-0.211	-0.379	0.070	0.162	0.221
PCA8	-0.254	-0.017	0.310	-0.129	0.184	0.087	-0.179	-0.189	0.125
PCA9	-0.039	0.046	-0.043	0.300	-0.012	-0.097	-0.518	-0.440	0.564

3. 2. 4. Spectral Angle Mapper Algorithm (SAM)

The SAM classification method that enables rapid mapping measures the spectral resemblance between the picture spectrums to reflectance spectra reported in the literature [50]. There are three ways to obtain the reference spectra: 1. Taking it from a laboratory, 2. Field measurements, 3. Direct extraction from an image. SAM calculates the spectral semblance by measuring the two spectra's angles, as if they are vectors in n-dimensional space [17]. Small angles forming in-between the two spectra indicate high similitude. Moreover, high angles are indications of dissimilarity. Solar illumination elements do not affect this methodology due to the independency of the angle the two vectors make of their lengths. It takes the arccosine of the dot product between the test spectrums "t" to a reference spectrum "r" with Equation (2) [51]:

$$\alpha = \cos^{-1} \left[\frac{\sum_{i=1}^{nb} t_i r_i}{(\sum_{i=1}^{nb} t_i^2)^{1/2} (\sum_{i=1}^{nb} r_i^2)^{1/2}} \right] \quad (2)$$

where nb is the number of bands, t_i is test spectrum, r_i is reference spectrum.

The SAM method was proposed by Bordman to measure the spectral similarity between the reference spectrum and the spectrum corresponding to each pixel [19]. In the present study, in the SAM method, the spectrum of each pixel of the ester image is compared with specific dimensions called member-end, which is the maximum absorption in the desired mineral. A variety of minerals from the USGS Spectral Library were used to access the member-end.

The spectral properties of the altered minerals in the SWIR bands of the ester images make it possible to determine the hydrothermal alteration zones using the minerals that are specific to that type of alteration. Muscovite, Illite and Cerussite minerals as the index of phyllite zone and kaolinite mineral as the index of argillic zone and Clacite, Dolomite and Epidote minerals as the index of propylitic zone are the characteristic minerals.

The deposits of the area are displayed at a higher magnification around the main map.

In this study, the member-end used for mineral's kaolinite was 6 and 5 bands (2.146-2.225 micrometers) and 6 and 7 bands (2.185-2.285 micrometers). The result of the SAM image is a black and white image whose color intensity is inversely related to the similarity between the member-end number and the spectrum of each particular pixel in the image (Figures 15-18) [52].

3. 3. Field Verification The identified alteration zones from processed ASTER images are verified with in-situ inspection. The field photographs of rock units, copper deposits and the geomorphology in the study area are shown in Figures 19 to 22.

Geological section 1 has a length of 3586 meters and is located in the western corner of the exploration area and has a north-south trend. This profile is composed of volcanic rocks and flysch sediments and is free of mineralization (Figure 19).

The identified alteration zones from processed ASTER images are verified with in-situ inspection. The field photographs of rock units, copper deposits and the geomorphology in the study area are shown in Figures 19 to 22.

Geological section 1 has a length of 3586 meters and is located in the western corner of the exploration area and has a north-south trend. This profile is composed of volcanic rocks and flysch sediments and is free of mineralization (Figure 19).

Geological section 2 has a length of 4546 meters and is located in the center of the exploration area and has a northeast-southwest trend. This profile is composed of volcanic rocks along with flysch units and radiofrequency shales that are intersected by siliceous veins and veins that contain copper mineralization (Figures 20-21).

Geological section 4 has a length of 4060 meters and is located in the west of the exploration area and has a

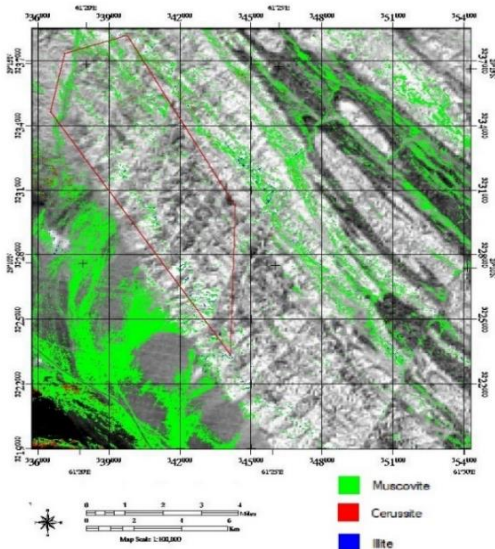


Figure 15. The result of spectral angle mapper (SAM) classification for phyllic zones

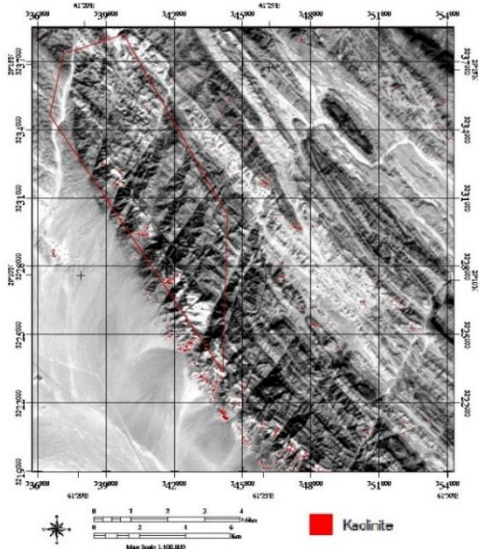


Figure 16. The result of spectral angle mapper (SAM) classification for Argilic zones

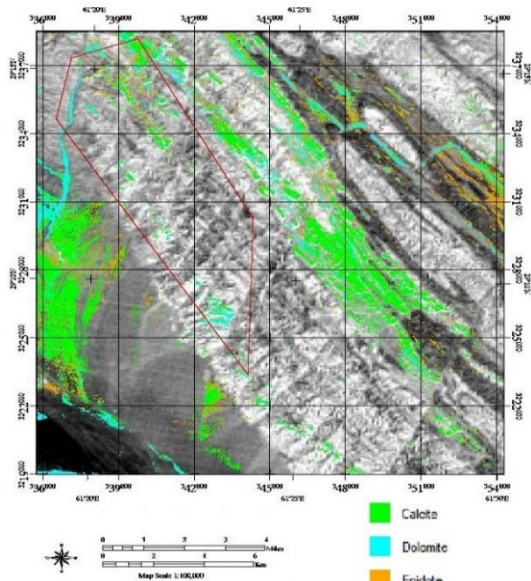


Figure 17. The result of spectral angle mapper (SAM) classification for Propylitic zones

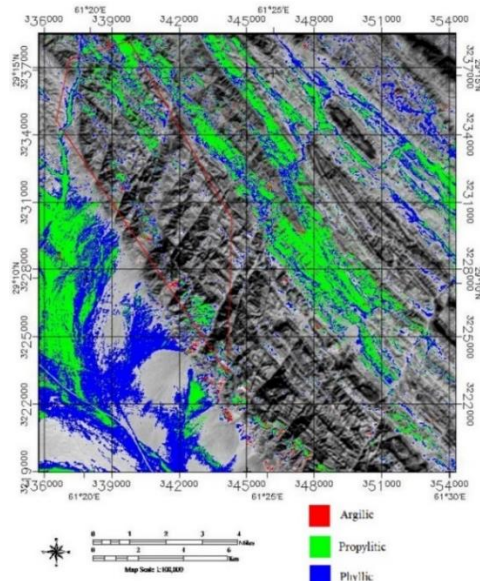


Figure 18. The result of spectral angle mapper (SAM) classification for alteration zones



Figure 19. Units in profile 1



Figure 20. View of copper mineralization in profile 2

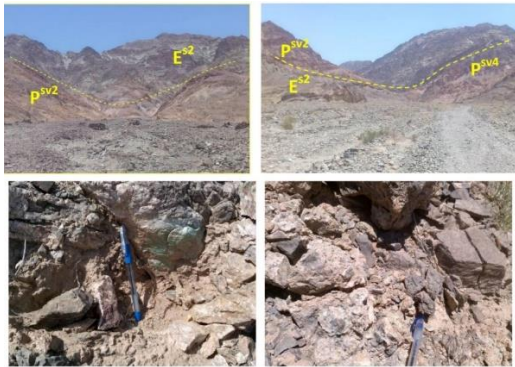


Figure 21. View of copper mineralization in the area along with siliceous veins



Figure 22. Units in profile 3

northeast-southwest trend. This profile is composed of volcanic rocks with flysch units, some of which are cut by siliceous veins and have no mineralization.

Geological section 3 has a length of 4976 meters and is located in the center of the exploration area and has a northwest-southeast trend. This profile is composed of volcanic rocks with flysch units, some of which are cut by siliceous veins and have no mineralization (Figure 22).

4. CONCLUSION

The new information extracted from ASTER specialized logical operators, PCA, and SAM defines several potential zones for copper exploration in Mirjaveh region. Statistical accuracy assessment and fieldwork data also verified the consistency of the results. Finally, based on remote sensing techniques, the diagnosis of potential Cu mineralization in the center portion of the research region was achieved owing to the identification of diverse and widespread changes (phyllic, propylitic, and argillic) in this area. Based on the investigations and their findings, the subsequent phases of exploration in the research area are economically justifiable, and the central, northern, and northwestern portions of the zone are presented as potential locations for exploration stages. This investigation emphasizes how remote sensing data can promote targeting high potential zones

for orogenic copper in Mirjaveh in EW Iran and in similar areas elsewhere.

5. REFERENCES

1. Pour, A.B. and Hashim, M., "The application of aster remote sensing data to porphyry copper and epithermal gold deposits", *Ore Geology Reviews*, Vol. 44, (2012), 1-9. <http://dx.doi.org/10.1016/j.oregeorev.2011.09.009>
2. Tripp, G.I. and Vearncombe, J.R., "Fault/fracture density and mineralization: A contouring method for targeting in gold exploration", *Journal of Structural Geology*, Vol. 26, No. 6-7, (2004), 1087-1108. <http://dx.doi.org/10.1016/j.jsg.2003.11.002>
3. Mars, J.C. and Rowan, L.C., "Regional mapping of phyllic-and argillic-altered rocks in the zagros magmatic arc, iran, using advanced spaceborne thermal emission and reflection radiometer (ASTER) data and logical operator algorithms", *Geosphere*, Vol. 2, No. 3, (2006), 161-186. <https://doi.org/10.1130/GES00044.1>
4. Paez, G.N., Ruiz, R., Guido, D.M., Jovic, S.M. and Schalamuk, I., "Structurally controlled fluid flow: High-grade silver ore-shoots at martha epithermal mine, deseado massif, argentina", *Journal of Structural Geology*, Vol. 33, No. 5, (2011), 985-999. <https://doi.org/10.1016/j.jsg.2011.02.007>
5. Pour, A.B. and Hashim, M., "Identification of hydrothermal alteration minerals for exploring of porphyry copper deposit using aster data, se iran", *Journal of Asian Earth Sciences*, Vol. 42, No. 6, (2011), 1309-1323. <http://dx.doi.org/10.1016/j.jseas.2011.07.017>
6. Rossetti, F., Aldega, L., Tecce, F., Balsamo, F., Billi, A. and Brilli, M., "Fluid flow within the damage zone of the boccheggiano extensional fault (larderello-travale geothermal field, central italy): Structures, alteration and implications for hydrothermal mineralization in extensional settings", *Geological Magazine*, Vol. 148, No. 4, (2011), 558-579. <http://dx.doi.org/10.1017/S001675681000097X>
7. Pour, A.B. and Hashim, M., "Identifying areas of high economic-potential copper mineralization using aster data in the urumieh-dokhtar volcanic belt, iran", *Advances in Space Research*, Vol. 49, No. 4, (2012), 753-769. <http://dx.doi.org/10.1016/j.asr.2011.11.028>
8. Alimohammadi, M., Alirezaei, S. and Kontak, D.J., "Application of aster data for exploration of porphyry copper deposits: A case study of daraloo-sarmeshk area, southern part of the kerman copper belt, iran", *Ore Geology Reviews*, Vol. 70, (2015), 290-304. <https://doi.org/10.1016/j.oregeorev.2015.04.010>
9. Safari, M., Maghsoudi, A. and Pour, A.B., "Application of landsat-8 and aster satellite remote sensing data for porphyry copper exploration: A case study from shahr-e-babak, kerman, south of iran", *Geocarto International*, Vol. 33, No. 11, (2018), 1186-1201. <https://doi.org/10.1080/10106049.2017.1334834>
10. Ahmadirouhani, R., Karimpour, M.-H., Rahimi, B., Malekzadeh-Shafaroudi, A., Pour, A.B. and Pradhan, B., "Integration of spot-5 and aster satellite data for structural tracing and hydrothermal alteration mineral mapping: Implications for cu-au prospecting", *International Journal of Image and Data Fusion*, Vol. 9, No. 3, (2018), 237-262. <https://doi.org/10.1080/19479832.2018.1469548>
11. Ge, W., Cheng, Q., Jing, L., Armenakis, C. and Ding, H., "Lithological discrimination using aster and sentinel-2a in the shibanjing ophiolite complex of beishan orogenic in inner mongolia, china", *Advances in Space Research*, Vol. 62, No. 7, (2018), 1702-1716. https://ui.adsabs.harvard.edu/link_gateway/2018AdSpR..62.1702G/doi:10.1016/j.asr.2018.06.036

12. Yazdi, Z., Jafari Rad, A., Aghazadeh, M. and Afzal, P., "Alteration mapping for porphyry copper exploration using aster and quickbird multispectral images, sonajeel prospect, nw iran", *Journal of the Indian Society of Remote Sensing*, Vol. 46, No., (2018), 1581-1593. <https://doi.org/10.1007/s12524-018-0811-1>
13. Mujabar, P.S. and Dajkumar, S., "Mapping of bauxite mineral deposits in the northern region of saudi arabia by using advanced spaceborne thermal emission and reflection radiometer satellite data", *Geo-spatial Information Science*, Vol. 22, No. 1, (2019), 35-44. <https://doi.org/10.1080/10095020.2018.1530857>
14. Sheikhrasimi, A., Pour, A.B., Pradhan, B. and Zoheir, B., "Mapping hydrothermal alteration zones and lineaments associated with orogenic gold mineralization using aster data: A case study from the sanandaj-sirjan zone, iran", *Advances in Space Research*, Vol. 63, No. 10, (2019), 3315-3332. <http://dx.doi.org/10.1016/j.asr.2019.01.035>
15. Son, Y.-S., Kim, K.-E., Yoon, W.-J. and Cho, S.-J., "Regional mineral mapping of island arc terranes in southeastern mongolia using multi-spectral remote sensing data", *Ore Geology Reviews*, Vol. 113, (2019), 103106. <https://doi.org/10.1016/j.oregeorev.2019.103106>
16. Chatteraj, S.L., Prasad, G., Sharma, R.U., van der Meer, F.D., Guha, A. and Pour, A.B., "Integration of remote sensing, gravity and geochemical data for exploration of cu-mineralization in alwar basin, rajasthan, india", *International Journal of Applied Earth Observation and Geoinformation*, Vol. 91, (2020), 102162. <https://doi.org/10.1016/j.jag.2020.102162>
17. Rowan, L.C. and Mars, J.C., "Lithologic mapping in the mountain pass, california area using advanced spaceborne thermal emission and reflection radiometer (ASTER) data", *Remote Sensing of Environment*, Vol. 84, No. 3, (2003), 350-366. [https://doi.org/10.1016/S0034-4257\(02\)00127-X](https://doi.org/10.1016/S0034-4257(02)00127-X)
18. Tangestani, M. and Moore, F., "Comparison of three principal component analysis techniques to porphyry copper alteration mapping: A case study, meiduk area, kerman, iran", *Canadian Journal of Remote Sensing*, Vol. 27, No. 2, (2001), 176-182. <https://doi.org/10.1080/07038992.2001.10854931>
19. Kruse, F.A., Boardman, J.W. and Huntington, J.F., "Comparison of airborne hyperspectral data and eo-1 hyperion for mineral mapping", *IEEE transactions on Geoscience and Remote Sensing*, Vol. 41, No. 6, (2003), 1388-1400. <https://doi.org/10.1109/TGRS.2003.812908>
20. Gersman, R., Ben-Dor, E., Beyth, M., Avigad, D., Abraha, M. and Kibreab, A., "Mapping of hydrothermally altered rocks by the eo-1 hyperion sensor, northern danakil depression, eritrea", *International Journal of Remote Sensing*, Vol. 29, No. 13, (2008), 3911-3936. <https://doi.org/10.1080/01431160701874587>
21. Bedini, E., Van Der Meer, F. and Van Ruitenbeek, F., "Use of hmap imaging spectrometer data to map mineralogy in the rodalquilar caldera, southeast spain", *International Journal of Remote Sensing*, Vol. 30, No. 2, (2009), 327-348. <https://doi.org/10.1080/01431160802282854>
22. Mars, J.C., "Mineral and lithologic mapping capability of worldview 3 data at mountain pass, california, using true-and false-color composite images, band ratios, and logical operator algorithms", *Economic Geology*, Vol. 113, No. 7, (2018), 1587-1601. <https://doi.org/10.5382/econgeo.2018.4604>
23. Bolouki, S.M., Ramazi, H.R., Maghsoudi, A., Beiranvand Pour, A. and Sohrabi, G., "A remote sensing-based application of bayesian networks for epithermal gold potential mapping in aharasbaran area, nw iran", *Remote Sensing*, Vol. 12, No. 1, (2019), 105. <https://doi.org/10.5382/econgeo.2018.4604>
24. Xiao-chang, M., Wen-can, L., Jian-guo, D. and Wei, X., "Comparison between etm+ and aster data for extraction of alteration information: A case study of fenghuangshan orefield, tongling, anhui province", *Geoscience*, Vol. 19, No. 2, (2005), 309.
25. WU, Z., GUO, F., LIU, L., Xie, C. and Jiang, Y., "Application of remote sensing alteration anomaly extraction with the method of composite algorithm based on tm/etm images", *Geology and Exploration*, Vol. 49, No. 3, (2013), 511-522.
26. Pilon, S., Bihong, F., Yuanxu, M. and Qiang, G., "Remote sensing detection for surface anomalies related to hydrocarbon in bashibulake uranium ore, southern tianshan", in 2016 IEEE International Geoscience and Remote Sensing Symposium (IGARSS), IEEE., (2016), 6374-6377.
27. Adiri, Z., El Harti, A., Jellouli, A., Lhissou, R., Maacha, L., Azmi, M., Zouhair, M. and Bachaoui, E.M., "Comparison of landsat-8, aster and sentinel 1 satellite remote sensing data in automatic lineaments extraction: A case study of sidi flah-bouskour inlier, moroccan anti atlas", *Advances in Space Research*, Vol. 60, No. 11, (2017), 2355-2367. <http://dx.doi.org/10.1016/j.asr.2017.09.006>
28. Rajendran, S. and Nasir, S., "Characterization of aster spectral bands for mapping of alteration zones of volcanogenic massive sulphide deposits", *Ore Geology Reviews*, Vol. 88, No., (2017), 317-335. <https://doi.org/10.1016/j.oregeorev.2017.04.016>
29. Govil, H., Gill, N., Rajendran, S., Santosh, M. and Kumar, S., "Identification of new base metal mineralization in kumaon himalaya, india, using hyperspectral remote sensing and hydrothermal alteration", *Ore Geology Reviews*, Vol. 92, (2018), 271-283. <https://doi.org/10.1016/j.oregeorev.2017.11.023>
30. Abubakar, A.J.a., Hashim, M. and Pour, A.B., "Remote sensing satellite imagery for prospecting geothermal systems in an aseismic geologic setting: Yankari park, nigeria", *International Journal of Applied Earth Observation and Geoinformation*, Vol. 80, (2019), 157-172. <https://doi.org/10.1016/j.jag.2019.04.005>
31. Guha, A., Yamaguchi, Y., Chatterjee, S., Rani, K. and Vinod Kumar, K., "Emittance spectroscopy and broadband thermal remote sensing applied to phosphorite and its utility in geoexploration: A study in the parts of rajasthan, india", *Remote Sensing*, Vol. 11, No. 9, (2019), 1003. <https://doi.org/10.3390/rs11091003>
32. Pour, A.B., Hashim, M., Hong, J.K. and Park, Y., "Lithological and alteration mineral mapping in poorly exposed lithologies using landsat-8 and aster satellite data: North-eastern graham land, antarctic peninsula", *Ore Geology Reviews*, Vol. 108, (2019), 112-133. <http://dx.doi.org/10.1016/j.oregeorev.2017.07.018>
33. Beiranvand Pour, A., Park, Y., Crispini, L., Läufer, A., Kuk Hong, J., Park, T.-Y.S., Zoheir, B., Pradhan, B., Muslim, A.M. and Hossain, M.S., "Mapping listvenite occurrences in the damage zones of northern victoria land, antarctica using aster satellite remote sensing data", *Remote Sensing*, Vol. 11, No. 12, (2019), 1408. <https://doi.org/10.3390/rs11121408>
34. Zoheir, B., El-Wahed, M.A., Pour, A.B. and Abdelnasser, A., "Orogenic gold in transpression and transtension zones: Field and remote sensing studies of the barramiya-mueilha sector, egypt", *Remote Sensing*, Vol. 11, No. 18, (2019), 2122. <https://doi.org/10.3390/rs11182122>
35. Zoheir, B., Emam, A., Abdel-Wahed, M. and Soliman, N., "Multispectral and radar data for the setting of gold mineralization in the south eastern desert, egypt", *Remote Sensing*, Vol. 11, No. 12, (2019), 1450. <https://doi.org/10.3390/rs11121450>
36. Crosta, A., De Souza Filho, C., Azevedo, F. and Brodie, C., "Targeting key alteration minerals in epithermal deposits in patagonia, argentina, using aster imagery and principal component analysis", *International Journal of Remote Sensing*, Vol. 24, No. 21, (2003), 4233-4240. <https://doi.org/10.1080/0143116031000152291>
37. Dai, J.-J., Wang, R.-J., Wang, R.-S., Qu, X.-M., Zhao, Y.-Y. and Xin, H.-B., "Porphyry copper deposit prognosis in the middle part of the bangong co-nuijiang river metallogenic belt in tibet based

- on alteration information extraction", *Diqiu Xuebao(Acta Geoscientica Sinica)*, Vol. 33, No. 5, (2012), 755-762. doi: <https://doi.org/10.1111/rge.12154>
38. Yang, R., Li, Z. and Cheng, X., "Information extraction of typical alteration mineral assemblage in porphyry copper using aster satellite data, arequipa province of south peru", *Journal of Geo-Information Science*, Vol. 14, No. 3, (2012), 411-418. <https://doi.org/10.3724/SP.J.1047.2012.00411>
 39. Zoheir, B. and Emam, A., "Field and aster imagery data for the setting of gold mineralization in western allaqi-heiani belt, egypt: A case study from the haimur deposit", *Journal of African Earth Sciences*, Vol. 99, (2014), 150-164. <https://doi.org/10.1016/j.jafrearsci.2013.06.006>
 40. Kumar, C., Shetty, A., Raval, S., Sharma, R. and Ray, P.C., "Lithological discrimination and mapping using aster swir data in the udaipur area of rajasthan, india", *Procedia Earth and Planetary Science*, Vol. 11, (2015), 180-188. <https://doi.org/10.1016/j.proeps.2015.06.022>
 41. Eldosouky, A.M., Abdelkareem, M. and Elkhateeb, S.O., "Integration of remote sensing and aeromagnetic data for mapping structural features and hydrothermal alteration zones in wadi allaqi area, south eastern desert of egypt", *Journal of African Earth Sciences*, Vol. 130, (2017), 28-37. <https://doi.org/10.1016/j.jafrearsci.2017.03.006>
 42. Fereydooni, H. and Mojeddfar, S., "A directed matched filtering algorithm (dmf) for discriminating hydrothermal alteration zones using the aster remote sensing data", *International Journal of Applied Earth Observation and Geoinformation*, Vol. 61, (2017), 1-13. <https://doi.org/10.1016/j.jag.2017.04.010>
 43. Beiranvand Pour, A., Park, T.-Y.S., Park, Y., Hong, J.K., Zoheir, B., Pradhan, B., Ayoobi, I. and Hashim, M., "Application of multi-sensor satellite data for exploration of zn-pb sulfide mineralization in the franklinian basin, north greenland", *Remote Sensing*, Vol. 10, No. 8, (2018), 1186. doi: 10.3390/rs10081186.
 44. Noori, L., Pour, A.B., Askari, G., Taghipour, N., Pradhan, B., Lee, C.-W. and Honarmand, M., "Comparison of different algorithms to map hydrothermal alteration zones using aster remote sensing data for polymetallic vein-type ore exploration: Toroud-chahshirin magmatic belt (TCMB), north iran", *Remote Sensing*, Vol. 11, No. 5, (2019), 495. doi: 10.3390/rs11050495.
 45. Chen, Q., Zhao, Z., Jiang, Q., Zhou, J.-X., Tian, Y., Zeng, S. and Wang, J., "Detecting subtle alteration information from aster data using a multifractal-based method: A case study from wuliang mountain, sw china", *Ore Geology Reviews*, Vol. 115, (2019), 103182. doi: 10.1016/j.oregeorev.2019.103182.
 46. Stöcklin, J., Eftekharneshad, J. and Hushmandzadeh, A., *Central lut reconnaissance east iran, geological survey of iran*. 1972, Report.
 47. Camp, V. and Griffis, R., "Character, genesis and tectonic setting of igneous rocks in the sisthan suture zone, eastern iran", *Lithos*, Vol. 15, No. 3, (1982), 221-239. doi: 10.1016/0024-4937(82)90014-7.
 48. Tirrul, R., Bell, I., Griffis, R. and Camp, V., "The sisthan suture zone of eastern iran", *Geological Society of America Bulletin*, Vol. 94, No. 1, (1983), 134-150. [http://dx.doi.org/10.1130/0016-6066\(1983\)94<134:TSSZOE>2.0.CO;2](http://dx.doi.org/10.1130/0016-6066(1983)94<134:TSSZOE>2.0.CO;2)
 49. Beygi, S., Talovina, I.V., Tadayon, M. and Pour, A.B., "Alteration and structural features mapping in kacho-mesqal zone, central iran using aster remote sensing data for porphyry copper exploration", *International Journal of Image and Data Fusion*, Vol. 12, No. 2, (2021), 155-175. doi: 10.1080/19479832.2020.1838628.
 50. Hunter, E. and Power, C., "An assessment of two classification methods for mapping thames estuary intertidal habitats using casi data", *International Journal of Remote Sensing*, Vol. 23, No. 15, (2002), 2989-3008. <https://doi.org/10.1080/01431160110075596>
 51. De Carvalho, O.A. and Meneses, P.R., "Spectral correlation mapper (scm): An improvement on the spectral angle mapper (sam)", in *Summaries of the 9th JPL Airborne Earth Science Workshop*, JPL Publication 00-18, JPL publication Pasadena, CA, USA. Vol. 9, No. Issue, (2000), 2.
 52. Gabr, S., Ghulam, A. and Kusky, T., "Detecting areas of high-potential gold mineralization using aster data", *Ore Geology Reviews*, Vol. 38, No. 1-2, (2010), 59-69. doi: <https://doi.org/10.1016/j.oregeorev.2010.05.007>

Persian Abstract

چکیده

در این تحقیق از تصاویر ماهواره‌ای ASTER و الگوریتم ترکیبی نسبت‌های باند با روش عملگرهای منطقی با تعیین حد آستانه بر اساس مطالعات میدانی، آزمایشگاهی و تجربی به منظور برجسته‌سازی دگرسانی‌های هیدروترمال استفاده شده است. تکنیک‌های تبدیل تصویر مانند نسبت باند تخصصی و تحلیل مؤلفه‌های اصلی برای نقشه‌برداری واحدهای سنگ‌شناسی و کانی‌های دگرسانی استفاده می‌شوند. تکنیک طبقه‌بندی نظارت‌شده، نقشه‌برداری زاویه طیفی (SAM) برای تشخیص تفاوت‌های ظریف بین کانی‌های شاخص دگرسانی مرتبط با محل‌های واقعی مس در منطقه اعمال می‌شود. نتایج نشان می‌دهد که ادغام تکنیک‌های تبدیل تصویر و طبقه‌بندی نظارت‌شده داده‌های ASTER با مطالعات میدانی و اکتشافات ژئوشیمیایی در پی جوی کانی‌سازی جدید مس بسیار موثر است. کانی‌سازی مس در محدوده همراه با رگه‌های سیلیسی مشاهده می‌شود. روند عمومی رگه‌های سیلیسی حاوی کانی‌زایی مس شمال-جنوبی تا شمال شرقی-جنوب غربی می‌باشد. شواهد دورسنجی وجود دگرسانی پروپلیتی و آرژیلیک را تایید می‌کند که می‌تواند برای پی‌جویی کانسارهای نوع مس-طلا مفید باشد. کائولینیت و پیروفیلیت در شناسایی زون‌های دگرسانی آرژیلیک نقش دارند و کانی‌های مسکوئیت، اپیدوت و کلریت در شناسایی زون‌های پیروفیلیتیک و فیلیک و در بحث اکتشاف مواد معدنی اهمیت فراوانی دارند. بر اساس پردازش‌های دورسنجی، با توجه به تشخیص دگرسانی‌های مختلف (فیلیک، پیروفیلیت و آرژیلیک) وسیع در این ناحیه، تشخیص کانی‌زایی احتمالی مس در بخش میانی منطقه مورد مطالعه حاصل شد. رویکرد مورد استفاده در این تحقیق ابزاری سریع و مقرون به صرفه برای شروع برنامه‌های اکتشافی جامع زمین‌شناسی و ژئوشیمیایی در منطقه مورد مطالعه و در مناطق مشابه فراهم می‌کند.



Experimental Investigation on the Effect of Flow Rate and Load on the Hydrodynamic Behavior and Performance of an Archimedes Screw Turbine

M. Zamani, R. Shafaghat*, B. Alizadeh Kharkeshi

Sea-Based Energy Research group, Babol Noshirvani University, Babol, Iran

PAPER INFO

Paper history:

Received 03 December 2022

Received in revised form 25 December 2022

Accepted 26 December 2022

Keywords:

Hydro Power

Experimental Study

Archimedes Screw Turbine

Performance

Economic Analysis

ABSTRACT

One of the best solutions to overcome problems caused by fossil fuel consumption is using renewable energy. In this research, effect of flow rate and load on the performance of an Archimedes turbine was experimentally studied. At first, Archimedes turbine with optimal size was made using 3D printer technology. Then it was placed in the river simulation setup. After the calibration and uncertainty analysis, tests were performed for three flow rates and five electrical resistances. The results showed that increasing the flow rate leads to a rise in power, torque, and angular velocity of the turbine, but it leads to a non-linear behavior in efficiency. On the other hand, an increase in electrical load has also led to a decrease in converter performance for all conditions. In addition, by implementing π -Buckingham theory, the converter's hydrodynamic behavior was studied by using Reynolds numbers, dimensionless flow, and power coefficient. The results showed that an increase in Reynolds number leads to a decrease in power coefficient. However, an increase in dimensionless flow increases the power coefficient first and then decreases (nonlinear behavior). In addition, the Archimedes screw turbine was also studied from an economic point of view, and the results showed that increasing discount rate leads to an increase in discounted payback period, and in the worst case, the payback period is 3.09 years, and in the best case, it is 1.6 years. Also, the construction of the Archimedean screw turbine in Iran can save currency for \$1439.5.

doi: 10.5829/ije.2023.36.04a.12

1. INTRODUCTION

Fossil fuels can cause many problems and have side effects including global warming [1], increased pollutants [2] and greenhouse gases [3]. Also, the usable sources of these fuels are limited. Therefore, renewable energies such as geothermal, solar, wind, biomass, wave energy, and hydropower are solutions to tackle the fossil fuel's problems and help to preserve the resources of fossil fuels [4].

Archimedes hydro screw turbine can generate power from the river currents. This turbine consists of a cylindrical shaft along with some spiral surfaces called blades and is a screw-like structure. The water flow enters the turbine from the top and moves along the screw between the blades, and this movement of the water flow causes the shaft to rotate and generate power. These

turbines have high efficiency in the low head and flow rates. Archimedes screw turbines can be installed and operated in rivers, channels, sloping places, dams, and places with variable currents [5].

Due to the ancient history of Archimedes screw turbine, many studies have been done on these turbines. The studies carried out in the field of Archimedes screw turbines are divided into two parts: studies related to changes in flow parameters and studies related to turbine geometric parameters. Nagel [6] presented an analytical and experimental equation for the rotational speed and the leakage width to avoid the decrease in efficiency due to the flow turbulence. Rorres [7] maximized the volume of water in each bucket in the Archimedes screw turbine. He has theoretically presented optimal dimensionless ratios for turbine radius, pitch, and water volume in the form of a table. Muller and Senior [8] compared the

*Corresponding Author Institutional Email: rshafaghat@NIT.ac.ir
(R. Shafaghat)

experimental results and the theoretical model of the Archimedes screw turbine to determine the effective parameters of turbine efficiency. The results showed that by increasing the turbine's rotational speed, decreasing the horizon angle and increasing the input flow rate, the efficiency of the turbine rises. Raza et al. [9] simulated this turbine in MATLAB with the help of mathematical equations. The simulation results showed that with an increase in the input flow rate to the turbine, the turbine's rotational speed and output power rise. Rohmer et al. [10] experimentally and numerically studied an Archimedes screw turbine model using the model presented by Rorres [7]. He has found that efficiency is a function of flow rate and torque. Hizhar et al. [11] studied the effect of flow rate and installation angle on the output power for an Archimedes screw turbine experimentally. Power increases with the growth of the flow rate, and also, at low flow rates, the efficiency declines with an increase in the turbine angle. Mulana et al. [12] conducted an experimental study on the maximum power and torque of Archimedes screw turbine and showed that maximum efficiency occurs at an average flow rate. Krystyadi et al. [13] used a governor to set the turbine's rotational speed in an optimal range to maximize efficiency. Abdullah et al. [14] experimentally and numerically studied the effect of changing the flow rate and installation angle on turbine performance. The results showed that with an increase in the input flow rate, the rotational speed and the output power always increase, but efficiency shows a non-linear behavior. Bustomi et al. [15] experimentally studied the mechanical and electrical characteristics of different inlet flow rates. The results showed that the rotational speed, torque and output power of the turbine increases with the rise in flow rate but an increase in electrical resistance leads to a decrease in the mentioned characteristics. Cahyono et al. [16] conducted an experimental study with the aim of determining the effect of changing the angle of Archimedes turbine on the rotational speed and output power of the turbine. The power shows a non-linear trend by slope. In 2022, Darmono and Pranoto [17] carried out a numerical simulation of the Archimedes screw turbine to find the effect of the number of blades on the torque and output power of the turbine. Three turbine models with nine, six and four blades were simulated, and the results showed that increasing the number of blades rises the torque and output power of the turbine, but the technical and economic limitations regarding increasing the number of blades should be considered.

Based on past studies, suitable analytical and experimental equations for the optimal design of Archimedes screw turbine have been presented. However, past studies have mainly relied on studying the performance characteristics of the turbine, such as rotational speed, torque and power. The study of turbine performance according to dimensionless numbers is not

presented. In this regard, dimensionless numbers affecting the performances of the turbine were extracted using the π -Buckingham theory, and the effect of dimensionless variables on the power coefficient was studied. For this purpose, an optimal Archimedes screw turbine was designed and built with the help of 3D printer technology. Also, to carry out the tests, a laboratory facility was designed and built to simulate the conditions of the river in the sea-based energy research group of Babol Noshirvani University of Technology. The effect of flow rate and electrical resistance on turbine performance characteristics such as rotational speed, torque, power, efficiency, blade tip speed ratio and power coefficient were studied. Then, by using Froude scaling method, the laboratory study results were scaled to the prototype model. Finally, the economic analysis for the payback period was performed.

2. EXPERIMENTAL STUDY

2. 1. Turbine Design This research aims to design an Archimedes screw turbine that can produce electricity for low-power applications. For the optimal design of the turbine, the model presented by Rorres [7] has been used.

$$0 \leq R_i \leq R_o \quad (1)$$

$$0 \leq R_i \leq \frac{2\pi R_o}{k} \quad (2)$$

$$p = \frac{R_i}{R_o} \quad (3)$$

$$\lambda = \frac{kp}{2\pi R_o} \quad (4)$$

The screw geometry is determined according to two types of parameters. The input parameters include the inner radius (R_i), pitch (p), and the number of blades (N) and the output parameters include radius ratio (ρ), pitch ratio (λ), and volume ratio (v) [18].

The input parameters of the turbine have a maximum outer diameter of 10 cm, a maximum length of 17 cm, and 4 blades. This optimal design for maximizing water volume in one screw cycle is calculated using Equation (5).

$$V_{tmax} = \pi R_o^2 p \quad (5)$$

And the volume of each duct is equal to:

$$V_c = \frac{\pi(R_o^2 - R_i^2)l}{N} \quad (6)$$

The volume of each bucket will be calculated by Equation (7).

$$V_b = \frac{V_c}{N} \quad (7)$$

The values of R_o and N are available as fixed values. Now it is necessary to maximize the value of V_t by finding

suitable values for R_i and p . For this purpose, the dimensionless parameters provided by Rorres [7] are used. In order to simplify the design process, three dimensionless parameters have been considered according to the number of blades used in the turbine design, whose value is between 0 and 1. They are radius ratio and volume ratio, which are obtained according to Equations (3) and (4), respectively and volume ratio which is calculated using Equation (8).

$$v = \frac{V_t}{\pi R_o^2} \quad (8)$$

Table 1 summarized the geometrical characteristics of designed Archimedes screw turbine in this article.

2. 2. Turbine Construction with 3D Technology

There are many ways to build an Archimedes screw turbine. Due to the complex geometry of this turbine, making it in the traditional way and using cutting and turning to create separate metal blades and welding the blades to the central hollow metal cylinder reduces the accuracy of the construction due to environmental and operator errors [19], [14],[20]. And it may affect the performance of the turbine. Also, the construction of turbine blades by machining aluminum sheets and sticking them to PVC pipes as the central cylinder can make the turbine lighter and reduce losses and friction [21]. But still, there will be errors in the correct construction of the design and it affects the performance

of the turbine. For this reason, in this article, the 3D printer of the Sea Based Energy Research Group of Noshirvani University of Technology, Babol is used to make the Archimedes screw turbine. Figure 1 and Table 2 show the used 3D printer and its specifications, respectively.

A 3D printer is a device that can turn a file designed in design software into a tangible object by successively adding materials on top of each other [22]. For this purpose, first Archimedes screw turbine is designed in SolidWorks software and is imported as input to the printer. In order to make the turbine lighter and reduce the losses and friction related to its rotation, the turbine is made of ABS Filament and hollow. This model made by 3D printer has all the details in the design of the turbine and helps the turbine to work better according to its optimal design. Figure 2 shows Archimedes screw turbine made using 3D technology.

2. 3. System Description

2. 3. 1. Experimental Tests Site

Figure 3 shows the device for conducting experimental tests of Archimedes screw turbine, designed and built in the sea-based energy research group. This site includes two water tanks and an open water channel. Water flows from the upstream water tank is transferred to the downstream water tank through an open water channel in which the Archimedes screw turbine is located. When the water flow passes through this channel, it passes through the

TABLE 1. Geometrical characteristics of designed Archimedes screw turbine

Turbine installation angle (degrees)	Screw turbine length (m)	Number of blades	Inner diameter (m)	Outer diameter (m)	Turbine pitch (m)	Turbine head (m)
25	0.17	4	0.05	0.1	0.17	0.0718



Figure 1. 3D printer used to make Archimedes screw turbine

TABLE 2. Printer specifications

Printer model	FDM
Printer dimensions	300*300*300 (mm)

Print speed	1800(mm/min)
Print accuracy	100 (μm)
Print material	ABS Filament

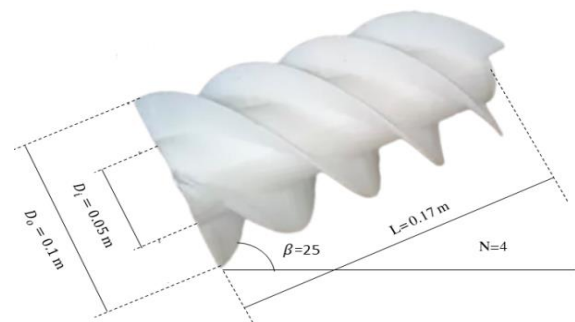


Figure 2. Archimedes screw turbine with 4 blades made with 3D printer technology and its geometrical characteristics

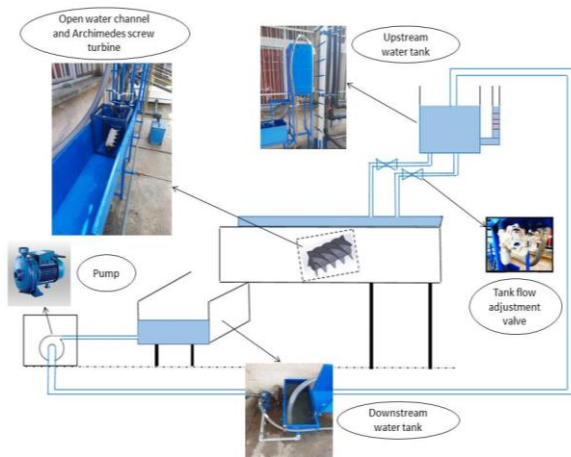


Figure 3. Schematic view of placement and experimental installation Archimedes screw turbine in the laboratory

turbine and causes the turbine to rotate and finally generate electricity through the generator connected to the turbine. A pump is also used to pump water to the upper tank and also a drain pipe has also been installed to prevent the tank from filling up and overflowing.

2. 3. 2. Archimedes Screw Turbine Performance Study

Turbine power equation is as follows.

$$P_{in} = \rho g Q H \quad (9)$$

where ρ is the water density, g is the gravitational acceleration, Q is the flow rate and H is the head of the turbine. Also, Equations (10) and (11) are used to calculate efficiency.

$$\eta = \frac{P_{out}}{P_{in}} \quad (10)$$

$$P_{out} = \eta P_{in} \quad (11)$$

The output power of the turbine is also calculated mechanically or electrically in the experimental tests according to Equations (12) and (13) [23].

$$P_{out\ mec} = T\omega = 2\pi nT \quad (12)$$

$$P_{out\ elc} = V.I \quad (13)$$

Also, the experimental equation presented by Nagel [6] for the rotational speed limit of Archimedes screw turbine, in order to prevent flow turbulence, is in the form of Equation (14).

$$n = \frac{0.85}{D_0^3} \quad (14)$$

The blade tip speed ratio (TSR) is another parameter evaluated in Archimedes screw turbine performance study. This ratio is the blade tip's linear velocity to the flow's speed entering the turbine and is expressed in the form of Equation (15).

$$TSR = \frac{r\omega}{V} \quad (15)$$

The angular velocity of the turbine is determined by Equation (16).

$$\omega = 2\pi f \quad (16)$$

2. 3. 3. Dimensionless Governing Equations

Dimensionless numbers are essential to create a dynamic similarity between the model and the prototype.

In the study of the performance of semi-submerged propellers, including Archimedes screw turbine, the dimensionless power coefficient is used to evaluate the performance. The power of an Archimedes screw turbine is a function several parameters given by Equation (17) [24].

$$P = f(Q, D_0, n, \rho, \mu) \quad (17)$$

According to the π -Buckingham theory [25], based on number of variables in Equation (17), three dimensionless groups can be made in the form of the following equations.

$$\pi_1 = \frac{P}{\rho n^3 D_0^5} \quad (18)$$

$$\pi_2 = \frac{Q}{n D_0^3} \quad (19)$$

$$\pi_3 = \frac{\rho V D_0}{\mu} \quad (20)$$

That respectively represents the dimensionless numbers of power coefficient, flow and Reynolds number for Archimedes screw turbine. Finally, the power coefficient of Archimedes screw turbine is calculated according to Equation (21).

$$C_p = \frac{P}{\rho n^3 D_0^5} = f\left(\frac{Q}{n D_0^3}, \frac{\rho V D_0}{\mu}\right) \quad (21)$$

2. 3. 4. Froude Scaling

For the scaling of semi-submerged propellers, including the Archimedes screw turbine, the dimensionless Froude number is used. This dimensionless number is defined as the ratio of inertial force to gravity force in the movement of a fluid and is expressed according to Equation (22) [26].

$$Fr = \frac{V}{\sqrt{g L_c}} \quad (22)$$

In this equation, V is the flow velocity and L_c is the characteristic length. For Archimedes screw turbine, L_c will be equal to the outer diameter of the turbine. Table 3 shows Froude scaling coefficient [27].

$$\lambda = \frac{(L_c)a}{(L_c)s} \quad (23)$$

2. 3. 5. Economic Study of Archimedes Screw Turbine

The cost of building micro hydropower

TABLE 3. Different parameters for the prototype scale

Parameters	Q	ω	R	P	T
coefficient	$\lambda^{2.5}$	$\lambda^{-0.5}$	λ^{-1}	$\lambda^{3.5}$	λ^4

plants in Iran is \$300 /kW and the income is \$0.025 /kWh. The Discounted Payback Period is the time required to offset investment costs with incoming cash flow. The payback period equation is as follows [28]:

$$DPP = \frac{-Ln(1 - \frac{Inv + Disc}{CF})}{Ln(1 + Disc)} \quad (24)$$

In this equation DPP is discounted payback period, Inv is the investment cost, Disc is the discount rate and CF is cash flow in one year. Another critical point in the economic analysis of the use of Archimedes screw turbine is the issue of currency savings.

2. 4. Design of Experiment The most important parameters affecting Archimedes screw turbine are the flow rate and the turbine's rotational speed. For this purpose, the test device is designed in a way to change the flow rate for three different flow rates. On the other hand, studying the turbine's performance should be possible according to the consumption load. Therefore, the turbine performance was also studied for 5 electrical resistances. A total of 75 tests (considering uncertainty analysis and repeating each test 5 times) should be

performed on the turbine's performance. Table 4 shows the design of the experiment.

2. 5. Laboratory Equipment in Experimental Tests

Essential parameters to measure in this study include rotational speed and output power. In order to calculate the power, the electrical current and voltage have been measured and also, a rheostat has been used to study the effect of electrical resistance on the performance of the turbine. Table 5 shows the equipment and measuring tools in experimental tests and their accuracy.

TABLE 4. Design of experiment

Flow rate (lit/s)	Resistance (ohm)	Flow rate (lit/s)	Resistance (ohm)
1.2	10	2.4	10
	20		20
	30		30
	40		40
	50		50
Flow rate (lit/s)	Resistance (ohm)		
3.6	10		
	20		
	30		
	40		
	50		

TABLE 5. Characteristics of measuring tools in experimental tests of Archimedes screw turbine

Device	Model	Device work	Measurement accuracy	Image
Tachometer	Dual Digital Tachometer DT-2268	Measuring the rotational speed of the turbine	0.1 rpm for values less than 1000 rpm	
Ammeter	HIOKI 3256-50	Measuring the current passing through the circuit	$\pm 1.5\%(rdg) \pm 4(dgt)$	
Voltmeter	HIOKI 3200	Measuring the voltage of both ends of the generator	$\pm 0.07\%(rdg) \pm 2(dgt)$	

Rheostat	-	Creating variable resistance in the circuit and changing the voltage and current of the circuit	1 ohm in the range of 1 to 55 ohms	
Chronometer	HS43	Measuring the duration of tank water discharge to calculate the flow rate	0.01 seconds	
Generator	127.P.02620 dunker motoren	Connecting to the output shaft of the turbine and generating electricity from the rotational movement of the turbine	-	

2. 6. Uncertainty Analysis Uncertainty is very important in experimental studies. First, the average of the parameters is obtained [29].

$$\bar{x} = \frac{\sum_{i=1}^m x_i}{m} \tag{25}$$

where x_i and \bar{x} will be the parameter's value in each experiment and the average value of the parameter, respectively. In the continuation of the uncertainty analysis process, the standard deviation of the measured values and the standard deviation of the average of the measured values are determined according to Equations (26) and (27), respectively [25].

$$s = \sqrt{\frac{\sum_{i=1}^m (x_i - \bar{x})^2}{m-1}} \tag{26}$$

$$\sigma_m = \frac{s}{\sqrt{m}} \tag{27}$$

According to these equations, Equation (30) is valid for uncertainty.

$$u = \sqrt{\sigma_m} \tag{28}$$

In the following, the expanded uncertainty is calculated according to Equation (29).

$$U = k \cdot u \tag{29}$$

Where k will be the overlap coefficient. Finally, the size range is calculated using Equation (30) [4].

$$x_f = \bar{x} \pm U \tag{30}$$

According to the measuring tools and the site of experimental tests of Archimedes screw turbine, experimental test parameters will include input flow rate, rotation speed, generator voltage, electric current and rheostat resistance, uncertainty analysis has been done in order to determine the number of tests required to achieve the acceptable result for each of these parameters. Uncertainty analysis for flow rate parameters, voltage and rotational speed are summarized in Table 6 (for instance) and the results show that each test should be repeated 5 times.

TABLE 6. Checking the uncertainty of different parameters

Value	1	2	3	4	5	Average value	Standard deviation	Average uncertainty	Uncertainty with overlap factor
circuit voltage at a flow rate of 3.6 (l/s) and resistance of 10 ohms (V)	1.20	1.19	1.23	1.22	1.21	1.21	0.01581	0.00707	0.01414
The rotational speed of the turbine at a flow rate of 3.6 (l/s) and a resistance of 10 ohms (rpm)	250	252	250	249	252	251	1.4142	0.6324	1.2648
Tank outlet valve flow rate (l/s)	1.19	1.19	1.22	1.22	1.18	1.2	0.01871	0.00836	0.01673

3. RESULTS

In this section, the results of the experimental tests are shown and related analyzes are performed. At first, the results of studying the performance characteristics of the Archimedes screw turbine are presented in the form of diagrams of variation in rotational speed, output power, torque and efficiency of the turbine according to different values of rheostat resistance for the inlet flow rates to the turbine. In the following, for a detailed investigation of the turbine efficiency diagram, the 3D diagram of efficiency is drawn and then, the diagrams of dimensionless power coefficient and blade tip speed ratio are studied according to the changes of flow and Reynolds numbers. Then, the results of the study of the performance of the turbine in the prototype scale are presented and the diagrams of the turbine in the prototype scale are shown. Finally, the results of the economic analysis were investigated.

3. 1. Turbine Performance

Figures 4(a) and 4(b) show the variations in turbine rotational speed and torque according to rheostat resistance for different flow rates. With an increase in the inlet flow rate of turbine, due to the rise in the momentum value, the rotational speed of the turbine always grows. Also, due to the fact that in the design and construction of Archimedes screw turbine, direct coupling of a DC motor was used as a generator to Archimedes screw turbine, the rheostat, which plays the role of a consumer in the electrical circuit output from the turbine, is used to create resistance in the circuit and variation the rotational speed of the turbine generator. According to the speed equation of the shunt electric motor [30], by increasing the resistance of the rheostat at a constant flow rate, the turbine's rotational speed will decrease. The gradient of this decrease in rotational speed increases with the rise in flow rate, so

that the slope decrease in the highest flow rate is 68% more than the lowest flow rate. This shows that the system is more sensitive to the consumer load at high flow rates. Figure 4(b) also shows the change of turbine output torque according to different rheostat resistances for different flow rates. According to this figure, changing the torque output from the turbine is the same as changing the rotating speed and always increases with the rise of flow rate within the range of experimental tests. In constant flow, it also decreases with increasing rheostat resistance. The torque reduction rate is almost constant for two flow rates of 2.4 and 3.6 (l/s), but for the flow rate of 1.2 (l/s), the rate of reduction with increasing resistance is small, and it can be said that the torque at low flow rates has a behavior independent of the electrical resistance (consumer load).

Figures 5(a) and 5(b) show the power and efficiency variations with electrical resistance for different flow rates. By increasing the inlet flow rate to the turbine, the output power of the turbine rises. This trend of output power variations with increasing flow rate is always upward in the range of experimental tests, and the maximum output power in experimental tests was 1.59 (W) at a flow rate of 3.6 (l/s). Also, at a constant flow rate, the output power of the turbine decreases with an increase in the rheostat resistance. Considering that the output power of Archimedes screw turbine is measured electrically by using an electric circuit connected to the generator, by increasing the resistance of the rheostat, the resistance value of the circuit increases and more power is consumed. Therefore, the output power decreases. Also, with the rise of the rheostat resistance at a constant flow rate, the turbine's rotational speed decreases; therefore, according to turbine power equation [23], the output power of the turbine decreases. Figure 5(b) also shows the diagram of the variations in turbine efficiency. According to this figure, for a constant flow rate, the

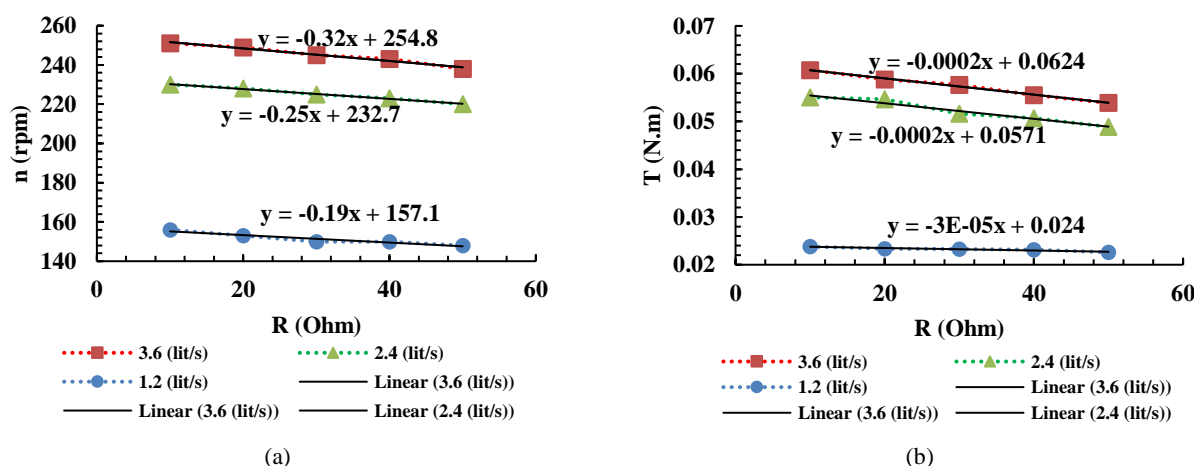


Figure 4. Diagram of a) rotational speed and b) output torque according to the value of rheostat electrical resistance for different conditions of the inlet flow rate to the turbine

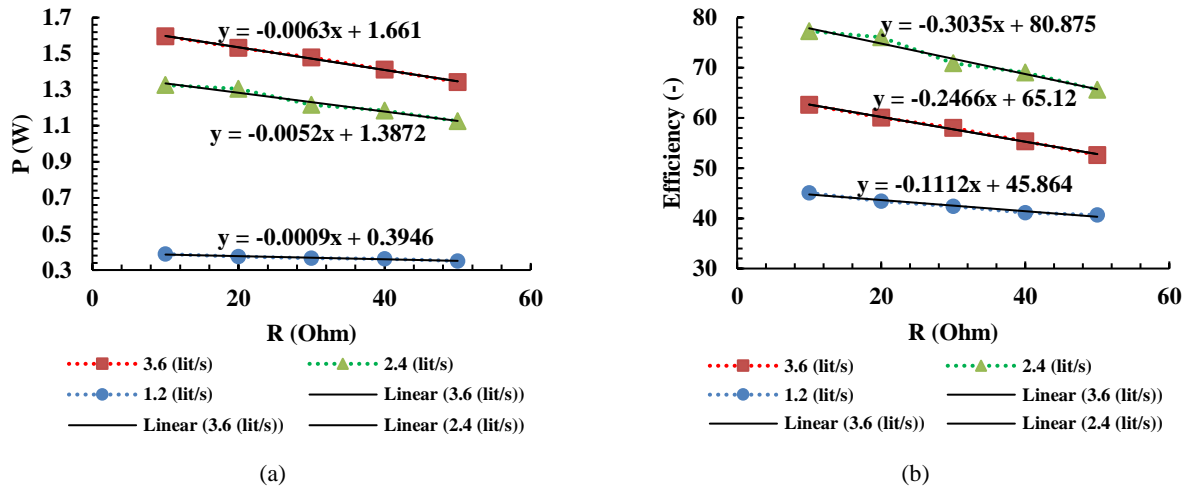


Figure 5. Diagram of a) output power and b) efficiency of turbine according to the value of rheostat electrical resistance for different conditions of the inlet flow rate to the turbine

efficiency value decreases with an increase in the rheostat resistance (reduction of the turbine's rotational speed). This reduction in efficiency is due to an decrease in the output power of the turbine with an increase in rheostat resistance. So, the output efficiency falls by reducing the output power according to turbine efficiency equation [23] for a constant flow rate. Also, in this figure, it is clear that the highest turbine efficiency will be at flow rate of 2.4 (l/s). As mentioned, with an increase in the flow rate, the turbine's rotational speed grows. According to rotational speed limit of Archimedes screw turbine equation [6], when the rotational speed exceeds this limit, the flow turbulence reduces the efficiency of the turbine. Since the rotational speeds measured in the experimental tests, in the flow rate of 3.6 (l/s), are higher than the speed limit provided by Nagel [6]. Consequently, the efficiency of the turbine has decreased in this flow rate.

By curve fitting the experimental data obtained for efficiency (by MATLAB CFTool), it is possible to draw

the efficiency variations for different flow rates and resistances (Figure 6). According to Figure 6, the efficiency of the Archimedes screw turbine initially increases with an increase in the input flow rate and by reaching its maximum value and passing the rotational speed limit at the same time as the flow turbulence increases, it starts to drop. According to the experimental tests, the maximum efficiency of Archimedes screw turbine is 77.28%, which occurs at the input flow rate of 2.4 (l/s), which is 23.47% higher than the flow rate of 3.6 (l/s).

3. 2. Dimensionless Study of Performance For analyzing of the power coefficient values for Archimedes screw turbine, diagram of power coefficient variations according to two dimensionless Reynolds and flow number is shown in Figure 7. According to this figure, with the increase of the Reynolds number, the power coefficient values always decrease due to the increase of

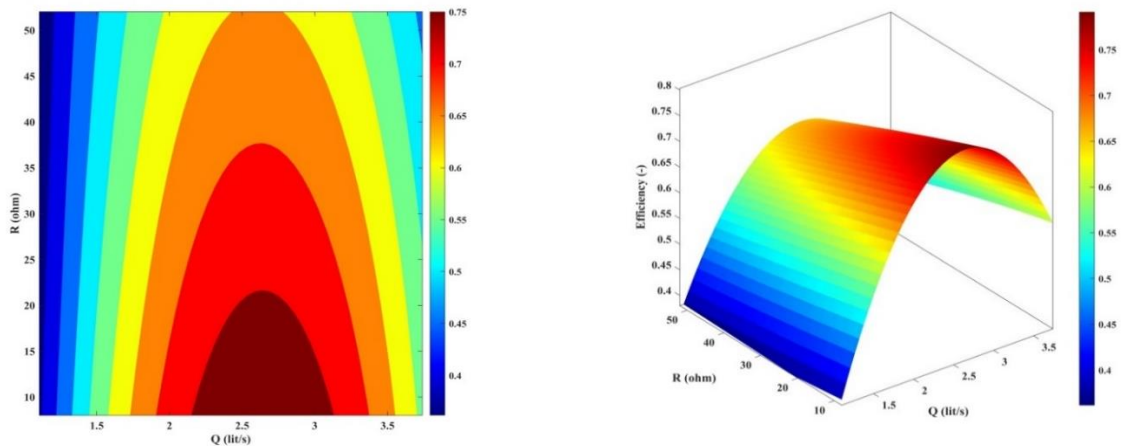


Figure 6. 3D diagram of turbine efficiency changes according to changes in inlet flow rate and resistance

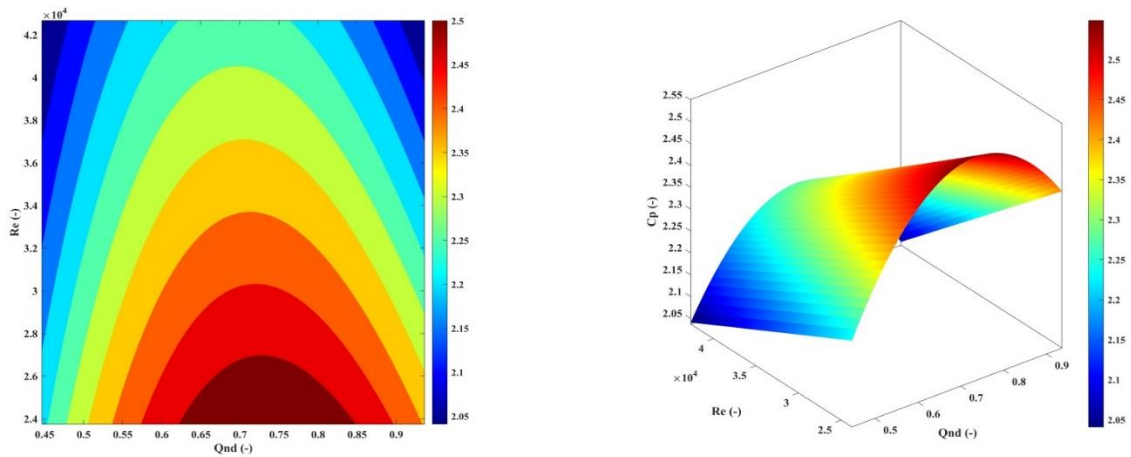


Figure 7. 3D diagram of power coefficient according to flow and Reynolds dimensionless numbers

the flow turbulence. Also, for constant Reynolds number, with an increase in the dimensionless number of flow, the power coefficient increases at the beginning like the changes in the turbine efficiency, and after reaching its maximum value, it begins to decrease.

Figure 8 shows the blade tip speed ratio variation according to flow and Reynolds numbers. According to this figure, with an increase in the Reynolds number, the value of the tip speed ratio rises. At a constant inlet flow rate, the turbine's rotational speed increases with the upturn of the Reynolds number and according to the Equation (15), the value of the blade tip speed ratio increases. Also, according to this figure, in a constant Reynolds number, the value of the blade tip speed ratio decreases with the rise in the dimensionless flow number. According to Equation (19), with this dimensionless number's rise, the turbine's flow rate increases or the turbine's rotational speed decreases. By growing this dimensionless number, the inlet flow rate of the turbine rises or the rotational speed of the turbine decreases, both

of these factors reduce the value of the dimensionless number of the blade tip speed ratio.

3. 3. Prototype Performance

The scaling has been considered 1:6, so it is possible to evaluate the performance of the Archimedes screw turbine in the prototype scale according to the results of the laboratory model performance and the equations in Table 3. Figure 9(a to c) shows the rotational speed, torque and power of prototype turbine to rheostat electrical resistance for different flow rates. Figure 9(a) shows the rotational speed of the Archimedes screw turbine in prototype scale. According to this figure, the behavior is similar to the diagram related to the laboratory model. Considering Archimedes screw turbine rotation speed limited equation [6] with an increase in the diameter of the Archimedes screw turbine, the rotational speed of the screw turbine decreases. In the diagram of Figure 9(a), this reduction in speed is evident in the prototype model compared to the laboratory model. The maximum

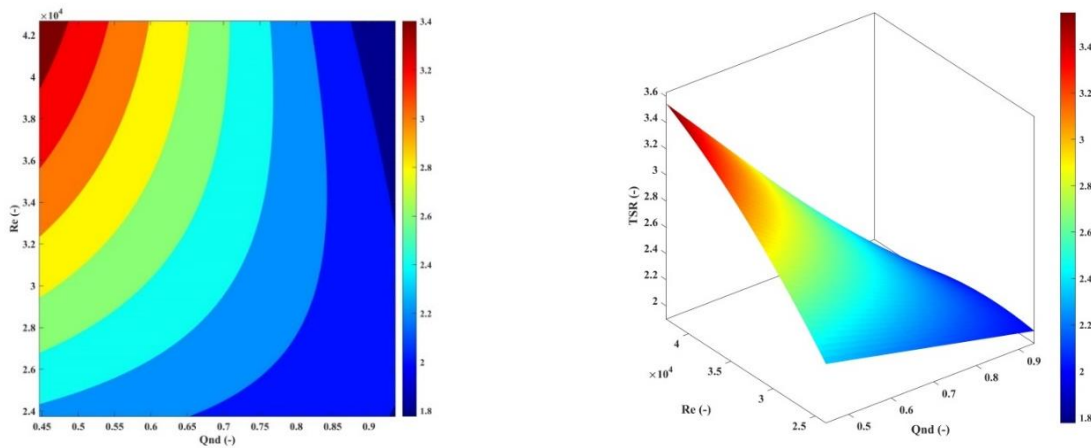


Figure 8. 3D diagram of blade tip speed ratio according to flow and Reynolds dimensionless numbers

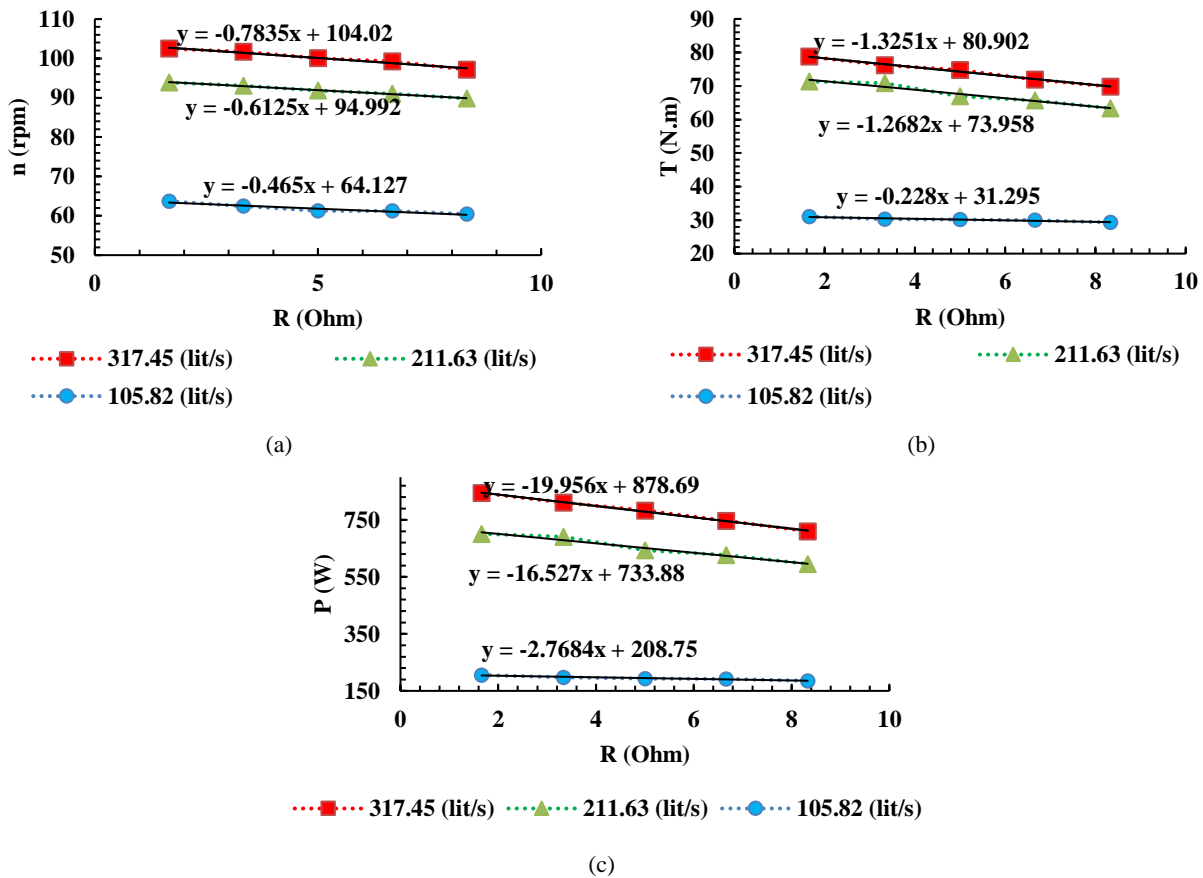


Figure 9. Prototype a) rotational speed, b) torque and c) power to rheostat electrical resistance for the different inlet flow rate to the turbine

rotational speed of the turbine will equal 102.47 (rpm) at flow rate of 317.45 (l/s). According to the gradient of the rotational speed variation diagram for laboratory and prototype model, the sensitivity of rotational speed to load changes in the prototype model has increased by about 145% compared to the laboratory model.

Figure 9(b) shows the torque variations of the Archimedes screw turbine on a prototype scale. According to the equations in Table 3 for prototype, the sensitivity of the torque variation to the electrical load has also increased significantly in prototype, according to the slope of the torque change diagrams for the laboratory model and prototype turbine. This rate is higher than the rate of changes in rotational speed and lower than the rate of variations in power.

Figure 9(c) also shows the diagram of power according to the changes in electrical resistance for different flow rates entering the turbine in the prototype scale. The behavior is just like the laboratory model. Due to an increase in the geometrical dimensions of the turbine in the prototype and the equations in Table 3 for different parameters, the head and flow rates of the input to the turbine have increased for the prototype. The maximum output power of the turbine in the prototype is

equal to 844.63 W at a flow rate of 317.48 (l/s). This power is about 527 times the output power of the laboratory model. Also, according to the slope of the output power diagrams for laboratory and prototype models, the sensitivity of the power to changes in the consumption load in the prototype compared to the laboratory model significantly increased.

3. 4. Economic Study

Using the results of the Archimedes screw turbine in the prototype scale, the turbine's design, construction and operation can be economically studied for the inlet flow rates and output powers. Table 7 shows the amount of annual power production, costs and income related to the operation of the Archimedes screw turbine for different flow rates tested. In this table, the power plant's maintenance cost equals 4% of its construction cost [31].

Figure 10 shows the effect of the discount rate on the payback period for the different conditions of the inlet flow rate to the Archimedes screw turbine. This figure shows that the payback period is not much further according to the costs and income of the construction and operation of the power plants for different flow rates entering the Archimedes screw turbine. According to this

TABLE 7. Specifications of production power and its costs and income for Archimedes screw turbine in prototype scale

Flow rate (l/s)	Annual electricity production (kWh)	Power plant construction cost (\$)	Power plant maintenance cost (\$)	Total costs (\$)	Annual income from selling electricity (\$)
105.82	1800.61	62	2.5	64.5	45
211.63	6143.47	210	8.5	218.5	153
317.45	7398.95	254	10.5	264.5	185

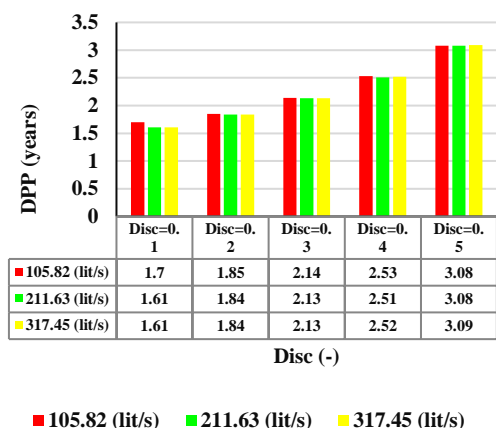


Figure 10. The effect of the discount rate on the payback period for different condition of inlet flow rate to the Archimedes screw turbine

diagram, the minimum payback period with a discount rate of 0.1 for the flow rates of 211.63 and 317.45 (l/s) is 1.7 years.

Figure 11 shows the amount of costs related to the construction of the Archimedes screw turbine power plant in Iran and the foreign model and the currency savings for different conditions of inlet flow rate to the Archimedes screw turbine. According to this figure, the values of Iranian and foreign model manufacturing cost and currency exchange for the flow rate of 317.45 (l/s) are more than the other flow rates of the Archimedes screw turbine.

And at the end of this paper, the performance results of the Archimedes screw turbine made with 3D printer technology in this paper are compared with the traditional turbine made by Yulistiyanto et al. [20]. The dimensions of these two turbines were different. For this reason, the results of Yulistitiano et al's [20] turbine close to the results of this paper by using Froude scaling. Figure 12 shows the power changes according to flow rate for these two turbines. In this figure, it is clear that the turbine made with a 3D printer in this paper has higher power values (with the exception of the flow rate of 1.2 (l/s)) compared to the turbine made with the traditional method. This shows the improvement of the performance of the turbine made with 3D technology compared to the traditional method.

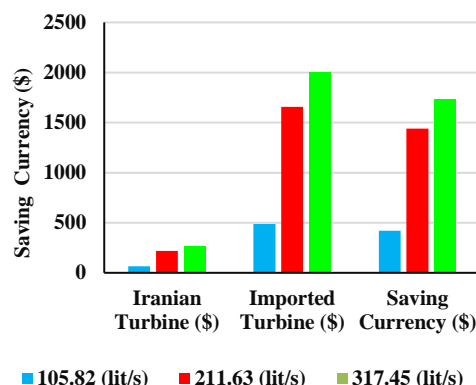


Figure 11. Amounts of costs related to the construction of the Archimedes screw turbine power plant in Iran and the foreign model and the amount of currency savings for different condition of inlet flow to the Archimedes screw turbine

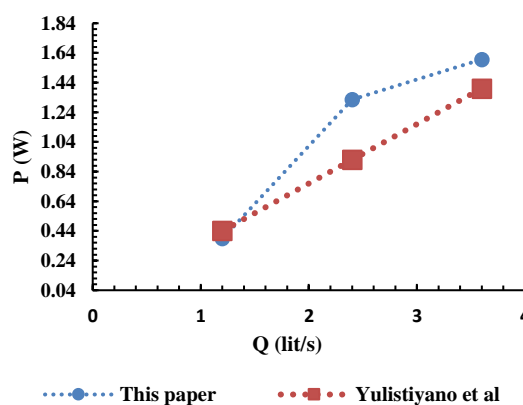


Figure 12. Comparing results

4. COCLUSIONS

In this article, the effects of changes in the inlet flow rate to the turbine and electrical resistance on the performance characteristics of the laboratory model of an Archimedes screw turbine, which include rotational speed, output power, output torque, and turbine efficiency, were discussed, and these results were scaled for the prototype by using Froude dimensionless number. Also, the effects of dimensionless flow and Reynolds numbers on power

coefficient and blade tip speed ratio of the turbine were investigated. Finally, the design, construction and operation of the Archimedes screw turbine in the prototype scale were analyzed from an economic viewpoint. The main results obtained from this study are as follows:

- The performance of the turbine made with 3D technology has a better performance than the turbines made with traditional methods.
- By increasing the value of rheostat resistance, the rotational speed, output power, torque and efficiency always decrease in the laboratory and prototype scale.
- The maximum value of turbine efficiency is equal to 77.28, which occurs in the flow rate of 2.4 (l/s).
- The maximum value of output power of the turbine for the laboratory model will be equal to 1.59 (W) and for the prototype it will be equal to 844.63 (W).
- Reynolds number increase lead to rise in blade tip speed ratio and the power coefficient decreases.
- Increasing dimensionless flow number cause decreases in the blade tip speed ratio and the power coefficient increases at first and decreases after reaching a maximum value.
- The discounted payback period depends on the discount rate and can be considered between 1.6 and 3 years according to the discount rate. Also, it can sell \$153 of electricity to the grid annually to achieve the best system efficiency.

5. REFERENCES

1. Zecca, A. and Chiari, L., "Fossil-fuel constraints on global warming", *Energy Policy*, Vol. 38, No. 1, (2010), 1-3. <https://doi.org/10.1016/j.enpol.2009.06.068>.
2. Perera, F., "Pollution from fossil-fuel combustion is the leading environmental threat to global pediatric health and equity: Solutions exist", *International Journal of Environmental Research and Public Health*, Vol. 15, No. 1, (2018), 16. <https://doi.org/10.3390/ijerph15010016>.
3. Covert, T., Greenstone, M. and Knittel, C.R., "Will we ever stop using fossil fuels?", *Journal of Economic Perspectives*, Vol. 30, No. 1, (2016), 117-138. doi: 10.1257/jep.30.1.117
4. Alizadeh Kharkeshi, B., Shafaghat, R., Jahanian, O. and Alamian, R., "Experimental evaluation of the effect of dimensionless hydrodynamic coefficients on the performance of a multi-chamber oscillating water column converter in laboratory scale", *Modares Mechanical Engineering*, Vol. 21, No. 12, (2021), 823-834. <http://mme.modares.ac.ir/article-15-52993-en.html>
5. Nuernbergk, D.M., *Archimedes screw in the twenty-first century, in Archimedes in the 21st century*. 2017, Springer.113-124. doi: 10.1007/978-3-319-58059-3_6
6. Nagel, G., "Archimedian screw pump handbook: Fundamental aspects of the design and operation of water pumping installations using archimedian screw pumps, RITZ-Pumpenfabrik OHG, (1968).
7. Rorres, C., "The turn of the screw: Optimal design of an archimedes screw", *Journal of Hydraulic Engineering*, Vol. 126, No. 1, (2000), 72-80. [https://doi.org/10.1061/\(ASCE\)0733-9429\(2000\)126:1\(72\)](https://doi.org/10.1061/(ASCE)0733-9429(2000)126:1(72)).
8. Müller, G. and Senior, J., "Simplified theory of archimedean screws", *Journal of Hydraulic Research*, Vol. 47, No. 5, (2009), 666-669. <https://doi.org/10.3826/jhr.2009.3475>.
9. Raza, A., Mian, M.S. and Saleem, Y., "Modeling of archimedes turbine for low head hydro power plant in simulink matlab", *International Journal of Engineering Research & Technology*, Vol. 2, No. 7, (2013), 2471-2477.
10. Rohmer, J., Knittel, D., Sturtzer, G., Flieller, D. and Renaud, J., "Modeling and experimental results of an archimedes screw turbine", *Renewable Energy*, Vol. 94, (2016), 136-146. <https://doi.org/10.1016/j.renene.2016.03.044>.
11. Hizhar, Y., Yulistianto, B. and Darmo, S., "Rancang bangun dan studi eksperimental pengaruh perbedaan jarak pitch dan kemiringan poros terhadap kinerja mekanik model turbin ulir 2 blade pada aliran head rendah", *METAL: Jurnal Sistem Mekanik dan Termal*, Vol. 1, No. 1, (2017), 27-34. <https://doi.org/10.25077/metal.1.1.27-34.2017>.
12. Maulana, M.I., Syuhada, A. and Kurniawan, R., "Experimental study on the effect of flow rate on the performance of two-blade archimedes screw turbine", *Journal of Advanced Research in Fluid Mechanics and Thermal Sciences*, Vol. 61, No. 1, (2019), 10-19. doi.
13. Kristiyadi, T., Aditya, R. and Nugraha, P., "Pengembangan governor elektrik berbasis arduino sebagai sistem kontrol turbin air screw", *ELKOMIKA: Jurnal Teknik Energi Elektrik, Teknik Telekomunikasi, & Teknik Elektronika*, Vol. 8, No. 3, (2020), 533.
14. Abdullah, O.S., Kamel, A.H. and Khalil, W.H., "Numerical and experimental modelling of small hydropower turbine", *Journal of Advanced Research in Fluid Mechanics and Thermal Sciences*, Vol. 80, No. 1, (2021), 112-127. <https://doi.org/10.37934/arfmts.80.1.112127>.
15. Bustomi, M.A., Indarto, B. and Putra, A.M.K., "Characteristics analysis of the archimedes screw turbine micro-hydro power plant with variation of turbine elevation angle", *JFA (Jurnal Fisika dan Aplikasinya)*, Vol. 17, No. 2, (2021), 56-61.
16. Cahyono, G.R., Amrullah, A., Ansyah, P.R. and Rusdi, R., "Pengaruh sudut kemiringan terhadap putaran dan daya hidrolisis pada turbin archimedes screw portable", *Jurnal Rekayasa Mesin*, Vol. 13, No. 1, (2022), 257-266. <https://doi.org/10.21776/ub.jrm.2022.013.01.25>.
17. Darmono, B. and Pranoto, H., "Archimedes screw turbines (ASTs) performance analysis using cfd software based on variation of blades distance and thread number on the pico hydro powerplant", *International Journal of Advanced Technology in Mechanical, Mechatronics and Materials*, Vol. 3, No. 1, (2022), 18-25. doi: 10.37869/ijatec.v3i1.53.
18. Borah, S., Chowdhury, B., Gogoi, S. and Askary, Z., "A theoretical study of design parameters of an archimedean screw turbine", *Journal of Material Science and Mechanical Engineering*, Vol. 2, (2015), 32-34.
19. Mwansa, G., "Design and construction of an archimedes turbine for rural electrification/lighting in zambia", *INDUSTRIAL AUTOMATION*, The Engineering Institute of Technology, Master of Engineering, (2017),
20. Yulistiyanto, B., Hizhar, Y. and Lisdiyanti, L., "Effect of flow discharge and shaft slope of archimedes (screw) turbin on the micro-hydro power plant", (2012). <http://hdl.handle.net/11617/3117>.
21. Nuramal, A., Bismantolo, P., Date, A., Akbarzadeh, A., Mainil, A.K. and Suryono, A.F., "Experimental study of screw turbine performance based on different angle of inclination", *Energy Procedia*, Vol. 110, (2017), 8-13. <https://doi.org/10.1016/j.egypro.2017.03.094>.

22. Shahrubudin, N., Lee, T.C. and Ramlan, R., "An overview on 3d printing technology: Technological, materials, and applications", *Procedia Manufacturing*, Vol. 35, (2019), 1286-1296. <https://doi.org/10.1016/j.promfg.2019.06.089>.
23. Stergiopoulou, A.V., Stergiopoulos, V.G., Tsvolas, D.I. and Stylianou, A., "Two innovative experimental archimedean screw energy models in the shadow of archimedes iii", in 5th International Conference on Experiments/Process/System Modeling/Simulation/Optimization. Vol., No. Issue.
24. White, F.M., "Fluid mechanics, Tata McGraw-Hill Education, (1979).
25. Alizadeh Kharkeshi, B., Shafaghat, R., Jahanian, O., Alamian, R. and Rezanejad, K., "Experimental study on the performance of an oscillating water column by considering the interaction effects of optimal installation depth and dimensionless hydrodynamic coefficients for the caspian sea waves characteristics", *Ocean Engineering*, Vol. 256, (2022), 111513. <https://doi.org/10.1016/j.oceaneng.2022.111513>. <https://www.sciencedirect.com/science/article/pii/S0029801822008836>
26. Kharkeshi, B.A., Shafaghat, R., Jahanian, O., Alamian, R. and Rezanejad, K., "Experimental study of an oscillating water column converter to optimize nonlinear pto using genetic algorithm", *Energy*, (2022), 124925. <https://doi.org/10.1016/j.energy.2022.124925>. <https://www.sciencedirect.com/science/article/pii/S0360544222018266>
27. Alizadeh Kharkeshi, B., Shafaghat, R., Alamian, R. and Aghajani Afghan, A.H., "Experimental & analytical hydrodynamic behavior investigation of an onshore owc-wec imposed to caspian sea wave conditions", *International Journal of Maritime Technology*, Vol. 14, No., (2020), 1-12. <http://ijmt.ir/article-1-712-en.html>.
28. Bhandari, S.B., "Discounted payback period-some extensions", *Journal of Business and Behavioral Sciences*, Vol. 21, No. 1, (2009), 28-38.
29. Shafaghat, R., Fallahi, M., Alizadeh Kharkeshi, B. and Yousefifard, M., "Experimental evaluation of the effect of incident wave frequency on the performance of a dual-chamber oscillating water columns considering resonance phenomenon occurrence", *Iranian (Iranica) Journal of Energy & Environment*, Vol. 13, No. 2, (2022), 98-110. <https://doi.org/10.5829/ijee.2022.13.02.01>.
30. Halliday, D., Resnick, R. and Walker, J., "Fundamentals of physics, John Wiley & Sons, (2013).
31. IRENA, W., *Hydropower*. 2012, IRENA Abu Dhabi, United Arab Emirates.44.

Persian Abstract

چکیده

یکی از بهترین راه‌حل‌ها برای غلبه بر مشکلات ناشی از مصرف سوخت‌های فسیلی استفاده از انرژی‌های تجدیدپذیر است. در این راستا، در این تحقیق تأثیر دبی و بار مصرفی بر عملکرد یک توربین پیچ ارشمیدس به صورت تجربی مورد بررسی قرار گرفت. در ابتدا توربین ارشمیدس با ابعاد بهینه با استفاده از فناوری چاپگر سه‌بعدی ساخته شد. سپس در سایت شبیه‌سازی رودخانه قرار گرفت. پس از کالیبراسیون و تجزیه و تحلیل عدم قطعیت، آزمایشات برای سه نرخ جریان و پنج مقاومت الکتریکی انجام شد. نتایج نشان داد که افزایش دبی منجر به افزایش توان، گشتاور و سرعت دورانی توربین می‌شود، اما باعث رفتار غیرخطی در راندمان می‌شود. از سوی دیگر، افزایش بار الکتریکی نیز منجر به کاهش عملکرد مبدل برای همه شرایط شده است. علاوه بر این، با استفاده از نظریه پی-باکینگهام، رفتار هیدرودینامیکی مبدل با استفاده از اعداد رینولدز، دبی بی‌بعد و ضریب توان مورد بررسی قرار گرفت. نتایج نشان داد که افزایش عدد رینولدز منجر به کاهش ضریب توان می‌شود. با این حال، افزایش دبی بدون بعد، ابتدا ضریب توان را افزایش و سپس کاهش می‌دهد (رفتار غیرخطی). علاوه بر این، توربین پیچ ارشمیدس از دیدگاه اقتصادی نیز مورد بررسی قرار گرفت و نتایج نشان داد که افزایش نرخ تورم منجر به افزایش دوره بازگشت سرمایه تنزیل شده می‌شود و در بدترین حالت، دوره بازپرداخت ۳/۰۹ سال و در بهترین حالت، ۱/۶ سال است. هم‌چنین ساخت توربین پیچ ارشمیدس در ایران می‌تواند ۱۴۳۹/۵ دلار صرفه جویی ارزی به همراه داشته باشد.



Development of Steel Yielding Seismic Dampers Used to Improve Seismic Performance of Structures: A Comprehensive Review

F. Behnamfar*, M. Almohammad-albakkar

Department of Civil Engineering, Isfahan University of Technology, Isfahan, Iran

PAPER INFO

Paper history:

Received 24 December 2022

Received in revised form 20 January 2023

Accepted 31 January 2023

Keywords:

Review Paper

Steel Yielding

Shear Panel

Pipe Damper

Curved Damper

Slit Damper

A B S T R A C T

Seismic excitation can cause significant energy to be released within structures. By using special devices, this energy can be consumed and dissipated without deforming structural members significantly. Due to this, structural damage is minimized, casualties are prevented during earthquakes, and structures are extended in their useful life. Over the past five decades, it has been widely acknowledged that steel yielding dampers are among the best energy dissipation devices. It has been stated that the hysteretic behavior of steel yielding dampers could vary slightly depending on their geometry. From a practical point of view, they are suitable for the improvement of seismic safety in new and existing structures. The purpose of this paper is to present a review related to steel yielding dampers, their development, various types, and applications, in order to help understand the role of these dampers in improving the seismic performance of structures. In terms of their shape, steel yielding dampers can be categorized as steel plate dampers, pipe dampers, curved dampers, and slit dampers. The most common use of steel plate, such as ADAS and TADAS, and pipe dampers is within braced frames, whereas U-shaped, J-shaped, and S-shaped dampers are mostly seen in frames with chevron bracing. Steel curved dampers with a 60° angle in a steel-braced frame, on the other hand, provide the best energy dissipation and frame strength. In this direction, until today, steel slit dampers have been found to be the most commonly used steel yielding dampers.

doi: 10.5829/ije.2023.36.04a.13

1. INTRODUCTION

A variety of dynamic and environmental loadings can affect civil structures, such as wind, traffic, and earthquakes. Especially during earthquake events, buildings structures can be significantly damaged. This observation has been experienced all over the earthquake prone countries of the world like those in the Middle East, southern Asia and Europe, North and South America, and Japan [1, 2]. Structural vibration control methods have been developed in a number of ways to minimize or prevent such damage, and they are being used skillfully in a variety of locations within civil structures [3-5]. There are four major classifications of structural vibration control systems: passive, active, semi-active, and hybrid systems [6-8] while several articles have addressed each of these categories in greater detail [6, 9-

18]. For example, the optimal control algorithm developed by Momeni and Bagchi [18] was designed to improve the efficiency of the semi-active controller. It combines replicator dynamics with an improved non-dominated sorting genetic algorithm (NSGA), NSGA-II. MR dampers, which are semi-active control devices, were then utilized in the new control system to alleviate the vibrations of the isolated highway bridge. Optimal replicator controllers achieve better performance than classical control algorithms, as mentioned in the results.

The passive energy dissipation device has been proposed, tested, and used as an effective tool for improving seismic performance and energy dissipation capacity of structures over the recent decades [19-21]. Passive energy dissipating devices do not require external power sources, unlike active, semi-active, or hybrid systems. In general, passive energy dissipating

*Corresponding Author Institutional Email: farhad@iut.ac.ir
(F. Behnamfar)

devices consume energy by yielding metals, rubbing surfaces together [22], and deforming viscous or viscoelastic materials [23]. Therefore, the wide variety of passive dampers is categorized based on their mechanism of action, including fluid viscous dampers [24-26], tuned liquid dampers [27-29], viscoelastic dampers [30, 31], hysteretic (or, yielding) dampers [32-34], and friction dampers [35]. As a result of their several advantages, steel-yielding devices have been widely used in structures among all kinds of passive energy dissipating devices. They are the focus of this review. Some of these advantages include resistance to fatigue due to low cycles and high displacements, bolted attachments, low fabrication costs, tolerance of large displacements, low sensitivity to ambient temperatures, and high long-term reliability [36-39]. For instance, Behnamfar and Soltanabadi [40, 41] developed a new type of damper that was both numerically and experimentally tested in order to enhance the seismic performance of steel moment connections, and to be repaired following an earthquake. A metal yielding damper can be divided into four types based on its way of yielding, namely axial yield, shear yield, flexural yield, and combined yield. Considering the versatility of steel yielding dampers in terms of application and development, these dampers are of great importance. A number of these yielding devices have been developed and applied to actual buildings, including shear panel damper, pipe damper, and steel plates with slits or with honeycomb-shaped openings subject to shearing [42-47].

To gather the scattered information on yielding dampers into an integrated literature compiling their chronological evolution and advancement from early 1970s to the current day devices, a comprehensive number of the related research tasks is reviewed in this paper to understand the role played by these dampers in improving seismic performance of structures. In this regard, steel yielding dampers can be categorized into four types based on their shape as steel plate dampers, pipe dampers, curved dampers, and slit dampers.

2. CLASSIFICATION OF STEEL YIELDING DAMPERS

In recent years, many solutions have been suggested to alleviate the effects resulting from earthquakes. This process was a reason to innovate a diverse number of control devices for dissipation of seismic energy. Most of these devices have advantages of being simple in construction and quick to repair or replace after an earthquake. Furthermore, as will be shown later, these energy dissipaters mostly not only could exhibit a high and stable energy absorption capacity, but also exhibit the same behavior under tension and compression. It is possible to further categorize steel yielding dampers into four types in terms of shape: steel plate damper, curved damper, pipe damper, and slit damper.

According to Figure 1, the review is conducted using the following flowchart. The review begins with the development of control systems and selecting the investigated control system. After that, the type of passive control system is selected. In this review, the steel yielding dampers are chosen and categorized into four types in terms of shape. The methods used to evaluate the yielding damper are discussed and a brief comparison is then conducted with the other passive dampers. At the end of the review paper, the conclusions and suggestion for future research are summarized.

2. 1. Steel Plate Dampers As early as the 1970s, Kelly et al. [48] invented the first steel dampers. Skinner et al. [32] developed and tested hysteretic dampers for earthquake-resistant structures, including U-strip dampers, torsional beam dampers, flexural beam dampers, and single-axis dampers. It is possible to install torsional beam dampers at the base of structures to prevent structural uplifting caused by severe earthquakes because they have a high load-bearing capacity. The flexural beam damper, however, is a bit more complicated where it can dissipate seismic loads bidirectionally. For the first time, trying out tapered-steel plates as energy dissipation devices has been proposed by

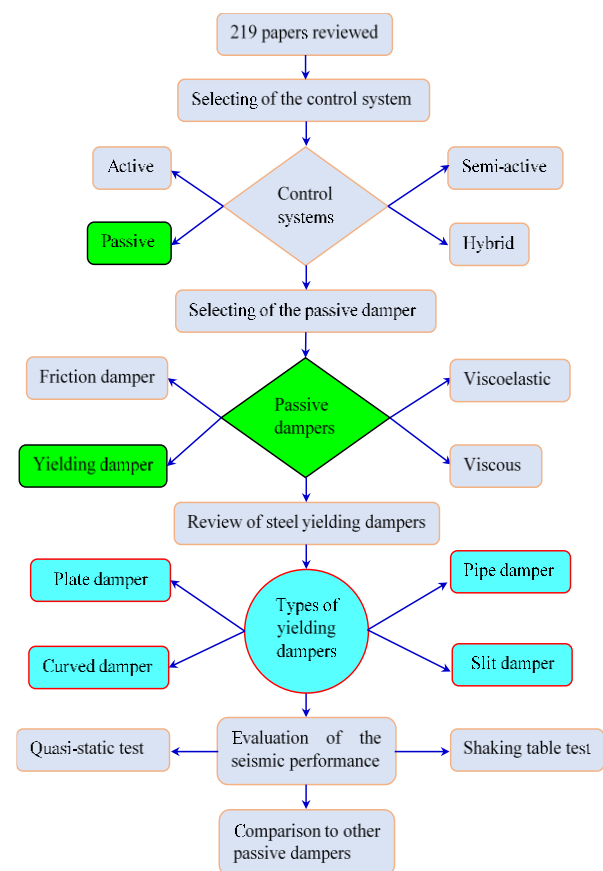


Figure 1. The flowchart adopted in this review paper

Tyler [49]. The damper consists of a steel plate that is welded to the anchorage plate at the base in order to form a cantilever and energy is consumed by steel material's plastic deformation. Thereafter, Bergman [50] suggested a steel damper and called it the added damping and stiffness (ADAS) damper, as shown in Figure 2(a). As proposed by Bergman, ADAS uses X-shaped steel plates that are bolted in parallel to the base plate to provide additional damping and stiffness. Steel X-plates ADAS elements, which are patented by Bechtel Power Corporation, were investigated in a study by Whittaker [51]. Two main goals were sought in the study: (a) investigating the effectiveness of ADAS in seismic applications, and (b) retrofitting ductile moment-resisting frames. A work hardening model based on elastic-perfectly plastic behavior was developed by Tsai and Chou [52] in order to accurately predict the hysteretic performance of the ADAS devices. Similarly, welded triangular-plates utilized for added damping and stiffness were developed and tested under cyclic loading by Tsai et al. [53-55] and Dargush and Soong [56], which are known as TADAS (see Figure 2(b)). TADAS devices are similar to ADAS and both of them can be used for moment resistant frames or braced frames [57-59]. Despite numerous yielding reversals, TADAS seemed to maintain stiffness and strength without deterioration. Afterwards, a one-dimensional fiber model was introduced by Tsai and Chou [60] to predict the experimental responses of the TADAS devices.

In the following years, Shih et al. [61, 62] created rhombic ADAS made of low yield strength steel. Experimental and numerical tests were conducted on this damper. Rhombic ADAS was shown to be capable of stably absorbing earthquake energy. According to the proposed model, rhombic low yield strength steel plates were capable of predicting the hysteretic energy dissipation behavior. Figure 2(c) illustrates a schematic view of this damper. Li and Li [63] invented what is called a dual-function metallic damper (DFMD), as depicted in Figure 2(d). DFMDs are able to achieve structural stiffness as well as reasonably good seismic energy dissipation. To assess the seismic performance of DFMDs quasi-static tests were conducted. As part of the seismic response and dynamic characteristics verification of a steel structure with DFMDs, shaking table tests were conducted on a steel structure with DFMDs under four earthquake ground motion records. It was also confirmed that placement of such X-plate dampers affects the response of buildings in a study by Pujari and Bakre [64]. As compared to the other placement schemes considered, it was reported that the optimal placement of the dampers resulted in a greater reduction of response. Equally, it is also important to note that the optimal placement of dampers is dependent upon the nature of the excitation force, the number of dampers used as well the way they are modelled. Especially, when structures equipped with

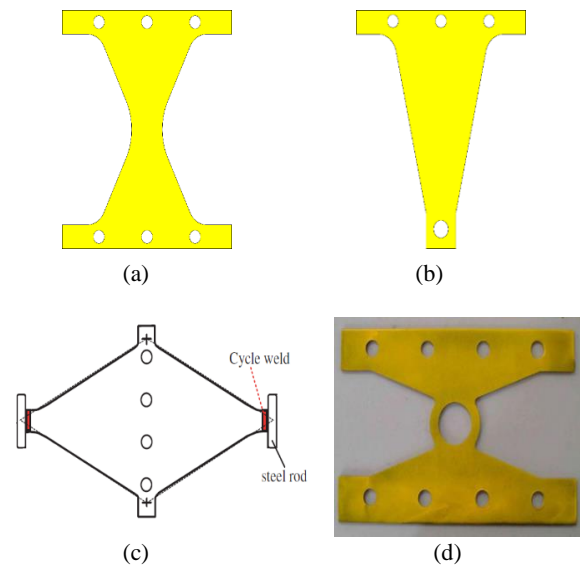


Figure 2. (a) ADAS damper; (b) TADAS damper; (c) Rhombic ADAS; (d) single round-hole steel damper [63]

TADAS dampers undergo large deformations, these members could be vulnerable to serious damage due to possible improper geometric characteristics [65]. It is therefore important to evaluate the behavior of TADAS dampers under large deformations. In this regard, in a study conducted by Mohammadi et al. [65], it was observed that stiffness of the TADAS damper increased abruptly when its pins hit the top of their holes, causing the damper to behave like a rigid element when subjected to large deformations. As a result of the stiffening behavior, the structure's beams and bracings were affected adversely.

Gray et al. [66-68], introduced the yielding brace system (YBS) by the work conducted in the development of ADAS and TADAS devices for which the YBS connectors are triangular in shape to promote spreading plasticity throughout. Due to the fact that "fingers" of the connection experience large deformations during a design level earthquake, the ends of the yielding fingers are bolted to the splice plates through long slotted holes that will accommodate the geometric changes in the fingers as they experience a large deformation like the TADAS. Based on the yielding brace system prototype design and testing program, it has been concluded that such braced frames can dissipate energy effectively and are capable of being displaced up to large displacements. Different applications of YBS in braced structures are shown in Figure 3.

In light of all of this, it should be noted that a hinge support should be used for this type of damper in order to reduce unfavorable axial force on the plate. In addition, low yield strength steel can be used to reduce local fractures in steel plate dampers, which enhances the damper's efficiency of dissipating energy and ductility.

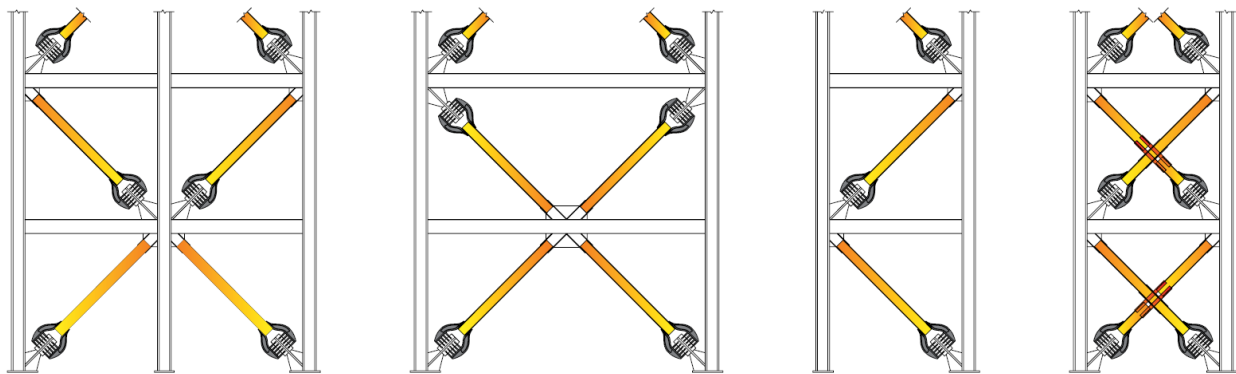


Figure 3. Different applications of YBS in braced structures [67]

On the other hand, it is possible to mitigate welding effects on damper performance by using damper symmetry like rhombic ADAS when clamped connections are achieved through welding. In terms of practicality, braced frames are most commonly equipped with ADAS and TADAS dampers to increase their damping and ductility.

Zibasokhan et al. [69] developed a pure bending yielding dissipater for seismic protection of structures with specially detailed concentrically braced configurations. Several transverse plates are inserted in this proposal into a box at the middle of a diagonal brace to form the device. The dissipater plates bend perfectly under the axial force of a concentric brace in a 4-point pure bending condition. Stable hysteretic behavior and excellent energy dissipation characteristic of the brace as well as similar behavior under tension and compression was observed when equipped with the proposed dissipater device. Labibi et al. [70] used the finite element method to simulate the behavior of a simple trapezoidal steel plate as a steel yielding damper and investigated geometrical parameters that affect absorption and cyclic behavior. In accordance with the results of the study, geometrical parameters can significantly influence energy absorption levels and improve damper hysteresis loops and ductility during specific cyclic loading conditions. In addition, use of the proposed steel damper will reduce the building's base shear and roof acceleration to a significant degree.

In a more recent study, a new damper with piston performance was presented by Ghandil et al. [71], which could be utilized effectively for controlling structures during earthquakes. The energy dissipating part of this device is a series of rectangular metallic yielding plates, which are contained within a rigid steel box and can move with only one degree of freedom. These plates were arranged in such a way that they would work in pure bending mode during cyclic motions of the damper. As a result of this configuration, the damper was able to produce a high level of force capacity and damping ratio.

Thus, the device was capable of being used as a tension/compression piston with sufficient stability in other directions as well. Various types of structural systems were shown to be able to be accommodated by the proposed metallic-yielding piston damper (MYP), including moment-resisting frames, braced frames, and even shear wall systems with the capability of multiple installations in every frame bay. Besides, it was able to significantly reduce the structural responses and residual deformations as well as the out-of-plane frame motions. The details of the damper can be seen in Figure 4.

2. 1. 1. Steel Shear Panel Dampers Yielding shear panel devices (YSPDs) are relatively new passive energy dissipation devices that are designed to absorb earthquake energy by exploiting the capacity of metallic plates to deform plastically in shear. Due to the YSPD's low cost and ease of manufacture and installation, it may prove to be a viable commercial product that can be directly used in the design practice [72, 73]. A shear panel is capable of sustaining large deformations without pinching hence without experiencing a sudden decrease of strength. This enables the use of it as a passive energy dissipating damper in building and bridge structures for the purpose of absorbing seismic energy through inelastic deformation of steel material [74-78]. Generally speaking, the shear-panel dampers are examples of metallic dampers made from low yield point steels, enabling them to dissipate seismic energy well [79-81]. This type of damper has been invented in 1994 by Nakashima et al. [79]. In a subsequent study by Nakashima et al. [82], an experimental program was conducted to investigate the hysteretic behavior of the low-yield steel shear panels. According to the results obtained, the amount of energy dissipated by the tested shear panels was 1.5-2.0 times greater than that consumed by an equivalent linearly elastic, perfectly plastic system. Furthermore, Takahashi and Shinabe [83] performed experimental studies on the restoring force characteristics of thin steel plate elements under shear.

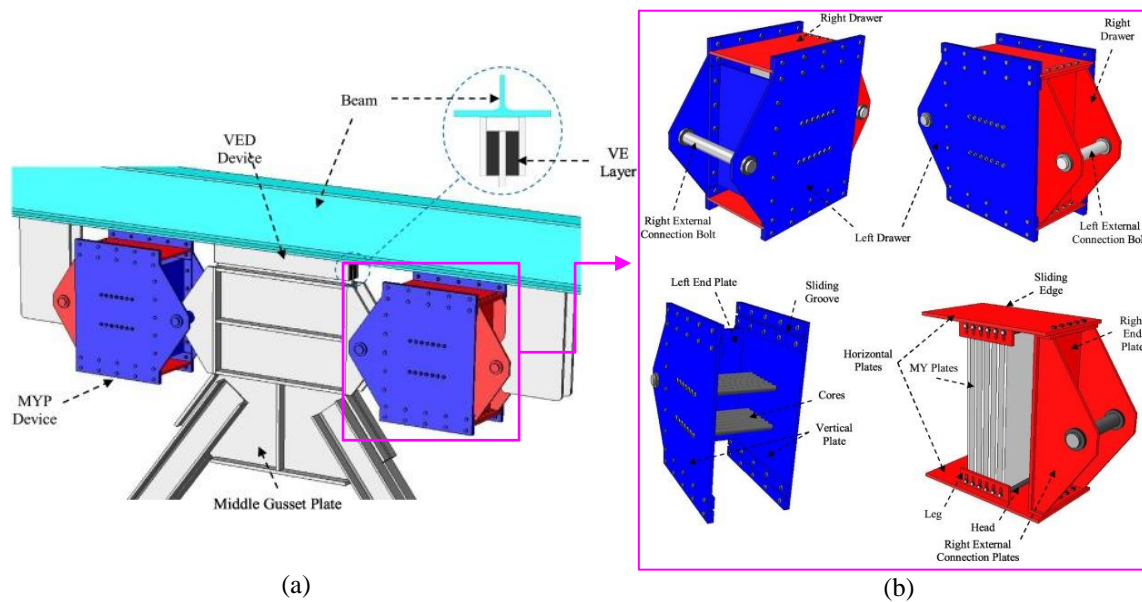


Figure 4. Metallic-yielding pistonic damper [71]: (a) chevron braced frame equipped with the MYP device; (b) details of the MYP device

Tanaka and Sasaki [84, 85] demonstrated in their studies that the curves of the panels using the same steel showed a common envelope irrespective of the width-thickness ratio of the panels.

Under cyclic loading, also, Tanaka and Sasaki [86] verified the hysteretic performance of shear panel dampers with ultra-low yield strength steel (100 MPa). These panels displayed an excellent cyclic performance, which is appropriate for hysteretic dampers [86]. Typical fracture modes of the specimens can be seen in Figure 5 [86]. Using this concept, Matteis et al. [87] studied the seismic response of MR steel frames with low-yield steel shear panels.

In the research works afterwards, Chan et al. [77] investigated a new earthquake damper, called yielding shear panel device (YSPD), for civil structures. This system was capable to dissipate the seismic energy through the plastic shear deformation of an external diaphragm steel plate that was welded inside a square hollow section. As mentioned before in this section, a metallic shear panel damper is commonly designed using low-yield-strength steel, owing to its high ductility [88, 89]. In this regard, Ming-hasiang et al. [61] reported that steel shear plate device with a low yield strength was capable of dissipating or absorbing input energy in a stable behavior. In order to simulate the hysteretic behavior of this device, the authors developed an analytical model and displayed the fact that the model was valid for simulating the reciprocal energy dissipation behavior. Dusicka et al. [90] investigated the cyclic behavior of a steel plate damper under large inelastic strains with constant amplitudes between 1% and 7%.

Study of different types of steel plates found that their fatigue life at low cycles was similar and that the strain rate had no significant effect on that. For conventional grade steel, the maximum cyclic stress exceeded the yield strength by approximately 2.0 times; for low yield point steel, it exceeded by 4.8 times. In response to the maximum cyclic stress, it was found that the manufacturing specifications were more important than the yield strength. Similarly, Aoki et al. [91, 92] performed a dynamic shear test of low-yield steel panel dampers to evaluate their seismic performance. In another study, YSPD finite element models were developed by Hossain et al. [73] using ANSYS. Additionally, Zhang et al. [93, 94] have previously focused on development and testing of a low-yield-strength steel shear panel damper (LYSPD) with an elongation ratio of around 60%. In addition to static and dynamic constant cyclic tests, further research was conducted on the performance characteristics of the developed LYSPD, including fatigue characteristics. Based on the test results, it appeared that the seismic performance of the LYSPD was likely to be underestimated by static tests. Dynamic tests were therefore necessary to ensure the reliability of LYSPD.

It should be noted that Narayanan et al. [95, 96] investigated the concept of perforated plates. Notably, it was reported that Chan et al. [97] in order to develop a new yielding shear panel device, perforated a thin yielding shear panel and welded it inside a short length square hollow section. It is considered a modified version of the Yielding Shear Panel Device (YSPD). This device is known as a Perforated Yielding Shear Panel Device

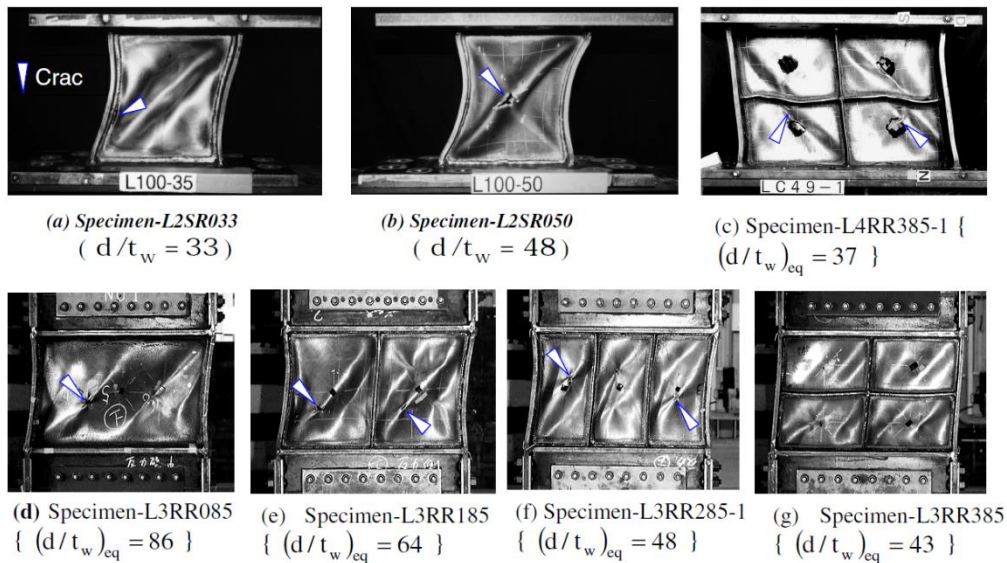


Figure 5. Fracture modes of the shear panel samples [86]

(PYSPD). The energy dissipation capability of devices with certain plate slenderness was large under quasi-static conditions and was characterized by a stable and repeatable force-displacement hysteresis. A perforated specimen has a lower elastic stiffness and yield strength than one that is not perforated. Due to the lack of study on the shape of the steel shear panel damper plate (SSPD), with the use of the finite element method, Liu and Shimoda [98] and Deng et al. [99] presented a shape optimization method for improving the deformation capacity [98] and the low cycle fatigue performance [99] of steel shear panel dampers. Using a shape optimization approach, a shear panel damper could be significantly improved in terms of deformation capacity. Moreover, a significant improvement in the low cycle fatigue performance of the SSPD was found, and the global optimal solution was found to be more effective than the local optimal solution [99]. Later, in a study by Sahoo et al. [100], an experimental investigations was conducted on a passive energy dissipation device made of steel plates that were capable of yielding under cyclic loads

both in flexure and shear. It was possible to dissipate energy through shear yielding on the rectangular web plate of the device while two end plates in an X-configuration were allowed to yield under flexural action (see Figure 6). The device was called SAFYD in brief. For the same level of lateral strength and energy dissipation, SAFYD devices could save considerable materials and costs. It was found that the hysteretic energy could be dissipated at drift levels up to 12.5% without fracture by X-shaped flexural plates and reentrant corners in SAFYD devices [100].

In a similar study by Zhu et al. [101] it was proved that optimized dampers exhibit a much more uniform distribution of plastic deformation than the non-optimized dampers, and the stress concentration was significantly reduced as compared to the non-optimized dampers. Whilst, Shi et al. [102] developed a theoretical model of the shape gradient function by using the Lagrange multiplier method that takes into account optimality conditions for maximizing the plastic work. The developed shape optimization method to design

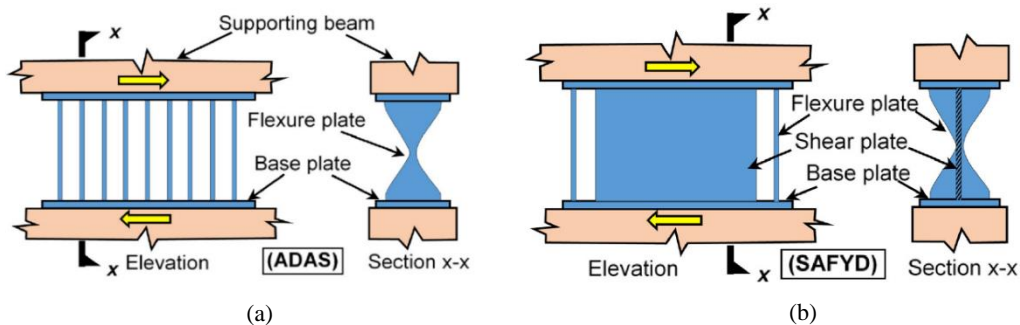


Figure 6. (a) ADAS device; (b) SAFYD device [100]

SPDs made of low yield steel was applied and results of the study indicated that the optimization method developed by the researchers enhanced the plastic work of SPDs effectively. In addition, this method had the advantage of allowing SPDs to be designed more efficiently when thickness variation was taken into account. Figure 7 presents a view of the low yield steel shear panel dampers, which includes an initial shape (Figure 7(a)) and the optimal shape without considering thickness variation (Figure 7(b) and (c)). Recently, buckling restrained shear panel damper was modified indirectly by Lin et al. [103] and was called the indirect buckling restrained shear panel damper (IBRSPD). This modified damper consists of stiffeners and energy dissipation units formed from hot-rolled H beams. It was found that the modified damper can reduce the seismic response. It has been indicated that the shear buckling of the core plates and the premature failure of the boundary plates are considered two of the most common challenges associated with shear panel dampers that cause insufficient energy dissipation and undesirable ultra-low cycle fatigue performance.

In a more recent study by Yao et al. [104], steel square tubes were used as out-of-plane stiffeners to support a low-yield-point steel core plate, and a reduced flange plate section was used to limit the fracture damage at the end (see Figure 8(b)). It has been demonstrated that steel perforated shear panel dampers may have detrimental hysteretic performance if pinching effects and softening occur due to cumulative damage caused by lateral-torsional buckling that may occur when plates are excessively thin and delimited by contiguous perforations [105]. Many research works have been conducted to investigate how geometric parameters affect panel hysteretic response, particularly with regard to pinching effects induced by buckling. Among the factors to be considered are the width-thickness ratio, corner perforation, stiffening rib size, perforation diameter, minimum spacing between holes, depth of the non-perforated area, and the boundary constraints of shear panel dampers [81, 105-107]. Moreover, the shear plastic behavior of SPDs was described with and without consideration of the cyclic hardening by Chaofeng et al. [108]. Their developed model is suitable for describing the mechanical properties of large plastic strains. A follow-up study was conducted to determine whether FEM could be used to assess the deformation capacity of a shear panel damper [109].

Steel shear panel dampers are often subject to low cycle fatigue damage near the welded stiffener, which negatively impacts their fatigue performance. In light of this fact, these dampers were stiffened to experience a high-performance. Experimental studies were also conducted on stiffened shear panel dampers in order to develop high-performance damping mechanisms by Koike et al. [110]. In parallel, a buckling restrained shear

panel damper (BRSPD) was introduced and proposed as a novel steel shear panel damper by Kailai et al. [111]. In their model, there are two main components of a BRSPD, an energy dissipation plate and two restraining plates. Energy dissipation plates do not have any stiffeners welded to them. Bolts on each side of the two restraining plates prevent out-of-plane buckling of the energy dissipation plate. Based on the results of the tests, it could be concluded that restraining plates of sufficient stiffness and strength can effectively prevent the out-of-plane buckling of the energy dissipation plate [111]. More recently, Quan et al. [112, 113] developed a classical shear panel damper using a corrugated steel plate. As a result of the experimental studies, it was demonstrated that direction of the corrugated shear panel modified the plastic failure modes of the dampers, which resulted in out-of-plane failure of a demountable horizontal corrugated shear panel damper (DCSPD-H) and the local buckling failure of a demountable vertical corrugated shear panel damper (DCSPD-V). Zhao et al. [114, 115] proposed a bent shear panel damper and examined it experimentally and numerically, which can be installed in eccentrically braced composite frames to effectively improve the stiffness and strength of such frames. On other hand, it should be noted that several previous studies have also studied and examined this idea in the context of walls [116-119].

In accordance with the previous research, low-yield-strength steel is typically used for steel shear panel dampers for dissipating or absorbing input energy. Whilst, it has been shown that steel shear panel dampers suffer from local buckling failure, which is considered to be the most common problem associated with shear panel dampers that result in inadequate energy dissipation caused by pinching effects induced by buckling and undesirable ultra-low cycle fatigue performance. In light of this fact, stiffening the shear plate will be helpful in overcoming the challenges associated with this drawback where stiffeners will prevent out-of-plane buckling, which will result in high plastic deformation. A second approach is that the steel shear panels can be perforated to prevent general buckling of the shear plates, thereby developing high performance.

2. 2. Steel Pipe Dampers Pipe dampers are among the steel yielding dampers, which can be utilized as a possible hysteretic damper. This system operates on the principle of passive energy dissipation. Some experimental studies have been conducted to investigate the effect of steel pipes on shear transmission. For instance, Frosch [120] tested the effect of steel pipe connectors on the transfer of shear between precast infill wall panels and concrete elements of the building frame.

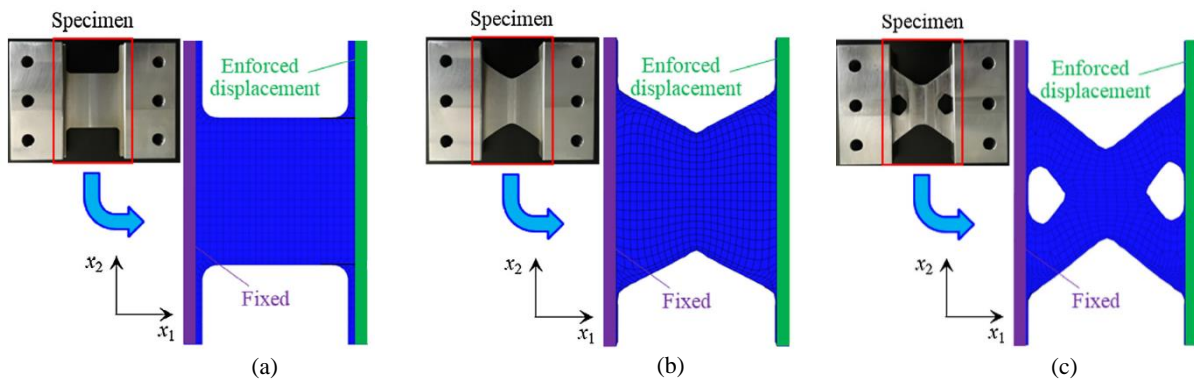


Figure 7. View of low yield steel shear panel dampers (SPDs) [102]: (a) The initial shape; (b) and (c) the optimal shape without considering thickness variation

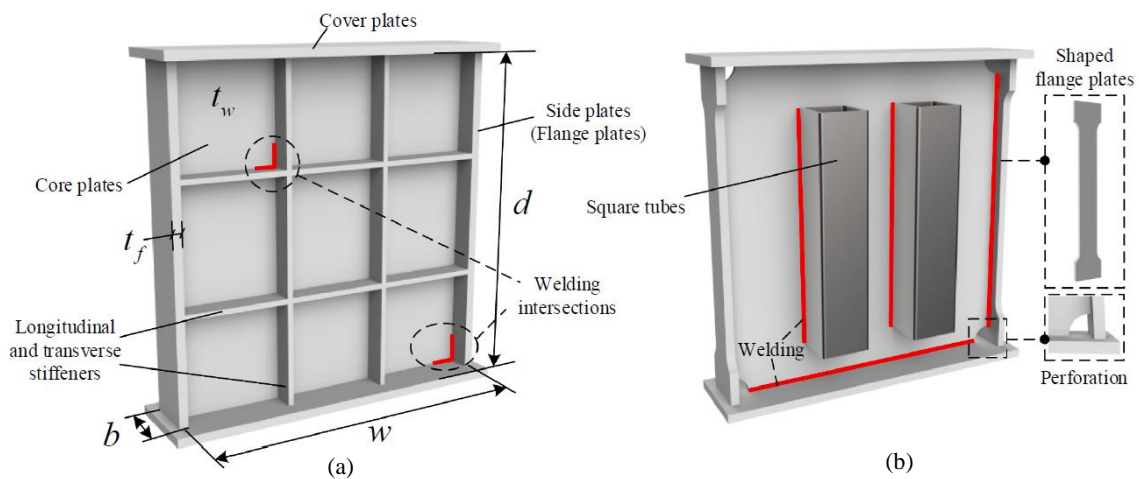


Figure 8. Schematic view of shear panel dampers: (a) with conventional stiffeners [99]; (b) with square steel tubes [104]

As well, Deam et al. [121] investigated transfer of shear force between a concrete slab and a laminated veneer lumber beam using steel pipe. Kafi [122] performed numerical and experimental research on the effects of hollow steel pipes on the seismic behavior of CBFs. It was shown that use of the hollow steel pipe significantly improved the ductility of the frames and delayed buckling of the braces. Maleki and Bagheri [123] studied two types of steel pipe dampers, filled and unfilled with concrete, under a cyclic shear load. Their study aimed to assess whether the segments can be used as seismic dampers. Under severe cyclic shear loading, the bare steel pipes exhibited a stable hysteretic behavior as they could absorb a considerable amount of energy. It has been demonstrated that concrete-filled pipes under shear loading fail in a non-ductile manner due to concrete crushing even though the pipe itself is unharmed. Further, according to Maleki and Mahjoubi [124], a new pipe damper was introduced, which was called the dual-pipe damper (DPD). The DPD was tested and investigated

analytically. In order to build the device, two pipes were welded at specific locations and loaded in shear at different points. The pipes dissipate the energy of the inelastic cyclic deformation by flexing their bodies. There are a number of advantages of the DPD, including its light weight, ease of fabrication, and affordability. About 36% of its height can be deformed without losing its structural integrity. In addition, it was reported that a DPD is more efficient than two single pipe dampers in terms of strength, stiffness, and energy dissipation. Installation of DPDs in structures can be classified into four types based on their application, as depicted in Figure 9. In a subsequent study by Maleki and Mahjoubi [125], the two welded pipes had main pipes and inner pipes and the spaces between the pipes were filled with metals such as lead, zinc, etc. This type of pipe dampers is named infilled-pipe damper or IPD. Compared to an equivalent DPD damper, IPD dampers have significantly higher strength and stiffness, as well as higher energy dissipation capacity. Due to the energy absorption

properties of lead, the lead-IPD exhibited a superior performance. Furthermore, lead-filled IPDs dissipate more energy than zinc-filled IPDs due to cracks that began forming in zinc during the initial loading cycles. It is generally recommended that the main pipe diameter be 1.5 and 1.40 times the inner pipe diameter for IPDs filled with lead and zinc, respectively. In terms of efficiency and reliability, IPDs with diameter-to-thickness and length-to-diameter ratios of 20 and less than 0.6, respectively, are extremely effective. The single pipe damper and dual-pipe damper can be seen in Figure 10(a). As another example, Javanmardi et al. [126] proposed an innovative vertical pipe damper (VPD) consisting of a short vertical pipe segment welded to two anchor plates. It was found that VPDs possess greater

ductility and energy dissipation capability than PDs and DPDs. VPDs are also capable of dissipating energy bidirectionally. An X-shaped pipe damper is constructed by welding two oppositely positioned pipe halves together to form an X-shaped core, and connecting the X-shaped core to the side plates by fillet welds or circumferential welding as depicted in Figure 10(c) [127]. With only half pipe usage, the XPDs can provide similar lateral load resistance as dual pipe dampers. In all cases, the XPD specimens showed stable and bulged hysteretic loops, and showed a steady increase in strength following yielding until fracture failure [127]. There was a general failure at welds in fillet weld specimens, as well as tensile tearing at the pipe plates in circumferential weld specimens.

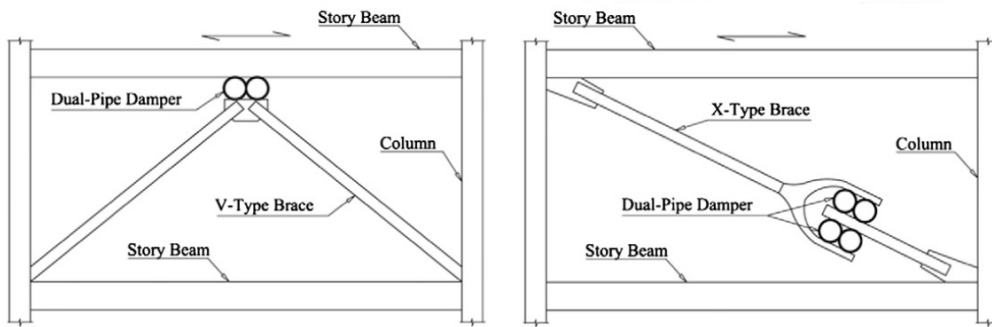


Figure 9. Schematics for DPD installation [124]

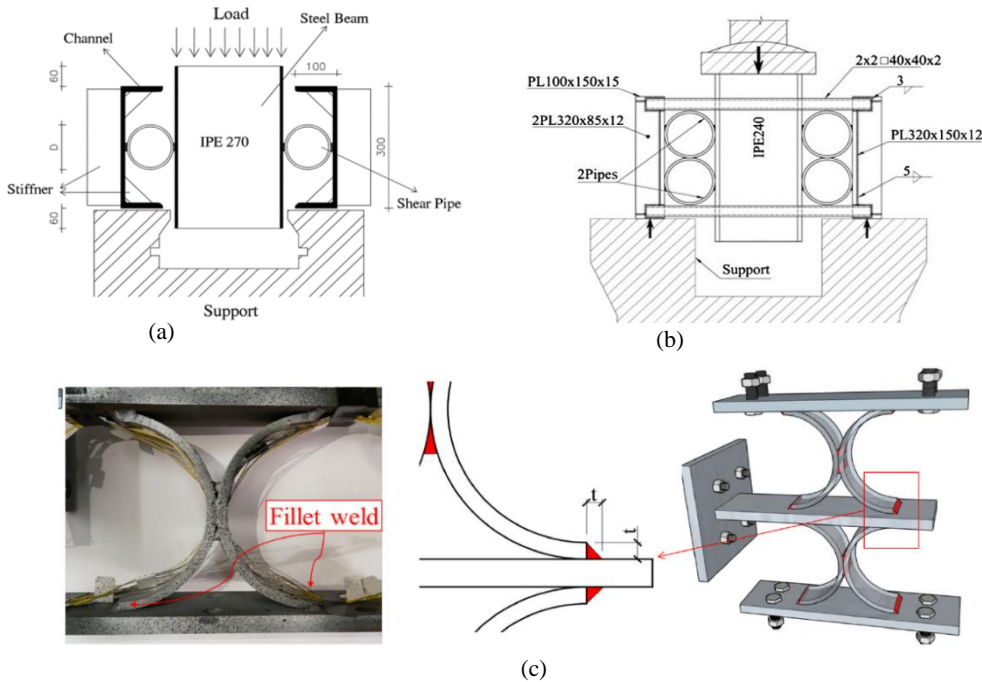


Figure 10. Details of steel pipe damper: (a) single pipe damper; (b) dual-pipe damper; (c) X-shaped pipe dampers

Recently, researchers have been interested in the application of two-level control systems. This system is based on the concept of combining two different control devices with different strengths and stiffness that results in dual seismic behavior as a result of their different energy dissipation levels. This concept has also been applied by using a multi-pipe damper.

Cheraghi and Zahrai [128, 129] evaluated the seismic performance of a multi-level pipe-in-pipe passive control system under cyclic loading analytically and experimentally. Afterwards, the attained hysteresis curves exhibited a highly ductile behavior. In addition, obtained hysteresis curves show that the multilevel system as expected can reliably dissipate energy at different energy levels leading to ductility ratios of about 15 to 37 and equivalent viscous damping ratios of about 36 to 50%. A modification of this system was made by the same authors [130] in another study in which zinc or lead was injected into the inner pipe or a diaphragm was slit within the pipe. According to the results, adding lead infill does not have a considerable effect on damper stiffness, whereas adding zinc infill and slit diaphragm can significantly increase damper stiffness, sometimes up to ten times, depending on the plate thickness and pipe diameter. It was found that the seismic response of steel structures equipped with multi-level pipe dampers [131], MPDs, was reduced and the maximum displacement and roof acceleration were lowered at 19-42% and 11-16%, respectively, in comparison to those of bare frames [131]. A new pipe-fuse damper (PFD) was proposed by Aghlara et al. [34] to enhance the seismic response of structures. This damper has been assessed experimentally and numerically and the location suggested for the installation of PFDs are illustrated in Figure 11. The damper showed a stable hysteretic behavior, easy replacement after each failure, less pinching effects and considerable energy dissipation. The effective dimensions of the pipes used in a DPD were recently

developed such that they can be implemented in a steel building frame [132, 133]. It was mentioned that the structures equipped with dual-pipe dampers [132, 133] and multi-pipe dampers exhibited better seismic retrofitting properties than bare frames.

Despite the pipe dampers being able to be manufactured easily without requiring casting or precision cutting tools, making them one of the most cost-effective passive metallic dampers, they have some challenges. To guarantee ductile behavior, mild steel pipes must have high elongation in tensile coupons. A further problem was that cracks originated in the pipe material adjacent to the welds which linked the pipe to the plates, propagated throughout the thickness and length of the pipe, causing the pipe to fail. Therefore, it is important to carefully choose the welding type and position so that this behavior is enhanced. In light of the above, it may be possible to consider better connecting methods such as bolted connections for pipe dampers in future studies.

2. 2. 1. Steel Ring Damper Steel ring dampers have been extensively used to improve seismic performance of structures. The use of steel ring dampers as passive seismic dampers has been confirmed by several studies [134-138]. Single and dual-ring damper have been sketched in Figure 12(a and b), respectively. A new system comprising one or two concentric steel rings installed vertically within cross-braced bays was proposed by Behnamfar et al. [138] This system was capable of increasing the ductility of cross-braced frames to levels comparable to those seen in ductile moment frames. It has been designed so that the steel rings fail in bending before the braces fail in compression. In this case, the rings serve as seismic fuses with multiple bending plastic hinges. Studies based on nonlinear pushover and cyclic analyses suggested the desirable use of the proposed system.

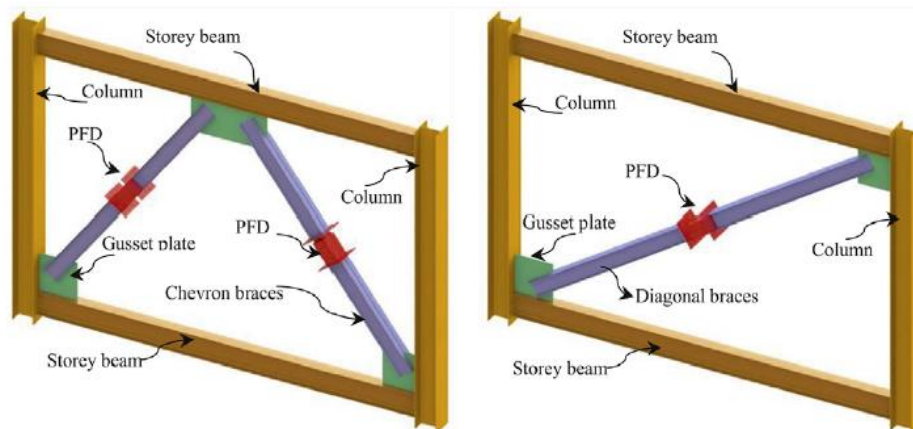


Figure 11. Location suggested for the installation of the pipe-fuse damper [34]



Figure 12. Steel ring dampers; (a) single ring; (b) dual-ring

2. 3. Steel Curved Dampers

2. 3. 1. Steel U-Shaped Plate Damper

The U-shaped plate damper has been invented by Kelly et al. [48] in 1972. It is a very simple damper. The strip begins in a semicircular configuration with two equal straight sections on either side. Once one side is moved relative to the other, the strip will take on a semicircular shape. The U-strip damper exhibits very large deformations in the elastic range because it is deformed in one direction. There is a common use for U-shaped dampers in isolation system. It starts working when the isolation layer is subjected to a relative displacement. Importance of seismic isolation systems in the world has been widely acknowledged following the Hanshin-Awaji (Kobe) earthquake. In this context, the displacement of isolators can be controlled by adding supplemental damping to the isolation systems. An example is the use of friction in base isolation systems by Abed et al. [139] to reduce structural response and enhance energy dissipation under lateral loads. They mentioned that these systems should be studied under bidirectional loading since further research and study is required before these systems can be implemented in practical applications in real life. Skinner [140] and Yoshikawa et al. [141] applied U-shaped dampers to base isolation systems with rubber bearings, which are described as typical hysteretic dampers. To evaluate the inelastic flexural deformation of U-shaped plates, Shultz and Magana [142] performed a number of experiments. According to Suzuki et al. [143], the horizontal property, velocity and temperature dependence of U-shaped steel dampers were discussed, as well as the results of experiments [143]. In a study by Kishiki et al. [144], a U-shaped damper that was capable of being used with an isolation bearing was designed (Figure 13(a)). In order to reduce the seismic demands of low- or medium-rise structures, Sang-Hoon et al. [145, 146] developed a base isolating system. This system was studied experimentally using shake table tests. In the study, they [145, 146] considered a base isolating system comprising of laminated-rubber bearings and U-shaped hysteretic (UH) dampers made of high toughness steel (HTS), and which are fabricated with slotted holes to increase deformation resistance. According to a shake-table test, a base-isolated structure with UH dampers could limit its seismic demands by extending the structural period. In addition, U-shaped dampers have

been added to the beam-column connection by Iwasaki et al. [147]. Tagawa and Gao [148] added this system to frames. The system depletes seismic energy into the structure by yielding U-shaped steel dampers (Figure 13(b)). As reported by Deng et al. [149], in their study, an innovative crawler steel damper was designed and installed in bridges, which can work with isolation bearings. The damper was composed of two U-shaped steel energy dissipation plates connected by two connection plates, and each U-shaped plate was bolted to the upper and lower connection plates. Among the most important controls on the damper performance are the thickness and height of the plates used for energy dissipation. According to Figure 13(C), plates were arranged according to a specific pattern. It was recommended that shape optimization be implemented in order to improve the hysteretic performance of the U-shaped damper [150].

Atasever et al. [151, 152] modeled the hysteretic behavior of U-shaped dampers (UDs) by ABAQUS finite element software and developed U-shaped steel dampers with perforated and nonparallel arm configurations (Figure 14). According to their study [151, 152], the developed damper device could be used in seismic applications. Qu et al. [153] introduced and described a new replaceable U-shaped steel damper. Stable hysteretic behaviors and satisfactory energy-dissipating capacities were obtained from their test results. In addition to being robust, the damper was also rupture-tolerant and it was demonstrated that the damper that was repaired following a severe earthquake by replacing the U-shaped steel plates continued to operate satisfactorily in the event of another earthquake. From an applied point of view, to combine the advantages of the yielding dampers and the buckling resistant braces (BRB), U-shaped dampers were utilized in braces by Taiyari et al. [154]. After several cycles of large inelastic deformations, the bracing system remained stable and dissipated energy well. More recently, U-shape dampers were added to a steel tank isolated by multiple friction pendulum bearings, which were studied by Yu et al. [155] where their effects on earthquake responses of an isolated inner steel tank were investigated. It was found that the U-shaped dampers were effective at controlling the displacement of the isolators.

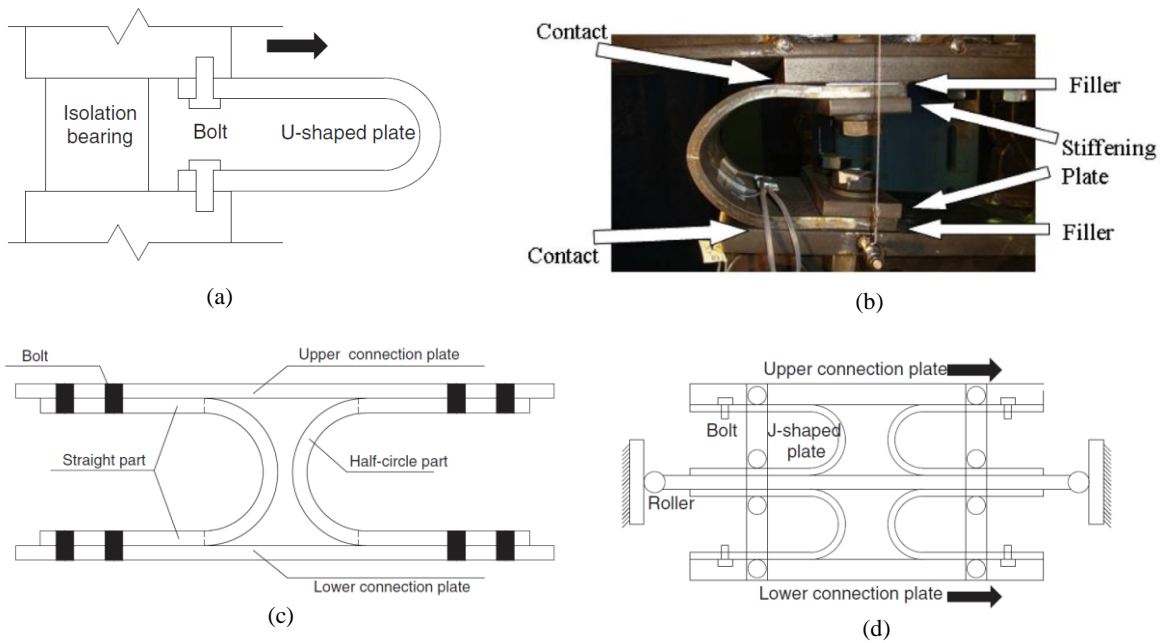


Figure 13. (a) U-shaped damper for bridges; (b) U-shaped damper under compression deformation; (c) Crawler steel damper and (d) schematic view of J-shaped damper

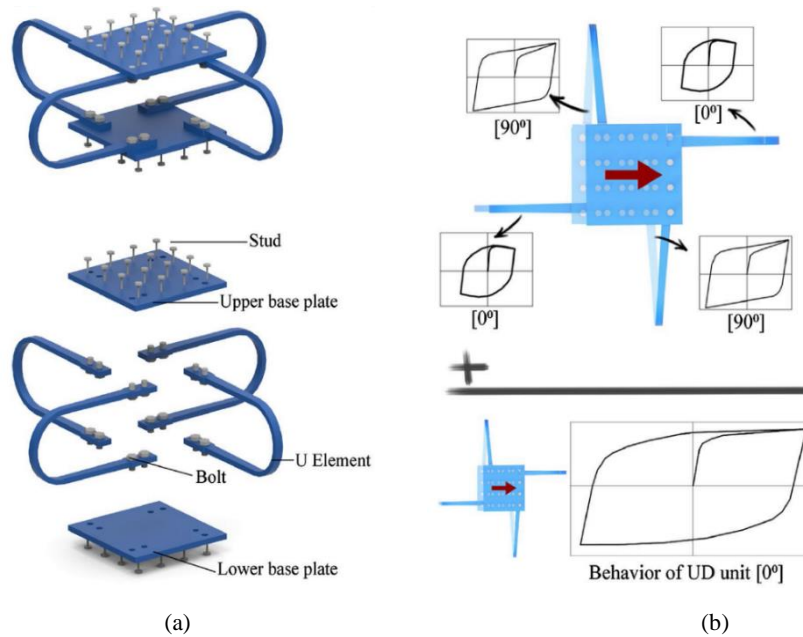


Figure 14. (a) configuration of UD; (b) hysteretic behavior of the UDs [151]

It is concluded from the previous results that the height and thickness of the U plates are the two most important factors that affect the dampers' performance where increasing thickness increases dissipation capacity, yield force, and initial stiffness, while increasing height decreases the mentioned parameters. In cases where higher levels of strength and energy

dissipation capacities are required for the damper, either thicker U-shaped steel plates can be used or U elements can be added or subtracted easily to modify seismic characteristics. The results of the tests indicate that the damper has a high level of robustness and is not easily damaged by ruptures in the U-shaped steel plates. Ultimately, a further investigation on the influence of the

thickness of the U-shaped steel plate on the fatigue life of the corresponding damper will be required in the future.

2. 3. 2. Steel Cushions Damper Steel cushions were invented by Özkaynak [156] and tested experimentally. In theory, they were supposed to be installed between chevron-type bracing elements and beams within an RC frame. It was determined by the numerical and experimental investigation that the steel cushions enhanced the RC frame's energy dissipation and damping properties.

2. 3. 3. Steel J-Shaped Damper Conventional approaches to earthquake-resistant building design are based on the assumption that the building's strength, stiffness, and inelastic deformation capacity are sufficient to withstand the effects of an earthquake at a given level. In most modern structures, however, seismic energy is mitigated before it reaches the structural elements as part of the modern approach.

The J-dampers were invented by Kato et al. [157, 158] in 2005 and used in a spatial structure at a location between the upper structure and the substructure of the system. It was demonstrated that J-dampers can experience large deformations during severe earthquakes. Following this study, hysteresis devices designed in the shape of Js were discussed in terms of their mechanical properties [159]. Figure 13(d) illustrates the schematic view of the J-shaped damper.

In addition, for the sake of practical applications, using steel cushions, and U- and J-shaped steel plates with longitudinally slotted holes on one flange makes the damper easy to install. Meanwhile, premature ruptures were observed at perforated plate cross-sections due to concentric plate yielding. As a consequence, it is

essential to design the working flange width in accordance with the maximum probable displacement demands on the damper.

2. 3. 4. S-Shaped Steel Plate Damper Zhai et al. [160] have developed a new metallic structural fuse for seismic resistant applications. This device is known as an S-shaped steel plate damper (SSPD), which has been tested experimentally and numerically. SSPDs are constructed from two S-shaped plates, which are easy to fabricate, install, inspect, and replace. The related damper, SSPD, is demonstrated in Figure 15. An S-shaped arc plate deforms flexibly in the plastic zone when it experiences small or medium displacements. This enables seismic energy to be dissipated. When a relatively large displacement is present, deformation changes from a flexural to a tensile pattern. There is a stable hysteresis loop characteristic for the SSPD, good energy dissipation and large deformation and ductility capacity. The predominant failure mode is characterized by fractures of the end plates as well as squeezed indents when there is a large displacement at which the fatigue performance becomes more critical. Dampers possess properties such as high strength-to-mass ratios, secondary stiffness, and overstrength coefficients as well as stable flexural-tensile behavior. In a study by Wang et al. [161], the axial tension and compression corrugated steel plate damper (ATCCSPD) was proposed for applications in axial tension and compression. It was demonstrated that the ATCCSPD specimens have stable and exhibit full hysteretic curves, as well as a satisfactory degree of ductility and energy dissipation capacity. The proposed formula was found to be conservative when compared with the test results and, therefore, suitable for engineering applications.

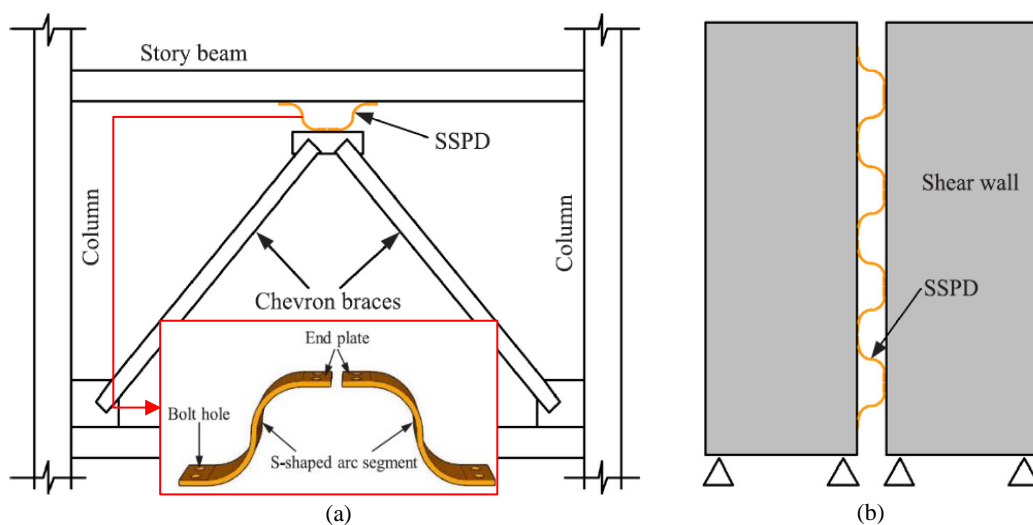


Figure 15. The potential applications of SSPD [160]: (a) Chevron braced frame equipped with SSPD; (b) Rocking wall system

The discussed U-shaped, J-shaped, and S-shaped steel plate dampers have the benefit of avoiding the drawbacks associated with standard damper systems that are commonly used with chevron bracing. On the other hand, these dampers have not been investigated regarding problems related to the use of them in braces. In order to assess design criteria for codification and practical applications, further experiments and numerical analyses of this scenario are needed in order to reach the final outcome.

2. 3. 5. Steel Curved Damper A metallic damper dispenses energy satisfactorily, is inexpensive, and is easy to install, which makes it widely used. In various applications, structural curved steel dampers are used to effectively mitigate damages at specific points in the structure. It has been highlighted that the shape of a curved-shaped damper determines the stability and saturation of hysteretic behavior in the in-plane direction [162]. The length and angle between the two ends of a curved damper influence its behavior. Curved plate dampers have three main parameters: thickness (t), width (b), and radius (R) and there is a relationship between the damper performance and these parameters.

A new generation of steel dampers was suggested and introduced by Hsu and Halim [163] by completing their previous investigation on knee braces, which is known as steel curved damper. Hsu and Halim [163] designed and installed this damper in moment-resisting frames. Steel plates are used to fabricate the damper, which has a curved shape. Afterwards, an experiment was conducted to test the performance of the damper in a beam-to-column connection. A result of the lateral movement was generation of eccentricity within the curved damper, which consequently increased the lateral stiffness of the beam-column connection. Based on the test results, it was proved that a smaller damper angle increased the frame strength. Moreover, the test results showed that the curved dampers significantly improved the strength, stiffness, and energy dissipation of the moment resisting frames when they were installed. Also, the curved damper was applied in a braced frame by Hsu and Halim [164]. The new brace equipped with the curved damper (see Figure 16(a)) displayed a significant viscous damping ratio of approximately 26–37%. It was found that the new system tolerated story drifts of around 5% without significant deterioration in strength, and displayed stable hysteretic behavior throughout the complete loading process, especially when the plate depth/thickness ratios of the curved dampers were lower than 4. Specifically, the curved plate damper was studied analytically and experimentally by Zheng et al. [165], and key parameters of the curved plate damper were derived, including elastic lateral stiffness, yield strength, and yield displacement. Based on the results of the

investigation, it was determined that the damper had a large initial stiffness, that no obvious damage was present, and that the hysteresis loop was full. In terms of deformation and energy dissipation, the dampers tested performed well.

Afterwards, Ghabussi et al. [166, 167] used this damper in frame structures to improve their seismic performance. In both the pitched roof symmetric portal frame and the mono pitch portal frame, dampers with a 30° and 60° angle were most effective at reducing energy dissipation and maintaining frame strength. Additionally, both types of portal frames showed marked improvements in seismic performance. Figure 16 illustrates the use of a curved damper in the braced frame and beam-to-column connections of the building, which can significantly improve the stiffness and ductility of the structure.

A combined damper was proposed by Shojaeifar et al. [168], which is combined of triangular added damping and stiffness (TADAS) dampers in combination with curved dampers and is called Curved-TADAS damper (Figure 17). This combined damper was installed in a moment resisting steel frame (MRSF) in the beam-column connection region and its seismic performance was assessed numerically using the finite element method by ABAQUS. Width of the curved damper, thickness of the TADAS damper and number of the TADAS dampers were considered as variable parameters. Based on the results of the study [168], Curved-TADAS dampers were successfully used to reduce structural responses to seismic loads and prevent structural failure as a result of dissipation of a large amount of seismic energy.

Furthermore, Using the recently developed curved dampers (CDs) with conventional steel trusses, a novel system called "curved damper truss moment frame" (CDTMF) was developed by Fathizadeh et al. [169, 170]. An illustration of the geometry of the curved damper truss moment frame can be seen in Figure 18. A comparison of this system was made with the recently proposed buckling restrained knee braced truss moment frame (BRKBTMF) system. Based on the results of the pushover analysis, CDTMF structures were much more ductile and have higher energy dissipation capacities than BRKBTMF structures. In a follow-up study by Fathizadeh et al. [171], seismic responses of multi-story buildings equipped with CDSRMFs were examined through the use of both nonlinear static and nonlinear dynamic analyses. Added curved dampers significantly enhanced the stiffness, strength, and energy dissipation of CDSRMFs compared to RMF and SRMF structures. For instance, there has been an increase of more than 100% in the energy absorption capacity of three-story CDSRMF structures compared to SRMF structures, followed by an increase of more than 190% for six- and

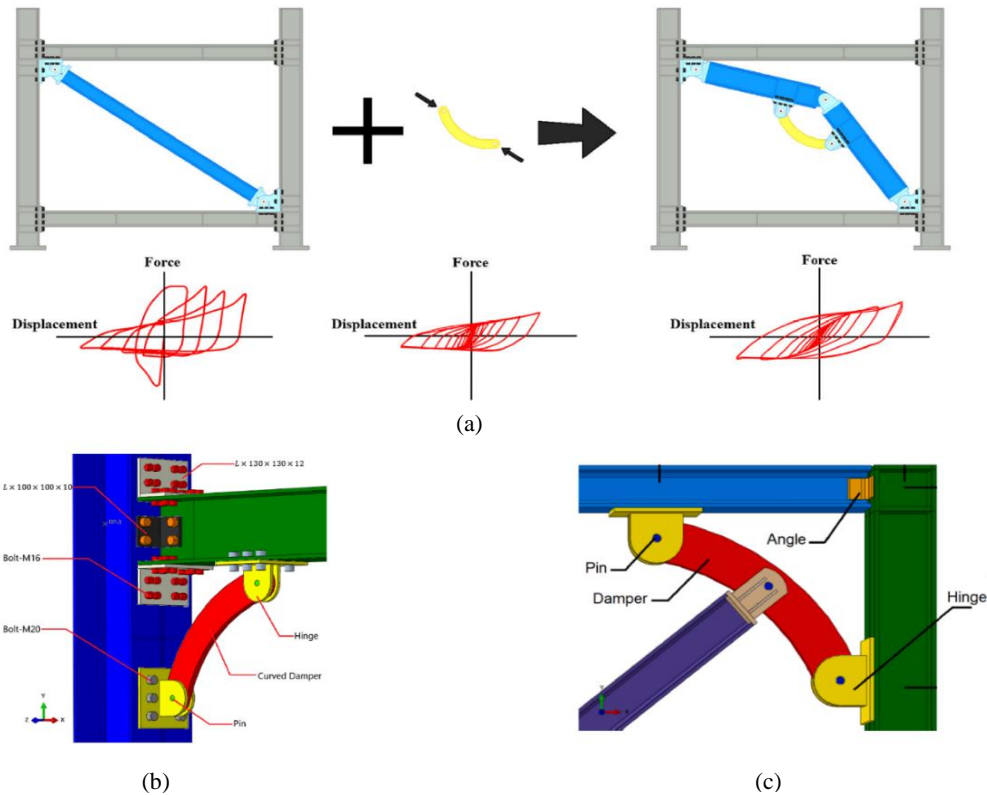


Figure 16. (a) brace with steel curved damper; (b) semi-rigid frame equipped with 60° steel curved damper (SRF-SCD); (c) braced frame equipped with steel curved dampers

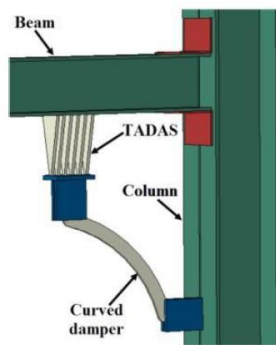


Figure 17. Curved-TADAS damper [168]

nine-story CDSRMF structures. Finally, based on the performed research tasks, it could be concluded that no visible cracks and no obvious damage were observed in curved dampers during the standard and the fatigue loadings. In addition, full hysteresis loops were observed under both loading conditions. In comparison with the knee system, curved damper elements have proved to be an effective structural fuse that absorbs earthquake energy and is easily interchangeable, as opposed to knee elements, which can form plastic hinges at the joints between the brace and column and the brace and beam.

According to the previous results, a curved steel damper can dissipate energy effectively in seismic applications. A final point worth mentioning is that the choice of the damper dimensions and angle affects seismic performance and can be investigated by optimization algorithms in future research. According to the recommendations, curved dampers should have an angle between 30° and 60°. A 60° damper in the steel-braced frame is the most effective steel curved damper in terms of energy dissipation and frame strength.

2. 4. Steel Slit Dampers There are various types of slit dampers, but on the whole, they are considered to be metallic yielding dampers owing to the fact that their damping behavior is influenced by the yielding of steel in one way or another. Steel slit dampers are the most commonly used passive energy dissipation devices [4]. This type of dampers was developed and applied experimentally by Benavent-Climent et al. [47] who conducted research on steel plate slit dampers subjected to shear deformation and attached to semi-rigid connections. Accordingly, Chan and Albermani [23] proposed installation of a slit steel damper as one of the first slit steel dampers in a V-braced system. They obtained analytical equations to predict the ultimate energy absorption capacity and mentioned that the

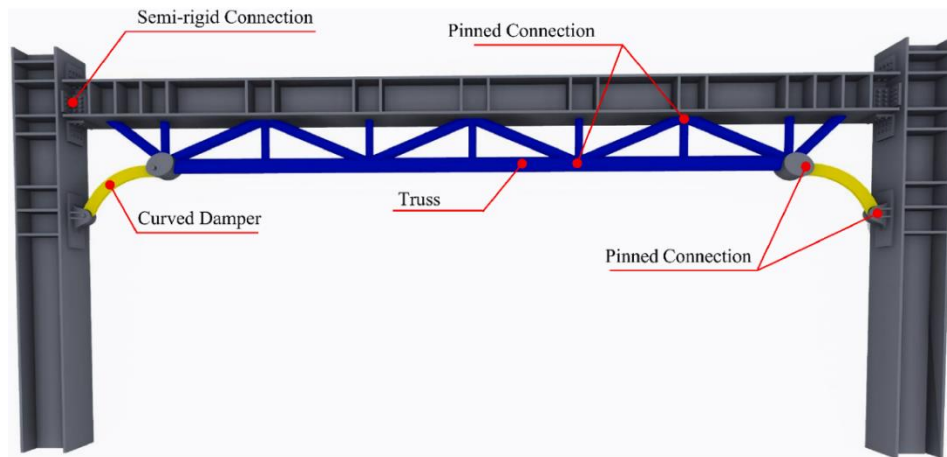


Figure 18. The geometry of the curved damper truss moment frame (CDTMF) [170]

energy dissipation attained could be analytically predicted and in fact, it was found that experimental and analytical results were in good agreement. The energy is consumed by these devices as a result of the flexural yielding of their strips evident between the slits when the device undergoes an inelastic cyclic deformation [23, 39, 172-174]. When a sufficient story drift is applied, each strip of the damper bends in double curvature, and therefore accepts plastic hinges at both ends [39]. In Figure 19, an idealized version of a slit damper is illustrated.

Afterwards, these dampers have been expanded in several other studies [173, 176-178]. For example, Benavent and Climent [179] proposed an alternative slit damper in braces that contained a series of strips in a tube-in-tube structure. Moreover, an effective

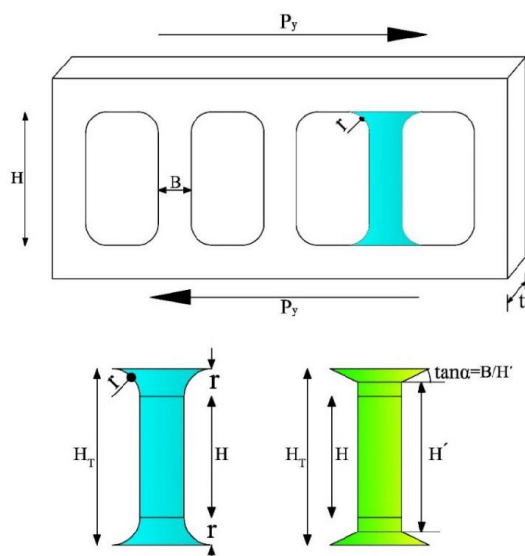


Figure 19. Idealization of a slit damper [175]

configuration was proposed by Ghabraie et al. [177, 180] for solving the strain concentration problem in slit dampers. As a result of using the suggested configuration, the device was able to dissipate more energy and was more resistant to low cycle fatigue. In a study conducted by Vaseghi et al. [181], a buckling restrained brace (BRB) and a tube-in-tube damper (TTD) were individually assessed for retrofitting steel structures. Due to their simplicity in construction and execution, TTD metal dampers have also garnered a great deal of attention in this field. As well as offering better performance than BRB, this damper could also be constructed more easily, leading to lower costs, which made it possible for countries without sophisticated technology to adopt it. In their study, Perform 3D software was used to perform a nonlinear dynamic analysis of the structures before and after retrofitting. As a result of the observation of both systems results, the positive effects of these energy dissipation systems were reduced with an increase in the number of building stories. This indicated that short-order structures are more benefited by such systems. The conductors of another study, Amiri et al [36], proposed a different type of the slit damper, described as a block slit damper. It consists of a box containing a steel block with several slits. In addition to its large shear strength, the damper also showed a high energy dissipation capacity, a stable hysteresis curve, and positive economic characteristics. Askariani et al. [182] suggested using slit link beams in EBFs. Their proposition was to create slits in the web of the link beam so that it could be divided into several vertical strips. An analytical formula was derived and applied in their study to characterize the behavior of the slit link beam. Later, Zhao et al. [183] developed a new damper. In their study [183], a number of slits in the H-profile brace were located along its length in the damper system. According to the results, the perforated webs

were yielded under the influence of in-plane shear, which resulted in dissipation of seismic energy. Meanwhile, it also showed full and stable hysteretic curves.

In a recent research by Almomhammad-albakkar and Behnamfar [39], in order to modify the seismic behavior of X-CBFs, the authors proposed a system consisting of two cross braces, each divided into two segments. In the middle of the bay, the four segments are connected by means of a grooved gusset plate damper (GGPD). By bending of strips developed in the gusset plate in its plane, strips in the GGPD dissipate the seismic energy. A mathematical formula was provided for determining the elastic stiffness as well as the yield and ultimate capacities of the damper. As a result of the calculations, it could be concluded that the analytical formulas and the numerical results were in good agreement. Further, specimens displayed full and stable hysteresis curves, and they behaved similarly in tension and compression. This system is also capable of dissipating significant amounts of energy and can tolerate more than 4% story drifts [39]. As shown in Figure 20, the cross-braced frame equipped with GGPDs undergoes no plastic deformation when subjected to lateral loads (Figure 20(b)).

Using slit dampers in the beam-to-column connections was also considered and applied. Specifically, after suffering of several steel buildings from severe damage during the Northridge (1994) and Kobe (1995) earthquakes, which had been designed firmly to prevent collapse, avoiding human deaths [184, 185]. A considerable amount of damage occurred at the welded connections between the beams and columns, including brittle fractures. Although there was no way to avoid this type of damage for older steel structures that had nonductile connections, it also occurred in some relatively new buildings designed in compliance with current seismic codes [186, 187]. Following the Northridge earthquake and the Kobe earthquake, significant experimental programs were implemented on beam-to-column connections and many improvements were applied [188-192].

In order for steel structures to be considered ductile and strong, beam-to-column connections must be able to achieve the same performance. It is important to note that classical steel connections have a limited rotational capacity due to their design. In this way, as mentioned above, the connection could fail prematurely and in a brittle manner before the plastic hinge could be formed

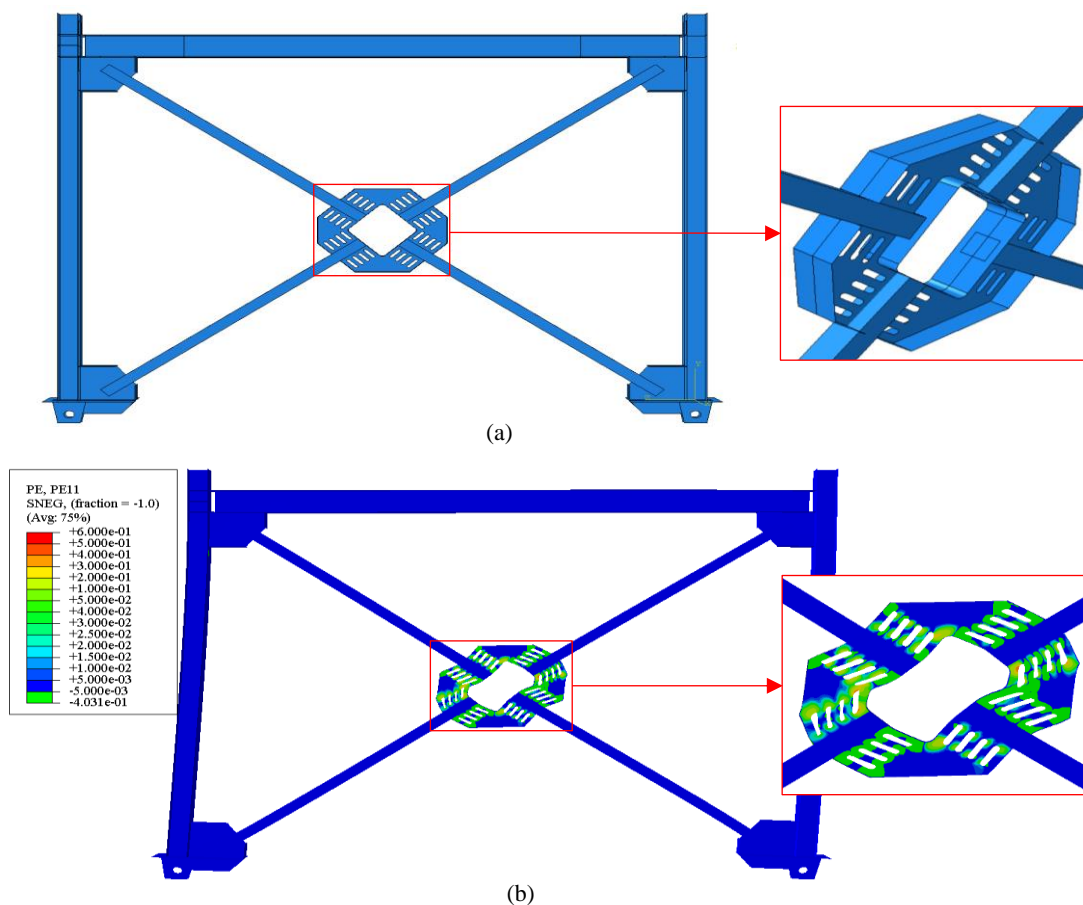


Figure 20. (a) cross-braced frame equipped with the GGPD; (b) distribution of plastic strain in GGPD [39]

in the beam, which is contrary to the principle of a “weak beam with a strong column”. It was proposed during these years that methods could be employed involving reducing the beam sections or strengthening the connections by dampers to provide rotation, stiffness, and strength at the proper level. Therefore, a number of studies have been conducted on the causes of premature and brittle failure of steel connections [193, 194]. In light of this, it would be considered a suitable option to design the moment connection using the plastic behavior of beam or additional devices. As has been mentioned in the previous section, to create a plastic hinge in a beam, an approach was developed by reducing the beam section where a part of the beam flange [195-199] or the beam web [200] was deliberately cut. This concept was first proposed and applied by Plumier in 1990 [201] through creating trapezoidal cut profiles in the beam flanges.

Considering the recent dampers, steel slit dampers are the most widely used. This damper has first been developed and applied in the beam-to-column connections by Oh et al. [173]. According to these authors, a slit damper was installed at the bottom beam flange to absorb seismic energy. One of the major advantages of this system was concentration of plastic deformation at the bottom of the flange in the slit damper. For the verification of the seismic performance of the proposed connection, specimens with conventional welded frame structures were cyclically tested along with three full-scale steel structures fitted with slit dampers. The seismic behavior of beam-to-column connections was studied in a similar study conducted by Shahri and Mousavi [174]. Elliptic slit dampers were installed at the bottom of the beam flange. The effect of steel slit dampers on beam-to-column connections was investigated experimentally and numerically by Köken and Koroğlu [202]. The same authors [203] have also tested beam to column connections with different shapes of steel slit dampers in another study [203] under cyclic

loading in both experimental and numerical experiments. It was concluded that the steel slit dampers can enhance several performance characteristics of the connections, including energy dissipation capacity, hysteretic behavior, and stiffness. Park and Oh [204] described an innovative connection. The proposed connection consists of two main components, which are the upper and lower connectors (see Figure 21). The beam and column were connected by bolts and the mentioned connectors. The lower part is a horizontally arranged steel slit damper that is used to absorb energy. It was found that when the connection is equipped with the proposed system, the plastic deformation is primarily concentrated in the damper. In addition, it was discovered that the hysteresis loops of the proposed connection had a similarly stable behavior in both negative and positive directions. This system complies with the SMF requirements since the full plastic moment of the beam was reached at a rotation angle of 0.04 rad. Therefore, this system can provide a design methodology for low- and mid-rise steel structures.

As a high-performance hysteretic damper, there are several characteristics that distinguish slit dampers from other types of dampers, including strength, ductility, and dissipative ability, which can be adjusted by altering the configuration of the slits. Additionally, these dampers are also distinguished by advantages over other dampers with their ability to be used for braced frames, beam-to-column connections, and shear walls. This makes slit dampers the most commonly used steel yielding dampers in steel structures. More importantly, slit dampers can be configured in several ways, including prismatic and hourglass configurations, which are very effective. Alternatively, it is possible to improve seismic performance of the slit dampers by obtaining their optimal shape. For beam-to-column connections, the effect of the beam effective length and bolt tightening force, etc., should be investigated in follow-up studies.

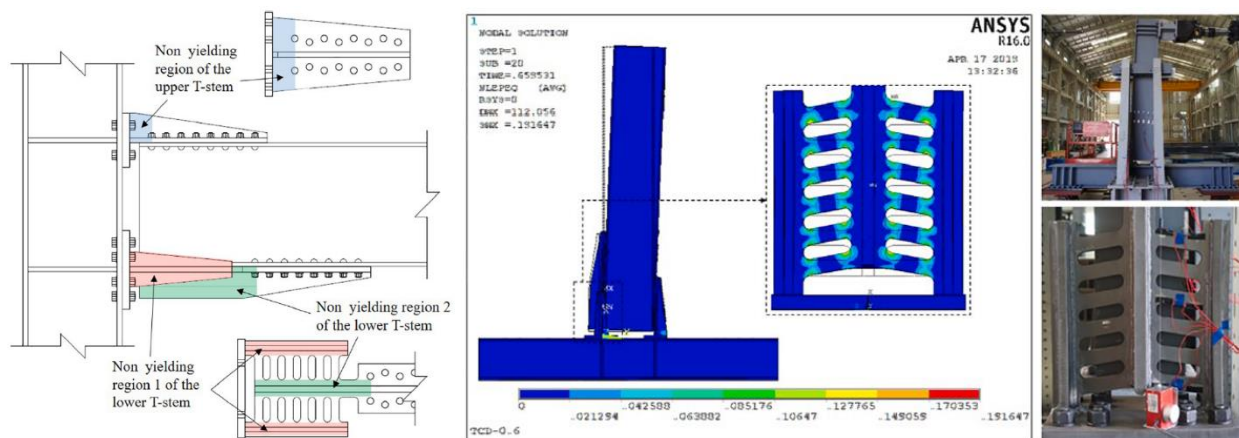


Figure 21. Distribution of the PEEQ and test ultimate state at a rotation angle of 0.04 rad of the proposed connection [204]

Generally, SSDs with short heights tend to buckle due to their shear behavior. It is a fundamental weakness of SSDs that needs to be addressed.

There is another kind of the yielding damper, referred to as the bar damper. This damper can be used for frame structures. The BDs are constructed from steel sections that are commonly used in the steel industry, such as hot-rolled Square Hollow Sections (SHS), C-Channels, plates, and bars [205]. An innovative form of this hysteretic metallic damper was developed by Ghaedi et al. [206, 207], called a bar damper (BD), which is composed of a number of solid bars sandwiched between two plates. As a result of flexural yielding, BD causes input energy due to vibration loads to be dissipated by the solid bars. It should be noted that the damper, despite its simplicity, can be optimized more by optimizing the geometry of the plates and the solid bars in order to ensure uniform stress and strain distributions. From the hysteresis loops of the tested specimens, a substantial cumulative displacement was obtained without significant loss of strength. A new device called fuse-bar damper (BFD) has been proposed by Aghlara and Tahir [205]. The device dissipates energy through use of replaceable bars that act as sacrificial elements. In addition to being economical and easy to install, it also doesn't require any special fabrication techniques. Round steel bars are used as energy absorbing components in the BFD, and these can be easily replaced if they are damaged. Under cyclic loads, this device exhibits stable hysteretic behavior with two important features: adequate energy dissipation and replaceable fuse parts. These factors make this device useful for protecting structures from plastic deformation and failure in multiple situations. In this regard, the BFD is capable of acting as a passive seismic damper.

3. EVALUATION OF THE SEISMIC PERFORMANCE OF STEEL YIELDING DAMPERS

3.1. Testing Methods Based on FEMA 461 [208], there are two tests that can be applied to assess the seismic performance of steel yielding dampers: (1) the quasi-static cyclic test and (2) the shaking table test. Outcomes of these tests, which are performed on steel yielding dampers, determine the mechanical factors of steel yielding dampers such as yield displacement (Δ_y), ultimate displacement (Δ_u), yield strength (P_y), ultimate strength (P_u), and ductility (μ). By analyzing the hysteresis curves of these dampers, the required information will be obtained and the seismic performance will be evaluated. A steel yielding device is tested in a quasi-static manner on its own or on a structure that is equipped with such a device. Cyclical quasi-static tests are standard procedures for determining the energy dissipating capacity of devices under deformation [208].

The quasi-static cyclic test is a displacement control procedure that involves multiple incremental or constant amplitudes of displacement cycles under testing conditions that include shear, bending, or torsion. Conversely, shaking table tests require dampers to be assembled on a scaled or full-scale structure, depending on the size of the shaking table. A ground motion record could be artificial or actual, depending on the input loading used in the test.

3.2. Loading Protocols Several loading protocols are more common for steel structures tests, including FEMA 461 [209], SAC [210], AISC 2005 [211], and ATC-24 [212]. In general, FEMA 461 (2007) has been created and developed for testing of drift sensitive nonstructural components and can be applied for testing of drift sensitive structural components such as dampers. In this case, the maximum amplitude of deformation is targeted as Δ_m and the loading begins with $a_1=0.048\Delta_m$, and $a_{i+1}=1.4a_i$. It is recommended to apply two cycles per amplitude. Targeted maximum deformation amplitude, Δ_m , can be obtained from a monotonic test where a value 0.03 is recommended in terms of story drift index (δ/h) [213]. In accordance with AISC 2005, cyclic loading protocols are expressed in terms of inter-story drift angle. The characteristics of this protocol is described in Table 1. For testing beam-to-column moment connections in special or intermediate moment frames, the American Institute of Steel Construction recommends using this loading protocol. The SAC protocol described here is identical to that used by AISC 2005 to test beam-to-column connections. As a result of the observed Northridge weld fractures that occurred before yielding, SAC and AISC include more small elastic cycles [214]. One of the first formal protocols developed for evaluating the seismic performance of steel components using a cyclic loading history was the ATC-24, which was specifically applied for steel structures components. In this case, the amplitude of deformation is based on the yield displacement, Δ_y , which can be calculated from a monotonic test.

3.3. Hysteresis Behavior A bilinear or trilinear elastoplastic model is often used to simplify the stress-strain relationship of steel materials. Steel yielding dampers may exhibit slightly different hysteretic behavior depending on their geometry. There is a similarity in the hysteresis trends of steel yielding dampers [38, 215]. An overview of the hysteresis loops of steel materials can be found in Figure 22 [38]. Steel material has a nonlinear behavior, which makes their hysteretic properties beneficial for dissipating dynamic energy, particularly in linear systems. In response to static loading, steel material undergoes plasticization when their elastic limit (Δ_y) is exceeded, and if the level of stress is increased, it undergoes stress hardening.

TABLE 1. Number of cycles and amplitudes of loading protocols

Step	Amplitudes				Number of cycles			
	FEMA [a_i/Δ_m]	SAC [rad]	AISC [rad]	ATC [Δ_y]	FEMA	SAC	AISC	ATC
1	0.048	0.00375	0.00375	Δ_y	4	6	6	3
2	1.4(0.048)	0.005	0.005	$2\Delta_y$	2	6	6	3
3	2.8(0.048)	0.0075	0.0075	$3\Delta_y$	2	6	6	3
4	4.2(0.048)	0.01	0.01	$4\Delta_y$	2	4	4	3
5	5.6(0.048)	0.015	0.015	$5\Delta_y$	2	2	2	3
6	7(0.048) ^a	0.02 ^b	0.02 ^b	$6\Delta_y$ ^c	2	2	2	3

^aKeep with increments of $a_{i+1}=1.4a_i$, and apply two cycles at each step

^bKeep with increments of 0.01 rad, and apply two cycles at each step

^cKeep with increments of $1\Delta_y$, and apply three cycles at each step

When a material is loaded cyclically, its elastic modulus (E) recovers as it is unloaded. In this context, when a material is subjected to a load in the opposite direction, this will lead to it yielding and softening at a lower stress level than its yield stress. This effect is called the Bauschinger effect [216]. Despite hysteretic behavior, the steel material can keep performing as long as the strain is not greater than the yield plateau, and the maximum positive and negative stresses are not greater than the yield stress ($\pm F_y$). Even after unloading from stresses greater than the yield plateau, the material retains its original elastic stiffness. All in all, when the material reaches the maximum strain, the Bauschinger effect will be more dramatic. In this range of cyclic loading, the material offers a certain level of post-yield stiffness, and the yield plateau disappears [216].

4. COMPARISON WITH OTHER DEVICES

Based on all previous discussions, results, and test observations, it can be said that steel yielding dampers, besides being inexpensive, easy to install, and less affected by temperature, are also easy to maintain, as a

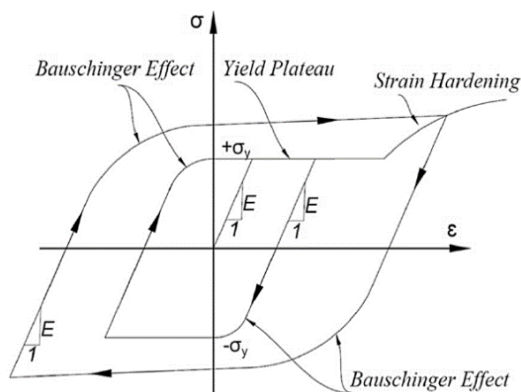


Figure 22. Idealization of cyclic stress-strain hysteresis of steel elements [38]

result, they can be used for all kinds of building structures. In addition, they are effective and economical for reinforcing and reconstructing existing and new structures. In general, as a result of elastic-plastic deformation of steel materials, the steel dampers can absorb and consume energy. The design and construction of earthquake-resistant structures is the most important factor in preventing human and financial losses due to the high energy of this natural disaster. As discussed in previous sections, the use of yielding dampers in recent decades has been suggested by researchers as one of the best ways to absorb and dissipate this destructive energy. In comparison to other passive energy dissipation devices, the steel yielding damper has a relatively larger hysteretic loop than its counterparts, indicating that it is capable of dissipating more energy per cycle. Additionally, performance of these devices is not affected by the ambient temperature [10]. In addition to increase of energy dissipation capacity, it should be highlighted that the simplicity in implementation, low cost, ease of adjustment, high speed of repair and replacement after an earthquake are among the other advantages of these damper [217]. Moreover, inexpensive maintenance and repair can be considered other benefits of using this new device. Generally, this dissipater not only can exhibit high energy dissipation capacity but also uniform force resistance in tension and compression and their hysteretic behavior are stable [10]. Then, in light of this review, it is noteworthy that this device can be used to design new structures as well as in the seismic improvement of existing structures which is considered another significant advantage. The design capacity of this damper can be easily selected since the number, width, thickness, geometry and shape of their plates can be chosen by the designer which can allow the designer to use the damper with diverse loads, drifts and energy dissipation capacities.

By comparison, a friction damper has similar characteristics to yielding dampers, including nonlinear behavior, insensitivity to ambient temperature, and stable hysteretic behavior. There are, however, a number of

uncertainties associated with sliding surfaces that cause its reliability to be questioned [218]. It is also somewhat difficult to analyze friction dampers due to their highly nonlinear behavior. It should also be mentioned that restoring incapability may result in permanent deformation if no external restoring mechanism is coupled with the damper [218]. In terms of controlling base shear, friction dampers outperform metallic

dampers slightly; however, when it comes to controlling the lateral displacement, metallic dampers are marginally better [219]. In contrast, viscoelastic dampers have restoring properties, and they are activated at low displacements in contrast to metallic, viscous, and friction dampers. The yielding damper is compared with other passive energy dissipation devices in Figure 23 [10].

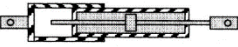
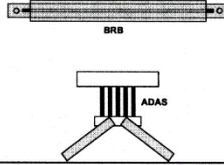
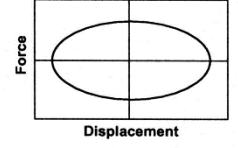
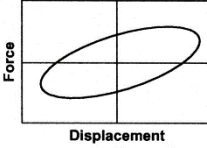
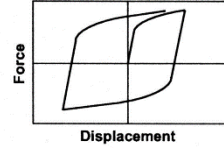
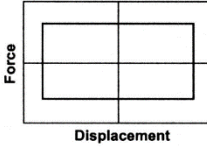
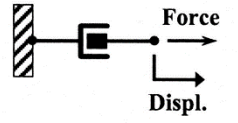
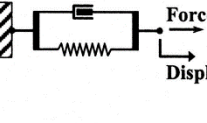
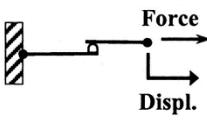
	Viscous Fluid Damper	Viscoelastic Solid Damper	Metallic Damper	Friction Damper
Basic Construction				
Idealized Hysteretic Behavior				
Idealized Physical Model			Idealized Model Not Available	

Figure 23. Yielding dampers compared to other passive energy dissipation devices [10]

5. CONCLUSIONS

Based on the information presented in this review, the following conclusions can be drawn:

- **Importance:** The state-of-the-art of steel yielding dampers since the 1970s is summarized in this comprehensive review. Steel yielding dampers can be classified according to their geometric configuration to four categories: steel plate damper, pipe damper, curved damper, and slit damper. These dampers are designed and used to provide safety during earthquakes and prevent the loss of lives. In addition to minimizing structural damage, they also enhance the structure's strength and life expectancy.
- **Main findings:**
 1. Steel plate dampers such as ADAS and TADAS should have hinge supports to reduce unfavourable axial forces. In terms of practicality, ADAS and TADAS dampers are most commonly used in braced frames to increase their damping and ductility.

2. In steel shear panel dampers, low-yield-strength steel is typically used to dissipate or absorb input energy. The most common failure associated with shear panel dampers is local buckling failure, which results in inadequate energy dissipation caused by pinching effects due to buckling. This fact makes stiffening the shear plate helpful in overcoming the challenges associated with out-of-plane buckling. This will result in high plastic deformation.
3. While pipe dampers are simple to manufacture without casting or precision cutting tools, they suffer from cracks that originate in the pipe material adjacent to the welds that linked the pipe to the plates and propagated throughout the pipe thickness and length. The welding type and position must therefore be carefully chosen.
4. The use of steel plate dampers such as U-shape, J-shape, and S-shape dampers is most common with chevron bracing since they can alleviate the disadvantages associated with other types of dampers.

5. Among the main factors affecting the seismic performance of curved dampers are their dimensions and angle. Curved dampers should be angled between 30° and 60° according to the recommendations. A 60° damper in the steel-braced frame is the most effective steel curved damper in terms of energy dissipation and frame strength.
6. Hysteretic slit dampers can be adjusted by altering the size and configuration of the slits, which are available in a variety of configurations, such as prismatic and hourglass designs, both of which are highly effective. Furthermore, these dampers offer advantages over other dampers for braced frames, beam-to-column connections, and shear walls. As a result, slit dampers are most commonly used in steel structures as steel yielding dampers.
 - **Suitability:** The performance of steel yielding dampers is not affected by the ambient temperature. The high energy dissipation capacity, simplicity in implementation, low cost, ease of adjustment, high speed of repair and replacement after an earthquake are among the other advantages of these dampers. Moreover, steel yielding dissipater displays a stable hysteretic behaviour and uniform force resistance in tension and compression. Besides, both new structures and existing structures can benefit from seismic improvements created by these dampers.
 - **Preference:** Preference between the dampers can be determined depending on the type of force applied, the damper location in structures, and the type of connection between the damper and the structure, i.e., welding or screws. The clamped connection between the damper plates and the support is accomplished through welding or screws such as ADAS, TADAS, and XPD. When welding is used to create an end connection in the plates, ductility of the steel in that area decreases unfavourably. SPDs are also characterized by stress concentration in the weld areas of the stiffeners connected. Also, in the areas around the places where welding is used to connect the SSDs to the support, ductility of the plate is reduced. Based on the above explanation, it is preferred to use a screw connection whenever possible for yielding dampers.
 - **Seismic performance:** Steel yielding dampers may exhibit slightly different hysteretic behavior depending on their geometry. There is a similarity in the hysteresis trends of steel yielding dampers. The seismic performance of steel yielding dampers can be evaluated in two ways: (1) the quasi-static cyclic test and (2) the shaking table test. Outcomes of these tests, which are performed on steel yielding dampers or on structures equipped with these devices, determine the mechanical factors of steel yielding dampers such as yield displacement, ultimate displacement, yield strength, ultimate strength, and ductility. By analysing the hysteresis curves of these dampers, the

required information will be obtained and the seismic performance will be evaluated. For performing cyclic tests, the most common loading protocols are FEMA 461, SAC, AISC, and ATC-24.

- **Limitations:** Even though yielding dampers can provide a variety of benefits, they suffer from several flaws where the use of a significant amount of welding reduces their ductility; in turn, this reduces the ductility of structures. Additionally, such dampers have the disadvantage that they absorb seismic energy only when they undergo inelastic deformation. Therefore, low yield strength steel is used because it has excellent ductility properties, which overcomes this limitation. On the other hand, during large deformations caused by second-order effects and/or gravity loads, an axial force is created inside the damper plates and in fact, the axial force reduces damper ductility fundamentally. In large lateral deformations, when the axial force increases, the stiffness of the plates increases, resulting in damper ductility being reduced. In parallel, shear plate dampers are characterized by high yielding force, in addition to shear buckling before yielding.

6. SUGGESTIONS FOR FUTURE RESEARCH

Steel yielding dampers are still a vast field that needs to be explored in terms of their development and application. As a result, the following recommendations have been summarized as a means of further understanding, developing, and applying steel yielding dampers:

- Studies on the effect of far-field and near-field earthquakes on steel yielding dampers are limited. To better understand, develop, and apply the general steel yielding damper, more investigations are required regarding the influence of near and far-field ground motions.
- As far as their use in braces is concerned, curved dampers have not been studied exhaustively. In order to assess design criteria for codification and practical applications, further experiments and numerical analyses of this scenario are needed. Also, there will need to be further studies in the future concerning the influence of the thickness of the curved steel plates on their fatigue life.
- Additionally, the quality of welding is an important consideration in the manufacture of metallic dampers as this can result in premature failure or reduce the ductility of the dampers during operation. So, this aspect should be investigated further. In future studies, it may be possible to consider more efficient methods of connecting pipe dampers, such as bolted connections.
- There has been limited research on the occurrence of buckling due to the shear behaviour of steel yielding

dampers with short heights. Future research should address this fundamental weakness.

- In most studies, axial force has not been taken into account when studying steel slit dampers. This force reduces the deformation of the damper before experiencing large deformation, particularly at the beam-to-column connections where the steel slit damper is installed in the beam.
- For beam-to-column connections equipped with slit dampers, the effect of beam effective length, bolt tightening force, etc., should be investigated in follow-up studies. Generally, SSDs with short heights tend to buckle due to their shear behaviour. It is a fundamental weakness of SSDs that needs to be addressed.
- In case of braced frames, it is important to consider the effects of the location and connection of the yielding damper. Thus, new configurations can be explored to address these issues in a constructive way.

7. REFERENCES

1. Ghaedi, K. and Ibrahim, Z., "Earthquake prediction", *Earthquakes-Tectonics, Hazard and Risk Mitigation*, (2017), 205-227. doi: 10.5772/65511.
2. Javanmardi, A., Ibrahim, Z., Ghaedi, K., Benisi Ghadim, H. and Hanif, M.U., "State-of-the-art review of metallic dampers: Testing, development and implementation", *Archives of Computational Methods in Engineering*, Vol. 27, No. 2, (2019), 455-478. doi: 10.1007/s11831-019-09329-9.
3. Boardman, P., Wood, B. and Carr, A., "Union house: A cross braced structure with energy dissipators", *Bulletin of the New Zealand Society for Earthquake Engineering*, Vol. 16, No. 2, (1983), 83-97.
4. Martinez-Romero, E., "Experiences on the use of supplementary energy dissipators on building structures", *Earthquake Spectra*, Vol. 9, No. 3, (1993), 581-625. doi: 10.1193/1.1585731.
5. Perry, C.L., Fierro, E.A., Sedarat, H. and Scholl, R.E., "Seismic upgrade in san francisco using energy dissipation devices", *Earthquake Spectra*, Vol. 9, No. 3, (1993), 559-579. doi: 10.1193/1.1585730.
6. Soong, T. and Spencer Jr, B., "Supplemental energy dissipation: State-of-the-art and state-of-the-practice", *Engineering Structures*, Vol. 24, No. 3, (2002), 243-259. doi: 10.1016/S0141-0296(01)00092-X.
7. Saaed, T.E., Nikolakopoulos, G., Jonasson, J.-E. and Hedlund, H., "A state-of-the-art review of structural control systems", *Journal of Vibration and Control*, Vol. 21, No. 5, (2015), 919-937. doi: 10.1177/1077546313478294.
8. Pourzangbar, A., Vaezi, M., Mousavi, S. and Saber, A., "Effects of brace-viscous damper system on the dynamic response of steel frames", *International Journal of Engineering, Transactions B: Applications*, Vol. 33, No. 5, (2020), 720-731. doi: 10.5829/ije.2020.33.05b.02.
9. Housner, G., Bergman, L.A., Caughey, T.K., Chassiakos, A.G., Claus, R.O., Masri, S.F., Skelton, R.E., Soong, T., Spencer, B. and Yao, J.T., "Structural control: Past, present, and future", *Journal of Engineering Mechanics*, Vol. 123, No. 9, (1997), 897-971. doi: 10.1061/(ASCE)0733-9399(1997)123:9(897).
10. Symans, M., Charney, F., Whittaker, A., Constantinou, M., Kircher, C., Johnson, M. and McNamara, R., "Energy dissipation systems for seismic applications: Current practice and recent developments", *Journal of Structural Engineering*, Vol. 134, No. 1, (2008), 3-21. doi: 10.1061/(ASCE)0733-9445(2008)134:1(3).
11. Li, H. and Huo, L., "Advances in structural control in civil engineering in china", *Mathematical Problems in Engineering*, Vol. 2010, (2010). doi: 10.1155/2010/936081.
12. Fisco, N. and Adeli, H., "Smart structures: Part i—active and semi-active control", *Scientia Iranica*, Vol. 18, No. 3, (2011), 275-284. doi: 10.1016/j.scient.2011.05.034.
13. Fisco, N. and Adeli, H., "Smart structures: Part ii—hybrid control systems and control strategies", *Scientia Iranica*, Vol. 18, No. 3, (2011), 285-295. doi: 10.1016/j.scient.2011.05.035.
14. Korkmaz, S., "A review of active structural control: Challenges for engineering informatics", *Computers & Structures*, Vol. 89, No. 23-24, (2011), 2113-2132. doi: 10.1016/j.compstruc.2011.07.010.
15. Ghaedi, K., Ibrahim, Z., Adeli, H. and Javanmardi, A., "Invited review: Recent developments in vibration control of building and bridge structures", *Journal of Vibration Engineering*, Vol. 19, No. 5, (2017), 3564-3580. doi: 10.21595/jve.2017.18900.
16. Dargush, G. and Sant, R., "Evolutionary aseismic design and retrofit of structures with passive energy dissipation", *Earthquake Engineering & Structural Dynamics*, Vol. 34, No. 13, (2005), 1601-1626.
17. Symans, M.D. and Constantinou, M.C., "Semi-active control systems for seismic protection of structures: A state-of-the-art review", *Engineering Structures*, Vol. 21, No. 6, (1999), 469-487. doi: 10.1016/S0141-0296(97)00225-3.
18. Momeni, Z. and Bagchi, A., "Intelligent control methodology for smart highway bridge structures using optimal replicator dynamic controller", *Civil Engineering Journal*, Vol. 9, No. 1, (2023), 1-16. doi: 10.28991/CEJ-2023-09-01-01.
19. Abdul Aziz, M., Muhtasim, S. and Ahammed, R., "State-of-the-art recent developments of large magnetorheological (mr) dampers: A review", *Korea-Australia Rheology Journal*, (2022), 1-32. doi: 10.1007/s13367-022-00021-2.
20. Saravanan, M., Goswami, R. and Palani, G., "Replaceable fuses in earthquake resistant steel structures: A review", *International Journal of Steel Structures*, Vol. 18, No. 3, (2018), 868-879. doi: 10.1007/s13296-018-0035-9.
21. Mousavi, H., Sabbagh Yazdi, S. and Almohammad-Albakkar, M., "A novel method for efficient design of frame structures equipped with nonlinear viscous dampers by using computational results of cylindrical friction damper", *Australian Journal of Structural Engineering*, (2022), 1-17. doi: 10.1080/13287982.2022.2088055.
22. Vaseghi, A.J. and Esmaeiltabar, N.P., "Response modification factor of chevron braced frame with pall friction damper", (2013). doi: 10.5829/idosi.ije.2013.26.02b.03.
23. Chan, R.W. and Albermani, F., "Experimental study of steel slit damper for passive energy dissipation", *Engineering Structures*, Vol. 30, No. 4, (2008), 1058-1066. doi: 10.1016/j.engstruct.2007.07.005.
24. McNamara, R.J. and Taylor, D.P., "Fluid viscous dampers for high-rise buildings", *The Structural Design of Tall and Special Buildings*, Vol. 12, No. 2, (2003), 145-154. doi: 10.1002/tal.218.
25. Lin, W.H. and Chopra, A.K., "Earthquake response of elastic sdf systems with non-linear fluid viscous dampers", *Earthquake Engineering & Structural Dynamics*, Vol. 31, No. 9, (2002), 1623-1642. doi: 10.1061/(ASCE)0733-9399(2003)129:6(597).
26. De Domenico, D., Ricciardi, G. and Takewaki, I., "Design strategies of viscous dampers for seismic protection of building structures: A review", *Soil Dynamics and Earthquake*

- Engineering*, Vol. 118, (2019), 144-165. doi: 10.1016/j.soildyn.2018.12.024.
27. Meshkat Rouhani, V., Zamani Ahari, G. and Saeedmonir, H., "Experimental and numerical study on a new double-walled tuned liquid damper", *International Journal of Engineering, Transactions A: Basics*, Vol. 35, No. 1, (2022), 29-44. doi: 10.5829/ije.2022.35.01a.04.
 28. Ashasi-Sorkhabi, A., Malekghasemi, H., Ghaemmaghami, A. and Mercan, O., "Experimental investigations of tuned liquid damper-structure interactions in resonance considering multiple parameters", *Journal of Sound and Vibration*, Vol. 388, (2017), 141-153. doi: 10.1016/j.jsv.2016.10.036.
 29. Zhang, C., Li, L. and Ou, J., "Swinging motion control of suspended structures: Principles and applications", *Structural Control and Health Monitoring*, Vol. 17, No. 5, (2010), 549-562. doi: 10.1002/stc.331.
 30. Zhang, R.-H. and Soong, T., "Seismic design of viscoelastic dampers for structural applications", *Journal of Structural Engineering*, Vol. 118, No. 5, (1992), 1375-1392. doi: 10.1061/(ASCE)0733-9445(1992)118:5(1375).
 31. Mahmoodi, P. and Keel, C.J., "Performance of viscoelastic structural dampers for the columbia center building", in *Building motion in wind*, ASCE., (1986), 83-106.
 32. Skinner, R.L., Kelly, J.M. and Heine, A., "Hysteretic dampers for earthquake-resistant structures", *Earthquake Engineering & Structural Dynamics*, Vol. 3, No. 3, (1974), 287-296. doi: 10.1002/eqe.4290030307.
 33. Skinner, R., Tyler, R., Heine, A. and Robinson, W., "Hysteretic dampers for the protection of structures from earthquakes", *Bulletin of the New Zealand Society for Earthquake Engineering*, Vol. 13, No. 1, (1980), 22-36. doi: 10.5459/bnzsee.13.1.22-36.
 34. Aghlara, R., Tahir, M.M. and Adnan, A.B., "Experimental study of pipe-fuse damper for passive energy dissipation in structures", *Journal of Constructional Steel Research*, Vol. 148, (2018), 351-360. doi: 10.1016/j.jcsr.2018.06.004.
 35. Sarwar, W. and Sarwar, R., "Vibration control devices for building structures and installation approach: A review", *Civil and Environmental Engineering Reports*, Vol. 29, No. 2, (2019), 74-100. doi: 10.2478/ceer-2019-0018.
 36. Amiri, H.A., Najafabadi, E.P. and Estekanchi, H.E., "Experimental and analytical study of block slit damper", *Journal of Constructional Steel Research*, Vol. 141, (2018), 167-178. doi: 10.1016/j.jcsr.2017.11.006.
 37. Soong, T.T. and Dargush, G.F., "Passive energy dissipation systems in structural engineering", Wiley, (1997).
 38. Christopoulos, C. and Filiatrault, A., "Principles of passive supplemental damping and seismic", IUSS Press, Pavia, Italy, (2006).
 39. Almohammad-Albakkar, M. and Behnamfar, F., "Numerical investigation of grooved gusset plate damper for using in cross-braced frames", *Journal of Constructional Steel Research*, Vol. 196, (2022), 107434. doi: 10.1016/j.jcsr.2022.107434.
 40. Behnamfar, F. and Soltanabadi, R., "Analytical studies on a combined rubber-steel damper for repairable steel moment connections", *Journal of Earthquake Engineering*, Vol. 24, No. 1, (2020), 37-58. doi: 10.1080/13632469.2017.1387618.
 41. Soltanabadi, R. and Behnamfar, F., "Experimental studies on a combined damper for repairable steel moment connections", *International Journal of Steel Structures*, Vol. 18, No. 1, (2018), 211-224. doi: 10.1007/s13296-018-0317-2.
 42. Fukumoto, T., "A study on steel damper with honeycomb shaped-openings", in *Annual Meeting (Summaries of AIJ)*, (1989).
 43. Naoki, T., "A study on steel plate d. With honeycomb-s. Openings s. To low cycle f", *AIJ*, Vol. 37, (1991). doi: 10003272681.
 44. Kobori, T., Miura, Y., Fukusawa, E., Yamada, T., Arita, T., Takenake, Y., Miyagawa, N., Tanaka, N. and Fukumoto, T., "Development and application of hysteresis steel dampers", in *Proceedings of the 10th World conference on earthquake engineering*. Vol. 2341, (1992), 2346.
 45. Wada, A., Huang, Y., Yamada, T., Ono, Y., Sugiyama, S., Baba, M. and Miyabara, T., "Actual size and real time speed tests for hysteretic steel damper", *Proceedings of STESSA*, Vol. 97, No., (1997), 778-785.
 46. Sugiyama, S., "Development and application of t-shaped elasto-plastic damper", in "Symposium on a new direction in seismic design" Tokyo. (1995). doi: 10003272680.
 47. Amadeo, B.C., OH, S.-H. and Akiyama, H., "Ultimate energy absorption capacity of slit-type steel plates subjected to shear deformations", *Journal of Structural and Construction Engineering (Transactions of AIJ)*, Vol. 63, No. 503, (1998), 139-147. doi: 10.3130/aijs.63.139_1.
 48. Kelly, J.M., Skinner, R. and Heine, A., "Mechanisms of energy absorption in special devices for use in earthquake resistant structures", *Bulletin of the New Zealand Society for Earthquake Engineering*, Vol. 5, No. 3, (1972), 63-88. doi: 10.5459/bnzsee.5.3.63-88.
 49. Tyler, R., "Tapered steel energy dissipators for earthquake resistant structures", *Bulletin of the New Zealand Society for Earthquake Engineering*, Vol. 11, No. 4, (1978), 282-294. doi: 10.5459/bnzsee.11.4.282-294.
 50. Bergman, D.M. and Goel, S.C., "Evaluation of cyclic testing of steel-plate devices for added damping and stiffness", Department of Civil Engineering, University of Michigan, (1987).
 51. WHITTAKER, A., "Earthquake simulatOr testing Of steel plate added damping", *Earthquake Engineering*, (1989). doi: 10.13140/RG.2.1.1455.3207.
 52. Tsai, K.-C. and Chou, C., "Plasticity models and seismic performance of steel plate energy dissipators", *Journal of the Chinese Institute of Civil and Hydraulic Engineering*, Vol. 8, No. 1, (1996), 45-54. doi: 246246/133915.
 53. Tsai, K.-C. and Hong, C., "Steel triangular plate energy absorber for earthquake resistant buildings", (1992). doi: 10.1193/1.1585727.
 54. Tsai, K.-C., Chen, H.-W., Hong, C.-P. and Su, Y.-F., "Design of steel triangular plate energy absorbers for seismic-resistant construction", *Earthquake Spectra*, Vol. 9, No. 3, (1993), 505-528. doi: 10.1193/1.1585727.
 55. Tsai, K., Li, J., Hong, C., Chen, H. and Su, Y., "Welded steel triangular plate device for seismic energy dissipation", *Proceedings, ATC-17-1 Semi-nar on Seismic Isolation, Passive Energy Dissipation and Active Control*, (1993).
 56. Dargush, G. and Soong, T., "Behavior of metallic plate dampers in seismic passive energy dissipation systems", *Earthquake Spectra*, Vol. 11, No. 4, (1995), 545-568. doi: 10.1193/1.1585827.
 57. Gray, M., Christopoulos, C. and Packer, J., "Full-scale testing of the cast steel yielding brace system", in *Proceedings of the 7th International Conference STESSA.*, (2012).
 58. Reddy, N.O. and Manchalwar, A., "Performance of moment resisting rc building equipped with x-plate damper under seismic and blast loading", *International Journal of Innovative Technology and Exploring Engineering (IJITEE)*, (2019). doi: 10.35940/ijitee.B6614.129219.
 59. Manchalwar, A. and Bakre, S., "Performance of rc structures equipped with steel and aluminium x-plate dampers", *Journal of The Institution of Engineers (India): Series A*, Vol. 97, No. 4, (2016), 415-425. doi: 10.1007/s40030-016-0180-0.
 60. Chou, C.C. and Tsai, K.C., "Plasticity-fibre model for steel triangular plate energy dissipating devices", *Earthquake*

- Engineering & Structural Dynamics*, Vol. 31, No. 9, (2002), 1643-1655. doi: 10.1002/eqe.180.
61. Ming-Hsiang, S., Wen-pei, S. and Cheer-Germ, G., "Investigation of newly developed added damping and stiffness device with low yield strength steel", *Journal of Zhejiang University-Science A*, Vol. 5, No. 3, (2004), 326-334. doi: 10.1007/BF02841018.
 62. Shih, M.-H. and Sung, W.-P., "A model for hysteretic behavior of rhombic low yield strength steel added damping and stiffness", *Computers & Structures*, Vol. 83, No. 12-13, (2005), 895-908. doi: 10.1016/j.compstruc.2004.11.012.
 63. Li, H.-N. and Li, G., "Experimental study of structure with "dual function" metallic dampers", *Engineering Structures*, Vol. 29, No. 8, (2007), 1917-1928. doi: 10.1016/j.engstruct.2006.10.007.
 64. Pujari, N.N. and Bakre, S., "Optimum placement of x-plate dampers for seismic response control of multistoried buildings", *International Journal of Earth Sciences and Engineering*, Vol. 4, No. 6, (2011), 481-485.
 65. Mohammadi, R.K., Nasri, A. and Ghaffary, A., "Tadas dampers in very large deformations", *International Journal of Steel Structures*, Vol. 17, No. 2, (2017), 515-524. doi: 10.1007/s13296-017-6011-y.
 66. Gray, M.G., Christopoulos, C. and Packer, J.A., "Cast steel yielding brace system for concentrically braced frames: Concept development and experimental validations", *Journal of Structural Engineering*, Vol. 140, No. 4, (2014), 04013095. doi: 10.1061/(ASCE)ST.1943-541X.0000910.
 67. Gray, M., Christopoulos, C., Packer, J. and Lignos, D., "Development, validation, and modeling of the new cast steel yielding brace system", in 20th analysis and computation specialty conference., (2012), 71-82.
 68. Gray, M.G., Christopoulos, C. and Packer, J.A., "Design and full-scale testing of a cast steel yielding brace system in a braced frame", *Journal of Structural Engineering*, Vol. 143, No. 4, (2017), 04016210. doi: 10.1061/(ASCE)ST.1943-541X.0001692.
 69. Zibasokhan, H., Behnamfar, F. and Azhari, M., "Experimental study of a new pure bending yielding dissipater", *Bulletin of Earthquake Engineering*, Vol. 17, No. 7, (2019), 4389-4410. doi: 10.1007/s10518-019-00616-1.
 70. Labibi, H., Gerami, M. and Hosseini, M., "Sensitivity analysis of behavior of simple trapezoidal steel plates to introduce a new yielding damper", *International Journal of Engineering, Transactions A: Basics*, Vol. 34, No. 10, (2021), 2302-2312. doi: 10.5829/IJE.2021.34.10A.11.
 71. Ghandil, M., Riahi, H.T. and Behnamfar, F., "Introduction of a new metallic-yielding piston damper for seismic control of structures", *Journal of Constructional Steel Research*, Vol. 194, (2022), 107299. doi: 10.1016/j.jcsr.2022.107299.
 72. Yadav, D. and Sahoo, D.R., "Experimental and analytical investigations of steel shear buckling-inhibited energy dissipation devices", *Journal of Constructional Steel Research*, Vol. 196, (2022), 107436. doi: 10.1016/j.jcsr.2022.107436.
 73. Hossain, M.R., Ashraf, M. and Albermani, F., "Numerical modelling of yielding shear panel device for passive energy dissipation", *Thin-Walled Structures*, Vol. 49, No. 8, (2011), 1032-1044. doi: 10.1016/j.tws.2011.03.003.
 74. Chen, Z., Ge, H. and Usami, T., "Hysteretic model of stiffened shear panel dampers", *Journal of Structural Engineering-New York*, Vol. 132, No. 3, (2006), 478. doi: 10.1061/(ASCE)0733-9445(2006)132:3(478).
 75. Kasai, A., Watanabe, T., Amano, M. and Usami, T., "Strength and ductility evaluation of stiffened steel plates subjected to cyclic shear loading", *Journal of Structural Engineering*, Vol. 47, No. 2, (2001), 761-770.
 76. Chen, Z., Ge, H. and Usami, T., "Hysteretic performance of shear panel dampers", in Fourth International Conference on Advances in Steel Structures, Elsevier. (2005), 1223-1228.
 77. Chan, R.W., Albermani, F. and Williams, M.S., "Evaluation of yielding shear panel device for passive energy dissipation", *Journal of Constructional Steel Research*, Vol. 65, No. 2, (2009), 260-268. doi: 10.1016/j.jcsr.2008.03.017.
 78. Aoki, T., Liu, Y., Takaku, T. and Fukumoto, Y., "A new type of shear panel dampers for highway bridge bearings", in Proceedings of the 5th European Conference on Steel and Composite Structures., (2008).
 79. Nakashima, M., Iwai, S., Iwata, M., Takeuchi, T., Konomi, S., Akazawa, T. and Saburi, K., "Energy dissipation behaviour of shear panels made of low yield steel", *Earthquake Engineering & Structural Dynamics*, Vol. 23, No. 12, (1994), 1299-1313. doi: 10.1002/eqe.4290231203.
 80. Zirakian, T. and Zhang, J., "Structural performance of unstiffened low yield point steel plate shear walls", *Journal of Constructional Steel Research*, Vol. 112, (2015), 40-53. doi: 10.1016/j.jcsr.2015.04.023.
 81. Xu, L.-Y., Nie, X. and Fan, J.-S., "Cyclic behaviour of low-yield-point steel shear panel dampers", *Engineering Structures*, Vol. 126, (2016), 391-404. doi: 10.1016/j.engstruct.2016.08.002.
 82. Nakashima, M., "Strain-hardening behavior of shear panels made of low-yield steel. I: Test", *Journal of Structural Engineering*, Vol. 121, No. 12, (1995), 1742-1749. doi: 10.1061/(ASCE)0733-9445(1995)121:12(1742).
 83. Takahashi, Y. and Shinabe, Y., "Experimental study on restoring force characteristics of shear yielding thin steel plate elements", *Journal of Structural and Construction Engineering (Transactions of AIJ)*, No. 494, (1997), 107-114. doi: 10.3130/aijs.62.107_3.
 84. Tanaka, K. and Sasaki, Y., "Study on energy absorbing performance of seismic control panel-dampers using low-yield-point steel under static loading; kyokutei kofukutenko wo mochiita seishin panel damper no seiteki rireki gensui seino ni kansuru kenkyu", Nippon Kenchiku Gakkai Kozo-kei Ronbunshu, (1998). doi: 10.3130/aijs.63.159_1.
 85. Tanaka, K., Torii, T., Sasaki, Y., Miyama, T., Kawai, H., Iwata, M. and Wada, A., "Practical application of damage tolerant structures with seismic control panel using low yield point steel to a high-rise steel building", Proceedings, Structural Engineering World Wide, Elsevier, CD-ROM, Paper T190-4, (1998). doi: 10.3130/aijt.3.126.
 86. Tanaka, K. and Sasaki, Y., "Hysteretic performance of shear panel dampers of ultra low yield-strength steel for seismic response control of buildings", in 12th World Conference on Earthquake Engineering, WCEE. New Zealand., (2000).
 87. De Matteis, G., Landolfo, R. and Mazzolani, F., "Seismic response of mr steel frames with low-yield steel shear panels", *Engineering Structures*, Vol. 25, No. 2, (2003), 155-168. doi: 10.1016/S0141-0296(02)00124-4.
 88. Liu, Y. and Aoki, T., "The strain measurement by image processing technique for shear panel damper made of low yield steel", in Fifth international conference on Thin-Walled Structures Brisbane, Australia, (2008).
 89. Liu, Y., Aoki, T., Takaku, T. and Fukumoto, Y., "Cyclic loading tests of shear panel damper made of low yield steel", *Journal of Structure Construction Engineering A*, Vol. 53, (2007), 560-567.
 90. Dusicka, P., Itani, A.M. and Buckle, I.G., "Cyclic response of plate steels under large inelastic strains", *Journal of Constructional Steel Research*, Vol. 63, No. 2, (2007), 156-164. doi: 10.1016/j.jcsr.2006.03.006.
 91. Aoki, T., Chaofeng, Z. and Huihui, Y., "Dynamic loading test of shear panel damper", (2012).
 92. Aoki, T., Dang, J., Zhang, C., Takaku, T. and Fukumoto, Y., "Dynamic shear tests of low-yield steel panel dampers for bridge bearing: T. Aoki, j. Dang & c. Zhang t. Takaku, in Behaviour of steel structures in seismic areas. 2009, CRC Press.665-670.

93. Zhang, C., Zhang, Z. and Zhang, Q., "Static and dynamic cyclic performance of a low-yield-strength steel shear panel damper", *Journal of Constructional Steel Research*, Vol. 79, (2012), 195-203. doi: 10.1016/j.jcsr.2012.07.030.
94. Zhang, C., Zhang, Z. and Shi, J., "Development of high deformation capacity low yield strength steel shear panel damper", *Journal of Constructional Steel Research*, Vol. 75, (2012), 116-130. doi: 10.1016/j.jcsr.2012.03.014.
95. Narayanan, R. and Chow, F., "Experiments on perforated plates subjected to shear", *The Journal of Strain Analysis for Engineering Design*, Vol. 20, No. 1, (1985), 23-34. doi: 10.1243/03093247V20I023.
96. Narayanan, R. and Der-Avanessian, N.G.V., "Analysis of plate girders with perforated webs", *Thin-Walled Structures*, Vol. 4, No. 5, (1986), 363-380. doi: 10.1016/0263-8231(86)90030-3.
97. Chan, R.W., Albermani, F. and Kitipornchai, S., "Experimental study of perforated yielding shear panel device for passive energy dissipation", *Journal of Constructional Steel Research*, Vol. 91, (2013), 14-25. doi: 10.1016/j.jcsr.2013.08.013.
98. Liu, Y. and Shimoda, M., "Shape optimization of shear panel damper for improving the deformation ability under cyclic loading", *Structural and Multidisciplinary Optimization*, Vol. 48, No. 2, (2013), 427-435. doi: 10.1007/s00158-013-0909-6.
99. Deng, K., Pan, P., Sun, J., Liu, J. and Xue, Y., "Shape optimization design of steel shear panel dampers", *Journal of Constructional Steel Research*, Vol. 99, (2014), 187-193. doi: 10.1016/j.jcsr.2014.03.001.
100. Sahoo, D.R., Singhal, T., Tarathia, S.S. and Saini, A., "Cyclic behavior of shear-and-flexural yielding metallic dampers", *Journal of Constructional Steel Research*, Vol. 114, (2015), 247-257. doi: 10.1016/j.jcsr.2015.08.006.
101. Zhu, B., Wang, T. and Zhang, L., "Quasi-static test of assembled steel shear panel dampers with optimized shapes", *Engineering Structures*, Vol. 172, (2018), 346-357. doi: 10.1016/j.engstruct.2018.06.004.
102. Shi, J.-X., Kozono, S., Shimoda, M., Takino, M., Wada, D. and Liu, Y., "Non-parametric shape design optimization of elastic-plastic shear panel dampers under cyclic loading", *Engineering Structures*, Vol. 189, (2019), 48-61. doi: 10.1016/j.engstruct.2019.03.049.
103. Lin, Y., Yang, S., Guan, D. and Guo, Z., "Modified strip model for indirect buckling restrained shear panel dampers", *Journal of Constructional Steel Research*, Vol. 175, (2020), 106371. doi: 10.1016/j.jcsr.2020.106371.
104. Yao, Z., Wang, W. and Zhu, Y., "Experimental evaluation and numerical simulation of low-yield-point steel shear panel dampers", *Engineering Structures*, Vol. 245, (2021), 112860. doi: 10.1016/j.engstruct.2021.112860.
105. De Matteis, G., Sarracco, G. and Brando, G., "Experimental tests and optimization rules for steel perforated shear panels", *Journal of Constructional Steel Research*, Vol. 123, (2016), 41-52. doi: 10.1016/j.jcsr.2016.04.025.
106. Lin, X., Wu, K., Skalomenos, K.A., Lu, L. and Zhao, S., "Development of a buckling-restrained shear panel damper with demountable steel-concrete composite restrainers", *Soil Dynamics and Earthquake Engineering*, Vol. 118, (2019), 221-230. doi: 10.1016/j.soildyn.2018.12.015.
107. Zhang, C., Zhu, J., Wu, M., Yu, J. and Zhao, J., "The lightweight design of a seismic low-yield-strength steel shear panel damper", *Materials (Basel)*, Vol. 9, No. 6, (2016), 424. doi: 10.3390/ma9060424.
108. Chaofeng, Z., Youchun, W., Longfei, W. and Meiping, W., "Hysteretic mechanical property of low-yield strength shear panel dampers in ultra-large plastic strain", *Engineering Structures*, Vol. 148, (2017), 11-22. doi: 10.1016/j.engstruct.2017.06.028.
109. Zhang, C., Wang, L., Sun, C. and Wu, M., "Feasibility of the evaluation of the deformation capacity of the shear panel damper by fem", *Journal of Constructional Steel Research*, Vol. 147, (2018), 433-443. doi: 10.1016/j.jcsr.2018.04.033.
110. Koike, Y., Yanaka, T., Usami, T., Ge, H., Oshita, S., Sagou, D. and Uno, Y., "An experimental study on developing high-performance stiffened shear panel dampers", *Journal of Structural Engineering, JSCE*, Vol. 54, (2008), 372-381. doi: 10.11532/structcivil.54a.372.
111. Deng, K., Pan, P., Li, W. and Xue, Y., "Development of a buckling restrained shear panel damper", *Journal of Constructional Steel Research*, Vol. 106, (2015), 311-321. doi: 10.1016/j.jcsr.2015.01.004.
112. Quan, C., Wang, W., Li, Y. and Lu, Z., "Cyclic behaviour of demountable metallic corrugated shear panel dampers", *Journal of Building Engineering*, Vol. 61, (2022), 105228. doi: 10.1016/j.job.2022.105228.
113. Quan, C., Wang, W. and Li, Y., "Hysteretic model and resilient application of corrugated shear panel dampers", *Thin-Walled Structures*, Vol. 178, (2022), 109477. doi: 10.1016/j.tws.2022.109477.
114. Zhao, J.-Z., Zhuang, L.-D. and Tao, M.-X., "Development of bent shear panel dampers for eccentrically braced composite frames", *Journal of Constructional Steel Research*, Vol. 193, (2022), 107292. doi: 10.1016/j.jcsr.2022.107292.
115. Zhao, J.-Z., Tao, M.-X., Wu, Z.-H. and Zhuang, L.-D., "Experimental and numerical study on bent shear panel damper made of bly160 steel", *Engineering Structures*, Vol. 260, (2022), 114229. doi: 10.1016/j.engstruct.2022.114229.
116. Vian, D., Bruneau, M., Tsai, K.-C. and Lin, Y.-C., "Special perforated steel plate shear walls with reduced beam section anchor beams. I: Experimental investigation", *Journal of Structural Engineering*, Vol. 135, No. 3, (2009), 211-220. doi: 10.1061/(ASCE)0733-9445(2009)135:3(211).
117. Purba, R. and Bruneau, M., "Finite-element investigation and design recommendations for perforated steel plate shear walls", *Journal of Structural Engineering*, Vol. 135, No. 11, (2009), 1367-1376. doi: 10.1061/(ASCE)ST.1943-541X.0000061.
118. Valizadeh, H., Sheidaii, M. and Showkati, H., "Experimental investigation on cyclic behavior of perforated steel plate shear walls", *Journal of Constructional Steel Research*, Vol. 70, (2012), 308-316. doi: 10.1016/j.jcsr.2011.09.016.
119. Choi, I.-R. and Park, H.-G., "Hysteresis model of thin infill plate for cyclic nonlinear analysis of steel plate shear walls", *Journal of Structural Engineering*, Vol. 136, No. 11, (2010), 1423-1434. doi: 10.1061/(ASCE)ST.1943-541X.0000244.
120. Frosch, R.J., "Shear transfer between concrete elements using steel pipe connection", *Structural Journal*, Vol. 96, No. 6, (1999), 1003-1008. doi: 10.14359/776.
121. Deam, B.L., Fragiaco, M. and Buchanan, A.H., "Connections for composite concrete slab and lvl flooring systems", *Materials and Structures*, Vol. 41, No. 3, (2008), 495-507. doi: 10.1617/s11527-007-9261-x.
122. Kafı, M., "Experimental research of the effect of steel pipes on concentric braced frame", Ph. D. thesis. University of Science and Technology, Department of Civil, (2009).
123. Maleki, S. and Bagheri, S., "Pipe damper, part i: Experimental and analytical study", *Journal of Constructional Steel Research*, Vol. 66, No. 8-9, (2010), 1088-1095. doi: 10.1016/j.jcsr.2010.03.010.
124. Maleki, S. and Mahjoubi, S., "Dual-pipe damper", *Journal of Constructional Steel Research*, Vol. 85, (2013), 81-91. doi: 10.1016/j.jcsr.2013.03.004.
125. Maleki, S. and Mahjoubi, S., "Infilled-pipe damper", *Journal of Constructional Steel Research*, Vol. 98, (2014), 45-58. doi: 10.1016/j.jcsr.2014.02.015.

126. Javanmardi, A., Ghaedi, K., Ibrahim, Z. and Muthu, K.U., "Seismic pounding mitigation of an existing cable-stayed bridge using metallic dampers", in IABSE Conf.-Eng. Dev. World, International Association for Bridge and Structural Engineering, Kuala Lumpur, Malaysia., (2018), 617-623. doi: 10.2749/kualalumpur.2018.0617.
127. Guo, W., Wang, X., Yu, Y., Chen, X., Li, S., Fang, W., Zeng, C., Wang, Y. and Bu, D., "Experimental study of a steel damper with x-shaped welded pipe halves", *Journal of Constructional Steel Research*, Vol. 170, (2020), 106087. doi: 10.1016/j.jcsr.2020.106087.
128. Cheraghi, A. and Zahrai, S.M., "Innovative multi-level control with concentric pipes along brace to reduce seismic response of steel frames", *Journal of Constructional Steel Research*, Vol. 127, (2016), 120-135. doi: 10.1016/j.jcsr.2016.07.024.
129. Cheraghi, A. and Zahrai, S.M., "Cyclic testing of multilevel pipe in pipe damper", *Journal of Earthquake Engineering*, Vol. 23, No. 10, (2019), 1695-1718. doi: 10.1080/13632469.2017.1387191.
130. Zahrai, S.M. and Cheraghi, A., "Improving cyclic behavior of multi-level pipe damper using infill or slit diaphragm inside inner pipe", *Structural Engineering and Mechanics*, Vol. 64, No. 2, (2017), 195-204. doi: 10.12989/sem.2017.64.2.195.
131. Zahrai, S.M. and Cheraghi, A., "Reducing seismic vibrations of typical steel buildings using new multi-level yielding pipe damper", *International Journal of Steel Structures*, Vol. 17, No. 3, (2017), 983-998. doi: 10.1007/s13296-017-9010-0.
132. Bincy, V. and Usha, S., "Seismic performance evaluation of steel building frames with modified dual-pipe damper", in IOP Conference Series: Materials Science and Engineering, IOP Publishing. Vol. 1114, (2021), 012004. doi: 10.1088/1757-899X/1114/1/012004.
133. Mahboubi, B., Zohari, A. and Abdollahiparsa, S., "Seismic behavior of braced steel frames with pipe damper (pd)", *Authorea Preprints*, (2020). doi: 10.1177/1369433220981653.
134. Abbasnia, R., Vetr, M., Ahmadi, R. and Kafi, M., "Experimental and analytical investigation on the steel ring ductility", *Sharif Journal of Science Technology*, Vol. 52, (2008), 41-48.
135. Andalib, Z., Kafi, M.A., Kheyroddin, A. and Bazzaz, M., "Experimental investigation of the ductility and performance of steel rings constructed from plates", *Journal of Constructional Steel Research*, Vol. 103, (2014), 77-88. doi: 10.1016/j.jcsr.2014.07.016.
136. Azandariani, M.G., Abdolmaleki, H. and Azandariani, A.G., "Numerical and analytical investigation of cyclic behavior of steel ring dampers (SRDS)", *Thin-Walled Structures*, Vol. 151, No., (2020), 106751. doi: 10.1016/j.tws.2020.106751.
137. Azandariani, M.G., Azandariani, A.G. and Abdolmaleki, H., "Cyclic behavior of an energy dissipation system with steel dual-ring dampers (SDRDS)", *Journal of Constructional Steel Research*, Vol. 172, (2020), 106145. doi: 10.1016/j.jcsr.2020.106145.
138. Behnamfar, F., Arman, S. and Zibasokhan, H., "Steel rings as seismic fuses for enhancing ductility of cross braced frames", *Earthquake Engineering and Engineering Vibration*, Vol. 21, No. 4, (2022), 1103-1117. doi: 10.1007/s11803-022-2135-y.
139. Abed, D., Al Thawabteh, J., Alzubi, Y., Assbeihat, J. and Al-Sahawneh, E., "Influence of earthquake parameters on the bi-directional behavior of base isolation systems", *Civil Engineering Journal*, Vol. 8, No. 10, (2022), 2038-2052. doi: 10.28991/CEJ-2022-08-10-02.
140. Skinner, R.I., "An introduction to seismic isolation/r. Ivan skinner, william h. Robinson, and graeme h. Meverry, (1993).
141. Yoshikawa, H., Saeki, E., Watanabe, A. and Suzuki, K., "Experimental study of u-shaped steel damper (part 2: Test of u-shaped dampers with rubber bearings)", in Summaries of Technical Papers of Annual Meeting, Architectural Institute of Japan, B-2, Structure II., (1999), 667-668.
142. Schultz, A. and Magana, R., "Seismic behavior of connections in precast concrete walls", *Special Publication*, Vol. 162, (1996), 273-312.
143. Suzuki, K., Watanabe, A. and Saeki, E., "Development of u-shaped steel damper for seismic isolation system", *Nippon Steel Technical Report*, Vol. 92, (2005), 56-61.
144. Kishiki, S., Ohkawara, Y., Yamada, S. and Wada, A., "Experimental evaluation of cyclic deformation capacity of u-shaped steel dampers for base-isolated structures", *Journal of Structural and Construction Engineering*, Vol. 73, No. 624, (2008), 333-340. doi: 10.3130/aijs.73.333.
145. Oh, S.-H., Song, S.-H., Lee, S.-H. and Kim, H.-J., "Seismic response of base isolating systems with u-shaped hysteretic dampers", *International Journal of Steel Structures*, Vol. 12, No. 2, (2012), 285-298. doi: 10.1007/s13296-012-2011-0.
146. Oh, S.-H., Song, S.-H., Lee, S.-H. and Kim, H.-J., "Experimental study of seismic performance of base-isolated frames with u-shaped hysteretic energy-dissipating devices", *Engineering Structures*, Vol. 56, (2013), 2014-2027. doi: 10.1016/j.engstruct.2013.08.011.
147. Iwasaki, A., Takeuchi, I., Inoue, K., Suita, K., Koetaka, Y. and Uno, N., "Study on damping mechanism for h-section beam-to-column connections", *Proceedings of AIJ Kinki Branch*, (2002), 197-200.
148. Tagawa, H. and Gao, J., "Evaluation of vibration control system with u-dampers based on quasi-linear motion mechanism", *Journal of Constructional Steel Research*, Vol. 70, (2012), 213-225. doi: 10.1016/j.jcsr.2011.09.004.
149. Deng, K., Pan, P. and Wang, C., "Development of crawler steel damper for bridges", *Journal of Constructional Steel Research*, Vol. 85, (2013), 140-150. doi: 10.1016/j.jcsr.2013.03.009.
150. Deng, K., Pan, P., Su, Y. and Xue, Y., "Shape optimization of u-shaped damper for improving its bi-directional performance under cyclic loading", *Engineering Structures*, Vol. 93, (2015), 27-35. doi: 10.1016/j.engstruct.2015.03.006.
151. Atasever, K., Celik, O.C. and Yuksel, E., "Development and cyclic behavior of u-shaped steel dampers with perforated and nonparallel arm configurations", *International Journal of Steel Structures*, Vol. 18, No. 5, (2018), 1741-1753. doi: 10.1007/s13296-018-0074-2.
152. Atasever, K., "Modelling hysteretic behaviour of u-shaped steel dampers and using such dampers with low damping rubber bearings as seismic isolator", *Istanbul Technical University*, (2015).
153. Qu, B., Dai, C., Qiu, J., Hou, H. and Qiu, C., "Testing of seismic dampers with replaceable u-shaped steel plates", *Engineering Structures*, Vol. 179, (2019), 625-639. doi: 10.1016/j.engstruct.2018.11.016.
154. Taiyari, F., Mazzolani, F.M. and Bagheri, S., "A proposal for energy dissipative braces with u-shaped steel strips", *Journal of Constructional Steel Research*, Vol. 154, (2019), 110-122. doi: 10.1016/j.jcsr.2018.11.031.
155. Yu, Q.-Q., Wu, J.-Y., Gu, X.-L. and Zhou, F.-Y., "Experimental study on effects of u-shape dampers on earthquake responses of a base-isolated lng inner tank", *Engineering Structures*, Vol. 269, (2022), 114841. doi: 10.1016/j.engstruct.2022.114841.
156. Özkaynak, H., "Model proposal for steel cushions for use in reinforced concrete frames", *KSCE Journal of Civil Engineering*, Vol. 21, No. 7, (2017), 2717-2727. doi: 10.1007/s12205-017-0477-1.
157. Kato, S., Ohya, T., Okamaoto, T. and Takayama, H., "Efficiency of steel hysteresis dampers to suppress earthquake responses of spatial structure", in Proceedings of IASS symposium., (2002), 583-590.

158. Kato, S., Kim, Y.-B., Nakazawa, S. and Ohya, T., "Simulation of the cyclic behavior of j-shaped steel hysteresis devices and study on the efficiency for reducing earthquake responses of space structures", *Journal of Constructional Steel Research*, Vol. 61, No. 10, (2005), 1457-1473. doi: 10.1016/j.jcsr.2005.03.006.
159. Kato, S. and Kim, Y.-B., "A finite element parametric study on the mechanical properties of j-shaped steel hysteresis devices", *Journal of Constructional Steel Research*, Vol. 62, No. 8, (2006), 802-811. doi: 10.1016/j.jcsr.2005.11.014.
160. Zhai, Z., Guo, W., Yu, Z., He, C. and Zeng, Z., "Experimental and numerical study of s-shaped steel plate damper for seismic resilient application", *Engineering Structures*, Vol. 221, (2020), 111006. doi: 10.1016/j.engstruct.2020.111006.
161. Wang, W., Song, J.-l., Su, S.-q., Cai, H.-l. and Zhang, R.-f., "Experimental and numerical studies of an axial tension-compression corrugated steel plate damper", *Thin-Walled Structures*, Vol. 163, (2021), 107498. doi: 10.1016/j.tws.2021.107498.
162. Kim, Y.-C., Mortazavi, S.J., Farzampour, A., Hu, J.-W., Mansouri, I. and Awoyera, P.O., "Optimization of the curved metal damper to improve structural energy dissipation capacity", *Buildings*, Vol. 12, No. 1, (2022), 67. doi: 10.3390/buildings12010067.
163. Hsu, H.-L. and Halim, H., "Improving seismic performance of framed structures with steel curved dampers", *Engineering Structures*, Vol. 130, (2017), 99-111. doi: 10.1016/j.engstruct.2016.09.063.
164. Hsu, H.-L. and Halim, H., "Brace performance with steel curved dampers and amplified deformation mechanisms", *Engineering Structures*, Vol. 175, (2018), 628-644. doi: 10.1016/j.engstruct.2018.08.052.
165. Zheng, J., Zhang, C. and Li, A., "Experimental investigation on the mechanical properties of curved metallic plate dampers", *Applied Sciences*, Vol. 10, No. 1, (2019), 269. doi: 10.3390/app10010269
166. Ghabussi, A., Marnani, J.A. and Rohanimanesh, M.S., "Improving seismic performance of portal frame structures with steel curved dampers", in *Structures*, Elsevier. Vol. 24, (2020), 27-40. doi: 10.1016/j.istruc.2019.12.025.
167. Ghabussi, A., Marnani, J.A. and Rohanimanesh, M.S., "Seismic performance assessment of a novel ductile steel braced frame equipped with steel curved damper", in *Structures*, Elsevier. Vol. 31, (2021), 87-97. doi: 10.1016/j.istruc.2021.01.073.
168. Shojaeifar, H., Maleki, A. and Lotfollahi-Yaghin, M.A., "Performance evaluation of curved-tadas damper on seismic response of moment resisting steel frame", *International Journal of Engineering, Transactions A: Basics*, Vol. 33, No. 1, (2020), 55-67. doi: 10.5829/ije.2020.33.01a.07.
169. Fathizadeh, S., Dehghani, S., Yang, T., Farsangi, E.N., Vosoughi, A., Hajirasouliha, I., Takewaki, I., Málaga-Chuquitaype, C. and Varum, H., "Trade-off pareto optimum design of an innovative curved damper truss moment frame considering structural and non-structural objectives", in *Structures*, Elsevier. Vol. 28, (2020), 1338-1353. doi: 10.1016/j.istruc.2020.09.060.
170. Dehghani, S., Fathizadeh, S., Yang, T., Farsangi, E.N., Vosoughi, A., Hajirasouliha, I., Málaga-Chuquitaype, C. and Takewaki, I., "Performance evaluation of curved damper truss moment frames designed using equivalent energy design procedure", *Engineering Structures*, Vol. 226, (2021), 111363. doi: 10.1016/j.engstruct.2020.111363.
171. Fathizadeh, S., Dehghani, S., Yang, T., Vosoughi, A., Farsangi, E.N. and Hajirasouliha, I., "Seismic performance assessment of multi-story steel frames with curved dampers and semi-rigid connections", *Journal of Constructional Steel Research*, Vol. 182, (2021), 106666. doi: 10.1016/j.jcsr.2021.106666.
172. Lee, M.-H., Oh, S.-H., Huh, C., Oh, Y.-S., Yoon, M.-H. and Moon, T.-S., "Ultimate energy absorption capacity of steel plate slit dampers subjected to shear force", *Steel Structures*, Vol. 2, No. 2, (2002), 71-79.
173. Oh, S.-H., Kim, Y.-J. and Ryu, H.-S., "Seismic performance of steel structures with slit dampers", *Engineering Structures*, Vol. 31, No. 9, (2009), 1997-2008. doi: 10.1016/j.engstruct.2009.03.003.
174. Shahri, S.F. and Mousavi, S.R., "Seismic behavior of beam-to-column connections with elliptic slit dampers", *Steel Composite and Structures*, Vol. 26, No. 3, (2018), 289-301. doi: 10.12989/scs.2018.26.3.289.
175. Lor, H.A., Izadina, M. and Memarzadeh, P., "Experimental and numerical study of i-shape slit dampers in connections", *Latin American Journal of Solids and Structures*, Vol. 15, (2018). doi: 10.1590/1679-78254416.
176. Karavasilis, T.L., Kerawala, S. and Hale, E., "Hysteretic model for steel energy dissipation devices and evaluation of a minimal-damage seismic design approach for steel buildings", *Journal of Constructional Steel Research*, Vol. 70, (2012), 358-367. doi: 10.1016/j.jcsr.2011.10.010.
177. Hedayat, A.A., "Prediction of the force displacement capacity boundary of an unbuckled steel slit damper", *Journal of Constructional Steel Research*, Vol. 114, (2015), 30-50. doi: 10.1016/j.jcsr.2015.07.003.
178. Zheng, J., Li, A. and Guo, T., "Analytical and experimental study on mild steel dampers with non-uniform vertical slits", *Earthquake Engineering and Engineering Vibration*, Vol. 14, No. 1, (2015), 111-123. doi: 10.1007/s11803-015-0010-9.
179. Benavent-Climent, A., "A brace-type seismic damper based on yielding the walls of hollow structural sections", *Engineering Structures*, Vol. 32, No. 4, (2010), 1113-1122. doi: 10.1016/j.engstruct.2009.12.037.
180. Ghabraie, K., Chan, R., Huang, X. and Xie, Y.M., "Shape optimization of metallic yielding devices for passive mitigation of seismic energy", *Engineering Structures*, Vol. 32, No. 8, (2010), 2258-2267. doi: 10.1016/j.engstruct.2010.03.028.
181. Vaseghi, A.J., Mirza, G.R.A. and Shafiei, S.H., "Effect of the height increasing on steel buildings retrofitted by buckling restrained bracing systems and ttd damper", (2013). doi: 10.5829/idosi.ije.2013.26.10a.05.
182. Askariani, S.S., Garivani, S. and Aghakouchak, A.A., "Application of slit link beam in eccentrically braced frames", *Journal of Constructional Steel Research*, Vol. 170, (2020), 106094. doi: 10.1016/j.jcsr.2020.106094.
183. Zhao, B., Lu, B., Zeng, X. and Gu, Q., "Experimental and numerical study of hysteretic performance of new brace type damper", *Journal of Constructional Steel Research*, Vol. 183, (2021), 106717. doi: 10.1016/j.jcsr.2021.106717.
184. Miller, D.K., "Lessons learned from the northridge earthquake", *Engineering Structures*, Vol. 20, No. 4-6, (1998), 249-260. doi: 10.1016/S0141-0296(97)00031-X.
185. Nakashima, M., Inoue, K. and Tada, M., "Classification of damage to steel buildings observed in the 1995 hyogoken-nanbu earthquake", *Engineering Structures*, Vol. 20, No. 4-6, (1998), 271-281. doi: 10.1016/S0141-0296(97)00019-9.
186. Tremblay, R., Filiatrault, A., Timler, P. and Bruneau, M., "Performance of steel structures during the 1994 northridge earthquake", *Canadian Journal of Civil Engineering*, Vol. 22, No. 2, (1995), 338-360. doi: 10.1139/195-046.
187. Japan, A.Lo., "Reconnaissance report on damage to steel building structures observed from the 1995 hyogoken-nanbu (hanshin/awaji) earthquake", (1997).
188. Engelhardt, M.D., "Experimental investigation of dogbone moment connections", *Engineering Journal*, Vol. 35, No. 4, (1999), 128-139. doi: 10012570852.
189. Suita, K., Tamura, T., Morita, S., Nakashima, M. and Engelhardt, M.D., "Plastic rotation capacity of steel beam-to-column connections using a reduced beam section and no weld access

- hole design-full scale tests for improved steel beam-to-column subassemblies-part 1", *Journal of Structure and Construction Engineering*, Vol. 526, (1999), 177-184. doi: 10.3130/aijs.64.177_3.
190. Oh, S.-H., Kim, Y.-J. and Moon, T.-S., "Cyclic performance of existing moment connections in steel retrofitted with a reduced beam section and bottom flange reinforcements", *Canadian Journal of Civil Engineering*, Vol. 34, No. 2, (2007), 199-209. doi: 10.1139/106-125.
 191. Venture, S.J. and Committee, G.D., "Recommended seismic design criteria for new steel moment-frame buildings", Federal Emergency Management Agency Washington, DC, USA, Vol. 350, (2000).
 192. Kim, Y.-J. and Oh, S.-H., "Effect of the moment transfer efficiency of a beam web on deformation capacity at box column-to-h beam connections", *Journal of Constructional Steel Research*, Vol. 63, No. 1, (2007), 24-36. doi: 10.1016/j.jcsr.2006.02.009.
 193. Hedayat, A. and Celikag, M., "Fracture moment and ductility of welded connections", *Proceedings of the Institution of Civil Engineers-Structures and Buildings*, Vol. 162, No. 6, (2009), 405-418. doi: 10.1680/stbu.2009.162.6.405.
 194. Mahin, S.A., "Lessons from damage to steel buildings during the northridge earthquake", *Engineering Structures*, Vol. 20, No. 4-6, (1998), 261-270. doi: 10.1016/S0141-0296(97)00032-1.
 195. Engelhardt, M. and Husain, A., "Cyclic-loading performance of welded flange-bolted web connections", *Journal of Structural Engineering*, Vol. 119, No. 12, (1993), 3537-3550. doi: 10.1061/(ASCE)0733-9445(1993)119:12(3537).
 196. Morrison, M., Schweizer, D. and Hassan, T., "An innovative seismic performance enhancement technique for steel building moment resisting connections", *Journal of Constructional Steel Research*, Vol. 109, (2015), 34-46. doi: 10.1016/j.jcsr.2015.02.010.
 197. Han, S.W., Moon, K.-H., Hwang, S.-H. and Stojadinovic, B., "Rotation capacities of reduced beam section with bolted web (rbs-b) connections", *Journal of Constructional Steel Research*, Vol. 70, (2012), 256-263. doi: 10.1016/j.jcsr.2011.09.001.
 198. Rahnavard, R., Hassanipour, A. and Siahpolo, N., "Analytical study on new types of reduced beam section moment connections affecting cyclic behavior", *Case Studies in Structural Engineering*, Vol. 3, (2015), 33-51. doi: 10.1016/j.csse.2015.03.001.
 199. Mirghaderi, S.R., Torabian, S. and Imanpour, A., "Seismic performance of the accordion-web rbs connection", *Journal of Constructional Steel Research*, Vol. 66, No. 2, (2010), 277-288. doi: 10.1016/j.jcsr.2009.09.007.
 200. Hassanipour, A., Rahnavard, R., Mokhtari, A. and Rahnavard, N., "Numerical investigation on reduced beam web section moment connections under the effect of cyclic loading", *Journal of Multidisciplinary Engineering Science and Technology*, Vol. 2, No. 8, (2015), 2054-2061. doi: JMESTN42350958.
 201. Plumier, A., "New idea for safe structures in seismic zones", in IABSE Symposium-Mixed Structures Including New Materials., (1990).
 202. Köken, A. and Köroğlu, M.A., "Experimental study on beam-to-column connections of steel frame structures with steel slit dampers", *Journal of Performance of Constructed Facilities*, Vol. 29, No. 2, (2015), 04014066. doi: 10.1061/(ASCE)CF.1943-5509.0000553.
 203. Köroğlu, M.A., Köken, A. and Dere, Y., "Use of different shaped steel slit dampers in beam to column connections of steel frames under cycling loading", *Advanced Steel Construction*, Vol. 14, No. 2, (2018), 251-273. doi: 10.18057/IJASC.2018.14.2.7.
 204. Park, H.-Y. and Oh, S.-H., "Structural performance of beam system with t-stub type slit damper", *Engineering Structures*, Vol. 205, (2020), 109858. doi: 10.1016/j.engstruct.2019.109858.
 205. Aghlara, R. and Tahir, M.M., "A passive metallic damper with replaceable steel bar components for earthquake protection of structures", *Engineering Structures*, Vol. 159, (2018), 185-197. doi: 10.1016/j.engstruct.2017.12.049.
 206. Ghaedi, K. and Ibrahim, Z., "A new metallic bar damper device for seismic energy dissipation of civil structures", in IOP Conference Series: Materials Science and Engineering, IOP Publishing. Vol. 431, (2018), 122009. doi: 10.1088/1757-899X/431/12/122009.
 207. Ghaedi, K., Ibrahim, Z., Javanmardi, A. and Rupakhety, R., "Experimental study of a new bar damper device for vibration control of structures subjected to earthquake loads", *Journal of Earthquake Engineering*, Vol. 25, No. 2, (2021), 300-318. doi: 10.1080/13632469.2018.1515796.
 208. Council, A.T., Center, M.-A.E., Research, M.C.f.E.E., Center, P.E.E.R. and Program, N.E.H.R., "Interim testing protocols for determining the seismic performance characteristics of structural and nonstructural components", Federal Emergency Management Agency, (2007).
 209. Agency, F.E.M., *Interim testing protocols for determining the seismic performance characteristics of structural and nonstructural components, fema 461*. 2007, Federal Emergency Management Agency Washington, DC.
 210. Venture, SAC Joint, "Protocol for fabrication, inspection, testing, and documentation of beam-column connection tests and other experimental specimens", Rep. No. SAC/BD-97, Vol. 2, (1997).
 211. Manual, AISC Seismic, *Seismic provisions for structural steel buildings*, (2005), 05-341.
 212. Council, A.T., "Guidelines for seismic testing of components of steel structures", Report of ATC-24, (1992).
 213. Jiao, Y., Kishiki, S. and Yamada, S., "Loading protocols employed in evaluation of seismic behavior of steel beams in weak-beam moment frames", in Proceeding of 15th World Conference on Earthquake Engineering, Lisbon, Portugal. (2012).
 214. Youssef, N.F., Bonowitz, D. and Gross, J.L., "A survey of steel moment-resisting frame buildings affected by the 1994 northridge earthquake, US National Institute of Standards and Technology, (1995).
 215. Azevedo, J. and Calado, L., "Hysteretic behaviour of steel members: Analytical models and experimental tests", *Journal of Constructional Steel Research*, Vol. 29, No. 1-3, (1994), 71-94. doi: 10.1016/0143-974X(94)90057-4.
 216. Bannantine, J., Comer, J. and Handrock, J., "Fundamentals of metal fatigue analysis(book)", Research supported by the University of Illinois. Englewood Cliffs, NJ, Prentice Hall, 1990, 286, (1990).
 217. Zhang, R., Wang, C., Pan, C., Shen, H., Ge, Q. and Zhang, L., "Simplified design of elastoplastic structures with metallic yielding dampers based on the concept of uniform damping ratio", *Engineering Structures*, Vol. 176, (2018), 734-745. doi: 10.1016/j.engstruct.2018.09.009.
 218. Jaisee, S., Yue, F. and Ooi, Y.H., "A state-of-the-art review on passive friction dampers and their applications", *Engineering Structures*, Vol. 235, (2021), 112022. doi: 10.1016/j.engstruct.2021.112022.
 219. Bagheri, S., Barghian, M., Saieri, F. and Farzinfar, A., "U-shaped metallic-yielding damper in building structures: Seismic behavior and comparison with a friction damper", in Structures, Elsevier. Vol. 3, (2015), 163-171. doi: 10.1016/j.istruc.2015.04.003.

Persian Abstract

چکیده

تحریک لرزه ای می تواند باعث آزاد شدن انرژی قابل توجهی در سازه ها شود. با استفاده از دستگاه های خاص می توان این انرژی را بدون تغییر شکل قابل توجهی در اعضای سازه مصرف و تلف کرد. به همین دلیل آسیب های سازه ای به حداقل می رسد، از تلفات جانی در هنگام زلزله جلوگیری می شود و عمر مفید سازه ها افزایش می یابد. در طول پنج دهه گذشته، به طور گسترده ای پذیرفته شده است که دمپره های تسلیم فولاد یکی از بهترین دستگاه های اتلاف انرژی هستند. بیان شده است که رفتار هیسترتیک دمپره های تسلیم فولاد بسته به هندسه آنها می تواند کمی متفاوت باشد. از نقطه نظر عملی برای بهبود ایمنی لرزه ای سازه های جدید و موجود مناسب هستند. هدف این مقاله ارائه مروری در رابطه با میراگرهای تسلیم فولاد، توسعه آنها، انواع مختلف و کاربردهای آن است تا به درک نقش این میراگرها در بهبود عملکرد لرزه ای سازه ها کمک کند. دمپره های تسلیم فولاد را از نظر شکل می توان به دمپره های صفحه فولادی، دمپره های لوله، دمپره های منحنی و دمپره های شکافی تقسیم کرد. رایج ترین استفاده از ورق فولادی مانند ADAS و TADAS و دمپره های لوله در قاب های مهاربندی شده است، در حالی که دمپره های U شکل، J و S شکل بیشتر در قاب هایی با مهاربندی شورون دیده می شوند. دمپره های منحنی فولادی با زاویه ۶۰ درجه در قاب فولادی مهاربندی شده، بهترین اتلاف انرژی و استحکام قاب را فراهم می کنند. در این راستا، تا به امروز، میراگرهای شکاف فولادی به عنوان متداول ترین دمپره های تسلیم فولادی شناخته شده اند.



An Economic Approach to the Confinement of Different Concrete Classes with Carbon and Glass Fibers Reinforced Polymers

S. A. Haj Seiyed Taghia^{*a}, H. R. Darvishvand^b, M. Pourhasan^b

^a Department of Civil and Environmental Engineering, University of Hawaii at Manoa, Honolulu, USA

^b Department of civil Engineering, Qazvin Branch, Islamic Azad University, Qazvin, Iran

PAPER INFO

Paper history:

Received 31 December 2022

Received in revised form 28 January 2023

Accepted 05 February 2023

Keywords:

Fiber Reinforced Polymer

Economic Analysis

Statistical Approach

Compressive Strength

Seismic Parameters

ABSTRACT

One of the current approaches for concrete retrofitting is called fiber reinforced polymer (FRP) wrapping. In this study, concrete retrofitting means compressive strength and seismic parameters improvement (such as failure strain, energy absorption, and ductility). Cost analysis may raise issues of concern regarding the economic value of this kind of retrofitting and for this reason, economic analysis was conducted based on experimental works. In this regard, 21 samples were prepared for three compressive strengths of concrete (20, 35, and 50MPa) and wrapped with different layers of carbon and glass fiber reinforced polymers (0, 1, 3, and 5 layers). Samples were subjected to stress-strain tests and concrete properties were estimated. The results showed that carbon and glass fibers, respectively, are more effective in improving the compressive strength and seismic parameters of concrete. But, the economic analysis indicated that glass fiber is more cost-benefit than carbon fiber in improving the concrete properties, especially for one layer of FRP. The economic analysis was not able to specify the application of FRP for which concrete samples are more economical, and for this reason, statistical analysis was used to respond to this vague and achieve a comprehensive assessment. The analysis indicated that the use of FRP is more cost-benefit for lower concrete strength.

doi: 10.5829/ije.2023.36.04a.14

1. INTRODUCTION

Study shows rehabilitation of structure is often a more practical and cost-effective choice in comparison to reconstruction for reducing seismic vulnerability. There are several techniques for retrofitting of older or damaged buildings such as the addition of a shear wall, steel bracing, steel jacketing, and fiber reinforced polymer (FRP). These techniques can reduce lateral deflections due to stiffen or strengthen of the structure, in addition, they prevent the brittle failure modes of structure through the increase of ductility.

1. 1. Fiber Reinforced Polymer (FRP) This research overviews the FRP application in structural retrofitting. FRP is composed of polymer matrix and fiber. The most common fiber reinforced polymers are carbon and glass, which they called CFRP and GFRP,

respectively [1, 2]. FRP advantages include fatigue resistance, low chemical reactivity, ease of application, and formation in various shapes. Besides, FRP has higher tensile strength and is lighter in weight in comparison to steel plate but, high expenditure and inadequate fire-protection are expressed as the most disadvantages of FRP [3, 4].

1. 2. Concrete Confined by FRP This section discusses the advantages of wrapping FRP in the strengthening concrete samples. As a solution to the seismic retrofitting issue, concrete is confined by FRP in the non-linear section of the structural element to increase compressive strength and ductility also, prevent bond slip and buckling of longitudinal reinforcement [3]. Regarding this issue, numerous experimental studies were carried out which confirm the validity of the solution. Youssf et al. [5] studied the capability of FRP

* Corresponding author email: taghia@hawaii.edu
(S. A. Haj Seiyed Taghia)

confinement on improving concrete behavior. The results were based on the stress-strain test. They demonstrated that the effect of confinement can be strongly improved if a corner of the rectangular column section is circularized. Zeng et al. [6] conducted similar research and confirmed the results obtained by Youssf et al. [5]. Taghia et al. [7] investigated the performance of FRP wraps in improving the mechanical and seismic properties of concrete classes. They figure out that FRP is more effective in developing the performance of low-strength concrete and also the growth rate of improvement declined by increasing the FRP layers. Sirach et al. [8] surveyed the effect of high-strain FRP wrapping on the behavior of high- and ultrahigh-strength concrete. They included three parameters in the study such as fiber type, concrete strength, and fiber thickness, and specified the role of these parameters on stress-strain behavior.

Studies illustrated that confinement provides noticeable increases in the final stress and strain of concrete [9-11].

Many researchers underlined the importance of the establishment of appropriate constitutive laws for confined concrete by FRP [4, 12].

Although, FRP contributes to the strength of the structure, but it can be costly for the structural retrofitting in comparison to other solutions (see section "1.1. Fiber Reinforced Polymer (FRP)"), therefore from a practical point of view, an economic analysis should be considered too.

1. 3. Cost-benefit Assessment Cost-benefit analysis is conducted to assess the efficiency of FRP application as a solution for structural retrofitting regarding financial considerations [13]. In this way, several researchers performed different types of assessments. Shapira et al. [14] achieved economic and constructability analyses of FRP cages used for strengthening of concrete beams. Although FRP is more expensive than steel reinforcement, in total, analyses revealed that FRP cages are more economical. Sahirman et al. [15] compared the application of FRP with steel reinforced concrete (SRC) for retrofitting of bridges. They improved a curve theory to estimate future costs of bridges. Based on the analysis of two data sets, their study proved that FRP application is more cost-beneficial than SRC for a period of 10 years. Berg et al. [16] conducted a cost-benefit analysis of concrete bridges in which FRP was applied for rehabilitation. The investigation demonstrated that FRP application reduces construction time and maintenance costs and increases concrete durability. Brayack [17] studied the technical and economic adequacy of FRP for retrofitting of concrete bridges. A cost-benefit analysis was performed to weight retrofitting with FRP and traditional methods. Based on some examples, it has been concluded that FRP

is a cost-effective strategy and can be replaced by the traditional methods. Yan et al. [18] implemented technical and economic analyses regarding the strengthening of the substation framework. They analyzed the economic aspects of two-span FRP and steel gantries and concluded that FRP application can reduce the total cost by 10%. As an economic solution for pipeline retrofitting with FRPs (carbon and glass fabrics), Sever and Ehsani [19] proposed an optimal design procedure. Chen et al. [20] studied the interply hybridization's effects of carbon, glass, and basalt fibers to enhance their flexural behavior and economic efficiency. They simultaneously applied the experiments and numerical simulation in their study. Investigations indicated higher efficiency for glass/carbon fibers regarding strength/cost and modulus/cost ratios. The results indicated that glass fiber demonstrates better behavior with reference to basalt fiber. Rodsin et al. [21] used accessible and inexpensive GFRP for concrete confinement and concluded that GFRP is very economical in order to improve compressive strength and ductility. It can be attributed to the improvement of stress and strain of wrapping concrete. Taghia et al. [22] compared the application of carbon and glass fiber wrappings on enhancing the mechanical properties and seismic parameters. They found that the carbon and glass fibers are more effective in improving compressive strength and seismic behavior respectively. seismic parameters consisted of failure strain, energy absorption, and ductility in their study. Shubhalakshmi et al. [23] conducted an economic analysis in the application of FRP wrapping used in strengthening of concrete slabs. The analysis was estimated according to the price of the material, wrapped area, and strength gained. They found that this technique can increase the bearing capacity of slabs by 6%. El Youbi et al. [24] performed a numerical simulation to estimate the effect of the CFRP warping on the compressive strength and the final strain of reinforced concrete. They developed a FE model associated with the parametric study to assess the impact of different layers of FRP. They indicated that CFRP has a noticeable impact on the ultimate load of eccentrically loaded columns relative to concentrically loaded ones. Salahaldin et al. [25] experimentally studied the capabilities of retrofitting of the damaged hybrid reinforced concrete beams having openings in the shear region. The research considered the difference in rehabilitation strategies of hybrid beams relative to conventional beams. They indicated that the traditional concrete beam reaches to the whole capacity for all kinds of openings. However, the hybrid beams just obtain 84% of ultimate strength.

In practical engineering, there are many structures that have low concrete strength for various reasons, and it is possible that they will not have proper seismic behavior in an earthquake and will suffer significant

damage. As mentioned before, to improve the performance of concrete, one of the best solutions is concrete confinement. Today, using fibers has expanded significantly due to their excellent features. But the high price of fibers is always a deterrent factor along with all the positive features. Therefore, it is necessary to academically optimize using fibers in order to achieve the greatest improvement in the behavior of concrete at the lowest cost. This forms the main idea of current research. The study aims to evaluate the impact of glass and carbon fiber wrapping (more available in the Iranian market) on improving the compressive strength and seismic characteristics of different concrete classes from an economic point of view.

1. 4. Research Significance

Simultaneous attention to the economic approach in the application of fibers along with considering their mechanical and seismic properties forms the importance of the current research. The study tries to fill the gap in previous research which mainly focused on the positive characteristics of fibers in improving the behavior of concrete and paid less attention to economic aspects in practical engineering. Another issue that highlights the importance of the current research is the use of glass and carbon fibers in a comparative manner, which in past research has often individually handled their characteristics in improving the performance of concrete. Meanwhile, there is a question about whether the concrete class is effective in the optimal selection of fibers or not. These are important issues that the current research tries to give a proper answer.

2. EXPERIMENTAL PROCEDURE

In this section, the material types, mix design, preparation, and curing are described, respectively.

2. 1. Material Types Ordinary Portland cement is used in the specimens. The samples are made according to ASTM C150 [26] standard. The gravel and sand aggregates are of river type in accordance with ASTM C33 [27] standard. The sand sizes range from 0 to 4.75 mm with an apparent weight of 2650 kg/m³ in the Saturated Surface Dry (SSD) state with 24-hour water absorption of 1.5%, and additionally, the super-plasticizer of P10-3R type is used based on ASTM C494 [28]. CFRP and GFRP are of type YC-N160 and EVR-200, respectively. The specifications of two types of polymers, and the epoxy DUR 300 resin, are presented in Tables 1 and 2, respectively.

2. 2. Sample Preparation With a practical approach to the subject, three classes of concrete are selected which

are common in construction projects in Iran (20, 35, and 50MPa). First, concrete is constructed and then inserted into pre-prepared cylindrical molds (with dimensions of 15 cm × 30 cm). They are kept in constant temperature and humidity to harden. After 24 hours, the specimens are removed from the molds and placed into a water pond at temperature of 20±2°C for curing. The curing time of the samples is equal to 28 days. Then, the samples are taken out from the pond and placed in the laboratory for drying the surface of the samples. Two days later, the concrete samples are wrapped with different numbers of layers (1, 3, and 5). Meanwhile, in order to compare the results and reach a comprehensive conclusion, a control sample without wrapping is also prepared. By taking into account different concrete classes and the number of different layers used, a total of 21 samples were prepared and, after 7 days, subjected to stress-strain tests. Tests are done in compliance with ASTM C469 [29] (see Figure 1).

In this study, Cs followed by the value mean the concrete class, and Ls followed by the value represent the number of the polymer sheet.

TABLE 1. The specifications of two types of polymers: (a) Carbon and (b) Glass

(a)	
Property	Specification
Type	YC-N160
Tensile strength	4900 MPa
Elastic modulus	230 GPa
Fracture strain	2.13%
Weight per unit area	160 g/m ²
Thickness	0.09 mm
(b)	
Property	Specification
Type	EWR200
Tensile strength	2200 MPa
Fracture strain	2.8 %
Weight per unit area	200 g/m ²
Moisture Content	<0.2 %

TABLE 2. Technical properties of Resin

Property	Specification
Mixing ratio	A: B = 100:34.5 by weight.
Tensile strength	Curing 7 days, +23°C: 45 N/mm ²
Flexural modulus	Curing 7 days, +23°C: 3000 N/mm ²
Tensile modulus	Curing 7 days, +23°C: 3500 N/mm ²

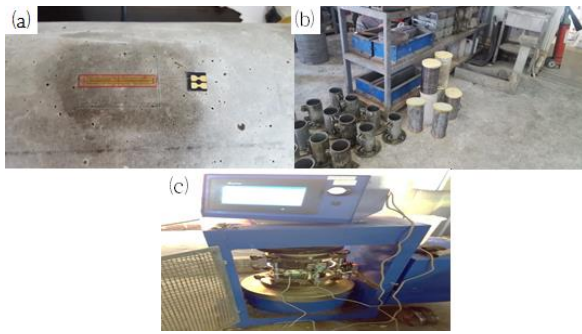


Figure 1. Preparing samples for experiments: (a) strain gauge installation; (b) FRP wrapping; (c) stress-strain device

3. EXPERIMENTAL DATA AND INTERPRETATION

To analyze the data, firstly, the effect of fiber reinforcement on characteristics of different concrete classes is investigated. Concrete characteristics include compressive strength and seismic properties of concrete (i.e. failure strain, energy absorption, and ductility). Then the cost-benefit analysis of fiber application is performed. The index in economic analyses is used to figure out the effect of FRP type, CFRP vs. GFRP, numbers of FRP layers, and compressive strength categories on the economic aspects for improving the strength and seismic properties of the concrete samples. The economic index is defined as an increase in compressive strength or seismic parameters of concrete samples strengthened with FRP wrapping divided by the expenses of strengthening these samples in Euros. The larger this index means, the greater performance improvement is achieved for a given cost of concrete wraps.

Table 3 shows the cost of CFRP and GFRP layers that are used for the wrapping of concrete samples. As it can be seen, the costs of strengthening are noticeable, therefore the number of FRP layers must be chosen, carefully.

Finally, a statistical approach is illustrated to reach a practical and comprehensive conclusion.

3. 1. The Stress-strain Experiments Figures 2-4 illustrate stress-strain plots for three classes of concrete (i.e. C20, C35, and C50) with different numbers of FRP layers. According to ACI 440.2R reference [30], concrete loses its integrity in a longitudinal strain greater than 1%

TABLE 3. The cost of CFRP and GFRP layers used for concrete samples

CFRP cost (€)			GFRP cost (€)		
One layer	Three layers	Five layers	One layer	Three layers	Five layers
2.25	6.83	11.08	0.89	2.56	4.23

and rebar reaches the failure strain and cohesion between concrete and rebar decreases, intensively. For this reason, in the current research, the failure strain values are limited to 1% in the entire Figures 2-4.

In the following sections, economic analysis is presented with respect to sample properties.

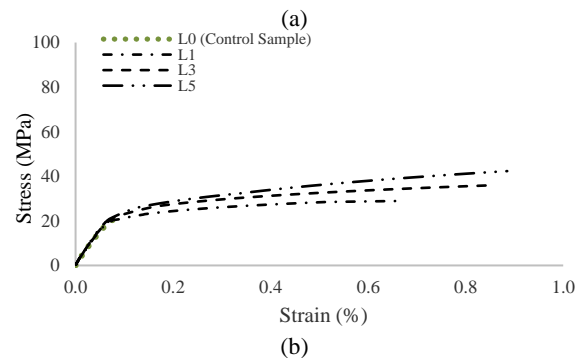
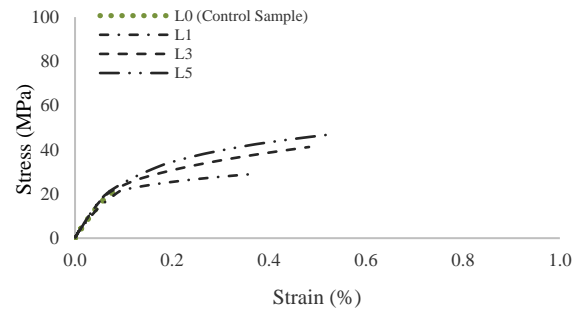


Figure 2. Stress-strain diagrams of samples for C20 class wrapped by: (a) CFRP; (b) GFRP

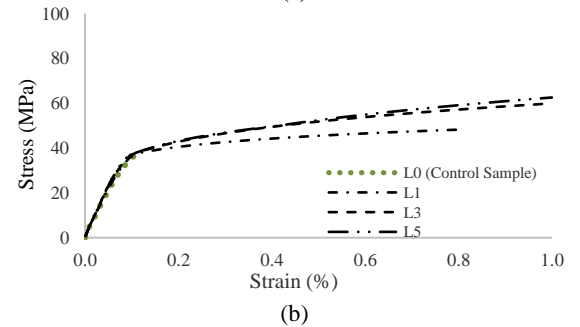
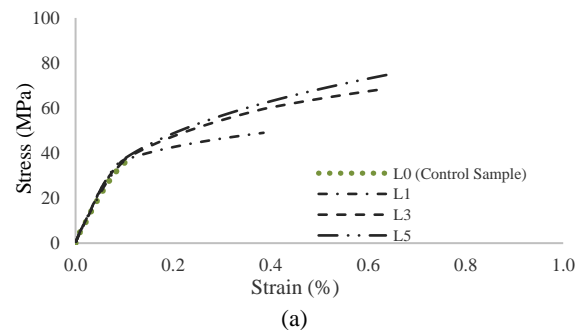


Figure 3. Stress-strain diagrams of samples for C35 class wrapped by: (a) CFRP; (b) GFRP

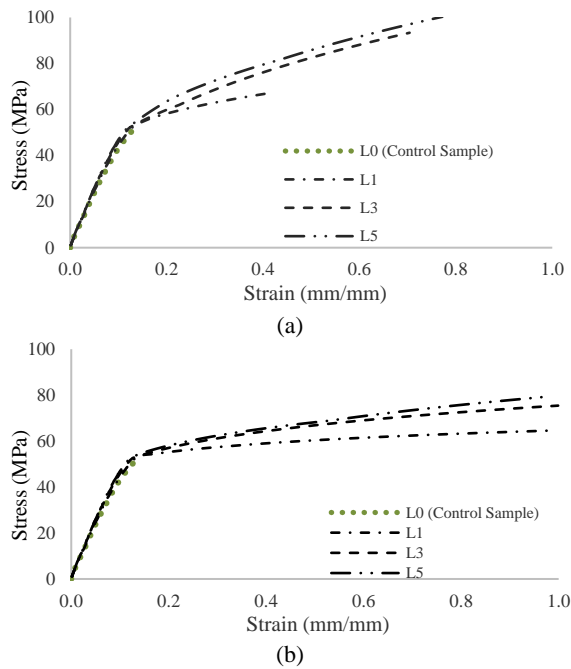


Figure 4. Stress-strain diagrams of samples for C50 class wrapped by: (a) CFRP; (b) GFRP

3. 1. 1. Compressive Strength In this study, the maximum values of stress in Figures 2-4 are determined and considered as compressive strength for designed samples. Figure 5 demonstrates the effects of FRP types and the number of polymer sheets on concrete strength for different concrete classes.

This figure indicates that the compressive strength of concrete samples raises with the increase of the number of FRP layers due to the development of the confinement effect, especially for higher strength concrete. Moreover, the compressive strength of samples wrapped by carbon fibers is higher than glass fibers. The reason can be attributed to the higher tensile strength of carbon fibers

with respect to glass fibers (see Table 1) which provides higher lateral pressure on concrete samples wrapped by CFRP.

The economic indices are estimated for the compressive strength of samples. The results are presented in Figure 6.

The plot in Figure 6, shows that the sample with one FRP layer is more economical. The analysis shows that additional FRP layers for improving the compressive strength are unworthy in order to strengthen the samples since this will increase the cost. The plot also indicates that FRP is more economical for higher concrete strength because FRP increases the compressive strength of higher concrete classes in comparison to the lower ones. (see Figure 5). Finally, the figure demonstrates that GFRP is more economical with respect to CFRP (Almost double). This means that the application of CFRP instead of GFRP, leads to more expenses for preparing the samples and not much gain in the compressive strength of concrete.

3. 1. 2. Failure Strain In Figures 2 through 4, final strains of samples with different concrete classes and FRP layers are specified and referred to as failure strains which are reported in Figure 7.

Figure 7 also, demonstrates that the longitudinal failure strains of samples wrapped by glass fiber are higher than the corresponding samples wrapped by carbon fiber, especially for higher concrete classes. This can be attributed to the more effective role of FRP to confine higher concrete strength and also higher failure strain of GFRP with respect to CFRP. However, GFRP has lower tensile strength relative to CFRP (see Table 1), but concrete withstands higher lateral strain prior to the breaking point without losing its integrity.

The economic indices are estimated regarding failure strains for entire samples. The results are presented in Figure 8.

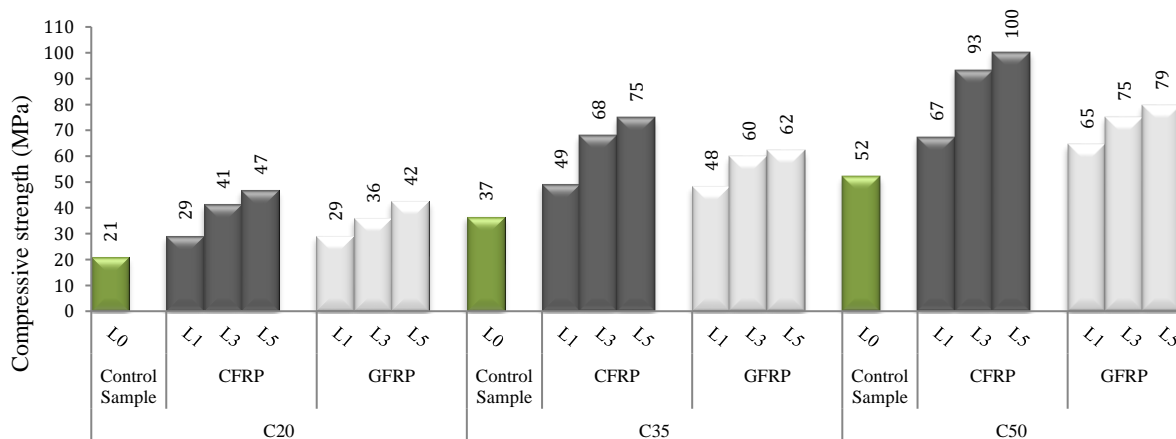


Figure 5. The values of compressive strength in the experiment

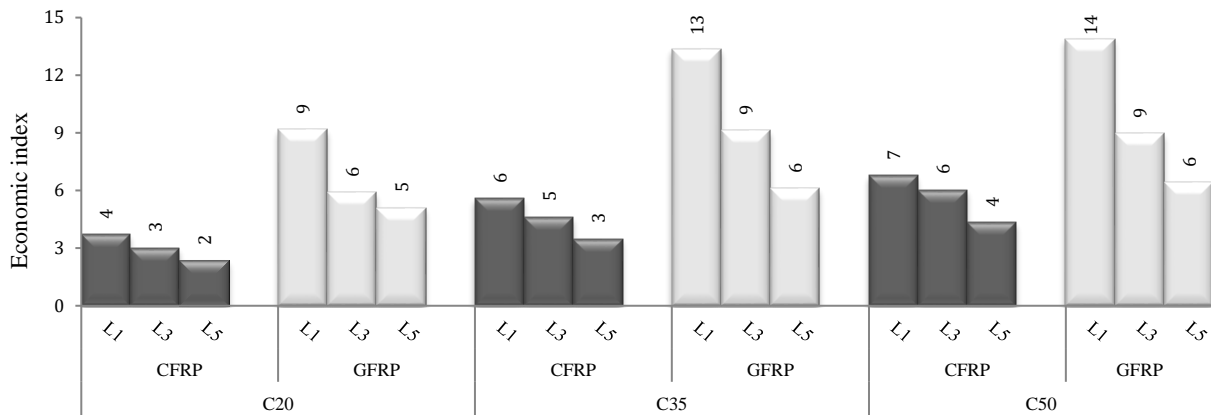


Figure 6. Economic analysis regarding compressive strength for entire samples

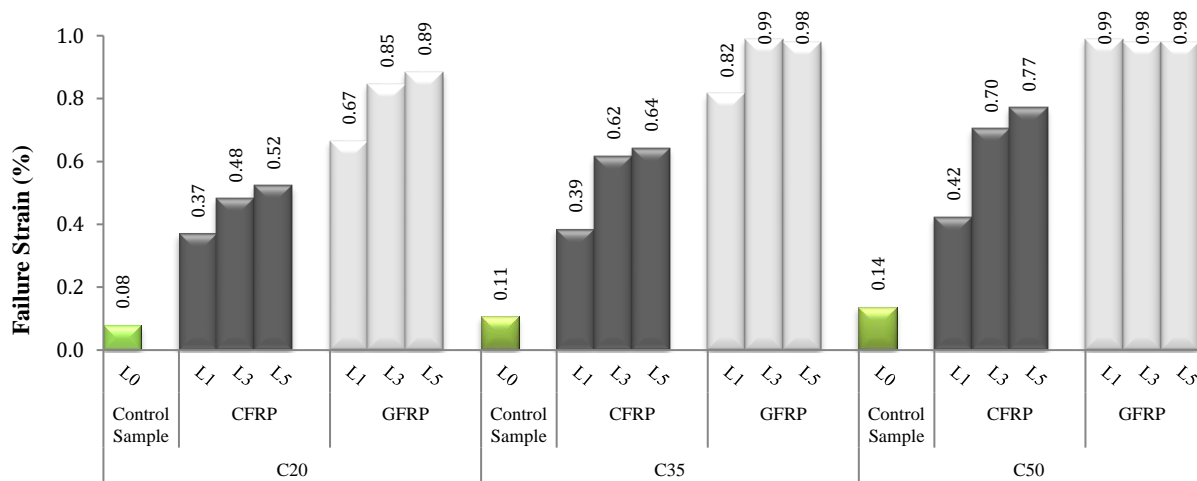


Figure 7. The values of failure strain in the experiment

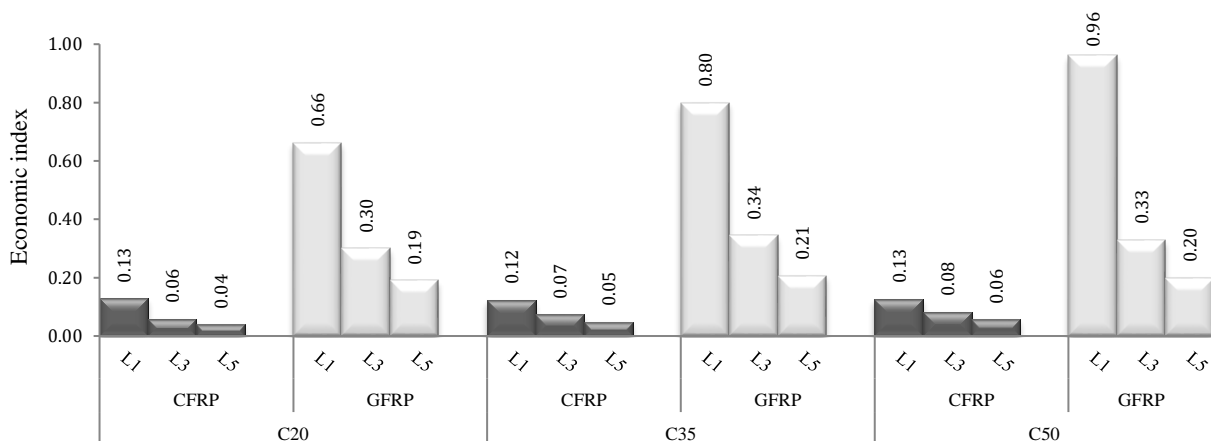


Figure 8. Economic analysis regarding failure strain for entire samples

With a similar argument stated in section “3.1.1.” regarding economic analysis of compressive strength, there is more cost-benefit for one layer of GFRP, especially for higher concrete strength. This clearly reveals in Figure 8.

3. 1. 3. Energy Absorption Energy absorption can be estimated from the areas under the curves of Figures 2 through 4 up to failure strain for the entire samples. The large scale of the area indicates that more energy is

absorbed. The area is calculated by applying the MATLAB program. In this process, the area of each curve is computed, individually and normalized to the area under the curve of the corresponding control sample. The normalized energy absorption of the samples is illustrated in Figure 9.

Figure 9 demonstrates that samples wrapped by GFRP have higher energy absorption than those wrapped by CFRP. The reason behind this is due to higher failure strain in glass fiber compared to carbon fiber.

The economic indices are estimated for entire samples corresponding the energy absorption, the results are shown in Figure 10.

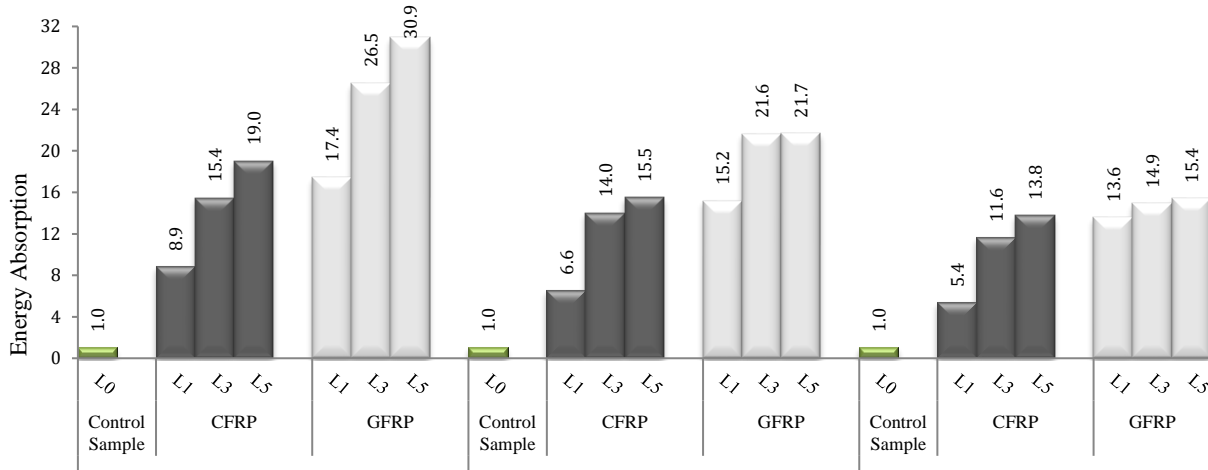


Figure 9. The values of energy absorption in the experiment

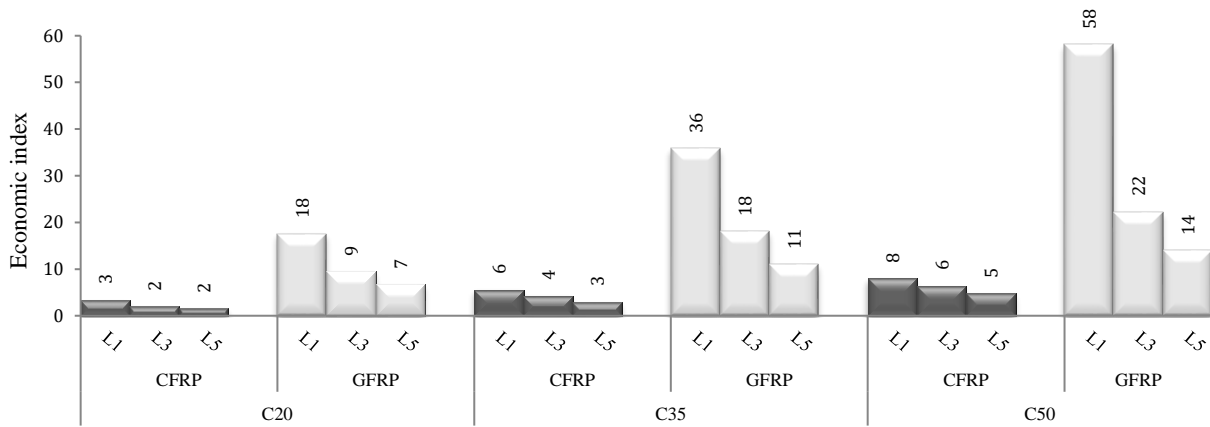


Figure 10. Economic analysis regarding energy absorption for entire samples

3. 1. 4. Ductility According to ASCE41 [31], the ductility of the samples (μ) is defined by dividing the failure strain (ϵ_f) over the yielding strain (ϵ_y). The yield strain is estimated by the following procedure: at first, the stress-strain curve of each sample is replaced by an equivalent bilinear form using MATLAB software, then the intersection of these two straight lines is introduced as the yield strain, ϵ_y . For instance, in Figure 11, the procedure is presented for the C20 class wrapped by three layers of GFRP (i.e. C20, GFRP-L3).

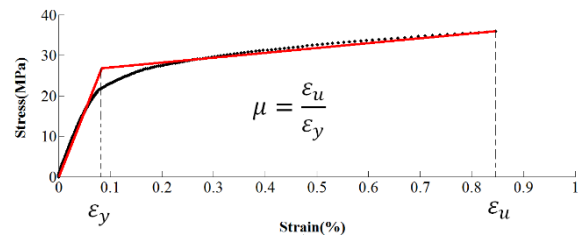


Figure 11. Ductility calculation for sample C20, GFRP-L3 using MATLAB software (2019)

The results of ductility calculation are reported in Figure 12 for the entire samples (corresponding to Figures 2 through 4).

In a similar fashion as explained in the previous section, Figure 12 reveals that the ductility in samples wrapped by GFRP is higher than those wrapped by CFRP due to the higher failure strain of glass fiber compared to carbon fiber.

The economic indices are estimated regarding ductility for entire samples. The results are illustrated in Figure 13. This figure is shown that more cost-benefit is obtained for one layer of GFRP and lower concrete classes.

Evaluation of plots in the economic analysis shown in Figures 6, 8, 10, and 13, indicates that FRP strengthening is more economical in regard to the improvement of compressive strength, failure strain, and energy absorption for higher concrete classes. In contradiction, the use of FRP is more cost-benefit regarding the improvement of ductility for lower concrete classes.

3. 2. Statistical Approach

The statistical approach is needed to achieve a full-scale cost analysis of entire research.

Paired t-test in statistical approach, provides the possibility of comparing two samples in different cases in which two-sample jams are essentially reduced to a one-sample case by using the computed differences d_1, d_2, \dots, d_n . Thus, the hypothesis reduces to:

$$H_0: \mu_1 - \mu_2 = d_0 \tag{1}$$

where μ_1 and μ_2 represent the population means.

H_0 is rejected at significance level α when the computed t-statistic:

$$t = \frac{\bar{d} - d_0}{s_d / \sqrt{n}} \tag{2}$$

exceeds $t_{\alpha/2, n-1}$ or is less than $-t_{\alpha/2, n-1}$ (critical regions). Parameter “n” is the sample size.

\bar{d} and s_d are parameters in relations (1) and (2). They represent the sample mean and standard deviation of the differences in the observations, respectively [32].

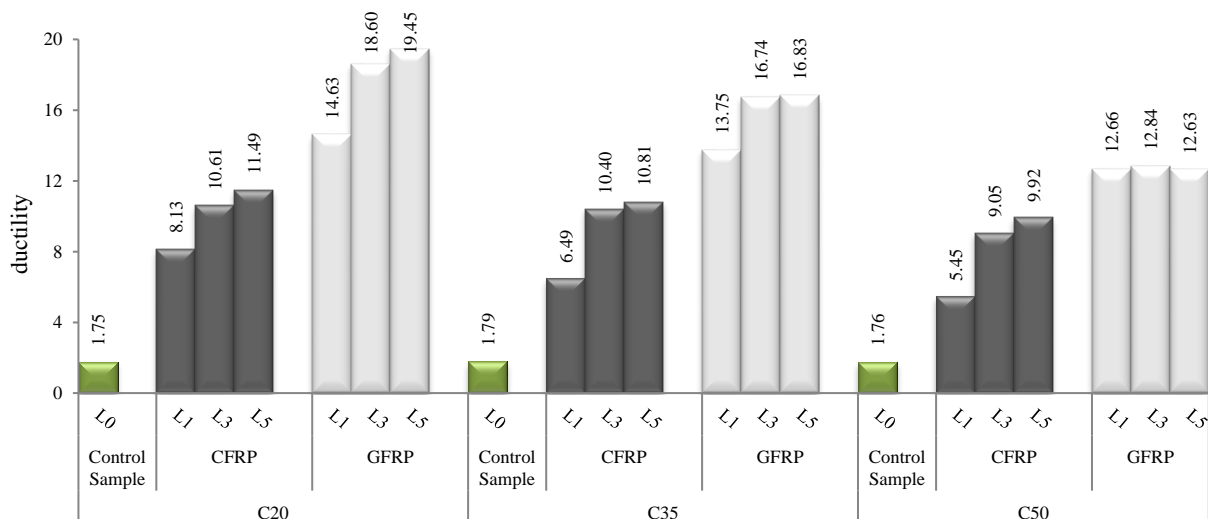


Figure 12. The values of ductility in the experiment

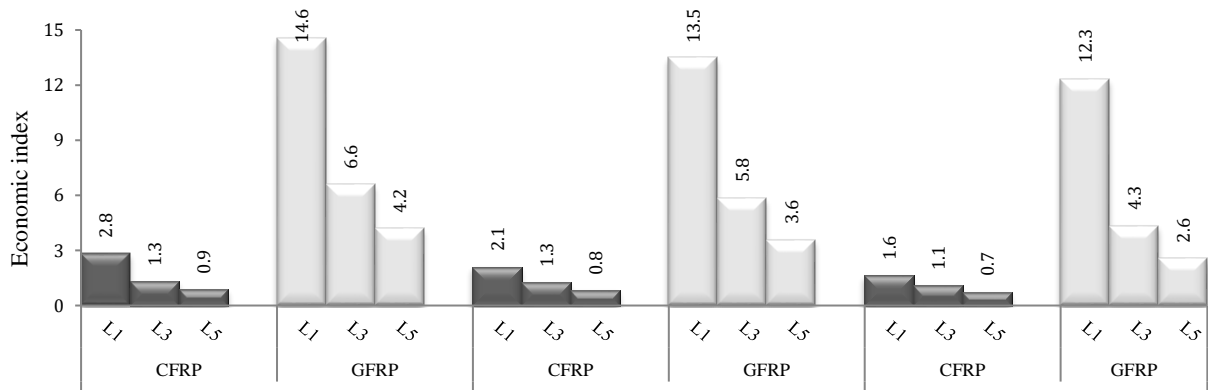


Figure 13. Economic analysis regarding ductility for entire samples

In the current study, the samples are economic indices related to concrete properties (reported in Figures 6, 8, 10, and 13), and d_0 variable, represents the improvement or decline of the index in comparison to the two samples.

Multiple comparisons of cases are conducted in the following:

Case 1: using glass fibers in comparison to carbon fibers for strengthening of concrete samples

Case 2: using different layers of FRP in comparison to one layer for wrapping of concrete samples

Case 3: strengthening of higher concrete classes in comparison to lowest concrete class by FRP wrapping

Cost-benefit analysis of the above cases is examined in the following three sections, respectively:

3. 2. 1. Case 1: Using Glass Fibers in Comparison to Carbon Fibers

The purpose of this section is to estimate the values of improvement or reduction in the economic index, d_0 in application of glass fibers (sample 1) in comparison to carbon fibers (sample 2) in concrete strengthening. This estimation is calculated for mechanical and seismic properties, individually. The results of Paired t-test are tabulated in Table 4.

Estimation showed that the values of d_0 are always positive which means that glass fibers are more cost-benefit than carbon fibers regarding the improvement of concrete properties. For more clarification, the values of d_0 are plotted in Figure 14.

Figure 14 reveals, the maximum and minimum improvement in the economic index is obtained for energy absorption and failure strain, respectively (6.05 vs. 0.17).

TABLE 4. amounts of \bar{d} , s_d and d_0 variables related to case 1

Concrete properties	\bar{d}	s_d	d_0
Concrete strength	4.25	2.11	2.63
Failure strain	0.36	0.26	0.17
Energy absorption	17.11	14.43	6.05
Ductility	6.09	4.01	3.00

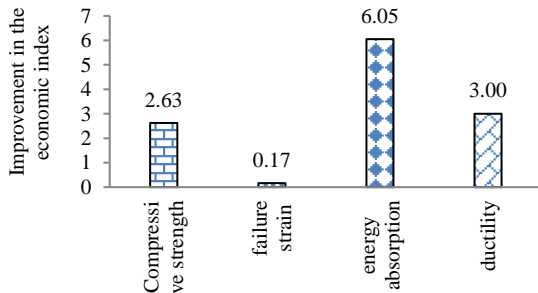


Figure 14. Values of d_0 in case 1 for different concrete properties and FRP types

From now on, evaluation of glass fibers will be the focus of the discussion, since the prior section has shown that the use of glass fibers is more economical than carbon fibers.

3. 2. 2. Case 2: Using Multiple Layers of FRP in Comparison to a Single Layer

The aim of the current section is to estimate the values of improvement or reduction in economic index d_0 when one layer of glass fibers, as in sample 1, is utilized in comparison to three and five layers of glass fibers, as in sample 2, for concrete strengthening. This estimation is performed for the entire concrete properties. The values of the Paired t-test are represented in Table 5.

Estimation reveals that the values of d_0 are always negative, which means that a single layer is more economical than three and five layers of glass fibers regarding the improvement of concrete properties. For more clarification, the values of d_0 are plotted in Figure 15.

Figure 15 shows that the maximum and minimum changes in the economic index belong to energy absorption and failure strain, respectively. Moreover, the graph reveals that the effect of an increase in GFRP layers from three to five layers is not noticeable in the economic index.

TABLE 5. Amounts of \bar{d} , s_d and d_0 variables related to case 2

Concrete properties	L3			L5		
	\bar{d}	s_d	d_0	\bar{d}	s_d	d_0
Concrete strength	-4.15	0.83	-6.23	-6.28	1.90	-11.00
Failure strain	-0.48	0.14	-0.83	-0.61	0.15	-0.97
Energy absorption	-20.58	14.07	-55.61	-26.63	16.71	-68.31
Ductility	-7.87	0.18	-8.32	-10.03	0.32	-10.81

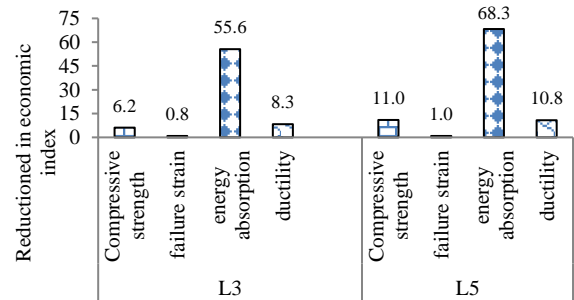


Figure 15. Values of d_0 in case 2 for different concrete properties and GFRP layers

3. 2. 3. Case 3: Strengthening of Higher Concrete Classes in Comparison to Lowest Concrete Class

The goal of the current section is to assess the values of improvement or reduction in economic index d_0 when lowest concrete class, as in sample 1, is compared to higher concrete classes, as in sample 2 for concrete strengthening with GFRP wrapping. Assessment is estimated for the entire concrete properties. The conclusions of the Paired t-test are tabulated in Table 6.

Table 6 shows that the values of d_0 are always negative, which implies that GFRP is more cost-benefit for the lowest concrete class regarding the improvement of concrete properties. For a better understanding, the values of d_0 are plotted in Figure 16.

Figure 16 demonstrates that the maximum and minimum changes in the economic index are related to energy absorption and failure strain, respectively.

TABLE 6. Amounts of \bar{d} , s_d and d_0 variables related to case 3.

Concrete properties	C35			C50		
	\bar{d}	s_d	d_0	\bar{d}	s_d	d_0
Concrete strength	2.81	1.64	-1.30	3.03	1.69	-1.16
Failure strain	0.07	0.06	-0.09	0.11	0.16	-0.29
Energy absorption	10.36	7.15	-7.45	20.19	17.83	-24.23
Ductility	-0.80	0.21	-1.33	-2.03	0.36	-2.94

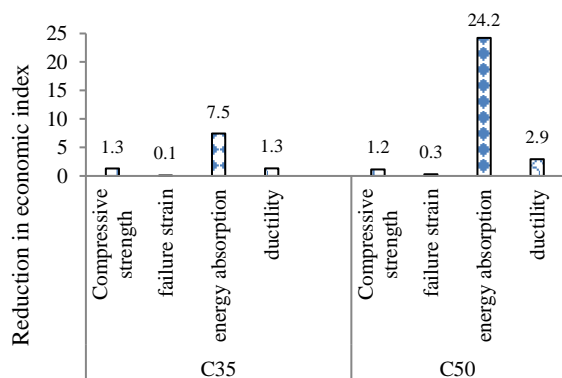


Figure 16. Values of d_0 in case 3 for different concrete properties and classes

4. CONCLUSIONS

Using fibers as an excellent solution in the improvement of non-resistant or earthquake-damaged structures is well known. Past research shows that carbon and glass fibers have proper performance in increasing the compressive strength and improving the seismic behavior of concrete,

respectively. Despite all the excellent FRP features, the considerable cost of fibers has always been an inhibiting factor in the development of the application of this method. Paying attention simultaneously to the economic approach in practical engineering in the application of FRPs (choosing the type and number of layers and concrete class) and considering their mechanical and seismic characteristics indicates the importance of the current research. The economic theoretical analysis performed in this study has been less discussed in past studies and is important in three ways (question form) and contributes to the new knowledge:

- Comparatively, which type of fiber (glass or carbon) is more economical in terms of improving the mechanical and seismic properties of concrete? Economic analysis revealed that the answer to this question is glass fibers.
- Choosing how many layers of fibers is more economical in concrete retrofitting? The economic analysis indicated that the lowest number of layers (one layer) is the answer to the problem and economic efficiency decreases with an increase in the number of FRP layers.
- Fibers are more economically effective on which concrete class in terms of improving performance? Statistical analysis clarified that fibers are more cost-effective in improving the behavior of low-strength concrete.

Regarding the limitations of the current research, it should be noted that the study was designed in response to the needs of the engineering society, and therefore its results are valid within the same scope. It is obvious that by choosing a wider range of concrete classes and the type and number of selected wraps, the research can be more comprehensive. Also, the effect of fibers from an economic aspect was focused on the compressive behavior of concrete. While the flexural behavior of concrete in the moment frame caused by an earthquake could be the subject of future research.

5. ACKNOWLEDGMENTS

The authors would like to acknowledge the following people, Mr. Borjali Darvishvand for his collaboration in editing the article and our colleagues in precast concrete structure laboratory for providing us their mechanical testing facilities.

6. REFERENCES

1. Correia, J., "Pultruded glass fiber (gfrp). Application in gfrp composite beams gfrp-concrete in construction", Master thesis, Instituto Superior Técnico (in Portuguese), (2004).
2. Cabral-Fonseca, S., "Polymeric composite material reinforced with fibers used in civil engineering—features and application",

- LNEC, Lisbon, Portuguese: Scientific and Technical Information, (2005).
3. GangaRao, H.V., Taly, N. and Vijay, P., "Reinforced concrete design with frp composites, CRC press, (2006).
 4. Gevin McDaniel, P.E., "Fiber reinforced polymer (FRP) composites", in America: American Composites Manufacturers Association. Vol., No. Issue, (2014 of Conference).
 5. Youssf, O., Hassanli, R. and Mills, J.E., "Retrofitting square columns using frp-confined crumb rubber concrete to improve confinement efficiency", *Construction and Building Materials*, Vol. 153, (2017), 146-156. <https://doi.org/10.1016/j.conbuildmat.2017.07.108>
 6. Zeng, J., Teng, J., Lin, G. and Li, L., "Large-scale frp-confined rectangular rc columns with section curvilinearization under axial compression", *Journal of Composites for Construction*, Vol. 25, No. 3, (2021), 04021020. [https://doi.org/10.1061/\(ASCE\)CC.1943-5614.0001129](https://doi.org/10.1061/(ASCE)CC.1943-5614.0001129)
 7. Taghia, S., Darvishvand, H.R., Ebrahimi, M. and Razavi, H.S.N., "Evaluating the performance and effect of the number of frp composite wrapping on strength and ductility for low strength concrete", in 16th European Conference on Earthquake Engineering (16ECEE), Thessaloniki, Greece., (2018), 18-21.
 8. Sirach, N., Smith, S.T., Yu, T. and Mostafa, A., "Experimental study on the confinement of concrete cylinders with large rupture-strain frp composites", *Journal of Composites for Construction*, Vol. 25, No. 4, (2021), 04021026. [https://doi.org/10.1061/\(ASCE\)CC.1943-5614.0001137](https://doi.org/10.1061/(ASCE)CC.1943-5614.0001137)
 9. Picher, F., "Confinement of concrete cylinders with cfrp, fiber composites in infrastructure", in Proceedings of the first International Conference on Composites in Infrastructure., (1996), 829-841.
 10. Matthys, S., Taerwe, L. and Audenaert, K., "Tests on axially loaded concrete columns confined by fiber reinforced polymer sheet wrapping", *Special Publication*, Vol. 188, (1999), 217-228. doi.
 11. Bisby, L.A. and Williams, B.K., "An introduction to frp strengthening of concrete structures", in ISIS Educational Module. Canada., (2004).
 12. Monti, G., Nisticò, N. and Santini, S., "Design of frp jackets for upgrade of circular bridge piers", *Journal of Composites for Construction*, Vol. 5, No. 2, (2001), 94-101. [https://doi.org/10.1061/\(ASCE\)1090-0268\(2001\)5:2\(94\)](https://doi.org/10.1061/(ASCE)1090-0268(2001)5:2(94))
 13. Abdelrahman, K. and El-Hacha, R., "Cost and ductility effectiveness of concrete columns strengthened with cfrp and sfrp sheets", *Polymers*, Vol. 6, No. 5, (2014), 1381-1402. doi: 10.3390/polym6051381.
 14. Shapira, A. and Bank, L.C., "Constructability and economics of frp reinforcement cages for concrete beams", *Journal of Composites for Construction*, Vol. 1, No. 3, (1997), 82-89. [https://doi.org/10.1061/\(ASCE\)1090-0268\(1997\)1:3\(82\)](https://doi.org/10.1061/(ASCE)1090-0268(1997)1:3(82))
 15. Sahirman, S., Creese, R.C., GangaRao, H.V. and Brown, C., "Economic analysis of fiber reinforced polymer (FRP) bridge decks", in IIE Annual Conference. Proceedings, Institute of Industrial and Systems Engineers (IISE)., (2003), 1.
 16. Berg, A.C., Bank, L.C., Oliva, M.G. and Russell, J.S., "Construction and cost analysis of an frp reinforced concrete bridge deck", *Construction and Building Materials*, Vol. 20, No. 8, (2006), 515-526. <https://doi.org/10.1016/j.conbuildmat.2005.02.007>
 17. Brayack, D.A., "Technical and economic effectiveness for repair with frp of concrete t-beam bridges: Case study for penn-dot-district 3", (2006). <https://doi.org/10.33915/etd.3243>
 18. Wang, Y., Li, L., Zhang, Y.F., Xu, M.X. and Sun, Q., "Techno-economic analysis of fiber reinforced polymer substitution", in Applied Mechanics and Materials, Trans Tech Publ. Vol. 357, No. Issue, (2013), 1194-1199.
 19. Sever, V.F. and Ehsani, M., Designing an economical frp system for pipeline rehabilitation, in Pipelines 2019: Planning and design. 2019, American Society of Civil Engineers Reston, VA.117-124.
 20. Chen, D., Sun, G., Meng, M., Jin, X. and Li, Q., "Flexural performance and cost efficiency of carbon/basalt/glass hybrid FRP composite laminates", *Thin-Walled Structures*, Vol. 142, (2019), 516-531. <https://doi.org/10.1016/j.tws.2019.03.056>
 21. Rodsin, K., Hussain, Q., Suparp, S. and Nawaz, A., "Compressive behavior of extremely low strength concrete confined with low-cost glass frp composites", *Case Studies in Construction Materials*, Vol. 13, (2020), e00452. <https://doi.org/10.1016/j.cscm.2020.e00452>
 22. Haj Seiyed Taghia, S.A., Darvishvand, H.R., Asadi, S. and Pourhasan, M., "A comparative study on the implementation of carbon and glass fibers wrappings to improve the compressive strength and seismic behavior of concrete", *Asian Journal of Civil Engineering*, Vol. 21, (2020), 1389-1398. <https://doi.org/10.1007/s42107-020-00285-5>
 23. Shubhalakshmi, B., Jagannatha Reddy, H., Prabhakara, R. and Kasi, A., "Performance-based economic evaluation of retrofitted slabs with different frp's and different configurations", Trends in Civil Engineering and Challenges for Sustainability: Select Proceedings of CTCS 2019, (2021), 323-331. https://doi.org/10.1007/978-981-15-6828-2_25
 24. El Youbi, M., Tbatou, T., Kadiri, I. and Fertahi, S.E.-D., "Numerical investigation of hsc columns retrofitted by cfrp materials under combined load", *Civil Engineering Journal*, Vol. 8, No. 4, (2022), 765-779.
 25. Salahaldin, A.I., Jomaa'h, M.M., Oukaili, N.A. and Ghaidan, D.J., "Rehabilitation of hybrid rc-i beams with openings using cfrp sheets", *Civil Engineering Journal*, Vol. 8, No. 01, (2022).
 26. Standard, A., "Astm c150: Standard specification for portland cement", Annual Book of ASTM Standards, American Society for Testing and Materials, West Conshohocken, PA, (2001).
 27. ASTM, A., "C33/c33m-18 standard specification for concrete aggregates", ASTM International: West Conshohocken, PA, USA, (2018).
 28. "ASTM C494, standard specification for chemical admixtures for concrete," ASTM International: West Conshohocken, PA, USA, (2017).
 29. ASTM, A., "C469/c469 m-14 (2014) standard test method for static modulus of elasticity and poisson's ratio of concrete in compression", ASTM International, West Conshohocken.
 30. Committee, A., "Guide for the design and construction of externally bonded frp systems for strengthening concrete structures (ACI 440.2 r-17)", American Concrete Institute, Farmington Hills, MI, (2017).
 31. Engineers, A.S.o.C., "Seismic evaluation and retrofit of existing buildings, American Society of Civil Engineers. (2017).
 32. Walpole, R.E., Myers, R.H., Myers, S.L. and Ye, K., "Probability and statistics for engineers and scientists, Macmillan New York, Vol. 5, (1993).

Persian Abstract

چکیده

یکی از رویکردهای حاضر برای مقاوم سازی بتن، دورپیچ FRP نام دارد. در این مطالعه، مقاوم سازی بتن به معنای بهبود مقاومت فشاری و پارامترهای لرزه‌ای (مانند کرنش شکست، جذب انرژی و شکل پذیری) است. تحلیل هزینه ممکن است مسائل نگران کننده ای را در رابطه با ارزش اقتصادی این نوع مقاوم سازی ایجاد کند و به همین دلیل، تحلیل اقتصادی بر اساس کارهای آزمایشگاهی انجام شد. در این راستا، ۲۱ نمونه برای سه رده مقاومت فشاری بتن (۲۰، ۳۵ و ۵۰ مگاپاسکال) آماده و با لایه‌های مختلف پلیمرهای تقویت شده با الیاف کربن و شیشه (۰، ۱، ۳ و ۵ لایه) دورپیچ شد. نمونه ها تحت آزمایش تنش-کرنش قرار گرفتند و خواص بتن برآورد شد. نتایج نشان داد که الیاف کربن و شیشه به ترتیب در بهبود مقاومت فشاری و پارامترهای لرزه ای بتن موثرتر هستند. اما، تحلیل اقتصادی نشان داد که الیاف شیشه نسبت به الیاف کربن در بهبود خواص بتن، به ویژه برای یک لایه FRP، از نظر هزینه-فایده مناسب تر است. تحلیل اقتصادی نتوانست مشخص کند که کاربرد FRP برای کدام نمونه های بتنی مقرون به صرفه تر است و به همین دلیل برای پاسخ به این ابهام و دستیابی به یک ارزیابی جامع از تحلیل آماری استفاده شد. تحلیل نشان داد که استفاده از FRP برای بتن کم مقاوم از نظر هزینه-فایده مناسب تر است.



High Energy Release-high Retraction Smart Polymer Fibers used in Artificial Muscle Fabrication

M. Karevan*, M. A. Motaleb, A. Jannesari, M. Zeinali

Department of Mechanical Engineering, Isfahan University of Technology, Isfahan, Iran

PAPER INFO

Paper history:

Received 07 January 2023

Received in revised form 23 December 2023

Accepted 06 February 2023

Keywords:

Blocked Force

Energy Release

Tensile Behavior

Smart Fiber

Shape-memory Polymer

ABSTRACT

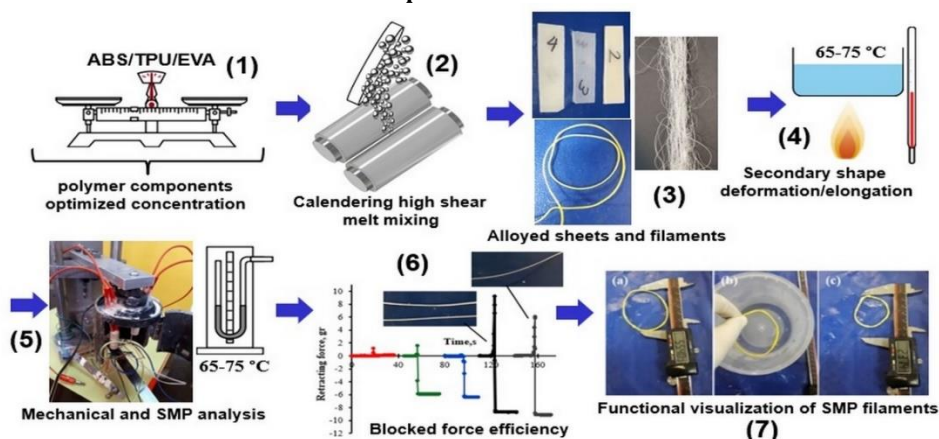
Shape-memory polymers (SMPs) could remember their original shape and then, return to their initial shape upon stimulus. So far, quantities such as fixity and recovery ratio of SMPs have been broadly reported. Nevertheless, one main issue is the existence and use of an appropriate approach to quantitatively estimate the SMPs released energy. In addition, it is hypothesized that the elastic behavior of SMPs plays an underlying role when SMP fibers need to exhibit high-tension and high-elongation capacity as required in synthetic muscles. Here, we present, for first time, SMP trinary bulk and filament systems of acrylonitrile butadiene styrene (ABS)/thermoplastic polyurethane (TPU)/ethylene vinyl acetate (EVA) fabricated under calendaring intense shear mixing and hot pressing. A digital blocked force load cell was used to record specimens energy released. The results exhibited high retraction from the specimens secondary shape correlated to the tensile behavior. It was shown the blended system of 50, 25 and 25% of TPU, ABS and EVA, respectively, resulted in ~640% and 3900% increase in the elastic modulus and energy release compared to EVA/TPU systems. The double SMP filaments led to a 50% increase in the energy release compared to single fibers. Nevertheless, the blended binary specimens with the TPU/ABS ratio of 50/50 exhibited 600% increase in tensile strength. It was confirmed the elastic modulus, number of fibers and elongation at break govern the SMP stored. The findings of the research lightened a new class of SMPs to be used as fiber-based artificial muscles and orthodontic products.

doi: 10.5829/ije.2023.34.04a.15

NOMENCLATURE

K	Equivalent stiffness (N/mm)	P_i	Forced applied on each fiber
K_i	Stiffness of each spring (N/mm)	W	total weight to be lifted
N	Number of fibers		

Graphical Abstract



¹ *Corresponding Author Institutional Email: mkarevan@iut.ac.ir (M. Karevan)

1. INTRODUCTION

Amongst smart materials shape-memory polymers (SMPs) could be listed due to their memory to return to their original shape with some approximation upon receiving an environmental trigger such as heat, moisture and chemicals [1, 2]. Thermal sensitive SMPs require temperature around the glass transition (T_g) or melt temperature (T_m) of the polymer components to implement the start of shape-memory cycle from the secondary to the original shape [3, 4]. Although, their mechanical performance limits their applications in structural sectors, they can find the wider exploitation in areas where mechanical response of the parts is of inferior issue. The latter has paved an avenue toward the utilization of SMPs in bio-medical parts [5, 6].

To develop muscle fibers, polymers of low transitional temperatures together with thermoplastic elastomers such as thermoplastic polyurethane (TPU) and ethylene vinyl acetate (EVA) blended with high stiffness polymers such as polylactic acid (PLA) have been widely reported in the literature [7-10]. The blend of such materials exhibits the network points and molecular switching phase that have been generated through covalent bonds, intermolecular interactions and cross-links [11]. The network points as hard segments serve as pivoting point for shape memory whilst the soft segment serves as an energy absorbing phase [12]. However, the ability of SMP parts to exhibit appropriate mechanical performance might be a pressing challenge as seen in the development of orthodontic filaments, surgical sutures and fibers in the devolvement of artificial muscles in humanoids or those used as scaffolds [13]. One underlying role of SMP parts derived from mechanical characteristics is the amount of energy stored in the secondary phase of SMPs to be released upon stimulus [14-16]. The higher the stored strain energy, the greater the recovery ratio of the specimens. The latter is proposed to be a criterion for SMP fibers able to lift heavier masses using two-way actuation or to tighten other objects upon being stimulated [17, 18]. The former could be correlated to the design and fabrication fiber-based muscles accommodating greater energy stored [19]. Therefore, whilst numerous studies have been elsewhere reported various SMP systems, less research so far has focused on the quality of SMP parts in energy release [14, 20]. In addition, along the ability of SMPs in energy release to perform a work by lifting masses, the extent SMP fibers could be stretched followed by their retraction (contraction) is of another requirement as seen in natural muscle fibers in human body [19]. The latter has been mostly correlated to the recovery ratio of SMPs [21]. However, the recovery ratio itself expresses the ability of SMPs to fully return to their initial shape regardless of the length difference in fibers of original

shape and that in the secondary shape status. It is hypothesized that the greater the said difference, the more capable the SMP fibers to be used as artificial muscle fibers as the nature suggested [22]. Therefore, the stretchability of SMP fibers whilst simultaneously retaining their shape-memory character is a crucial factor. The soft region so far called the amorphous phase is mostly responsible for the fixation ability whilst the crystalline phase is ascribed to the SMPs recovery ratio. Whilst the apomorphs phase contributed to the stretchability upon heating, the net points are expected to enhance the recovery of SMP fibers. As understood, such effects contradicts and, thus, the formulation of SMP blends of high stored energy could be a serious challenge to be addressed [23, 24].

Mirvakili and Hunter [25] used nylon fiber actuators fabricated on the basis of highly oriented nylon filaments representing a 5% deformation with a temperature change from 25 to 140 °C with reservable amplitude. Xie et al. [26] used poly (ethylene-co-vinyl acetate)/graphene (cEVA/G) to develop shape-memory actuators. Their EVA-carbon fiber based composites (EVA/CF) resulted on a significant enhanced recovery stress. Ma et al. [27] developed a mixed-matrix membrane strategy to fabricate photo-induced SMP artificial muscles that were able to lift masses with a fast light response and the high elastomer properties. Yip and Niemeyer [28] employed conductive polyamide 6.6 sewing thread to design high-performance robotic muscles using electric heating. Xiao et al. [29] used liquid crystal polymer (LCP) in the preparation of Janus flower-like structure to design and fabricate soft robots based on the concept of order-disorder phase transition. Although the incorporation of micro- and nanofillers into polymers has been considered to improve SMP properties, the use of pure polymers of right blending ratio could be still a more reasonable approach in terms of processability and cost [30].

Here, we proposed a shape-memory ternary blend system of Acrylonitrile butadiene styrene (ABS)/thermoplastic polyurethane (TPU)/Ethylene vinyl acetate (EVA) bulk and fiber fabricated through melt mixing method on a two-roller mixing calendaring followed by hot pressing. The filaments were manually fabricated by applying tensile tension on the hot melt pieces of alloyed strips. Blocked force method and tensile testing were performed to determine the optimized level of polymer components in terms of energy recovery and tensile response of the parts. The findings of the research expressed a methodology in formulation and fabrication high energy release SMPs containing an optimized level of polymer ratios which are capable of being transformed to filaments. The latter may suggest application of the formulated compounds in design and fabrication of polymer fibers to be used in design of artificial muscles due to their high elastic stored energy.

2. EXPERIMENTAL

2.1. Material In the current work, PLA (KAS GmBh, Austria), TPU (EPAFLEX, Italy) and EVA granules (28%, EPAFLEX, Italy) were used as the thermoplastic matrices. No additional treatment and chemicals modification was performed on the polymer granules.

2.2. Shape-memory Film and Fiber Fabrication

To fabricate SMP alloyed films, a two-roller calendaring device was utilized to melt mixed the polymer components of TPU (0 to 70%), ABS (0 to 70%) and EVA (0 to 50%) under heat and intense shear forces. To decide on the loading fraction of each polymer phase, expected mechanical properties of each polymer was taken into consideration followed by a simple rule of mixtures method to estimate overall mechanical behavior of the parts. It was hypothesized that the higher the fraction of the EVA and TPU part, the greater the elongation and processability of the alloyed systems [31, 32]. On the other hand, it was expected that the ABS would contribute to the tensile strength and modulus of the fabricated parts. The temperature of rollers in the calendaring machine was set to ~140° to 160°C at 5-10 rpm and the granules were first gradually fed into the rollers gap to ensure the melting state onto the heated rolls under intense shear forces. To fabricate the films, the gap between the rollers then was decreased to the desired sheet thickness followed by gradual temperature decrease of the rollers in air. The melt alloyed compound was removed from the rollers surface for the hot press processing under the temperature of 150°C to fabricate the films. The fabricated specimens in form of sheets are displayed in Figure 1.

The strips (bulk specimens) per ASTM D882 standard were cut from the sheets of less than 1 mm for the tensile and energy release characterization steps as displayed in Figure 2. The same dimensions were used for the specimens in the blocked force measurement analysis. The SMP fibers were fabricated using a pre-tension onto the melt compound of the ternary polymer systems at the melt state of the compound collecting from the roller's surface drawn so that a diameter of 200 to 800 μm is achieved for blocked force measurements as shown in Figure 3.



Figure 1. Blended polymer systems onto the calendaring rolls in form of thin layer sheets after hot pressing

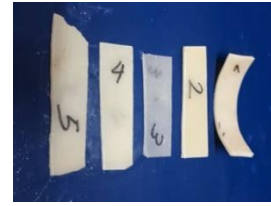


Figure 2. Polymer blended strips (bulk) of ABS/TPU/EVA

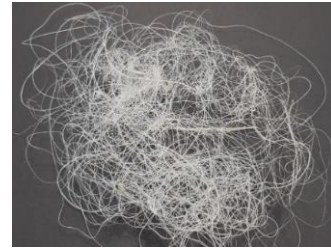


Figure 3. Fabricated SMP fibers of ABS/TPU/EVA

Figure 4 represents the fabricated fibers (filaments) that are in the form of single, multiple bundled, twisted or numerous paralleled fibers from Figures 4(a) to 4(d), respectively.

It is hypothesized that the number of fibers in the form of yarn or bundled filaments affects the amount of energy stored in the softer phases of the alloyed systems to be returned to the fibers initial length upon heating influenced by the presence of net points (hard regions) in either polymer phases [15, 33].

It is noted that multiple fibers parallelly aligned would behave similar to a stronger muscle containing fibers which mimic elastic springs whose equivalent stiffness (K) is the sum of the stiffness of each spring (k_i).

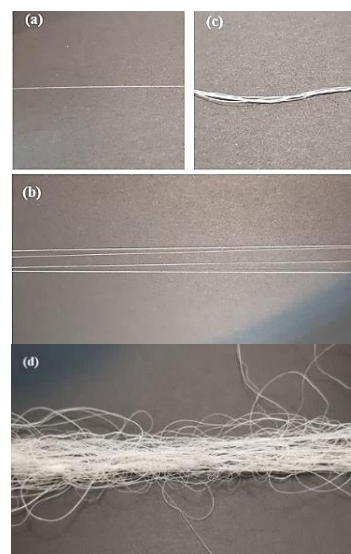


Figure 4. Polymer blended fibers in the form of a) single, b) multiple aligned (bundled), c) twisted (yarn) and d) numerous paralleled

It is clearly understood that each spring (fiber) tolerates a portion of weight collectively applied as expressed by Equation (1):

$$P_i = \frac{W}{N} \quad \text{and} \quad i=1 \text{ to } N \quad (1)$$

where P_i is the forced applied on each fiber, N the number of fibers in a bundle or yarn and W the total weight to be lifted. Therefore, the overall stiffness of the bundle (multiple fibers) as given by Equation (2) as follows:

$$K = K_1 + K_2 + \dots + K_N \quad (2)$$

2. 3. Characterization of ABS/TPU/EVA SMPs

2. 3. 1. Tensile Testing

The tensile response of the ABS/TPU/EVA alloyed systems including the Young's modulus, elongation and tensile strength was determined based on ASTM D882 using a universal tensile testing machine (Sanaf Co., Iran). Specimens measuring the length of 100 mm and width of 10 mm with the thickness of less than 1 mm were cut from the blended sheets as mentioned earlier. The gage length of 50 mm was considered in the experiment as the grip separation. Measurements were obtained at the deformation rate (stroke speed) of 12.5 mm/min at the ambient temperature.

2. 3. 2. Blocked Force

The shape-memory recovery measuring the released energy stored in the specimens in the second SMP cycle (heating-deformation-cooling) at their secondary state above their transitional temperature was measured using the blocked force method. The measurements were conducted on both fibers and strips to understand the correlations amongst the mass, shape, number of fibers and the energy stored in the SMPs. The heat was applied onto their temporary shape and the force applied by specimens release energy was assessed using a home-made strain gage transducer. To apply heat, two parallel heating elements within a cylindrical chamber surrounding the specimens as the built-in accessory of the load cell was used. The transition temperature of the specimens was specified once the load cell started showing changes in its output current. Due to the low average T_g values of EVA and TPU (being around ~ -25 to -30 °C and -50 to 10 °C, respectively [34, 35]), it was found that the specimens started contraction at temperatures in the range of 65 - 75 °C as their SMP transition temperature. To perform the test, two ends of the pre-tensioned SMP wires/yarn were initially fixed at two rigid and deflectable supports of the blocked force system. Upon fibers or strips shortening, the single cantilever beam deflected and linked to the applied force made by the SMP fibers or strips. The block force apparatus was initially calibrated to gain the input-output slope as shown in Figure 5.

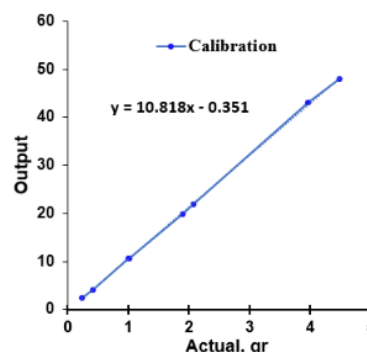


Figure 5. Calibration curves exhibiting input vs output values

The SMP filament and bulk specimens and the used loadcell setup showing the specimens fixed are illustrated in Figure 6(a) and (b). Figure 6(c) further represents the bulk flexed specimens in the secondary SMP shape upon fixation in the cold water to be activated by thermal stimulus on the blocked force set-up (also revisit Figure 2). Based on the former information provided as the transition temperature initiation, the bulk specimens were placed into water with the temperature in the range of 65 - 75 °C followed by quick mechanical deformation around a curved surface to obtain their secondary fixed shape (temporary shape). In case of fibers, it is noted that the fibers were initially stretched in water with the said temperature up to a diameter reduction of around 25% compared to their original diameter (~ 200 to 800 μm). It is concluded that considering the total contraction of the fibers (above 50%) as explained in next part, a diameter swelling of $\sim 12\%$ is expected upon thermal stimulation.

3. RESULTS AND DISCUSSION

3. 1. Tensile Properties

Figure 7 represents the tensile testing results on the ABS/TPU/EVA specimens as a function of the polymer ratios used. It is illustrated

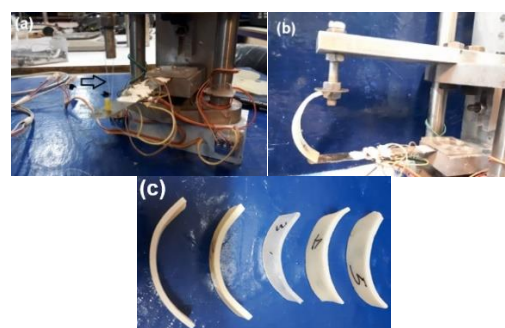


Figure 6. Blocked force load cell measuring the energy released by (a) fibers, (b) bulk specimens and (c) the bulk specimens in the secondary (flexed) shape before thermal activation

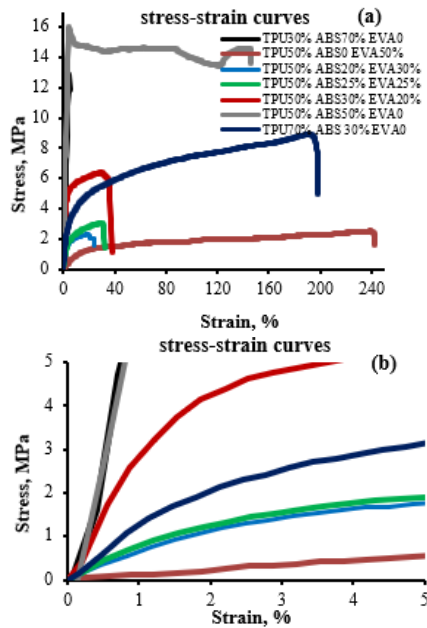


Figure 7. (a) Tensile stress-strain curves of ABS/TPU/EVA alloyed systems and (b) of which the inset at low-strain regions

in Figure 7(a) that the presence of ABS as the harder polymer significantly affects the overall tensile strength as expected as shown by the gray and black curves [36].

Further, it is confirmed that when EVA is incorporated into the alloyed systems, the elongation of the sheets increases, and the more the EVA content, the greater strain at break of the parts which is in good agreement with results reported elsewhere [31]. It is clearly shown in the figure that lower amount of ABS and greater fraction of EVA result in low tensile behavior of the specimens as exhibited by ABS content less than 25% and that in the case of EVA above 20%. It is shown, however, that lack of EVA in the specimens as seen in the case of TPU/ABS ratio of 70/30 leads to an optimized level of both tensile elongation and strength (dark blue line). It is shown that upon the addition of EVA replaced by the same fraction of TPU, the elongation and tensile strength decrease as shown by the red curve. To better examine the effect of the polymer ratios on the elastic modulus of the specimens, an inset of the graph was prepared at low strain regions as demonstrated in Figure 7(b).

It is clearly shown that similar to the tensile strength performance of the specimens, the addition of ABS phase leads to greater modulus values. Nevertheless, when EVA is added into the blends, the modulus of the specimens sharply drops shown by lower slop of the curves represented in the inset graph. It could be understood that both EVA and TPU negatively contribute to the tensile modulus whilst the former more noticeably influences the tensile behavior of the fabricated

specimens. To compare the obtained results, the tensile strength and modulus values are reported and summarized in Figures 8 and 9, respectively. It is shown that the high loading of EVA in overall results in the lowest tensile strength of the specimens unlike addition of ABS (~2.3 MPa). It is understood that equal fraction of ABS and TPU leads to the greatest strength value of ~16 MPa. It is demonstrated in Figure 8 that the blended system containing 50, 50 and 0% of TPU, ABS and EVA, respectively, exhibits the tensile strength above 600% greater than in the case of parts with the loading of 50, 20 and 30% of TPU, ABS and EVA, respectively, as the worse blending scenario. In meantime, blended specimens composing of 50, 25 and 25% of TPU, ABS and EVA, respectively, lead to the greatest elastic modulus 640% higher than that in parts with the mixture of only 50 and 50% of TPU and EVA, respectively, as understood from modulus values in Figure 9. The former is hypothesized to exhibit favorable SMP energy release, too. As shown in Figure 7(a), the latter system results in the greatest elongation at break of 240% as expected.

Figure 9 illustrates that EVA can help to increase modulus at specific fractions of ABS and TPU unlike its general effects on the tensile performance (addition of 25% of EVA into 50% and 25% of TPU and ABS, respectively). However, both EVA and TPU as soft

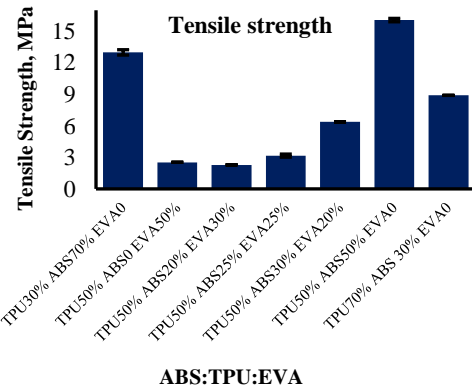


Figure 8. Tensile strength of the blended specimens

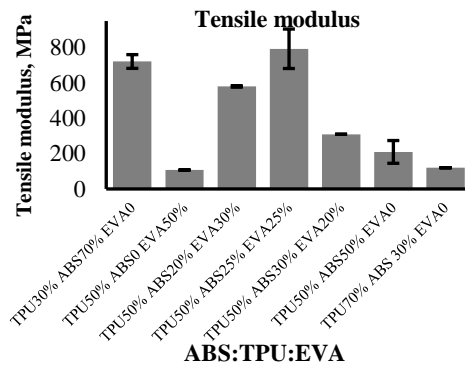


Figure 9. Tensile modulus of the blended specimens

regions compared to the ABS phase exhibit adverse effect on the modulus of the specimens as widely reported in literature [37].

3. 2. Blocked Force Energy Release

The blocked force values of the alloyed specimens are shown in Figure 10. The results represent that the amount of released energy upon activation of the specimens is markedly sensitive to the type and percentage of polymer component used. It is clearly shown that TPU and high ABS ratios would lead to minimal energy released. However, it is exhibited that when 50% of TPU is mixed with ABS and EVA of the same ratio the greatest degree of energy released (blocked force) is obtained shown by the black solid curve.

It is concluded that the number and quality of net points (represented by rigid regions within the amorphous phases) significantly contribute to the amount of stored energy in the fixation cycle (cooling and secondary shape) of SMPs used in this study as reported elsewhere in other studies [38, 39]. Nevertheless, it is shown that the larger the loading of softer polymers such as EVA and soft TPU, the lower the level of the energy released upon thermal activation of bulk specimens (shown by green and blue curves).

It is noted that the drop displayed on the curved vs time is correlated to the soft nature of polymer components upon heating and a contraction due to the forced applied by the elastic and rigid supports in the load cell. It is clearly shown that the ABS/TPU ratio of 50/50 still results in low energy released due to lack of enough soft region to be recoiled upon actuation. One needs to keep in mind that the flexed bulk specimens as shown in Figure 6(c) are placed between two load cell supports when the parts are in their secondary bent state. Upon heating, the specimens incline to recover to their original straight state and thus exerting deflection onto the elastic single-cantilever support of the blocked force system. It is noted based on Figure 10 that the higher the modulus of the specimens, the greater the energy released [40, 41].

As easily understood from the figure, bulk specimens resulting in the greatest modulus (50, 25 and 25% of

TPU, ABS and EVA) also exhibit the greatest energy release of ~6 grf that is above 3900% greater than the blended SMP systems showing the least energy release. When double filaments are used, the energy release increases by 50% with respect to the single wire case (9.25 grf vs 6 grf) which is in overall 6000% greater than blended systems with the TPU/EVA ratio of 50/50 with absence of ABS phase.

The same measurements were conducted on the alloyed fibers of the same polymer components as illustrated in Figure 11. Based on tensile and blocked force values on bulk specimens demonstrated in Figure 7 and 10, respectively. It was decided to use specific fractions of polymers in the fabrication of the fibers followed by their blocked force analysis. One main limitation is the capability of polymer alloys to be converted to filament. Therefore, an optimized level of polymer components needs to be incorporated into the blends. As shown in the figure, the binary alloyed systems result in minimal released energy upon heating and consequent shortening (contracting) of the fibers as shown by the green, blue and red solid curve [12, 16]. However, ABS systems loaded with 50 and 25wt% of TPU and EVA, respectively, lead to greater energy released as shown by the gray and black solid curve. The results are in good agreement with the bulk specimens of the same ternary systems. Nevertheless, by the use of a single fiber specimen, the amount of force applied on the load cells decreases (gray curve) as shown by the inset image.

To better understand the effect of parallel springs constants, two wires were used and their SMP released energy was determined. It is clearly shown that such filaments result in a greater energy release. It is demonstrated that the mass of fibers as well as their secondary length significantly contribute to the applied force onto the load cell cantilever upon stimulation. The greater the contraction of the fibers, the greater the energy released due to the increased overall stiffness of the material as proved by relations 1 and 2 stated earlier. To better show the retraction of the fibers fabricated, visual performance of the fibers was recorded as presented in next part.

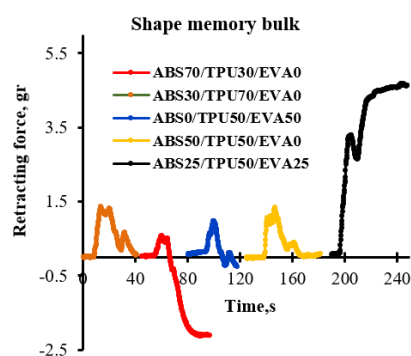


Figure 10. Blocked force values as a function of ABS based alloyed systems and TPU in bulk specimens

3. 3. Visual Performance

Figure 12 demonstrates the length difference between secondary temporary shape and shortened filaments before and after thermal activation. It is clearly illustrated that upon activation, the SMP fiber is shortened as shown by the scale ruler (a retraction above 50% was observed). The difference between two stages governs the generated forces and energy released as discussed earlier. The more the filament is retracted, the higher the energy released [42]. Factors including the ratio and type of polymers, activation temperature and the degree of net points define the energy released [43]. Figure 13 rephrases the length difference in Figure 12 whilst the filament is circled

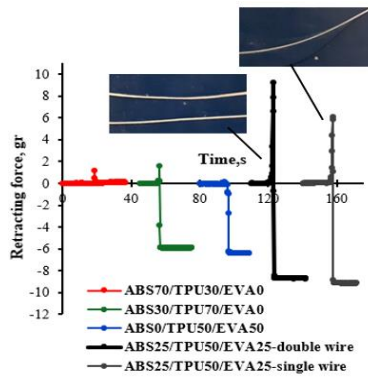


Figure 11. Blocked force values as a function of ABS based alloyed systems and TPU in filament specimens. The insets represent the number of fibers tested

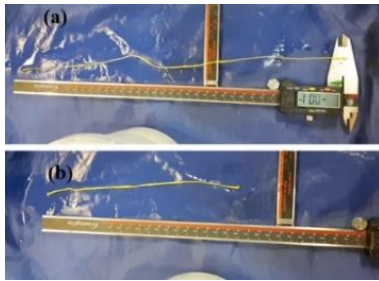


Figure 12. SMP filaments (a) long before and (b) contracted (shortened) upon thermal activation

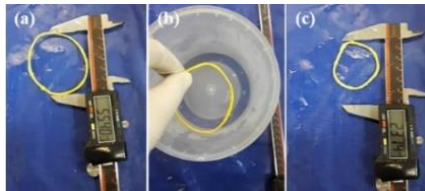


Figure 13. (a) SMP circle filament of larger diameter before activation, (b) thermal activation in warm water and (c) smaller diameter after recovery

mimicking a knot. It is shown that upon activation, the diameter of the circle decreases. The representation of the diameter change is used in simulation of a self-tightening suture knot over an open wound which is tightened upon an activation as another potential application of the current research [44]. The latter conveys that the difference in fiber lengths causes an internal exerted force that is able to close the wound edges as an external force [45].

4. CONCLUSIONS

Successful fabrication of trinary SMPs was demonstrated using ABS/TPU/EVA blended systems fabricated in bulk and filament geometries. To ensure complete blending of

the polymers component, high intense shear mixing on a calendering device was employed. Hot press was used to fabricated sheets SMPs after the melt mixing process. Fibers were produced between the two calendering rolls during the melt mixing process and were able to be collected due to their high surface tension. Blocked forced measurement was performed to quantitatively estimate the SMP stored energy of the bulk and fiber specimens. The results confirmed tight correlations amongst the tensile behavior, retraction and energy release of SMPs upon thermal actuation. It was shown specific fractions of the trinary blended SMPs containing 50, 25 and 25% of TPU, ABS and EVA, respectively, led to the greatest elastic modulus and recovery energy release by 640% and 3900% increase, respectively, with respect to binary systems. The dependence of the energy release values on the number of fibers was also represented. The latter showed governing synergistic effect of SMPs parallelly aligned as parallel springs contributing to an increase in the overall spring constant of the system. To better understand the effect of polymer fractions, contraction (retraction) of fabricated filaments upon thermal stimulus was further visually demonstrated. The latter together with the obtained high shape-memory strain stored in the SMPs suggested the application of the trinary formulation of the blends in the design and development of fibers used as synthetic muscles elements or self-tightening surgical sutures.

4. REFERENCES

- Xia, Y., He, Y., Zhang, F., Liu, Y. and Leng, J., "A review of shape memory polymers and composites: Mechanisms, materials, and applications", *Advanced Materials*, Vol. 33, No. 6, (2021), 2000713. DOI: 10.1002/adma.202000713.
- Jahangir, H. and Bagheri, M., "Evaluation of seismic response of concrete structures reinforced by shape memory alloys", *International Journal of Engineering*, Vol. 33, No. 3, (2020), 410-418 DOI: 10.5829/ije.2020.33.03c.05.
- Wang, L., Zhang, F., Liu, Y. and Leng, J., "Shape memory polymer fibers: Materials, structures, and applications", *Advanced Fiber Materials*, Vol. 4, No. 1, (2022), 5-23. DOI: 10.1007/s42765-021-00073-z.
- Yakacki, C.M. and Gall, K., "Shape-memory polymers for biomedical applications", *Shape-memory Polymers*, (2009), 147-175. DOI: 10.1002/adfm.201909047.
- Pineda-Castillo, S.A., Stiles, A.M., Bohnstedt, B.N., Lee, H., Liu, Y. and Lee, C.-H., "Shape memory polymer-based endovascular devices: Design criteria and future perspective", *Polymers*, Vol. 14, No. 13, (2022), 2526. DOI: 10.3390/polym14132526.
- Ramaraju, H., Akman, R.E., Safranski, D.L. and Hollister, S.J., "Designing biodegradable shape memory polymers for tissue repair", *Advanced Functional Materials*, Vol. 30, No. 44, (2020), 2002014. DOI: 10.1002/adfm.202002014.
- Chen, Y., Zhao, X., Luo, C., Shao, Y., Yang, M.-B. and Yin, B., "A facile fabrication of shape memory polymer nanocomposites with fast light-response and self-healing performance", *Composites Part A: Applied Science and Manufacturing*, Vol. 135, (2020), 105931. DOI: 10.1016/j.compositesa.2020.105931.

8. Mitchell, K., Raymond, L. and Jin, Y., "Material extrusion advanced manufacturing of helical artificial muscles from shape memory polymer", *Machines*, Vol. 10, No. 7, (2022), 497. DOI: 10.1002/adfm.202002014.
9. Sonjaya, M.L. and Hidayat, M.F., "Construction and analysis of plastic extruder machine for polyethylene plastic waste", *EPI International Journal of Engineering*, Vol. 3, No. 2, (2020), 132-137. DOI: 10.25042/epi-ije.082020.07.
10. Zhang, H.-C., Huang, J., Zhao, P.-F. and Lu, X., "Bio-based ethylene-co-vinyl acetate/poly (lactic acid) thermoplastic vulcanizates with enhanced mechanical strength and shape memory behavior", *Polymer Testing*, Vol. 87, (2020), 106537.
11. Schönfeld, D., Chalissery, D., Wenz, F., Specht, M., Eberl, C. and Pretsch, T., "Actuating shape memory polymer for thermoresponsive soft robotic gripper and programmable materials", *Molecules*, Vol. 26, No. 3, (2021), 522. DOI: 10.3390/molecules26030522.
12. Lendlein, A. and Gould, O.E., "Reprogrammable recovery and actuation behaviour of shape-memory polymers", *Nature Reviews Materials*, Vol. 4, No. 2, (2019), 116-133. DOI: 10.1038/s41578-018-0078-8.
13. Jose, S., George, J.J., Siengchin, S. and Parameswaranpillai, J., "Introduction to shape-memory polymers, polymer blends and composites: State of the art, opportunities, new challenges and future outlook", *Shape Memory Polymers, Blends and Composites*, (2020), 1-19. DOI: 10.1007/978-981-13-8574-2_1.
14. Yu, K., Xie, T., Leng, J., Ding, Y. and Qi, H.J., "Mechanisms of multi-shape memory effects and associated energy release in shape memory polymers", *Soft Matter*, Vol. 8, No. 20, (2012), 5687-5695. DOI: 10.1039/C2SM25292A.
15. Hornat, C.C., Nijemeisland, M., Senardi, M., Yang, Y., Pattyn, C., van der Zwaag, S. and Urban, M.W., "Quantitative predictions of maximum strain storage in shape memory polymers (smp)", *Polymer*, Vol. 186, (2020), 122006. DOI: 10.1016/j.polymer.2019.122006.
16. Wei, W., Liu, J., Huang, J., Cao, F., Qian, K., Yao, Y. and Li, W., "Recent advances and perspectives of shape memory polymer fibers", *European Polymer Journal*, (2022), 111385. DOI: 10.1016/j.eurpolymj.2022.111385.
17. Posada-Murcia, A., Uribe-Gomez, J.M., Förster, S., Sommer, J.-U., Dulle, M. and Ionov, L., "Mechanism of behavior of two-way shape memory polymer under constant strain conditions", *Macromolecules*, Vol. 55, No. 5, (2022), 1680-1689. DOI: 10.1021/acs.macromol.1c02564.
18. Namathoti, S. and PS, R.S., "A review on progress in magnetic, microwave, ultrasonic responsive shape-memory polymer composites", *Materials Today: Proceedings*, Vol. 56, No., (2022), 1182-1191. DOI: 10.1016/j.matpr.2021.11.151.
19. Scalet, G., "Two-way and multiple-way shape memory polymers for soft robotics: An overview", in *Actuators*, MDPI. Vol. 9, No. 1, (2020), 10.
20. Sun, L. and Huang, W.M., "Mechanisms of the multi-shape memory effect and temperature memory effect in shape memory polymers", *Soft Matter*, Vol. 6, No. 18, (2010), 4403-4406. DOI: 10.1039/C0SM00236D.
21. Nissenbaum, A., Greenfeld, I. and Wagner, H., "Shape memory polyurethane-amorphous molecular mechanism during fixation and recovery", *Polymer*, Vol. 190, (2020), 122226. DOI: 10.1016/j.polymer.2020.122226.
22. Staszczak, M., Nabavian Kalat, M., Golasinski, K.M., Urbański, L., Takeda, K., Matsui, R. and Pieczyńska, E.A., "Characterization of polyurethane shape memory polymer and determination of shape fixity and shape recovery in subsequent thermomechanical cycles", *Polymers*, Vol. 14, No. 21, (2022), 4775. DOI: 10.3390/polym14214775
23. Fan, J. and Li, G., "High performance and tunable artificial muscle based on two-way shape memory polymer", *RSC advances*, Vol. 7, No. 2, (2017), 1127-1136. DOI: 10.1039/C6RA25024F.
24. Mirvakili, S.M. and Hunter, I.W., "Artificial muscles: Mechanisms, applications, and challenges", *Advanced Materials*, Vol. 30, No. 6, (2018), 1704407. DOI: 10.1002/adma.201704407.
25. Mirvakili, S.M. and Hunter, I.W., "Multidirectional artificial muscles from nylon", *Advanced Materials*, Vol. 29, No. 4, (2017), 1604734 DOI: 10.1002/adma.201604734.
26. Xie, H., Li, L., Deng, X.-Y., Cheng, C.-Y., Yang, K.-K. and Wang, Y.-Z., "Reinforcement of shape-memory poly (ethylene-co-vinyl acetate) by carbon fibre to access robust recovery capability under resistant condition", *Composites Science and Technology*, Vol. 157, (2018), 202-208. DOI: 10.1016/j.compscitech.2018.01.031.
27. Yu, Q., Yang, X., Chen, Y., Yu, K., Gao, J., Liu, Z., Cheng, P., Zhang, Z., Aguila, B. and Ma, S., "Fabrication of light-triggered soft artificial muscles via a mixed-matrix membrane strategy", *Angewandte Chemie International Edition*, Vol. 57, No. 32, (2018), 10192-10196. DOI: 10.1002/anie.201805543.
28. Yip, M.C. and Niemeyer, G., "High-performance robotic muscles from conductive nylon sewing thread", in 2015 IEEE International Conference on Robotics and Automation (ICRA), IEEE., (2015), 2313-2318.
29. Xiao, Y.Y., Jiang, Z.C., Tong, X. and Zhao, Y., "Biomimetic locomotion of electrically powered "janus" soft robots using a liquid crystal polymer", *Advanced Materials*, Vol. 31, No. 36, (2019), 1903452. DOI: 10.1002/adma.201903452.
30. Pradhan, S., Sahu, S.K., Pramanik, J. and Badgayan, N.D., "An insight into mechanical & thermal properties of shape memory polymer reinforced with nanofillers; a critical review", *Materials Today: Proceedings*, Vol. 50, (2022), 1107-1112. DOI: 10.1016/j.matpr.2021.07.504.
31. Lim, W.L.Y., Rahim, F.H.A., Johar, M. and Rusli, A., "Tensile and shape memory properties of polylactic acid/ethylene-vinyl acetate blends", *Materials Today: Proceedings*, Vol. 66, (2022), 2771-2775. DOI: 10.1016/j.matpr.2022.06.513.
32. Bernardes, G.P., da Rosa Luiz, N., Santana, R.M.C. and de Camargo Forte, M.M., "Influence of the morphology and viscoelasticity on the thermomechanical properties of poly (lactic acid)/thermoplastic polyurethane blends compatibilized with ethylene-ester copolymer", *Journal of Applied Polymer Science*, Vol. 137, No. 31, (2020), 48926. DOI: 10.1002/app.48926.
33. Ke, D., Chen, Z., Momo, Z.Y., Jiani, W., Xuan, C., Xiaojie, Y. and Xueliang, X., "Recent advances of two-way shape memory polymers and four-dimensional printing under stress-free conditions", *Smart Materials and Structures*, Vol. 29, No. 2, (2020), 023001. DOI: 10.1088/1361-665X/ab5e6d.
34. Voda, A., Beck, K., Schaubert, T., Adler, M., Dabisch, T., Bescher, M., Viol, M., Demco, D.E. and Blümich, B., "Investigation of soft segments of thermoplastic polyurethane by nmr, differential scanning calorimetry and rebound resilience", *Polymer Testing*, Vol. 25, No. 2, (2006), 203-213. DOI: 10.1016/j.polymertesting.2005.10.007.
35. Stark, W. and Jaunich, M., "Investigation of ethylene/vinyl acetate copolymer (eva) by thermal analysis dsc and dma", *Polymer Testing*, Vol. 30, No. 2, (2011), 236-242. DOI: 10.1016/j.polymertesting.2010.12.003.
36. Memarian, F., Fereidoon, A. and Ahangari, M.G., "The shape memory, and the mechanical and thermal properties of tpu/abs/cnt: A ternary polymer composite", *RSC Advances*, Vol. 6, No. 103, (2016), 101038-101047. DOI: 10.1039/C6RA23087C.
37. Chatterjee, T., Dey, P., Nando, G.B. and Naskar, K., "Thermo-responsive shape memory polymer blends based on alpha olefin

- and ethylene propylene diene rubber", *Polymer*, Vol. 78, (2015), 180-192. DOI: 10.1016/j.polymer.2015.10.007.
38. Dao, T.D., Goo, N.S. and Yu, W.R., "Blocking force measurement of shape memory polymer composite hinges for space deployable structures", *Journal of Intelligent Material Systems and Structures*, Vol. 29, No. 18, (2018), 3667-3678. DOI: 10.1177/1045389X18798950.
39. Zhao, Q., Behl, M. and Lendlein, A., "Shape-memory polymers with multiple transitions: Complex actively moving polymers", *Soft Matter*, Vol. 9, No. 6, (2013), 1744-1755. DOI: 10.1039/C2SM27077C.
40. Sun, L., Huang, W., Wang, C., Zhao, Y., Ding, Z. and Purnawali, H., "Optimization of the shape memory effect in shape memory polymers", *Journal of Polymer Science Part A: Polymer Chemistry*, Vol. 49, No. 16, (2011), 3574-3581.
41. Hornat, C.C. and Urban, M.W., "Shape memory effects in self-healing polymers", *Progress in Polymer Science*, Vol. 102, (2020), 101208. DOI: 10.1016/j.progpolymsci.2020.101208.
42. Prasad, A., Moon, S. and Rao, I.J., "Thermo-mechanical modeling of viscoelastic crystallizable shape memory polymers", *International Journal of Engineering Science*, Vol. 167, (2021), 103524. DOI: 10.1016/j.ijengsci.2021.103524.
43. Nie, D., Yin, X., Cai, Z. and Wang, J., "Effect of crystallization on shape memory effect of poly (lactic acid)", *Polymers*, Vol. 14, No. 8, (2022), 1569. DOI: 10.3390/polym14081569
44. Li, Y., Min, L., Xin, J., Wang, L., Wu, Q., Fan, L., Gan, F. and Yu, H., "High-performance fibrous artificial muscle based on reversible shape memory uhmwpe", *Journal of Materials Research and Technology*, Vol. 20, (2022), 7-17. DOI: 10.1016/j.jmrt.2022.07.045.
45. Duarah, R., Singh, Y.P., Gupta, P., Mandal, B.B. and Karak, N., "Smart self-tightening surgical suture from a tough bio-based hyperbranched polyurethane/reduced carbon dot nanocomposite", *Biomedical Materials*, Vol. 13, No. 4, (2018), 045004. DOI: 10.1088/1748-605X/aab93c.

Persian Abstract

چکیده

پلیمرها با حافظه شکلی قادر به خاطرآوری شکل اولیه خود بوده و پس تحریک می‌توانند به آن شکل اولیه بازگردند. تاکنون مقادیری نظیر نسبت تثبیت و بازیابی بسیار گزارش شده است. با این وجود، یک چالش اصلی وجود و استفاده از یک روش مناسب برای تخمین کمی مقدار انرژی رهایش حافظه داری است. بعلاوه، اینگونه فرضیه سازی می‌شود که خواص الاستیک الیاف حافظه دار نقش کلیدی در الیاف موقعی که نیاز است رفتار با درصد تغییر طول زیاد و کشش زیاد داشته باشد دارد همانطور که در ماهیچه های مصنوعی مورد نیاز است. در این تحقیق، ما برای اولین بار، ترکیب پلیمرهای حافظه دار بصورت بالک و یا فیلامنت بصورت دو و یا سه جزئی حاصل از ترکیبات پلیمرهای اکریل بوتادین استایرن (ABS)، پلی یورتان ترموپلاستیک (TPU) و اتیلین وینیل استات (EVA) از طریق ترکیب مذاب با غلتک کلندرینگ تحت تنش برشی شدید و پرس گرم را ارائه می‌دهیم. یک لودسل دیجیتال برای بررسی نیروی مقید و تثبیت نتایج انرژی رهایش استفاده شد. نتایج رفتار حافظه داری عالی را که توسط اندازه گیری نیروی مقید و انقباض از حالت ثانویه را در ارتباط با رفتار کششی نمایش دارد. نشان داده شد که ترکیب پلیمری حافظه دار TPU، ABS و TPU به ترتیب با درصدهای ۲۰٪ و ۲۵٪ منجر به افزایش ۶۴۰ درصدی و ۳۹۰۰ درصدی در مدول الاستیک و مقدار انرژی رهایش حافظه داری نسبت به سامانه های ترکیبی دوجزئی تنها با ترکیبات EVA و TPU می‌شود. همچنین نشان داده شد که نمونه های دو فیلامنتی منجر به افزایش ۵۰ درصدی در انرژی رهایش نسبت به تک سیمی شد. با این وجود، ترکیب دوجزئی TPT/ABS با درصد ترکیب ۵۰/۵۰ افزایش ۶۰۰ درصدی در استحکام کششی در مقایسه با سامانه های سه جزئی گردید. تأیید شد که مدول الاستیک، تعداد الیاف و درصد ازدیاد طول در شکست به طور چشمگیری حاکم بر خواص حافظه داری در خصوص مقدار کرنش حافظه داری ذخیره شده است. یافته های این تحقیق گروه جدیدی از پلیمرهای حافظه دار را نمایش داد که می‌تواند در طراحی و ساخت مواد با رهایش انرژی بالا و انقباض زیاد به منظور کاربردها نظیر ماهیچه مصنوعی پایه الیاف و محصولات ارتودنسی استفاده گردد.



Efficient Sampling-based for Mobile Robot Path Planning in a Dynamic Environment Based on the Rapidly-exploring Random Tree and a Rule-template Sets

M. A. R. Pohan*, J. Utama

Electrical Engineering Department, Universitas Komputer Indonesia, Jl. Dipatiukur 102-116, Bandung 40132, Indonesia

PAPER INFO

Paper history:

Received 12 December 2022

Received in revised form 30 December 2022

Accepted 16 January 2023

Keywords:

Efficient Sampling

Path Planning

Dynamic Environment

Rapidly-exploring Random Tree

Rule-template Sets

ABSTRACT

This study presents an efficient path planning method for mobile robots in a dynamic environment. The method is based on the rapidly-exploring random tree (RRT) algorithm. The two primary processes in mobile robot path planning in a dynamic environment are initial path planning and path re-planning. In order to generate a feasible initial path with fast convergence speed, we used a hybridization of rapidly-exploring random tree star and ant colony systems (RRT-ACS). When an obstacle obstructs the initial path, the path re-planner must be executed. In addition to the RRT-ACS algorithm, we proposed using a rule-template set based on the mobile robot in dynamic environment scenes during the path re-planner process. This novel algorithm is called RRT-ACS with Rule-Template Sets (RRT-ACS+RT). We conducted many benchmark simulations to validate the proposed method in a real dynamic environment. The performance of the proposed method is compared to the state-of-the-art path planning algorithms: RRT*FND and MOD-RRT*. Numerous experimental results demonstrate that the proposed method outperforms other comparison algorithms. The results show that the proposed method is suitable for the use on robots that need to navigate in a dynamic environment, such as self-driving cars.

doi: 10.5829/ije.2023.36.04a.16

1. INTRODUCTION

Path planning is one of the most researched problems in robotics [1-3]. Any path planning algorithm's primary goal is to provide a collision-free path from a start state to an end state within the robot's configuration space [4, 5]. The Rapidly Exploring Random Tree (RRT) is a simple and fast algorithm that generates a tree in the configuration space incrementally until the goal is reached [6]. The RRT is one of the most widely used probabilistic planning algorithms [7-9]. On the other hand, the RRT has never converged to an asymptotically optimal solution [10, 11]. As a result, Karaman developed the RRT* [12]. Since the introduction of the RRT* algorithm, research has expanded to discover new ways to improve the RRT* algorithm in the path planning application [13-16]. However, the operational environment of path planning is dynamic in many scenarios [17, 18]. The path from a single query is frequently obstructed during execution. As a result, the

topic of dynamic and re-planning is critical to robotic path planning [19].

Many methods for dynamic path planning algorithms have been presented in the literature. Sampling-based planners, such as RRT-related methods, are widely used among existing mobile robot path planning in a dynamic environment [6, 17]. Meng et al. [20] proposed an improved two-way RRT algorithm to solve the path re-planning problem for Unmanned Aerial Vehicles (UAV) in dynamic environments. Before the UAV takes off, offline path planning is performed. If a pop-up threat is detected during the flight, the affected nodes will be removed while the remaining tree structure will be preserved. The improved two-way RRT is then used for path re-planning. Chen and Wang [21] present a novel RRT-based path planning algorithm that allows UAVs to fly safely in dynamic threat environments. Chen and Wang [21] proposed a pruning-reconnecting mechanism to avoid collisions with dynamic threats and repair the path when new obstacles appear. Adiyatov and Varol

*Corresponding Author Institutional Email:

muhammad.aria@email.unikom.ac.id (M. A. R. Pohan)

Please cite this article as: M. A. R. Pohan, J. Utama, Efficient Sampling-based for Mobile Robot Path Planning in a Dynamic Environment Based on the Rapidly-exploring Random Tree and a Rule-template Sets, *International Journal of Engineering, Transactions A: Basics*, Vol. 36, No. 04, (2023), 797-806

[22] proposed a novel RRT-based algorithm for dynamic motion planning and named it RRT*FND. Adiyatov and Varol [22] extends the memory-efficient RRT*FN algorithm to dynamic scenarios. Adiyatov and Varol [22] then used two greedy heuristics to repair the solution rather than restarting the entire motion planning process. Qi et al. [23] present an RRT algorithm suitable for robot navigation in an undetermined dynamic environment. The algorithm includes two procedures: initial path planning and re-planning. To determine the initial path, a modified RRT* is employed. If the current path is not feasible, a different method is intended to reroute it. This algorithm is called MOD-RRT*. Wei et al. [24] proposed a Bi-RRT* dynamic path planning approach based on an improved exploring function with a goal direction to deal with re-planning paths for a robotic manipulator to avoid dynamic obstacles. A multi-step expansion strategy with greedy heuristics is also used in the Bi-RRT* proposal. Meng and Dai [25] updated the current path with the advanced RRT algorithm for local path planning to avoid obstacles based on the obstacle map. Meng's method solved the problem of avoiding dynamic obstacles during real-time autonomous robot navigation. However, the RRT algorithm is still used in the methods described above.

Numerous techniques have been developed to enhance the performance of the RRT* algorithm. Klemm et al. [13] introduced the RRT*-connect algorithm, a dual-tree variant of RRT*. RRT*-connect could find the solution faster than RRT, especially in a narrow passage environment where the planner must traverse to find solutions. However, to optimize their paths, RRT*-connect must search all states. Gammel et al. [14] introduced the informed RRT* algorithm, which employs informed sampling on RRT* once the first solution has been determined. The informed RRT* algorithm can find the optimal solution 1.2–10.3 times faster than the RRT* algorithm. However, informed RRT* encounters difficulty when the target node is concealed behind a narrow passage. The informed RRT*-connect algorithm was developed by Mashayekhi et al. [15], which combines RRT*-connect with informed RRT*. Therefore, informed RRT*-connect can find the optimal solution faster than informed RRT* in a narrow passage environment. Pohan et al. [16] created the RRT-ACS algorithm, a hybrid of the RRT algorithm and the Ant Colony System (ACS). In Friedman's nonparametric test, Pohan et al. [16] reported that the RRT-ACS algorithm outperformed the informed RRT*, informed RRT*-connect, RRT*-connect, and RRT* algorithms. To the authors' best of knowledge, no research has used the RRT-ACS algorithm in a path planning mobile robot in a dynamic environment.

This study presents an effective mobile robot path planning method in a dynamic environment. The method is based on the RRT algorithm. Initial path generation

and path re-planning are the two primary processes in path planning for mobile robots in dynamic environments. In order to generate a feasible initial path with fast convergence speed, we used the RRT-ACS algorithm. The path re-planner must be executed when an obstruction blocks the initial path. During the path re-planner process, we propose using a rule-template set based on the mobile robot in dynamic environment scenes. A rule-template set consists of multiple rule templates generated offline based on the context of an environment scene. At the start of the algorithm, the rule-template set is loaded, and a suitable rule template can be chosen automatically based on the scene of the environment. If some nodes in the rule template are not collision-free, these nodes will be discarded, and the remaining nodes will be added to the root. Thus, the tree likely possesses a portion of branches and leaves at this time. If this tree has reached the goal state, then random searching is no longer necessary, and this strategy will reduce the time needed for re-planning. However, if the goal state has yet to be reached, the RRT-ACS algorithm will be implemented to accelerate the growth rate of the search tree in order to reach the goal state. RRT-ACS with Rule-Template Sets (RRT-ACS+RT) is the name of this proposed algorithm. We ran numerous benchmark simulations to validate the proposed method in a dynamic environment. The performance of the proposed method is compared to RRT*FND and MOD-RRT*, the state-of-the-art path planners in a dynamic environment. Numerous experimental results indicate that the proposed method outperforms other comparative algorithms. The results show that the proposed method is suitable for use on robots that need to navigate in a dynamic environment, such as self-driving cars.

The remaining sections of this paper are structured as follows. The RRT-ACS+RT algorithm is described in section II. In section III, the performance of the RRT-ACS+RT algorithm in comparison to RRT*FND and MOD-RRT*, the state-of-the-art path planners for a dynamic environment, is evaluated and discussed. Finally, section IV presents some conclusions.

2. PROPOSED ALGORITHM: RRT-ACS+RT

2.1. Proposed Algorithm This section details the proposed algorithm. Algorithm 1 depicts the RRT-ACS+RT algorithm. Compared with RRT-ACS, the improvement is the addition of rule templates. By introducing path rule templates, more vertices and edges will be derived from rule templates than constructed online during the re-planning phase when obstacles block the initial path. The concept of using rule templates to speed up the re-planning process was inspired by the research of Ma et al. [26]. Ma et al. use rule templates for cases of autonomous on-road driving.

A set of rule templates contains multiple rule templates, which are generated offline according to the context of the environment. Figure 1 shows an example of a rule template created offline for a straight-line initial path blocked by an obstacle.

At the start of the proposed algorithm, the rule template set T is loaded (line 2). This template is then parsed and saved as a tree-like structure. If some of the vertices and path edges in the rule template are not collision-free with obstacles or road boundaries, these sections are discarded, and the remainder in the rule template is preserved and added to the root (line 3). Therefore, at this point, the tree may already have some branches and leaves before searching randomly. If the tree from this template can immediately plot a path to the current destination state without any obstructions, then the algorithm stops and returns the tree. If the function fails, then the algorithm starts the following iteration step.

In the iteration step process, a random variable value will be generated at each iteration to determine whether the exploration or exploitation process will be used (line 8). If the exploration process is chosen, the random sample will determine the random state $q_{rndstate}$ (line 14). If the exploitation process is selected, the random state will be determined using pheromone distribution data (lines 10-12).

After obtaining the value of the random state, the following process is to look for nodes in T that are less than a threshold value to the random state. The nodes are named Q_{near} (line 16). Then the node in Q_{near} that is closest to $q_{rndstate}$ is selected. The node with the shortest distance is named $q_{nearest}$ (line 17). Next, a new branch will be created from the $q_{nearest}$ node that goes to $q_{rndstate}$ with a distance of Δq from $q_{nearest}$. The new node is named q_{new} (line 18). If there are no obstacles between $q_{nearest}$ and q_{new} (line 19), then the q_{new} node will be entered into T (lines 20-22). Next, it will be checked whether there are nodes in the current T close enough to the destination node or q_{goal} (line 23). If a node is close enough to the destination node, an X^{bs} route will be built (line 24). This process will repeat until the stop condition is met. The looping process can have several conditions that vary to stop, for example, if the maximum number of iterations has been met.

The RRT-ACS+RT algorithm determines the new path using pheromone information to ensure the quality

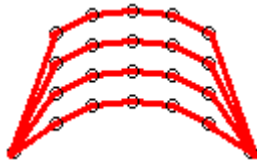


Figure 1. Example of a rule template for a straight line initial path blocked by an obstacle

Algorithm 1 : $X^{bs} \leftarrow \text{RRT-ACS+RT}(\text{map})$

```

1:  % ===== Initialization
2:   $T \leftarrow \text{Load Template}()$ 
3:   $T \leftarrow \text{TrimTree}(T)$ 
4:   $s \leftarrow 0$ 
5:  while termination condition not met do
6:    for  $k = 1$  to  $m$  do
7:      while  $s = 0$  do
8:         $q \leftarrow \text{randvar}[0,1]$  and  $\tau \neq 0$ 
9:        if  $q \leq q_o$ 
10:          $q_{samp} \leftarrow \text{SampleFrom}$ 
11:            $10\text{LastNode}(T)$ 
12:          $\tau_{near} \leftarrow \text{Near}(\tau, q_{samp})$ 
13:          $q_{rndstate} \leftarrow \text{RouletteWhell}(\tau_{near})$ 
14:         else
15:            $q_{rndstate} \leftarrow \text{RandomSample}(k)$ 
16:         end if
17:          $Q_{near} \leftarrow \text{Near}(T, q_{rndstate})$ 
18:          $q_{nearest} \leftarrow \text{NearestNeighbor}$ 
19:            $(q_{rndstate}, Q_{near}, T)$ 
20:          $q_{new} \leftarrow \text{GrowTree}$ 
21:            $(q_{nearest}, q_{rndstate}, \Delta q)$ 
22:         if  $\text{Obstaclefree}(q_{nearest}, q_{new})$  then
23:            $Q_{near} \leftarrow \text{Near}(T, q_{new})$ 
24:            $q_{min} \leftarrow \text{ChooseParent}$ 
25:              $(q_{new}, Q_{near}, q_{nearest})$ 
26:            $T \leftarrow \text{InsertNode}(q_{min}, q_{new}, T)$ 
27:           if  $\text{CanConnected}(q_{goal}, T)$  then
28:              $X^{bs} \leftarrow \text{UpdateBestPath}(T)$ 
29:           end if
30:         end if
31:       end while
32:        $X(k) \leftarrow \text{MakePath from } T$ 
33:     end for
34:      $X^{bs} \leftarrow \text{LocalSearch}(X^{bs}, \text{map})$ 
35:      $X^w \leftarrow \text{Select } w \text{ best Path}(X)$ 
36:      $\tau \leftarrow \text{Add Pheromone Node on the } w \text{ best}$ 
37:        $\text{Path}(X^w, \tau)$ 
38:      $\tau \leftarrow \text{Evaporate Pheromone Node}(\tau)$ 
39:   end while

```

of the final result. This motivation is based on the principle of learning by doing. A procedure for updating pheromone data has been implemented (lines 31-33). Only ants with the best path will contribute to providing additional pheromones at each iteration. This restriction is intended to provide additional reinforcement only to the good paths. The function LocalSearch (line 30) will optimize RRT's existing branches to improve the quality of found paths.

The RRT-ACS+RT algorithm was designed to deal with dynamic obstacles. Algorithms 2 - 4 depict the RRT-ACS+RT-based dynamic path planning algorithm. In order to generate a feasible initial path with fast convergence speed, the RRT-ACS algorithm, as described by Pohan et al. [16], is used (line 2 in algorithm 2). After that, the robot will set its velocity (line 4 in algorithm 2). The robot's position is updated based on the

speed. This process is described in algorithm 3. When the vertex is reached, the robot changes the velocity vector to move toward the next node (line 2-5 in algorithm 2).

Algorithm 2 : ExecutePath()

```

1: map ← SetRobotEnvironment()
2:  $X^{bs} \leftarrow$  RRT-ACS(map)
3: RobotDestinaton ← NextWaypnt( $X^{bs}$ )
4: Set RobotVelocity()
5: SetObstacleDestination(NumberObstacles)
6: SetObstacleVelocities(NumberObstacles)
7: while RobotLocation ≠ GoalLocation do
8:   UpdateRobotLoc( $X^{bs}$ )
9:   UpdateObstaclesLoc(NumObstacles)
10: end while

```

Algorithm 3 : UpdateRobotLoc(X^{bs})

```

1: RobotLocation = RobotLocation +
   RobotVelocity
2: If RobotLocation == RobotDestination
   then
3:   RobotDestinaton ← NextWaypnt( $X^{bs}$ )
4:   Set RobotVelocity()
5: end
6: ObsDistance ← GetDistance(
   RobotLocation,
   ObstacleLoc)
7: if ObsDistance < RobotRange then
8:   if ObstacleLoc blocks the path do
9:      $X^{bs} \leftarrow$  DoReplan(map)
10:  end if
11: end if

```

Algorithm 4 : $X^{bs} \leftarrow$ DoReplan(map)

```

1: T ← InvalidateNodes()
2: map ← SetReplanStartLocation()
3: map ← SetReplanGoalLocation()
4:  $X^{replan} \leftarrow$  RRT-ACS+RT(map)
5: while RobotLocation ≠
   ReplanGoalLocation do
6:   UpdateRobotLoc( $X^{replan}$ )
7:   UpdateObstaclesLoc(NumObstacles)
8: end while

```

When the simulation begins, the moving obstacles choose several random adjacent vertices as the destination points for movement (lines 5 and 6 in algorithm 2). During the simulation, the obstacle will move towards several random adjacent vertexes (line 9 of algorithm 2).

As the robot approaches the RobotDestination, it will determine if there are any dynamic obstacles within the robot's detection range. Furthermore, the dynamic obstacle movement must be observed in at least two steps to predict the dynamic obstacle's speed and direction. If the dynamic obstacle is predicted to block the path that the vehicle should take, DoReplan will be executed (lines 7 - 9 in algorithm 3).

The DoReplan algorithm works on the principle of determining the current vehicle position node as ReplanStartLocation (line 2 in algorithm 4). Following that, the DoReplan algorithm will determine the next position on the global path that is not blocked by dynamic obstacles (line 3 in algorithm 4). ReplanGoalLocation is the name of this position. The RRT-ACS+RT algorithm will then modify and expand the nodes surrounding the dynamic obstacle that connects ReplanStartLocation and ReplanGoalLocation (line 4 in algorithm 4). In principle, a path will be found that will circle the dynamic obstacle to ReplanGoalLocation. Any nodes that collide with a random moving obstacle are invalidated rather than deleted. After that, the robot will follow the re-planning result path until it reaches the ReplanGoalLocation (lines 5-8 in algorithm 4). Once the ReplanGoalLocation is reached (and the obstacle has been overcome), the robot will retrace the initial path determined previously.

2. 2. The Illustration

Figures 2 – 10 depict illustrations of the proposed algorithm. This illustration mimics the scenario proposed by Connell et al. [6], Jin et al. [27], and Wei and Ren [28]. The illustration shows a robot path planning process in a maze environment with a dynamic object. Figure 2 shows the scenario of the maze environment used and a unicycle robot model (big grey circle) moving from the starting location (red dot) to the destination location (blue dot). Robots are currently treated as particles. Furthermore, certain safe distances are set aside to form obstacles. The barriers are expanded to ensure the robot's safety during operation, as shown in Figure 3.

The next step is to perform path planning using the RRT-ACS algorithm, with the results displayed in Figure 4. In Figure 4, it is evident that the path generated by the RRT-ACS algorithm is close to the optimal path, as the path's corner points are close to the corners of the obstacle. Figure 5 depicts the results of path planning on the original map (without obstacle expansion). Based on Figure 5, the resulting path is safe for the robot to traverse, as it will not cause it to collide with the wall. The illustration of a robot moving through a given path is shown in Figure 6.

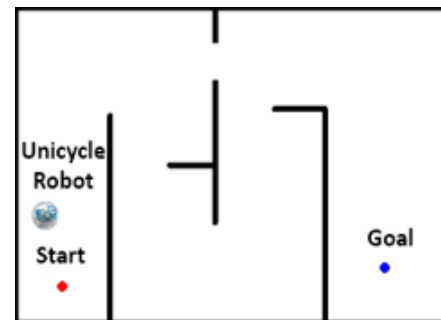


Figure 2. Maze environment scenario used for testing

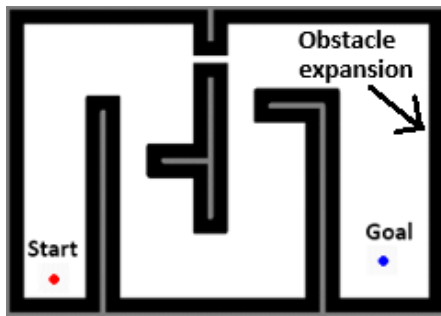


Figure 3. Obstacle expansion

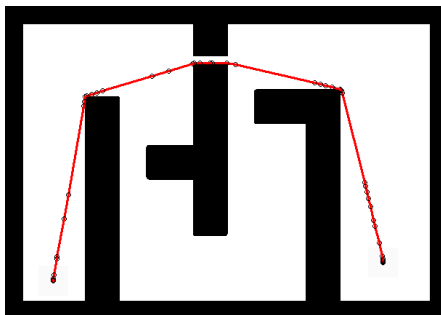


Figure 4. The results of path planning using the RRT-ACS algorithm

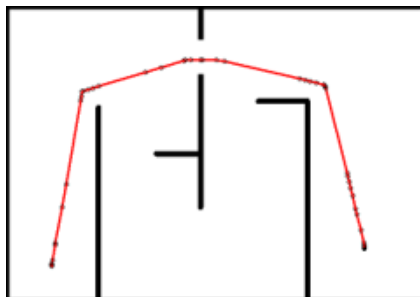


Figure 5. The results of the path planning using the RRT-ACS algorithm on the initial map

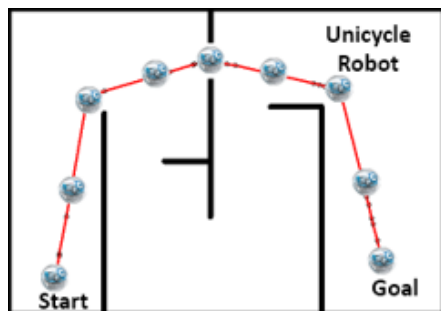


Figure 6. Illustration of a robot moving through a given path

Furthermore, a dynamic obstacle in the form of a basketball is given, as shown in Figure 7. It can be seen that the dynamic obstacle blocks the path that the robot

must pass. The robot will crash into these dynamic obstacles if re-planning is not carried out. So that in the proposed algorithm, if an obstacle is detected that blocks the robot, it will be detected by the sensor. The algorithm will update the environmental map, as shown in Figure 8.

Next, the RRT-ACS+RT algorithm is run again to produce a re-planning algorithm to avoid dynamic constraints. The first stage of the RRT-ACS+RT algorithm for the re-planning process is to use the tree of rule templates, as shown in Figure 9. If the tree of rule templates can be connected to the destination node, then the re-planning process is complete. If not, the RRT-ACS algorithm will start iterating to connect the tree with the destination node. The resulting re-planning path is shown in Figure 10.

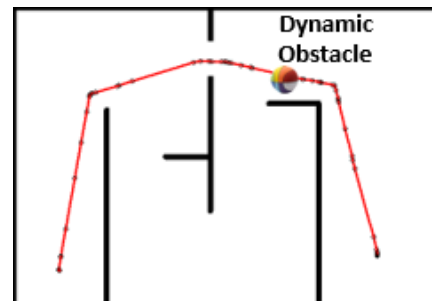


Figure 7. Given an obstacle on the path traversed by the robot

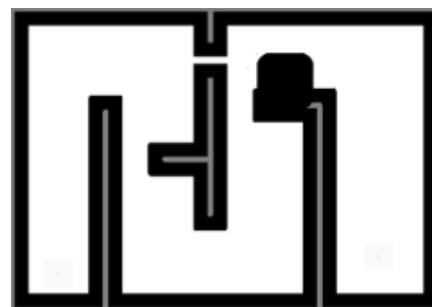


Figure 8. Update the environmental map after the robot detects a dynamic obstacle

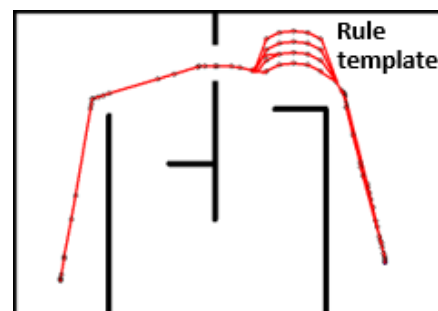


Figure 9. Use of rule template to speed up the re-planning process

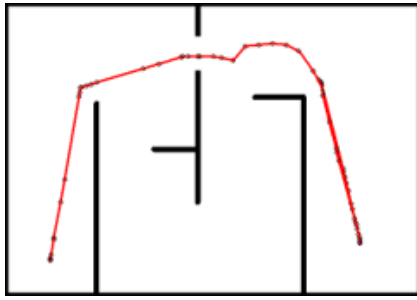


Figure 10. Path re-planning results to avoid dynamic obstacle

3. RESULTS AND DISCUSSION

To validate the performance of the proposed path planning mobile robot in a dynamic environment using the RRT-ACS+RT algorithm, we ran it through a three-dynamic environment simulation scenario (as shown in Figures 11 – 13). The three scenarios replicate the test scenario proposed by Wang et al. [29]. In each scenario, the robot's initial location is indicated by a red dot, while a blue dot indicates the robot's goal location. The simulation tests were carried out on a PC with a Core i5 3.20 GHz CPU and 4 GB RAM running Windows 10 64-bit, with LabVIEW 7.1 as the compilation environment.

The first scenario is shown in Figure 11(a). In this scenario, there are five static obstacles (black box) and one dynamic obstacle (in the form of a basketball). First, the robot will create an initial path, as shown in Figure 11(b). Then, when the robot moves, a dynamic obstacle will be placed that will block the initial path, as shown in Figure 11(c) or Figure 11(d). The robot must then re-plan in order to find a new path to the goal state that avoids the newly-placed dynamic obstacles. Figure 11(c) shows an example of the re-planning path generated by the proposed algorithm. It can be seen that the robot simply circles around the dynamic obstacle to avoid colliding with it. As for the case of Figure 11(d), the dynamic obstacle covers the narrow path that the robot wants to pass (making the robot unable to pass through the narrow path). The RRT-ACS+RT algorithm then searches for a new route that takes a right turn to reach the goal state while avoiding collisions with dynamic obstacles.

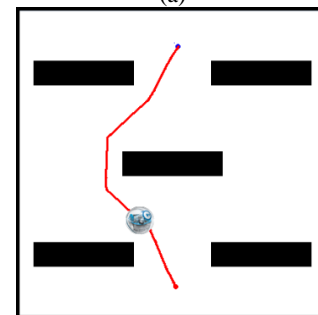
The second scenario is shown in Figure 12(a). In this scenario, there are two static obstacles and two dynamic obstacles. First, the robot will create an initial path, as shown in Figure 12(b). Then, when the robot begins to move, it will place the first dynamic obstacle that will block the initial path, as shown in Figure 12(c). The robot must then re-plan to find a new path to the goal state without being impeded by the newly placed dynamic obstacles. Figure 12(c) shows an example of the re-planning path generated by the proposed algorithm. It can be seen that the robot simply circles around the dynamic obstacle to avoid a collision.

Furthermore, a second dynamic obstacle will be placed when the robot moves again to block the initial path on the other side, as shown in Figure 12(d). Then the robot must re-do the re-planning to find a new path to reach the goal state and not be hindered by the second dynamic obstacle. Figure 12(d) shows an example of the second re-planning path generated by the RRT-ACS+RT algorithm.

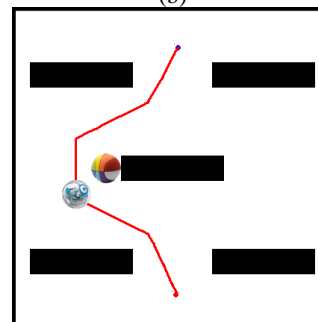
Meanwhile, the third scenario is shown in Figure 13(a). The initial path generated by the proposed algorithm is also shown in Figure 13(a). In this scenario, there are four static obstacles and three dynamic obstacles. The three dynamic obstacles will be placed in turn to block the initial path of the robot, as shown in Figure 13(b) – 13(d). It can be seen in the three figures that every time a dynamic obstacle blocks the robot's path; the robot will re-plan to find a new path to reach the goal state and not be hindered by dynamic obstacles. Figures 13(b) – 13(d) show an example of the re-planning path generated by the RRT-ACS+RT algorithm every time the robot detects a dynamic object.



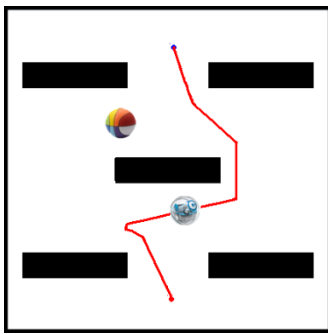
(a)



(b)

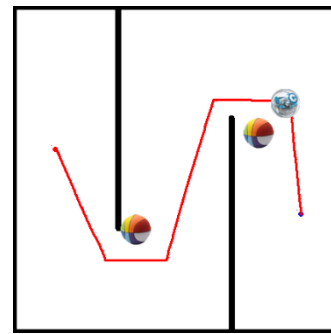


(c)



(d)

Figure 11. First test scenario: (a) test scenario, initial location and goal location of the robot, (b) an example of the initial path generated by the proposed algorithm, (c) and (d) dynamic obstacle is placed that will block the initial path and the robot must re-planning the path to reach the goal location while avoiding collisions with dynamic obstacles

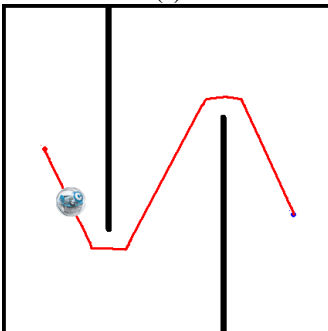


(d)

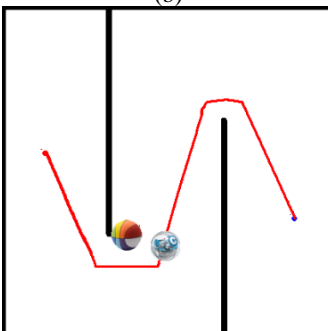
Figure 12. Second test scenario: (a) test scenario, initial location and goal location of the robot, (b) an example of the initial path generated by the proposed algorithm, (c) and (d) the first and the second dynamic obstacle is placed that will block the initial path and the robot must re-planning the path to reach the goal location while avoiding collisions with dynamic obstacles



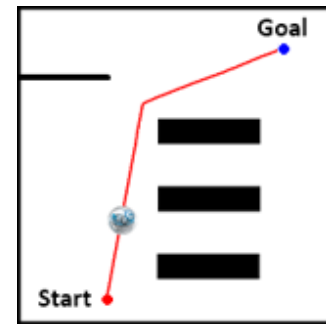
(a)



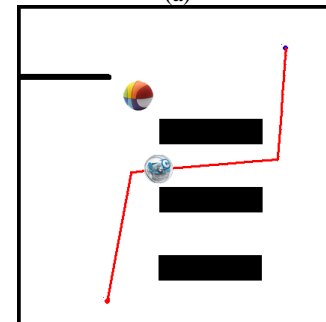
(b)



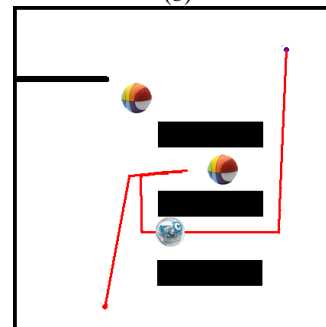
(c)



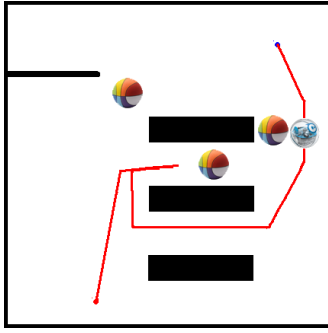
(a)



(b)



(c)



(d)

Figure 13. Third test scenario: (a) test scenario, initial location, goal location, and the initial path generated by the proposed algorithm, (b) - (d) the first, the second, and the third dynamic obstacle is placed that will block the initial path and the robot must re-planning the path to reach the goal state while avoiding collisions with dynamic obstacles

The performance of the re-planning process of the mobile robot in a dynamic environment using the RRT-ACS+RT algorithm is compared to the RRT*FND, MOD-RRT*, and RRT* algorithms. Testing was carried out using the three scenarios that have been described. The results are summarized in Tables 1-3. Performance measurements include the best, the worst, and the mean computation time of each algorithm.

Based on the data in Tables 1-3, we will compare how fast the RRT-ACS+RT, RRT*FND, and MOD-RRT* algorithms perform the re-planning process compared to the RRT* algorithm. The results of this comparison are stated in Table 4.

Based on the data reported in Table 4, it can be seen that the average time for the RRT-ACS+RT algorithm to carry out the re-planning process is 65.5% faster than the RRT* algorithm. These results are consistent with the RRT-ACS algorithm performance measurement results reported by Pohan et al. [16]. They have also reported that the speed of the RRT-ACS algorithm was 59.4%

TABLE 1. Comparison of the time required for each algorithm to re-planning in the first scenario. The time is in milliseconds

Computation time performance	RRT-ACS+RT	RRT* FND	MOD-RRT*	RRT*
The dynamic obstacle's location as shown in Figure 11(c)				
Best	478.9	1216.2	1577.0	1770
Mean	565.3	1451.0	2617.8	3113
Worst	1158.1	1935.9	4050.3	5296
The dynamic obstacle's location as shown in Figure 11(d)				
Best	763.8	1385.5	1649.7	1875
Mean	936.5	2340.9	2549.5	2932.2
Worst	2824.5	19670.1	4289.6	4965

TABLE 2. Comparison of the time required for each algorithm to re-planning in the second scenario. The time is in milliseconds

Computation time performance	RRT-ACS+RT	RRT* FND	MOD-RRT*	RRT*
The first dynamic obstacle is placed as in Figure 12(c)				
Best	615.5	1003.8	1028.2	1154
Mean	921.7	1086.6	1696.1	2017
Worst	943.1	1329.1	2207.2	2886
The second dynamic obstacle is placed as in Figure 12(d)				
Best	266.8	360.0	1525.7	1734
Mean	1427.7	1861.0	2327.6	2677
Worst	2593.5	4060.7	3627.8	4199

TABLE 3. Comparison of the time required for each algorithm to re-planning in the third scenario. The time is in milliseconds

Computation time performance	RRT-ACS+RT	RRT* FND	MOD-RRT*	RRT*
The first dynamic obstacle is placed as in Figure 13(b)				
Best	286.2	794.3	798.3	896
Mean	312.8	980.0	1709.7	2033.2
Worst	441.6	1254.3	3501.2	4578
The second dynamic obstacle is placed as in Figure 13(c)				
Best	869.8	1577.7	1343.5	1527
Mean	1245.8	2092.6	3123.2	3592
Worst	1147.2	6019.3	4884.9	5654
The third dynamic obstacle is placed as in Figure 13(d)				
Best	482.1	801.3	805.4	904
Mean	753.7	1038.2	1256.2	1493.8
Worst	922.6	2069.1	1804.9	2360

TABLE 4. Comparison of the average time for each algorithm executes the re-planning process relative to the RRT* algorithm

Dynamic obstacle position	RRT-ACS+RT	RRT* FND	MOD-RRT*
First scenario, Figure 11(c)	81.8%	53.4%	15.9%
First scenario, Figure 11(d)	68.1%	20.2%	13.1%
Second scenario, Figure 12(c)	54.3%	46.1%	15.9%
Second scenario, Figure 12(d)	46.7%	30.5%	13.1%
Third scenario, Figure 13(b)	84.6%	51.8%	15.9%
Third scenario, Figure 13(c)	73.7%	41.7%	13.1%
Third scenario, Figure 13(d)	49.5%	30.5%	15.9%
Average percentage	65.5%	39.2%	14.7%

faster than the RRT* algorithm in reaching the optimal path. Based on the data in Table 4, it can be apparent that the average time for the RRT*FND algorithm to carry out the re-planning process is 39.2% faster than the RRT* algorithm. These results are consistent with the performance measurement results of the RRT*FND algorithm reported by Adiyatov et al. [22]. Adiyatov et al. [22] also reported that the speed of the RRT*FND algorithm in reaching the optimal path was 43.5% faster than the RRT* algorithm. Based on Tables 1 - 4, it is clear that the RRT-ACS+RT algorithm outperforms other algorithms in terms of best path length, worst path length, and mean path length.

4. CONCLUSION

This study implements a path planning mobile robot based on the RRT-ACS+RT algorithm in a dynamic environment. The simulation was carried out to validate the proposed method in a real dynamic environment. The proposed method's performance is compared to the RRT*FND and MOD-RRT algorithms. The test results demonstrate that the proposed method outperforms other comparison algorithms. The findings indicate that the proposed method is appropriate for use on robots navigating in a dynamic environment, such as self-driving cars.

5. ACKNOWLEDGMENTS

This research was funded by Universitas Komputer Indonesia through the UNIKOM Internal Research program in 2023.

6. REFERENCES

- Ganeshmurthy, M. S., and Suresh, G. R. "Path planning algorithm for autonomous mobile robot in dynamic environment." In 2015 3rd International Conference on Signal Processing, Communication and Networking (ICSCN), (2015), 1-6. <https://doi.org/10.1109/icscn.2015.7219901>
- Ab Wahab, M. N., Lee, C. M., Akbar, M. F., and Hassan, F. H. "Path planning for mobile robot navigation in unknown indoor environments using hybrid PSOFS algorithm." *IEEE Access*, Vol. 8, (2020), 161805-161815. <https://doi.org/10.1109/access.2020.3021605>
- Nascimento, L. B., Morais, D. S., Barrios-Aranibar, D., Santos, V. G., Pereira, D. S., Alsina, P. J., and Medeiros, A. A. "A Multi-Robot Path Planning Approach Based on Probabilistic Foam." In 2019 Latin American Robotics Symposium (LARS), 2019 Brazilian Symposium on Robotics (SBR) and 2019 Workshop on Robotics in Education (WRE), (2019), 329-334. <https://doi.org/10.1109/lars-sbr-wre48964.2019.00064>
- Aria, M. "Optimal Path Planning using Informed Probabilistic Road Map Algorithm." *Journal of Engineering Research-ASSEEE Special Issue*, (2021), 1-15. <https://doi.org/10.36909/jer.asseee.16105>
- Teshnizi, M. M., Kosari, A., Goliaei, S., and Shakhesi, S. "Centralized Path Planning for Multi-aircraft in the Presence of Static and Moving Obstacles." *International Journal of Engineering, Transactions B: Applications*, Vol. 33, No. 5, (2020) 923-933. <https://doi.org/10.5829/ije.2020.33.05b.25>
- Connell, D., and Manh La, H. "Extended rapidly exploring random tree-based dynamic path planning and replanning for mobile robots." *International Journal of Advanced Robotic Systems*, Vol. 15, No. 3 (2018), 1729881418773874. <https://doi.org/10.1177/1729881418773874>
- Zhang, H., Wang, Y., Zheng, J., and Yu, J. "Path planning of industrial robot based on improved RRT algorithm in complex environments." *IEEE Access*, Vol. 6, (2018) 53296-53306. <https://doi.org/10.1109/access.2018.2871222>
- Li, X., Jiang, H., Shi, W., Chen, S., and Wang, Y. "Path planning of multipoint region attraction RRT* algorithm in complex environment." In 2019 Chinese Control Conference (CCC), (2019) 4409-4414. <https://doi.org/10.23919/chicc.2019.8865834>
- Taheri, E. "Any-time randomized kinodynamic path planning algorithm in dynamic environments with application to quadrotor." *International Journal of Engineering, Transactions A: Basics*, Vol. 34, No. 10, (2021) 2360-2370. <https://doi.org/10.5829/ije.2021.34.10a.17>
- Wang, J., Li, X., and Meng, M. Q. H. "An improved rrt algorithm incorporating obstacle boundary information." In 2016 IEEE International Conference on Robotics and Biomimetics (ROBIO), (2016) 625-630. <https://doi.org/10.1109/robio.2016.7866392>
- Zhang, Y., Wang, R., Song, C., and Xu, J. "An Improved Dynamic Step Size RRT Algorithm in Complex Environments" In 2021 33rd Chinese Control and Decision Conference (CCDC), (2021) 3835-3840. <https://doi.org/10.1109/ccdc52312.2021.9602069>
- Solovey, K., Janson, L., Schmerling, E., Frazzoli, E., and Pavone, M. "Revisiting the asymptotic optimality of RRT." In 2020 IEEE International Conference on Robotics and Automation (ICRA), (2020) 2189-2195. <https://doi.org/10.1109/icra40945.2020.9196553>
- Klemm, S., Oberländer, J., Hermann, A., Roennau, A., Schamm, T., Zollner, J. M., and Dillmann, R. "RRT-connect: Faster, asymptotically optimal motion planning." In 2015 IEEE International conference on robotics and biomimetics (ROBIO), (2015) 1670-1677. <https://doi.org/10.1109/robio.2015.7419012>
- Gammell, J. D., Barfoot, T. D., and Srinivasa, S. S. "Informed asymptotically optimal anytime search." in *International Journal of Robotics Research*, (2017) 1-27. <https://doi.org/10.1177/0278364919890396>
- Mashayekhi, R., Idris, M. Y. I., Anisi, M. H., Ahmedy, I., and Ali, I. "Informed RRT*-connect: An asymptotically optimal single-query path planning method." *IEEE Access*, Vol. 8, (2020) 19842-19852. <https://doi.org/10.1109/access.2020.2969316>
- Pohan, M. A. R., Trilaksono, B. R., Santosa, S. P., and Rohman, A. S. "Path Planning Algorithm Using the Hybridization of the Rapidly-Exploring Random Tree and Ant Colony Systems." *IEEE Access*, Vol. 9, (2021) 153599-153615. <https://doi.org/10.1109/access.2021.3127635>
- Connell, D., and La, H. M. "Dynamic path planning and replanning for mobile robots using RRT." In 2017 IEEE International Conference on Systems, Man, and Cybernetics (SMC), (2017) 1429-1434. <https://doi.org/10.1109/smc.2017.8122814>
- Yaghmaee, F., and Koohi, H. "Dynamic obstacle avoidance by distributed algorithm based on reinforcement learning." *International Journal of Engineering, Transactions B:*

- Applications*, Vol. 28, No. 2, (2015) 198-204. <https://doi.org/10.5829/idosi.ije.2015.28.02b.05>
19. Kala, R., Shukla, A., and Tiwari, R. "Robot path planning using dynamic programming with accelerating nodes." *Paladyn*, Vol. 3, No. 1, (2012) 23-34. <https://doi.org/10.2478/s13230-012-0013-4>
 20. Meng, L., Qing, S., and Jun, Z. Q. "UAV path re-planning based on improved bidirectional RRT algorithm in dynamic environment." In 2017 3rd International Conference on Control, Automation and Robotics (ICCAR), (2017) 658-661. <https://doi.org/10.1109/iccar.2017.7942779>
 21. Chen, Y., and Wang, L. "Adaptively Dynamic RRT*-Connect: Path Planning for UAVs Against Dynamic Obstacles." In 2022 7th International Conference on Automation, Control and Robotics Engineering (CACRE), (2022) 1-7. <https://doi.org/10.1109/cacre54574.2022.9834188>
 22. Adiyatov, O., and Varol, H. A. "A novel RRT*-based algorithm for motion planning in Dynamic environments." In 2017 IEEE International Conference on Mechatronics and Automation (ICMA), (2017) 1416-1421. <https://doi.org/10.1109/icma.2017.8016024>
 23. Qi, J., Yang, H., and Sun, H. "MOD-RRT*: A sampling-based algorithm for robot path planning in dynamic environment." *IEEE Transactions on Industrial Electronics*, Vol. 68, No. 8, (2020) 7244-7251. <https://doi.org/10.1109/tie.2020.2998740>
 24. Wei, K., Chu, Y., and Gan, H. "An improved Rapidly-exploring Random Tree Approach for Robotic Dynamic Path Planning." In 2021 11th International Conference on Intelligent Control and Information Processing (ICICIP), (2021) 181-187. <https://doi.org/10.1109/icicip53388.2021.9642182>
 25. Meng, C., and Dai, H. "An Obstacle Avoidance Method Based on Advanced Rapidly-exploring Random Tree for Autonomous Navigation." In 2021 IEEE International Conference on Parallel & Distributed Processing with Applications, Big Data & Cloud Computing, Sustainable Computing & Communications, Social Computing & Networking (ISPA/BDCLOUD/SocialCom/SustainCom), (2021) 1118-1125. IEEE. <https://doi.org/10.1109/ispa-bdcloud-socialcom-sustaincom52081.2021.00154>
 26. Ma, L., Xue, J., Kawabata, K., Zhu, J., Ma, C., and Zheng, N. "Efficient sampling-based motion planning for on-road autonomous driving." *IEEE Transactions on Intelligent Transportation Systems*, Vol. 16, No. 4, (2015) 1961-1976. <https://doi.org/10.1109/tits.2015.2389215>
 27. Jin, Q., Tang, C., and Cai, W. "Research on Dynamic Path Planning Based on the Fusion Algorithm of Improved Ant Colony Optimization and Rolling Window Method." *IEEE Access*, Vol. 10, (2021) 28322-28332. <https://doi.org/10.1109/access.2021.3064831>
 28. Wei, K., and Ren, B. "A method on dynamic path planning for robotic manipulator autonomous obstacle avoidance based on an improved RRT algorithm." *Sensors*, Vol. 18, No. 2 (2018), 571. <https://doi.org/10.3390/s18020571>
 29. Wang J., Meng M. Q. -H., and Khatib, O. "EB-RRT: Optimal Motion Planning for Mobile Robots," in *IEEE Transactions on Automation Science and Engineering*, Vol. 17, No. 4 (2020), 2063-2073, <https://doi.org/10.1109/TASE.2020.2987397>

Persian Abstract

چکیده

این مطالعه یک روش برنامه ریزی مسیر کارآمد برای ربات های متحرک در یک محیط پویا ارائه می دهد. این روش بر اساس الگوریتم درخت تصادفی در حال کاوش سریع (RRT) است. دو فرآیند اصلی در برنامه ریزی مسیر ربات متحرک در یک محیط پویا، برنامه ریزی مسیر اولیه و برنامه ریزی مجدد مسیر است. به منظور ایجاد یک مسیر اولیه امکان پذیر با سرعت همگرایی سریع، ما از ترکیبی از سیستم های مستعمره ای از درختان تصادفی که به سرعت در حال کاوش هستند (RRT-ACS) استفاده کردیم. هنگامی که مانعی مسیر اولیه را مسدود می کند، برنامه ریزی مجدد مسیر باید اجرا شود. علاوه بر الگوریتم RRT-ACS، ما استفاده از یک مجموعه الگو-قانون مبتنی بر ربات متحرک را در صحنه های محیط پویا در طول فرآیند برنامه ریزی مجدد مسیر پیشنهاد کردیم. این الگوریتم جدید RRT-ACS با مجموعه های الگو-قانون (RRT-ACS+RT) نامیده می شود. ما شبیه سازی های معیار زیادی را برای اعتبارسنجی روش پیشنهادی در یک محیط پویا واقعی انجام دادیم. عملکرد روش پیشنهادی با الگوریتم های پیشرفته برنامه ریزی مسیر مقایسه می شود: RRT*FND و MOD-RRT*. نتایج تجربی متعدد نشان می دهد که روش پیشنهادی بهتر از سایر الگوریتم های مقایسه عمل می کند. نتایج نشان می دهد که روش پیشنهادی برای استفاده در روبات هایی که نیاز به جهت یابی در یک محیط پویا، مانند اتومبیل های خودران دارند، مناسب است.



Enhanced Face Presentation Attack Prevention Employing Feature Fusion of Pre-trained Deep Convolutional Neural Network Model and Thepade's Sorted Block Truncation Coding

S. D. Thepade*, M. R. Dindorkar, P. R. Chaudhari, S. V. Bang

Computer Engineering Department, Pimpri Chinchwad College of Engineering, Pune, India

PAPER INFO

Paper history:

Received 23 October 2022

Received in revised form 24 November 2022

Accepted 24 November 2022

Keywords:

Face Presentation Attack

Transfer Learning

DensNet121

VGG16

Xception

VGG19

Pretrained Deep CNN

InceptionV3

MobileNet

Thepade's SBTC

ABSTRACT

The evolution and improvements of deep learning are being used to tackle any research obstacles that could be converted into classification problems in all spheres of life. Each Deep convolutional neural network (DCNN) design's output is determined by the depth and value of the hyperparameters, which explains why so many of them have been proposed. These DCNN architectures must be created entirely from scratch, and they can only be used for the applications for which they were intended. Transfer learning may be used to modify these pre-trained networks so they are more appropriate for particular purposes. This article aims to evaluate the empirical performance of the applicability of pre-trained DCNN models to identify human face presentation threats (FPAD). Human FPAD is one of the most significant and crucial areas of research right now because of the introduction of ambient computing, which necessitates contact-free identification of persons with the help of their biometric traits. Six pre-trained DCNN models are taken into account for an experimental evaluation in human FPAD alias VGG19, VGG16, DensNet121, MobileNet, Xception, and InceptionV3. The investigation makes use of the NUAA and Replay-Attack benchmark FPAD datasets. Thepade's sorted block truncation coding (SBTC) 10-ary features are merged with deep learning features produced from the finest performing finetuned DCNNs to enhance the FPAD capabilities of analyzed machine learning (ML) classifiers. The integration of features of Thepade's SBTC 10-ary and DCNN has considerably increased the FPAD accuracy of ML classifiers with slightly more computations of feature extraction.

doi: 10.5829/ije.2023.36.04a.17

1. INTRODUCTION

The security and access management of assets in the contemporary era of pervasive computing is largely dependent on the biometric characteristics of a person, such as a face [1-4], iris [5-7], fingerprints [8, 9], etc. Due to the numerous traits shown by the face and the simplicity of using face recognition algorithms, face recognition has emerged as an important physiological biometric technique utilized in information security [10]. Attackers trick these systems by using a variety of spoofing techniques, including photo, video, cut-photo, mask attacks, etc. Existing facial recognition systems should be modified to counteract these threats. Current

antispoofing techniques use features based on shape, motion, depth, color, texture, and deep learning for spoof identification. Convolutional neural networks (CNN) are being researched in several fields of image processing [11-13]. For image classification tasks, there are numerous accessible pre-trained deep CNN models similar to Inception V3, VGG19, VGG16 etc.

A very precise model must have huge annotated datasets as a minimum requirement. It is difficult to obtain such massive datasets for any domain. A method called transfer learning was developed to reduce this requirement. Transfer learning, in general, is a method that adapts a model which has already been trained to execute one job to perform another. The transfer learning

*Corresponding Author Institutional Email:
sudeepthepade@gmail.com (S. D. Thepade)

method accelerates the development of new models while also enhancing their functionality. Several transfer learning strategies are employed depending on the study domain and the available data. However, manually created features use less computational power and let us extract global texture data from various parts of the image. Handcrafted features occasionally give CNN more data in a variety of classification tasks. As a result, the current work suggests an FPAD technique by combining deep learning features and manually creating texture characteristics from Thepade's SBTC [14-18].

The following are the key contributions of the current paper:

- Performance assessment of 6 different pre-trained DCNNs for FPAD.
- Capability evaluation of Thepade's SBTC features of 10-ary for different Machine Learning (ML) classifiers in FPAD.
- Improving the FPAD capability of a classifier by fusing Thepade's SBTC 10-ary texture features and auto-extracted DCNN features.

The sections in the paper are placed as given here. Section 1 has an introduction; section 2 surveys pertinent literature; section 3 elaborates on current deep CNN models; section 4 contains the proposed technique; section 5 illustrates the environment set up for experimentation; section 6 converses the observed results, and section 7 has concluding remarks.

2. LITERATURE SURVEY

Recent attempts to use pre-trained CNN models for FPAD have had some notable success. Here is a quick summary of their endeavours.

A CNN architecture called FASNet, which is a modified version of VGG16, is proposed by Lucena et al. [19]. The authors used back-propagation to adjust the weights to the uppermost layers starting from the fourth block. The findings were produced on the datasets 3DMAD (3D Mask Attack Dataset) and Replay-Attack to appraise the significance of the suggested strategy.

The method using the Rotation Invariant Local Binary Pattern (RILBP) and the ResNet-18 pre-trained CNN model was proposed by Chen et al. [20]. Support Vector Machine (SVM) is trained with the fused features from ResNet-18 and RILBP for binary classification. In intra- and cross-database testing, better results were obtained using a pre-trained CNN model. Tang et al. [21] suggest a method for obtaining class probabilities that involve feeding colour, temporal, and patch-based characteristics to a pre-trained CNN architecture called ResNet-18. To create a class-probability vector, these class probabilities are further concatenated. Therefore, SVM receives a vector of class probability for binary categorization.

The suggested approach by Tu et al. [22] locates pertinent hidden features from an input facial image using a pre-trained CNN model called ResNet-50. ResNet-50, which learns temporal properties from frame sequence, is put on top of LSTM with the exception of the top layers. The face's authenticity can be determined using these learning attributes.

Das et al. [23] suggest a novel human face antispooofing method that combines hand-crafted features extracted from an input face image using an LBP descriptor with deep features derived via VGG16.

Two Presentation Attack Detection (PAD) techniques are developed by Elloumi et al. [24] based on deep learning with the quality evaluation of the image. The first strategy uses the LBP histogram computation and VGG16 finetuning, whereas the other strategy relies on Image Quality Measures.

The work of Song and Hongbin [25] makes use of the feature extractors like ULTP (Uniform Local Ternary Pattern) and ULBP (Uniform Local Binary Pattern) with G-R color (color-INF and color-MMT). The SVM classifier uses these extracted features to further combine them and decide if the given face image is real or fake. On three separate face antispooofing datasets, the approach has produced notable results.

These nine different types of features as MeanRGB, SSIM, Energy, MeanYCbCr, Entropy, SBTC, BTC, LBP, and Luminance, are extracted and explored by Jagdale and Thepade [26], Thepade et al. [27]. To determine if a face is alive, the further fusion of these features is given to SVM. Although Thepade's SBTC produces notable results, the method is only tested on the NUAA dataset.

Thepade et al. [28] studied two ML classifiers, three ensembles, and three colour spaces: YCrCb, Kekre-LUV, and CIE-LUV. By computing a histogram over the colorspace under consideration, features are derived. These features are used to train the classifiers and ensembles indicated above. The combination of CIE-LUV, YCrCb, and RandomForest produces impressive results for FPAD. The method's performance is evaluated on two datasets, Replay-attack and NUAA.

The fusion of features formed by using pre-trained DCNN models and conventional content features is presented by Abdullakutty et al. [29]. Colour LBP was extracted in YCbCr and HSV colour spaces for content features. The ResNet-50 with CLBP has given better performance over the three datasets used.

For 2D face PAD, a video preprocessing method called Temporal Sequence Sampling (TSS) by removing the predicted inter-frame 2D affine motion with the features of a Convolutional Neural Network (CNN) through a self-supervised representation learning scheme is proposed by Usman et al. [30].

Face presentation attack detection using various openly available datasets and their combinations are

presented by Abdullakutty et al. [31], where the binary classification using transfer learning is explored for attack detection.

3. EXISTING DCNN MODELS

The six well-known DCNN models, MobileNet, VGG16, InceptionV3, Xception, Densenet121, and VGG19, are empirically evaluated here. With the aid of the transfer learning method for FPAD, all of these well-known DCNN models are explored.

Simonyan et al. [32] trained a CNN model known as VGG16 having a total of 16 layers (3 fully connected preceded by 13 convolutional) with the ImageNet data, having about 1000 classes and 14 million images. A total of 19 layers (3 fully connected preceded by 16 convolutional) make up VGG19 [25]. The VGG19 was significantly improved by enhancing the layer count from 16 to 19.

The 42 layers-deep InceptionV3 [33] network took the first runner-up in the ILSVRC-2015 because of its low error rate achievement (ImageNet Large Scale Visual Recognition Competition). Despite having a 2.5-fold higher computational cost than InceptionV1 (GoogleNet), InceptionV3 is more effective than VGGNet.

DenseNet121 is available in four different versions: DenseNet201, DenseNet169, DenseNet161, and DenseNet121. Each layer of DenseNet is connected as feed-forward [34]. The main benefits of these networks are 'encouragement to feature reuse' and 'reduction in concerns of vanishing gradient.' The DenseNet121 architecture has 121 layers.

The architecture of Xception [35] is 36 layers thick. The architecture of Xception was inspired by that of Inception, where depth-wise removable convolutions were used in place of the inception modules. There are exactly the same amount of parameters in Xception and InceptionV3.

The MobileNet [36] architecture comprises 28 layers when the pointwise and depthwise convolutions are considered separate layers. The pointwise and depthwise convolutions created in the form of piles are used to organise the separable convolution modules found in the MobileNet.

4. PROPOSED APPROACH

A stored network that has been trained on a sizable dataset to do general image categorization is the pre-trained model. The machine learning (ML) algorithm learns from the specific dataset and applies that information to others during the transfer learning process. Two methods can be used to implement transfer

learning, (i) The pre-trained model is taken as an automatic feature extractor in a particular image categorization task. (ii) Fine-tuning the pre-trained model, which involves either retraining the entire model or only a section of it using fresh data. Transfer learning is frequently used when there is little data to prevent overfitting. Transfer learning provides the advantage of reducing 'time' and 'computation resources' needed in the training stage.

The gray version of the input face image is taken in work proposed here (Figure 1), which is followed by passing it through the Haar-cascade classifier to determine the area of interest (ROI), which is shrunk to fit within a '224 x 224' pixel window. The suggested methodology leverages the finetuning strategy on various pre-trained DCNN models for FPAD tasks after preprocessing. For each pre-trained model, a classification head having two fully connected layers with sizes "1" and "256" correspondingly replaces the final fully connected layers (FC). Between these FC layers is a dropout layer with a 0.2% dropout rate in order to prevent overfitting. The adam optimizer is used with a learning rate of 10^{-4} and weight decay at a rate of 10^{-6} (refer to Table 1). Additionally, sigmoid is employed (rather than softmax) decision function, which is suitable in binary categorization.

Finetuning the model using a randomly initialized classification head (depicted by pink color in Figures 2 to 7) may make the pre-trained base model disremember what it learned due to massive gradient updates. Hence here, the base pre-trained model is set to be non-trainable, and the classification head is trainable for the first 5

TABLE 1. Optimizer parameter set for DCNN Models in experimentation for person face liveness detection

Optimizer Parameters	Value
Optimizer	Adam
Beta-1	0.9
Learning rate	0.0001
Beta-2	0.999
Batch size	10^2
Epsilon	1×10^{-8}

TABLE 2. Parameters used to enhance the data during the DCNN model's training

Parameter for Data Augmentation	Value
Rescale	1/0.255
Fill mode	nearest
Rotation range	20°
Range of Width shift/ Shear/ Height Shift/ Zoom	0.2

epochs of training. Then the last two blocks of the base pre-trained model (shown in the red-marked rectangle) are set to be trainable (unfrozen). Further, the classification head and the base model are jointly trained using Keras's¹ early stopping criteria with parameter 'patience' equal to 10, indicating the training process will be automatically terminated if enhancement is not detected in test accuracy over 10 epochs. Further, to mitigate overfitting in training, data augmentation is carried out on the training dataset using the parameters

listed in Table 2. The last 2 convolution blocks enclosed with a red border are finetuned in the case of VGG16, VGG19 and DenseNet121, as specified in Figures 2, 3, and 4, respectively. As depicted in Figure 5, the lattermost 2 inception blocks are chosen for finetuning in the case of InceptionV3. The bottommost 2 separable convolution blocks are finetuned for Xception (see Figure 6). Similarly, as per Figure 7, the last 2 depthwise separable convolution blocks are finetuned for MobileNet.

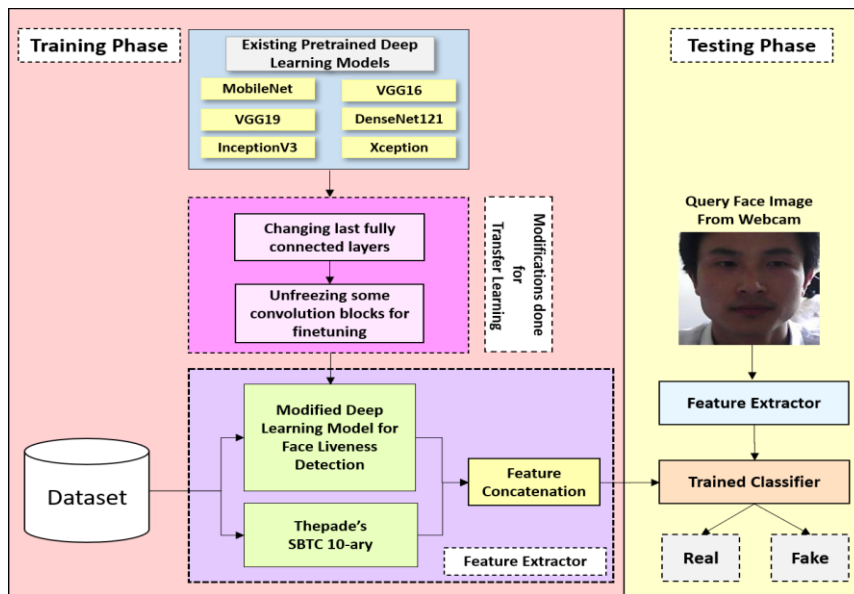


Figure 1. Flowchart illustrating the proposed method of human face liveness detection



Figure 2. Custom-made VGG16 model indicating the finetuned convolution blocks with red borderline



Figure 3. Custom-made VGG19 model depicting the finetuned convolution blocks with the red borderline (Output of dense layer indicated by a yellow color, is utilized to extract deep learning features that are used for feature fusion with Thepade's SBTC 10-ary)

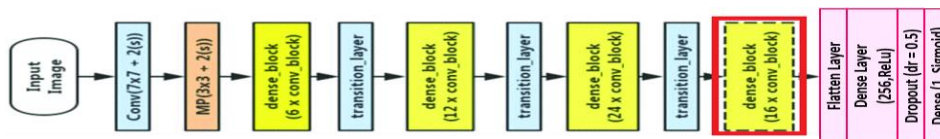


Figure 4. Custom-made DenseNet121 model indicating the finetuned convolution block with red borderline

¹ www.keras.io

5. EXPERIMENTATION ENVIRONMENT

Here, experimental evaluation is conducted using a platform made available by Kaggle¹, an online community for machine learning professionals and data scientists. The Python code written in Kaggle notebooks is run using the GPU as an accelerator for experimentation here.

Here, two widely used datasets for human FPAD, dubbed "Replay-Attack" and "NUAA," are investigated to validate the performance of current DCNN models using transfer learning. For each improved DCNN model, the testing accuracy is employed as a performance metric.

The Replay-Attack dataset [38] was generated by the IDIAP Research Institute and contained 1300 movies of 50 people under two different brightness settings as controlled and unfavourable during the acquisition (shown in Figure 8). The collection contains only videos that were shot at a 25 Hertz frame rate.

The NUAA dataset was generated by the Nanjing University of Aeronautics and Astronautics [39]. A web camera is used to capture 15 people's real and faked face photos. 5105 genuine and 7509 artificial face photos make up the data split over training and testing. Each facial image is 640 x 480 pixels in size. Only a sort of spoofing assault, 'a photo attack', is listed in the database, which includes changes in appearance, such as gender, light, and whether or not glasses are worn. The NUAA dataset's few candidate faces are given in Figure 9. Table 3 lists the count of training and testing sets collected from real and fake face photos for the datasets "Replay-Attack" and "NUAA." False Rejection Rate (FRR), Half Total Error Rate (HTER), False Acceptance Rate (FAR), and accuracy are each represented by Equations (7), (8), (9), and (10), correspondingly.

$$\text{False Rejection Rate (FRR)} = \frac{FN}{TP+FN} \quad (7)$$

$$\text{Half Total Error Rate (HTER)} = \left(\frac{FAR+FRR}{2} \right) * 100 \quad (8)$$

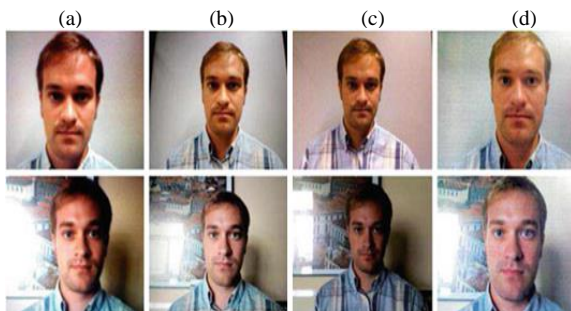


Figure 8. Candidate images taken from the Replay attack dataset [40] Top row represents the Controlled Scenario while the Last Row depicts Adverse Scenario. (a) LCD Photo Attack and (b) HD Photo Attack, (c) Real face samples, (d) Print Photo Attack



Figure 9. Candidate images taken from the NUAA dataset [41] Row one depicts real access face images, and row two gives fake access face images from the NUAA dataset

$$\text{False Acceptance Rate (FAR)} = \frac{FP}{TN+FP} \quad (9)$$

$$\text{Accuracy} = \left(\frac{TP+TN}{TP+TN+FP+FN} \right) * 100 \quad (10)$$

where, TP => True Positives (Quantity of Live human faces predicted as Live), TN => True Negatives (Quantity of Spoofed human faces predicted as Spoofed). FP => False Positives (Quantity of Spoofed human faces predicted as Live). FN => False Negatives (Quantity of Live human faces predicted as Spoofed)

6. RESULTS AND DISCUSSION

Six of the current pre-trained deep learning CNN models, referred to here as VGG19, VGG16, DensNet121, Xception, MobileNet, and InceptionV3, are taken into consideration for performance evaluation and to ensure appropriateness in human FPAD. These models are changed for the human FPAD to achieve transfer learning. The investigated transfer learning performance is validated using the "NUAA" and "Replay-Attack" face spoofing detection datasets.

It is clear from Tables 4 and 5 that tuned VGG19 outperforms other DCNNs in terms of FPAD test accuracy. Deep learning characteristics are extracted from the second-to-last FC layer, which consists of 256 neurons, to improve the FPAD capability (highlighted in yellow in Figure 3).

Thepade's SBTC 10-ary features are attached with these automatically derived 256-dimension deep learning

TABLE 3. The count of human face images used from the datasets for evaluation of the proposed FPAD method

Face Class	Replay-Attack		NUAA	
	Training	Testing	Training	Testing
Live Face	900	1200	1743	3362
Spoofed Face	900	1200	1748	5761
	Spoofed by four sorts		Spoofed by only a sort	

¹ <https://www.kaggle.com>

TABLE 4. Percentage test accuracy of considered finetuned DCNN models for face liveness detection over the NUAA dataset

Finetuned DCNN model	Test Accuracy
VGG16	90.07
VGG19	94.31
MobileNet	78.18
Xception	71.6
InceptionV3	68
DenseNet121	70.9

features. The weighting of handcrafted and automatically derived features is displayed in Table 6 to provide a thorough knowledge of the feature combinations used in the current experiment. Different ML classifiers, including RandomForest, ExtraTree, SVM (kernel = "linear"), and RandomForest + ExtraTree + SVM ensemble, are trained for the FPAD task using these feature combinations.

On the NUAA dataset and using various types of features to train them. Table 7 compares the performance of several ML classifiers taken into account for FPAD. With a test accuracy of 94.52% for the NUAA dataset, it is noted that the RandomForest classifier trained with VGG19 + VGG19 + Thepade's SBTC 10-ary fused features outperforms all other investigated classifier and feature combinations.

According to Table 8, where the percentage test accuracy of considered ML classifiers trained over different features for face liveness detection on the Replay-Attack dataset is compiled, the SVM trained by VGG19 + VGG19 + Thepade's SBTC 10-ary fused features beats other classifiers for the Replay-Attack dataset by reaching 98.67% test accuracy. Tables 7 and 8 show that utilising VGG19 + VGG19 + Thepade's SBTC 10-ary fused features gives classifiers more FPAD capability compared to simply using deep learning features from VGG19.

Table 9 compares a few face presentation attack detection methods that have been suggested in the literature, with the best results found in the current study for two datasets known as NUAA and Replay-Attack. It is difficult to compare performance because each existing approach uses a different testing environment, performance measurements, and datasets.

TABLE 5. Percentage test accuracy of considered finetuned DCNN models for face liveness detection over Replay-Attack dataset

Finetuned DCNN model	Test Accuracy
VGG16	97.59
VGG19	98.11
MobileNet	94.54
Xception	86.8
InceptionV3	81.76
DenseNet121	78.97

TABLE 6. Dissection of handcrafted and auto-extracted features across considered different feature combinations

Sr No.	Feature combination	VGG19 feature	Thepade's SBTC 10-ary features	Total dimension of feature vector
1.	VGG19 feature	256 (1/1 part)	0	256
2.	Thepade's SBTC 10-ary features	0	30 (1/1 part)	30
3.	VGG19 + Thepade's SBTC 10-ary feature fusion	256 (1/2 part)	30 (1/2 part)	286
4.	VGG19 + VGG19 + Thepade's SBTC 10-ary feature fusion	512 (2/3 part)	30 (1/3 part)	542

TABLE 7. Percentage test accuracy of considered ML classifiers trained over different features for face liveness detection on the NUAA dataset

ML Classifier	Thepade's SBTC 10-ary features	Finetuned VGG19 feature	VGG19 + Thepade's SBTC 10-ary feature fusion	VGG19 + VGG19 + Thepade's SBTC 10-ary feature fusion	Average across all types of features
RandomForest	70.31	93.92	93.95	94.56	88.19
Extratree	70.59	93.46	93.49	94.25	87.95
SVM	62.54	93.25	94.16	94.40	86.09
RandomForest + ExtraTree + SVM	69.96	93.37	93.93	94.09	87.83
Average across all ML classifiers	68.35	93.50	93.88	94.33	--

TABLE 8. Percentage test accuracy of considered ML classifiers trained over different features for face liveness detection on the Replay-Attack dataset

ML Classifier	Thepade's SBTC 10-ary features	Finetuned VGG19 feature	VGG19 + Thepade's SBTC 10-ary feature fusion	VGG19 + VGG19 + Thepade's SBTC 10-ary Feature fusion	Average across all types of features
Randomforest	91.66	95.78	95.96	96.47	94.97
Extratree	87.48	95.35	95.57	95.66	93.51
SVM	87.18	95.61	98.54	98.67	95.00
RandomForest+ ExtraTree + SVM	89.55	95.44	95.87	96.47	94.33
Average across all ML classifiers	88.97	95.55	96.49	96.82	

TABLE 9. Comparison of the existing face liveness detection methods of literature with the proposed method

Face Anti-spoofing Method	Pre-trained DCNN model	Performance Metric	Dataset Explored	Testing Accuracy (%)	HTER (%)	EER (%)
Proposed method VGG19 + VGG19 + Thepade's SBTC 10-ary + RandomForest	VGG19	HTER, Test Accuracy	Replay-Attack	98.67	1.35	-
Proposed method VGG19 + VGG19 + Thepade's SBTC 10-ary + SVM	VGG19	HTER, Test Accuracy	NUAA	94.56	4.71	-
ResNet50 + RI-LBP [20]	ResNet-50	HTER, EER	Replay-Attack	-	2.6	2.3
			NUAA	-	-	0.5
			CASIA-FASD	-	-	4.4
			MSU-MFSD	-	-	3.1
VGG16 + LBP [23]	VGG16	Test Accuracy	Replay-Attack	75.25	-	-
			SSIJRI	92.05	-	-
			3DMAD	96.97	-	-
			Replay-Mobile	90.52	-	-
VGG16 [24]	VGG16	HTER	Replay-Attack	-	2.5	-
			CASIA-FASD	-	0.0	-
			Replay-Mobile	-	0.0	-
ResNet-50 + CLBP [29]	ResNet-50	HTER, Test Accuracy	CASIA-FASD	94.65	8.68	-
			Replay-Attack	98.56	2.64	

The HTER and testing accuracy noticed in the suggested work provided here using VGG19; however, are better than the regarded existing equivalent attempts from the literature [20, 23, 24, 29] when one compares the explorations carried out utilising datasets NUAA and Replay-Attack (as presented in Table 9 for comparison of existing methods with the proposed approach).

7. CONCLUSION

One of the more clever methods for adapting the learned DCNN architecture of an existing system to newer applications is transfer learning. Depending on its

specifics, each architecture may represent a different performance for newer applications. In the ambient computing environment of today, where person identity is confirmed using the collected contactless biometric features, human FPAD has assumed paramount importance. This study empirically evaluated six such pre-trained DCNN models (Xception, InceptionV3, MobileNet, DenseNet121, VGG16 and VGG19) to detect person face presentation attacks. To adapt all pre-trained DCNN models for use with human FPAD, certain changes have to be made. Performance measures for contrasting the effectiveness of the proposed method with current human FPAD methodologies include test

accuracy and HTER. According to experimental findings, among all fine-tuned DCNNs taken into account, the VGG19 network architecture provides the highest test accuracy for FPAD across the NUAA and Replay-Attack datasets. Additionally, compared to using simply the deep learning features of VGG19, VGG19 + VGG19 + Thepade's SBTC 10-ary fused features improve the FPAD capacity for all classifiers with slight additional computations of feature extraction. Future research on datasets like 3DMAD and others can test the robustness of the approach suggested in the current work against mask attacks.

8. REFERENCES

- Kekre, H., Thepade, S.D. and Maloo, A., "Face recognition using texture features extracted from walshlet pyramid", *ACEEE International Journal on Recent Trends in Engineering and Technology (IJRTET)*, Vol. 5, No. 1, (2011), 186-190. <https://doi.org/10.5120/1672-2256>
- Kekre, H., Thepade, S.D. and Chopra, T., "Face and gender recognition using principal component analysis", *International Journal on Computer Science and Engineering*, Vol. 2, No. 4, (2010), 959-964.oi.
- Shahbakhsh, M.B. and Hassanpour, H., "Empowering face recognition methods using a gan-based single image super-resolution network", *International Journal of Engineering, Transactions A: Basics*, Vol. 35, No. 10, (2022), 1858-1866. https://www.ije.ir/article_150976.html
- Asghari Beirami, B. and Mokhtarzade, M., "Ensemble of log-euclidean kernel svm based on covariance descriptors of multiscale gabor features for face recognition", *International Journal of Engineering, Transactions B: Applications*, Vol. 35, No. 11, (2022), 2065-2071. https://www.ije.ir/article_153711.html
- Thepade, S.D. and Bidwai, P., "Iris recognition using fractional coefficients of transforms, wavelet transforms and hybrid wavelet transforms", in 2013 International Conference on Control, Computing, Communication and Materials (ICCCCM), IEEE., (2013), 1-5.
- Kekre, H., Thepade, S.D., Jain, J. and Agrawal, N., "Iris recognition using texture features extracted from walshlet pyramid", in Proceedings of the International Conference & Workshop on Emerging Trends in Technology., (2011), 76-81.
- Thepade, D.S. and Mandal, P.R., "Novel iris recognition technique using fractional energies of transformed iris images using haar and kekre transforms", *International Journal of Scientific & Engineering Research*, Vol. 5, No. 4, (2014), 305-308. <https://www.ijser.org/researchpaper/Novel-Iris-Recognition-Technique-using-Fractional-Energies.pdf>
- Khade, S. and Thepade, S.D., "Novel fingerprint liveness detection with fractional energy of cosine transformed fingerprint images and machine learning classifiers", in 2018 IEEE Punecon, IEEE., (2018), 1-7.
- Khade, S., Thepade, S.D. and Ambedkar, A., "Fingerprint liveness detection using directional ridge frequency with machine learning classifiers", in 2018 Fourth International Conference on Computing Communication Control and Automation (ICCCUBEA), IEEE., (2018), 1-5.
- Kekre, H., Thepade, S.D. and Maloo, A., "Eigenvectors of covariance matrix using row mean and column mean sequences for face recognition", *International Journal of Biometrics and Bioinformatics (IJBB)*, Vol. 4, No. 2, (2010), 42-50.
- Keramati Hatkeposhti, R., Yadollahzadeh Tabari, M. and GolsorkhtabariAmiri, M., "Fall detection using deep learning algorithms and analysis of wearable sensor data by presenting a new sampling method", *International Journal of Engineering, Transactions A: Basics*, Vol. 35, No. 10, (2022), 1941-1958. https://www.ije.ir/article_151530.html
- Fallah, A., Soleymani, A. and Khosravi, H., "A method for automatic lane detection using a deep network", *International Journal of Engineering, Transactions A: Basics*, Vol. 35, No. 4, (2022), 802-809. https://www.ije.ir/article_143621.html
- Azimi, B., Rashno, A. and Fadaei, S., "Fully convolutional networks for fluid segmentation in retina images", in 2020 International Conference on Machine Vision and Image Processing (MVIP), IEEE., (2020), 1-7.
- Thepade, S.D. and Chaudhari, P.R., "Land usage identification with fusion of thepade sbtc and sauvola thresholding features of aerial images using ensemble of machine learning algorithms", *Applied Artificial Intelligence*, Vol. 35, No. 2, (2021), 154-170. <https://doi.org/10.1080/08839514.2020.1842627>
- Thepade, S.D., Chaudhari, P.R. and Das, R., "Identifying land usage from aerial image using feature fusion of thepade's sorted n-ary block truncation coding and bernsen thresholding with ensemble methods", *International Journal of Engineering and Advanced Technology (IJEAT)*, Vol. 9, No. 3, (2020), 2612-2621. doi.
- Thepade, S.D., Subhedarpage, K.S. and Mali, A.A., "Performance rise in content based video retrieval using multi-level thepade's sorted ternary block truncation coding with intermediate block videos and even-odd videos", in 2013 International Conference on Advances in Computing, Communications and Informatics (ICACCI), IEEE., (2013), 962-966.
- Madane, M. and Thepade, S., "Score level fusion based bimodal biometric identification using thepade's sorted n-ary block truncation coding with varied proportions of iris and palmprint traits", *Procedia Computer Science*, Vol. 79, (2016), 466-473. doi: 10.1016/j.procs.2016.03.060.
- Thepade, S.D. and Patil, P.H., "Novel visual content summarization in videos using keyframe extraction with thepade's sorted ternary block truncation coding and assorted similarity measures", in 2015 International Conference on Communication, Information & Computing Technology (ICCICT), IEEE. (2015), 1-5.
- Lucena, O., Junior, A., Moia, V., Souza, R., Valle, E. and Lotufo, R., "Transfer learning using convolutional neural networks for face anti-spoofing", in Image Analysis and Recognition: 14th International Conference, ICIAR 2017, Montreal, QC, Canada, July 5-7, 2017, Proceedings 14, Springer., (2017), 27-34.
- Chen, F.M., Wen, C., Xie, K., Wen, F.Q., Sheng, G.Q. and Tang, X.G., "Face liveness detection: Fusing colour texture feature and deep feature", *IET Biometrics*, Vol. 8, No. 6, (2019), 369-377. <https://doi.org/10.1049/iet-bmt.2018.5235>
- Tang, Y., Wang, X., Jia, X. and Shen, L., "Fusing multiple deep features for face anti-spoofing", in Biometric Recognition: 13th Chinese Conference, CCBR 2018, Urumqi, China, August 11-12, 2018, Proceedings 13, Springer., (2018), 321-330.
- Tu, X. and Fang, Y., "Ultra-deep neural network for face anti-spoofing", in Neural Information Processing: 24th International Conference, ICONIP 2017, Guangzhou, China, November 14-18, 2017, Proceedings, Part II 24, Springer. (2017), 686-695.
- Das, P.K., Hu, B., Liu, C., Cui, K., Ranjan, P. and Xiong, G., "A new approach for face anti-spoofing using handcrafted and deep network features", in 2019 IEEE International Conference on Service Operations and Logistics, and Informatics (SOLI), IEEE., (2019), 33-38.

24. Elloumi, W., Chetouani, A., Charrada, T.B. and Fourati, E., "Anti-spoofing in face recognition: Deep learning and image quality assessment-based approaches", *Deep Biometrics*, (2020), 51-69. https://doi.org/10.1007/978-3-030-32583-1_4
25. Song, L. and Ma, H., "Face liveness detection based on texture and color features", in 2019 IEEE 4th International Conference on Cloud Computing and Big Data Analysis (ICCCBDA), IEEE., (2019), 418-422.
26. Jagdale, P. and Thepade, S., "Face liveness detection using feature fusion using block truncation code technique", *International Journal on Recent and Innovation Trends in Computing and Communication*, Vol. 7, No. 8, (2019), 19-22. <https://doi.org/10.17762/ijritcc.v7i8.5348>
27. Thepade, S., Jagdale, P., Bhingurde, A. and Erandole, S., "Novel face liveness detection using fusion of features and machine learning classifiers", in 2020 IEEE international conference on informatics, IoT, and enabling technologies (ICIoT), IEEE. (2020), 141-145.
28. Thepade, S.D., Chaudhari, P., Dindorkar, M., Bang, S. and Bangar, R., "Improved face spoofing detection using random forest classifier with fusion of luminance chroma", *International Journal of Computer Information Systems and Industrial Management Applications*, Vol. 12, No. 2020, (2020), 374-386.
29. Abdullakutty, F., Johnston, P. and Elyan, E., "Fusion methods for face presentation attack detection", *Sensors*, Vol. 22, No. 14, (2022), 5196.
30. Muhammad, U., Yu, Z. and Komulainen, J., "Self-supervised 2d face presentation attack detection via temporal sequence sampling", *Pattern Recognition Letters*, Vol. 156, (2022), 15-22.
31. Abdullakutty, F., Elyan, E., Johnston, P. and Ali-Gombe, A., "Deep transfer learning on the aggregated dataset for face presentation attack detection", *Cognitive Computation*, Vol. 14, No. 6, (2022), 2223-2233. <https://doi.org/10.1007/s12559-022-10037-z>
32. Simonyan, K. and Zisserman, A., "Very deep convolutional networks for large-scale image recognition", arXiv preprint arXiv:1409.1556, (2014).
33. Szegedy, C., Vanhoucke, V., Ioffe, S., Shlens, J. and Wojna, Z., "Rethinking the inception architecture for computer vision", in Proceedings of the IEEE conference on computer vision and pattern recognition., (2016), 2818-2826.
34. Huang, G., Liu, Z., Van Der Maaten, L. and Weinberger, K.Q., "Densely connected convolutional networks", in Proceedings of the IEEE conference on computer vision and pattern recognition., (2017), 4700-4708.
35. Chollet, F., "Xception: Deep learning with depthwise separable convolutions", in Proceedings of the IEEE conference on computer vision and pattern recognition., (2017), 1251-1258.
36. Howard, A.G., Zhu, M., Chen, B., Kalenichenko, D., Wang, W., Weyand, T., Andreetto, M. and Adam, H., "Mobilenets: Efficient convolutional neural networks for mobile vision applications", arXiv preprint arXiv:1704.04861, (2017).
37. Badre, S.R. and Thepade, S.D., "Novel video content summarization using thepade's sorted n-ary block truncation coding", *Procedia Computer Science*, Vol. 79, (2016), 474-482. <https://doi.org/10.1016/j.procs.2016.03.061>
38. Chingovska, I., Anjos, A. and Marcel, S., "On the effectiveness of local binary patterns in face anti-spoofing", in 2012 BIOSIG-proceedings of the international conference of biometrics special interest group (BIOSIG), IEEE., (2012), 1-7.
39. Tan, X., Li, Y., Liu, J. and Jiang, L., "Face liveness detection from a single image with sparse low rank bilinear discriminative model", *ECCV* (6), Vol. 6316, (2010), 504-517. https://doi.org/10.1007/978-3-642-15567-3_37

Persian Abstract

چکیده

تکامل و پیشرفت‌های یادگیری عمیق برای تمام مشکلات تحقیقاتی که ممکن است به چالش‌های طبقه‌بندی در هر زمینه‌ای از زندگی تبدیل شوند، استفاده می‌شوند. عمق و مقدار فرآیندها خروجی هر طراحی شبکه عصبی پیچیده عمیق (DCNN) را تعیین می‌کند، به همین دلیل است که تعداد زیادی از آنها پیشنهاد شده‌اند... چنین معماری‌های DCNN باید کاملاً از ابتدا توسعه داده شوند و نمی‌توان از آنها برای برنامه‌هایی که پیشرفته‌تر از آن‌هایی که برای آن طراحی شده‌اند استفاده کرد. این شبکه‌های از پیش آموزش دیده را می‌توان از طریق آموزش انتقال تغییر داد تا برای کاربردهای خاص تر مناسب تر شوند. این مقاله تلاش می‌کند تا اثربخشی و کاربرد معماری‌های DCNN از پیش آموزش دیده فعلی را برای تشخیص حملات نمایش چهره انسانی (FPAD) ارزیابی کند. توجه به توسعه محاسبات محیطی، که نیاز به شناسایی بدون تماس افراد با استفاده از ویژگی‌های بیومتریک آنها دارد، FPAD انسانی یکی از مهم‌ترین و حیاتی‌ترین حوزه‌های تحقیقاتی امروزی است. برای ارزیابی تجربی در FPAD انسانی، شش مدل DCNN از پیش آموزش دیده - Xception, MobileNet, DensNet, VGG, VGG, InceptionV3 و VGG - دو مجموعه داده معیار FPAD، Replay-Attack و NUAA، برای کاوش استفاده می‌شوند. به منظور بهبود قابلیت FPAD طبقه‌بندی‌کننده‌های یادگیری ماشینی تحلیل شده (ML)، ویژگی‌های ۱۰ ساله Thepade's Sorted Block Truncation Coding (SBTC) با ویژگی‌های عمیق مشتق شده از DCNN‌های بالاترین عملکرد تنظیم شده ترکیب شده‌اند. با توجه به ادغام ویژگی‌های DCNN و ۱۰-ary SBTC، دقت FPAD طبقه بندی کننده های ML به طور قابل توجهی بهبود یافته است.



Numerical Simulation of Embankment Settlement in Vacuum Preloading Systems

I. B. Mulyawati*^a, M. Riza^a, H. Dermawan^a, V. Pratiwi^b

^a Department of Civil Engineering Education, Universitas Pendidikan Indonesia, Bandung, Indonesia

^b Department of Civil Engineering, Universitas Komputer Indonesia, Bandung, Indonesia

PAPER INFO

Paper history:

Received 13 December 2022

Received in revised form 21 January 2023

Accepted 27 January 2023

Keywords:

Soft Soil

Settlement

Vacuum Preloading

Prefabricated Vertical Drain

Geostudio

ABSTRACT

In Indonesia, the construction of the road has challenges because the road was built on soft clay soil. The vacuum preloading method was used to improve the shear strength and compressibility properties of soft soil in this project. Moreover, what needs to be a concern for practitioners is the issue of increasing simulation accuracy in predicting soil settlement in a vacuum preloading system. The research objective of this study was to determine changes in soil settlement behavior that occurred from the vacuum preloading system using a numerical simulations Geostudio with the 2D Multi Drain-Plane Strain approach and the settlement result of the simulation will be compare with instrumentation data. In this study the vacuum pressure distribution is modeled using water total head negative pore water pressure and the pressure value used following vacuum gauge data in the field with distribution approach is 100% at the surface of the sand platform, 85% to a depth of 5 m, then 60% to the end of the PVD. Based on the simulations, the conclusion is the vacuum pressure applied along the vertical drainage is not modeled constant, but changes with depth, the value of 60% at the bottom of the vertical drainage is quite representative of the conditions in the field and the settlement from the simulation is quite good at approaching the field observation with a prediction of the settlement due to vacuum preloading of ± 0.93 m, when compared to the field observation data there is a difference of about 1.6%.

doi: 10.5829/ije.2023.36.04a.18

1. INTRODUCTION

Indonesia has accelerated the building of roads to enhance connections between regional corridors and support the nation's economic growth. Soil conditions need to be considered because in Indonesia soft clay and peat are evenly distributed around 20 million hectares or about 10 percent of the total land area [1]. It will be going to be challenging to build roads on soft soil. The fact that one of Indonesia's roads is built on soft clay soil that has a low shear strength value and a relatively high compressibility. For civil engineering engineers, resolving problems in settlement and stability during construction would be a significant challenge [2]. Vacuum Preloading which was first discovered by Kjellman [3] is a method of improving soft soil that can accelerate the consolidation process so that the shear strength of the soil will increase and can reduce excessive settlement after the construction period. The basic

concept of vacuum preloading pressure vacuum of about 40 – 90 kPa to the soil so as to create a pressure difference between the drainage channel usually used Prefabricated Vertical Drain (PVD) and the surrounding soil. Utilization of PVD has become an economical and feasible option because of its fast installation with simple equipment [4]. Then, the applied negative pressure will continue to pull the pore water out of the soil, thus accelerating the consolidation process [5, 6]. so that the soil will decrease in a relatively fast time.

Analysis of soil settlement behavior due to vacuum preloading has become important and in recent years the popularity of numerical modeling has increased to predict soil settlement behavior. In general, vacuum preloading still uses 1D numerical modeling [7, 8] where the results show that the decreased value is lower than the actual conditions in the field. Following the development of the previous simulation, the analysis was further expanded using 2D numerical modeling of plane strain

*Corresponding Author Institutional Email:

isahbelamulyawati@upi.edu (I. B. Mulyawati)

with multi-drain to include the smear zone as in the study [9-11]. Increasing accuracy in numerical modeling is a challenge for geotechnical engineers in predicting soil settlement behavior using vacuum preloading so that the results are close to actual conditions in the field.

The research objective of this study was to determine the changes in soil settlement behavior that occurred from the vacuum preloading system using a numerical simulation, namely Geostudio. Numerical simulations were carried out using a 2D Multi Drain -Plane Strain approach, where the clay soil zone was modeled using Modified Cam Clay material and the vacuum pressure distribution was modeled using negative pore water pressure. The smear zone due to PVD penetration is modeled using soil clusters with lower permeability compared to the surrounding undisturbed soil.

2. METHODS

2. 1. Procedure for Plane Strain Condition in Numerical Simulation

Based on the theory of Indraratna and Redana [12], Indraratna et al. [13] pressure simulation approach vacuum for vertical drains is shown in Figure 1. In this theory, the three-dimensional model can be converted to equivalent plane strain in the following three ways.

- a. Geometric approach, where the vertical drain changes but the permeability of the soft clay soil is constant.
- b. Permeability approach, where the soil permeability is changed to an equivalent value, but the drain remains unchanged.
- c. The combined permeability and geometric approach, where the equivalent permeability value is determined by the spacing drain.

Indraratna et al. [14] proposed a solution for vacuum preloading with vertical drains equation strain [15] and assumed a trapezoidal along the vertical drain to describe the possible loss of vacuum pressure, as illustrated in Figure 2. Permeability parameters of undisturbed and smeared conditions plane strain can be calculate by the following equation [16]:

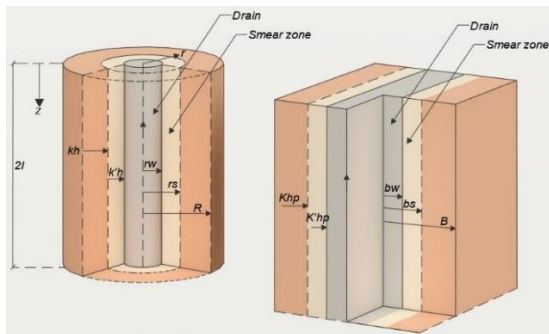


Figure 1. Conversion of axisymmetric unit cell to plane strain condition

$$\frac{k_{h,ps}}{k_{h,ax}} = \frac{0.67}{[\ln(n)-0.75]} \tag{1}$$

where, $n = B/b_w$, $k_{h,ps}$ is the coefficient horizontal permeability for plane strain condition, and $k_{h,ax}$ is the coefficient horizontal permeability for axisymmetric condition.

For the smear is determined by the following Equations (2) to (5) [16].

$$\frac{k_{s,ps}}{k_{h,ps}} = \frac{\beta}{\frac{k_{h,ps}}{k_{h,ax}} \left[\ln\left(\frac{n}{s}\right) + \left(\frac{k_{h,ax}}{k_{s,ax}}\right) \ln(s) - 0.75 \right] - \alpha} \tag{2}$$

where:

$$s = b_s/b_w \tag{3}$$

$$\alpha = \frac{2}{3} - \frac{2b_s}{B} \left(1 - \frac{b_s}{B} + \frac{b_s^2}{3B^2} \right) \tag{4}$$

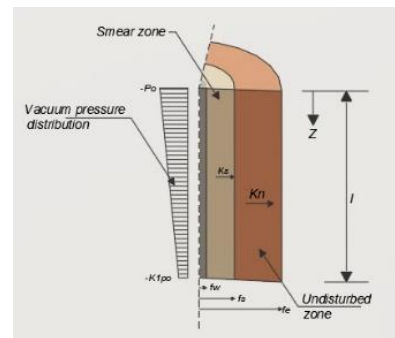
$$\beta = \frac{1}{B^2} (b_s - b_w)^2 + \frac{b_s}{3B^3} (3b_w^2 - b_s^2) \tag{5}$$

$k_{s,ps}$ = the coefficient horizontal permeability in the smear zone for plane strain condition

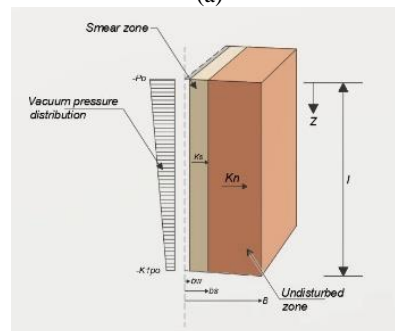
$k_{s,ax}$ = the coefficient horizontal permeability in the smear zone for axisymmetric condition

2. 2. Numerical Simulation Set-up

One of the road constructions in Indonesia is planned to use a vacuum preloading. In general, the soil condition in the project is soft clay soil. Where the soil stratification based



(a)



(b)

Figure 2. Distribution of vacuum pressure in the unit cell (a) Axisymmetric conditions, (b) Plane strain conditions

on soil investigation at a depth of 0 - 13 m is very soft clay to soft clay consistency, then at a depth of 13 - 15.5 m is a medium clay. The vacuum preloading uses a membrane type with a sand platform layer thickness of 1.6 m, and a 2.7 m embankment and 13.5 m long PVD. Table 1 is the PVD parameters installed with 1 m spacing and a typical cross section can be observed in Figure 3.

In this case, a numerical simulation was carried out using SIGMA/W Geostudio to describe the consolidation behavior of the soft clay soil due to vacuum preloading. Simulation 2D multi-drain-plane strain based on Equations (1) to (5) and the constitutive model of Modified Cam-Clay [17] were used in this analysis. Based on several studies that have been collected by Iskandar [18], the value of the ratio of kh/ks ranges from 2 - 14. In this analysis, the value of kh/ks of 12 is used. The design soil parameters used in the analysis are determined based on the test results field, laboratory data, and empirical correlations are summarized in Table 2. Then, constitutive model of sand platform and embankment material using Elastic Plastic, parameters can be seen in Table 3.

Numerical simulation done by modeling PVD, smear, and undisturbed soil as a whole. The boundary conditions in this simulation use joint placement at the bottom (displacement on the horizontal and vertical axes = 0, $U_x = U_y = 0$) and on both right and left sides are used roller placement (displacement on the horizontal axis = 0, $U_x = 0$). For the mesh use a Global Element Size of 0.75 m consisting of 3800 and 3730 Nodes elements (Figure 4).

The vacuum preloading simulated using SIGMA/W is divided into two stages as follows:

- a. Before the vacuum pressure was activated, the sand platform was spread with a thickness of 1.6 m, PVD

TABLE 1. Vertical Drain Parameter

Vertikal Drain Parameter	Value
Spacing, s	1 m
PVD Width, a	0.003 m
PVD Thickness, b	0.1 m
Discharge Capacity, q_w	0.00008 m ³ /s
PVD Length	13.5 m

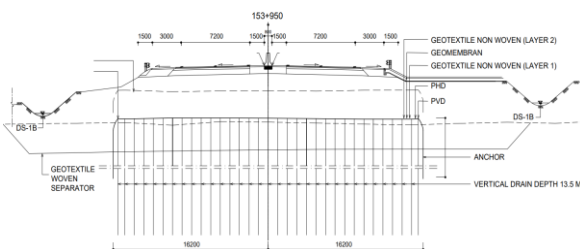


Figure 3. Typical cross section of road construction

installation and horizontal drainage were carried out for 200 days.

- a. When the vacuum pressure is activated, on the 50th day the embankment load started. The vacuum pressure was stopped after 240 days.

The vacuum pressure was modeled with the negative total head water boundary condition on the PVD according to the vacuum gauge pressure distribution vacuum changing with depth as is reported by Indraratna and Chu [16], Tuan Vu and You Yang [17]. The vacuum

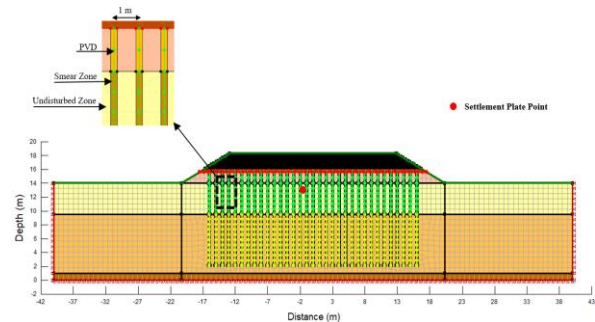


Figure 4. Plane Strain multi drain simulation

TABLE 2. Vertical Drain Parameter

Parameter	Symbol	Clay, Very Soft	Clay, Soft	Clay, Medium
Depth, (m)	-	0 - 4.5	4.5 - 13	13 - 15.5
Wet weight, (kN/m ²)	γ_{sat}	15	15	16
Poisson's ratio	ν	0.35	0.35	0.43
Effective Friction Angle, (°)	ϕ'	24	25	26
Void ratio	e	1.2	1.1	1
Slope of critical state line	M	0.941	0.984	1.027
Slope of The Isotropic NC Line	λ	0.096	0.208	0.167
Slope of The Isotropic OC (swelling) line	κ	0.019	0.042	0.033
Vertical Permeability, (m/s)	k_v	2.50E-07	2.00E-07	1.80E-07
Horizontal Permeability, (m/s)	k_h	5.00E-07	4.00E-07	3.60E-07
Undisturbed Plan Strain Permeability, (m/s)	k_{hp}	5.00E-07	4.00E-07	3.60E-07
Smearred Plan Strain Permeability, (m/s)	k'_{hp}	2.08E-10	1.66E-10	1.49E-10

TABLE 3. Sand Platform and Embankment Parameters

Parameter	Symbol	Unit	Sand Platform	Backfill
Wet weight	γ_{sat}	kN/m ³	16	16
Young modulus	E	kN/m ²	30000	10000
Poisson's ratio	ν	-	0.35	0.35
Friction Angle	ϕ	°	30	-
Cohesion	c	kN/m ²	10	30

pressure distribution approach in this study is 100% at the surface of the sand platform, 85% to a depth of 5 m, then 60% to the end of the PVD.

3. RESULTS AND DISCUSSION

The stages of vacuum implementation are divided into 5 stages as follows:

- Preparation stage

Preparation starts from determining the location for research, determining the area to be vacuum preloading, the type of instrumentation to be used, and the number of instrumentation installation points, as well as determining the point of installation test for in-situ testing/laboratory test.

- Instrumentation installation stage

At this stage the installation of instrumentation tools corresponds to the initial planning. The instrumentation tools used included:

- Inclinometer, this instrument is used to monitor the lateral movement of the soil due to vacuum.
- Settlement plate, this instrument is used to monitor the total decrease soil due to vacuum and applied loads.
- Extensometer, this tool is used to determine the decrease at a certain depth (layered settlement).
- Piezometer, this tool is used to monitor changes pore water pressure value at a certain depth.
- Vacuum gauge, this tool is used to monitor the vacuum pressure applied to the repair area.

The instrumentation that will be used as a reference in this study is a settlement plate and a vacuum gauge as shown in the schematic drawn in Figure 5.

- Stage of implementation of vacuum preloading and instrumentation monitoring

At this stage vacuum preloading work in the study area is carried out. During the vacuum preloading work, instrumentation monitoring is carried out daily on the value of the drop, lateral deformation, vacuum pressure, and pressure spread, unless there is data showing settlement rate or pore water pressure that is drastically reduced, there is an indication that this vacuum activity will be completed so that the instrumentation readings will be enlarged.

- Stage of interpretation of the results of monitoring and evaluation of work in the field

At this stage the results of the instrumentation monitoring data are interpreted whether the vacuum preloading work worked has shown good results or needs additional data, so that this work can provide sufficient data for later analysis. Furthermore, field and laboratory testing is carried out for soil conditions after the vacuum work is completed.

After the last stage is carried out, then in this study will be compared how the settlement behavior of the results of finite element analysis with monitoring data in the field.

The analysis finite element results of the changes in soil settlement behaviour, total stress, and shear stress due to vacuum preloading are shown in Figures 6 to 8. It can be seen from the contour of the settlement that the

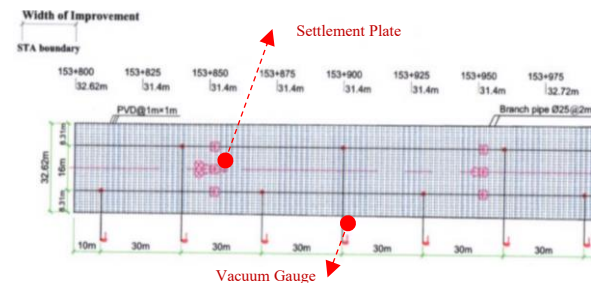


Figure 5. Settlement plate and vacuum gauge location

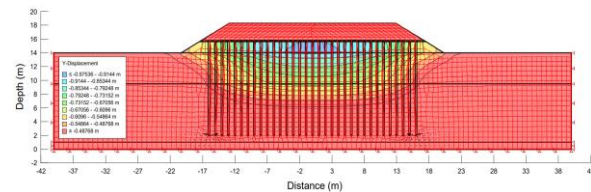


Figure 6. Contour of Settlement after construction 240 days

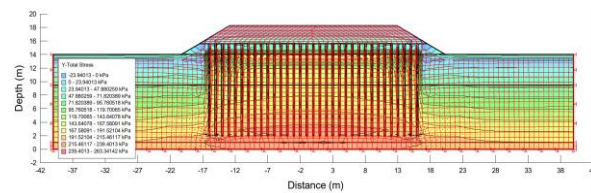


Figure 7. Contour of Y-Total Stress

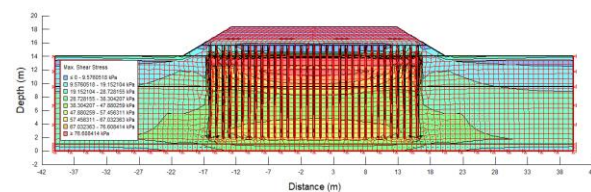


Figure 8. Contour of Shear Stress

embankment area experienced greater deformation and tended to move inwards the repair area. The results of the analysis will be verified based on observations of the settlement plate installed in the repair area as shown in Figure 9.

Figure 9 is a comparison curve for settlement from numerical simulations and field monitoring plotted against construction time. The soil settlement recorded at the end of construction in the field was ± 0.945 m while the numerical simulation results of ± 0.93 m contained a difference of about 1.6%. In general, the settlement trendline on the 130th to 240th days gives results that are very close to field monitoring. However, there is a different settlement trendline on day 50 between the results of numerical analysis and field monitoring (the difference is about 23%). The monitoring data vacuum gauge (Figure 9) that in the first 50 days the vacuum pressure tends to be unstable due to improvements to the geomembrane and the vacuum area, but after 50 days the vacuum pressure tends to be constant around 80 – 82 kPa even though there are several times the generator stops.

As stated by Feng et al. [18] the Finite Element model using Plaxis 2D gave a different settlement result compared to field monitoring (a difference of about 62%) in the first 10 days (Figure 10). This is because the FE

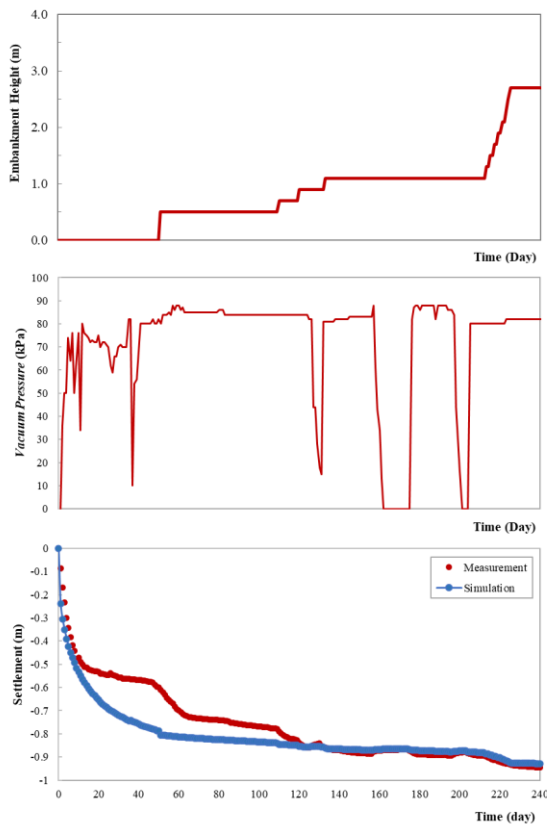


Figure 9. Typical monitoring data and calculated time-settlement curve used SIGMA/W

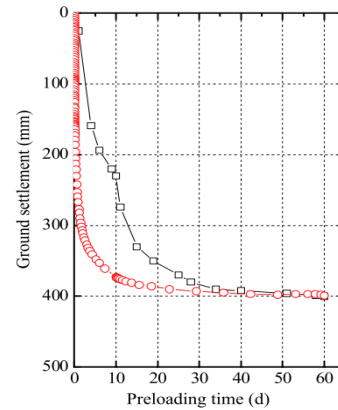


Figure 10. Settlement of conventional vacuum preloading [18]

model uses a constant value of hydraulic conductivity in the field, this value can decrease when there is an increase in pressure. Then, in the first 10 days is the vacuum pressure test phase, so that the monitoring data was incomplete because there was a process of checking the tightness of the membrane. But beyond that stage, the vacuum pressure tends to be stable.

In addition, the vacuum preloading 2D multi-drain plane simulation was conducted by Pardsouie et al. [19] the model used Geostudio with constant value of vacuum pressure and also without smear zone showed that there was a good correlation between the prediction of settlement and the measurements in the field except that in the first 50 days. That simulation results gave overestimate the settlement value (Figure 11).

The constitutive model of the material that was used, the determination of the permeability value of the plane-strain condition, and the distribution of vacuum pressure to depth are the parameters that significantly affect the settlement results. The discussion above shows that the numerical simulations carried out give a settlement pattern that matches quite well with the observed points of the settlement plate after carrying out various approaches such that the simulation stages approach the conditions in the field.

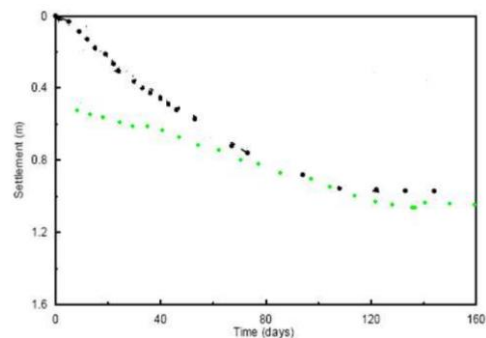


Figure 11. Comparison of Model Simulation Results with Monitored Field Data's [19]

4. CONCLUSION

Based on the results of the vacuum preloading with SIGMA/W that has been carried out, it can be concluded several things that is the simulation of vertical drainage and smear in 2D multi-drain-plane strain, the permeability value of the axisymmetric must be converted into plane strain, and then the vacuum pressure applied along the vertical drainage is not modeled constant, but changes with depth, the value of 60% at the bottom of the vertical drainage is quite representative of the conditions in the field. Afterward, the settlement pattern generated from the simulation is quite good at approaching the field observation points with a prediction of the magnitude of the settlement due to vacuum preloading of ± 0.93 m, when compared to the field observation data there is a difference of about 1.6%.

5. REFERENCES

1. Arisikam, D., Purwadinata, A.H. and Mulyawati, I.B., "Perencanaan stabilisasi dan perkuatan tanah dasar jalur kereta api", *Jurnal Ilmiah Teknologi Infomasi Terapan*, Vol. 8, No. 2, (2022). <https://doi.org/10.33197/jitter.vol8.iss2.2022.860>
2. Long, P., Bergado, D., Nguyen, L. and Balasubramaniam, A., "Design and performance of soft ground improvement using pvd with and without vacuum consolidation", *Geotechnical Engineering Journal of the SEAGS & AGSSEA*, Vol. 44, No. 4, (2013), 36-51.
3. W. Kjellman, "Consolidation of clayey soils by atmospheric pressure", in Proceedings of a Conference on Soil Stabilization Massachusetts Institute of Technology., Boston. (1952), 258-263.
4. Shang, J., Tang, M. and Miao, Z., "Vacuum preloading consolidation of reclaimed land: A case study", *Canadian Geotechnical Journal*, Vol. 35, No. 5, (1998), 740-749.
5. Indraratna, B., Rujikiatkamjorn, C., Baral, P. and Ameratunga, J., "Performance of marine clay stabilised with vacuum pressure: Based on queensland experience", *Journal of Rock Mechanics and Geotechnical Engineering*, Vol. 11, No. 3, (2019), 598-611.
6. Gouw, T.-L., "Case histories on the application of vacuum preloading and geosynthetic-reinforced soil structures in indonesia", *Indian Geotechnical Journal*, Vol. 50, (2020), 213-237. doi: 10.1007/s40098-019-00391-5.
7. Mohamedelhassan, E. and Shang, J., "Vacuum and surcharge combined one-dimensional consolidation of clay soils", *Canadian Geotechnical Journal*, Vol. 39, No. 5, (2002), 1126-1138. <https://doi.org/10.1139/t02-052>
8. Saowapakpiboon, J., Bergado, D., Voottipruex, P., Lam, L. and Nakakuma, K., "Pvd improvement combined with surcharge and vacuum preloading including simulations", *Geotextiles and Geomembranes*, Vol. 29, No. 1, (2011), 74-82. doi: 10.1016/j.geotexmem.2010.06.008.
9. Indraratna, B., Rujikiatkamjorn, C. and Sathananthan, I., "Analytical and numerical solutions for a single vertical drain including the effects of vacuum preloading", *Canadian Geotechnical Journal*, Vol. 42, No. 4, (2005), 994-1014. doi: 10.1139/t05-029.
10. Indraratna, B. and Redana, I., "Numerical modeling of vertical drains with smear and well resistance installed in soft clay", *Canadian Geotechnical Journal*, Vol. 37, No. 1, (2000), 132-145. doi: 10.1139/t99-115.
11. Chai, J., Bergado, D.T. and Shen, S.-L., "Modelling prefabricated vertical drain improved ground in plane strain analysis", *Proceedings of the Institution of Civil Engineers-Ground Improvement*, Vol. 166, No. 2, (2013), 65-77. doi: 10.1680/grim.11.00007.
12. Indraratna, B. and Redana, I., "Plane-strain modeling of smear effects associated with vertical drains", *Journal of Geotechnical and Geoenvironmental Engineering*, Vol. 123, No. 5, (1997), 474-478.
13. Indraratna, B., Sathananthan, I., Rujikiatkamjorn, C. and Balasubramaniam, A., "Analytical and numerical modeling of soft soil stabilized by prefabricated vertical drains incorporating vacuum preloading", *International Journal of Geomechanics*, Vol. 5, No. 2, (2005), 114-124. [https://doi.org/10.1061/\(ASCE\)1532-3641\(2005\)5:2\(114\)](https://doi.org/10.1061/(ASCE)1532-3641(2005)5:2(114))
14. Indraratna, B., Sathananthan, I., Bamunawita, C. and Balasubramaniam, A., Theoretical and numerical perspectives and field observations for the design and performance evaluation of embankments constructed on soft marine clay, in Elsevier geoenvironmental book series. 2005, Elsevier.51-89.
15. Barron, R.A., "Consolidation of fine-grained soils by drain wells by drain wells", *Transactions of the American Society of Civil Engineers*, Vol. 113, No. 1, (1948), 718-742.
16. Chu, J.J. and Rujikiatkamjorn, C., "Ground improvement: Case histories, Elsevier, (2005).
17. Vu, V.-t. and Yang, Y.-y., "Numerical modelling of soft ground improvement by vacuum preloading considering the varying coefficient of permeability", *International Journal of Geotechnical Engineering*, Vol. 12, No. 3, (2018), 258-266. doi: 10.1080/19386362.2016.1270793.
18. Feng, S., Lei, H. and Lin, C., "Analysis of ground deformation development and settlement prediction by air-boosted vacuum preloading", *Journal of Rock Mechanics and Geotechnical Engineering*, Vol. 14, No. 1, (2022), 272-288. doi: 10.1016/j.jrmge.2021.05.006.
19. Pardouie, M.M., Momeni, M., Nasehi, S.A. and Pardouie, M.H., "2d numerical investigation of the effectiveness of surcharge and vacuum preloading along with pvds", in 13th National Congress on Civil Engineering Isfahan University of Technology, Isfahan, IranAt: Isfahan, Iran, Esfahan, Iran. Vol. 5, (2022), 22.

Persian Abstract

چکیده

در اندونزی، ساخت جاده با چالش‌هایی همراه است، زیرا جاده بر روی خاک رسی نرم ساخته شده است. برای بهبود مقاومت برشی و خواص تراکم پذیری خاک نرم در این پروژه از روش پیش بارگذاری خلاء استفاده شد. علاوه بر این، آنچه باید برای پزشکان نگران باشد، مسئله افزایش دقت شبیه‌سازی در پیش‌بینی نشست خاک در یک سیستم پیش بارگذاری خلاء است. هدف تحقیق این مطالعه تعیین تغییرات رفتار نشست خاک ناشی از سیستم پیش بارگذاری خلاء با استفاده از شبیه‌سازی عددی **Geostudio** با رویکرد **Multi Drain – Plane Strain** بود و نتیجه نشست شبیه‌سازی با داده‌های ابزار دقیق مقایسه می‌شود. در این مطالعه توزیع فشار خلاء با استفاده از فشار آب منفذ منفی کل سر آب مدل‌سازی شده است و مقدار فشار استفاده شده به دنبال داده‌های گیج خلاء در میدان با رویکرد توزیع 100 درصد در سطح سکوی ماسه، 85 درصد تا عمق 5 متر، سپس 60٪ تا پایان **PVD** بر اساس شبیه‌سازی‌ها، نتیجه این است که فشار خلاء اعمال شده در طول زهکشی عمودی ثابت مدل‌سازی نمی‌شود، اما با عمق تغییر می‌کند، مقدار 60 درصد در پایین زهکشی عمودی کاملاً معرف شرایط مزرعه و نشست است. از شبیه‌سازی در نزدیک شدن به مشاهدات میدانی با پیش‌بینی نشست به دلیل پیش بارگذاری خلاء ± 0.93 متر بسیار خوب است، در حالی که در مقایسه با داده‌های مشاهدات میدانی تفاوت حدود 1.6٪ وجود دارد.

AIMS AND SCOPE

The objective of the International Journal of Engineering is to provide a forum for communication of information among the world's scientific and technological community and Iranian scientists and engineers. This journal intends to be of interest and utility to researchers and practitioners in the academic, industrial and governmental sectors. All original research contributions of significant value focused on basics, applications and aspects areas of engineering discipline are welcome.

This journal is published in three quarterly transactions: Transactions A (Basics) deal with the engineering fundamentals, Transactions B (Applications) are concerned with the application of the engineering knowledge in the daily life of the human being and Transactions C (Aspects) - starting from January 2012 - emphasize on the main engineering aspects whose elaboration can yield knowledge and expertise that can equally serve all branches of engineering discipline.

This journal will publish authoritative papers on theoretical and experimental researches and advanced applications embodying the results of extensive field, plant, laboratory or theoretical investigation or new interpretations of existing problems. It may also feature - when appropriate - research notes, technical notes, state-of-the-art survey type papers, short communications, letters to the editor, meeting schedules and conference announcements. The language of publication is English. Each paper should contain an abstract both in English and in Persian. However, for the authors who are not familiar with Persian, the publisher will prepare the latter. The abstracts should not exceed 250 words.

All manuscripts will be peer-reviewed by qualified reviewers. The material should be presented clearly and concisely:

- *Full papers* must be based on completed original works of significant novelty. The papers are not strictly limited in length. However, lengthy contributions may be delayed due to limited space. It is advised to keep papers limited to 7500 words.
- *Research notes* are considered as short items that include theoretical or experimental results of immediate current interest.
- *Technical notes* are also considered as short items of enough technical acceptability with more rapid publication appeal. The length of a research or technical note is recommended not to exceed 2500 words or 4 journal pages (including figures and tables).

Review papers are only considered from highly qualified well-known authors generally assigned by the editorial board or editor in chief. Short communications and letters to the editor should contain a text of about 1000 words and whatever figures and tables that may be required to support the text. They include discussion of full papers and short items and should contribute to the original article by providing confirmation or additional interpretation. Discussion of papers will be referred to author(s) for reply and will concurrently be published with reply of author(s).

INSTRUCTIONS FOR AUTHORS

Submission of a manuscript represents that it has neither been published nor submitted for publication elsewhere and is result of research carried out by author(s). Presentation in a conference and appearance in a symposium proceeding is not considered prior publication.

Authors are required to include a list describing all the symbols and abbreviations in the paper. Use of the international system of measurement units is mandatory.

- On-line submission of manuscripts results in faster publication process and is recommended. Instructions are given in the IJE web sites: www.ije.ir-www.ijeir.info
- Hardcopy submissions must include MS Word and jpg files.
- Manuscripts should be typewritten on one side of A4 paper, double-spaced, with adequate margins.
- References should be numbered in brackets and appear in sequence through the text. List of references should be given at the end of the paper.
- Figure captions are to be indicated under the illustrations. They should sufficiently explain the figures.
- Illustrations should appear in their appropriate places in the text.
- Tables and diagrams should be submitted in a form suitable for reproduction.
- Photographs should be of high quality saved as jpg files.
- Tables, Illustrations, Figures and Diagrams will be normally printed in single column width (8cm). Exceptionally large ones may be printed across two columns (17cm).

PAGE CHARGES AND REPRINTS

The papers are strictly limited in length, maximum 8 journal pages (including figures and tables). For the additional to 8 journal pages, there will be page charges. It is advised to keep papers limited to 3500 words.

Page Charges for Papers More Than 8 Pages (Including Abstract)

For International Author ***	\$55 / per page
For Local Author	100,000 Toman / per page

AUTHOR CHECKLIST

- Author(s), bio-data including affiliation(s) and mail and e-mail addresses).
- Manuscript including abstracts, key words, illustrations, tables, figures with figure captions and list of references.
- MS Word files of the paper.



THOMSON REUTERS

WEB OF SCIENCE



Scopus®



CAS®

A DIVISION OF THE
AMERICAN CHEMICAL SOCIETY



 Crossref



Scientific Indexing Services

Google
Scholar